Istituto Nazionale di Fisica Nucleare
LABORATORI NAZIONALI DI FRASCATI

Supported by ICFA

Supported by EU
Via IFAST, GA 101004730

65th ICFA Advanced Beam Dynamics Workshop on High Luminosity Circular e^+e^- Colliders
eeFACT2022

12-16 September 2022

INFN Frascati National Laboratories (Italy)

International Organizing Committee
M.E. Biagini (INFN-LNF, Italy) (LOC chair)
A. Blondel (CERN)
Y. Funakoshi (KEK, Japan)
Y. Li (IHEP, China)
Q. Qin (ESRF, France)
F. Zimmermann (CERN, Switzerland)

Scientific Program Committee

R. Appleby R (Univ. of Manchester)
R. Assmann (DESY)
F. Bedeschi (INFN)
M.E. Biagini (INFN)
A. Blondel (CERN)
A. Bogomyagkov (BINP)
M. Boscolo (INFN)
P. Branchini (INFN)
O. Brunner (CERN)
Y. Cai (SLAC)
Y. Chi (IHEP)
W. Chou (IHEP)
M. Dam (Niels Bohr Inst.)
A. Faus Golfe (IJCLab)
Y. Funakoshi (KEK)
K. Furukawa (KEK)
J. Gao (IHEP)
P. Giacomelli (INFN)
E. Gianfelice (FNAL)
H. Ikeda (KEK)
P. Janot Patrick (CERN)
R. Kersevan (CERN)
I. Koop (BINP)
E. Levichev (BINP)
Y. Li (IHEP)
A. Novokhatski (SLAC)
K. Oide (CERN)
Y. Onishi (KEK)
Q. Qin (ESRF)
B. Parker (BNL)
P. Ratoff (Cockcroft)
R. Rimmer (JLAB)
D. Sagan (Cornell)
J. Seeman (SLAC)
Y. Suetsugu (KEK)
M. Sullivan (SLAC)
M. Tobiyama (KEK)
M. Wendt (CERN)
J. Wenninger (CERN)
U. Wienands (ANL)
F. Willeke (BNL)
Y. Zhang (IHEP)
F. Zimmermann (CERN)
M. Zobov (INFN)

Local Organizing Committee
M.E. Biagini (chair) (*INFN-LNF, Italy*)
F. Casarin (*INFN-LNF, Italy*)
M. Giabbai (*INFN-LNF, Italy*)
S. Guiducci (*INFN-LNF, Italy*)
M.G. Iungo (*INFN-LNF, Italy*)

PROCEEDINGS

Photo by M. Biagini

Istituto Nazionale di Fisica Nucleare
LABORATORI NAZIONALI DI FRASCATI

Foreword: Welcome to the eeFACT22 Workshop Proceedings

The 65th ICFA Advanced Beam Dynamics Workshop on High Luminosity Circular e^+e^- Colliders (eeFACT2022) was hosted by INFN Frascati National Laboratories on September 12-16, 2022.

The workshop was organized in the context and with sponsoring of the ICFA Beam Dynamics Panel and EU/IFAST funded European Network for Accelerator Performance and Concepts (APEC), under GA 101004730. This is a bi-annual meeting, but due to the Covid-19 pandemic the 2020 edition had to be postponed.

Previous editions were held at Fermilab (2012), Beijing (2014), Daresbury (2016), Hong Kong (2018).

The eeFACT workshop series scope is:

- Reviewing and documenting the state of the art in e^+e^- factory design;
- Reviewing and drawing lessons from SuperKEKB phase 3 commissioning;
- Catalyzing further contributions to the SuperKEKB, FCC, CEPC & tau-charm design efforts;
- Fostering synergies and new collaborations across communities, in particular with low-emittance light sources and other colliders (muon, linear, e-ion) and between continents;
- Jointly developing novel solutions to outstanding problems.

The complete agenda can be found on the workshop website at: https://agenda.infn.it/event/21199/overview.

Because of the COVID-19 pandemic restrictions, the workshop was organized both in-person and remote format. 112 delegates registered and 61% participated in person.

Topics were divided in 13 Working Groups, each assigned to 2 conveners, and the program built accordingly. Two EXTRA sessions were organised after the Workshop, on Thursday 15th afternoon and Friday 16th morning, to address the "*Luminosity and Electrical power projections for various e^+e^- Factories*" topic. The total number of talks (including the EXTRA sessions) was 105. However, only 67 abstracts were presented for the proceedings with 44 paper submissions. A list of the WGs topics and conveners is shown in the table below.

	Conveners	
WG1	Levichev/Biagini	Overview of colliders (including muon & e-ion colliders)
WG2	Branchini/Dam	Physics & Detector
WG3	Oide/Gao	Optics & Beam Dynamics
WG4	Zobov/Zimmermann	Beam-beam & Instabilities
WG5	Boscolo/Sullivan	Interaction Region & MDI & Backgrounds
WG6	Seeman/Furukawa	Injection
WG7	Ikeda/Wendt	Instrumentation
WG8	Bogomyagkov/Gianfelice	Polarization and energy calibration
WG9	Kersevan/Shibata	Vacuum
WG10	Parker/Koop/Li	Magnets
WG11	Brunner/Rimmer	RF
WG12	Qin/Funakoshi	Infrastructures, Cryogenics, Commissioning & Operation
WG13	Faus-Golfe/Wenninger	Monochromatization

The participating delegates per geographical area and per Institution are shown in the figure below. Unfortunately Russian scientists could not be allowed to participate due to the conflict in Ukraine.

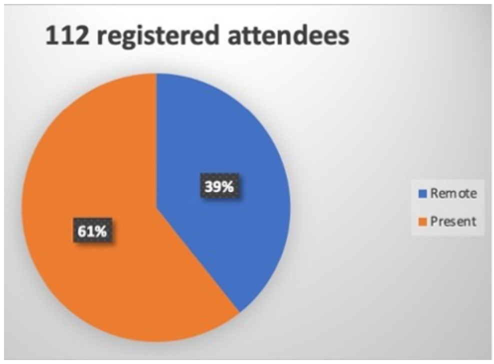

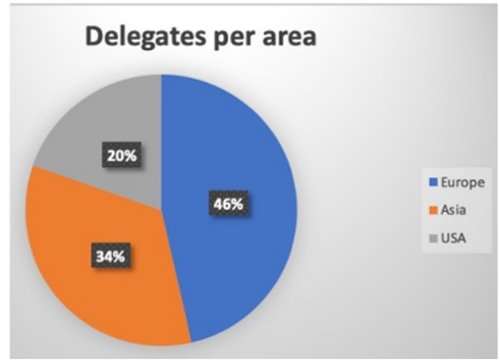

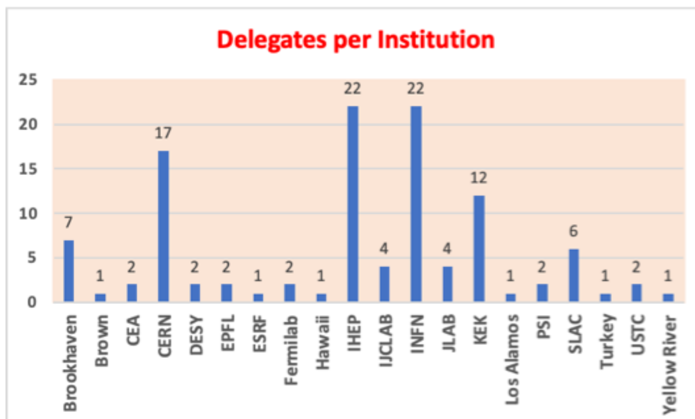

The Organizing Committee warmly thanks all participants for the interesting talks and enthusiastic participation.

Maria Enrica Biagini, Chair
INFN-Frascati National Laboratories
Frascati, Rome, Italy

Scientific Program Committee (SPC)

R. Appleby	Univ. of Manchester	UK
R. Assmann	DESY	Germany
F. Bedeschi	INFN	Italy
M. E. Biagini	INFN	Italy
A. Blondel	CERN	Switzerland
A. Bogomyagkov	BINP	Russia
M. Boscolo	INFN	Italy
P. Branchini	INFN	Italy
O. Brunner	CERN	Switzerland
Y. Cai	SLAC	USA
Y. Chi	IHEP	China
W. Chou	IHEP	China
M. Dam	Niels Bohr Inst.	Denmark
A. Faus Golfe	IJCLab	France
Y. Funakoshi	KEK	Japan
K. Furukawa	KEK	Japan
J. Gao	IHEP	China
P. Giacomelli	INFN	Italy
E. Gianfelice	FNAL	USA
H. Ikeda	KEK	Japan
P. Janot Patrick	CERN	Switzerland
R. Kersevan	CERN	Switzerland
I. Koop	BINP	Russia
E. Levichev	BINP	Russia
Y. Li	IHEP	China
A. Novokhatski	SLAC	USA
K. Oide	CERN	Switzerland
Y. Onishi	KEK	Japan
Q. Qin	ESRF	France
B. Parker	BNL	USA
P. Ratoff	Cockcroft Inst.	UK
R. Rimmer	JLab	USA
D. Sagan	Cornell	USA
J. Seeman	SLAC	USA
Y. Suetsugu	KEK	Japan
M. Sullivan	SLAC	USA
M. Tobiyama	KEK	Japan
M. Wendt	CERN	Switzerland
J. Wenninger	CERN	Switzerland
U. Wienands	ANL	USA
F. Willeke	BNL	USA
Y. Zhang	IHEP	China
F. Zimmermann	CERN	Switzerland
M. Zobov	INFN	Italy

International Organizing Committee (IOC)

M. E. Biagini	INFN-LNF	Italy
A. Blondel	CERN	Switzerland
Y. Funakoshi	KEK	Japan
Y. Li	IHEP	China
Q. Qin	ESRF	France
F. Zimmermann	CERN	Switzerland

Local Organizing Committee (LOC)

M. E. Biagini	**Chair**	INFN-LNF	Italy
F. Casarin		INFN-LNF	Italy
M. Giabbai		INFN-LNF	Italy
S. Guiducci		INFN-LNF	Italy
M. G. Iungo		INFN-LNF	Italy
G. Vinicola		INFN-LNF	Italy

JACoW Editorial Team (JET)

M. E. Biagini	**Editor-in-Chief**	INFN-LNF	Italy
J. Chrin		PSI	Switzerland
M. Giabbai		INFN-LNF	Italy
M.G. Iungo		INFN-LNF	Italy
Volker RW Schaa	**Technical Editor**	GSI	Germany

Contents

ISBN: 978-3-95450-236-3 ISSN: 2673-7027 doi:10.18429/JACoW-eeFACT2022-MOXAT0103

SuperKEKB LUMINOSITY QUEST*

Y. Ohnishi†, KEK, Tsukuba, Japan
on behalf of the SuperKEKB and Belle II commissioning groups

Abstract

SuperKEKB is a positron-electron collider with a nano-beam scheme and continues to achieve the world's highest luminosity for the production of B meson pairs. The luminosity performance has been improved by the full-scale adoption of the crab-waist scheme. The nano-beam scheme allows the vertical beta function at the interaction point (IP) to be much smaller than the bunch length. The vertical beta function and the beam size at the collision point are the smallest in the world among colliders. As the result, the peak luminosity of 4.65×10^{34} cm^{-2}s^{-1} has been achieved with the Belle II detector in 2022. Recent progress will be presented, and then the problems and issues to be overcome from the beam physics point of view will be discussed for further improvement of luminosity performance in the future.

INTRODUCTION

The SuperKEKB accelerator [1, 2] is a positron-electron collider whose main purpose is B meson pair production. The target integrated luminosity is 50 ab^{-1}. The accelerator will be stopped for the first long-term shutdown (LS1) after about 3 years and half of the operation from March 2019, when Phase 3 began, to June 2022. The LS1 will cover upgrades to the Belle II detector [3] and minor modifications to the accelerator. This paper reports on the accelerator performance achieved until 2022. The run from February to the end of March is denoted as *a*, the run from April to July as *b*, and the run from October to December as *c*, with each denoted at the end of the calendar year. The run preceding LS1, the most recent operating period, is represented as 2022b.

The SuperKEKB accelerator consists of an electron ring (HER) with the beam energy of 7 GeV and a positron ring (LER) with the beam energy of 4 GeV, an electron-positron injector [4] with a positron damping ring [5], and beam transport lines connecting them. In the main ring, which has a circumference of about 3 km, the Belle II detector is placed at a collision point.

In order to achieve collisions with asymmetric energies, a double ring is required. It makes to accumulate many bunches while maintaining a single collision point. In addition, a large horizontal crossing angle at the collision point realizes a nano-beam scheme [6, 7]. A final focusing system (QCS) [8] consists of superconducting magnets is placed in the interaction region (IR) to strongly squeeze the beam.

In the LER, ARES RF accelerating cavities [9], which are normal-conducting cavities, are installed, and ARES cavities and superconducting RF accelerating cavities (SCC) [10, 11] are installed in the HER. The linac injector provides beams of the same energy as the main ring with a top-up injection. The energy lost by emitting synchrotron radiation is compensated by the RF cavities. The arc section employs non-interleaved chromaticity correction similar to that of the KEKB accelerator [12], and the emittance can be adjusted in combination with wiggler magnets in the straight sections (OHO and NIKKO). This enables the low emittance required by the nano-beam scheme.

Local chromaticity correction is placed in the straight section (TSUKUBA) where the IR is located, and the chromatic aberration generated in the drift space from the final focus quadrupole magnets to the collision point is efficiently corrected. The sextupole magnets for the local chromaticity correction are also used to perform the crab-waist scheme [13, 14].

The optical functions are calculated by using *SAD* [15] for the model lattice to compare with the measured optical functions and correct them [16]. Typical residual errors after optics corrections are 5 % for the beta functions (rms of $\Delta\beta_{x,y}/\beta_{x,y}$), 5 mm for dispersions (rms of $\Delta\eta_y$). The X-Y couplings as the leakage orbit in the vertical direction from the horizontal single-kick orbit (ratio of rms of Δy to rms of Δx) are obtained to be 0.012–0.016.

LUMINOSITY PERFORMANCE

The highest luminosity achieved through June 2022 is 4.65×10^{34} cm^{-2}s^{-1}. The unofficial record without data acquisition by the Belle II detector is 4.71×10^{34} cm^{-2}s^{-1}. These records are more than twice the highest luminosity achieved with the KEKB accelerator. The integrated luminosity provided by the accelerator is 491 fb^{-1}, of which 428 fb^{-1} (4 fb^{-1} is data not used in the analysis) was recorded at the Belle II detector. Table 1 shows the best integrated luminosity records per 8 hours(per shift), per day, and per 7 days.

Table 1: Integrated Luminosity Records

	Recorded	**Delivered**	**Unit**
Shift (8 hours)	958	1036	pb^{-1}
1 day	2.5	2.9	fb^{-1}
7 days	15.0	16.6	fb^{-1}

The maximum beam current is 1.46 A for the LER and 1.14 A for the HER. The maximum number of bunches achieved is 2346 which corresponds to about 4 nsec for a 2-bucket spacing. The vertical beta function at the IP is

* WORK SUPPORTED BY KEK, MINISTRY OF EDUCATION, CULTURE, SPORTS, SCIENCE AND TECHNOLOGY (MEXT), AND JSPS KAKENHI GRANT NUMBER 17K05475, JAPAN.
† yukiyoshi.onishi@kek.jp

ISBN: 978-3-95450-236-3 ISSN: 2673-7027 doi:10.18429/JACoW-eeFACT2022-MOXAT0103

mainly 1 mm for the operation, with a minimum value of 0.8 mm. When the vertical beta function at the IP is 0.8 mm, there are issues of beam lifetime and injection efficiency that depend on the optimization of the dynamic aperture with sextupole settings and physical aperture limited by movable collimators [17]. Both rings use the crab-waist scheme, which applies the crab-waist ratio of 80 % for the LER and 40 % for the HER. It is found that the crab-waist scheme reduces the effect of resonance lines that deteriorate luminosity, while significantly reducing the dynamic aperture. The machine parameters that achieved the highest luminosity are shown in Table 2. The σ_y^* shown in Table 2 is estimated by

Table 2: Machine Parameters

	LER	HER	Unit
Emittance, ε_x	4.0	4.6	nm
Beam current, $I_\pm$	1321	1099	mA
Number of bunches, n_b	2249		
Bunch current, $I_{b\pm}$	0.587	0.489	mA
Hor. size at IP, σ_x^*	17.9	16.6	μm
Ver. size at IP, σ_y^*	0.215		μm
Hor. betatron tune, ν_x	44.525	45.532	
Ver. betatron tune, ν_y	46.589	43.573	
Hor. beta at IP, β_x^*	80	60	mm
Ver. beta at IP, β_y^*	1.0	1.0	mm
Piwinski angle, Φ	10.7	12.7	
Crab-waist ratio	80	40	%
Beam-Beam, ξ_y	0.041	0.028	
Luminosity, L	4.65×10^{34}		1/cm^2/s

the Σ_y^* calculated from the luminosity divided by $\sqrt{2}$ with assuming $\sigma_{y+}^* = \sigma_{y-}^*$. The bunch length, σ_z used in the calculation is a nominal value. Luminosity is

$$L = \frac{N_+ N_- n_b f_0}{2\pi\phi_x \Sigma_z \Sigma_y^*}, \tag{1}$$

where $N_\pm$ is a number of particles, f_0 is a revolution frequency,

$$\Sigma_z = \sqrt{\sigma_{z+}^2 + \sigma_{z-}^2} \quad \text{and} \quad \Sigma_y^* = \sqrt{\sigma_{y+}^{*2} + \sigma_{y-}^{*2}}. \tag{2}$$

Piwinski angle is defined by

$$\Phi = \frac{\sigma_z}{\sigma_x^*}\tan\phi_x, \tag{3}$$

where ϕ_x is a half crossing-angle of 41.5 mrad. A feature of the nano-beam scheme is that the Piwinski angle is 10 or more, which is about 10 times larger than that of conventional colliders. This allows the vertical beta function at the IP to be squeezed to the bunch length divided by the Piwinski angle. However, the effect of bunch length on luminosity is introduced, so the vertical beam size needs to be reduced to compensate for the reduction of geometrical luminosity. The nominal bunch length is 4.6 mm for the LER and 5.1 mm for the HER. Practically, the bunch length is measured to be about 6 mm at the bunch current of 0.4 mA in the LER.

Crab-Waist Scheme

The advantage of the crab-waist scheme is not only to compensate for geometric luminosity loss but also to reduce betatron or synchro-betatron resonances caused by beam-beam interactions [18, 19]. For a crab-waist ratio of 100 %, the required K value (1/m^2) of a sextupole magnet is

$$K_2 = \frac{1}{\cos\Delta\psi_x \sin^2\Delta\psi_y}\frac{1}{\tan 2\phi_x}\frac{1}{\beta_y^s\beta_y^*}\sqrt{\frac{\beta_x^*}{\beta_x^s}}, \tag{4}$$

where β_x^s and β_y^s are the beta functions at the crab-waist sextupole magnet, and $\Delta\psi_{x,y}$ is the phase advance to the IP. The phase advances are designed and adjusted to have $|\cos\Delta\psi_x| = 1$ and $\sin^2\Delta\psi_y = 1$. The crab-waist scheme enables collision experiments with high bunch currents and improves specific luminosity [20, 21].

Specific Luminosity

Figure 1 shows the relationship between the specific luminosity and the bunch current product. The cases where $\beta_y^* = 1$ mm and 0.8 mm are shown. The specific luminosity is expressed by

$$L_{sp} = \frac{L}{n_b I_{b+} I_{b-}} \propto \frac{1}{\Sigma_z \Sigma_y^*}. \tag{5}$$

The beam size is constant with respect to the bunch current product unless a blowup occurs. It has been found that even with the setting of 1 mm, the deviation of the horizontal beam orbit in the local chromaticity correction causes a beta-beat and a deviation of the vertical beta function at the IP. In this case, the estimated beta function at the IP is also shown in the figure. This is more significant for the HER than for the LER.

In the case of $\beta_y^* = 0.8$ mm, higher specific luminosity was obtained with the bunch current product of 0.05 mA^2, but it decreases sharply around 0.1 mA^2. This may suggest that the correction of chromatic X-Y couplings is not optimized enough.

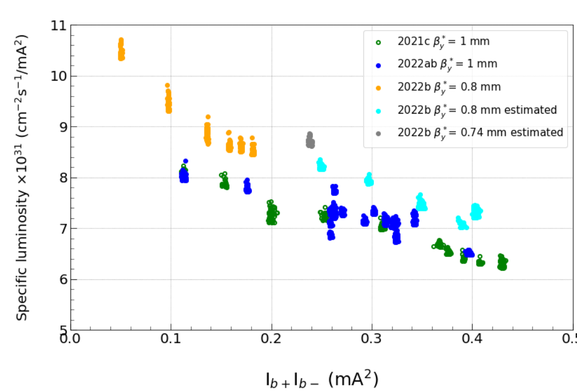

Figure 1: Specific luminosity.

ISBN: 978-3-95450-236-3 ISSN: 2673-7027 doi:10.18429/JACoW-eeFACT2022-MOXAT0103

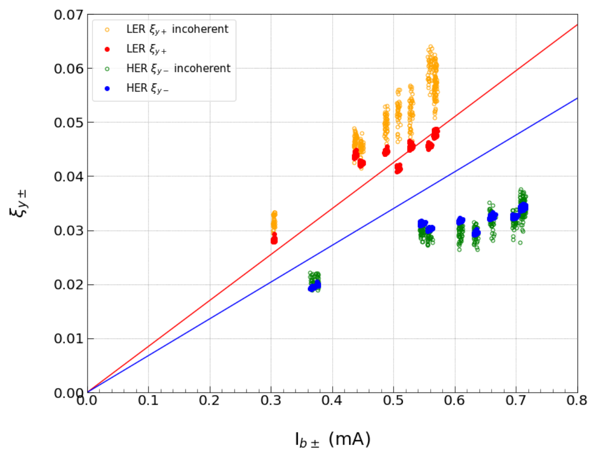

Figure 2: Beam-Beam parameter for the LER and HER, respectively. The red line shows calculated beam-beam parameter in the LER and blue line for the HER without a beam-beam blowup where the vertical emittance is 25 pm in the LER and 40 pm in the HER.

Beam-Beam Interaction

As squeezing the vertical beta function at the IP, the vertical beam-beam parameter decreases, usually according to $\sqrt{\beta_y^*}$. However, if the vertical emittance can also be reduced in proportion to β_y^*, the beam-beam parameter remains constant for the same bunch current. In other words, the luminosity increases only by $1/\sqrt{\beta_y^*}$ when β_y^* is squeezed, but if the vertical emittance can be decreased at the same time, the luminosity improves proportional to $1/\beta_y^*$. Figure 2 shows the beam-beam parameters for the bunch current of the opposite beam. The figure shows two types of beam-beam parameters in the physics run. The beam-beam parameters calculated from the luminosity is

$$\xi_{y\pm} = 2er_e \frac{\beta_{y\pm}^* L}{\gamma_\pm I_\pm}. \tag{6}$$

On the other hand, the incoherent beam-beam parameter is written by

$$\xi_{y\pm} = \frac{r_e}{2\pi\gamma_\pm}\left(\frac{I_{b\mp}}{ef_0}\right)\frac{\beta_{y\pm}^*}{\phi_x\sigma_{z\mp}\sigma_{y\mp}^*} \propto I_{b\mp}\sqrt{\frac{\beta_{y\pm}^*}{\varepsilon_{y\mp}}}, \tag{7}$$

where $\beta_{y+}^* = \beta_{y-}^*$. The reason why the beam-beam parameters of the HER are smaller than those of the LER is mainly because the beam current of the HER is increased compared to the energy ratio in the process of optimizing luminosity. When the HER beam current becomes smaller, the HER beam size tends to a blowup. In the bunch current region (0.8 mA or less) used in the physical run, the optimum ratio of the LER to the HER is 5 : 4. When the beam current is increased while maintaining this current ratio, the increase of beam-beam parameter in the electron beam slows down when the LER bunch current exceeds 0.6 mA. The highest beam-beam parameter seems to be 0.03 to 0.035 for the physics run. However, in the high-bunch current collision study with a small number of bunches, an optimization was performed specifically for the luminosity performance, the beam-beam parameter of 0.045 was achieved.

Correction of Chromatic X-Y Couplings in the LER

The LER is equipped with sextupole magnets rotating around the beam axis of 6 families on each side across the IP [22]. Both of chromatic X-Y couplings at the IP and chromaticity can be corrected by the rotatable sextupole magnets. There are four parameters for the X-Y couplings: r_1, r_2, r_3, and r_4. The chromatic X-Y couplings of r_1' and r_2', which have a direct effect on the luminosity, were corrected. To estimate the magnitude of the chromatic X-Y couplings, we focus on the resonance-line strengths $\nu_x - \nu_y - \nu_s$ =integers and $\nu_x - \nu_y - 2\nu_s$ =integers. Fix the horizontal tune, the vertical tune was scanned with measuring the vertical beam size by using the X-ray beam size monitor (XRM) [23]. Figures 3 and 4 show the relationship between the measured vertical emittance and the vertical tune (in the model) when r_1' and r_2' at the IP are changed. Based on these measurements, we decided to adopt $r_1' = -1$ and $r_2' = 0$ m as the combination with the weakest resonance-line strength.

OBSTACLES TO LUMINOSITY IMPROVEMENT

Beam Blowup in the LER

No beam blowup due to electron cloud effect in the LER was observed up to 0.35 mA/bunch/bucket spacing which corresponds to the maximum beam current of 1.64 A. However, the blowup for single-beam and single-bunch have been observed [24]. When observing the tune spectrum, the -1 mode side band ($\nu_y - \nu_s$) appears with a high bunch current. This -1 mode instability is thought to be related to the beam blowup, but the whole picture has not been fully understood. There are three sources of -1 mode instability; the impedance due to the movable collimators, the tuning of the bunch-by-bunch feedback system, and the vertical

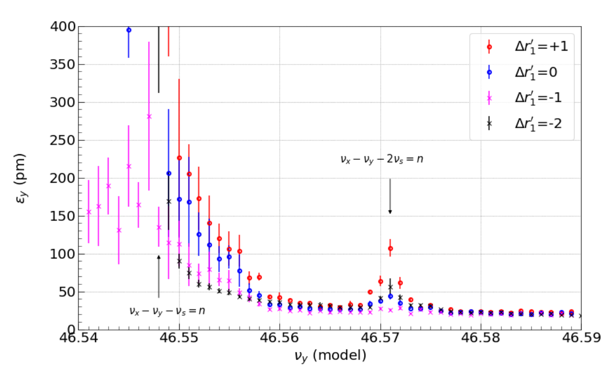

Figure 3: Vertical emittance as a function of vertical tune with different r_1'.

ISBN: 978-3-95450-236-3 ISSN: 2673-7027 doi:10.18429/JACoW-eeFACT2022-MOXAT0103

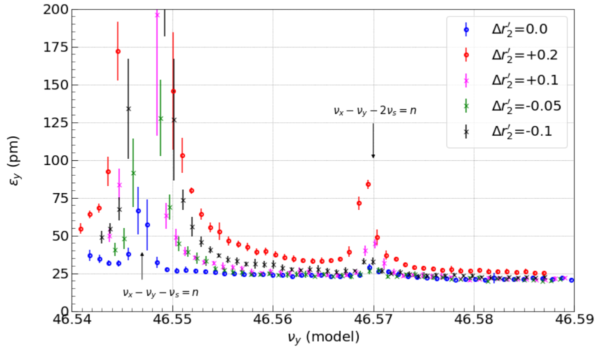

Figure 4: Vertical emittance as a function of vertical tune with different r_2'. The unit of $\Delta r_2'$ is m.

tune. After minimizing the impedance of the collimators and adjusting the bunch-by-bunch feedback system, it has been demonstrated that the beam blowup can be suppressed. In particular, simulation results show that reducing the number of taps in the bunch-by-bunch feedback system does not induce the blowup due to -1 mode instability. Selecting a higher vertical tune also helps to suppress the beam blowup.

It has been observed that when the collimator head is damaged by large beam loss, the bunch current dependence of the vertical tune shift increases. A damaged collimator is assumed to have an increased impedance. Collimator damage causes the beam blowup and increases beam backgrounds, which is a serious problem in the accelerator operation.

Sudden Beam Loss

There are events that cause beam loss in a few turns and lead to beam abort. In most cases, the beam loss is detected and the beam is aborted by the loss monitor, but if the amount of beam loss is too large, it causes damage to the collimator head and QCS quench. It is observed that the fast beam loss occurs near these collimators. We call the fast beam loss "sudden beam loss".

For the LER, we mainly use three movable collimators in the vertical direction, D06V1, D06V2, and D02V1, from the upstream of the IP. A large beam loss near D02V1 often quenches the QCS and increases the dose in the Belle II detector. Among the QCS, the superconducting coil for the LER called QC1LP, which is the closest to the downstream of the IP, is quenched, and in the case of a larger beam loss, the superconducting coil called QC1RP on the upstream side is also quenched. It can also damage the D06V1 and D02V1 collimator heads. Simultaneously, a vacuum pressure rise near the collimator is observed. The superconducting coil for the HER has never been quenched during the normal accelerator operation. Large sudden beam losses tend to become noticeable when the LER bunch current exceeds 0.7 mA. Also, if the collimator head is damaged and the impedance increases, the bunch current threshold that causes such sudden and large beam loss tends to be low.

Collimator Impedance

A movable collimator plays a major role in reducing the beam background for the Belle II detector. The beam background is caused by injected beams and stored beams [25]. For the stored beam, the beam background is caused by a scattering due to residual gas in the vacuum pipes, a particle scattering in a bunch, and a scattering due to collisions with opposite beams which becomes more pronounced as the luminosity increases. Residual gas decreases as the vacuum baking progresses. For the low emittance, a probability of intra-beam scattering increases and the dynamic aperture of the optics containing the IP decreases, so that the scattered particles move out of the stable region and become the background. If the emittance or energy spread of the injected beam is larger than required, or if the coherent oscillation due to the top-up injection is large, the injected beam causes the background. The physical aperture of the movable collimator is adjusted to reduce these beam backgrounds. In that case, an optimization is performed while balancing injection efficiency and beam lifetime. Compared to the horizontal collimator, the physical aperture of the vertical collimator is considered to be very small and the impedance is large since the vertical aperture of QC1s determines the physical aperture.

The short-range wake field due to the movable collimators makes single-bunch tune shift. The vertical tune shift is expressed by

$$\frac{\Delta \nu_y}{I_b} = -\frac{T_0}{4\pi(E/e)} \sum_i \beta_{yi} \kappa_i(d), \tag{8}$$

where T_0 is the revolution frequency (about 10 μsec), $\kappa_i(d)$ is the loss factor of each movable collimator which is a function of physical aperture of d. Figure 5 shows the relationship between the measured bunch current dependence of the vertical tune-shift in the LER and the estimated product of the loss factor and β_y at the vertical collimator for each β_y^*. If the impedance near QCS is dominant, there should be a difference in the tune shift due to the beta function at the IP, but this is not observed. On the other hand, it can be seen that the change in impedance due to the physical aperture of the collimator has a significant effect on the tune shift. In the physics run, the sum of $\beta_y \kappa(d)$ of the LER is about 33 kV/pC and the tune shift is about -0.011 mA^{-1} which corresponds to about half of the synchrotron tune in the LER. However, as described in the previous section, if a large beam loss occurs and the collimator head is damaged, the tune shift becomes further larger.

Optics Changes due to Beam-Line Deformation

In the HER, a significant vertical tune shift was observed with increasing beam current. Recently, it has been found that the horizontal orbit at strong sextupole magnets deviates from the reference orbit with the beam current, even with performing the continuous closed orbit correction (CCC) every 15 seconds. The deviation of the horizontal orbit in the sextupole magnet causes a tune shift due to create a quadrupole

ISBN: 978-3-95450-236-3 ISSN: 2673-7027 doi:10.18429/JACoW-eeFACT2022-MOXAT0103

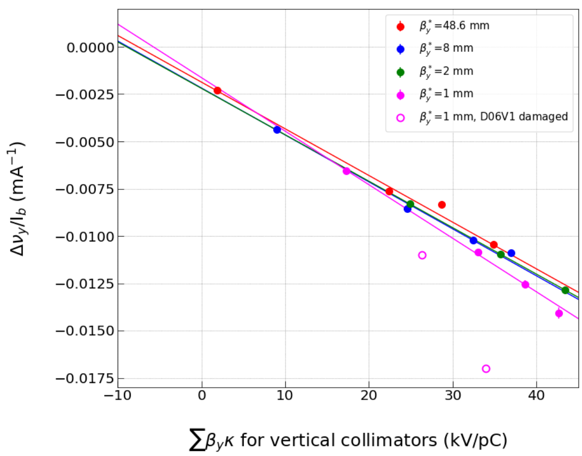

Figure 5: Slope of vertical tune as a function of $\sum \beta_y \kappa$.

magnetic field component. In particular, in the case of sextupole magnets for the local chromaticity correction, the horizontal beta function is small and the vertical beta function is large. Therefore, mainly the vertical tune shift occurs. Assuming that as the beam current increases, the beam line is deformed by the synchrotron radiation heating and the deviation of the orbit in the horizontal direction increases, the resulting vertical tune shift is consistent with the measured value. We observed the horizontal tune shift which can be explained by resistive wall impedance. Tune shift due to the resistive wall impedance should also contribute in the vertical direction. Regarding the vertical tune shift, amount of the tune shift due to the horizontal orbit deviation at the sextupole magnet and the resistive wall impedance is not clear, so further detailed investigation is required.

The quadrupole magnetic field components produced by horizontal orbital deviations at strong sextupole magnets cause beta-beats as well as tune shifts. As a result of beta-beat, the vertical beta function at the IP also changes. In the case of the HER, as the beam current increases, the horizontal beam orbit at the pair of sextupole magnets in the local chromaticity correction tends to shift toward the outside of the ring. The orbit deviation is in the direction that the vertical beta function at the IP becomes smaller, and with a shift of 20 μm, β_y^*=1 mm is reduced to be about 0.8 mm. A local bump orbit placed at the sextupole magnet is used to correct horizontal beam orbit deviations. As a result, the reproducibility of optics corrections at low current (50 mA) was improved. In addition, the injection efficiency in the high current region recovered to the same level as that in the low current region, and the beam background was reduced. The vertical beta function in the arc section is smaller compared to the local chromatic aberration correction, but there are strong sextupole magnets in the arc. Further more, the vertical orbit deviation at the sextupole magnet produces X-Y couplings. Since there is a similar problem in the LER, we should understand the deformation of the beam line as a whole ring, and consider the system that keeps the beam orbit constant in the entire beam current at the level of 10 μm order.

Lifetime and Beam Injection

The characteristics of the nano-beam scheme are low emittance and small beta function at the IP. These make it difficult to ensure sufficient dynamic aperture. Simulations show that the crab-waist scheme reduces the dynamic aperture for particles with momentum deviations. The physical aperture of the movable collimator for beam background reduction also affects the beam lifetime. If the vertical beta function at the IP is squeezed, the injection efficiency decreases. Moreover, since the injection efficiency depends on the bunch current, the beam-beam effect can not be ignored for the injection. In the future, it will be a big challenge to squeeze the beta functions at the IP and increase the beam current to achieve a luminosity exceeding 10^{35} cm^{-2}s^{-1}.

SUMMARY

The recent operation status of the SuperKEKB accelerator was reported in this article. In the operation of 2022*b*, the LER beam current exceeded 1 A and became stable, then the maximum beam current reached 1.4 A. The number of bunches could be increased to 2346 bunches (2-bucket spacing). As a result, the maximum luminosity of 4.65×10^{34} cm^{-2}s^{-1} was achieved. Figure 6 shows the history of the beam current, luminosity and integrated luminosity. The accelerator was operated as Phase 3 from spring in 2019 to summer in 2022, but it entered a long-term shutdown (LS1) after that. The accelerator will be upgraded, including the adoption of a nonlinear collimator and the modification of vacuum pipe at injection region in the HER in LS1. We plan to achieve 10^{35} cm^{-2}s^{-1} within 2 years after LS1 and an integrated luminosity of 15 ab^{-1} in 10 years.

ACKNOWLEDGMENTS

We would like to thank all those involved in the operation of the SuperKEKB accelerator. The research results were widely supported by the INFN(LNF), CERN, and KEK collaborations, for which we would like to thank them here.

REFERENCES

[1] Y. Ohnishi *et al.*, *Prog. Theor. Exp. Phys.*, vol. 2013, p. 03A011, 2013. doi:10.1093/ptep/pts083

[2] K. Akai *et al.*, *Nucl. Instrum. Methods*, vol. A907, p. 188, 2018. doi:10.1016/j.nima.2018.08.017

[3] Belle II, *Technical Design Report*, 2010. arXiv:1011.0352.

[4] K. Furukawa *et al.*, in *Proc. IPAC'18*, Vancouver, Canada, Apr.-May 2018, pp. 300–303. doi:10.18429/JACoW-IPAC2018-MOPMF073

[5] M. Kikuchi *et al.*, in *Proc. IPAC'10*, Kyoto, Japan, May 2010, paper TUPEB054, pp. 1641–1643.

[6] P. Raimondi, Presented at the 2nd Workshop on Super B-Factory, Frascati, 2006.

[7] *SuperB Conceptual Design Report*, INFN/AE-07/2, SLAC-R-856, LAL 07-15 March, 2007.

ISBN: 978-3-95450-236-3 ISSN: 2673-7027 doi:10.18429/JACoW-eeFACT2022-MOXAT0103

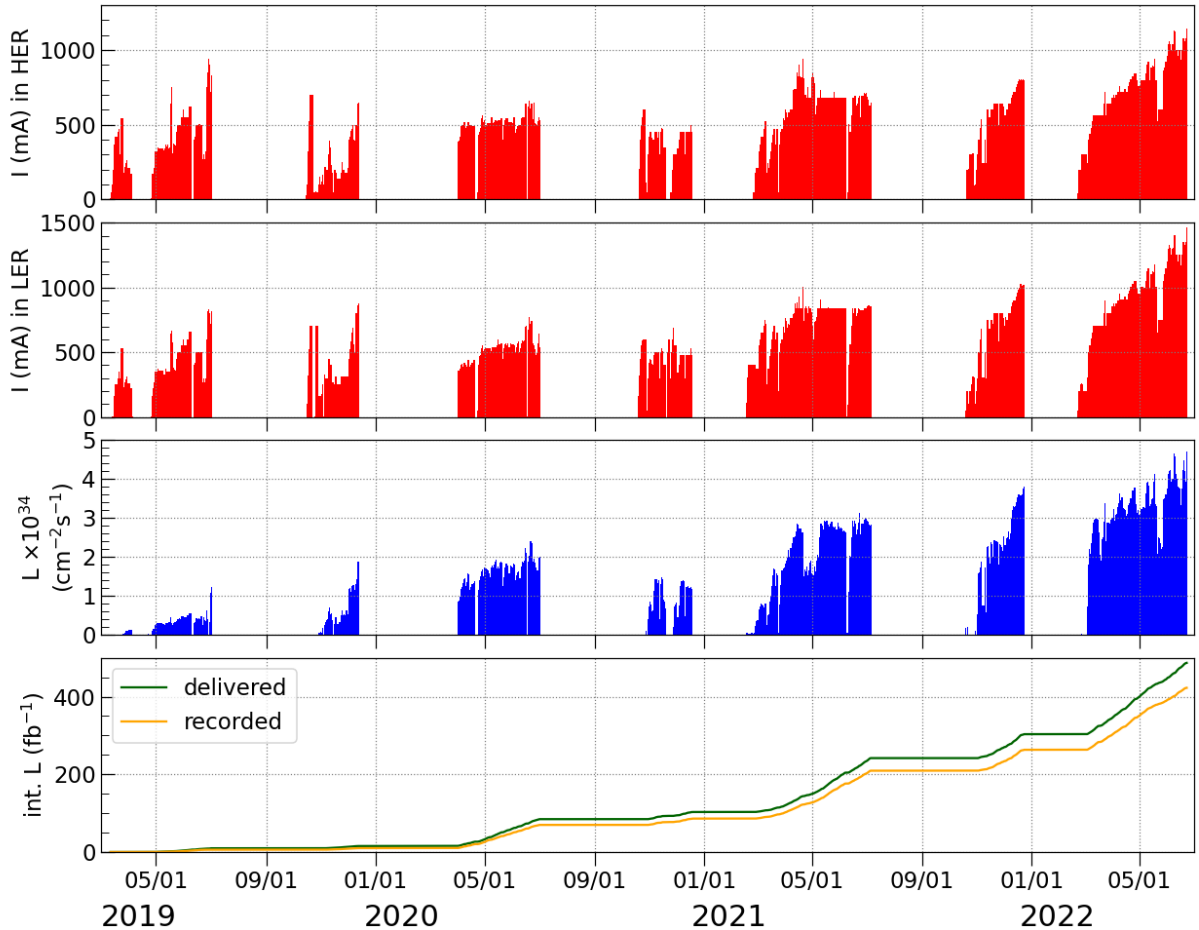

Figure 6: History of SuperKEKB since 2019.

[8] N. Ohuchi *et al.*, in *Proc. IPAC'18*, Vancouver, Canada, Apr.-May 2018, pp. 1215–1219. doi:10.18429/JACoW-IPAC2018-TUZGBE2

[9] K. Watanabe *et al.*, in *Proc. IPAC'19*, Melbourne, Australia, May 2019, pp. 619–621. doi:10.18429/JACoW-IPAC2019-MOPRB022

[10] T. Furuya *et al.*, in *Proc. SRF'95*, Gif-sur-Yvette, France, Oct.1995, paper SRF95F35, pp. 729–733.

[11] T. Tajima *et al.*, in *Proc. 2nd Superconducting Linear Accelerator Meeting in Japan*, KEK-PROC–99-25.

[12] T. Abe *et al.*, *Prog. Theor. Exp. Phys.*, vol. 2013, p. 03A001, 2013. doi:10.1093/ptep/pts102

[13] *SuperB Conceptual Design Report*, INFN/AE-07/2, SLAC-R-856,LAL 07-15 March, 2007.

[14] K. Oide *et al.*, *Phys. Rev. Accel. Beams*, vol. 19, p. 111005, 2016. doi:10.1103/PhysRevAccelBeams.19.111005

[15] *Strategic Accelerator Design*, http://acc-physics.kek.jp/SAD.

[16] H. Sugimoto *et al.*, in *Proc. eeFACT2022*, Frascati, Italy, Sep. 2022. Paper TUXAT0103, this conference

[17] T. Ishibashi *et al.*, *Phys. Rev. Accel. Beams*, vol. 23, p. 053501, 2020. doi:10.1103/PhysRevAccelBeams.23.053501

[18] M. Zobov *et al.*, *Phys. Rev. Lett.*, vol. 104, p. 174801, 2010. doi:10.1103/PhysRevLett.104.174801

[19] D. Shatilov *et al.*, *Phys. Rev. ST Accel. Beams*, vol. 14, p. 014001, 2011. doi:10.1103/PhysRevSTAB.14.014001

[20] Y. Ohnishi *et al.*, *Eur. Phys. J. Plus*, vol. 136, p. 1023, 2021. doi.org/10.1140/epjp/s13360-021-01979-8

[21] D. Zhou *et al.*, in *Proc. IPAC'22*, Bangkok, Thailand, Jun. 2022, pp. 2011–2014. doi:10.18429/JACoW-IPAC2022-WEPOPT064

[22] R. Sugahara *et al.*, *IEEE Trans. Appl. Supercond.*, vol. 26, 2016. doi:10.1109/TASC.2016.2534760

[23] J. W. Flanagan, in *Proc. IBIC'18*, Shanghai, China, Sep. 2018, pp. 361–365. doi:10.18429/JACoW-IBIC2018-WEOC02

[24] S. Terui *et al.*, in *Proc. IPAC'22*, Bangkok, Thailand, Jun. 2022, pp. 2169–2172. doi:10.18429/JACoW-IPAC2022-WEPOTK050

[25] H. Nakayama *et al.*, in *Proc. IPAC'21*, Campinas, Brazil, May 2021, pp. 2532–2535. doi:10.18429/JACoW-IPAC2021-WEXA07

ISBN: 978-3-95450-236-3 ISSN: 2673-7027 doi:10.18429/JACoW-eeFACT2022-MOXAT0104

FCC-ee FEASIBILITY STUDY PROGRESS*

Michael Benedikt, Frank Zimmermann†, CERN, Geneva, Switzerland

Abstract

The Future Circular Collider (FCC) "integrated programme" consists of a proposed high-luminosity e+e- collider, FCC-ee, serving as Higgs and electroweak factory, which would, in a second stage, be succeeded by a 100 TeV hadron collider, FCC-hh. FCC-ee and FCC-hh share the same 91 km tunnel and technical infrastructure. In summer 2021 a detailed FCC Feasibility Study (FCC FC), focused on siting, tunnel construction, environmental impact, financing, operational organisation, etc., was launched by the CERN Council. This FCC Feasibility Study (FCC FS) should provide the necessary input to the next European Strategy Update expected in 2026/27. In this paper we briefly review the FCC key design features, status and plans.

This paper is an updated, slightly modified version of an article submitted to the proceedings of NA-PAC'22 [1] (published under the Creative Commons Attribution 3.0 license). Sections on two planned accelerator mock-ups and on regional activities were taken from an article in the ECFA Newsletter [2].

INTRODUCTION

This paper is an updated, slightly modified version of an article submitted to the proceedings of NA-PAC'22 [1] (published under the Creative Commons Attribution 3.0 license). Sections on two planned accelerator mock-ups and on regional activities were taken from an article in the ECFA Newsletter [2].

The Future Circular electron-positron Collider, FCC-ee, is a proposed new storage ring of 91 km circumference, designed to carry out a precision study of Z, W, H, and $t\bar{t}$ with an extremely high luminosity, ranging from 2×10^{36} cm^{-2}s^{-1} per interaction point (IP), on the Z pole (91 GeV c.m.), 7×10^{34} cm^{-2}s^{-1} per IP at the ZH production peak and 1.3×10^{34} cm^{-2}s^{-1} per IP at the $t\bar{t}$. In the case of four experiments, the total luminosity on the Z pole will be close to 10^{37} cm^{-2}s^{-1}. FCC-ee will also offer unprecedented energy resolution, both on the Z pole and at the WW threshold.

The FCC-ee represents a low-risk technical solution for an electroweak and Higgs factory, which is based on 60 years of worldwide experience with e^+e^- circular colliders and particle detectors. R&D is being carried out on components for improved performance, but there is no need for "demonstration" facilities, as LEP2, VEPP-4M, PEP-II, KEKB, DAΦNE, or SuperKEKB already demonstrated many of the key ingredients in routine operation.

The FCC shall be located in the Lake Geneva basin and be linked to the existing CERN facilities. The FCC utility requirements are similar to those in actual use at CERN. The FCC "integrated programme" consists of the FCC-ee Higgs and electroweak factory as a first stage, succeeded by a 100 TeV hadron collider, FCC-hh, as the ultimate goal. This sequence of FCC-ee and FCC-hh is inspired by the successful past Large Electron Positron collider (LEP) and Large Hadron Collider (LHC) projects at CERN. A similar two-stage project is under study in China, under the name CEPC/SPPC [3].

The FCC technical schedule foresees the start of tunnel construction around the year 2030, the first e^+e^- collisions at the FCC-ee in the mid or late 2040s, and the first FCC-hh hadron collisions by 2065–70.

* Work supported by the European Union's H2020 Framework Programme under grant agreement no. 951754 (FCCIS).
† frank.zimmermann@cern.ch

DESIGN OUTLINE

The FCC-ee is conceived as a double ring e^+e^- collider. It shares a common footprint with the 100 TeV hadron collider, FCC-hh, that would be the second stage of the FCC integrated programme.

The FCC-ee design features a novel asymmetric interaction-region (IR) layout and optics to limit the synchrotron radiation emitted towards the detector (a lesson from LEP [4]), and to generate the large crossing angle of 30 mrad, required for the crab-waist collision scheme [5].

The latest FCC layout features a superperiodicity of four, and can accommodate either two or four experiments, in four 1.40 km long straight sections, which are alternating with 2.03 km straight sections hosting technical systems, in particular radiofrequency (RF) cavities. Each of the 8 separating arc sections has a length of 9.6 km. Figure 1 sketches the layout and possible straight-section functions for the FCC-ee.

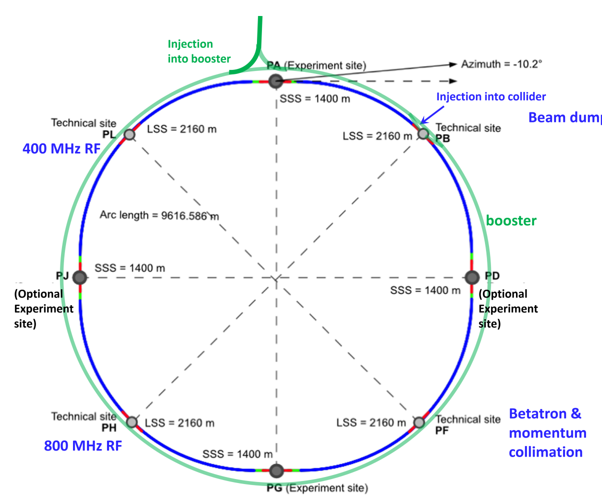

Figure 1: Schematic layout of the FCC-ee collider with a circumference of 91.1 km and four-fold superperiodicity. The full-energy booster and part of its injection transfer line are also indicated.

65th ICFA Adv. Beam Dyn. Workshop High Luminosity Circular e+e− Colliders eeFACT2022, Frascati, Italy JACoW Publishing
ISBN: 978-3-95450-236-3 ISSN: 2673-7027 doi:10.18429/JACoW-eeFACT2022-MOXAT0104

FCC-ee key parameters, evolved from those of the Conceptual Design Report (CDR) [6], are summarized in Table 1. Thanks to self-polarisation at the two lower energies (Z and W operation) [7], a precision energy calibration by resonant depolarisation is possible, down to 100 keV accuracy for m_Z and 300 keV for m_W [8, 9].

An important ingredient is the crab waist collision scheme, which was first demonstrated at DAΦNE, where it tripled the collider luminosity [10]. More recently, in 2020, at SuperKEKB the "virtual" crab waist collision, first developed for the FCC-ee [5], was successfully implemented, and is now used in routine operation [11]. SuperKEKB is also already operating with a vertical IP beta function β_y^* of 1 mm in regular operation, and, during accelerator studies, further squeezed β_y^* down to 0.8 mm, the smallest value considered for FCC-ee (see Table 1). Both the natural bunch lengths due to synchrotron radiation (SR) and their values in collision including the effect of beamstrahlung (BS) are shown in Table 1. The FCC-ee considers a combination of 400 MHz radiofrequency systems (at the first three energies, up to 2.1 GV) and 800 MHz (additional cavities, with up to 9.2 GV, for $t\bar{t}$ operation), with respective voltage strengths in each running mode as indicated. For ZH and $t\bar{t}$ operation, the RF cavities are shared by the two beams. The beam lifetime shown represents the combined effect of the luminosity-related radiative Bhabha scattering and beamstrahlung. The assumed cross section for radiative Bhabha scattering is pessimistic, since it was computed without the beam density cutoff introduced in Ref. [12]. As shown in Table 1, the synchrotron radiation power of FCC-ee is assumed to be limited to 50 MW per beam. As the centre-of-mass energy is increased, the synchrotron radiation power is kept constant, primarily by reducing the number of bunches. Top-up injection requires a full-energy booster synchrotron in the collider tunnel.

PROJECT COST AND PROFILE

The FCC CDR of 2019 included a cost estimate for the first stage, the FCC-ee, which is reproduced in Table 2.

A draft spending profile for FCC-ee is displayed in Fig. 2. This figure assumes civil engineering construction from 2032 to 2040, installation of technical infrastructure from

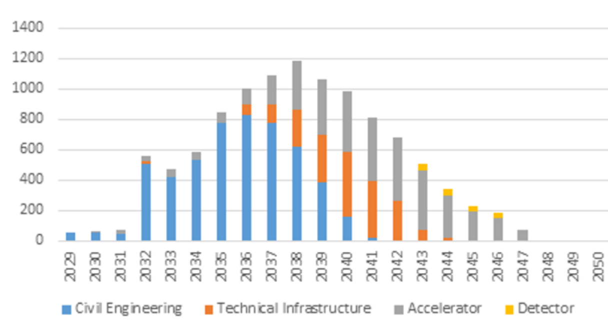

Figure 2: Example draft spending profile for FCC-ee, in units of MCHF versus the year.

Table 1: Preliminary key parameters of FCC-ee, now with a circumference of 90.7 km, and a new arc optics for Z and W running. Luminosity values are given per interaction point (IP), for a scenario with 4 IPs.

Running mode	Z	W	ZH	$t\bar{t}$
Number of IPs		4		
Beam energy (GeV)	45.6	80	120	183
Bunches/beam	10000	880	248	40
Beam current [mA]	1280	135	26.7	5.0
Luminosity/IP [nb^{-1} s^{-1}]	1820	194	73	12.5
Energy loss / turn [GeV]	0.04	0.37	1.87	10.0
Synchr.rad.power [MW]		100		
RF volt. 0.4 GHz [GV]	0.12	1.0	2.1	2.1
RF volt. 0.8 GHz [GV]	0	0	0	9.2
Bunch length σ_z w/o	4.4	3.6	3.3	1.9
and with BS [mm]	15.4	8.0	6.0	2.7
Hor. emit. ε_x [nm]	0.71	2.16	0.64	1.49
Vert. emit. ε_y [pm]	1.42	4.32	1.29	2.98
Long. damp. time [turns]	1168	217	64.5	18.5
Vert. IP beta β_y^* [mm]	0.8	1.0	1.0	1.6
Hor. IP beta β_x^* [m]	0.1	0.2	0.3	1.0
Beam lifetime [min.]	8	18	6	10

Table 2: Construction cost estimate for FCC-ee considering a machine configurations at the Z, W, and H working points. A baseline configuration with 2 detectors is assumed. The CERN contribution to 2 experiments is included.

Cost Category	MCHF	%
Civil engineering	5,400	50
Technical infrastructure	2,0009	18
Accelerator	3,300	30
Detector	200	2
Total Cost (2018 prices)	10,900	100

2037 to 2043, construction of accelerator and experiments during the years 2032–2045, and, finally, commissioning and start of operation in the period 2045–2048.

FCC-ee R&D

Many of the technologies required for constructing an FCC-ee exist [13]. Ongoing FCC-ee research and development (R&D) efforts focus on further improving the overall energy efficiency, on obtaining the measurement precision required, and on achieving the target performance in terms of beam current and luminosity. Work is also ongoing on an alternative collider optics with potentially much better performance.

Key FCC-ee R&D items for improved energy efficiency include high-efficiency continuous wave (CW) radiofrequency (RF) power sources (klystrons, IOTs and/or solid state), high-Q superconducting (SC) cavities for the 400–800 MHz range, and possible applications of high-temperature superconduc-

ISBN: 978-3-95450-236-3 ISSN: 2673-7027 doi:10.18429/JACoW-eeFACT2022-MOXAT0104

tor (HTS) magnets. For ultra high precision centre-of-mass energy measurements, the R&D should also cover advanced beam measurements (inv. Compton, beamstrahlung, etc.) and spin-polarisation simulations. Finally, for high luminosity, high current operation, FCC-ee requires a next generation beam stabilization and feedback system to suppress instabilities arising over a few turns, a robust low-impedance collimation scheme, and a machine tuning system based on artificial intelligence.

SRF Cavity Developments

Since PETRA, TRISTAN and LEP-2, superconducting RF systems are the underpinning technology for modern circular lepton colliders. The FCC-ee baseline foresees the use of single-cell 400 MHz Nb/Cu cavities for high-current low-voltage beam operation at the Z production energy, two-cell 400 MHz Nb/Cu cavities at the W and H (ZH) energies, and a complement of five-cell bulk Nb 800 MHz cavities at 2 K for low-current high-voltage $t\bar{t}$ operation [6]. In the full-energy booster, only multi-cell 400 and 800 MHz cavities may be installed. The necessity of 400 MHz systems in the booster is under study. For the FCC-ee collider, also alternative RF scenarios, with possibly fewer changes between operating points, are being explored, such as novel 600 MHz slotted waveguide elliptical (SWELL) cavities [14].

R&D for the FCC-ee Arcs

Aside from the various RF systems, another major component of the FCC-ee is the regular arc, covering about 77 km. Indeed, the arc half-cell is the most recurrent assembly of mechanical hardware in the accelerator (about 1500 similar FODO cells). Therefore, as part of the FCC R&D plan, an arc half-cell mock up is foreseen to be constructed at CERN by 2025. It will include girder, a vacuum system with antechamber and pumps, dipole, quadrupole and sextupole magnets, beam position monitors, cooling and alignment systems, and technical infrastructure interfaces. The mock-up will lead to functional prototype(s), and then further to a pre-series plus, finally, series production. Building the mock-up allows optimizing and testing fabrication, integration, installation, assembly, transport, maintenance, by working, where required, with structures of equivalent volumes, weights, and stiffness.

Similarly, for the interaction region the construction of a mock up is proposed at INFN Frascati [15]. Starting from the central interaction point vacuum chamber made from AlBeMet162, cooled by paraffin and held by a strong outer support tube, a steel transition plus bellows, the mock up could later be extended to also include the trapezoidal vacuum chamber with remote vacuum connection, a placeholder luminosity monitor, a compensation solenoid, and the first superconducting quadrupole with cryostat, more beam pipes, support structures for quadrupole and cryostat, and vibration and alignment sensors.

Constructing some of the magnets for the FCC-ee final focus or arcs with advanced high-temperature superconductor (HTS) technology [16] could lower the energy consumption and increase operational flexibility. The focus of this HTS R&D will not be on reaching extremely high field, but on operating lower-field SC magnets at temperatures between 40 and 77 K. Nevertheless, this development could also be a first step towards higher field HTS magnets for the hadron collider FCC-hh, where operation at 20 K or 40 K instead of 2 K, would dramatically reduce the electric power consumption.

Centre-of-Mass Energy Calibration

Highly precise centre-of-mass energy calibration at c.m. energies of 91 GeV (Z pole) and 160 GeV (WW threshold), a cornerstone of the precision physics programme of the FCC-ee, relies on using resonant depolarisation of wiggler-pre-polarised pilot bunches [9]. The operation with polarised pilot bunches requires constant and high precision monitoring of the residual 3-D spin-polarisation of the colliding bunches, which — if nonzero — would affect the physics measurements.

FCC-ee Pre-Injector

Concerning the FCC-ee pre-injector, the CDR design foresaw a pre-booster synchrotron. At present, this choice is under scrutiny. As an alternative, and possibly new baseline, it is proposed to extend the energy of the injection linac to 10–20 GeV, for direct injection into the full-energy booster [17]. The higher-energy linac could be based on state-of-the-art S-band technology as employed for the FERMI upgrade at the ELETTRA synchrotron radiation facility. Alternatively, a C-band linac could be considered, possibly based on the SLAC C^3 technology [18].

It is also envisaged to design, construct and then test with beam a novel positron source [17, 19] plus capture linac, and measure the achievable positron yield, at the PSI SwissFEL facility, with a primary electron energy that can be varied from 0.4 to 6 GeV.

Full-Energy Booster

The injection energy for the full-energy booster is defined by the field quality of its low-field magnets. Magnet development and prototyping of booster dipole magnets, along with field measurements (presently only available for the twin collider CEPC [20]), should guide the choice of the injection energy. Maintaining beam stability at injection into the booster may require the installation of wiggler magnets for increasing the beam energy spread. An alternative optics, which may both increase the SR energy spread and avoid very low magnetic fields, is based on alternating the polarity of arc dipole magnets at injection, reminiscent of what is being planned for the Electron Storage Ring (ESR) of the US Electron Ion Collider (EIC) [21, 22], although the FCC-ee booster is fast ramping, while the ESR will operate at different constant beam energies.

Role of SuperKEKB

The SuperKEKB collider, presently being commissioned [23], features many of the key elements of FCC-ee: double

65th ICFA Adv. Beam Dyn. Workshop High Luminosity Circular e⁺e⁻ Colliders eeFACT2022, Frascati, Italy JACoW Publishing
ISBN: 978-3-95450-236-3 ISSN: 2673-7027 doi:10.18429/JACoW-eeFACT2022-MOXAT0104

ring, large crossing angle, low vertical IP beta function β_y^* (design value ~0.3 mm), short design beam lifetime of a few minutes, top-up injection, and a positron production rate of up to several 10^{12}/s. SuperKEKB has achieved, in both rings, the world's smallest ever β_y^* of 0.8 mm, which also is the lowest value considered for FCC-ee. Profiting from a new "virtual" crab-waist collision scheme, first developed for FCC-ee [5], in July 2022 SuperKEKB reached a world record luminosity of 4.7×10^{34} cm^{-2}s^{-1}. However, several issues still need to be resolved, such as a vertical emittance blow up, the transverse machine impedance and the associated single-bunch instability threshold, sudden beam losses, poor quality of the injected beam, etc.

SuperKEKB is pushing the frontiers of accelerator physics with a vertical rms beam spot size of about 300 nanometer, the lowest of any operating collider. The future goal is pushing the luminosity to 6×10^{35} cm^{-2}s^{-1}, and a beam spot size of 50 nm. SuperKEKB serves as an important testbed for FCC-ee and other future electron-positron colliders, and also as a unique facility for training the next generation of accelerator physicists, who will be commissioning these future colliders.

Collaboration with EIC

The EIC ESR [22] has almost identical beam parameters as FCC-ee, but it will operate with close to twice the maximum electron beam current, or half the bunch spacing, and it will operate at lower beam energy. These differences make it more challenging. About ten domains of common interest have been identified by the FCC and EIC design teams, for each of which a joined EIC-FCC working group is being set up. The EIC will start beam operation about a decade prior to FCC-ee. It would, thereby, provide another invaluable opportunity to train the next generation of accelerator physicist on an operating collider, to test hardware prototypes, beam control schemes, etc.

OPTIMIZED PLACEMENT

In 2021, the placement and layout of the FCC (common for both FCC-ee and FCC-hh) was optimized, taking into account numerous constraints and considerations, including geological conditions, depth of access shafts, vicinity of access roads, railway connections, etc., while avoiding surface sites in water protection zones, densely urbanized areas, and high mountains. The number of surfaces sites was reduced from 12 in the CDR to 8, which facilitates the placement and decreases the required surface area from 62 ha to less than 40 ha, In addition, the 8 surface sites and the new layout are arranged with a perfect 4-fold superperiodicity, which allows for either two or four collision points and experiments.

Four different FCC-ee detectors placed at the maximum number of four collision points could be optimized, respectively, for the Higgs factory programme, for ultraprecise electroweak and QCD physics, for Heavy Flavour physics, and for searching feebly coupled particles (LLPs) [24]. For the FCC-hh, two high-luminosity general-purpose experiments and two specialized experiments are foreseen [25], similar to the present LHC detectors.

By suppressing 3/4 of the resonances in the tune diagram, the superperiodicity of four will ensure the best possible beam-dynamics performance for both lepton and hadron collider. The resulting optimized placement is illustrated in Fig. 3, and the corresponding long section showing the geological situation and the depths of access shafts in Fig. 4. More than 90% of the collider tunnel are situated in the so-called "molasse" layer, which is ideally suited for tunnel boring machines. The depths of the access shafts varies from 100 m to 400 m, with most shaft depths around 200–250 m. All proposed surface sites are close to existing road infrastructures, so that in total less than 5 km of new road constructions is required for all sites together. Several sites are located in the vicinity of 400 kV electricity grid lines. Finally, the good road connections of Points PD, PF, PG, PH suggest a second operation pole around Annecy (CNRS LAPP) in the South. Detailed site investigations are planned for the period 2024–2025, with about 40 to 50 drillings and some 100 km of seismic lines.

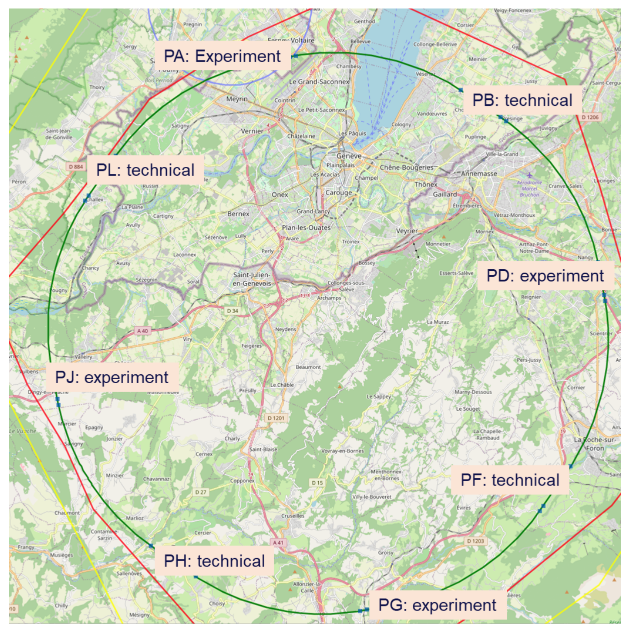

Figure 3: Optimized placement of the FCC.

SUSTAINABILITY

According to the conceptual design, the FCC-ee is the most sustainable of all the proposed Higgs and electroweak factory proposals, in that it implies by far the lowest energy consumption for a given value of total integrated luminosity, over the collision energy range from 90 to 365 GeV [26, 27].

The electrical power consumption depends on the centre-of-mass energy. An estimation of the upper limit of the power drawn by the various FCC-ee systems for each mode of operation was first presented in [28] and updated recently [29]. Depending on the collision energy the total facility power extends from about 238 MW at the Z to 388 MW at

ISBN: 978-3-95450-236-3 ISSN: 2673-7027 doi:10.18429/JACoW-eeFACT2022-MOXAT0104

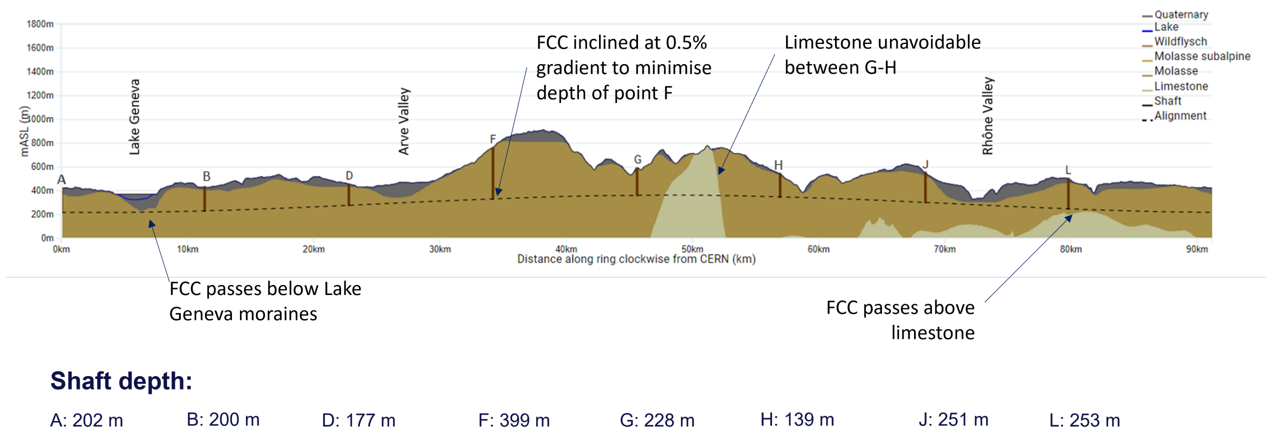

Figure 4: Long section of the optimally placed FCC.

the $t\bar{t}$ energy. These values are comparable in order of magnitude with CERN's present power consumption of about 200 MW, when LHC is operating, or with a total CERN power consumption of up to ~240 MW at the time of the previous LEP collider. The numbers include the power required for cooling and ventilation, for general services, for two experiments, for data centres, and for the injector complex. Although the FCC-ee is three to four times larger than LEP, and achieves about 10^5 times the LEP luminosity, the design concept leads to an overall electrical peak power of only about 2.5 times the one of LEP, which alone consumed ~120 MW. Adding to FCC-ee operation also the powering required for the present CERN site running various lower-energy hadron accelerators, and for a parallel fixed target proton programme at the existing CERN SPS North Area, the total annual energy consumption is expected to range from about 1.8 TWh at the Z to 2.5 TWh at the $t\bar{t}$ [29]. Additional technology advancements and design optimisation, such as the introduction of HTS magnets in the collider rings or of permanent magnets in the damping ring, will further reduce the FCC-ee energy consumption.

The FCC-ee will be powered by a mixture of renewable and other carbon-free sources. Today, the electricity produced and consumed in France and Switzerland is already more than 90% carbon-free, an order of magnitude better than in most other countries [30]. By 2045, the electricity in France and Switzerland is expected to be 100% carbon free.

The FCC-ee power consumption can be rapidly and easily adjusted to the power available on the European electricity grid, by varying the number of bunches in the collider.

Lastly, the results from the"Mining the Future®" competition [31] have established several credible re-use pathways for the excavation materials (molasse), which, in combination with a local re-use scheme, promise material management with a low environmental and carbon footprint.

FUTURE UPGRADES AND USES

The FCC-ee is not only a Higgs, but also a Z and W factory ("TeraZ"). The upgrade to $t\bar{t}$ running is foreseen, at a cost of about 1 BCHF for additional systems.

In addition to the 4 baseline running modes listed in Table 1, another optional operation mode, presently under investigation for FCC-ee, is the direct s-channel Higgs production, $e^+e^- \to H$, at a centre-of-mass energy of 125 GeV, which would allow a direct measurement of the electron Yukawa coupling. Here, a monochromatization scheme should reduce the effective collision energy spread in order for the latter to become comparable to the width of the Higgs [32].

Following the FCC-ee, the FCC integrated programme foresees as a second stage, a hadron collider, FCC-hh, which shall provide proton-proton collisions at a centre-of-mass energy of at least 100 TeV. It will also enable heavy-ion collisions at the equivalent ion energy. The FCC-hh will be installed in the tunnel which earlier houses the FCC-ee and share/re-use much of the FCC-ee technical infrastructure, including electric distribution sytems, cooling and ventilation, RF, cryogenics, experimental caverns, etc. The sequence of FCC-ee and FCC-hh would support a comprehensive long-term program maximising physics opportunities.

Numerous other possible extensions are under study, such as lepton-proton and lepton-hadron collisions (FCC-eh) [25], LHC- and FCC-based Gamma factories [33], and a Lemma-type 100 TeV muon collider, FCC-$\mu\mu$ [34, 35], which could reuse key elements of the FCC-ee and FCC-hh accelerators.

FCC FEASIBILITY STUDY

The 2013 European Strategy Update (ESU) requested a Conceptual Design of the FCC, the four-volume report of which was delivered in 2019 [6, 25, 36], describing the physics cases, the design of the lepton and hadron colliders, and the underpinning technologies and infrastructures. Following the 2020 ESU [37], an FCC Feasibility Study (FCC

ISBN: 978-3-95450-236-3 ISSN: 2673-7027 doi:10.18429/JACoW-eeFACT2022-MOXAT0104

FS) has been launched by CERN Council in 2021 [38, 39], with a Feasibility Study Report (FSR) expected by the end of 2025. The FSR will address not only the technical design, but also numerous other key feasibility aspects, including tunnel construction, financing, and environment. The FSR will be an important input to the next European Strategy Update expected in 2026/27.

The FCC FS is organized as an international collaboration with, presently, about 150 participating institutes from around the world. The FCC FS and a possible future project will profit from CERN's decade-long experience with successful large international accelerator projects, e.g., the LHC and HL-LHC, and the associated global experiments, such as ATLAS and CMS.

REGIONAL ACTIVITIES

Concerning progress with regional activities [2], elected representatives from the French "départements" of Haute Savoie and Ain and from the Swiss Canton of Geneva visited CERN, while information meetings and exchanges were being organised with the presidents and prefects of Ain and Haute Savoie, in preparation of the next steps. All communities concerned by the FCC trace were approached directly via information letters co-signed by the Prefect of the region Auvergne-Rhone-Apes and by the CERN Director-General (DG) for France, and by the Conseiller d'État de Genève and the CERN DG for Switzerland. Consultations with individual communities are ongoing. Technical discussions on territorial implementation, water use, excavation material reuse, etc., have started with the French department no. 74, Haute Savoie.

OUTLOOK

A comprehensive R&D program and implementation preparation is presently being carried out in the frameworks of the FCC FS, the EU co-financed FCC Innovation Study, the Swiss CHART program, and the CERN High-Field Magnet Programme.

The first stage of FCC could be approved within a few years after the 2027 Strategy Update, if the latter is supportive. The tunnel construction could then start in the early 2030s and the FCC-ee physics program begin in the second half of the 2040s, a few years after the completion of the HL-LHC physics runs expected by 2041.

ACKNOWLEDGEMENTS

This talk was given on behalf of the global FCC Collaboration, and reports work from close to 2000 international experts. We are indebted, in particular, to I. Agapov, A. Blondel, M. Boscolo, O. Brunner, J.-P. Burnet, I. Chaikovska, P. Charitos, P. Craievich, M. Giovannozzi, A. Grudiev, J. Gutleber, K. Hanke, M. Hofer, P. Janot, J. Keintzel, M. Koratzinos, R. Losito, V. Mertens, K. Oide, J. Osborne, P. Raimondi, T. Raubenheimer, D. Shatilov, F. Sonnemann, and T. Watson for helpful discussions and material included in this article.

REFERENCES

[1] F. Zimmermann, M. Benedikt, K. Oide, and T. O. Raubenheimer, "The Electron-Positron Future Circular Collider (FCC-ee)," Albuquerque, New Mexico, USA, Aug. 2022, presented at NAPAC'22, Albuquerque, New Mexico, USA, Aug. 2022, paper TUZD1.

[2] M. Benedikt and F. Zimmermann, *FCC Feasibility Study*, 10th ECFA Newsletter, `https://ecfa.web.cern.ch/sites/default/files/10th\%20ECFA\%20Newsletter_v6.pdf`, 2022.

[3] The CEPC Study Group, *CEPC Conceptual Design Report: Volume 1 - Accelerator*, arXiv: 1809.00285, 2018, `doi:10.48550/ARXIV.1809.00285`

[4] M. Boscolo, H. Burkhardt, and M. Sullivan, "Machine detector interface studies: Layout and synchrotron radiation estimate in the future circular collider interaction region," *Phys. Rev. Accel. Beams*, vol. 20, p. 011 008, 1 2017, `doi:10.1103/PhysRevAccelBeams.20.011008`

[5] K. Oide *et al.*, "Design of beam optics for the future circular collider e^+e^- collider rings," *Phys. Rev. Accel. Beams*, vol. 19, p. 111 005, 11 2016, `doi:10.1103/PhysRevAccelBeams.19.111005`

[6] A. Abada *et al.*, "FCC-ee: The Lepton Collider: Future Circular Collider Conceptual Design Report Volume 2," *Eur. Phys. J. ST*, vol. 228, no. 2, pp. 261–623, 2019, `doi:10.1140/epjst/e2019-900045-4`

[7] E. Gianfelice-Wendt, "Investigation of beam self-polarization in the future e^+e^- circular collider," *Phys. Rev. Accel. Beams*, vol. 19, p. 101 005, 10 2016, `doi:10.1103/PhysRevAccelBeams.19.101005`

[8] A. Blondel and E. Gianfelice, "The challenges of beam polarization and keV-scale centre-of-mass energy calibration at the FCC-ee," *Eur. Phys. J. Plus*, vol. 136, p. 1103, 2021, `doi:10.1140/epjp/s13360-021-02038-y`

[9] A. Blondel, P. Janot, J. Wenninger, *et al.*, "Polarization and Centre-of-Mass Energy Calibration at FCC-ee," *arXiv 1909.12245*, 2019.

[10] M. Zobov *et al.*, "Test of "Crab-Waist" Collisions at the DAΦNE Φ Factory," *Phys. Rev. Lett.*, vol. 104, p. 174 801, 17 2010, `doi:10.1103/PhysRevLett.104.174801`

[11] Y. Funakoshi *et al.*, "The SuperKEKB has Broken the World Record of the Luminosity," Bangkok, Thailand, Jun. 2022, IPAC'22, Bangkok, Thailand, Jun. 2022, paper MOPLXGD1.

[12] H. Burkhardt and R. Kleiss, "Beam Lifetimes in LEP," in *Proc. EPAC'94*, London, UK, Jun.-Jul. 1994, pp. 1353–1356.

[13] B. Richter, "Very high-energy electron-positron colliding beams for the study of the weak interactions," *Nucl. Instrum. Methods*, vol. 136, 47–60. 31 p, 1976, `doi:10.1016/0029-554X(76)90396-7`

[14] I. Syratchev, F. Peauger, I. Karpov, and O. Brunner, "A Superconducting Slotted Waveguide Elliptical Cavity for FCC-ee," version 1.0, 2021, `doi:10.5281/zenodo.5031953`

[15] M. Boscolo, *FCC-ee IR MOCK-UP*, FCC-EIC Joint & MDI Workshop, 26 Oct. 2022 `\https://indico.cern.ch/event/1186798/contributions/5074714/`, 2022.

[16] I. Agapov *et al.*, "Future Circular Lepton Collider FCC-ee: Overview and Status," 2022, `doi:10.48550/ARXIV.2203.08310`

[17] P. Craievich *et al.*, "The FCCee Pre-Injector Complex," Bangkok, Thailand, Jun. 2022, presented at IPAC'22,

ISBN: 978-3-95450-236-3 ISSN: 2673-7027 doi:10.18429/JACoW-eeFACT2022-MOXAT0104

Bangkok, Thailand, Jun. 2022, paper WEPOPT063.

[18] M. Bai *et al.*, *C^3: A "Cool" Route to the Higgs Boson and Beyond*, arXiv: 2110.15800, 2021.

[19] B. Humann *et al.*, "Radiation Load Studies for the FCC-ee Positron Source with a Superconducting Matching Device," Bangkok, Thailand, Jun. 2022, presented at IPAC'22, Bangkok, Thailand, Jun. 2022, paper THPOTK048.

[20] W. Kang *et al.*, "Development of the CEPC booster prototype dipole magnets," *Int. J. Mod. Phys. A*, vol. 36, no. 22, p. 2 142 008, 2021, doi:10.1142/S0217751X21420082

[21] D. Marx *et al.*, "Designing the EIC Electron Storage Ring Lattice for a Wide Energy Range," Bangkok, Thailand, Jun. 2022, presented at IPAC'22, Bangkok, Thailand, Jun. 2022, paper WEPOPT042.

[22] F. Willeke and J. Beebe-Wang, "Electron Ion Collider Conceptual Design Report 2021," 2021, doi:10.2172/1765663

[23] Y. Ohnishi, "Status and perspectives of the SuperKEKB project," *presented at EPS-HEP2021*, 2021.

[24] M. Dam, "Detector R&D requirements for future circular high energy e^+e^- machine, presented as ECFA Detector R&D Roadmap Input from Future Facilities," 2021, https://indico.cern.ch/event/994685/

[25] A. Abada *et al.*, "FCC-hh: The Hadron Collider: Future Circular Collider Conceptual Design Report Volume 3," *Eur. Phys. J. ST*, vol. 228, no. 4, pp. 755–1107, 2019, doi:10.1140/epjst/e2019-900087-0

[26] M. Benedikt, A. Blondel, P. Janot, et al., "Future circular colliders succeeding the LHC," *Nature Physics*, vol. 16, p. 402, 2020, doi:10.1038/s41567-020-0856-2

[27] P. Janot and A. Blondel, "The carbon footprint of proposed e+e- Higgs factories," *Eur. Phys. J. Plus*, vol. 137, p. 1122, 2022, doi:10.1140/epjp/s13360-022-03319-w

[28] S. Aull *et al.*, "Electrical Power Budget for FCC-ee," in *7th IPAC*, 2016, pp. 3828–3831, doi:10.18429/JACoW-IPAC2016-THPOR024

[29] J. P. Burnet, "Update of the power demand for fcc-ee," *FCC Week 2022, Paris*, 2022, https://indico.cern.ch/event/1064327

[30] Carbon Brief web site, https://www.carbonbrief.org/

[31] Mining the Future, https://indico.cern.ch/event/1001465/

[32] A. Faus-Golfe, M. Valdivia Garcia, and F. Zimmermann, "The Challenge of Monochromatization Direct s-Channel Higgs Production: $e^+e^- \rightarrow H$," *Eur. Phys. J. Plus*, vol. 137, 31 2022, doi:10.1140/epjp/s13360-021-02151-y

[33] M. W. Krasny, *The Gamma Factory proposal for CERN*, arXiv: 1511.07794, 2015, doi:10.48550/ARXIV.1511.07794

[34] F. Zimmermann, "LHC/FCC-based muon colliders," *Journal of Physics: Conference Series*, vol. 1067, p. 022 017, 2018, doi:10.1088/1742-6596/1067/2/022017

[35] F. Zimmermann, A. Latina, A. P. Blondel, M. Antonelli, M. Boscolo, and J. P. Farmer, "Muon Collider Based on Gamma Factory, FCC-ee and Plasma Target," no. 13, p. 1691, presented at IPAC'22, Bangkok, Thailand, Jun. 2022, paper WEPOST009.

[36] A. Abada et al. (The FCC Collaboration), "FCC Physics Opportunities: Future Circular Collider Conceptual Design Report Volume 1," *European Physical Journal C*, vol. 79, 2019, doi:10.1140/epjc/s10052-019-6904-3

[37] European Strategy Group, "2020 Update of the European Strategy for Particle Physics (Brochure)," *CERN-ESU-015*, 2020, https://cds.cern.ch/record/2721370

[38] CERN Council, *Organisational structure of the FCC feasibility study. Restricted CERN Council - Two-Hundred-and-Third Session*, CERN/SPC/1155/Rev.2, 2021, http://cds.cern.ch/record/2774006

[39] CERN Council, *Main deliverables and timeline of the FCC feasibility study. Restricted CERN Council - Two-Hundred-and-Third Session*, CERN/SPC/1161, 2021, http://cds.cern.ch/record/2774007

ISBN: 978-3-95450-236-3 ISSN: 2673-7027 doi:10.18429/JACoW-eeFACT2022-MOXAT0105

CEPC ACCELERATOR TDR STATUS OVERVIEW

Yuhui Li
Institute of High Energy Physics, Beijing, China

Abstract

The Circular Electron-Positron Collider (CEPC) was proposed in the year of 2012, shortly after the observation of Higgs boson. After years of pre-studies, the CEPC study group has completed the Conceptual Design Report (CDR) in 2018. Since then a series of key technology R&D was carried out, and the accelerator design has been kept optimizing as well. The accelerator design can meet the scientific objectives by allowing the operation in different energies for W/Z, Higgs and ttbar with high luminosities. Key technologies required for the mass production have been developed, such as the superconducting accelerating cavities, high efficiency RF power source, magnets and vacuum systems etc. The accelerator Technical Design Report (TDR) is scheduled to be finished in the cross period of 2022-2023. All of the key technology R&D accomplishments will presented and the optimized accelerator parameters will be updated in it.

INTRODUCTION

The Higgs boson was discovered in July 2012. It plays an important role as the unique "elementary particle" in the SM. Chinese scientists proposed the Circular Electron-Positron Collider (CEPC) in September 2012. CEPC is an electron-positron Higgs factory which can produce 4 million Higgs bosons in a clean background, hence it will boost the precision of the Higgs by about 1 order of magnitude compare to HL-LHC. Except for Higgs, CEPC is expected to generate hundreds of millions W bosons, and 4 trillions of Z bosons with 4-5 orders of magnitude higher than that of the latest generation of the Large Electron Positron Collider. Moreover, CEPC can be upgraded in its center of mass energy to 360 GeV, and produces roughly 1 million top or anti-top quarks. Beyond the electron-positron collision, since the cross size of the CEPC tunnel is wide enough it can accommodate an independent proton-proton collider in the long term plan.

Since 2013, the CEPC has carried out design and key technology R&D. It has received total funding of roughly 260 million CNY from the MOST, the NSFC, the CAS, and some local governments. The Conceptual Design Report (CDR) was published in 2018 [1], followed by significant key technology achievements among the systems that require a high budget ratio in the accelerator construction. What's more, in the years after the CDR was released the design of CEPC was kept being optimized and its luminosity is competitive among the suggested Higgs factories in the world, as shown in Fig. 1.

CEPC aims at getting approved and then commencing the accelerator construction in the years between 2025-2030, thereby the machine operation and data collection can start in the decade of 2030's. Based on the achievements since the publication of CDR, the Technical Design Report (TDR) is planned to be finished in early 2023, in which the optimized accelerator design and the key technology R&D status will be presented in detail.

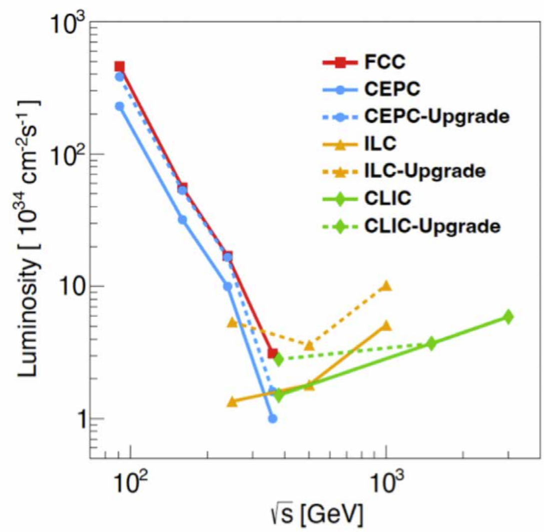

Figure 1: Comparison of the design luminosity of the CEPC and those of other electron-positron Higgs factories.

CEPC DESIGN

The majority CEPC accelerator complex consists of the 100 km collider and booster rings and the Linac including a positron damping ring as the injector. Table 1 lists the major parameters of CEPC at the power of 30 MW [2, 3].

Table 1: Margin Specifications

	Higgs	W	Z	top
Number of IPs	2	2	2	2
Circumference [km]	100	100	100	100
Energy [GeV]	120	80	45	180
Bunch number	249	1297	11951	35
Beam current [mA]	16.7	84.1	803.5	3.3
βx/βy at IP [m/mm]	0.33 /1	0.21 /1	0.13 /0.9	1.04 /2.7
Bunch length (SR/total) [mm]	2.3 /3.9	2.5 /4.9	2.5 /8.7	2.2 /2.9
Beam-beam parameters (ξx/ξy)	0.015 /0.11	0.012 /0.113	0.004 /0.127	0.071 /0.1
RF frequency [MHz]	650	650	650	650
Luminosity per IP [10^{34}/cm^2/s]	5.0	16	115	0.5

CEPC adopts a compatible design with the partial or full double-rings collider for electrons and positrons. A special

ISBN: 978-3-95450-236-3 ISSN: 2673-7027 doi:10.18429/JACoW-eeFACT2022-MOXAT0105

bypass scheme is designed to allow an easy switch in various operations of Higgs, W and Z. As shown in Fig. 2, in the stage 1 the 2-cells 650 MHz SRF accelerator modules are divided into two parts. In the operation of Higgs, electron and positron beams pass both parts and the energy loss caused by the Synchrotron Radiation (SR) is compensated. In the lower energy operations of W and Z the electron and positron beams only pass one part of the accelerator modules since the needed energy compensation is lower. In stage 2 the high luminosity Z operation, not only the 2-cells but also the 1-cell cavities are used. The 2-cells SRF module are placed at the centre of the RF station and the 1-cell modules are placed on both sides. In the Higgs and Z energy operations the beams pass all SRF modules while in the high luminosity Z operation beams only pass through the 1-cell modules. In this way the side effect of HOM is mitigated. Finally, in the stage 3 the ttbar upgrade operation, the additional 5-cell cavities are induced adjacent to the 2-cell modules that the 180 GeV beam can be kept in the storage ring.

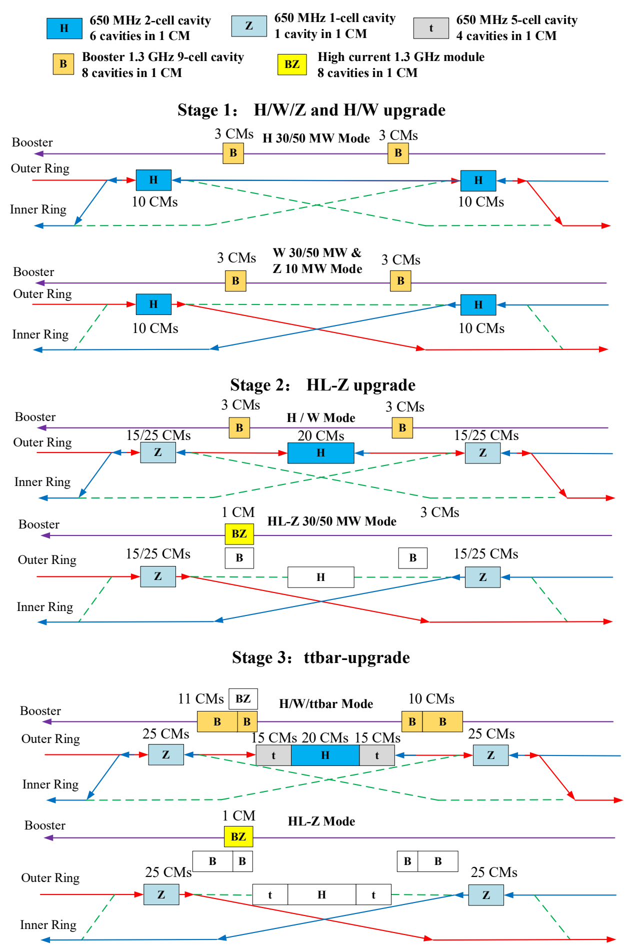

Figure 2: The bypass scheme for the RF station in different operations.

The optics is carefully optimized for all energies based on which high luminosities are expected [4]. The design of the interaction region provides local chromaticity and the crab-waist collision [5] is implemented. The FODO structure is applied to the arc region and the filling factor of dipoles in this region is maximized. In the operation of Higgs and ttbar the phase advance is 90/90 degrees and the aberration is cancelled. Whereas the phase advance in the operations of W and Z is 60/60 degrees. In the RF straight section a 75 m drift is reserved to transversely separate the electron/positron beams for about 10 cm. Two triplets are used to constrain the beta functions. The beams are further separated with dipoles outside of the drift space. The deflection of the outgoing beam is 35 cm in the Higgs mode while increasing to 1.0 m in the W and Z modes where the RF cryostat needs to be bypassed. The optics in half collider ring for all of the operation modes were designed and optimized. The beta and dispersion functions are shown in Fig. 3.

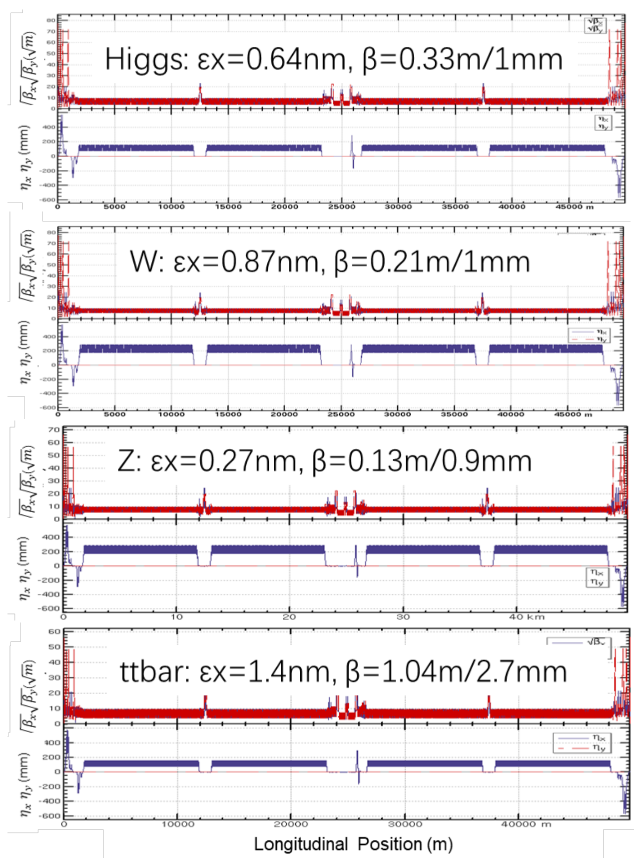

Figure 3: The half collider ring optics of all operation modes.

A certain Dynamic Aperture (DA) is required for the efficient injection and adequate beam life time. Systematic DA studies have been done for all operation modes. For example, The required DA for Higgs is $8\sigma_x \times 15\sigma_y \times 1.7\%$, event to the lattice with errors. Both magnet alignment and field errors were included for the simulations. By applying the closed orbit distortion correction and dispersion correction the errors are corrected and the required DA is feasible. Figure 4 shows the DA with bare lattice and with magnets errors.

ISBN: 978-3-95450-236-3 ISSN: 2673-7027 doi:10.18429/JACoW-eeFACT2022-MOXAT0105

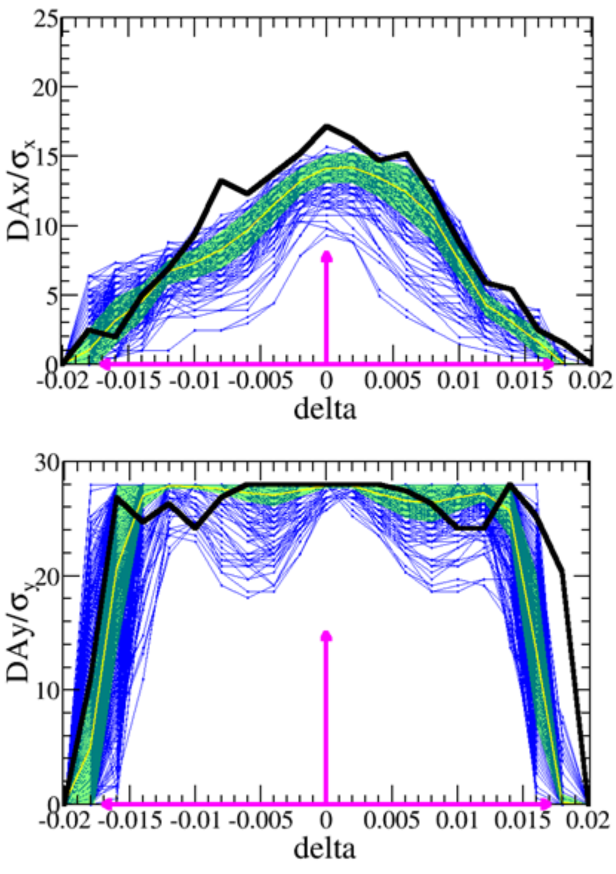

Figure 4: The Dynamic Apertures with respect to the energy deviation. The blue lines are DA with different simulated error seeds, yellow line is the mean value and the black line is the DA with bare lattice.

Beam-beam interactions impact the luminosity a lot. A number of beam parameters effect [6]. The comprehensive simulations were carried out. For example, the energy spread blows up and the bunch is lengthened due to the Beamstrahlung. Bunches are lengthened by the impedance as well which is also taken into accounted in the relevant simulations. For Higgs the beam-beam effect simulation is done with the luminosity of 5 x 10^{34}cm^{-2}s^{-1}. Figure 5 illustrates the luminosity and horizontal bunch size with respect to the horizontal tune. It is seen that the width of the stable tune area is 0.004, which satisfies the requirement.

Interaction of an intense charged particles with the vacuum chamber leads to collective instabilities. These instabilities degrade beam quality and expedite beam loss. The impedance thresholds for different operation modes are estimated. The limitation on the longitudinal broadband impedance mainly comes from the microwave instability and it results in bunch lengthening. Boussard or Keil-Schnell criteria is used to estimate the threshold of microwave instability. The limitation of the transverse broadband impedance mainly comes from the transverse mode coupling instability. Gaussian bunches are assumed and the threshold current is expressed with the transverse kick factor. The narrowband impedances are mainly contributed by the cavity alike structures. They induce coupled bunch instabilities in both longitudinal and transverse planes. The limitation on the shunt impedance of a HOM is evaluated in the resonant condition.

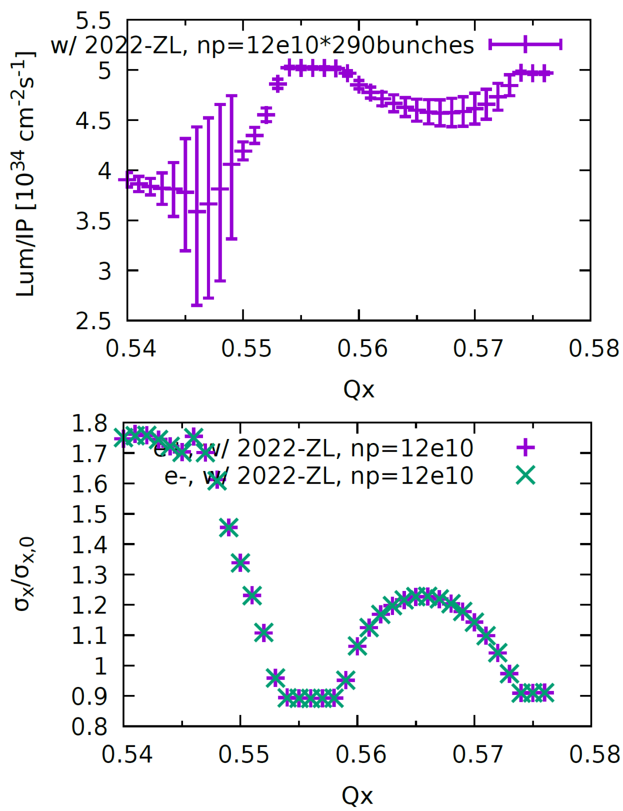

Figure 5: The luminosity and the beam size with respect to the horizontal tune.

According to the collider design, the impedance and wake are calculated both with formulas and with numerical codes. The microwave instability degrades the luminosity by lengthening the bunch and increasing the energy spread. The transverse mode coupling instability is estimated with the Eigen mode analysis which gives the dependence of the head-tail mode frequencies with respect to the bunch intensity. Careful simulations demonstrate that the transverse coupling effect is tolerable. To the narrow band instabilities one dominant contribution is the resonance of the transverse resistive wall impedance at zero frequency. The threshold exists at the high luminosity operation of Z pole where the most dangerous instability mode is about 2 ms much faster than the radiation damping of 840 ms. Therefore, an effective transverse feedback system is required for the correction. Another important narrow band impedance is contributed by the RF HOMs. The threshold value mainly depends on the actual tolerances of the cavity construction. With a HOM frequency scattering of 1 MHz, all the transverse and longitudinal modes below the cut-off frequency can be well damped for all operation scenarios. Other instabilities such as electron cloud effects, beam-ion instability were also investigated.

The booster raises the electron/positron output energy of the linac to different target collider operation energies

ISBN: 978-3-95450-236-3 ISSN: 2673-7027 doi:10.18429/JACoW-eeFACT2022-MOXAT0105

(Higgs, W, Z and ttbar). In the high luminosity optimization, the linac extraction energy increases from 10 GeV, the CEPC-CDR baseline, to 30 GeV. The booster is accommodated in the same 100 km tunnel together with the collider, hanging on the tunnel ceiling. The booster not only fills the empty collider but also top-up injects bunches for the beam loss compensation in the collider. The on-axis scheme is used for the injection from the linac to booster and the Higgs injection from the booster to collider. The off-axis injection is adopted for the other energies from the booster to collider. The most sophisticated procedure is the top-up injection for Higgs: in the first step 240 bunches are injected from the linac, followed by the second step that 7 bunches are selected and extracted from collider to booster and the bunches from linac and collider merge by damping, then they are injected back to the collider. These steps iterate until all bunches in collider are full of charge.

In order to meet the beam dynamics requirement two types of lattice were investigated for the booster arc cells. One is FODO and the other is TME (Theoretical Minimum Emittance). It turns out that TME lattice brings larger DA and requires lower magnet cost. Thereby TME is chosen. The Dynamic Aperture is calculated and shown in Fig. 6. The thick solid lines are the DA with bare lattice at different energy deviations. The dot lines indicate the shrunken DA with 100 error seeds simulation of magnets misalignment and field imperfection where close orbit distortion and dispersion correction were applied. The centre half elliptical circle indicates the least requirement of DA and it is well satisfied.

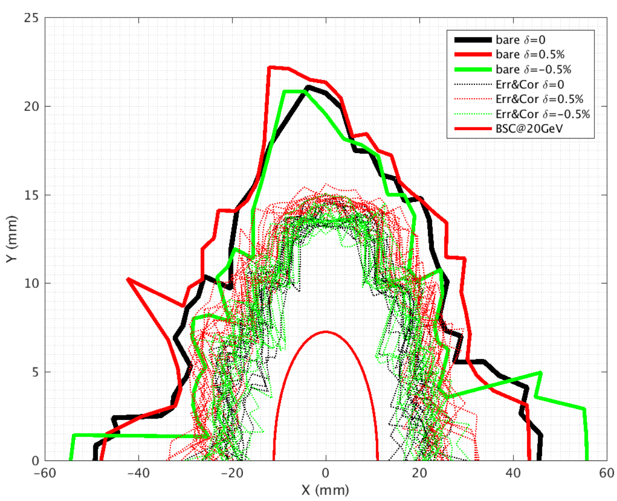

Figure 6: The booster DA with bare lattice and errors.

In the CEPC-CDR the linac uses normal conducting S-band cavities with the frequency of 2860 MHz to accelerate 10 GeV electron/positron energy. However, the correlated study for the booster dipole reveals that the economical iron-based magnet does not satisfy the quality requirement. It only works for the higher energy than 20 GeV. For this reason, the linac energy is increased from 10 to 30 GeV which allows the use of the diluted iron dipoles for the mass production. Moreover, the linac mainly uses C-band accelerator to increase the beam energy with high gradient.

KEY TECHNOLOGY R&D

Since 2013, the CEPC has carried out a series of key technology R&D. The fanatical support from various funding sources boosted the relevant studies in a wide range, covering most of the systems, such as RF power source, superconducting RF cavity, magnet system, vacuum chamber and so on. In addition, a significant part of the technology required by CEPC was validated in other large-scale accelerator facilities that the Institute of High Energy Physics (IHEP) is in charge of.

Among these key technology studies the high efficiency klystron is one of the most important exploration. The standard klystron energy transfer rate is about 60%. With an improved efficiency of 80% the P-band klystron along will save the operation fee more than 100 M CNY per year. Except for the economic benefit, the higher efficiency also makes CEPC an environmental friendly facility. For this purpose, the research team has planned three prototypes. The first one aims at a 650 MHz klystron with the standard 60% energy transfer rate. The second klystron aims at the high efficiency of 77% and the third one takes use for the Multi-Beam-Klystron (MBK) technology to reach the efficiency of 80%. The first prototype accomplished its commissioning in 2021 and the efficiency is 62%. The second prototype is still in the test and the efficiency already reached 70.5%. The third MBK prototype has been designed and is in the manufacture. Figure 7 shows the efficiency of the second klystron prototype with respect to the input voltage.

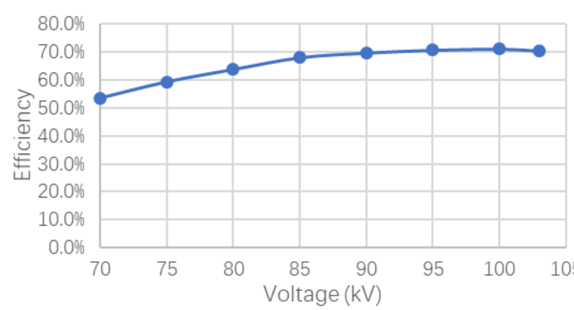

Figure 7: The 2nd klystron prototype efficiency *vs* input voltage.

CEPC relies on high quality superconducting RF cavity. Not only the widely used 9-cell 1.3 GHz but also the 1/2-cell 650 MHz superconducting RF cavities were developed in-house. Important technology breakthroughs have been achieved in the past years and the technology reaches states-of the-art level. As an example, Fig. 8 shows the test results of three 1-cell 650 MHz SRF cavities with different surface treatments such as EP and middle temperature annealing. The quality factor with respect to the acceleration field, voltage and the peak surface field is demonstrated, which exceed the specifications of CEPC. Efforts are continuously spent to reach even higher Q factor at high gradient.

The CEPC booster share the 100 km tunnel with the collider and lots of civil construction fee is saved. However, the ultra-long booster needs very weak dipoles to ramp up

ISBN: 978-3-95450-236-3 ISSN: 2673-7027 doi:10.18429/JACoW-eeFACT2022-MOXAT0105

low energy beams: the minimum beam energy of 20 GeV asks for 56 Gs dipole field. It is very weak field and the prototype with anisotropic steel shows that the field homogeneity is better than 0.1% and fulfils the specification. With higher injection energy to the booster of 30 GeV, the cheaper isotropic steel can be used and can heavily reduce the construction fee. Figure 9 shows the weak field dipole cross section and the field distribution.

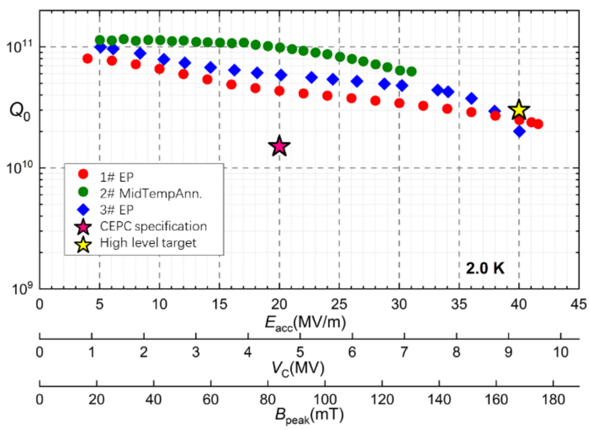

Figure 8: Q factor with respect to the acceleration field, voltage and peak field for three 650MHz 1-cell prototype.

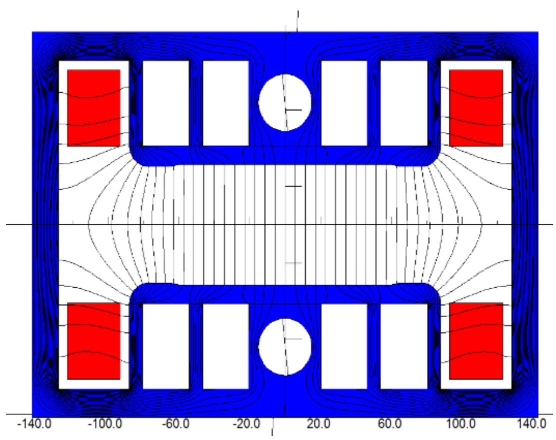

Figure 9: The cross section of the weak field dipole and its field distribution.

SUMMARY

Since the CEPC-TDR publication in 2018 the accelerator team has kept on the design optimization in a consistent way and the key technology R&D. The lattice and collision design were updated and higher luminosities at different energies are foreseen. The baseline SR power is 30 MW but the design is upgradable to the higher power of 50 MW. A series of key technology R&D has been carried out as well. The fruitful achievement of the pre-studies as well as the experience accumulated from other large-scale accelerator facilities undertook by IHEP guarantees the readiness of construction around the year of 2026.

ACKNOWLEDGEMENT

This overview paper is presented on behalf of the CEPC accelerator team. The relevant materials including the table data, plots etc. are collected from various talks given by the CEPC colleagues.

REFERENCES

[1] CEPC Study Group, "CEPC Accelerator CDR", arXiv:1809.00285 [physics.acc-ph], 2018. doi:10.48550/arXiv.1809.00285

[2] J. Gao, "CEPC and SppC Status from the completion of CDR towards TDR", *Int. J. Mod. Phys. A*, vol. 36, no. 22, p. 2142005, 2021. doi:10.1142/S0217751X21420057

[3] CEPC Accelerator Study Group, "Snowmass 2021 White Paper AF3-CEPC", arXiv:2203.09451[physics.acc-ph], 2022. doi:10.48550/arXiv.2203.09451

[4] Yiwei Wang *et al.*, "Lattice design for the CEPC double ring scheme", *Int. J. Mod. Phys. A*, vol. 33, no. 2, p. 1840001, 2018. doi:10.1142/S0217751X18400018

[5] M. Zobov *et al.*, "Test of "Crab-Waist" Collisions at the DAΦNE Φ Factory", *Phys. Rev. Lett.*, vol. 104, p. 174801, 2010. doi:10.1103/PhysRevLett.104.174801

[6] Yuan Zhang *et al.*, "Self-consistent simulations of beam-beam interaction in future e⁺e⁻ circular colliders including beamstrahlung and longitudinal coupling impedance", *Phys. Rev. Accel. Beams*, vol. 23, p. 104402, 2020. doi:10.1103/PhysRevAccelBeams.23.104402

ISBN: 978-3-95450-236-3 ISSN: 2673-7027 doi:10.18429/JACoW-eeFACT2022-MOXAT0106

REALIZATION, TIMELINE, CHALLENGES AND ULTIMATE LIMITS OF FUTURE COLLIDERS

V. Shiltsev[1,*], Fermilab, Batavia, IL 60510, USA

Abstract

This paper consists of two parts: in first, we briefly summarize the US particle physics community planning exercise "Snowmass'21" that was organized to provide a forum for discussions among the entire particle physics community to develop a scientific vision for the future of particle physics in the U.S. and its international partners. The Snowmass'21 Accelerator Frontier activities include discussions on high-energy hadron and lepton colliders, high-intensity beams for neutrino research and for "Physics Beyond Colliders", accelerator technologies, science, education and outreach as well as the progress of core accelerator technologies, including RF, magnets, targets and sources. We also discuss main outcomes of the Snowmass'21 Implementation Task Force which was changed to carry our comparative evaluation of future HEP accelerator facilities, their realization strategies, timelines, and challenges.

In the second part, we present an attempt to evaluate limits on energy, luminosity and social affordability of the ultimate future colliders - linear and circular, proton, electron positron and muon, based on traditional as well as on advanced accelerator technologies.

SNOWMASS'21

Snowmass is a particle physics community study that takes place in the US every 7-9 years (the last one was in 2013). The Snowmass'21 study (the name is historical, originally held in Snowmass, Colorado) took place in 2020-22, it was organized by the the American Physical Society divisions (DPF, DPB, DNP, DAP, DGRAV) and strived to define the most important questions for the field and to identify promising opportunities to address them, to identify and document a scientific vision for the future of particle physics in the U.S. and its international partners - see [1]. The P5, Particle Physics Project Prioritization Panel, chaired by H.Murayama (UC Berkeley), has taken the scientific input from Snowmass'21 to develop (by the Spring of 2023) a strategic plan for U.S. particle physics that can be executed over a 10 year timescale in the context of a 20-year global vision for the field.

Snowmass'21 activities are managed along the lines of ten "Frontiers": Energy Frontier (EF), Neutrino Physics Frontier (NF), etc, with the Accelerator Frontier (AF) among them. More than three thousand scientists have taken part in the Snowmass'21 discussions and about 1500 people participated in the final Community Summer Study workshop (Seattle, July'22) in person and remotely. In general, the international community was very well represented and many scientists from Europe and Asia have been either organizers of sessions and events, or conveners of topical groups, or submitted numerous Letters of Interest (short communications) or White Papers (extended input documents).

* shiltsev@fnal.gov

More than 300 Letters of Interest and 120 White Papers have been submitted to the Snowmass'21 AF topical groups. There were more than 30 topical workshops, 8 cross-Frontier *Agoras* (5 on various types of colliders: $e+e-/\gamma\gamma$, linear/circular, $\mu\mu$, pp, advanced ones and three on experiments and accelerators for rare processes physics), and several special cross-Frontier groups were organized such as *the eeCollider Forum, the Muon Collider Forum, the Implementation Task Force* (see below), the 2.4MW proton power upgrade design group at FNAL, etc.

Most important outcomes of the Snowmass AF deliberations are presented in the topical groups' reports and summarized in the Accelerator Frontier report (all available in [2]):

Facilities for Neutrino Frontier: The needs of neutrino physics call for the next generation, higher-power, megawatt and multi-MW-class superbeams facilities. There is a broad array of accelerator and detector technologies and expertise to design and construct a 2.4 MW beam power upgrade of the Fermilab accelerator complex for the LBNF/DUNE Phase II, a world leading neutrino experiment, expand the volume of Liquid Argon detectors by 20 ktons, and build a new neutrino near-detector on the Fermilab site.

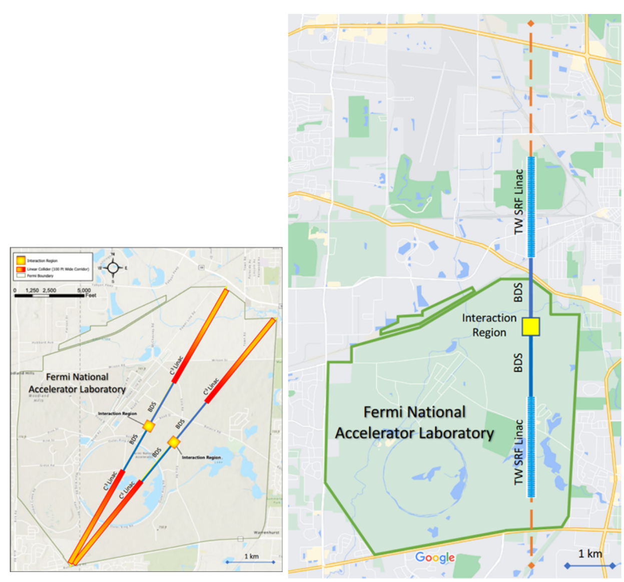

Figure 1: Possible placements of future linear e^+e^- Higgs/EW factory colliders C^3 and HELEN on the Fermilab site map - both about the same length: (left) 250 GeV c.m.e. options with a 7-km footprint, and (right) higher c.m. energy options (12 km dashed line) (from the AF report [2]).

ISBN: 978-3-95450-236-3 ISSN: 2673-7027 doi:10.18429/JACoW-eeFACT2022-MOXAT0106

Facilities for Rare Processes Frontier: Several possibilities for Rare Processes Frontier (searches for axions, charged lepton flavor violation, dark matter) have been identified that call for broad use of existing and future facilities, such as the SLAC 4-8 GeV electron linac, Fermilab's PIP-II proton linac beam and PAR (PIP-II Accumulator Ring), etc.

Facilities for the Energy Frontier: The Energy Frontier community calls for an active program toward post-LHC colliders. In particular, the world community has called for a Higgs/EW Factory as the next major accelerator project and this might be followed by a O(10 TeV/parton c.m.e.) collider. At present, there are as many as eight Higgs/EW factories under consideration, and also about two dozen energy frontier collider concepts that go beyond HL-LHC in their discovery potential.

In the course of the AF discussions, clearly identified was the need of an integrated future collider R&D program in the US DOE Office of HEP to engage in the design and to coordinate the development of next generation collider projects such as: FCC-ee (circular collider), C3/HELEN/CLIC (linear Higgs factory colliders, the first two fitting the Fermilab site - see Fig.1), multi-TeV Muon Collider, and FCC-hh, in order to enable an informed choice by the next Snowmass/P5 ca. 2030. The proposal of such a program will need to be approved by the P5.

General Accelerator R&D, Education, and Training Major goals for the accelerator R&D for the next decade have been identified as: a)development of efficient high intensity high brightness $e+$ sources and multi-MW proton targets for neutrino production (2.4 MW for PIP-III, 4-8 MW for a future muon collider); b) design and testing of 16 T dipoles, 40T solenoids, and $O(1000\ \mathrm{T/s})$ fast cycling magnets; c) development of efficient RF sources and 70-150 MV/m C^3 and 70 MV/m TW SRF cavities and structures, exploration and testing of new materials with the potential of sustaining higher gradients with high Q_0; d) demonstration of collider quality beams in advanced acceleration methods, efficient drivers and staging, and development of self-consistent parameter sets of potential far-future colliders based on wakefield acceleration in plasma and structures; e) focus in the beam physics should be on experimental, computational and theoretical studies on acceleration and control of high intensity/high brightness beams, high performance computer modeling and AI/ML approaches, and design integration and optimization, including the overall energy efficiency of future facilities.

There is also a recognized need to strengthen and expand education and training programs, enhance recruiting (especially international talent), promote the field (e.g., via colloquia at universities), and creating a national undergraduate level recruiting program structured to draw in women and underrepresented minorities (URM), with corresponding efforts at all career stages to support, include and retain them in the field.

	CME (TeV)	Lumi per IP (10^34)	Years, pre-project R&D	Years to 1st Physics	Cost Range (2021 B$)	Electric Power (MW)
FCCee-0.24	0.24	8.5	0-2	13-18	12-18	280
ILC-0.25	0.25	2.7	0-2	<12	7-12	140
CLIC-0.38	0.38	2.3	0-2	13-18	7-12	110
HELEN-0.25	0.25	1.4	5-10	13-18	7-12	110
CCC-0.25	0.25	1.3	3-5	13-18	7-12	150
CERC(ERL)	0.24	78	5-10	19-24	12-30	90
CLIC-3	3	5.9	3-5	19-24	18-30	~550
ILC-3	3	6.1	5-10	19-24	18-30	~400
MC-3	3	2.3	>10	19-24	7-12	~230
MC-10-IMCC	10-14	20	>10	>25	12-18	$O(300)$
FCChh-100	100	30	>10	>25	30-50	~560
Collider-in-Sea	500	50	>10	>25	>80	»1000

Figure 2: Main parameters of the submitted Higgs factory proposals (FCCee, ILC, CLIC, C^3, HELEN, and CERC - ERL based collider in the FCCee tunnel) and multi-TeV colliders (CLIC, ILC, 3 TeV and 10 TeV c.m.e. Muon Collider options, FCChh, and 1900-km circumference "Collider in the Sea"). Years of the pre-project R&D indicate required effort to get to sufficient technical readiness. Estimated years to first physics are for technically limited timeline starting at the time of the decision to proceed. The total project cost ranges are in 2021$ (based on a parametric estimator and without escalation and contingency). The peak luminosity and power consumption values have not been reviewed by ITF and represent proponent inputs. (Adapted from the ITF report [3].)

Implementation Task Force

A very important and useful development of the Snowmass'21 Accelerator Frontier was organization of the Implementation Task Force [3] charged with developing metrics and processes to facilitate comparisons between projects. More than 30 collider concepts have been comparatively evaluated by the ITF using parametric estimators to compare physics reach (impact), beam parameters, size, complexity, power, environment concerns, technical risk, technical readiness, validation and R&D required, cost and schedule – see Fig. 2. The significant uncertainty in these values was addressed by giving a range where appropriate. Note that by using the proponent-provided luminosity and power consumption values (for a fully operational facility including power consumption of all necessary utilities), ITF chose not to evaluate the risk of not achieving this aspects of facilities' performance.

The years of required pre-project R&D is just one aspect of the technical risk, but it provides a relevant and comparable measure of the maturity of a proposal and an estimate of how much R&D time is required before a proposal could be considered for a project start (CD0 in the US system). The time to first physics in a technically limited schedule includes the pre-project R&D, design, construction and commissioning of the facility, and is most useful to compare the scientific relevance of the proposals.

ISBN: 978-3-95450-236-3 ISSN: 2673-7027 doi:10.18429/JACoW-eeFACT2022-MOXAT0106

The total project cost follows the US project accounting system *but without escalation and contingency*. Various parametric models were used by ITF to estimate this cost, including the cost estimated by the proponents. The cost estimate uses known costs of existing installations and reasonably expected costs for novel equipment. For future technologies, pre-project cost reduction R&D may further reduce the cost estimates used by the ITF.

ON ULTIMATE COLLIDERS

Charged particle colliders – arguably the most complex and advanced scientific instruments – have been at the forefront of scientific discoveries in high-energy and nuclear physics since the 1960s [4]. There are seven colliders in operation and the Large Hadron Collider now represents the "accelerator energy frontier" with its 6.8 TeV energy per beam, $2.1{\cdot}10^{34}$ cm^{-2}s^{-1} luminosity and some 1.2 TWh of annual total site electric energy consumption. The Super-KEKB is an asymmetric e^+e^- B-factory with 4 and 7 GeV beam energies, respectively. Since the startup in 2018, it has achieved the world record luminosity (for any collider type) of $4.7{\cdot}10^{34}$ cm^{-2}s^{-1}, and aspires to reach $60{\cdot}10^{34}$ cm^{-2}s^{-1}– a whopping 30-times over its predecessor KEK-B (1999-2010).

Naturally, the question of the limits of the colliding beams technique of of utmost importance for long-term planning of the particle physics. From the discussion above, one can see the some future energy frontier colliders have been discussed as part of the Snowmass'21 AF and ITF discussions, namely: the 3 TeV CLIC option (100 MV/m accelerating gradient, 50 km long), a 10-14 TeV c.m.e. $\mu^+\mu^-$ collider (10-14 km circumference, 16 T magnets), two roughly 100 km circumference pp colliders - SPPC in China (75-125 TeV c.m.e., based on 12-20 T IBS SC magnets) and FCChh at CERN (100 TeV, 16-17 T Nb_3Sn SC dipoles), and "Collider in Sea" (500 TeV, 1900 km, ~ 4 T magnets). Are those machines at the limit of colliders? Which factors set those limits? Are they different for different types of colliders (linear, circular, lepton, hadron, etc)? Discussion on these important questions has been ongoing for over a decade - see, e.g., in Refs. [4–8].

Any of the future collider projects constitute one of, if not, the largest science facility in particle physics. The cost, the required resources and, maybe most importantly, the environmental impact in the form of large energy consumption will approach or exceed the limit of affordability. The discussion below is a modest update of the analysis Ref. [7] and starts with general introduction to the issue: definitions of the scope and units, approaches to the limits of on the energy, luminosity, and social cost of the ultimate colliders. Then, we take a more detail look into the limits of the circular pp, ee and $\mu\mu$ colliders, linear and plasma-based $ee, \gamma\gamma, \mu\mu$ ones, and briefly discuss exotic schemes, such as the crystal muon colliders. The social cost considerations (power consumption, financial costs, availability of experts, carbon footprint and time to construct) are best defined for the machines based on existing core accelerator technologies (RF and magnets), and less so for the emerging or exotic technologies (ERLs, plasma, crystals, etc).

Each type of the ultimate future colliders to be evaluated on base of feasibility of energy E, feasibility of luminosity L, and feasibility of the cost C. For each machine type (technology) we start with the current state-of-the-art machines – see Ref. [4] – and attempt to make several (1,2,...) orders of magnitude steps in the energy and see how that affects the luminosity and the cost. This study does not include discussion on where are the lower limits on the luminosity or the upper limits of the cost.

Units and Limits on E, L and C

Everywhere below we will use TeV for the units for E, understood as the c.m.e. equal to twice the beam energy. The units of L are ab^{-1}/yr that is equal, e.g., 10^{35} cm^{-2}s^{-1} over 10^7 sec/yr. For reference, the HL-LHC will deliver 0.3 ab^{-1}/yr. Due to spread of expectations for the machine availability, there might be a factor of ~2 uncertainty in peak luminosity demands for any ab^{-1}/yr value. The units of total facility electric power consumption are TWh/yr and, e.g., at present CERN with operational LHC takes requires P=200MW of the average power and 1.1-1.3 TWh/yr. The cost is evaluated in "LHC-Units". 1 LHCU is the cost of the LHC construction (≃10B$). The cost of large accelerators is set by the scale (energy, length, power) and technology. Typically, accelerator components (NC or/and SC magnets and RF systems) account for 50 ± 10% of the total cost, while the civil construction takes 35 ± 15%, and power production, delivery and distribution technology adds the remaining 15 ± 10% [9]. While the last two parts are mostly determined by industry, the magnet, RF and wakefield accelerator technology is a linchpin of the progress of accelerators and would dominate the accelerator cost without progress from the R&D programs. For most of the future machines, the cost is estimated using $\alpha\beta\gamma$ model $C = \alpha\sqrt{Length} + \beta\sqrt{Energy} + \gamma\sqrt{Power}$ that is claimed to end up with good estimate within a $O(2)$ range [9]. While the $\alpha\beta\gamma$ model still needs to be properly extended to the advanced technologies (plasma, lasers, crystals, etc), it was found to be within a factor of 2 w.r.t. more detail models used in the ITF analysis of the three dozens of already proposed medium- and far-future machines [3].

Synchrotron radiation sets up the first limit of the energy reach if one demands the SR loss per turn to be less than the total beam energy $\Delta E \le E/2$. That defines the absolute c.m.e. limit for the circular colliders as :

$$E[\mathrm{TeV}] \le (m/m_e)^{4/3}(R/10[\mathrm{km}])^{1/3} \;, \qquad (1)$$

that is ~1 TeV for electrons, some 1.2 PeV for muons ($m \approx 210 m_e$) and 25 PeV for protons ($m \approx 2000 m_e$), R is the radius of the machine. Beyond these energies, the colliders will have be linear (thus, needing no dipole magnets). Other energy limits are set by the survival of the particles. Indeed, if, for example, an advanced 5 TeV linear collider consist of

ISBN: 978-3-95450-236-3 ISSN: 2673-7027 doi:10.18429/JACoW-eeFACT2022-MOXAT0106

M = 1000 5 GeV acceleration stages, then the stage-to-stage transfer efficiency must be better than $\eta = 1 - 1/M$. Also, if the particles are unstable with the lifetime at rest τ_0, then to guarantee delivery to the collision point, the minimum accelerator gradient must significantly exceed $G \gg mc/\tau_0$ – that is, e.g., 0.3 MeV/m for muons and 0.3 TeV/m for tau-leptons [5]. Of course, inevitable might be corollary limits as higher E usually demands higher C, P or facility size. For example, the machine of 100 km circumference with $B \leq$ 16T magnets will have $E \lesssim$ 100 TeV; or 40,000 km circumference with 1 T magnets will have $E \lesssim$ 2.6 PeV; or a linear accelerators with the total length limit of 50 km and gradient $G \leq$ 0.1 GV/m will stay under $E \lesssim$ 5 TeV; or under $E \lesssim$ 10 PeV if the length is 10 km and $G \leq$ 1 TV/m.

Performance (luminosity) reach of the ultimate colliders can be limited by a large number of factors and effects – particle production, beamstrahlung, synchrotron radiation power per meter, IR radiation damage, neutrino-radiation dose, beam instabilities, jitter/emittance growth, etc – which are machine specific and will be considered below. But the most fundamental is the limit on the total beam power $P_b = f_0 n_b N \gamma m c^2$. Indeed, from the standard luminosity formula $L = f_0 n_b N^2/4\pi\sigma^2$ one gets:

$$L = P_b^2/(4\pi\gamma n_b \varepsilon \beta^* m^2 c^4) \propto P_b^2/E\,, \qquad (2)$$

see [4] for standard description of the variables. The luminosity scaling with energy $L \propto 1/E$ in Eq.(2) is markedly different from the usual HEP requirement for the luminosity to follow the cross-section scaling $L \propto E^2$.

Of course, there are societal limits on the machine's total cost, total "carbon footprint" and environmental impact. While the total cost C is dependent on the technology (core accelerator technology, civil construction technology, power production, delivery and distribution technology, etc), the probability of (a technically feasible) facility scales down with the cost, possibly as $\propto C^2/(1 + C^\kappa)$, with $\kappa \approx 4 - 5$ as for the real estate sales price distributions. Also, to note: i) the costs of civil construction and power systems are mostly driven by larger economy, ii) having an injector complex available (sometimes up to 1/3 of the total cost) results in potential factor of 2 in the energy reach; iii) the collider cost is usually relatively weak function of luminosity (the latest example is the HL-LHC 1B$ project that will increase luminosity of the 10B$ LHC by a factor of 5); iv) so, one can consider starting future machines with high E and relatively low L in anticipation of eventual performance upgrades (e.g., CESR and Tevatron witnessed L increase by a factor of $O(100)$, LHC by a factor ≥10, etc); v) C is a moderate function of length/circumference; vi) cost is a strong function of E and technology.

Construction time of large accelerator projects to date is usually between 5 and 11 years and approximately scales as $T \propto \sqrt{C}$ [3]. It is often limited by the peak annual spending rate, at present thought to be O(0.5 B$/yr) – compare to the world's global HEP budget 4B$ – and on the number of available technical experts (now, about 4500 worldwide). Technical commissioning time ("one particle reaches the design energy") can be as short as one-few years – and it is shorter for known technologies and longer for new ones and for larger number of accelerator elements. Progress towards the design (or ultimate) luminosity is dependent on the machine's "complexity" [10] and for the luminosity risk of 100 (ratio of initial to ultimate L) it can take as long as $T \approx ln(100) \cdot 2$=9 yrs - see also corresponding discussion in the ITF report [3].

Ultimate Colliders

Below we attempt to explore ultimate limits of various types of future colliders.

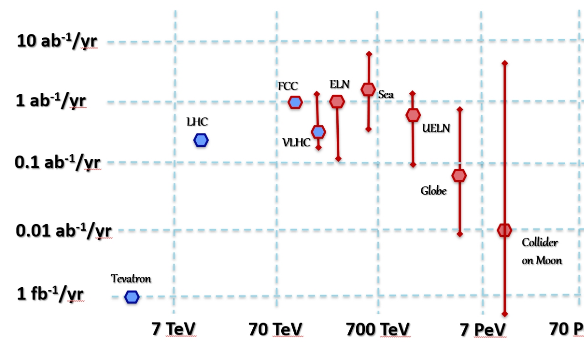

Figure 3: Estimated performance of the circular pp colliders vs c.m.energy.

Circular pp colliders Tevatron (E=2 TeV, B =4.5T, 6.3 km circumference) and 14 TeV LHC (8T, 27km) can be used as reference points while discussing future circular pp colliders. Also, there are parameter sets available for SCC (40 TeV, 6.6T, 87km), SppC (75 TeV, 12T, 100km), FCC-hh (100 TeV, 16T, 100km), VLHC (175 TeV, 12T, 233km), Eloisatron (200 TeV, 10T, 300km), "Collider-in-Sea" (500 TeV, 4T, 1,900km),a very old E.Fermi's concept of "Globaltron" (3-5 PeV, ~1T, 40,000km)) [4,11], and, since very recently, collider on Moon (14PeV=14,000 TeV, 20 T, 11,000km) [12]. Often cited advantages of such colliders are known technology and beam physics and good power efficiency in terms of ab^{-1}/TWh. Their major limitations include i) large size (related to the magnetic field B technological limit), ii) high total facility power; iii) high cost; iv) beam-beam effects, beam burn-off, and instabilities; v) synchrotron radiation power P_{SR} deposition in the SC magnets environment. Considering the beam-beam limit ξ and the P_{SR} per meter to be the major luminosity limitations, one gets $L \propto (\xi/\beta^*)(P_{SR}/2\pi R)(R^2/\gamma^3))$. Fig. 3 presents estimates of performance of circular pp colliders vs c.m.energy. Power consumption of these colliders approaches 3 TWh/yr (about 3 times the LHC one) starting at the 100 TeV FCC. Cost optimization of these gargantuan machines usually ends up with the estimates exceeding 2 LHCU above about E =30 TeV. Of course, under continuous exploration are such cost saving ideas as superferric magnets, permanent magnets, better/cheaper conductors (such as, e.g., iron-based SC cables),

ISBN: 978-3-95450-236-3 ISSN: 2673-7027 doi:10.18429/JACoW-eeFACT2022-MOXAT0106

graphene, etc. It is highly questionable at present whether they can result in a factor of ~5 saving in the magnet cost per (Tm).

Circular ee Colliders

Due to quickly growing SR power with E, circular ee colliders have very limited energy range to expand, even with the use of the ERL technologies [13]. For example, a E ~1 TeV machine will be need to be big (~200-300 km circumference), low luminosity O(10-100 fb^{-1}/yr) and require a lot of expensive RF acceleration, that would drive its cost above 2-3 LHCU.

Circular $\mu\mu$ Colliders

There are parameter sets available for 1.5, 3, 6, 10, 14 TeV circular $\mu\mu$ colliders [4]. Their major advantages are thought to be [14]: i) factor of ×7 in equivalent E reach compared to pp colliders; ii) arguably the best power efficiency in terms of ab^{-1}/TWh and iii) traditional core technologies. Major limitations include efficient muon production, fast muon cooling and potential neutrino radiation hazard.

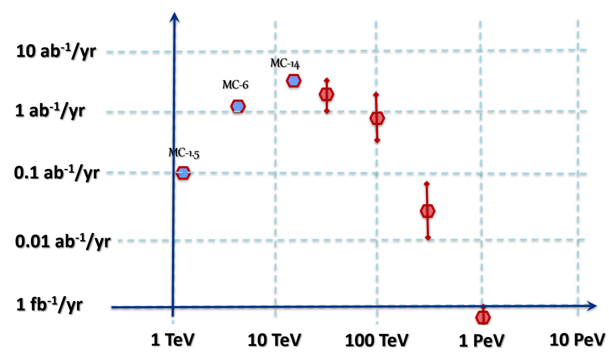

Figure 4: Estimated performance of the circular $\mu\mu$ colliders.

For the muon colliders $L \propto B$ and grows with the average particle production rate $dN/dt = f_r N$. At some energy, neutrino radiation dose $D \propto (dN/dt)E^3/\Phi$ sets the limit and the ultimate luminosity depends on suppression "neutrino flux dilution factor Φ, which some believe can be as high as 10-100:

$$L \propto B \frac{D\Phi}{E^2} \frac{N}{4\pi\epsilon_n\beta^*} . \tag{3}$$

That results in a scaling with energy as $L \propto 1/E^k$, where k=1...2 depending on whether the beta-function at the IP can be reduced as $\beta^* \propto 1/E$ – see Fig. 4. Above approximately 14-30 TeV, the power consumption of the muon colliders exceeds 2 TWh/yr and the construction cost estimates goes over 2 LHCU.

Traditional and Advanced Linear ee Colliders

In principle, linear colliders (LCs) can operate in e^+e^-/e^-e^- and $\gamma\gamma$ regimes (muons are possible, but their sources are expensive and of limited production rate; protons are possible, too, but pp collisions lose factor of 7 ineffective c.m. energy reach w.r.t. leptons) and be based on the NC RF, SC RF, plasma, wakefields, etc. Major advantages of such machines are: i) no SR power losses; ii) RF acceleration is a well developed technology. Their major limitations include: i) luminosity scales with total beam power as $L \propto (P/E)(N_\gamma/\sigma_y)$, ii) the last factor (N_γ/σ_y) determines the beamstrahlung energy spread while small beam size - often used to compensate for the loss of luminosity with E - makes jitter tolerances extremely challenging [15]; iii) plasma and wakefield acceleration is not fully matured acceleration technique yet (there are many unknowns such as the energy staging, production and acceleration of e^+, power efficiency of large facilities, cost, etc). Of course, there are some appealing alternatives under study: positron production and acceleration in plasma can be avoided by switching to ee operation and conversion into $\gamma\gamma$ at the IP, the beamstrahlung issues can be solved by colliding ultrashort bunches or switching to $\gamma\gamma$ or $\mu\mu$, etc. But in general, there are always some unavoidable challenges and limits, such as instabilities in the RF structures or plasma cells, jitter/emittance control problems that grow with the number of cells and elements, smaller and smaller beam sizes are required at the IP (approaching the limit of 1 A) [16].

Figure 5 presents estimated luminosities of very high energy linear lepton colliders, starting with the 1 TeV ILC (40 km) and 3 TeV CLIC (50 km). The cost of the latter is already 2.5 LHCU and P is about 3 TWh/yr. Higher energy 10-30 TeV LCs based on beam-plasma, laser-plasma and dielectric plasma wakefield acceleration – see Ref. [3, 17–19]), not speaking of 100 TeV and 1 PeV options, are extremely power hungry and costly beyond any reasonable limits on P and C.

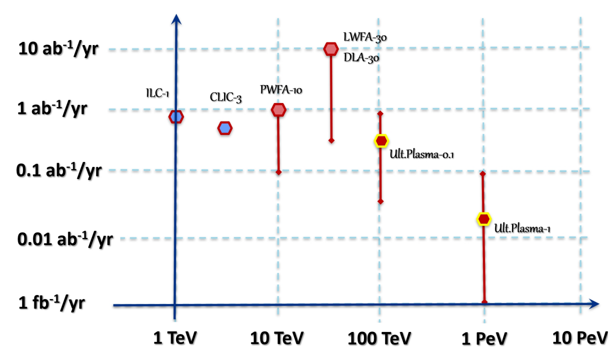

Figure 5: Estimated performance of the linear lepton colliders.

Exotic Linear $\mu\mu$ Colliders

An interesting opportunity of acceleration of muons in structured solid media, e.g., CNTs or crystals [20], promises extreme gradients 1-10 TV/m, continuous focusing and acceleration (no cells, one long channel, particles get strongly cooled betatron radiation), small facility size (10 km for 10 TeV) - and, therefore, promise of low cost - but very low luminosity 0.001-0.1 ab^{-1}/yr at best - see Fig. 6. Of course,

ISBN: 978-3-95450-236-3 ISSN: 2673-7027 doi:10.18429/JACoW-eeFACT2022-MOXAT0106

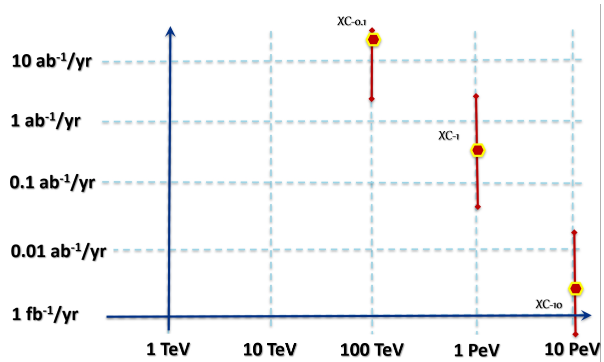

Figure 6: Estimated performance of the linear crystal $\mu\mu$ colliders.

such exotic technique is still under study [21] and awaits the proof-of-principle E336 experiment at the FACET-II [22].

SUMMARY

Recent US particle physics community planning exercise “Snowmass’21" was extremely instrumental as a forum for discussions among the entire particle physics community to develop a scientific vision for the future of particle physics. In particular, the Snowmass’21 Accelerator Frontier outlined community views on future high-energy hadron and lepton colliders, high-intensity beams for neutrino research and for “Physics Beyond Colliders”, beam physics, education and outreach as well as pointed out most promising directions in core accelerator technologies R&D, including RF, magnets, targets and sources. The Snowmass’21 Implementation Task Force report which presented a comparative evaluation of three dozens of proposed future HEP accelerator facilities, their realization strategies, timelines, and challenges, and has become a very useful document for the strategic HEP Planning.

Our analysis of ultimate limits of colliders emphasized the primary factors such as attainment of the highest possible energy E, high luminosity L and within socially affordable C. The cost is critically dependent on core acceleration technology. Employment of already existing injectors and infrastructure can greatly help to reduce C. For most collider types we found that the pursue of high energy typically results in low(er) luminosity. For example, one should not expect more than 0.1-1 ab^{-1}/yr at $E \geq 30$ TeV to 1 PeV. In the luminosity calculations, one might also assume the total facility (and, therefore, the beam) annual power consumption should better be limited to 1-3 TWh/yr.

For the considered collider types we found that : i) for circular pp colliders the overall $E-L-C$ feasibility limit is close or below 100 TeV (~14 TeV cme per parton); ii) for circular ee colliders the limit is below ~1 TeV; iii) for circular $\mu\mu$ colliders the limit is about 30 TeV; iv) for linear RF-based lepton colliders as well as for plasma $ee/\gamma\gamma$ colliders the limit is between 3 and 10 TeV; v) there are exotic schemes, such as crystal channeling muon colliders, which have promise of 0.1-1 PeV c.m.e. though with small Luminosity. All in all, muons seems to be the particles of choice the future ultimate HEP colliders [23].

ACKNOWLEDGEMENTS

This paper is mostly based on various reports and summaries of the Snowmass’21 "Accelerator Frontier" (which author was co-convener of, together with Steve Gourlay and Tor Raubenheimer [2, 25]), presentation at the Snowmass Workshop on the "Physics Limits of Ultimate Beams" [24] (January 22, 2021), IPAC’21 presentation [7] and recent review [4]. Author greatly appreciates input from and very helpful discussion on the subject of this paper with F. Zimmermann, M. Bai, W. Barletta, S. Gourlay, V. Kashikhin, V. Lebedev, M. Palmer, T. Raubenheimer, D. Schulte and A. Zlobin.

This manuscript has been supported by the Fermi Research Alliance, LLC under Contract No. DE-AC02-07CH11359 with the U.S. Department of Energy, Office of Science, Office of High Energy Physics.

REFERENCES

[1] Snowmass’21, `https://snowmass21.org/`

[2] Snowmass Accelerator Frontier, `https://snowmass21.org/accelerator/`

[3] T.Roser*et al.*, “Report of the Snowmass 2021 collider implementation task force”, *arXiv preprint arxiv:2208.06030*. `doi:10.48550/arXiv.2208.06030`

[4] V.Shiltsev and F.Zimmermann, “Modern and future collider”, *Rev. Mod. Physics*, vol. 93, no. 1, p. 015006, 2021. `doi:10.1103/RevModPhys.93.015006`

[5] V.Shiltsev, “High-energy particle colliders: past 20 years, next 20 years, and beyond”, *Physics Uspekhi*, vol. 55, no. 10, p.1033, 2012. `doi:10.3367/UFNe.0182.201210d.1033`

[6] F.Zimmermann, “Future colliders for particle physics — ‘Big and small’ ”, *Nucl. Instrum. Methods A*, vol. 909, p.33, 2018. `doi:10.1016/j.nima.2018.01.034`

[7] V. D. Shiltsev, “General Approach to Physics Limits of Ultimate Colliders”, in *Proc. 12th Int. Particle Accelerator Conf. (IPAC’21)*, Campinas, Brazil, May 2021, pp. 2624–2627. `doi:10.18429/JACoW-IPAC2021-WEPAB017`

[8] M. Bai, F. Zimmermann, and V. D. Shiltsev, “Ultimate limits of future colliders”, presented at the North American Particle Accelerator Conf. (NAPAC’22), Albuquerque, New Mexico, USA, Aug. 2022, paper TUZD3, unpublished.

[9] V. Shiltsev, “A phenomenological cost model for high energy particle accelerators”, *J. Instrum.*, vol. 9, p. T07002, 2013. `doi:10.1088/1748-0221/9/07/T07002`

[10] V. Shiltsev, “On performance of high energy particel colliders and other complex scientific systems”, *Mod. Phys. Lett. A*, vol. 26, no. 11, p. 761, 2011. `doi:10.1142/S0217732311035699`

[11] W. Barletta, “Maximizing the luminosity of eloisatron, a hadron supercollider at 100 TeV per beam”, *AIP Conf. Proc.*, vol. 351, no. 1, p. 56, 1996. `doi:10.1063/1.49331`

ISBN: 978-3-95450-236-3 ISSN: 2673-7027 doi:10.18429/JACoW-eeFACT2022-MOXAT0106

[12] J. Beacham and F. Zimmermann. “A very high energy hadron collider on the Moon”, *New J. Phys.* vol. 24, no. 2, p. 023029, 2022. 10.1088/1367-2630/ac4921

[13] V. Litvinenko, T. Roser, and M. Chamizo-Llatas, “High-energy high-luminosity e+ e collider using energy-recovery linacs"”, *Phys. Lett. B* vol. 804, p. 135394, 2020. doi:10.1016/j.physletb.2020.135394

[14] K. Long *et al.*, “Muon colliders to expand frontiers of particle physics”, *Nature Physics*, vol. 17, p.289, 2021. doi:10.1038/s41567-020-01130-x

[15] T. Raubenheimer, “Estimates of emittance dilution and stability in high-energy linear accelerators”, *Phys. Rev. Spec. Top. Accel. Beams*, vol. 3, p. 121002, 2000. doi:10.1103/PhysRevSTAB.3.121002

[16] D.Schulte, “Application of advanced accelerator concepts for colliders”, *Rev. Accel. Sci. Tech.*, vol. 9, p. 209, 2016. doi:10.1142/S1793626816300103

[17] C. Schroeder *et al.*, “Physics considerations for laser-plasma linear colliders”, *Pys. Rev. Spec. Top. Accel. Beams*, vol. 13, p. 101301, 2010. doi:10.1103/PhysRevSTAB.13.101301

[18] Input to the European Strategy Particle Physics Update 2018-2020, Granada, Spain, May 2019, #007a, https://cafpe.ugr.es/eppsu2019/

[19] C. Geddes, M. Hogan, P. Musumeci, and R. Assmann, “Report of Snowmass 21 Accelerator Frontier Topical Group 6 on Advanced Accelerators”, *arXiv preprint arxiv:2208.13279*. 10.48550/arXiv.2208.13279

[20] T. Tajima and M. Cavenago, “Crystal x-ray accelerator”, *Phys. Rev. Lett.*, vol. 59, p. 1440, 1987. doi:10.1103/PhysRevLett.59.1440

[21] T.Tajima *et al.* (eds.), *Beam Acceleration in Crystals and Nanostructures*, World Scientific, 2020.

[22] R. Arinello *et al.*, “Channeling acceleration in crystals and nanostructures and studies of solid plasmas: new oppportunities”, *arXiv preprint arxiv:2203.07459*. doi:10.48550/arXiv.2203.07459

[23] I.Strakovsky *et al.*, *Modern Muon Physics: Selected Issues*, Nova, 2020.

[24] C. Schroeder *et al.*, “Physics Limits of Ultimate Beams”, https://indico.fnal.gov/event/47217/

[25] S. Gourlay, T. Raubenheimer, and V. Shiltsev, “Challenges of future accelerators for particle physics research”, *Front. Phys.*, p. 557, 2022.

ISBN: 978-3-95450-236-3 ISSN: 2673-7027 doi:10.18429/JACoW-eeFACT2022-MOXAT0107

FUTURE PROJECTS FOR THE NEXT GENERATION TAU-CHARM FACTORIES IN CHINA AND RUSSIA*

Q. Luo, School of Nuclear Science and Technology and National Synchrotron Radiation Laboratory, University of Science and Technology of China, Hefei, China

Abstract

Based on the key scientific questions in the frontier of particle physics field, the current status and future development trend globally and domestically of accelerator-based particle physics experiments, new generation electron-positron colliders in tau-charm energy region (around 4 GeV center-of-mass) are proposed both in China and Russia. This paper discussed the general collision scheme and the key issues of accelerator physics and technologies. Also, the accelerator research and the progress of the projects in Russia and China are presented.

INTRODUCTIONS

As we know, there're two frontiers for accelerator-based particle physics. One is high energy frontier, in which scientists search for new physics beyond the standard model with very high beam energy. Meanwhile, a super particle factory usually refers to a collider which operates in the high luminosity frontier of particle physics with relatively lower energy. With a center-of-mass energy of around 4 GeV (tau-charm region), the super particle factory collider will operate in the quantum chromodynamics (QCD) perturbative and non-perturbative transition region and have unique features, such as rich resonance structures, threshold production, quantum correlation, etc, and will provide unique opportunities to study the internal structure of hadrons and explore the nature of non-perturbative QCD, to measure charge-parity (CP) violations and test the electroweak models precisely, and search for the new physics beyond-standard-model [1]. As the most successful tau charm factory of the world, the Beijing Electron Positron Collider II (BEPCII) will finish its historical mission in the next decade and certainly need a successor. Therefore, a new super tau charm factory which will have abundant physics program and great potential for scientific discoveries in high energy physics fields is required. It is expected to achieve major breakthroughs in tau-charm and hadron physics fields in future.

Both Chinese and Russian scientists have made their efforts in conceptual design study of the next generation tau charm factory and applied for funds to develop key technologies and construct test facilities since 2010s. Scientists from other countries also played an important part in related discussion. There're annual international joint workshops since the year 2018, first held in Paris, then Moscow and Hefei.

* Work supported by the National Key Research and Development Program of China (2022YFA1602201), the international partnership program of the Chinese Academy of Sciences Grant No. 211134KYSB20200057 and "the Fundamental Research Funds for the Central Universities".
† luoqnig@ustc.edu.cn

As a next generation facility, a super tau charm factory will be a dual-ring electron-positron collider with high current symmetric and flat beams, which have very small transversal size at interaction point (IP) so as to reach 50-100 times as BEPCII's luminosity. Compared to head-on collision and large emittance beams for BEPCII, the new super tau charm factory will utilize a fundamentally new scheme called Crab Waist and large Piwinski angle [2, 3]. Although this scheme has been successfully applied in low luminosity situation by the Φ-factory DAΦNE (INFN LNF, Frascati) [4], there're still a lot of work to do if we want to achieve much higher current and luminosity in tau-charm region, especially based on SuperKEKB experience [5]. This paper discusses the key issues of accelerator physics and technologies and presented the progress of the accelerator research and the situation of the projects in China and Russia.

MAJOR CHALLENGES FOR SUPER TAU CHARM ACCELERATORS

The new approach of large Piwinski angle and Crab Waist (CW) scheme allows raising the luminosity by one or two orders of magnitude without significant increase in the intensity of the beams or the dimensions of the installation or decrease in the bunch length. The idea was first offered by P. Raimondi, M. Zobov and D. Shatilov [6], see Fig. 1.

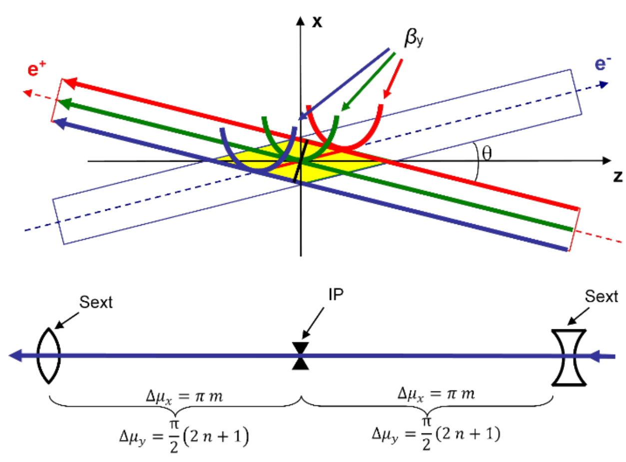

Figure 1: Large Piwinski angle and Crab Waist.

The theoretical luminosity satisfies $L = \frac{\gamma}{2er_e} \cdot \frac{I_{tot}\xi_y}{\beta_y^*} R_H$. With a Piwinski angle $\phi = \sigma_z/\sigma_x \tan(\theta/2)$ large enough, the hourglass effect will be suppressed and the bunch length doesn't have to be decreased. Crab waist sextupoles suppress the betatron and synchro-betatron resonances so the luminosity is increased [7].

ISBN: 978-3-95450-236-3 ISSN: 2673-7027 doi:10.18429/JACoW-eeFACT2022-MOXAT0107

Based on experience since then, there're several major challenges for the accelerator complex.

Since the bunch current is relatively high and the bunch size is very small at IP, the collective effects will increase and the beam instability should be carefully dealt with.

Due to strong focusing in interaction region, there will be local chromatic correcting sextupoles, together with the crab sextupoles, they will introduce strong non-linearity, which will reduce the apertures.

Beam lifetime due to Bremsstrahlung is not decisive in super tau charm factories. But both the dynamic aperture and energy aperture will be smaller than they are in last generation colliders such as BEPCII, result in much shorter Touschek lifetime.

Generally speaking, the key accelerator physics and technologies involved in a super tau charm accelerator can be categorized into the following three parts:

Firstly, physics and technologies for high peak luminosity. A physical design of storage rings that can achieve high enough peak luminosity. Devices to compress the bunch in the interaction region, such as a double-aperture superconducting magnet with high precision in the interaction region, superconducting solenoids and collimators.

Secondly, technologies of advanced beam instrumentations and diagnostics to ensure the stable operation of the accelerator and adequate integrated luminosity accumulation. Such as feedback system to suppress the instabilities and increase the current limit, fast feedback at the interaction point, precision measurement (submicron) of bunch transversal size to monitor the beam blow-up, and other important beam diagnostic devices.

Last, to meet the requirements of top-up operation, the physical design and key technologies of injectors that offer high current, low emittance and high-quality electron and positron beams for the storage ring. For example, a photocathode gun with large charge, low emittance and enough repetition rate will be a good choice of electron source if we want to achieve lower injecting background and high quality positron beam.

THE SUPER TAU CHARM FACILITY IN CHINA

General Description

The Super Tau Charm Facility (STCF) has a center-of-mass energy of covering 2 to 7 GeV and a peak luminosity of 1×10^{35} cm^{-2} s^{-1} at a center-of-mass energy of 4 GeV and was firstly proposed in the year 2013. In 2018-2021, the Chinese scientists completed a preliminary physical design report. The STCF consists of an accelerator, including double storage rings of circumference approximately 800 m, a linear injector of length approximately 400 m, and a particle spectrometer. The planned STCF is estimated to have an approximate cost of 4.5 billion RMB for construction, taking approximately 10 years for technology research and development (R&D) as well as construction, and of a territory covering area one km square.

Physical Design Progress

The preliminary physical design progress was published in 2021 [8]. After that several modifications had been made. The Hybrid 7BA (H-7BA) was altered to high order achromat H-7BA to get larger dynamic aperture and momentum aperture. The tune between CCY and Final Doublet (FD) was changed, with additional sextupoles at small β position, to get large momentum aperture. A higher harmonic cavity was adopted to control the bunch length so as to adjust the beam-beam effects and get the optimum luminosity. Table 1 shows the beam parameters under further optimization.

Table 1: STCF Accelerator Parameters

Parameters	**Value**
Peak Luminosity	1×10^{35} cm^{-2} s^{-1}
Beam Energy	2 GeV optimized 1-3.5 GeV tunable
Circumference	617.06 m
Current	2 A
Beam Emittance $\varepsilon_x/\varepsilon_y$ (with IBS)	4.29/0.02 nm·rad
β_x^*/β_y^*	90/0.6 mm
Crossing Angle	60 mrad
Bunch Length	10 mm with IBS
ξ_y	0.1
$\tau_{Touschek}$	200 s

Figure 2 shows the lattice function and layout of the STCF.

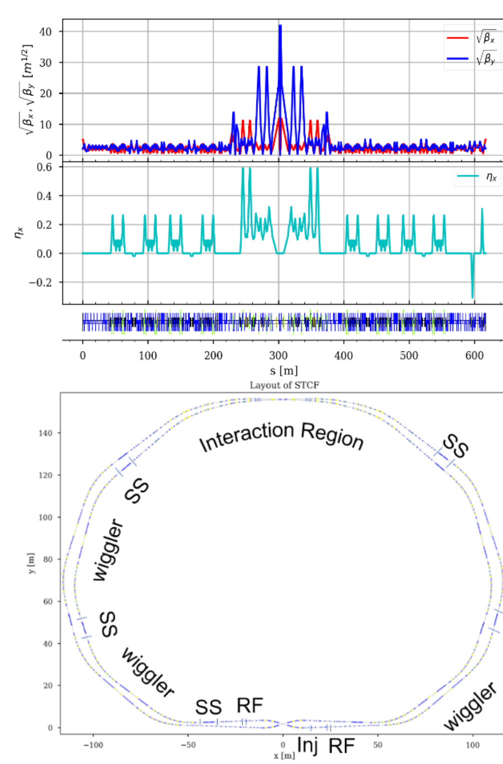

Figure 2: STCF lattice and layout.

ISBN: 978-3-95450-236-3 ISSN: 2673-7027 doi:10.18429/JACoW-eeFACT2022-MOXAT0107

Figure 3 shows the dynamic aperture on and off momentum with crab sextupoles on and off. The Touschek lifetime was increased from 35s to 200s after new IR and arcs were adopted.

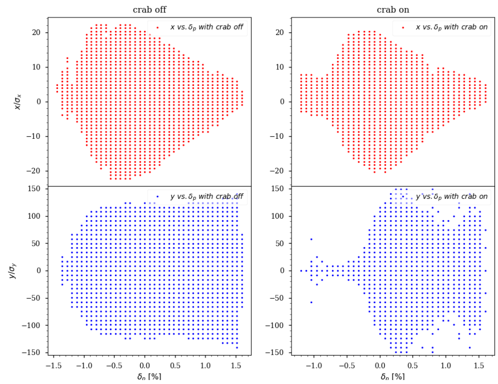

Figure 3: STCF dynamic apertures.

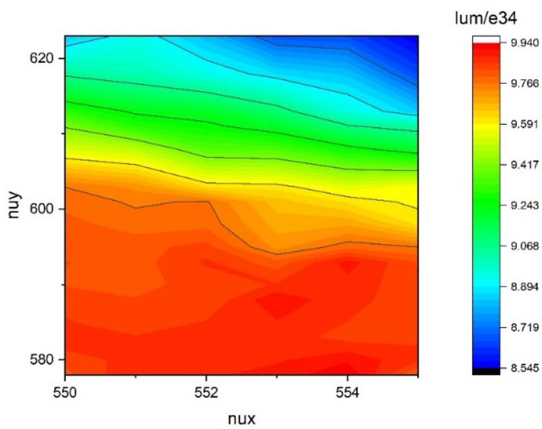

Figure 4: First STCF beam simulations results.

The preliminary beam simulation results, Fig. 4, showed that in a range of 37.550~37.555 ν_x and 27.575~27.590 ν_y a higher than 0.95×10^{35} $cm^{-2}\,s^{-1}$ luminosity can be achieved after 3 times as damping time.

Future Plans

We can see that further work is still needed to get better lifetime and aperture. So, in next several years accelerator physics will be a key point. Also, three series of key techniques should be prepared.

Recently, Anhui Province is actively supporting the key technology R&D of STCF, and considering to see the STCF as part of the "Fifteenth Five Year Plan" at Hefei Comprehensive National Science Center. The full R&D and construction process will be divided into three stages: at the R&D stage (2023-2025), scientists will finish a technical design report and a test facility of high intensity injector, then apply for full support to build the whole facility. At the second stage (2026-2032) the main accelerators will be built and achieve a luminosity of about 5×10^{34} $cm^{-2}\,s^{-1}$ pilot. At the third stage, after an upgrade, a luminosity of 1×10^{35} $cm^{-2}\,s^{-1}$ will be achieved with the electron beam longitudinally polarized at the IP.

THE SUPER CHARM TAU FACTORY AT BINP

General Description

The Super Charm Tau Factory (SCTF) at Novosibirsk is a project of new colliding beam experiment proposed in Budker Institute of Nuclear Physics (BINP). In 2011, scientists from BINP had published their first version of CDR [9], with Machine Detector Interface (MDI) design, lattice optimization and high performance operation at all energies. In 2018, the second version of CDR had upgraded the lattice design and given more technical details [10]. From 2019 to now, the SCTF is under technical design stage, finished further optimization work, showed shorter rings, better dynamics, realistic design of MDI, lens and injection facility [11, 12]. Differs from STCF in China, SCTF will be a more ambitious project with a luminosity of 1×10^{35} $cm^{-2}\,s^{-1}$ at almost all energy range and with a polarized electron beam in the first place.

Conceptual and Technical Design Progress

Figure 5 shows the lattice function and layout of the BINP STCF.

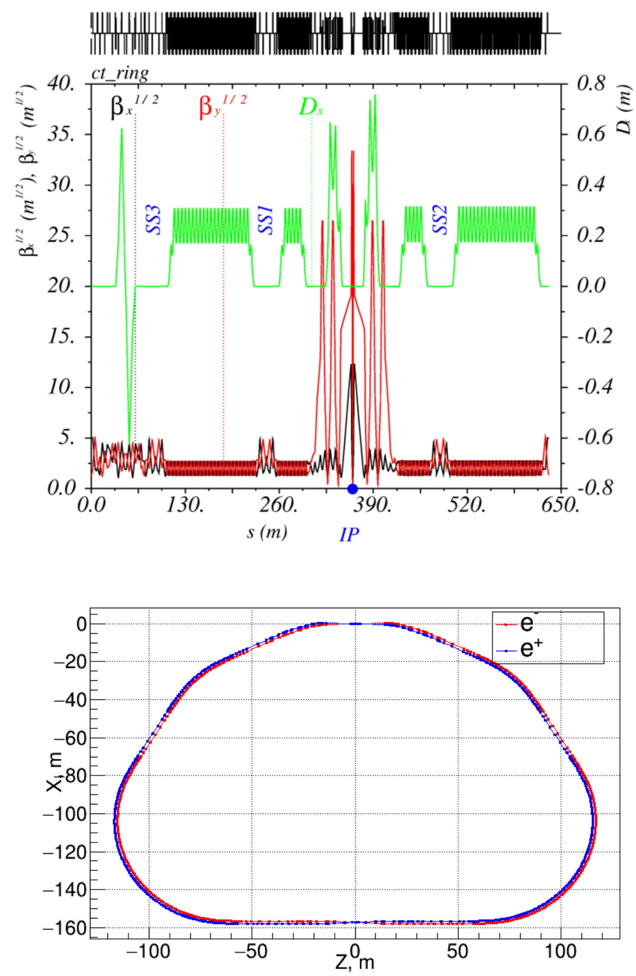

Figure 5: SCTF lattice and layout.

ISBN: 978-3-95450-236-3 ISSN: 2673-7027 doi:10.18429/JACoW-eeFACT2022-MOXAT0107

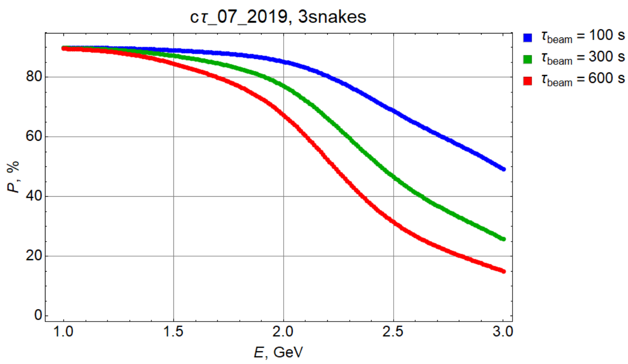

Figure 6: SCTF polarization simulation.

From Fig. 6 we can see that the linear lattice and parameters provide the desired luminosity and polarization. Recently, a realistic design of new injection facility 2×10^{11} e^{+}/s for 200 s of beam lifetime. The detailed design of the Interaction Region and MDI, and the 3D design of Final Focus quadrupoles are also finished, while maximum strength is reduced from 100 T/m to 40 T/m.

Future Plans

There's almost the same situation as STCF that off momentum dynamic aperture with CRAB ON is not good enough. And also, efforts in longer Touschek lifetime is always needed.

The united team with several powerful organizations, labs and institutes as supporters keeps steadily pushing the Russian government to approve the project. In spite the whole budget is still under discussion by Russian government, there was a decision to start with R&D and prototypes and money were allocated for 2022-2023 for key components. SuperKEKB experience show that there are still problems with implementation of the CW collision in real life. Therefore, to reduce risks for large super charm-tau, BINP is considering a test facility in the range of 1-1.5 GeV beam energy with all main CW features (large Piwinski angle, small emittance, large current, low βy, complicated IR, etc.).

CONCLUSION

Based on the research results from China and Russia, we can see that a super tau charm factory reaches a luminosity of 1×1035 cm^{-2} s^{-1} is feasible. But there's still a lot of work to do, both in accelerator physics and key technologies. Experienced accelerator physicists and engineers are needed all around the world, therefore, besides world-wide recruitment, work together with international colleagues should definitely be an option for either project.

ACKNOWLEDGEMENTS

The author would like to thank Hefei Comprehensive National Science Center for their strong support. The colleagues from INFN, IHEP, BINP and other institutes kindly gave the author a lot of information. Special thanks to Dr E. Levichev from BINP.

REFERENCES

[1] Z. Zhao, "Introduction to Future High Intensity Collider @ 2-7 GeV in China", presented at Workshop on Physics at Future High Intensity Collider @ 2-7GeV in China, Hefei, China, January 2015.

[2] M. Bona *et al.*, "SuperB a high-luminosity heavy flavour factory conceptual design report", presented at INFN March 2007.

[3] K. Hirata, "Analysis of beam-beam interactions with a large crossing angle", *Phys. Rev. Lett.*, vol. 74, p. 2228, 1995. doi:10.1103/PhysRevLett.74.2228

[4] M Zobov *et al.*, "Test of 'Crab-Waist' Collisions at the DAΦNE Φ Factory", *Phys. Rev. Lett.*, vol. 104, p. 174801, 2010. doi:10.1103/PhysRevLett.104.174801

[5] Y.Ohnishi *et al.*, "SuperKEKB operation using crab waist collision scheme", *Eur. Phys. J. Plus*, vol. 136, 1023, 2021. doi:10.1140/epjp/s13360-021-01979-8

[6] P. Raimondi, D. Shatilov, M. Zobov, "Beam-Beam Issues for Colliding Schemes with Large Piwinski Angle and Crabbed Waist", *LNF-07-003-IR*, 2007. doi:10.48550/arXiv.physics/0702033

[7] M. E. Biagini *et al.*, "Tau/Charm Factory Accelerator Report", INFN Report INFN-13-13/LNF, 2013. doi:10.48550/arXiv.1310.6944

[8] J.Q. Lan, Q. Luo, C. Zhang, W. W. Gao, Y. Xu, and Y. Bai, "Design of beam optics for a Super Tau-Charm Factory", *J. Instrum.*, vol. 16, no. 7, p. T07001, 2021. doi:10.1088/1748-0221/16/07/T07001

[9] V. V. Anashin *et al.*, "Super Charm-Tau Factory Conceptual Design Report", 2011.

[10] V. V. Anashin *et al.*, "Super Charm-Tau Factory Conceptual Design Report Part Two", 2018.

[11] A. Bogomyagkov, "Status of Novosibirsk SCTF", presented at the 2021 Joint International Workshop for Super-Charm Tau Facility, September 2021.

[12] E. Levichev, private communication, 2022.

ISBN: 978-3-95450-236-3 ISSN: 2673-7027 doi:10.18429/JACoW-eeFACT2022-TUXAS0101

LATEST RESULTS ON KAON PHYSICS AT KLOE-2

A. Di Domenico*, Sapienza University of Rome and INFN Sez. Roma, Rome, Italy
on behalf of KLOE-2 Collaboration

Abstract

The most recent results obtained by the KLOE-2 collaboration with entangled neutral kaons produced at DAΦNE are briefly reviewed: (i) an improved search for decoherence and $\mathcal{CPT}$ violation effects in the process $\phi \to \mathrm{K_S K_L} \to \pi^+\pi^-\pi^+\pi^-$, constraining with the utmost precision several phenomenological models; (ii) the first direct test of the $\mathcal{T}$ and $\mathcal{CPT}$ symmetries in neutral kaon transitions between flavor and $\mathcal{CP}$ eigenstates, by studying the processes $\phi \to \mathrm{K_S K_L} \to \pi^+\pi^- \pi e \nu$, $\phi \to \mathrm{K_S K_L} \to \pi e \nu\, 3\pi^0$; (iii) a new measurement of the $\mathrm{K_S} \to \pi e \nu$ branching fraction, that in combination with the previous KLOE result improves the total precision by almost a factor of two, and allows a new derivation of $f_+(0)|V_{us}|$.

KLOE AND DAΦNE

DAΦNE, the Frascati ϕ-factory [1], is an e^+e^- collider working at a center of mass energy of $\sqrt{s} \sim 1020$ MeV, corresponding to the peak of the ϕ resonance. The ϕ production cross section is ~3 μb, and the $\phi \to \mathrm{K^0\bar{K}^0}$ decay has a branching fraction of 34%. The neutral kaon pair is produced into a fully anti-symmetric entangled state with quantum numbers $J^{\mathcal{PC}} = 1^{--}$:

$$|i\rangle = \frac{1}{\sqrt{2}}\{|\mathrm{K^0}\rangle|\mathrm{\bar{K}^0}\rangle - |\mathrm{\bar{K}^0}\rangle|\mathrm{K^0}\rangle\} = \frac{\mathcal{N}}{\sqrt{2}}\{|\mathrm{K_S}\rangle|\mathrm{K_L}\rangle - |\mathrm{K_L}\rangle|\mathrm{K_S}\rangle\} \quad (1)$$

with $\mathcal{N} = \sqrt{(1+|\epsilon_S|^2)(1+|\epsilon_L|^2)}/(1-\epsilon_S\epsilon_L) \simeq 1$ a normalization factor, and $\epsilon_{S,L}$ the small $\mathcal{CP}$ impurities in the mixing of the physical states $\mathrm{K_{S,L}}$ with definite widths $\Gamma_{S,L}$ and masses $m_{S,L}$.

The double differential decay rate of the state $|i\rangle$ into decay products f_1 and f_2 at proper times t_1 and t_2, respectively, is an observable quantity at a ϕ-factory. After integration on (t_1+t_2) at fixed time difference $\Delta t = t_2 - t_1 \geq 0$, the decay intensity can be written as follows [2]:

$$I(f_1,f_2;\Delta t) = C_{12}\{|\eta_2|^2 e^{-\Gamma_L \Delta t} + |\eta_1|^2 e^{-\Gamma_S \Delta t} -2|\eta_1||\eta_2| e^{-\frac{(\Gamma_S+\Gamma_L)}{2}\Delta t}\cos[\Delta m \Delta t + \phi_1 - \phi_2]\} . \quad (2)$$

with $\Delta m = m_L - m_S$, $\eta_i \equiv |\eta_i|e^{i\phi_i} = \frac{\langle f_i|T|\mathrm{K_L}\rangle}{\langle f_i|T|\mathrm{K_S}\rangle}$, and $C_{12} = \frac{|\mathcal{N}|^2}{2(\Gamma_S+\Gamma_L)}|\langle f_1|T|\mathrm{K_S}\rangle\langle f_2|T|\mathrm{K_S}\rangle|^2$.

The detection of a kaon at large times t_2 satisfying the condition $e^{-(\Gamma_S-\Gamma_L)\Delta t}/|\eta_2| \ll 1$ *post-tags* a $\mathrm{K_S}$ state in the opposite direction. This is a unique feature at a ϕ-factory, not possible at fixed target experiments, that can be exploited to select very pure $\mathrm{K_S}$ beams [3].

The KLOE experiment operated at DAΦNE with a detector mainly consisting of a large volume drift chamber [4] surrounded by an electromagnetic calorimeter [5], both immersed in a 0.52 T uniform magnetic field provided by a superconducting coil. KLOE completed its data taking campaign in 2006 collecting an integrated luminosity of 2.5 fb^{-1}. A second data taking campaign was carried out in years 2014-2018 by the KLOE-2 experiment [6], the successor of KLOE, at an upgraded DAΦNE collider [7, 8], collecting an integrated luminosity of 5.5 fb^{-1}. In total KLOE and KLOE-2 collected 8 fb^{-1} of data, corresponding to $\sim 2.4\times10^{10}$ ϕ-mesons and $\sim 8\times10^{9}$ $\mathrm{K_S K_L}$ pairs produced. All the results presented in this paper have been obtained using the KLOE data sample.

SEARCH FOR DECOHERENCE AND $\mathcal{CPT}$ VIOLATION EFFECTS

The quantum interference between the decays of the entangled kaons in state (1) is studied in the $\mathcal{CP}$-violating process $\phi \to \mathrm{K_S K_L} \to \pi^+\pi^-\pi^+\pi^-$, which exhibits the characteristic Einstein–Podolsky–Rosen correlations that prevent both kaons to decay into $\pi^+\pi^-$ at the same time. The measured Δt distribution can be fitted with the distribution:

$$I(\pi^+\pi^-,\pi^+\pi^-;\Delta t) \propto e^{-\Gamma_L\Delta t} + e^{-\Gamma_S \Delta t} -2(1-\zeta_{\mathrm{SL}})e^{-\frac{(\Gamma_S+\Gamma_L)}{2}|\Delta t|}\cos(\Delta m \Delta t) , \quad (3)$$

where the quantum mechanical expression (2) in the $\{\mathrm{K_S},\mathrm{K_L}\}$ basis has been modified with the introduction of a decoherence parameter ζ_{SL}, and a factor $(1-\zeta_{\mathrm{SL}})$ multiplying the interference term. Analogously, a $\zeta_{0\bar{0}}$ parameter can be defined in the $\{\mathrm{K^0},\mathrm{\bar{K}^0}\}$ basis [9]. Δt resolution and detection efficiency effects, as well as background contributions due to $\mathrm{K_S}$-regeneration on the beam pipe wall, and the non-resonant $e^+e^- \to \pi^+\pi^-\pi^+\pi^-$ process, are all taken into account in the fit. Figure 1 shows as an example the result in the case of the ζ_{SL} decoherence model. The analysis of a data sample corresponding to L ~ 1.7 fb^{-1} yields the following results [10]:

$$\begin{aligned}\zeta_{\mathrm{SL}} &= (0.1 \pm 1.6_{\mathrm{stat}} \pm 0.7_{\mathrm{syst}})\times10^{-2} \\ \zeta_{0\bar{0}} &= (-0.5 \pm 8.0_{\mathrm{stat}} \pm 3.7_{\mathrm{syst}})\times10^{-7} ,\end{aligned} \quad (4)$$

compatible with the prediction of quantum mechanics, i.e. $\zeta_{SL} = \zeta_{0\bar{0}} = 0$, and no decoherence effect. In particular the result on $\zeta_{0\bar{0}}$ has a high precision, $\mathcal{O}(10^{-6})$, due to the $\mathcal{CP}$ suppression present in the specific decay channel; it is an improvement of five orders of magnitude over the limit obtained by a re-analysis of CPLEAR data [9, 11]. This

* antonio.didomenico@roma1.infn.it

ISBN: 978-3-95450-236-3 ISSN: 2673-7027 doi:10.18429/JACoW-eeFACT2022-TUXAS0101

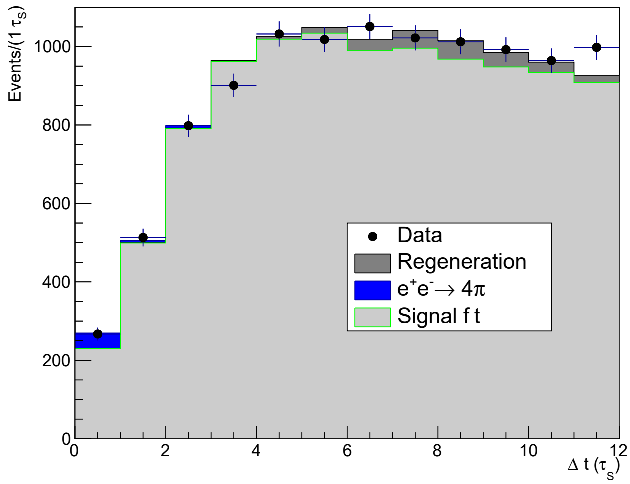

Figure 1: Data and fit distribution for the ζ_{SL} decoherence model with background contributions displayed.

result can also be compared to a similar test in the B meson system [12], where an accuracy of $\mathcal{O}(10^{-2})$ is reached.

Decoherence effects may appear in a quantum gravity scenario in connections with $\mathcal{CPT}$ violation, being the quantum mechanical operator generating $\mathcal{CPT}$ transformations *ill-defined*. In this case a model for decoherence can be formulated [13, 14] in which neutral kaons are described by a density matrix ρ that obeys a modified Liouville-von Neumann equation. In this context γ is one of the relevant parameters describing decoherence and $\mathcal{CPT}$ violation. It has mass units and in a quantum gravity scenario it is presumed to be at most of $\mathcal{O}(m_K^2/M_{\rm Planck}) \sim 2 \times 10^{-20}$ GeV. Fitting the same $I(\pi^+\pi^-, \pi^+\pi^-; \Delta t)$ distribution as in the ζ parameters analysis, the following result is obtained [10]:

$$\gamma \;=\; \left(1.3 \pm 9.4_{\rm stat} \pm 4.2_{\rm syst}\right) \times 10^{-22}\ {\rm GeV}\,, \quad (5)$$

compatible with no decoherence and $\mathcal{CPT}$ violation, improving the previous result by CPLEAR [15], while the sensitivity reaches the interesting Planck's region.

As discussed above, in a quantum gravity framework inducing decoherence, the $\mathcal{CPT}$ operator is ill-defined. This consideration has intriguing consequences in entangled neutral kaon states, where the resulting loss of particle-antiparticle identity could induce a breakdown of the correlation in state (1) imposed by Bose statistics [16]. As a result the initial state (1) can be parametrized in general as:

$$\begin{aligned} |i\rangle \;=\; & \frac{1}{\sqrt{2}}[|{\rm K}^0\rangle|\bar{\rm K}^0\rangle - |\bar{\rm K}^0\rangle|{\rm K}^0\rangle \\ & +\omega\left(|{\rm K}^0\rangle|\bar{\rm K}^0\rangle + |\bar{\rm K}^0\rangle|{\rm K}^0\rangle\right)]\,, \end{aligned} \quad (6)$$

where ω is a complex parameter describing a novel $\mathcal{CPT}$ violation phenomenon, and in this scenario its order of magnitude is expected to be at most:

$$|\omega| \sim \left[(m_K^2/M_{\rm Planck})/\Delta\Gamma\right]^{1/2} \sim 10^{-3}$$

with $\Delta\Gamma = \Gamma_S - \Gamma_L$. The study performed on the Δt distribution of the $\phi \to {\rm K_S K_L} \to \pi^+\pi^-\pi^+\pi^-$ process including in the fit the modified initial state Eq. (6), yields the most precise measurement of the complex parameter ω [10]:

$$\begin{aligned} \Re(\omega) &= \left(-2.3^{+1.9}_{-1.5\,\rm stat} \pm 0.6_{\rm syst}\right) \times 10^{-4} \\ \Im(\omega) &= \left(-4.1^{+2.8}_{-2.6\,\rm stat} \pm 0.9_{\rm syst}\right) \times 10^{-4}\,, \end{aligned} \quad (7)$$

with an accuracy that already reaches the interesting Planck scale region.

Results (4), (5), and (7) represent a sizeable improvement with respect to previous measurements [9, 11, 15, 17]. They are consistent with no deviation from quantum mechanics and $\mathcal{CPT}$ symmetry, while for some parameters the precision reaches the interesting level at which – in the most optimistic scenarios – quantum gravity effects might show up. They provide the most stringent limits up to date on the considered models.

DIRECT $\mathcal{T}$, $\mathcal{CP}$, $\mathcal{CPT}$ TESTS

In order to realize direct tests of $\mathcal{T}$, $\mathcal{CP}$, $\mathcal{CPT}$ symmetries in neutral kaon transition processes, it is necessary to compare the probability of a reference transition with its symmetry conjugate. The exchange of *in* and *out* states required for a genuine test involving an anti-unitary transformation implied by time-reversal $\mathcal{T}$, can be implemented exploiting the entanglement of ${\rm K}^0\bar{\rm K}^0$ pairs [18, 19], as briefly described in the following.

The initial kaon pair produced in $\phi \to {\rm K}^0\bar{\rm K}^0$ decays can be rewritten in terms of any pair of orthogonal states:

$$\begin{aligned} |i\rangle &= \frac{1}{\sqrt{2}}\{|{\rm K}^0\rangle|\bar{\rm K}^0\rangle - |\bar{\rm K}^0\rangle|{\rm K}^0\rangle\} \\ &= \frac{1}{\sqrt{2}}\{|{\rm K}_+\rangle|{\rm K}_-\rangle - |{\rm K}_-\rangle|{\rm K}_+\rangle\}\,. \end{aligned} \quad (8)$$

Here the states $|{\rm K}_-\rangle$, $|{\rm K}_+\rangle$ are defined as the states which cannot decay into pure $\mathcal{CP} = \pm 1$ final states, $\pi\pi$ or $3\pi^0$, respectively [18, 19]. The condition of orthogonality $\langle {\rm K}_-|{\rm K}_+\rangle = 0$, corresponds to assume negligible direct $\mathcal{CP}$ and/or $\mathcal{CPT}$ violation contributions in the decay, while the $\Delta S = \Delta Q$ rule is also assumed, so that the two flavor orthogonal eigenstates $|{\rm K}^0\rangle$ and $|\bar{\rm K}^0\rangle$ are identified by the charge of the lepton in semileptonic decays. Thus, exploiting the perfect anticorrelation of the states implied by Eq. (8), it is possible to have a "flavor-tag"or a "$\mathcal{CP}$-tag", i.e. to infer the flavor (${\rm K}^0$ or $\bar{\rm K}^0$) or the $\mathcal{CP}$ (${\rm K}_+$ or ${\rm K}_-$) state of the still alive kaon by observing a specific flavor decay ($\pi^+\ell^-\nu$ or $\pi^-\ell^+\bar{\nu}$, in short ℓ^+ or ℓ^-) or $\mathcal{CP}$ decay ($\pi\pi$ or $3\pi^0$) of the other (and first decaying) kaon in the pair. Then the decay of the surviving kaon into a semileptonic (ℓ^+ or ℓ^-), $\pi\pi$ or $3\pi^0$ final state, filter the kaon final state as a flavor or $\mathcal{CP}$ state.

In this way one can identify a reference transition (e.g. ${\rm K}^0 \to {\rm K}_-$) and its symmetry conjugate (e.g. the $\mathcal{CPT}$-conjugated ${\rm K}_- \to \bar{\rm K}^0$), and directly compare them through the corresponding ratios of probabilities. The observable

ISBN: 978-3-95450-236-3 ISSN: 2673-7027 doi:10.18429/JACoW-eeFACT2022-TUXAS0101

ratios for the various symmetry tests can be defined as follows [20]:

$$
\begin{aligned}
R_{2,\mathcal{T}} &\equiv \frac{I(\ell^-,3\pi^0;\Delta t \gg \tau_S)}{I(\pi\pi,\ell^+;\Delta t \gg \tau_S)}\cdot\frac{1}{D_{\mathcal{CPT}}} \\
&= 1-4\Re\epsilon+4\Re x_+ +4\Re y\,, \qquad (9)\\
R_{4,\mathcal{T}} &\equiv \frac{I(\ell^+,3\pi^0;\Delta t \gg \tau_S)}{I(\pi\pi,\ell^-;\Delta t \gg \tau_S)}\cdot\frac{1}{D_{\mathcal{CPT}}} \\
&= 1+4\Re\epsilon+4\Re x_+ -4\Re y\,, \qquad (10)\\
R_{2,\mathcal{CP}} &\equiv \frac{I(\ell^-,3\pi^0;\Delta t \gg \tau_S)}{I(\ell^+,3\pi^0;\Delta t \gg \tau_S)} \\
&= 1-4\Re\epsilon_S-4\Re x_- +4\Re y\,, \qquad (11)\\
R_{4,\mathcal{CP}} &\equiv \frac{I(\pi\pi,\ell^+;\Delta t \gg \tau_S)}{I(\pi\pi,\ell^-;\Delta t \gg \tau_S)} \\
&= 1+4\Re\epsilon_L-4\Re x_- -4\Re y\,, \qquad (12)\\
R_{2,\mathcal{CPT}} &\equiv \frac{I(\ell^-,3\pi^0;\Delta t \gg \tau_S)}{I(\pi\pi,\ell^-;\Delta t \gg \tau_S)}\cdot\frac{1}{D_{\mathcal{CPT}}} \\
&= 1-4\Re\delta+4\Re x_+ -4\Re x_-\,, \qquad (13)\\
R_{4,\mathcal{CPT}} &\equiv \frac{I(\ell^+,3\pi^0;\Delta t \gg \tau_S)}{I(\pi\pi,\ell^+;\Delta t \gg \tau_S)}\cdot\frac{1}{D_{\mathcal{CPT}}} \\
&= 1+4\Re\delta+4\Re x_+ +4\Re x_-\,. \qquad (14)
\end{aligned}
$$

where $I(f_1,f_2;\Delta t \gg \tau_S)$ is the double decay rate (2) in the asymptotic region $\Delta t \gg \tau_S$ [2, 18, 19], with f_1 occurring before f_2 decay and $\Delta t > 0$. The constant factor $D_{\mathcal{CPT}}$ is defined as:

$$
D_{\mathcal{CPT}} = \frac{\left|\langle 3\pi^0|T|\mathrm{K}_-\rangle\right|^2}{\left|\langle \pi^+\pi^-|T|\mathrm{K}_+\rangle\right|^2} = \frac{\mathrm{BR}\left(\mathrm{K_L}\to 3\pi^0\right)}{\mathrm{BR}\left(\mathrm{K_S}\to \pi^+\pi^-\right)}\frac{\Gamma_L}{\Gamma_S}\,,
$$

and can be determined from measurable branching fractions and lifetimes of $\mathrm{K_{S,L}}$ states [19, 20]. For $\Delta t = 0$ one has by construction no symmetry violation, within our assumptions. The measurement of any deviation from the prediction $R_{i,s} = 1$ (with $s = \mathcal{T}, \mathcal{CP}$, or $\mathcal{CPT}$, and $i = 2, 4$) imposed by the symmetry invariance is a direct signal of the symmetry violation built in the time evolution of the system. The following double ratios independent of the factor $D_{\mathcal{CPT}}$ can also be defined:

$$
\begin{aligned}
DR_{\mathcal{T},\mathcal{CP}} &\equiv \frac{R_{2,\mathcal{T}}}{R_{4,\mathcal{T}}} \equiv \frac{R_{2,\mathcal{CP}}}{R_{4,\mathcal{CP}}} = 1-8\Re\epsilon+8\Re y\,, \qquad (15)\\
DR_{\mathcal{CPT}} &\equiv \frac{R_{2,\mathcal{CPT}}}{R_{4,\mathcal{CPT}}} = 1-8\Re\delta-8\Re x_-\,. \qquad (16)
\end{aligned}
$$

The r.h.s. of Eqs.(9)-(16) is evaluated to first order in small parameters; ϵ and δ are the usual $\mathcal{T}$ and $\mathcal{CPT}$ violation parameters in the neutral kaon mixing, respectively, and $\epsilon_{S,L} = \epsilon \pm \delta$ the $\mathcal{CP}$ impurities in the physical states $\mathrm{K_S}$ and $\mathrm{K_L}$; the small parameter y describes a possible $\mathcal{CPT}$ violation in the $\Delta S = \Delta Q$ semileptonic decay amplitudes, while x_+ and x_- describe $\Delta S \neq \Delta Q$ semileptonic decay amplitudes with $\mathcal{CPT}$ invariance and $\mathcal{CPT}$ violation, respectively. Therefore the r.h.s. of Eqs.(9)-(16) shows the effect of symmetry violations only in the effective Hamiltonian description of the neutral kaon system according to the Weisskopf-Wigner approximation, without the presence of other possible sources of symmetry violations. The small spurious effects due to the release of our assumptions are also shown, including possible $\Delta S = \Delta Q$ rule violations ($x_+, x_- \neq 0$) and/or direct $\mathcal{CPT}$ violation effects ($y \neq 0$). It is worth noting that the direct $\mathcal{CP}$ ϵ' effects are fully negligible in the asymptotic region $\Delta t \gg \tau_S$ [18, 19].

The KLOE-2 collaboration recently completed the analysis of a data sample corresponding to an integrated luminosity $L = 1.7\ \mathrm{fb}^{-1}$ collected at the DAΦNE ϕ-factory, and measured all eight observables defined in Eqs.(9)-(16). The Δt distributions of the $\phi \to \mathrm{K_S K_L} \to \pi^+\pi^-\ \pi e\nu$ and $\phi \to \mathrm{K_S K_L} \to \pi e\nu\ 3\pi^0$ processes are studied in the asymptotic region $\Delta t \gg \tau_S$. A time of flight technique is used to identify semileptonic decays for both $\mathrm{K_S}$ and $\mathrm{K_L}$. $\mathrm{K_L} \to 3\pi^0$ decays are identified reconstructing the decay position and time using a trilateration method applied to the best candidate set of six reconstructed photons from π^0 decays. Residual background for the $\phi \to \mathrm{K_S K_L} \to \pi e\nu\ 3\pi^0$ channel is evaluated with the aid of Monte Carlo (MC) simulation and subtracted. Signal selection efficiencies are evaluated from MC and corrected with data using independent control samples. The Δt distributions of observables ratios (9)-(16) are then constructed and fitted with a constant.

The final results obtained for the eight observable ratios (9)-(16) are summarized in Fig.2, and compared with the expected values from $\mathcal{CPT}$ invariance and $\mathcal{T}$ violation extrapolated from observed $\mathcal{CP}$ violation in the $\mathrm{K}^0-\bar{\mathrm{K}}^0$ mixing [21].

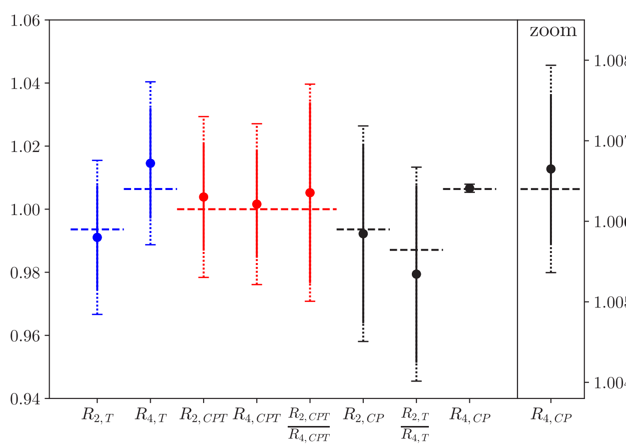

Figure 2: Comparison of the measured symmetry-violation-sensitive single and double ratios (9)-(16) and their expected values (horizontal dashed lines). Solid error bars denote statistical uncertainties and dotted error bars represent total uncertainties (including systematic uncertainties and the error on the $D_{\mathcal{CPT}}$ factor in case of single $\mathcal{T}$ and $\mathcal{CPT}$-violation sensitive ratios). The right-hand-side panel magnifies the region of the $\mathcal{CP}$-violation-sensitive ratio $R_{4,\mathcal{CP}}$.

For the $\mathcal{T}$ and $\mathcal{CPT}$ single ratios a total error of 2.5 % is reached, while for the double ratios (15) and (16) the total error is increased to 3.5 %, with the advantage of in principle a doubled sensitivity to violation effects, and of

ISBN: 978-3-95450-236-3 ISSN: 2673-7027 doi:10.18429/JACoW-eeFACT2022-TUXAS0101

independence from the $D_{\mathcal{CPT}}$ factor. The measurement of the single ratio $R_{4,\mathcal{CP}}$ benefits of highly allowed decay rates for the involved channels, reaching an error of 0.13 %.

The double ratio $DR_{\mathcal{CPT}}$ is our best observable for testing $\mathcal{CPT}$, free from approximations and model independent, while $DR_{\mathcal{T},\mathcal{CP}}$ assumes no direct $\mathcal{CPT}$ violation and is even under $\mathcal{CPT}$, therefore it does not disentangle $\mathcal{T}$ and $\mathcal{CP}$ violation effects, contrary to the genuine $\mathcal{T}$ and $\mathcal{CP}$ single ratios.

No result on $\mathcal{T}$ and $\mathcal{CPT}$ observables shows evidence of symmetry violation. We observe $\mathcal{CP}$ violation in transitions in the single ratio $R_{4,\mathcal{CP}}$ with a significance of 5.2σ, in agreement with the known $\mathcal{CP}$ violation in the $\mathrm{K}^0 - \bar{\mathrm{K}}^0$ mixing [21] using a different observable.

NEW MEASUREMENT OF $\mathcal{B}(\mathrm{K_S} \to \pi e \nu)$

The branching fraction for semileptonic decays of charged and neutral kaons together with the lifetime measurements are used to determine the $|V_{us}|$ element of the Cabibbo–Kobayashi–Maskawa quark mixing matrix. The relation among the matrix elements of the first row, $|V_{ud}|^2 + |V_{us}|^2 + |V_{ub}|^2 = 1$, provides the most stringent test of the unitarity of the quark mixing matrix.

Different factors contribute to the uncertainty in determining $|V_{us}|$ from kaon decays, discussed in Refs. [22–25] and among the six semileptonic decays the contribution of the lifetime uncertainty is smallest for the $\mathrm{K_S}$ meson. Nevertheless, given the lack of pure high-intensity $\mathrm{K_S}$ meson beams compared with $\mathrm{K}^{\pm}$ and $\mathrm{K_L}$ mesons, the measurements of $\mathrm{K_S}$ semileptonic decays from the KLOE [26,27] and NA48 [28] experiments provide the least precise determination of $|V_{us}|$.

A data sample corresponding to an integrated luminosity of $L = 1.63\ \mathrm{fb}^{-1}$ collected by KLOE was analyzed by the KLOE-2 collaboration. $\mathrm{K_S}$ states are tagged by identifying the interaction of their entangled partners in the calorimeter ($\mathrm{K_L}$-crash). The $\mathrm{K_S} \to \pi e \nu$ signal selection exploits a boosted decision tree (BDT) classifier built with kinematic variables measured with DC only together with time-of-flight measurements from EMC. The signal yield is provided by the fit to the reconstructed electron mass distribution shown in Fig.3, and is then normalised to $\mathrm{K_S} \to \pi^+\pi^-$ decays in the same data set. $\mathrm{K_L} \to \pi e \nu$ data control samples are used to evaluate signal selection efficiencies. Finally the branching fraction is derived [29]:

$$\mathcal{B}(\mathrm{K_S} \to \pi e \nu) = (7.211 \pm 0.046_{\mathrm{stat}} \pm 0.052_{\mathrm{syst}}) \times 10^{-4}.$$

The previous result from KLOE [26], based on an independent data sample corresponding to $0.41\ \mathrm{fb}^{-1}$ of integrated luminosity, is $\mathcal{B}(\mathrm{K_S} \to \pi e \nu) = (7.046 \pm 0.076_{\mathrm{stat}} \pm 0.049_{\mathrm{syst}}) \times 10^{-4}$. The combination of the two results, accounting for correlations between the two measurements, gives

$$\mathcal{B}(\mathrm{K_S} \to \pi e \nu) = (7.153 \pm 0.037_{\mathrm{stat}} \pm 0.043_{\mathrm{syst}}) \times 10^{-4},$$

reducing the overall uncertainty on the branching fraction at the 0.8% level. The value of $|V_{us}|$ is related to the $\mathrm{K_S}$ semileptonic branching fraction by the equation

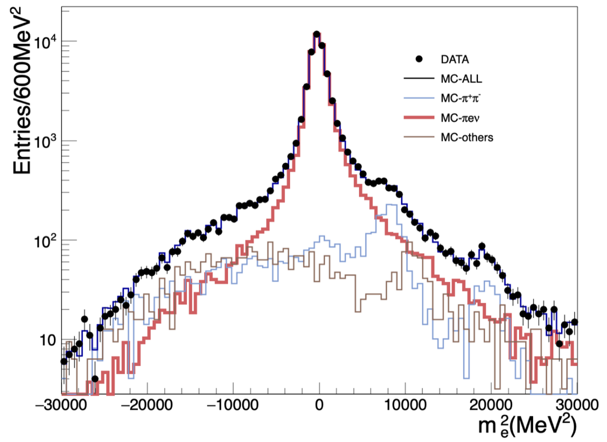

Figure 3: The m_e^2 distribution for data, MC signal and background compared with the fit result.

$$\mathcal{B}(\mathrm{K_S} \to \pi \ell \nu) = \frac{G^2 (f_+(0)|V_{us}|)^2}{192\pi^3} \tau_S m_K^5 I_K^{\ell} S_{\mathrm{EW}} (1 + \delta_{\mathrm{EM}}^{K\ell}),$$

where I_K^{ℓ} is the phase-space integral, which depends on measured semileptonic form factors, S_{EW} is the short-distance electro-weak correction, $\delta_{\mathrm{EM}}^{K\ell}$ is the mode-dependent long-distance radiative correction, and $f_+(0)$ is the form factor at zero momentum transfer for the $\ell\nu$ system. Using the values $S_{\mathrm{EW}} = 1.0232 \pm 0.0003$ [30], $I_K^e = 0.15470 \pm 0.00015$ and $\delta_{\mathrm{EM}}^{Ke} = (1.16 \pm 0.03)\ 10^{-2}$ from Ref. [25], and the world average values for the $\mathrm{K_S}$ mass and lifetime [21] we derive

$$f_+(0)|V_{us}| = 0.2170 \pm 0.0009,$$

with a sizable reduction of the uncertainty with respect to the previous derivation, from 0.6% to 0.4%.

CONCLUSION

Recent analyses by the KLOE-2 collaboration on entangled neutral kaons yielded improved precision tests of Quantum Mechanics and $\mathcal{CPT}$ symmetry, the first direct tests of $\mathcal{T}$ and $\mathcal{CPT}$ symmetries in neutral kaon transitions, and a new measurement of the $\mathrm{K_S} \to \pi e \nu$ branching fraction.

The analysis of the total $8\ \mathrm{fb}^{-1}$ of data collected by KLOE and KLOE-2 is in progress and will constitute a unique opportunity to push forward a rich Physics program including these kind of studies on discrete symmetries, and on the properties of the entanglement of neutral kaons.

REFERENCES

[1] A. Gallo *et al.*, “DAΦNE status report”, *Conf. Proc.*, vol. C060626, p. 604, 2006.

[2] A. Di Domenico (Ed.), “Handbook on Neutral Kaon Interferometry at a ϕ-factory”, *Frascati Phys. Ser.*, vol. 43 INFN-LNF, Frascati, 2007; available online at `http://www.lnf.infn.it/sis/frascatiseries/Volume43/volume43.pdf`

ISBN: 978-3-95450-236-3 ISSN: 2673-7027 doi:10.18429/JACoW-eeFACT2022-TUXAS0101

[3] J. Bernabeu and A. Di Domenico, "Can future observation of the living partner post-tag the past decayed state in entangled neutral K mesons?", *Phys. Rev. D*, vol. 105, p. 116004, 2022.

[4] M. Adinolfi *et al.*, "The tracking detector of the KLOE experiment", *Nucl. Instrum. Methpds A*, vol. 488, p. 51, 2002.

[5] M. Adinolfi *et al.*, "The KLOE electromagnetic calorimeter", *Nucl. Instrum. Methods A*, vol. 482, p. 364, 2002.

[6] G. Amelino-Camelia *et al.*, "Physics with the KLOE-2 experiment at the upgraded DAΦNE", *Eur. Phys. J. C*, vol. 68, p. 619, 2010.

[7] M. Zobov *et al.*, "Test of crab-waist collisions at the DAΦNE Φ factory", *Phys. Rev. Lett.*, vol. 104, p. 174801, 2010.

[8] C. Milardi *et al.*, "High luminosity interaction region design for collisions inside high field detector solenoid", *J. Instrum.*, vol. 7, p. T03002, 2012.

[9] R. A. Bertlmann, W. Grimus, and B. C. Hiesmayr, "Quantum mechanics, Furry's hypothesis, and a measure of decoherence in the $K^0\ \bar{K}^0$ system", *Phys. Rev. D*, vol. 60, p. 114032, 1999.

[10] KLOE-2 Collaboration, D. Babusci *et al.*, "Precision tests of quantum mechanics and CPT symmetry with entangled neutral kaons at KLOE", *J. High Energy Phys.*, vol. 04, p. 059, 2022.

[11] A. Apostolakis *et al.*, "An EPR experiment testing the non-separability of the K^0 anti-K^0 wave function", *Phys. Lett. B*, vol. 422, p. 339, 1998.

[12] A. Go *et al.*, "Measurement of Einstein-Podolsky-Rosen-Type Flavor Entanglement in $\Upsilon(4S) \to B^0\bar{B}^0$ Decays", *Phys. Rev. Lett.*, vol. 99, p. 131802, 2007.

[13] J. Ellis, J. S. Hagelin, D. V. Nanopoulos, and M. Srednicki, "Search for violations of quantum mechanics", *Nucl. Phys. B*, vol. 241, p. 381, 1984.

[14] J. Ellis, J. L. Lopez, N. .E. Mavromatos, and D. V. Nanopoulos, "Precision tests of CPT symmetry and quantum mechanics in the neutral kaon system", *Phys. Rev. D*, vol. 53, p. 3846, 1996.

[15] R. Adler *et al.*, "Tests of CPT symmetry and quantum mechanics with experimental data from CPLEAR", *Phys. Lett. B*, vol. 364, p. 239, 1995.

[16] J. Bernabeu, N. Mavromatos, and J. Papavassiliou, "Novel Type of CPT Violation for Correlated Einstein-Podolsky-Rosen States of Neutral Mesons", *Phys. Rev. Lett.*, vol. 92, p. 131601, 2004.

[17] F. Ambrosino *et al.*, "First observation of quantum interference in the process $\phi \to K_S K_L \to \pi^+\pi^-\pi^+\pi^-$: a Test of quantum mechanics and CPT symmetry", *Phys. Lett. B*, vol. 642, p. 315, 2006.

[18] J. Bernabeu, A. Di Domenico, and P. Villanueva-Perez, "Direct test of time reversal symmetry in the entangled neutral kaon system at a ϕ-factory", *Nucl. Phys. B*, vol. 868, p. 102, 2013.

[19] J. Bernabeu, A. Di Domenico, and P. Villanueva-Perez, "Probing CPT in transitions with entangled neutral kaons", *J. High Energy Phys.*, vol. 10, p. 139, 2015.

[20] A. Di Domenico, "Testing discrete symmetries in transitions with entangled neutral kaons", *Acta Phys. Polonica B*, vol. 48, p. 1919, 2017.

[21] P. Zyla *et al.*, (Particle Data Group), "Review of Particle Physics", *Prog. Theor. Exp. Phys.*, vol. 2020, p. 083C01, 2020.

[22] M. Antonelli *et al.*, "An evaluation of $|V_{us}|$ and precise tests of the Standard Model from world data on leptonic and semileptonic kaon decays", *Eur. Phys. J. C*, vol. 69, p. 399, 2010.

[23] M. Moulson and E. Passemar, "Status of $|V_{us}|$ determination for kaon decays", in *Proc. 10th Int. Workshop on the CKM Unitarity Triangle*, University of Heidelberg, Germany, Sep., 2018. doi:10.5281/zenodo.2565479

[24] E. Blucher and W.J. Marciano, "V_{ud}, V_{us}, the Cabibbo angle, and CKM unitarity", in The Review of Particle Physics, (Particle Data Group), *Prog. Theor. Exp. Phys*, vol. 2020, p. 083C01, 2020.

[25] C.-Y. Seng, D. Galviz, W. J. Marciano, and U.-G. Meissner, "Update on $|V_{us}|$ and $|V_{us}/V_{ud}|$ from semileptonic kaon and pion decays", *Phys. Rev. D*, vol. 105, p. 013005, 2002.

[26] F. Ambrosino *et al.*, "Study of the branching ratio and charge asymmetry for the decay $K_S \to \pi e \nu$ with the KLOE detector", *Phys. Lett. B*, vol. 636, p. 173, 2006.

[27] D. Babusci *et al.*, "Measurement of the branching fraction for the decay $K_S \to \pi \mu \nu$ with the KLOE detector", *Phys. Lett. B*, vol. 805, p. 135378, 2020.

[28] J.R. Batley *et al.*, "Determination of the relative decay rate $K_S \to \pi e \nu / K_L \to \pi e \nu$", *Phys. Lett. B*, vol. 653 p. 145, 2007.

[29] D. Babusci *et al.*, "Measurement of the $K_S \to \pi e \nu$ branching fraction with the KLOE experiment", *arXiv preprint*, arXiv:2208.04872, submitted for publication.

[30] W. J. Marciano and A. Sirlin, "Radiative Corrections to $\pi_{\ell 2}$ Decays", *Phys. Rev. Lett.*, vol. 71, p. 3629, 1993.

ISBN: 978-3-95450-236-3 ISSN: 2673-7027 doi:10.18429/JACoW-eeFACT2022-TUXAT0103

SuperKEKB OPTICS TUNING AND ISSUES

H. Sugimoto*, Y. Ohnishi, A. Morita, H. Koiso
High Energy Accelerator Research Organization, Tsukuba, Japan

Abstract

SuperKEKB is an electron-positron double-ring asymmetric-energy collider at the High Energy Accelerator Research Organization (KEK) in Japan. It adopts a novel collision method named nano-beam scheme to avoid the so-called hourglass effect. In the nano-beam scheme, two beams are squeezed to extremely small sizes at the interaction point and are collided with a large crossing angle between them. Since starting the collision operation in April 2018, numerous machine tunings and beam studies have been performed to improve the machine performance. The highest peak luminosity so far is 4.65×10^{34} cm^{-2}s^{-1} reached in June 8th, 2022. This record is the world's highest instantaneous luminosity and is more than two times higher than that of the previous KEKB collider This paper presents some important topics related to beam optics tuning in the SuperKEKB operation. Major issues to be resolved to boost the machine performance are also addressed.

INTRODUCTION

SuperKEKB [1] is a 7 GeV electron (HER) and 4 GeV positron (LER) double ring collider. Beam commissioning without final focusing system (QCS) was carried out from February 2016 to June 2016 [2]. Beam commissioning with QCS was started March 2018 [3]. SuperKEKB adopts a novel collision scheme named nano-beam scheme to open up new luminosity frontier. In the nano beam scheme, two beams collide with a large horizontal crossing angle with extremely small beam sizes. The nano beam scheme realizes small betatron function at the interaction point (IP) while avoids so-called hourglass effect which limits the luminosity performance.

Luminosity L is written by beam current I, vertical beam-beam parameter ξ_y, vertical betatron function at IP β_y^* and a reduction factor R as,

$$L = \frac{\gamma_\pm}{2er_e} \frac{I_\pm \xi_{y\pm}}{\beta_y^*} R, \tag{1}$$

where e, r_e, and $\gamma_\pm$ are elementary charge, classical electron radius and the Lorentz gamma factor, respectively. Since the beam-beam parameter ξ_y is proportional to $\sqrt{\beta_y^*/\varepsilon_y}$, the vertical emittance ε_y should be also very small as well as β_y^* to realize the nano-beam collision. Therefore the low emittance tuning is one of the important machine parameters in the SuperKEKB machine tuning.

The nominal β_y^* in the present operation is $\beta_y^* = 1$ mm while the final target of β_y^* is $\beta_y^* = 0.3$ mm. The operation with $\beta_y^* = 0.8$ mm was carried out for short-term trial. The achievable bunch currents is smaller than of $\beta_y^* = 1$ mm case due to poor injection efficiency. Improvement of the injection efficiency is a major issue in both squeezing β_y^* and increasing stored beam current.

Crab waist scheme (CW) [4, 5] is incorporated to both LER and HER in 2020 to mitigate a sort of hourglass effect in the transverse direction. CW is realized by applying different filed strength to sextupole magnets (SLY) used in the vertical local chromaticity correction (Y-LCC) as shown in Fig. 1. The vertical betatron function at SLY and field strength of SLY are quite large owing to the extremely small β_y^* and the resultant large chromaticity. Therefore beam optics is easily distorted by a tiny amount of lattice or orbit errors. Optics tuning and the machine operation should be performed with careful attention to the Y-LCC section as well as the interaction region (IR).

OPTICS TUNING

Beam Position Monitor and Corrector

Beam Position Monitor (BPM) is attached to each of quadrupole magnets for precise orbit and optics control. The BPM system is successfully used in the beam tuning with an averaging mode of 0.25 Hz. In addition to closed orbit measurement, more than 100 BPMs per ring can be used as gated turn-by-turn BPMs. The gated turn-by-turn BPMs are very helpful in the beam injection tuning. Optics measurement with turn-by-turn beam position is performed only for dedicated beam study. Usual optics tuning is based on closed orbit measurement.

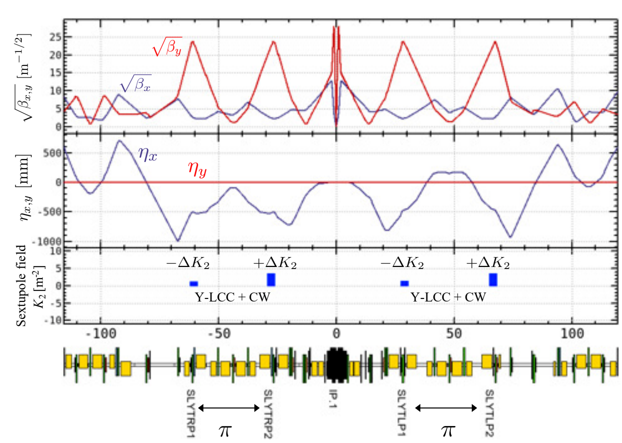

Figure 1: Betatron and dispersion functions at the Y-LCC section in LER. Two sextupoles pairs installed in both left and right sides of the interaction region. The sextupole pairs are utilized for Y-LCC and CW. Betatron phase advance between the two sextupoles is π.

* hiroshi.sugimoto@kek.jp

ISBN: 978-3-95450-236-3 ISSN: 2673-7027 doi:10.18429/JACoW-eeFACT2022-TUXAT0103

The SuperKEKB main rings have about 900 quadrupole magnets and about 200 sextupole magnets. Horizontal and vertical steering magnets are installed near the focusing and de-focusing quadrupole magnets, respectively. Almost all quadrupole magnets have independent power supply for their auxiliary coil to enable robust optics tuning. Skew quadrupole coils are installed to all sextupole magnets and utilized in optics correction and luminosity tuning.

Measurement

Beam optics at BPMs are extracted by analyzing closed orbit distortion induced by horizontal and vertical dipole kicks. Closed orbit at i-th BPM $\Delta\chi_i$ excited by j-th dipole kick $\Delta\theta_j$ is written by

$$\Delta\chi_i = \frac{\sqrt{\beta_i\beta_j}}{2\sin\pi\nu}\Delta\theta_j\cos\left(|\phi_i-\phi_j|-\pi\nu\right), \qquad (2)$$

where β, ϕ and ν are betatron function, betatron phase and betatron tune, respectively. Betatron function and its phase are determined so that Eq. (2) reproduces measured orbit distortion. Six kinds of closed orbit distortion per each direction are analyzed in the optics measurement at SuperKEKB.

Dispersion function is measured by varying the beam revolution frequency f_{rev} with Δf_{rev}. Beam orbit deviation at i-th BPM $\Delta\chi_i$ caused by the frequency change Δf_{rev} is proportional to dispersion function η_i at the BPM as

$$\Delta\chi_i = -\frac{\eta_i}{\alpha_p-\gamma^{-2}}\frac{\Delta f_{\mathrm{rev}}}{f_{\mathrm{rev}}}, \qquad (3)$$

where α_p is the momentum compaction factor of the ring. Dispersion function is calculated with measured orbit response and Eq. (3) assuming the model value for α_p. The momentum compaction factor is $\alpha_p = 3.0\times10^{-4}$ in LER and $\alpha_p = 4.5\times10^{-4}$ in HER. The amount of the relative frequency change $\Delta f_{\mathrm{rev}}/f_{\mathrm{rev}}$ is about $\pm6\times10^{-7}$, and it corresponds to 0.2 % and 0.13 % beam energy deviations in LER and HER, respectively.

The other important tuning item in SuperKEKB is coupling between horizontal and vertical betatron motions (xy-coupling). There are several parametrization techniques for betatron coupling in accelerators. Four optical functions r_{1-4} used in the SuperKEKB operation. The coupled transverse motions in four-dimensional phase space (x, p_x, y, p_y) are decomposed to two independent betatron motions as

$$\begin{pmatrix} u \\ p_u \\ v \\ p_v \end{pmatrix} = \begin{pmatrix} \mu & 0 & -r_4 & r_2 \\ 0 & \mu & r_3 & -r_1 \\ r_1 & r_2 & \mu & 0 \\ r_3 & r_4 & 0 & \mu \end{pmatrix}\begin{pmatrix} x \\ p_x \\ y \\ p_y \end{pmatrix}, \qquad (4)$$

where $\mu^2 = 1-(r_1r_2-r_3r_4)$. The xy-coupling parameter is a correlation between horizontal and vertical betatron motions. Therefore vertical leakage orbit induced by a horizontal dipole kick contains information of xy-coupling parameters. Although it is possible to infer the coupling parameters r_{1-4} from the leakage orbits with some model dependent assumptions, numerical simulations show that the optics correction based on vertical leakage orbit itself sufficiently reduces r_{1-4}. Therefore the vertical leakage orbit is used in the global optics correction for simplicity. Six kinds of vertical leakage orbits are used in xy-coupling correction.

Optics measurement and correction are performed with a low stored beam current (<50mA) to avoid dangerous beam loss during the measurement.

Global Optics Correction

Global optics correction is performed so that difference between measured beam optics and that of model optics is minimized. Strength of corrector magnets are obtained with measured beam optical parameters and response matrix of the model lattice. Betatron functions, dispersions and xy-coupling are in general coupled to each others. However, correction of each optical parameter is independently and iteratively performed in SuperKEKB to break down the size of problem to be solved.

An example of vertical leakage orbits in HER before and after the optics correction are shown in Fig. 2(a) and (b), re-

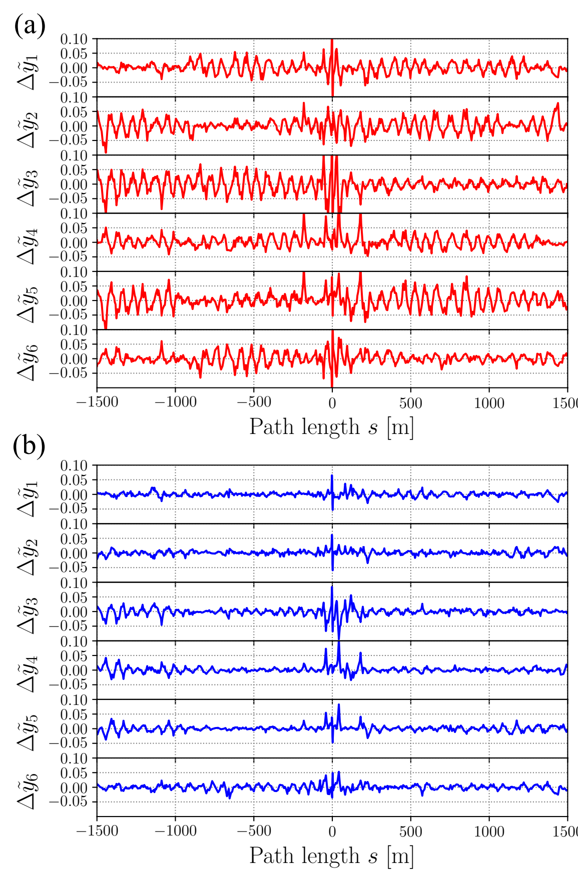

Figure 2: Measured vertical leakage orbits in HER before (a) and after (b) the optics correction. The vertical axis is normalized by root-mean-squared (RMS) amplitude of the horizontal orbits. IP is located on $s = 0$.

ISBN: 978-3-95450-236-3 ISSN: 2673-7027 doi:10.18429/JACoW-eeFACT2022-TUXAT0103

spectively. The skew quadrupole corrector coils in sextupole magnets are mainly utilized. Skew quadrupole magnets near IR are also used depending on the situation.

One of essential optical parameter in the nano-beam scheme is vertical emittance. Therefore the vertical emittance is considered as the main figure of merit in the optics tuning. Each storage ring has one X-ray beam size monitor to monitor horizontal and vertical beams sizes. The vertical emittance evaluated by measured vertical beam size is used to confirm the validity of the optics correction.

Figure 3 shows time evolution of vertical emittance in HER during a series of optics correction performed on a machine maintenance day. The vertical emittance is reduced from more than 100 pm to 30 – 40 pm. Typical residual of optical parameters and vertical emittance is summarized in Table 1. The vertical emittance after the optics correction depends on daily machine condition. The urgent issue is how to keep the beam optics during physics experiment rather than the performance of optics correction itself.

Tuning of IP Parameters

Experience on SuperKEKB operation shows r_1^* and r_2^* are effective for luminosity performance. Vertical dispersion is also effective for beam size control. On the other hand r_3^* and r_4^* are not so effective for luminosity performance, but these parameters affect beam background (BG).

Several machine studies were carried out to evaluate optical parameters at IP by means of both closed orbit response and turn-by-turn beam positions. It is however difficult to determine their absolute values due to poor sensitivity of IP orbit and uncertainty in the complicated IR modeling. Therefore, the tuning of IP parameters are performed based on the observed machine performance.

One of important parameter to be optimized is xy-coupling at IP (r_{1-4}^*). Global optics correction presented in this paper does not take care IP parameters itself. Eventually a tuning knob named IPTiltKnob which can control xy-coupling and vertical dispersion at IP by using skew quadrupole coils is

Table 1: Typical Residual of Optical Parameters

Optical Parameter	LER	HER
$(\Delta\beta_x/\beta_x)^{\text{rms}}$ [%]	5	5
$(\Delta\beta_y/\beta_y)^{\text{rms}}$ [%]	5	5
$\Delta y^{\text{rms}}/\Delta x^{\text{rms}}$ $[10^{-3}]$	16	12
$\Delta\eta_x^{\text{rms}}$ [mm]	15	30
$\Delta\eta_y^{\text{rms}}$ [mm]	5	5
ε_y [pm]	20 ~ 40	20 ~ 40

developed for luminosity tuning. The IPTiltKnob calculates field strength of skew quadrupoles which produces desired change of IP parameters assuming the model lattice.

Figure 4 shows an example of luminosity tuning using IPTiltKnob with r_2^*. IP parameters are routinely adjusted during physics experiment to keep or improve machine performance by carefully watching not only luminosity but also BG and injection efficiency.

In addition to beam optics, vertical crossing angle at IP Δp_y^* has huge impact on the luminosity performance. Figure 5 shows luminosity performance for four different values of Δp_y^* in LER. Luminosity performance was improved by about 20 % by optimizing Δp_y^*. It is also confirmed that the tuning of Δp_y^* reduces BG.

ISSUES

Optics correction is originally scheduled every two weeks on a machine maintenance day. It is also performed when the optics distortion is suspected by degradation in machine performance such as beam size, injection efficiency, BG and luminosity. Unexpected optics distortion is observed more frequently in the recent operation. Eventually, optics correction is required once every 2 or 3 days.

Beam optics of the SuperKEKB main ring are very sensitive to perturbation owing to the large betatron function at IR and SLY. Therefore the fluctuation and drifting of machine condition should be understood and minimized. Some

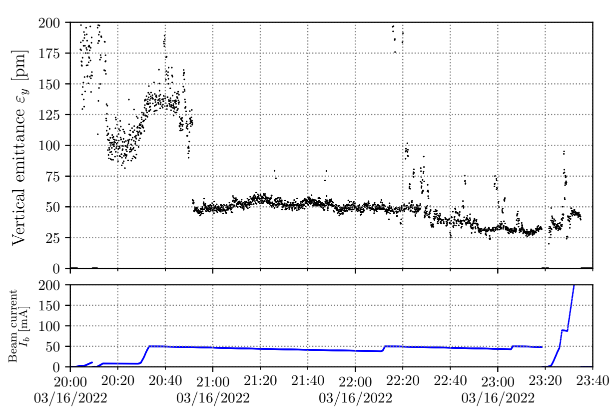

Figure 3: Time evolution of the vertical emittance together with beam current in HER during a series of optics correction.

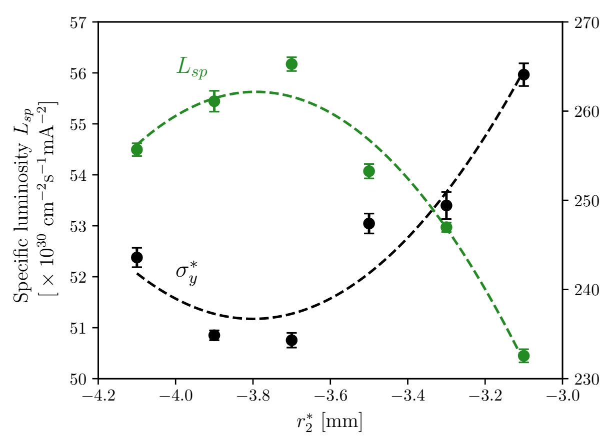

Figure 4: Specific luminosity and vertical beam size as a function of r_2^*.

ISBN: 978-3-95450-236-3 ISSN: 2673-7027 doi:10.18429/JACoW-eeFACT2022-TUXAT0103

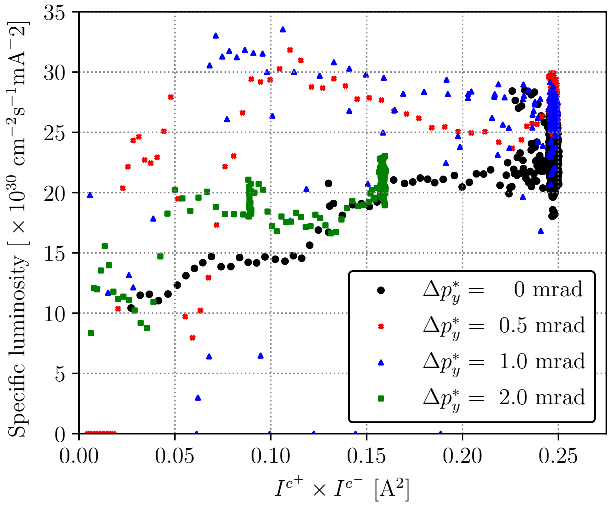

Figure 5: Specific luminosity as a function of beam current products with different four vertical crossing angle at IP.

topics related to beam optics degradation during operation are presented in this section.

Field Drifting of QCS

Unexpected vertical tune drifting was suspected in 2021 as shown Fig. 6(a), where the tune drifting is estimated by the amount of a tune feedback for the operation. The vertical beta-beating is also observed as shown in Fig. 7. It is confirmed by numerical calculation that the measured tune drifting and beta-beating are explained by QCS's quadrupole error of 10^{-2} %. It was also pointed out that the tune drifting starts just after the QCS startup. These observations and numerical calculations imply the field drifting of QCS.

Experiments on field drifting of QCS were carried out with a QCS prototype [6]. The field measurement shows drifting qudrupole field of 10^{-3}~10^{-2} % depending on ramp cycle of the magnet. Based on the measurements the ramp cycle of QCS was modified to mitigate the field drifting. Figure 6(b) shows remarkable reduction of tune drifting by the modification.

Beam Current Dependent Optics Degradation

Betatron tune is kept a constant by a tune feedback system which adjusts some quadrupole magnets in matching sections. The amount of adjustment is calculated by the model lattice. The feedback system was originally developed to compensate beam current dependent tune shift.

It is possible to estimate the beam current dependency of tune by the amount of feedback. Figure 8 shows HER horizontal and vertical tunes as a function of stored beam current I_b in various days. The amount of horizontal tune shift dose not depend on the day while that of vertical tune depends on the day. It was considered that the major source of current dependent tune shift in HER is quadrupolar components of resistive wall wake due to non-circular shape of vacuum chamber. However, Fig. 8 implies that the existence

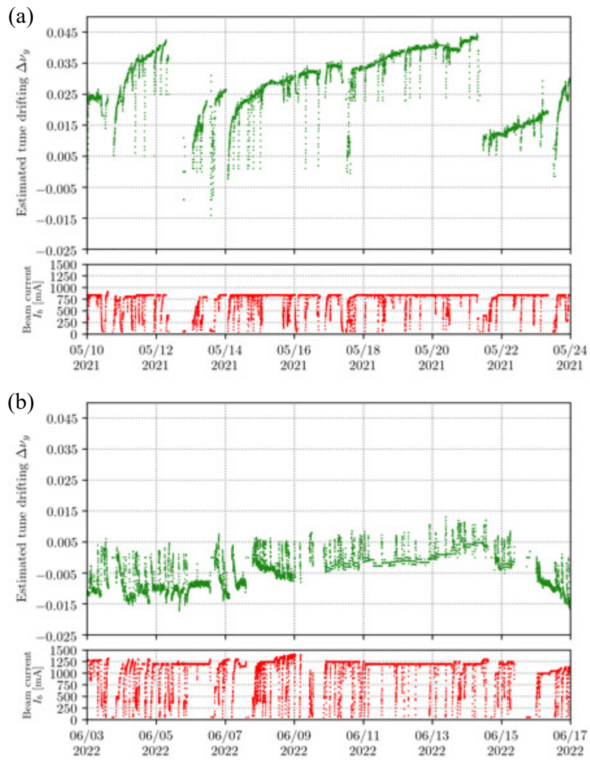

Figure 6: Vertical tune drifting in LER estimated with amount of tune feedback in 2021 (a). Tune drifting is reduced in 2022 by the modification for the ramp cycle of QCS

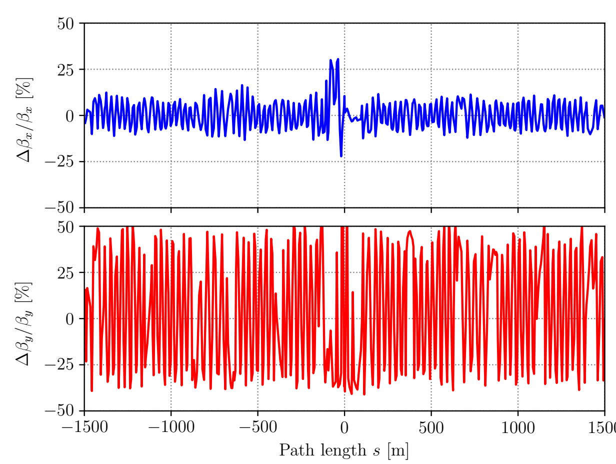

Figure 7: Measured beta-beating in LER. The measurement was performed on May 21st, 2021.

of other sources which causes a relatively large vertical tune shift and the amount of tune shift depends not only on the beam current but also on the day.

An possible source of the observed vertical tune shift is beam orbit fluctuation at strong sextupole magnets. The most crucial magnets are SLY because of the strong field strength and large betatron function β_y^s. Because the betatron phase advance between the two sextupoles is π, it is useful to consider cosine-like and sine-like orbits. The

ISBN: 978-3-95450-236-3 ISSN: 2673-7027 doi:10.18429/JACoW-eeFACT2022-TUXAT0103

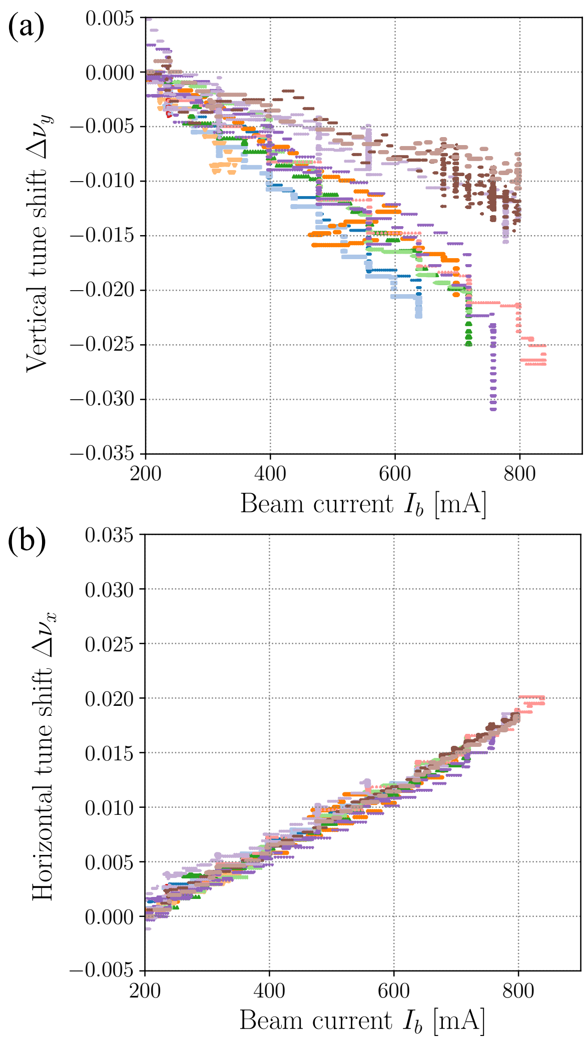

Figure 8: Horizontal (a) and vertical (a) tune shifts estimated by the amount of tune feedback as a function of stored beam current in HER. Each marker represents a measurement day.

tune shifts $\Delta\nu_{x,y}$ caused by cosine-like and sine-like orbits whose amplitude is Δx are respectively given by

$$\Delta\nu_{x,y} = \pm\frac{\beta^s_{x,y}}{4\pi}(K_2^1 + K_2^2)\Delta x, \quad (5)$$

$$\Delta\nu_{x,y} = \pm\frac{\beta^s_{x,y}}{4\pi}(K_2^1 - K_2^2)\Delta x, \quad (6)$$

where $K_2^{1,2}$ are field strengths of the two sextupole magnets. Only the cosine-like orbit causes tune shift when CW is turned off because of $K_2^1 = K_2^2$. When CW is turned on, both cosine-like and sine-like orbits cause tune shift. Assuming cosine-like orbit with $\Delta x = 10\,\mu\text{m}$ in HER for example, and inserting $\beta_y = 700$ m and $K_2^1 + K_2^2 = 16\,\text{m}^{-2}$ to Eq. (5) , the resultant vertical tune shift is $\Delta\nu_y \sim -0.009$ and comparable to the measured tune shift shown in Fig. 8.

Figure 9 shows the dependence of the beam orbits at SLYs on the stored beam current. The orbits at SLYTLE1 and SLYTLE2 move in same direction as beam current increase.

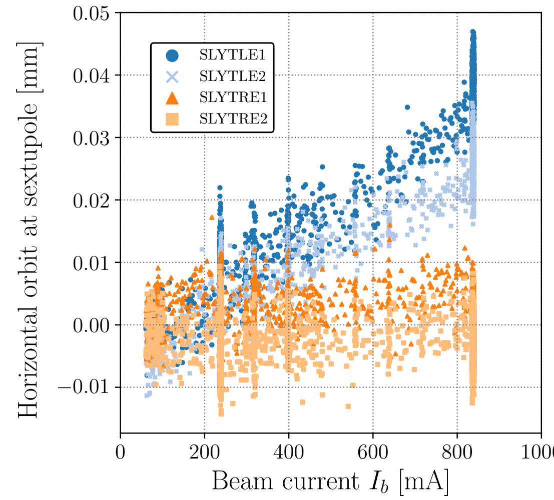

Figure 9: Horizontal beam orbits at SLYs (SLYTLE1, SLYTLE2, SLYTRE1 and SLYTRE2) and stored beam current in HER.

The vertical tune shift due to the observed beam orbit changes is evaluated by model calculations. The orbits at SLYs are imported to the model lattice as misalignments of SLYs. The betatron tune shift calculated with the misaligned SLYs as a function of stored beam current is shown in Fig. 10 together with the observed tune shifts. The measured orbit drifting causes almost no horizontal tune shift. On the other hand the measured vertical tune shift is reproduced by the orbit drifting at SLYs. It is also confirmed that the variation of the amount of vertical tune shift shown in Fig. 8 is attributed to the day to day variation of the orbit drifting.

The orbit change at SLY causes not only tune shift but also beta-beating in the whole ring. Figure 11 shows estimated vertical beta-beating as a function of stored beam current

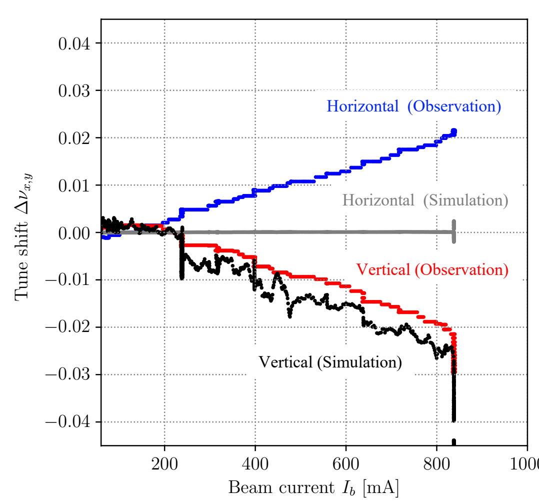

Figure 10: Current dependent tune shift estimated by orbit at SLYs together with that of observation.

ISBN: 978-3-95450-236-3 ISSN: 2673-7027 doi:10.18429/JACoW-eeFACT2022-TUXAT0103

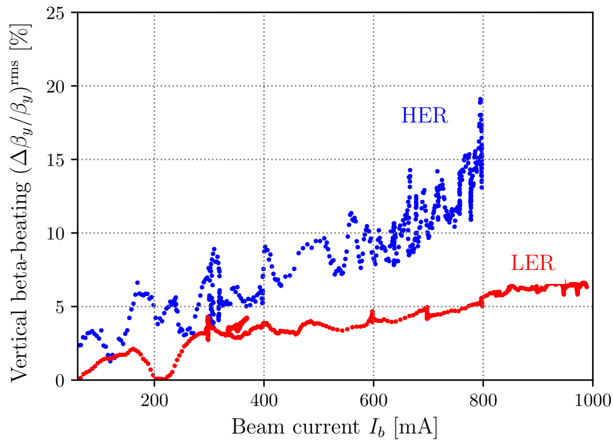

Figure 11: Estimated vertical beta-beating as a function of stored beam current, where the residual beta-beating is calculated with root-mean-squared of beta-beating at all BPMs.

for both rings. The estimated optics distortion in high beam current operation is considerably large.

The vertical betatron function at IP β_y^* is estimated in Fig. 12. It is known empirically that direction of beam orbit movement in SLYTLE1 and SLYTLE2 is somehow always same. Therefore both beams are always squeezed too much in high beam current operation. The smaller β_y^* results large vertical betatron function in QCS and makes stable machine operation more difficult because of poor injection efficiency and high BG level.

The source of beam current dependence of beam orbit is not understood yet. A possible reason is deformation of beamline due to beam pipe heating caused by synchrotron radiation from the beam. Although some experiments on the deformation is now carried out to clarify the movement of BPM and beam pipes, any scenario which explains measured orbit drifting is found so far.

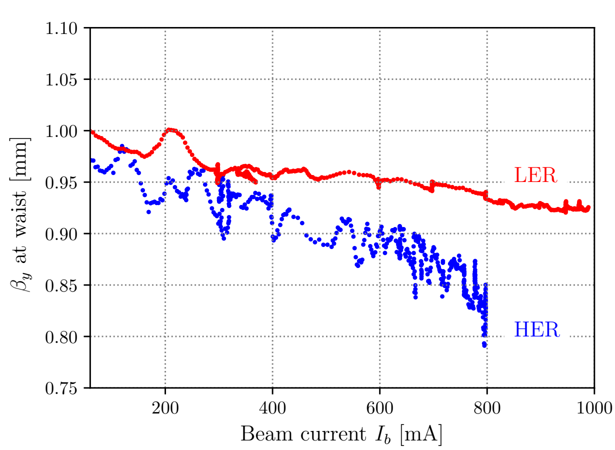

Figure 12: Estimated vertical betatron function at IP as a function of stored beam current.

Localized orbit at SLYs are applied to mitigate the optics distortion following to the above consideration. Figure 13 shows results of the beam orbit tuning at SLYs. It was confirmed that the orbit tuning improves both beam injection efficiency and BG. The localized orbit is now utilized as one of tuning knob in machine operation especially in high beam current operation.

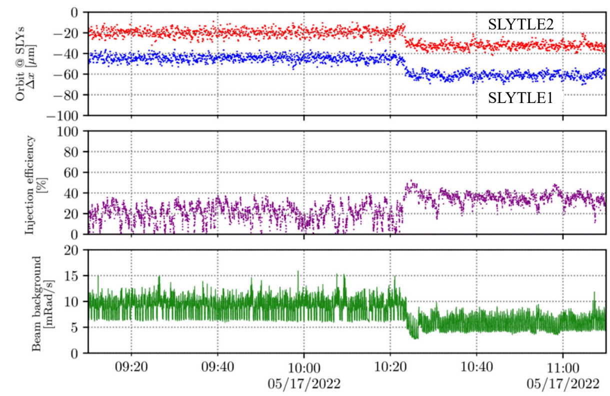

Figure 13: Tuning of orbit at SLYs with a localized orbit in HER, where time histories of orbit at SLYs, injeciton efficiency and BG are shown.

Earthquake

Japan is a country of many earthquakes. Earthquake causes beam abort in both rings in most cases. In addition, HER beam becomes unstable after earthquake in some cases. Figure 14 shows the unexpected luminosity degradation after recovery from earthquake. The vertical beam size blowup in HER can not be suppressed by tuning of IP parameters. Global optics correction is eventually necessary to recover the stable operation. Although numerical calculation implies that skew quadrupole components at SLY and/or QCS explain the observed distortion of *xy*-coupling, a clear reason for the skew quadrupole components is not found so far.

Stability of Beam Orbit and Optics

Although optics correction is originally scheduled every other week, more frequent optics correction is necessary in high beam current operation. Figure 15 shows time history of some machine parameters for few days. The vertical emittance gradually increases in a few days. As the results, beam injection efficiency becomes worse and BG increases. Eventually, optics correction is necessary every 2 or 3 days to resume stable operation.

A possible reason of the optics degradation is orbit changes during operation. Closed orbit in each of the SuperKEKB main rings is maintained by a slow (~0.1 Hz) orbit feedback system. The feedback system applies orbit correction with steering magnets to keep the closed orbit during machine operation. The residual of closed orbit is about 20 ~ 30 μm for both horizontal and vertical directions

ISBN: 978-3-95450-236-3 ISSN: 2673-7027 doi:10.18429/JACoW-eeFACT2022-TUXAT0103

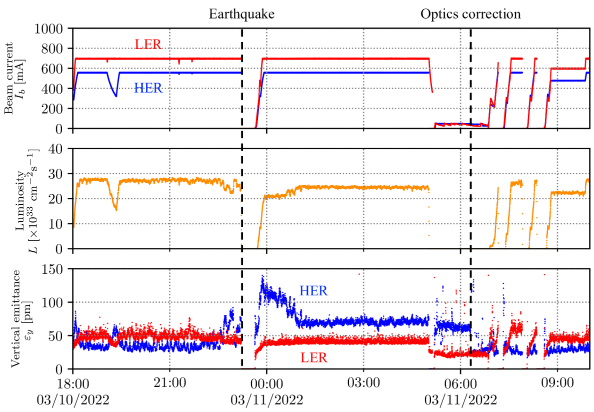

Figure 14: Machine parameters before and after an earthquake. Time histories of stored beam current, luminosity and vertical emittance are shown.

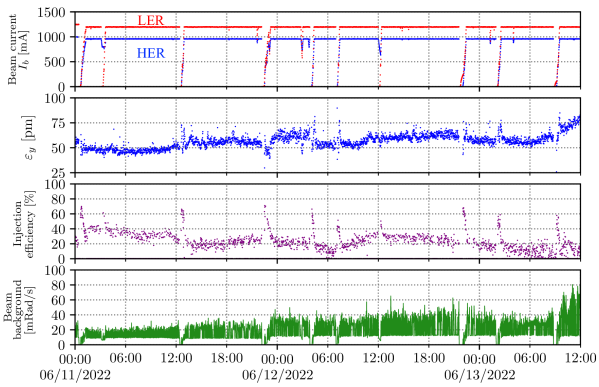

Figure 15: Degradation of machine performance within a few days in HER, where time histories of stored beam current, vertical emittance, beam injection efficiency and BG are shown.

in the RMS sense. One the other hand, numerical estimation indicates that the orbit fluctuation at strong sextupole magnets in arc cells of a few ten μm has non-negligible impact on beam optics.

Identification of error source is not trivial because tiny amount of beam orbit changes should be discussed carefully. The BPM reading used in the orbit feedback depends not only on beam orbit itself but also on various effects such as deformation of beamline, air temperature, electrical characteristics of the BPM system, etc. More systematic and precise investigation is essential to improve orbit and optics stability.

SUMMARY

Global optics tuning in SuperKEKB is based on analysis of closed orbit response. Correction of betatron function, *xy*-coupling and dispersion function are independently and iteratively applied until the residual error is converged. Correction of optical parameters at IP is performed by observing machine performance, such as beam size, luminosity, injection efficiency, BG, etc.

Field drifting of QCS was suspected by the unexpected drifting of tune feedback system in 2021. It is confirmed by field measurement with a QCS prototype magnet that the amount of field drifting depends on ramp cycle of QCS. Following to the field measurements, ramp cycle for QCS's startup was modified. The tune drifting is much reduced by the modification.

Investigation on amount of tune feedback and orbit at SLYs indicates that beam current dependence of vertical tune shift is attributed to the beam orbit change at SLYs. The orbit fluctuation at SLY causes beta-beating and makes stable operation more difficult in high beam current operation. It is demonstrated that the orbit tuning at SLYs improves both injection efficiency and BG level. The orbit at SLYs is very important parameter to be carefully monitored in the machine operation. The mechanism of the beam current dependence of the orbit is not understood yet.

Optics degradation in a few days is an urgent issue in high beam current operation. It seems that a few ten μm orbit change at strong sextupoles is not negligible according to numerical estimations. Systematic and detailed investigation on BPM reading including the BPM system itself and deformation of beamline is necessary to clarify the real beam orbit and its effects on beam optics.

ACKNOWLEDGEMENTS

The authors would like to thank the entire SuperKEKB accelerator group for developing the hardware system and supporting the beam measurement presented in this paper.

REFERENCES

[1] Y. Ohnishi *et al.*, "Accelerator design at SuperKEKB", *Prog. Theor. Exp. Phys.*, vol. 2013, p. 03A011, 2013. doi:10.1093/ptep/pts083

[2] Y. Funakoshi *et al.*, "Beam commissioning of SuperKEKB", in *Proc. 7th Int. Particle Accelerator Conf. (IPAC'16)*, Busan, Korea, May 2016, pp. 1019–1021. doi:10.18429/JACoW-IPAC2016-TUOBA01

[3] Y. Ohnishi, "Report on SuperKEKB Phase 2 Commissioning", in *Proc. 9th Int. Particle Accelerator Conf. (IPAC'18)*, Vancouver, Canada, Apr.-May 2018, pp. 1–5. doi:10.18429/JACoW-IPAC2018-MOXGB1

[4] P. Raimondi, "Introduction to Super B-Accelerators presented at the 2nd SuperB Workshop", presented at the 2nd SuperB Workshop, Frascati, Italy, Mar. 16-18 2006.

[5] K. Oide *et al.*, "Design of beam optics for the future circular e^+e^- collider collider rings", *Pys. Rev. Accel. Beams*, vol. 19, p. 111005, 2016. doi:10.1103/PhysRevAccelBeams.19.111005

[6] Y. Arimito *et al.*, "Lessons learned from the SuperKEKB IR magnet upgrade and plans for the future", in *Proc. 65th ICFA Advanced Beam Dynamics Workshop on High Luminosity Circular e+e- Colliders (eeFACT'22)*, Frascati (RM), Italy, Sep. 2022, paper WEZAT0202, this workshop.

ISBN: 978-3-95450-236-3 ISSN: 2673-7027 doi:10.18429/JACoW-eeFACT2022-TUYAT0101

BEAM PHYSICS FRONTIER PROBLEMS*

Frank Zimmermann†, CERN, Geneva, Switzerland

Abstract

The main challenges for far-future higher-energy particle colliders are discussed along with possible technological paths to overcome them.

COLLIDER LANDSCAPE

This workshop paper is mostly an abbreviated version of an article published in the "Frontiers in Physics" journal [1] (open access under the Creative Commons Attribution 4.0 International licence). The topic of electric power generation using accelerators has been added.
High-energy physics calls for particle colliders with much higher energy and/or luminosity than any past or existing machine. Various types of future particle colliders are being proposed and under development.

Technically closest to construction are the International Linear Collider (ILC) in Japan, the Future Circular electron-positron Collider (FCC-ee) in Europe, and the Circular Electron Positron Collider (CEPC) in China. The ILC design is grounded in more than 30 years of dedicated and successful R&D efforts. Another type of linear collider, CLIC, is based on higher-gradient normalconducting RF cavities, and powered with a novel two-beam acceleration scheme. The two circular collider designs, FCC-ee and CEPC, build on 60 years of experience with operating colliding beam storage rings, and in particular, they include ingredients of the former LEP collider at CERN, and of the KEKB, PEP-II and SuperKEKB B factories. Combining successful concepts and introducing a few new ones allows for an enormous jump in performance. For example, FCC-ee, when running on the Z pole is expected to deliver more than 100,000 times the luminosity of the former LEP collider. The circular lepton colliders FCC-ee and CEPC would be succeeded by energy frontier hadron colliders, FCC-hh and SPPC, respectively, providing proton collisions at a centre-of-mass energy of about 100 TeV or higher.

Several colliders based on energy-recovery linacs (ERLs) also are under discussion. A Large Hadron electron Collider (LHeC), with an electron beam from a dedicated ERL, could extend the physics programme at the LHC [2, 3]. A similar collider option, called FCC-eh [4], is considered for the FCC-hh. Recently, high-energy, high-luminosity ERL-based versions of the FCC-ee [5] and of the ILC [6, 7] have been proposed.

The above proposals are complemented by still others, presumably in the farther future, such as photon colliders, muon colliders, or colliders based on plasma acceleration.

Technical feasibility, affordability, and sustainability are among the questions which the collider designers may need to address.

ACCELERATOR CHALLENGES

Five major challenges are driving the design and, ultimately, the feasibility of future high-energy colliders. These are: (1) synchrotron radiation, (2) the bending magnetic field, (3) the accelerating gradient, (4) the production of rare or unstable particles (positrons or muons), and (5) cost and sustainability.

A charged particle deflected transversely to its velocity vector emits electromagnetic radiation which, if emitted due to the influence of an external magnetic field, is called synchrotron radiation. Denoting the charge of the particle by e, its relativistic Lorentz factor by γ, and considering a particle that follows a circular orbit of bending radius ρ, the energy loss per turn is given by

$$U_0 = \frac{e^2}{3\epsilon_0}\frac{\gamma^4}{\rho} \ . \tag{1}$$

If there is not a single particle but a beam with current I_{beam}, the power of the emitted synchrotron radiation becomes

$$P_{\mathrm{SR}} = \frac{I_{\mathrm{beam}}}{e} U_0 \ . \tag{2}$$

To provide some examples, the maximum synchrotron radiation power at the former Large Electron Positron collider (LEP) was about 23 MW, while for the proposed future circular electron-positron collider FCC-ee a total constant value of 100 MW has been adopted as a design constraint.

For the same particle energy, the Lorentz factor of protons is much (about 2000 times) lower than for electrons. Consequently, until now, synchrotron radiation power for proton beams has been much less significant, even if not fully negligible. For the Large Hadron Collider (LHC), it amounts to about 10 kW. However, this value increases to a noticeable 5 MW for the proposed future circular hadron collider FCC-hh. Removal of this heat from inside the cold magnets of the collider arcs, requires more than 100 MW of electric cryoplant power. These numbers reveal that for both future electron-positron and hadron circular colliders, synchrotron radiation alone implies more than 100 MW of electric power needs.

Possible mitigation measures to limit or suppress the synchrotron radiation include:

- increasing the bending radius ρ, which translates into a large(r) circular collider, and is a key part of the FCC concept;
- the construction of a linear collider, which features only minor arcs, but still faces the issues of radiation in the

* Work supported by the European Union's Horizon 2020 Research and Innovation programme under grant agreement no. 101004730 (iFAST).
† frank.zimmermann@cern.ch

ISBN: 978-3-95450-236-3 ISSN: 2673-7027 doi:10.18429/JACoW-eeFACT2022-TUYAT0101

final quadrupole magnets (Oide effect) and in collision (beamstrahlung) — see below;
- the construction of a muon collider;
- miniaturizing the beam vacuum chamber of a large ring; and
- shaping the beam to suppress radiation.

We will now look at these five possibilities in greater detail.

Size of Circular Colliders

The construction cost of different collider elements increases or decreases with the size of the ring. The optimum size is a function of the maximum beam energy. In 1976, B. Richter performed a cost optimisation of circular electron-positron colliders [8]. For a maximum c.m. energy of about 365 GeV (top quark production), he found that a collider diameter of 100 km is close to the optimum. A similar circumference value of about 90 km is obtained when extrapolating from the size and energy of more recent machines (PETRA, TRISTAN and LEP) [9].

Serendipitously, a circumference of 90–100 km is exactly the size required for a 100 TeV hadron collider. Namely, the beam energy of a hadron collider is given by

$$E = ecB\rho \ , \tag{3}$$

where B is the dipole field, ρ the bending radius. Doubling the field compared with the LHC, and increasing the radius or circumference by a factor 3–4 yields a factor 6–8 increase in proton energy to about 100 TeV in the centre of mass.

In addition, the size of 90–100 km required for both FCC lepton and hadron colliders also matches the local topology of the Lake Geneva basin, where possible tunnel locations are bounded on two sides by the Jura and (Pre-)Alpes, respectively, and where, in addition, the collider should pass around the Salève mountain.

Linear Colliders

A linear collider still features moderate arcs in its beam delivery system, and also faces the issues of synchrotron radiation emitted in the final quadrupole magnets and in collision, which ultimately limit the achievable beam size and the maximum beam energy of such colliders.

Indeed, some bending magnets are an integral part of the beam delivery systems, e.g., for the collimation of off-energy particles, and for the chromatic correction of the final focus. Synchrotron radiation emitted in these bending magnets can increase the beam size at the interaction point (IP), either directly due to the resulting increase of the horizontal emittance, or due to incomplete chromatic correction for particle energy changes that occur within the system [10]. These effects call for reduced bending as the beam energy is increased. At the same time, at higher energy the incoming geometric beam emittance adiabatically decreases, allowing for stronger sextupole magnets. In consequence, the geometry and the length of the beam delivery system change with beam energy. As an example, the CLIC beam-delivery footprint and length greatly changes when increasing the collision energy from 500 GeV to 3 TeV [11, 12]. The initial tunnel layout for a linear-collider beam-delivery system should be designed so as to accommodate, and provide space for, a higher-energy geometry. Even with the modified, optimised geometry, synchrotron radiation is by no means negligible. For example, synchrotron radiation in the bending magnets caused a factor of about 2 loss in luminosity in the 2003 CLIC BDS design at 3 TeV [11]; a similar situation was found for the SLC at a beam energy of only 45.6 GeV [13]. Such questions will also need to be addressed for a proposed 3 TeV energy upgrade of the International Linear Collider [14], or for upgrades of linear colliders to even higher energies, based on plasma acceleration.

A second limit set by synchrotron radiation in linear colliders arises in the final quadrupole magnets, where photon emission leads to an energy change, and thereby to a different focal length and increase in the vertical spot size ("Oide effect") [15].

The third, and perhaps most important limitation due to synchrotron radiation at linear colliders relates to the one emitted during the collision in the electromagnetic field of the opposite beam, also called "beamstrahlung". The strength of the beamstrahlung is characterized by the parameter Υ, defined as [16, 17] $\Upsilon \equiv \gamma B/B_c = (2/3)\hbar\omega_c/E_e$, with $B_c = m_e^2c^2/(e\hbar) \approx 4.4$ GT the Schwinger critical field, $\hbar\omega_c = (3/2)\hbar c\gamma^3/\rho$ the critical photon energy as introduced by Sands [18], E_e the electron (or positron) energy before radiation, B the local magnetic field, $\rho = e/(pB)$ the local bending radius, γ the relativistic Lorentz factor corresponding to E_e, $p \approx E_e/c$ the particle momentum, e the electron charge, and c the speed of light. The average Υ during the collision of three-dimensional Gaussian bunches is

$$\langle\Upsilon\rangle = \frac{5r_e^2}{6\alpha}\frac{N_b}{\sigma_z(\sigma_x^* + \sigma_y^*)} \ , \tag{4}$$

where α denotes the fine structure constant ($\alpha \approx 1/137$), $r_e \approx 2.8 \times 10^{-15}$ m the classical electron radius, N_b the bunch populaiton σ_z the rms bunch length, and $\sigma^*_{x(y)}$ the rms horizontal (vertical) spot size at the collision point.

In the classical regime $\Upsilon \ll 1$, and for flat Gaussian beams, the number of photons emitted per beam particle during the collision is [19]

$$n_\gamma \approx 2.12\frac{\alpha N_b r_e}{\sigma_x^* + \sigma_y^*} \ . \tag{5}$$

The parameter n_γ is important, since it describes the degradation of the luminosity spectrum. Namely, the emission of beamstrahlung photons changes the energy of the emitting electron or positron, and, thereby, the energy of its later collision. The fraction of the total luminosity $L_{\rm tot}$ at the target centre-of-mass energy L_0 is determined by n_γ as [20]

$$\frac{L_0}{L_{\rm tot}} = \frac{1}{n_\gamma^2}\left(1 - e^{-n_\gamma}\right)^2 \ , \tag{6}$$

ISBN: 978-3-95450-236-3 ISSN: 2673-7027 doi:10.18429/JACoW-eeFACT2022-TUYAT0101

To illustrate this degradation with an example, for CLIC at 380 GeV 60% of the total luminosity lies within 1% of the target energy, while at 3 TeV this fraction decreases to only 34%. In this way, at TeV energies, e^+e^- collisions in linear colliders lose their distinct energy precision.

Muon Colliders

The muon is about 200 times heavier than the electron, which, according to Eq. (1), implies close to 2×10^9 times less radiation at the same energy and bending radius. On the other hand, muon beams have two drawbacks: their production is not trivial, and the muons decay, with a rather short lifetime of only 2.2 µs at rest. In the later section on unstable ot rare particles, we will present an innovative approach to the muon collider.

Shielding the Radiation

The radiation emission is suppressed at wavelengths larger than $\lambda_{\mathrm{sh}} \approx 2\sqrt{d^3/\rho}$ with d signifying the pipe diameter [21]. Therefore, miniature accelerators with extremely small beam pipe, on the micron or nanometre scale, combined with a large bending radius ρ could suppress almost all radiation. An extreme case would be the use of bent-crystals, where d becomes comparable to the inter-atom distance in the crystal lattice.

Shaping the Beam

It is noteworthy that classically a uniform time-independent beam does not emit any synchrotron radiation [22, 23]. As an example, the CERN ISR operated with high-current stationary beams. In the case of such a coasting beam, residual radiation could arise from shot noise or from beam instabilities. The shot noise might be reduced by suitable manipulations — see e.g. [24] — or by stochastic cooling. The shot noise and, therefore, the associated synchrotron radiation can be markedly suppressed in case the cooling is so strong as to produce a crystalline beam [25]. The acceleration of a “DC” (or near-DC) beam may be accomplished by induction acceleration [26].

HIGH-FIELD MAGNETS

The energy reach of hadron colliders, and of hypothetical future muon colliders, is determined by their size and by the magnetic field — see Eq. (3).

All SC hadron storage rings built to date used magnets based on Nb-Ti conductor, for which the maximum reachable magnetic field is 8–9 T, as for the LHC dipole magnets. To go beyond this field level, the High Luminosity LHC (HL-LHC) upgrade foresees the installation of a few tens of higher-field magnets made from Nb_3Sn superconductor, with a design peak field of 11–12 T. The FCC-hh is designed with a few 1000s of Nb_3Sn magnets with a higher field of 16 or 17 T, which is close to the maximum field that can be reached with this type of conductor. To achieve even higher fields, high-temperature superconductors are under consideration. At CERN magnets based on REBCO are being developed. In China iron-based superconductor, with a field of up to 24 T, is the material of choice for the SPPC.

The coils of the SC magnets for future hadron colliders must withstand extreme pressure and forces, without any quench and without any degradation in performance. In dipole accelerator magnets, the horizontal forces per quadrant approach 10 MN/m for a field of 20 T [27].

ACCELERATING SYSTEMS

SC Radiofrequency Systems

As for the bending fields, also for the accelerating systems, superconducting materials have gained widespread use. Superconducting radiofrequency (RF) cavity systems underpin many modern facilities, the latest examples being the European XFEL at DESY Hamburg, the LCLS-II at SLAC, and FRIB in Michigan. Accelerating fields have been increased from a few MV/m to more than 30 MV/m for multicell cavities, and close to twice this value for single cells. Most SC cavities to date have been based on bulk Nb or in Nb-on-Cu cavities. New cavity treatments (nitrogen doping or nitrogen infusion [28]), innovative production methods (chemical vapor deposition [29], high impulse power magnetron sputtering [30]) and new materials, e.g. Nb_3Sn [31], as for the magnets, etc. promise further significant advances in performance, by factors of 2–10 in quality factor Q_0 and of 2–3 in maximum accelerating gradient. As an example, for Nb_3Sn, the theoretical ultimate “superheating” field [32] corresponds to a maximum accelerating gradient of ~ 100 MV/m, about twice the corresponding value for Nb, while the latter is not far from the currently achieved peak values of about 50 MV/m for Nb cavities [31].

Plasma Acceleration and Crystals

Other advanced accelerating concepts can reach much higher gradients. For example, plasma acceleration routinely achieves fields of 100 GV/m, which is 3000 times higher than the Nb cavities proposed for the International Linear Collider. The accelerating plasma waves can be driven either by a high-energy charged particle beam or by a laser. Comprehensive concepts have been developed for electron-positron colliders based on either beam-driven [33, 34] or laser-driven plasma acceleration [35, 36]. Beam quality, pulse-to-pulse stability, and energy efficiency of plasma accelerators [37] are critical issues addressed by ongoing R&D programs. High-energy colliders are arguably the most demanding application of plasma acceleration. Possible ultimate limits of plasma acceleration arise from the scattering of beam particles off plasma nuclei and plasma electrons, and from the emission of betatron radiation [38]. Both of these effects might be partially mitigated by accelerating in a hollow plasma channel. For realizing e^+e^- colliders, not only electrons but also positrons must be accelerated in the plasma, while preserving the beams' transverse and longitudinal emittance. For this purpose, more complex plasma excitation schemes may need to be developed, e.g. [39, 40].

ISBN: 978-3-95450-236-3 ISSN: 2673-7027 doi:10.18429/JACoW-eeFACT2022-TUYAT0101

Thanks to their higher electron density, even larger gradients can be generated in crystals. The maximum field is given by [41]

$$E_0 \approx \frac{m_e c \omega_p}{e} \approx 100 \left[\frac{\mathrm{GeV}}{\mathrm{m}}\right] \sqrt{n_0[10^{18}\ \mathrm{cm}^{-3}]}\,, \quad (7)$$

with ω_p the angular plasma frequency and n_0 the electron density. With $n_0 \approx 10^{22}$ cm^{-3} to 5×10^{24} cm^{-3} in a crystal, peak gradients of 10–1000 TV/m would be within reach. Accelerating crystal waves could be excited by X-ray lasers [41].

UNSTABLE OR RARE PARTICLES

Several future colliders require unprecedented production rates of positrons (linear colliders) and muons (muon collider), while future circular colliders need positrons at a level already demonstrated.

The present world record positron production rate of about 5×10^{12} e$^+$ per second was established at the SLC in the 1990s. Even achieving, or reproducing, this SLC rate is not trivial. The SLC target failed after 5 years of operation. For a dedicated failure analysis performed at LANL, the failed SLC positron target was cut into pieces and metallographic studies were carried out to examine the level of deterioration of material properties due to radiation exposure. The hardness of the target material in units of kg/mm^2 was found to be decreased by about a factor of 2, over the first 10 mm. However, whether this degradation had been due to radiation damage, work hardening, or temperature cycling could not be clearly resolved.

To push the production rate of e$^+$ and μ's much beyond the state of the art, a candidate ultimate source of positrons and muons is the Gamma factory [42, 43], which we discuss in the following subsection.

Gamma Factory

The Gamma Factory [42] is based on resonant scattering of laser photons off partially stripped heavy-ion beam in the existing LHC or in the planned FCC-hh. Profiting from two Lorentz boosts, the Gamma Factory acts as a high-stability laser-light-frequency converter, with a maximum photon frequency equal to $\nu_{\gamma,\max} = 4\gamma^2 \nu_{\mathrm{laser}}$, where γ is the relativistic Lorentz factor of the partially stripped ion beam. This allows the production of intense bursts of gamma rays with photon energies of up to several 100 MeV. Importantly, the LHC-based Gamma Factory can also be used to drive a subcritical nuclear reactor, producing of order 300 MW electric power, while performing a transmutation of nuclear waste [44].

In particular, the Gamma Factory can serve as a powerful source of e$^+$ (yielding 10^{16}–10^{17} e$^+$/s — five orders of magnitude higher than the state of the art), μ (10^{11}–10^{12}/s), π, etc. [42, 43]. The positron rate available from the Gamma factory would be sufficient for a LEMMA type muon collider [45, 46]. The Gamma Factory would also allow for Doppler laser cooling of high-energy beams, and, thereby, provide an avenue to a High Luminosity LHC based on laser-cooled isocalar ion beams [47].

Induction Acceleration and Positron Annihilation in Plasma Target

The LEMMA scheme for a muon collider is based on the annihilation of positrons with electrons at rest [45]. The cross section for continuum muon pair production e$^+$e$^-$ $\rightarrow$ $\mu^+\mu^-$ has a maximum value of about 1 µb at a centre-of-mass energy of ~0.230 GeV, which corresponds to a positron beam energy of about 45 GeV, exactly as required for the FCC-ee operating as a TeraZ factory and provided by the FCC-ee full-energy booster [48].

Challenges with the LEMMA-type muon production scheme relate to the emittance preservation of muons and muon-generating positrons upon multiple traversals through a target, and the merging of many separate muon bunchlets, due to production by many separate positron bunches or positron bunch passages.

These challenges may potentially be overcome by [49]:

- Operating the FCC-ee booster with a barrier bucket and induction acceleration, so that all positrons of a cycle are merged into one single superbunch [50], instead of $\sim 10,000$ separate bunches.
- Sending the positron superbunch from the booster into a plasma target, where, during the passage of the positron superbunch, the electron density is enhanced 100–1000 fold without any significant density of nuclei, hence with bremsstrahlung and Coulomb scattering largely absent.

Since the positron bunch will be mismatched to the nonlinear plasma channel, filamentation and significant transverse emittance growth may result [49].

For a typical initial plasma electron density of n_e = 10^{23} m^{-3}, and assuming a density enhancement by a factor of 1000, due to the electron pinch in the positive electric field of the positron beam, the positrons annihilate into muon pairs at a rate of 10^{-8} m^{-1}.

As described in the CDR [51], the FCC-ee booster can accelerate 3.5×10^{14} positrons every 50 s. Using the much more powerful Gamma Factory positron source, with a rate of 10^{16}–10^{17} e$^+$ s^{-1} [42], and injecting into the booster during one or a few seconds, of order 10^{17} e$^+$ can be accumulated, at the booster injection energy of ~20 GeV. The positrons can be captured into a single barrier RF bucket, with a final length of $\sim$ 5 m, at which the longitudinal density would be about 1000 times higher than the peak bunch density in the collider ring (without collision), possibly compromising the beam stability.

Accelerating the long positron superbunch containing 10^{17} e$^+$ by 25 GeV, from 20 to 45 GeV, requires a total energy of 0.4 GJ, or, if accelerated over 2 s, about 200 MW of RF power. This translates into an induction acceleration voltage of ~2 MV per turn, which is three orders of magnitude higher than the induction voltage of the KEK digital accelerator [52], but about 10 times lower than the induction RF voltage produced at the LANL DARHT-II [53], at much higher or lower repetition rate, respectively. On the ramp and at top energy, the full bunch length l_b can conceivably

ISBN: 978-3-95450-236-3 ISSN: 2673-7027 doi:10.18429/JACoW-eeFACT2022-TUYAT0101

be compressed to the assumed $l_b \approx 5$ m, by squeezing the gap of the barrier bucket (which requires substantially more voltage for the barrier RF system) – also see [26, 52]. Tentative parameters of the positron superbunch are compiled in Ref. [49]. We assume that the booster ring runs near the coupling resonance so that the emittance is shared between the two transverse planes.

When the accelerated and compressed positron bunch is sent into a plasma, the plasma electron distribution quickly acquires a nearly stationary shape, while any remaining plasma ions are slowly repelled away from the positron beam [54]. In the stationary phase, the electron distribution approaches a form that resembles the one of the positron beam, with a density

$$n_{e,\mathrm{stat}} \approx \frac{N_b}{2\pi l_b \sigma_\perp^2} \, , \tag{8}$$

so as to neutralize the electric field. With an average rms size of $\sigma_\perp \approx 10\,\mu$m, we obtain $n_{e,\mathrm{stat}} \approx 10^{26}$ m^{-3}. Considering a 100 m long plasma channel yields $\sim 10^{11}$ μ pairs, with an initial muon energy of ~22 GeV, and an initial lifetime of 0.5 ms at this energy.

In particular, once the electron distribution is nearly stationary, the longitudinal fields inside the plasma can be neglected. The resulting transverse emittance of the produced muons can be optimized by adjusting positron beam parameters and the optical functions at the entrance to the plasma [49]. In addition, a phase rotation (bunch compression) of the muons may be required, since the initial bunch length ~ 5 m, of the positrons or resulting muons, will still be too long for collider operation.

Overall, the described scheme would produce about 10^{12} muon pairs per cycle, with a cycle length of order 3 s. Even at an energy of 50 TeV, the muons would decay with a lifetime of only 1.1 s. This kind of cycle/lifetime ratio of about 3:1 might still be considered acceptable. On the other hand, for collision at a muon beam energy of 7 TeV in the existing LHC ring, the muon lifetime would be only 0.15 s, and the scheme would be considerably more challenging.

COST AND SUSTAINABILITY

Efficient RF Power Sources

Radiofrequency (RF) systems are used to keep a charged particle beam bunched, and to feed energy to the beam, be it for purposes of acceleration or to compensate for the energy lost due to synchrotron radiation. In superconducting continuous-wave RF cavities, almost no power is lost to the cavity wall and all RF power entering the cavity can be transferred to the beam highly efficiently. Then, in the overall power budget, the RF power source is the most inefficient element. For RF frequencies above about 400 MHz, and for high power applications, historically klystrons have been the RF power source of choice on particle accelerators.

It is most remarkable that about 80 years after the invention of the klystron by the Varian brothers, a revolution in klystron technology is underway. Using advanced bunching techniques, it is expected that the klystron efficiency can be raised from the present 50–60% level to about 90%, which would translate into a significant energy saving [55]. Prototypes of such novel highly-efficient klystrons are being manufactured both by CERN, in collaboration with industry, for FCC, CLIC and ILC, and, in China, for the CEPC project.

In parallel, the efficiency of alternative RF power sources, such as inductive output tubes or solid-state amplifiers [56], is also being improved.

While at present the RF power sources are the dominant contributors to overall grid-to-beam power transmission inefficiency, a few percent additional losses each occur in the electrical network between utility high-voltage interconnect point and RF power source, and in the wave guides and couplers feeding the generated RF power into the accelerating cavities, respectively.

Efficient Magnets

For high fields, superconducting magnets are most efficient, as no energy is lost, and electric power is mostly required for the cryogenic system. Namely, significant heat from synchrotron radiation and (in the case of muons) particle decay needs to be removed from the cold magnet environment. Approximately 1000 W of electric power is required to remove 1 W of heat at 1.9 K. Increasing the operating temperature of the high-field superconducting magnets from presently 1.9 or 4.5 K to 10–20 K or higher, would greatly improve the cryogenic efficiency [57], and reduce overall power consumption. This temperature step may be achieved through advanced magnets based on high temperature superconductor [58].

For lower fields, up to of order 1 T, permanent magnets are most energy efficient. An example is the Fermilab Recycler Ring [59], which was built almost entirely from permanent magnets. Even adjustable permanent magnets have been designed and built for applications at light sources, colliders, and plasma accelerators [60]. Other ingenious solutions for energy saving can be found, depending on the respective application. For example, for the FCC-ee double-ring collider, twin dipole and quadrupole magnets at low field (of order 0.05 T, for the dipoles) have been designed [61], which promise a significant power reduction compared with the magnets of similar fields at earlier colliders.

Energy Recovery Linacs (ERLs)

Recovering the energy of the spent beam after one or several collisions is another effective measure to improve overall energy efficiency, if a significant fraction of the overall electric power is stored in the beam, as typically is the case for beams accelerated in superconducting linacs [62].

A comparison of ERL-based colliders proposed half a century ago with several recent concepts is presented in Table 1. The main differences between proposals from the 1970s and today are the collision of flat beams instead of round beams, and much smaller (vertical) beam sizes, combined with higher beam current, yielding, on paper, of order

ISBN: 978-3-95450-236-3 ISSN: 2673-7027 doi:10.18429/JACoW-eeFACT2022-TUYAT0101

Table 1: A comparison of ERL-based colliders proposed in the 1960s [62] and 1970s [63, 64], and in the recent period 2019–2021 [7, 65, 66].

Proposal	Tigner 1965	Amaldi 1976	Gerke & Steffen 1979	Litvinenko et al. 2019		Telnov 2021		Litvinenko et al. 2022	
c.m. energy [GeV]	1–6	300	200	240	600	250	500	240	3000
av. beam current [mA]	120	10	0.3	2.5	0.16	100	100	38	40
vert. rms IP beam size [nm]	40,000 (round)	2,000 (round)	900 (round)	6	5	6.1	7.4	2.7	4.1
luminosity [10^{34} cm^{-2}s^{-1}]	0.0003	0.01	0.004	73	8	90	64	343	94

~10,000 times higher luminosity than the proposals from half a century ago.

Beam Loss Control and Machine Protection

Also minimisation of beam loss can improve the energy efficiency of accelerators, such as ERLs. For proposed future higher-energy facilities, machine protection and beam collimation systems become ever more challenging due to their unprecedented beam power or stored energy. For example, the FCC-hh design features a stored beam energy of 8.3 GJ [67], which is more than a factor 20 higher than for the LHC.

NOVEL DIRECTIONS

Storage rings constructed as high energy physics colliders could also serve for other intriguing applications. In this section, we mention a few examples.

Ultimate Light Sources

Large circular storage rings like the FCC-ee, and even the FCC-hh, can serve as ultimate storage-ring light sources, with diffraction limited emittances down to photon wavelengths of

$$\lambda_{\min} \approx 4\pi\varepsilon_x \, . \tag{9}$$

For FCC-ee the geometric emittance ε_x, of the collider or of the full-energy booster, scales as γ^2, and the lowest value of $\varepsilon_x \approx 50$ pm is reached at the injection energy of 20 GeV, resulting in $\lambda_{\min,ee} \approx 650$ pm. With a beam current of 1.5 A or higher, this could represent a formidable light source. Conversely, for FCC-hh the normalized proton beam emittance $\gamma\varepsilon_x$ shrinks during proton beam storage at 50 TeV to ~ 0.2 µm [67], corresponding to a geometric emittance of 4 pm, and the associated minimum wavelength is $\lambda_{\min,ee} \approx$ 50 pm, still more than an order of magnitude lower than for the FCC-ee. The FCC-hh design beam current is 0.5 A.

The FCC-ee ring emittance could be further reduced by factors of 10–100 through the addition of damping wigglers, pushing the accessible wavelength into the ten picometre regime.

A more detailed study of synchrotron light produced by such low-emittance FCC-ee beams passing through realistic undulator configurations has been performed recently [68]. The use of hadron storage rings as light sources was discussed in the past, e.g., for the Superconducting Super Collider (SSC) [69].

In addition, also Free Electron Lasers (FELs) based on ERLs designed for high-energy physics colliders can offer outstanding performance in terms of average brightness, and in their wavelength reach down into the few picometre range [70], e.g., in the case of the LHeC-ERL based FEL, with a beam current of ~20 mA.

Detection of Gravitational Waves

Various approaches have been suggested for using beams in a storage ring for the detection of gravitational waves [71–74] including the construction of special optics with regions of extremely high beta functions that would serve as "gravitational wave antennae" [74, 75]. Exploration of such possibilities continues.

Storage Rings as Quantum Computers

With advanced cooling and manipulation schemes, storage rings might eventually be used as quantum computers [76, 77]. Indeed, combining the storage rings of charged particles with the linear ion traps used for quantum computing and mass spectrometry would enable a large leap in the number of ions serving as qubits for a quantum computer. Such an approach holds the promise of significant advances in general quantum calculations and, especially, in simulations of complex quantum systems.

Electric Power Generation

Future accelerators could generate significant rates of electric energy, and, thereby, contribute to ongoing efforts to slow down, or reverse, global warming.

One approach is power generation through inertial fusion with ion accelerators [78, 79]. This would be an alternative to nuclear fusion reactors like ITER.

Accelerators can also drive subcritical fission reactors and, thereby, generate energy more safely and in a better controlled way than classical nuclear power plants. Importantly, they can also offer an important solution to nuclear waste treatment.

As an example, the Multi-purpose hybrid Research Reactor for High-tech Applications (MYRRHA) in Belgium is being developed for demonstrating the large scale feasibility of nuclear waste transmutation using an Accelerator Driven System (ADS) [80]. The MYRRHA design is based on a

ISBN: 978-3-95450-236-3 ISSN: 2673-7027 doi:10.18429/JACoW-eeFACT2022-TUYAT0101

cw 600 MeV proton linac with a high average beam power of 2.4 MW. A major concern is the reliability and availability of this accelerator. Only 10 beam trips longer than 3 s are allowed per 3-month operation cycle, translating into an overall required Mean Time Between Failure of at least 250 hours [80].

Similarly, in Asia, the China initiative Accelerator Driven System (CiADS) equally aims at building the first ADS experimental facility to demonstrate nuclear waste transmutation. The CiADS driving linac can accelerate 5 mA proton beam to 500 MeV at a beam power of up to 2.5 MW with state-of-the-art accelerator technologies [81].

In Japan, at J-PARC, a Transmutation Experimental Facility (TEF) is being developed. In this facility, a beam of negative hydrogen ions, with a power of 250 kW, will be sent onto a Lead-Bismuth Eutectic target, placed in the ADS Target Test Facility (TEF-T). In addition, a laser charge exchange technique will be employed to deliver a low-intensity beam of 10 W to the Transmutation Physics Experimental Facility (TEF-P) [82].

Above, in the section on unstable or rare particles, we already indicated a novel approach to driving subcritical reactors, namely by using high-energy photons from a Gamma Factory, as proposed for CERN [42]. This Gamma Factory, based on laser collisions with a partially stripped LHC ion beam, would produce high-energy photons with tunable angle-dependent energies, which could be tailored to transform specific radioactive isotopes. Waste isotopes may be suitably arranged as a function of radial distance from the central photon axis. Such a subcritical nuclear reactor driven by photons from the Gamma Factory is predicted to produce an electric power of order 300 MW, while processing the nuclear waste [44].

BEYOND THE EARTH

To reach the Planck scale of 10^{28} eV, linear or circular colliders would need to have a size of order 10^{10} m, which is about a tenth of the distance between the earth and the sun, if operated close to the Schwinger critical field [83, 84].

Following the FCC a possible next or next-next step in this direction could be a circular collider on the moon (CCM) [85]. With a circumference of about 11 Mm, a centre-of-massage energy of about 14 PeV (1000 times the energy of the LHC), based on 6×10^5 dipoles with 20 T field, either ReBCO, requiring ~7–13 k tons of rare-earth elements, or iron-based superconductor (IBS), requiring of order a million tons of IBS [85]. Many of the raw materials needed to construct machine, injector complex, detectors, and facilities can potentially be sourced directly on the Moon. The 11000-km tunnel should be constructed a few 10 to 100 m under lunar surface to avoid lunar day-night temperature variations, cosmic radiation damage, and meteoroid strikes. A "Dyson band" or "Dyson belt" could be used to continuously collect sun power. Operating this collider would require the equivalent of 0.1% of the sun power incident on Moon surface [85].

SUMMARY AND OUTLOOK

Particle colliders boast an impressive 70 year long history, with dramatic improvements in performance, and they will also be the cornerstone for a long and exciting future in high-energy physics. Future colliders should heed the lessons from the previous generations of colliders, like LEP, SLC, KEKB, PEP-II, LHC, and SuperKEKB.

Present collider-accelerator R&D trends include the development of more powerful positron sources; the widespread application of energy recovery; "nanobeam" handling — with stabilisation, positioning, and tuning; the polarization control at the 0.1% level; monochromatization; the use of machine learning and artificial intelligence, e.g. for automated design and for accelerator operation; and the introduction of novel uses, such as for generating electrical power, probing gravity or developing high-throughput quantum computing; plus, last not least, bringing advanced acceleration schemes to maturity.

Considering the desired higher intensity and energy for future machines, a major challenge will be to make the future colliders truly "green", that is energy-efficient and sustainable. In this context, suppressing synchrotron radiation or mitigating its impact becomes a key objective for the long term. Concerning the near term, it is important to observe that the Future Circular lepton Collider, FCC-ee, is the most sustainable of all the proposed Higgs and electroweak factory proposals, in that it implies the lowest energy consumption for a given value of total integrated luminosity [86, 87], over the collision energy range from 90 to 365 GeV.

For the Future Circular Collider (FCC) effort, the next concrete steps encompass the local/regional implementation scenario to be worked out in collaboration with the CERN host states, machine design optimization, physics studies, and technology R&D, performed via a global collaboration and supported by the EC H2020 FCC Innovation Study, to prove the FCC feasibility by 2025/26.

ACKNOWLEDGMENTS

The author would like to thank R. Aßmann, J. Beacham, M. Benedikt, G. Franchetti, K. Oide, V. Shiltsev, and many other colleagues for helpful discussions.

This work was supported, in parts, by funding from the European Union's Horizon 2020 Research and Innovation programme under Grant Agreement No 101004730 (iFAST).

REFERENCES

[1] F. Zimmermann, "Accelerator Technology and Beam Physics of Future Colliders," *Frontiers in Physics*, vol. 10, 2022, doi:10.3389/fphy.2022.888395

[2] J. Abelleira Fernandez *et al.*, "A Large Hadron Electron Collider at CERN: Report on the Physics and Design Concepts for Machine and Detector," *J. Phys. G*, vol. 39, p. 075 001, 2012, doi:10.1088/0954-3899/39/7/075001

[3] F. Zimmermann, O. Bruning, and M. Klein, "The LHeC as a Higgs Boson Factory," 2013, http://cds.cern.ch/record/1575158

ISBN: 978-3-95450-236-3 ISSN: 2673-7027 doi:10.18429/JACoW-eeFACT2022-TUYAT0101

[4] O. Brüning, A. Seryi, and S. Verdú-Andrés, "Electron-Hadron Colliders: EIC, LHeC and FCC-eh," *Front. Phys.*, vol. 10, p. 886 473, 2022, doi:10.3389/fphy.2022.886473
[5] V. N. Litvinenko, T. Roser, and M. Chamizo-Llatas, "High-energy high-luminosity e+e- collider using energy-recovery linacs," *Physics Letters B*, vol. 804, p. 135 394, 2020, doi:https://doi.org/10.1016/j.physletb.2020.135394
[6] V. I. Telnov, "A high-luminosity superconducting twin e^+e^- linear collider with energy recovery," *arXiv*, 2021.
[7] V. N. Litvinenko *et al.*, *The relic: Recycling linear e^+e^- collider*, 2022, doi:10.48550/ARXIV.2203.06476
[8] B. Richter, "Very High-Energy electron-Positron Colliding Beams for the Study of the Weak Interactions," *Nucl. Instrum. Meth.*, vol. 136, pp. 47–60, 1976, doi:10.1016/0029-554X(76)90396-7
[9] S. Myers, "FCC: Building on the shoulders of giants," *Eur. Phys. J. Plus*, vol. 136, no. 10, p. 1076, 2021, doi:10.1140/epjp/s13360-021-02056-w
[10] K. Oide, "A Final Focus System for Flat Beam Linear Colliders," *Nucl. Instrum. Meth. A*, vol. 276, pp. 427–432, 1989, doi:10.1016/0168-9002(89)90567-6
[11] M. Aleksa *et al.*, "CLIC Beam Delivery System," *CERN Report*, vol. CLIC-Note-551, 2003, http://cds.cern.ch/record/602202
[12] G. Zamudio and R. Tomas, "Optimization of the CLIC 500 GeV Final Focus system and design of a new 3 TeV Final Focus system with L*=6.0 M," CERN, Tech. Rep., 2010, http://cds.cern.ch/record/1368480
[13] F. Zimmermann, "Magnet alignment tolerances in the 1994 SLC final focus system," *SLAC SLC Collider Note*, vol. SLAC-CN-398, 1994.
[14] H. Padamsee, "ILC Upgrades to 3 TeV," *arXiv*, vol. 2108.11904, 2021.
[15] K. Oide, "Synchrotron Radiation Limit on the Focusing of Electron Beams," *Phys. Rev. Lett.*, vol. 61, pp. 1713–1715, 1988, doi:10.1103/PhysRevLett.61.1713
[16] K. Yokoya, "Quantum Correction to Beamstrahlung Due to the Finite Number of Photons," *Nucl. Instrum. Meth.*, vol. A251, p. 1, 1986, doi:10.1016/0168-9002(86)91144-7
[17] K. Yokoya and P. Chen, "Beam-beam phenomena in linear colliders," *Lect. Notes Phys.*, vol. 400, pp. 415–445, 1992, doi:10.1007/3-540-55250-2_37
[18] M. Sands, "The Physics of Electron Storage Rings: An Introduction," *Conf. Proc. C*, vol. 6906161, pp. 257–411, 1969.
[19] P. Chen, "Review of linear collider beam-beam interaction," *AIP Conf. Proc.*, vol. 184, pp. 633–679, 1989, doi:10.1063/1.38047
[20] P. Chen, "Differential luminosity under multiphoton beamstrahlung," *Phys. Rev. D*, vol. 46, pp. 1186–1191, 3 1992, doi:10.1103/PhysRevD.46.1186
[21] R. L. Warnock, "Shielded coherent synchrotron radiation and its effect on very short bunches," in *4th Advanced ICFA Beam Dynamics Workshop: Collective Effects in Short Bunches*, 1990.
[22] J. S. Schwinger, "On radiation by electrons in a betatron: Transcription of a paper by J. Schwinger, 1945," pp. 307–331, 1945, doi:10.2172/1195620
[23] L. Arzimovitch and I. Pomeranchuk, "The Radiation of Fast Electrons in the Magnetic Field," *J. Phys. (USSR)*, vol. 9, 1945.
[24] D. Ratner and G. Stupakov, "Observation of shot noise suppression at optical wavelengths in a relativistic electron beam," *Phys. Rev. Lett.*, vol. 109, p. 034 801, 3 2012, doi:10.1103/PhysRevLett.109.034801
[25] H. Primack and R. Blümel, "Synchrotron radiation of crystallized beams," *Phys. Rev. E*, vol. 60, pp. 957–967, 1 1999, doi:10.1103/PhysRevE.60.957
[26] K. Takayama and R. J. Briggs, Eds., *Induction Accelerators*. Springer, 2011, doi:10.1007/978-3-642-13917-8
[27] L. Bottura, "High Field Magnets," *Future Collider Forum: 1st Workshop, DESY 6–8 October, 2021*, 2021.
[28] P. Dhakal, "Nitrogen doping and infusion in SRF cavities: A review," *Physics Open*, vol. 5, p. 100 034, 2020, doi:https://doi.org/10.1016/j.physo.2020.100034
[29] M. Ge *et al.*, "Cvd coated copper substrate srf cavity research at cornell university," in *Proc. 19th Int. Conf. RF Superconductivity (SRF'19)*, Dresden, Germany, 2019, pp. 381–386, doi:10.18429/JACoW-SRF2019-TUFUB8
[30] M. Sayeed, H. Elsayed-Ali, G. V. Eremeev, M. J. Kelley, C. E. Reece, and U. Pudasaini, "Magnetron Sputtering of Nb3Sn for SRF Cavities," in *Proc. 9th Int. Particle Accelerator Conf. (IPAC'18)*, Vancouver, Canada, 2018, pp. 3946–3949, doi:10.18429/JACoW-IPAC2018-THPAL129
[31] S. Posen, M. Liepe, G. Eremeev, U. Pudasaini, and C. E. Reece, "Nb3Sn Superconducting Radiofrequency Cavities: a Maturing Technology for Particle Accelerators and Detectors," in *2022 Snowmass Summer Study*, 2022.
[32] H. Padamsee, K. W. Shepard, and R. Sundelin, "Physics and accelerator applications of rf superconductivity," *Annual Review of Nuclear and Particle Science*, vol. 43, no. 1, pp. 635–686, 1993, https://doi.org/10.1146/annurev.ns.43.120193.003223
[33] E. Adli *et al.*, "A beam driven plasma-wakefield linear collider: From higgs factory to multi-tev," *arXiv*, vol. 1308.1145, 2013.
[34] J. B. B. Chen, D. Schulte, and E. Adli, "e^+e^- Beam-Beam Parameter Study for a TeV-scale PWFA Linear Collider," *arXiv*, vol. 2009.13672, 2021.
[35] W. Leemans and E. Esarey, "Laser-driven plasma-wave electron accelerators," *Phys. Today*, vol. 62N3, pp. 44–49, 2009, doi:10.1063/1.3099645
[36] C. B. Schroeder, C. Benedetti, E. Esarey, and W. P. Leemans, "Laser-plasma-based linear collider using hollow plasma channels," *Nucl. Instrum. Meth. A*, vol. 829, pp. 113–116, 2016, doi:10.1016/j.nima.2016.03.001
[37] V. Lebedev, A. Burov, and S. Nagaitsev, "Efficiency versus instability in plasma accelerators," *Phys. Rev. Accel. Beams*, vol. 20, p. 121 301, 12 2017, doi:10.1103/PhysRevAccelBeams.20.121301
[38] F. Zimmermann, "Possible limits of plasma linear colliders," *J. Phys.: Conf. Ser.*, vol. 874, 012030. 8 p, 2017, doi:10.1088/1742-6596/874/1/012030
[39] Z. Y. Xu *et al.*, "New injection and acceleration scheme of positrons in the laser-plasma bubble regime," *Phys. Rev. Accel. Beams*, vol. 23, no. 9, p. 091 301, 2020, doi:10.1103/PhysRevAccelBeams.23.091301
[40] C. S. Hue *et al.*, "Efficiency and beam quality for positron acceleration in loaded plasma wakefields," *Phys. Rev. Research*, vol. 3, p. 043 063, 4 2021, doi:10.1103/PhysRevResearch.3.043063
[41] V. D. Shiltsev, "High energy particle colliders: past 20 years,

ISBN: 978-3-95450-236-3 ISSN: 2673-7027 doi:10.18429/JACoW-eeFACT2022-TUYAT0101

next 20 years and beyond," *Phys. Usp.*, vol. 55, pp. 965–976, 2012, doi:10.3367/UFNe.0182.201210d.1033

[42] M. W. Krasny, "The Gamma Factory proposal for CERN," *arXiv*, vol. 1511.07794, 2015.

[43] A. Apyan, M. W. Krasny, and W. Placzek, *Gamma Factory high-intensity muon and positron source – exploratory studies*, 2022, doi:10.48550/ARXIV.2212.06311

[44] M.W. Krasny, *Gamma Factory driven subcritical reactor*, https://indico.cern.ch/event/1137276/contributions/4950792/, 2022.

[45] M. Antonelli, M. Boscolo, R. Di Nardo, and P. Raimondi, "Novel proposal for a low emittance muon beam using positron beam on target," *Nucl. Instrum. Meth. A*, vol. 807, pp. 101–107, 2016, doi:10.1016/j.nima.2015.10.097

[46] F. Zimmermann, "LHC/FCC-based muon colliders," *Journal of Physics: Conference Series*, vol. 1067, p. 022 017, 2018, doi:10.1088/1742-6596/1067/2/022017

[47] M. W. Krasny, A. Petrenko, and W. Płaczek, "The Gamma Factory path to high-luminosity LHC with isoscalar beams," *PoS*, vol. ICHEP2020, p. 690, 2021, doi:10.22323/1.390.0690

[48] M. Benedikt and F. Zimmermann, "Future Circular Collider: Integrated Programme and Feasibility Study," *Submitted to Frontiers of Physics*, 2022.

[49] F. Zimmermann, A. Latina, A. Blondel, M. Antonelli, and M. Boscolo, "Muon Collider based on Gamma factory, FCC-ee and Plasma Target," *Submitted to IPAC'22*, 2022.

[50] A. Blondel, *Private communication*, 2021.

[51] The FCC Collaboration, "FCC-ee: The Lepton Collider," *Eur. Phys. J. Spec. Top.*, vol. 228, 2019, https://doi.org/10.1140/epjst/e2019-900045-4

[52] K. Takayama *et al.*, "Induction acceleration of heavy ions in the KEK digital accelerator: Demonstration of a fast-cycling induction synchrotron," *Phys. Rev. ST Accel. Beams*, vol. 17, no. 1, p. 010 101, 2014, doi:10.1103/PhysRevSTAB.17.010101

[53] J. Barraza *et al.*, "Upgrades to the DAHRT Second Axis Induction Cells," *Conf. Proc. C*, vol. 070625, p. 2385, 2007, doi:10.1109/PAC.2007.4441258

[54] F. Zimmermann, A. Latina, J. Farmer, A. Blondel, M. Antonelli, and M. Boscolo, "Muon Collider Based on Gamma Factory, FCC-ee and Plasma Target," no. 13, p. 1691, presented at *IPAC'22*, Bangkok, Thailand, Jun. 2022, paper WEPOST009.

[55] A. Y. Baikov, C. Marrelli, and I. Syratchev, "Toward High-Power Klystrons With RF Power Conversion Efficiency on the Order of 90%," *IEEE Trans. Electron. Dev.*, vol. 62, no. 10, pp. 3406–3412, 2015, doi:10.1109/TED.2015.2464096

[56] N. Barov, X. Chang, D. J. Newsham, and D. Wu, "Development of the Energy-Efficient Solid State RF Power Source for the Jefferson Laboratory CEBAF Linac," *Conf. Proc. C*, vol. 1205201, pp. 3455–3457, 2012.

[57] M. Seidel, "Towards Efficient Particle Accelerators - A Review," in *Proc. IPAC'22*, Bangkok, Thailand, 2022, pp. 3141–3146, doi:10.18429/JACoW-IPAC2022-FRPLYGD1

[58] L. Bottura and F. Zimmermann, *HE-LHC Options*, invited article for a book on the LHC and its potentials edited by O. Brüning, M. Klein, L. Rossi, and P. Spagnolo, 2022.

[59] J. T. Volk, "Experiences with permanent magnets at the fermilab recycler ring," *Journal of Instrumentation*, vol. 6, no. 08, T08003–T08003, 2011, doi:10.1088/1748-0221/6/08/t08003

[60] B. Shepherd, "Permanent Magnets for Accelerators," *JACoW*, vol. IPAC2020, MOVIRO05, 2020, doi:10.18429/JACoW-IPAC2020-MOVIRO05

[61] A. Milanese, "Efficient twin aperture magnets for the future circular e^+/e^- collider," *Phys. Rev. Accel. Beams*, vol. 19, p. 112 401, 11 2016, doi:10.1103/PhysRevAccelBeams.19.112401

[62] M. Tigner, "A possible apparatus for electron clashing-beam experiments," *Nuovo Cim.*, vol. 37, pp. 1228–1231, 1965, doi:10.1007/BF02773204

[63] U. Amaldi, "A Possible Scheme to Obtain e- e- and e+ e- Collisions at Energies of Hundreds of GeV," *Phys. Lett. B*, vol. 61, pp. 313–315, 1976, doi:10.1016/0370-2693(76)90157-X

[64] H. Gerke and K. Steffen, "Note on a 45-GeV - 100-GeV 'Electron Swing' Colliding Beam Accelerator," *DESY Report*, vol. DESY-PET-79-04, 1979.

[65] V. N. Litvinenko, T. Roser, and M. Chamizo-Llatas, "High-energy high-luminosity e^+e^- collider using energy-recovery linacs," *Phys. Lett. B*, vol. 804, p. 135 394, 2020, doi:10.1016/j.physletb.2020.135394

[66] V. I. Telnov, "A high luminosity superconducting twin e^+e^- linear collider with energy recovery," in *International Workshop on Future Linear Colliders*, 2021.

[67] The FCC Collaboration, "FCC-hh: The Hadron Collider," *Eur. Phys. J. Spec. Top.*, vol. 228, 2019, https://doi.org/10.1140/epjst/e2019-900087-0

[68] S. Casalbuoni, M. Benedikt, M. Doser, and F. Zimmermann, "First thoughts on the synergetic use of the FCC-ee collider and its injector complex for photon science and other applications," *CERN/FCC Internal Note*, 2020.

[69] S. K. Dutt, "Synchrotron radiation from protons," in *Workshop on 4th Generation Light Sources*, 1992.

[70] Z. Nergiz, N. S. Mirian, A. Aksoy, D. Zhou, F. Zimmermann, and H. Aksakal, "Bright ångstrom and picometer free electron laser based on the large hadron electron collider energy recovery linac," *Phys. Rev. Accel. Beams*, vol. 24, p. 100 701, 10 2021, doi:10.1103/PhysRevAccelBeams.24.100701

[71] D. Zer-Zion, "On the detection of gravitational waves through their interaction with particles in storage rings," 1998.

[72] J. W. van Holten, "Cyclotron motion in a gravitational wave background," 1999.

[73] S. Rao, M. Brüggen, and J. Liske, "Detection of gravitational waves in circular particle accelerators," *Phys. Rev. D*, vol. 102, p. 122 006, 12 2020, doi:10.1103/PhysRevD.102.122006

[74] A. Berlin *et al.*, "Storage Rings and Gravitational Waves: Summary and Outlook," in *ARIES WP6 Workshop: Storage Rings and Gravitational Waves*, 2021.

[75] K. Oide, "Response of a storage-ring beam to a gravitational wave - preliminary considerations," *presented at ARIES SRGW2021 workshop*, 2021.

[76] K. A. Brown and T. Roser, "Towards storage rings as quantum computers," *Phys. Rev. Accel. Beams*, vol. 23, p. 054 701, 5 2020, doi:10.1103/PhysRevAccelBeams.23.054701

[77] T. Shaftan and B. B. Blinov, "Cold ion beam in a storage ring as a platform for large-scale quantum computers and simulators: Challenges and directions for research and development," *Phys. Rev. Accel. Beams*, vol. 24, p. 094 701, 9 2021, doi:10.1103/PhysRevAccelBeams.24.094701

[78] I. Hofmann, "The Challenge of Inertial Fusion Driven by

ISBN: 978-3-95450-236-3 ISSN: 2673-7027 doi:10.18429/JACoW-eeFACT2022-TUYAT0101

Heavy Ion Accelerators," in *Proc. LINAC'98*, Chicago, IL, USA, Aug. 1998, https://jacow.org/l98/papers/FR2001.pdf

[79] S. A. Slutz *et al.*, "Scaling magnetized liner inertial fusion on z and future pulsed-power accelerators," *Physics of Plasmas*, vol. 23, no. 2, p. 022 702, 2016, doi:10.1063/1.4941100

[80] H. Podlech *et al.*, "The MYRRHA Project," in *Proc. NAPAC'19*, Lansing, MI, USA, Sep. 2019, pp. 945–950, doi:10.18429/JACoW-NAPAC2019-THZBA2

[81] Z. J. Wang *et al.*, "The Status of CiADS Superconducting LINAC," in *Proc. IPAC'19*, Melbourne, Australia, May 2019, pp. 994–997, doi:10.18429/JACoW-IPAC2019-MOPTS059

[82] S.-i. Meigo, H. Iwamoto, H. Matsuda, and H. Takei, "Target test facility for ads and cross-section experiment in j-parc," *Journal of Physics: Conference Series*, vol. 1021, no. 1, p. 012 072, 2018, doi:10.1088/1742-6596/1021/1/012072

[83] P. Chen and R. J. Noble, "Crystal channel collider: Ultrahigh-energy and luminosity in the next century," *AIP Conf. Proc.*, vol. 398, no. 1, pp. 273–285, 1997, doi:10.1063/1.53055

[84] F. Zimmermann, "Future colliders for particle physics—big and small," *Nuclear Instruments and Methods in Physics Research Section A: Accelerators, Spectrometers, Detectors and Associated Equipment*, vol. 909, pp. 33–37, 2018, 3rd European Advanced Accelerator Concepts workshop (EAAC2017), doi:https://doi.org/10.1016/j.nima.2018.01.034

[85] J. Beacham and F. Zimmermann, "A very high energy hadron collider on the moon," *New Journal of Physics*, vol. 24, no. 2, p. 023 029, 2022, doi:10.1088/1367-2630/ac4921

[86] M. Benedikt, A. Blondel, P. Janot, *et al.*, "Future Circular Colliders succeeding the LHC," *Nature Physics*, vol. 16, p. 402, 2020, doi:https://doi.org/10.1038/s41567-020-0856-2

[87] P. Janot, A. Blondel, "The carbon footprint of proposed e+e-Higgs factories," *Eur. Phys.'J. Plus*, vol. 137, p. 1122, 2022, doi:10.1140/epjp/s13360-022-03319-w

ISBN: 978-3-95450-236-3 ISSN: 2673-7027 doi:10.18429/JACoW-eeFACT2022-TUYAT0102

FCC-ee LATTICE DESIGN

J. Keintzel*, A. Abramov, M. Benedikt, M. Hofer, K. Oide,
R. Tomás, F. Zimmermann, CERN, Geneva, Switzerland
P. Hunchak, University of Saskatchewan, Saskatoon, Canada
T. O. Raubenheimer, SLAC National Accelerator Laboratory, USA

Abstract

Within the framework of the Future Circular Collider Feasibility and Design Study, the design of the electron-positron collider FCC-ee is being optimised, as a possible future double collider ring, currently foreseen to start operation during the 2040s. FCC-ee is designed to operate at four different energy stages, allowing for precision measurements: from the Z-pole up to above the $t\bar{t}$-threshold. This synchrotron with almost 100 km circumference is designed including advanced accelerator concepts, such as the crab-waist collision scheme or one combined off-momentum and betatron collimation insertion. Furthermore, numerous optics tuning and measurement studies are being performed to drive the collider design at an early stage and guarantee its feasibility and efficient operation.

INTRODUCTION

The Future Circular electron positron Collider [1], FCC-ee, is the first part of the so-called integrated FCC program [2], which foresees, first, the construction of an almost 100 km long tunnel infrastructure and the integration and commissioning of the FCC-ee. After completion of its physics program, it is then envisaged to decommission the FCC-ee, followed by integration of the hadron FCC [3], FCC-hh, into the same tunnel infrastructure. First collisions are presently foreseen in the mid-2040s for the FCC-ee and around 2065 for the FCC-hh [4].

A flexible high energy electron-positron collider such as the FCC-ee, offers the potential for high precision physics experiments at various particle physics resonances [5, 6]. In case of the FCC-ee beam energies from 45.6 GeV, corresponding to the Z-pole, and up to above the top-pair-threshold with 182.5 GeV are foreseen. To limit the synchrotron radiation (SR) power to 50 MV per turn the beam current decreases with increasing energy. Each energy stage leads, therefore, to unique beam dynamics challenges, and solutions need to be found in accordance with the general layout.

Within the framework of the FCC feasibility study, launched in 2021, it is aimed to provide a self-consistent design of the required technical infrastructure and the accelerator complex for the FCC-ee by end of 2025 with a mid-term review in mid-2023 [7, 8].

REVISED PLACEMENT

The tunnel infrastructure required to host the FCC in the Geneva basin is assumed to be constructed approximately 100 m below ground, similar to the tunnel which presently hosts the Large Hadron Collider, LHC [9]. Tunnel construction is one of the main cost drivers, and depends on the tunnel dimensions, depth and composition of the ground material. Additionally, shafts and surface sites around the circumference are required to host various infrastructures, demanding dedicated civil engineering solutions. Geographic constraints to integrate a circular collider into the Franco-Swiss-Basin are the various mountain ranges surrounding it, including the Jura-mountains in the north-west and the Plateau des Bornes in the south-east in addition to the Geneva lake in the north-east. Furthermore, a possible circular tunnel should surround the Salève-mountain and, hence, these constraints already limit the circumference to about 80 km to 100 km.

Considering all described constraints it has been found that a 90 km tunnel with a four-fold symmetry together with 8 surface sites and straight sections is the most suitable layout. Figure 1 shows the FCC and the LHC placement schematically. The FCC-hh and the FCC-ee lattices have, therefore, been adapted to follow this new tunnel infrastructure and the latter is described in the following.

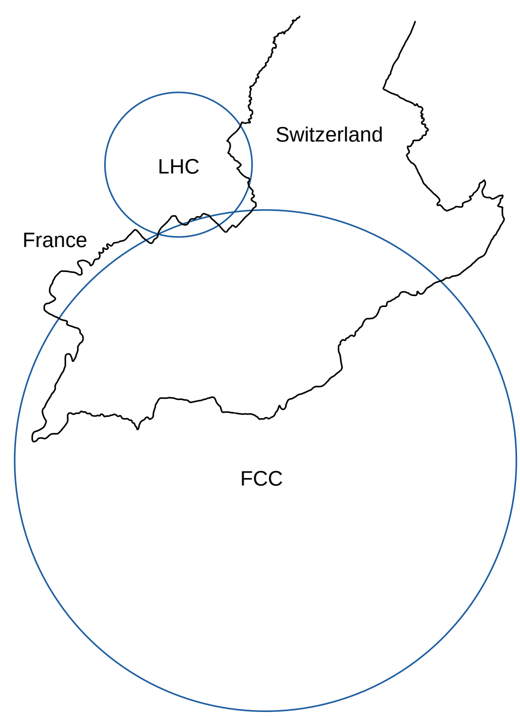

Figure 1: Comparison between the LHC, the FCC and the Franco-Swiss border.

* jacqueline.keintzel@cern.ch

ISBN: 978-3-95450-236-3 ISSN: 2673-7027 doi:10.18429/JACoW-eeFACT2022-TUYAT0102

Table 1: Latest FCC-ee beam optics parameters for the lattice with four interaction points [12].

		Z	**WW**	**ZH**	**$t\bar{t}$**
Circumference	[km]	91.174			
Bending radius	[km]	9.937			
SR power per beam	[MW]	50			
Half crossing angle	[mrad]	15			
Beam Energy	[GeV]	45.6	80	120	182.5
Beam Current	[mA]	1280	135	26.7	5.0
Bunches/beam	[-]	10000	880	248	40
Bunch population	[10^{11}]	2.43	2.91	2.04	2.37
Horizontal emittance	[nm]	0.71	2.16	0.64	1.49
Vertical emittance	[pm]	1.42	4.32	1.29	2.98
Arc cell phase advance	[°]	90/90			
Arc cell length	[m]	100		50	
Momentum compaction factor	[10^{-6}]	28.5		7.33	
Arc sextupole families	[-]	75		146	
Betatron tunes	[-]	214.260 / 214.380		402.224 / 394.360	
Synchrotron tune	[-]	0.0370	0.0801	0.0328	0.0826
β_x^* / β_y^*	[mm]	100 / 0.8	200 / 1.0	300 / 1.0	1000 / 1.6
Energy spread with SR/BS	[%]	0.038 / 0.132	0.069 / 0.154	0.103 / 0.185	0.157 / 0.221
Bunch length with SR/BS	[mm]	4.38 / 15.4	3.55 / 8.01	3.34 / 6.00	1.95 / 2.75
RF-frequency	[MHz]	400	400	400	400 + 800
Total RF voltage	[GV]	0.120	1.0	2.08	11.25
Long. damping time	[turns]	1168	217	64.5	18.5
Energy acceptance	[%]	±1.3	±1.3	±1.7	−2.8 +2.5
Luminostiy / IP	[10^{34} cm^{-2}s^{-1}]	182	19.4	7.26	1.25
Polarization time	[s]	15000	900	120	4.6
SR losses/turn	[GeV]	0.039	0.370	1.869	10.0

GENERAL LAYOUT

Compared to the FCCC-ee CDR version numerous changes have been made, including a shorter circumference and the possibility of integrating four instead of two experiments [11]. The FCC-ee lattice follows the new, so-called lowest risk tunnel scenario with approximately 91.1 km circumference, eight straight sections, (PA, PB, PD, PF, PG, PH, PJ and PL) and is schematically shown in Fig. 2. It offers the possibility of up to four experimental insertion regions (IRs) in PA, PD, PG and PL, where the beams are brought to collision from the inside outwards. Thus, beams are required to change from the inside to the outside aperture in all IRs. The beam collimation section is placed in PF. RF-cavities are foreseen to be integrated in one to two IRs, PL and PH. The electron and the positron beams are presumed to be injected continuously at nominal beam energy in PB (top-up injection) from the High Energy Booster (HEB). The HEB is designed to be installed in the same tunnel infrastructure and thus its lattice design must also be compatible with the one for the colliding rings. Thus, the lattice design of the FCC-ee must comply with all three rings hosted in the same tunnel, and thus two IRs are dedicated for the RF-cavities of the three rings.

Designed at four different beam energies of 45.6, 80, 120 and 182.5 GeV, the FCC-ee allows for physics precision experiments at the Z-pole, the W-pair-threshold, the ZH-maximum and above the top-pair-threshold [6]. It is presently presumed to operate the FCC-ee with increasing beam energy over years, which, among others, requires a flexible lattice and optics design, allowing for fast transitions including upgrades of the RF-cavities to compensate increasing SR energy losses. The latest FCC-ee lattice and optics parameters are summarized in Table 1 [12].

ARCS

The eight arcs are designed using FODO cell structures, consisting of horizontally focusing and defocusing quadrupoles (QF and QD in the lattice) with bending dipoles in-between, with a transverse phase advance of 90° at all energy stages. Although the transverse phase advance is constant over all energies, we note that at the Z-pole and the WW-threshold the cell length is 100 m, while at ZH- and $t\bar{t}$-operation it is reduced to about 50 m by inserting additional quadrupole magnets [12]. Non-interleaved individually powered 76 or 146 sextupole pairs, respectively for the two lower or higher beam energy modes, are installed with a $-I$-transformation between them. The periodic structure within the arc, named super-cell, consists of five FODO cells and contains one focusing and one defocusing sextupole pair. Therefore also additional sextupole magnets are required to

ISBN: 978-3-95450-236-3 ISSN: 2673-7027 doi:10.18429/JACoW-eeFACT2022-TUYAT0102

be installed when switching to the shorter FODO cells arc lattice for the higher beam energies. Due to fewer quadruple magnets in the arc optics for the lower beam energies at the Z- and WW-mode, the arc β-functions are roughly a factor 2 larger and the horizontal dispersion by almost a factor 4. A schematic plot of one or two super-cells, respectively, for the lower and higher beam energy arc designs is shown in Fig. 3.

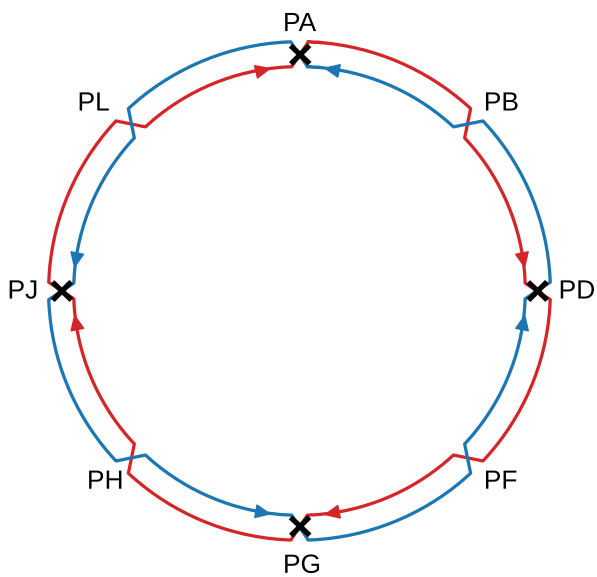

Figure 2: FCC-ee general layout with four-fold periodicity and super-symmetry with 8 straight sections. The positron and the electron beam are circulating, respectively, clock and counter-clock wise. The four experimental straight sections are marked with a black cross.

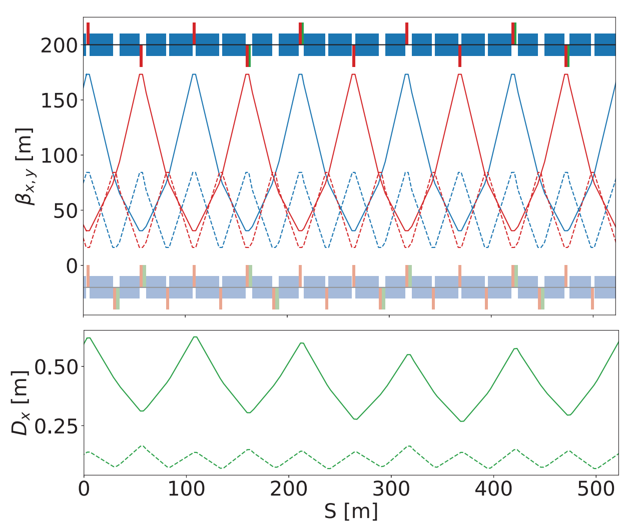

Figure 3: FCC-ee arc lattice and optics for five FODO cells (equivalent to one super-cell) for the Z- and WW-mode (solid lines); and ten FODO cells (equivalent to two super-cells) for ZH- and $t\bar{t}$-mode (dashed lines). Horizontal and vertical β-functions are shown in, respectively, blue and red. Dipoles, quadrupoles and sextupoles are shown, respectively, in blue, red and green. Focusing and defocusing elements, respectively, are shown below and above the horizontal axis.

The sextupole families are optimized to maximize the momentum aperture up to about 2.8 % at 182.5 GeV, since beamstrahlung and synchrotron radiation lead to a wide momentum spread. Additionally, horizontal on-momentum dynamic aperture of about 15 σ is achieved, required for top-up injection. The possibility of using fewer than 75 and 146 sextupole pairs, respectively, for the lower energy and higher energy operation modes, while reaching the required momentum aperture, is envisaged to be explored.

EXPERIMENTAL INSERTIONS

All four experimental IRs feature the same optics design with horizontal and vertical β-functions at the interaction point (IP) of as low as $\beta^*_{x,y} = 100, 0.8$ mm at the Z-pole, shown in Fig. 4, and a crossing angle of 30 mrad. Although β^*_y is about 3 times larger than the SuperKEKB design [13], the generated chromaticity around the IP is in the same order of magnitude for both colliders. It has to be noted, that the minimum β^*_y achieved so far in SuperKEKB is 0.8 mm and thus approximately a factor 3 larger than its design.

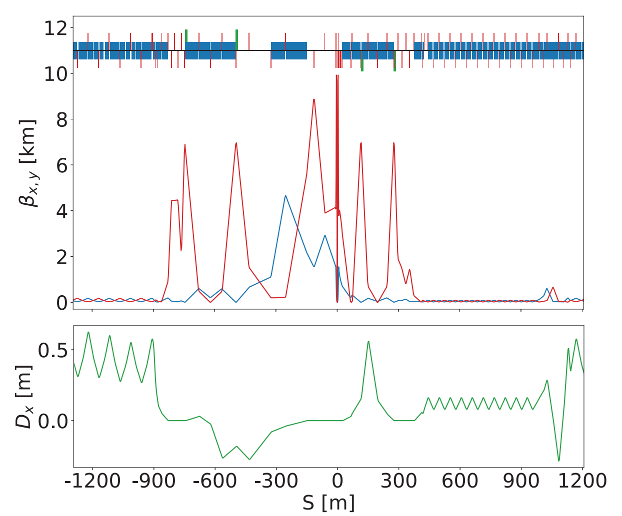

Figure 4: Lattice and optics for the experimental interaction region for the Z-pole. $S = 0$ marks the IP. Horizontal and vertical β-functions are shown in, respectively, blue and red. The beam direction is from left to right. Dipoles, quadrupoles and sextupoles are shown, respectively, in blue, red and green. Focusing and defocusing elements, respectively, are shown below and above the horizontal axis.

To control the generated chromaticity, a local chromaticity correction scheme (LCCS) consisting of non-interleaved sextupole pairs, for the vertical plane is integrated on both IP sides. The outer sextupoles of the LCCS are also the ones used for the crab-waist transformation [14–16]. For the crab-waist collision scheme vertical beam sizes in the order of a few nano-meter are brought to collision with a large Piwinksi-angle aligning the waist of the β-functions on

ISBN: 978-3-95450-236-3 ISSN: 2673-7027 doi:10.18429/JACoW-eeFACT2022-TUYAT0102

the axis of the other beam via adequate sextupole powering. The crab-waist sextupoles correspond to the outer ones of each pair and are placed at a horizontal and vertical phase advance of, respectively, 2π and 2.5π with respect to the IP on both sides, as schematically shown in Fig. 5, together with the presently used terminology of the IR quadrupoles. This scheme has first been tested successfully at DAΦNE [14–16] with dedicated crab-sextupoles and is presently also used in SuperKEKB [13] using the virtual crab-waist collision scheme which is also foreseen for the FCC-ee [5].

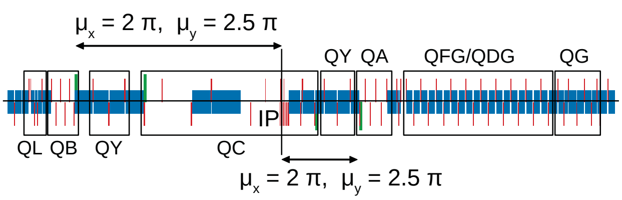

Figure 5: Betatron phase advance between the IP and the LCCS sextupoles and terminology of quadrupoles in the experimental IRs. Dipoles, quadrupoles and sextupoles are shown, respectively, in blue, red and green. Focusing and defocusing elements, respectively, are shown below and above the horizontal axis.

In each IP beams cross from the inside to the outside aperture as shown in Fig. 6, to mitigate synchrotron radiation at the detector. This requires weaker dipole magnets downstream of the IP, and stronger ones upstream of it. Since the beams are crossing from the inside aperture at all experimental IRs (PA, PD, PG and PJ), beam crossings from the outside towards the inside are required at all other straight sections (PB, PF, PH and PL). In the experimental IRs no common magnets are foreseen for the electron and the positron beam [17]. Recent progress on Machine Detector Interface (MDI) studies is being reported in [18–20].

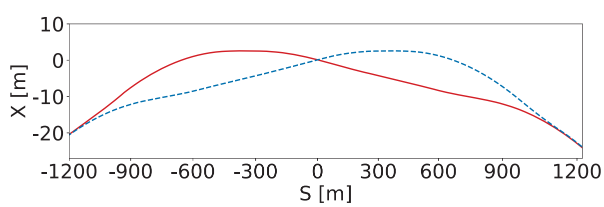

Figure 6: Beam crossing at the IP from the inner towards the outer aperture. $S = 0$ marks the IP.

INJECTION

The positron and the electron beams are injected continuously from the HEB in PB at nominal energy, known as top-up injection. One can distinguish in principle between on- and off-momentum injection, and using a conventional orbit bump or a multipole kicker injection (MKI), resulting in four possible scenarios presently investigated for the FCC-ee [21]. For multipole-kicker injection a dedicated optics has been designed and the on-momentum one is shown in Fig. 7. It features a large horizontal β-function of about 2000 m at the injection point, centered between the MKI and a corrector magnet, MKIC. Previous tracking studies have shown that by integrating an additional MKIC beam size blow-up at the IP is successfully corrected [22]. We note that this optics is optimized for the 2-IP version and significant changes for the 4-IP lattice will need to be applied [23]. Furthermore, if the RF-cavities are not located in the same IR for the HEB and the main rings, the energy saw tooth could lead to different local beam energies between the injector, the electron and the positron ring which must be considered [24]. Future studies will show the most suitable injection technique for the 4-IP FCC-ee lattice.

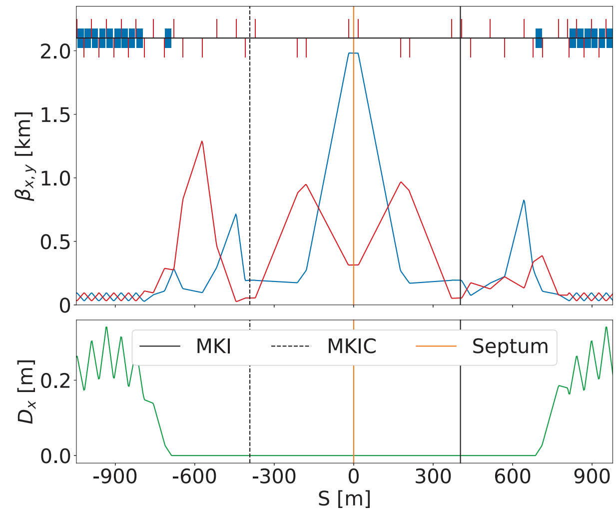

Figure 7: Optics and lattice for on-momentum injection using a multipole kicker (MKI) and a correction magnet (MKIC) for a 2-IP lattice. Horizontal and vertical β-functions are shown in, respectively, blue and red. The beam direction is from left to right. Dipoles, quadrupoles and collimators are shown, respectively, in blue, red and black. Focusing and defocusing elements, respectively, are shown below and above the horizontal axis.

COLLIMATION

The stored beam energy in the FCC-ee reaches up to 20.7 MJ [25], and is, therefore, comparable to heavy ion operation at the Large Hadron Collider, LHC [10]. One collimation insertion with beam crossing in its center, is integrated into the FCC-ee lattice in PF [26]. This insertions optics, as shown in Fig. 8 for the $t\bar{t}$-mode combines halo and off-momentum collimation, located, respectively, upstream and downstream of the beam crossing. In each plane there is a two-stage collimation system, with 1 primary and 2 secondary colliamtors. While for the halo-collimation the horizontal dispersion is kept low, it reaches up to about ±0.6 m for the momentum collimation, which allows independent cuts in betatron amplitude and in momentum offset [26]. The horizontal and vertical primary collimators are set at 15 σ_x and 80 σ_y respectively, while the off-momentum

ISBN: 978-3-95450-236-3 ISSN: 2673-7027 doi:10.18429/JACoW-eeFACT2022-TUYAT0102

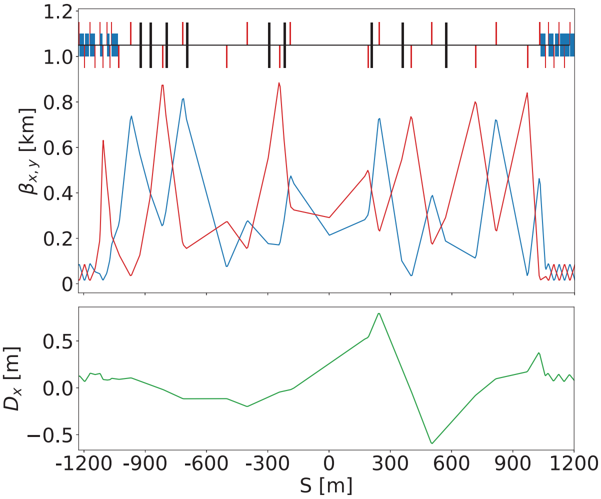

Figure 8: Optics and lattice for the collimation insertion for $t\bar{t}$-mode. Betatron and off-momentum collimation are located, respectively, upstream and downstream of the beam crossing in the center, located at $S = 0$. Horizontal and vertical β-functions are shown in, respectively, blue and red. The beam direction is from left to right. Dipoles, quadrupoles and collimators are shown, respectively, in blue, red and black. Focusing and defocusing elements, respectively, are shown below and above the horizontal axis.

primary is set at 23.0 σ_x, corresponding to a $\mathrm{d}p/p$ cut of 2.9 %, just outside the RF bucket acceptance. The location of the collimators for $t\bar{t}$-operation are also shown in the same figure.

First loss map studies for the 4-IP lattice are performed for betatron collimation at 182.5 GeV beam energy using the newly-developed Xtrack-BDSIM coupling framework [25]. 5×10^6 primary positrons are tracked for 700 turns without radiation and optics tapering, and the FCC-ee aperture model [27] is used. The resulting loss map over the circumference, assuming a molybdenum-graphite primary collimator, are shown in Fig. 9. In addition to the collimators in PF, significant warm and cold losses are also observed in the four experimental IRs. The results are preliminary and further studies, including a comparison with beam loss scenarios and equipment loss tolerances, are required to assess the performance of the collimation system.

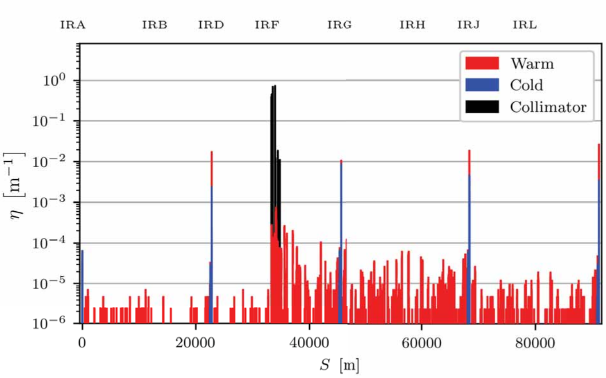

Figure 9: Loss map studies for betatron collimation for the positron ring at 182.5 GeV beam energy with 5×10^6 primary particles using a molybdenum-graphite primary collimator.

RF-INSERTIONS

Although beams are injected at the nominal energy into the main rings, energy is lost due to, for example, synchrotron radiation, beamstrahlung or longitudinal impedance sources. The present baseline foresees elliptical cavities with frequencies of 400 MHz and 800 MHz, whereby novel studies investigate the so-called slotted waveguide elliptical cavities with 600 MHz. More details can be found in [28].

Two RF-sections are presently foreseen at the highest beam energy stage and only one for all lower operation energies. Especially at the Z-pole and the WW-threshold, placing the collider RF-cavities in only one straight section is crucial for precision physics requirements [6], since this allows for keeping the center-of-mass energy, ECM, constant within a few keV at all IPs when considering losses from SR and beamstrahlung, as also demonstrated in [29]. At the Z- and the WW-operation separate RF-cavities are foreseen for the electron and the positron beam with a beam crossing in the center of the straight section. Contrarily, at the ZH- and $t\bar{t}$-mode the present design has common RF-cavities and thus beams must cross before or after being accelerated. To reduce SR power on the RF-cavities only the outgoing beam is deflected [5]. The lattices and terminology of quadrupoles for the IR hosting the RF-system are shown schematically in Fig. 10 for Z- and $t\bar{t}$-mode. Additionally, the optics are shown in Fig. 11.

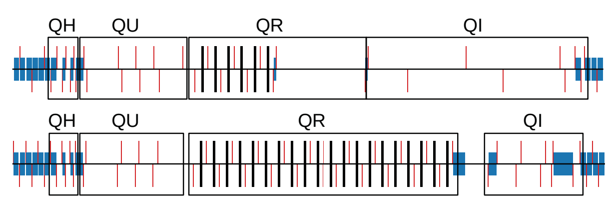

Figure 10: Terminology of quadrupoles in the RF IRs. Dipoles, quadrupoles and RF-cavities are shown, respectively, in blue, red and black. Focusing and defocusing elements, respectively, are shown below and above the horizontal axis.

ENERGY LOSSES

Severe synchrotron radiation losses in lepton storage rings lead naturally to energy losses over each turn. While for the lowest beam energy only roughly 40 MeV are lost due to SR, in case of the highest beam energy about 5.5 % (10 GeV) of the total beam energy is lost per turn. SR power losses depend on the Lorentz-factor by γ_{rel}^4 and thus, also on the local beam energy throughout the circumference. In addition to

ISBN: 978-3-95450-236-3 ISSN: 2673-7027 doi:10.18429/JACoW-eeFACT2022-TUYAT0102

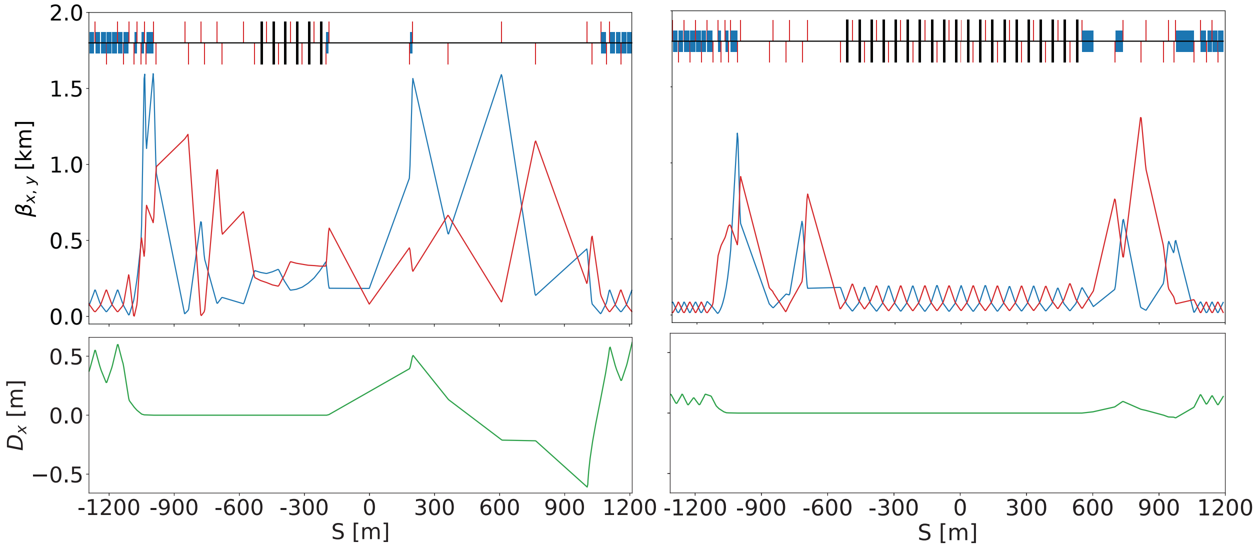

Figure 11: Optics for the RF insertion for Z- (left) and t$\bar{\text{t}}$-modes (right). Horizontal and vertical β-functions are shown in, respectively, blue and red. The beam direction is from left to right. Dipoles, quadrupoles and RF-cavities are shown, respectively, in blue, red and black. Focusing and defocusing elements, respectively, are shown below and above the horizontal axis.

SR, energy losses from beamstrahlung for colliding bunches and longitudinal impedance or energy shifts due to crossing angles also impact the local beam energy. Furthermore, energy drifts are also a result of machine circumference change caused by e.g. Earth tides. All systematic energy losses must be compensated by the RF-cavities. First studies aiming to determine the beam energy over the circumference include SR and beamstrahlung losses for the positron and the electron beam. Figure 12 shows the beam energy variation for both beams without and with beamstrahlung losses at each IP of 14 MeV simulated with MAD-X. In this example two RF-sections are assumed with 400 MHz 5 GV cavities in PH and 800 MHz 6.7 GV in PL. The difference between the lowest and the highest beam energy is 7.56 GeV.

Without adjusting the element's strengths to the local beam energy, large orbits and optics beatings would be generated. To avoid these, the strengths of lattice elements are scaled according to the local beam energy. This is known as tapering, and is included in the lattice design [38]. While

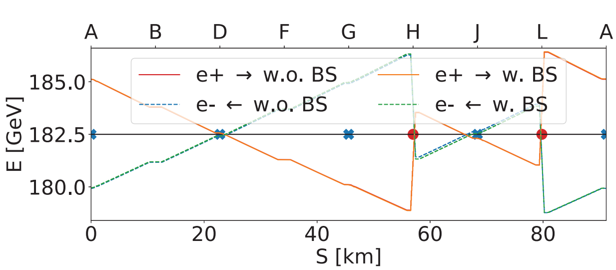

Figure 12: Beam energies at the t$\bar{\text{t}}$-mode with and without beamstrahlung (BS) at the IPs for RF-sections located in PL and PH.

ideal tapering of all elements individually is optimal to mitigate optics aberrations, a huge number of power supplies and, possibly, corrector coils would be required.

ENERGY CALIBRATION, POLARIZATION AND MONOCHROMATIZATION

Since the discovery potential of the FCC-ee is directly linked to the achieved precision on the ECM measurement, huge effort is put into energy calibration, polarization and monochromatization (EPOL) studies in a dedicated working group [30] and numerous reports have recently been made, e.g. in [31] and in a dedicated workshop [32]. Due to the unprecedented luminosity a statistical precision of 4 keV and 100 keV, respectively, for the Z- and the W-mass measurements is predicted [6]. It is, therefore, envisaged achieving a systematic precision in the same order of magnitude by depolarizing transversely polarized low-intensity (10^{10} particles per bunch) non-colliding pilot bunches, which requires dedicated hardware to be integrated in the lattice.

The natural polarization time is 250 h and 15 h and the Z- and WW-mode, respectively. To enhance polarization it is foreseen to integrate wiggler magnets, following the three-block design of those installed in the Large Electron Positron Collider (LEP) [33]. They are presently integrated in each experimental straight section downstream the IP in a dispersion free section (see also Fig. 4). In total 24 units providing 0.7 T magnetic field are foreseen for the FCC-ee, which reduce the polarization time to 12 h while increasing the energy spread to 64 MeV in case of the Z-pole [34]. Furthermore, the integration of wigglers leads to photon generation with a critical energy in the order of MeV and, therefore, possibly imposing radiation protection constraints.

ISBN: 978-3-95450-236-3 ISSN: 2673-7027 doi:10.18429/JACoW-eeFACT2022-TUYAT0102

Wigglers are only used to achieve up to approximately 5 to 10 % polarization on roughly 200 low intensity pilot bunches, and are switched off once this goal is fulfilled. Subsequently all nominal intensity bunches are injected and brought to collision. A transverse kicker depolarizes the pilot bunches and the impact on the polarization is measured using polarimeters.

Foreseen polarimeters are based on inverse Compton scattering processes of the beam with laser photons (532 nm wavelength) travelling in the opposite direction of the beam. Approximately 2 m are required for the Laser Interaction Region (LIR), followed by an about 2 mrad bending dipole and a 100 m long drift space. The back-scattered photons and the scattered leptons with the minimum energy are then measured with silicon-pixel detectors, allowing to reconstruct the 3D polarization vector. One suitable location would be upstream of the straight section hosting the RF-cavities, where one polarimeter for each beam could be installed. Another suitable lattice location for integration of polarimeters could also be upstream of the IP, using the last arc dipole with 1.6 mrad. However, the subsequent drift space is only roughly 50 m, which could impose reducing the laser photon wavelength by a factor 2 or could require higher resolution silicon-pixel detectors, which remains to be explored in future studies [35]. While the baseline foresees only one polarimeter per beam, it has recently been suggested investigating in the feasibility and necessity of installing one polarimeter per beam and IP [36].

TUNING STUDIES

One of the most crucial challenges of the FCC-ee is achieving the design performance for a lattice including non-homogeneous beam energy, misalignments and multipole field errors together with dedicated correction techniques. Numerous aspects are addressed in a dedicated working group, where the most recent meeting can be found in [37]. Furthermore, findings from tuning studies will also feedback into the lattice design and a few examples are given in the following.

The current FCC-ee layout does not explicitly include Beam Position Monitors (BPMs), orbit correctors or skew quadrupoles. It is assumed that orbit correctors and skew quadrupoles coils can be added to every sextupole. However current emittance tuning studies [39] assume the integration of orbit corrector magnets next to every quadrupole, which implies more than a factor 2 larger number of orbit correctors than currently foreseen by placing them at sextupoles. Preliminary simulations show that the length of the orbit correctors should be between 10 cm and 25 cm [40].

SuperKEKB has recently observed shifts of the transverse sextupoles position in the order of 10 µm due to temperature changes between low and high beam current operation [41]. Low beam current is needed for the optics tuning as this involves orbit changes around the ring. The feed-down from the sextupole shifts distorts the optics and is potentially affecting injection efficiency and luminosity. In FCC-ee Z-mode a 3 µm horizontal shift of one IR sextupole changes the vertical tune by about $5{\times}10^{-3}$ units and introduces a 20 % β-beating. For arc sextupoles the required shift to generate comparable aberrations is 250 µm. The FCC-ee will therefore require accurate beam-based sextupole alignment techniques to the 1 µm level, together with the capability to measure optics aberrations at high beam currents. Notably, studies for CEPC are assuming beam-based sextupole alignment with an accuracy of 10 µm [42]. The technology to achieve these ambitious challenges should be investigated. It should include robust sextupole-to-quadrupole alignment or attaching BPMs to sextupoles should be considered.

Suitable optics measurements techniques for the FCC-ee are essential for the control of the beam optics. Turn-by-Turn (TbT) optics measurements have found to be a promising and fast solution in obtaining the beam optics for the FCC-ee [43], since they are regularly used in numerous existing circular storage rings such as the LHC [44, 45] or are presently being explored for SuperKEKB [46]. To apply existing TbT measurement techniques, the beam needs to be excited to increase the action, either by single kicks or by a continuous excitation to force betatronic oscillations. The latter could be applied during high beam current operation to one or few bunches to limit risks related to beam losses or synchrotron radiation and allowing optics tuning in parallel with luminosity production. This requires BPMs with bunch-by-bunch and TbT capabilities together with high frequency kickers which need to be allocated in the machine layout.

SUMMARY AND OUTLOOK

An updated FCC-ee lattice and optics have been designed which follow the novel tunnel layout. Hence, it features a four-fold symmetry and super-periodicity with eight IRs and the possibility of hosting up to four experiments in PA, PD, PG and PJ, where an electron and a positron beam are brought to collision. To limit the SR power on the detectors, the beams always cross from the inside towards the outside in the experimental insertions. Consequently, this demands beams crossing from the outside inwards in all auxiliary IRs. Top-up injection at the nominal energy is foreseen for both beams in PB from the high energy booster, located in the same tunnel infrastructure. Halo-collimation and betatron collimation systems are combined in PF. PL and PH are foreseen to host the RF-cavities for the main rings and the booster.

The FCC-ee optics features a large dynamic and momentum aperture, while simultaneously achieving beam sizes in the nano-meter regime at the IP. Generated chromaticity from the final focus is corrected using a local chromaticity correction in the vertical plane with sextupoles, which are also used for the virtual crab-waist collision scheme.

Complementary studies aiming to determine the ECM as precise as possible have shown the necessity for the integration of wiggler magnets and polarimeters in each beam, which have already successfully been integrated into the lattice. Lastly, tuning studies explore the best location and parameters for BPMs and corrector magnets and will influence the final FCC-ee lattice design.

To conclude, great progress has been made since the CDR and the latest lattice and optics design have been shown here. Large combined effort in defining the first FCC-ee baseline design is presently ongoing, aimed to be delivered in the framework of the FCC-IS with a mid-term review in 2023 and the final report end of 2025.

ACKNOWLEDGMENTS

The work is also supported by the FCC-IS project, receiving funding from the European Union's H2020 Framework Programme under grant agreement no. 951754. Furthermore, the authors would like to that R. Bruce and G. Wilkinson for fruitful discussions and comments on the manuscript.

REFERENCES

[1] M. Benedikt *et al.* (eds.), "Future Circular Collider study, Volume 2: The Lepton Collider (FCC-ee) Conceptual Design Report", in Eur. Phys. J. ST. **228**, pp. 261–623, 2019.

[2] M. Benedikt, A. Blondel, P. Janot, M. Mangano, and F. Zimmermann, "Future circular colliders succeeding the LHC", in Nat. Phys. **16**, pp. 402–407, 2020. doi:10.1038/s41567-020-0856-2

[3] M. Benedikt *et al.* (eds.), "Future Circular Collider study, Volume 3: The Hadron Collider (FCC-hh) Conceptual Design Report", in Eur. Phys. J. ST. **228**, pp. 755–1107, 2019.

[4] F. Gianotti, "Welcome and introduction from CERN", presented at the FCC-Week 2022, Paris, France, 2022. indico.cern.ch/event/1064327/contributions/4891231/

[5] K. Oide *et al.*, "Design of beam optics for the future circular collider e+e- collider rings", Phys. Rev. Accel. Beams **19**, pp. 1111005, 2016.

[6] A. Blondel *et al.*, "Polarization and centre-of-mass energy calibration at FCC-ee", doi:arXiv:1909.12245v1, 2019.

[7] M. Benedikt and F. Zimmermann, "Future Circular Collider: Integrated Programme and Feasibility Study", Front. in Physics **10**, pp. 888078, 2022. doi:10.3389/fphy.2022.888078

[8] F. Zimmermann *et al.*, "FCC-ee Feasibility Study progress", presented at the 65th ICFA Advanced Beam Dynamics Workshop on High Luminosity Circular e+e- Colliders (eeFACT22), Frascati (RM), Italy, Sept. 2022, this workshop.

[9] O. Brüning *et al.*, "LHC Design Report", CERN, Geneva, Switzerland, Rep. No. CERN-2004-003-V-1, 2004.

[10] R. Bruce *et al.*, "Performance and luminosity models for heavy-ion operation at the CERN Large Hadron Collider", *Eur. Phys. J. Plus*. **136** pp. 745, 2021, https://doi.org/10.1140/epjp/s13360-021-01685-5

[11] J. Gutleber, "Update of the layout and placement development", presented at the FCC-Week 2022, Paris, France, 2022. indico.cern.ch/event/1064327/contributions/4888577/

[12] K. Oide "IR Optics for FCC-ee", presented at the FCC-EIC Joint & MDI Workshop 2022, 17th to 28th October 2022. indico.cern.ch/event/1186798/contributions/5062582

[13] Y. Ohnishi *et al.*, "Accelerator design at SuperKEKB", in Progr. of Theoretical and Experimental Physics, **2013** (3), 2013. doi:10.1093/ptep/pts083

[14] P. Raimondi, "Crab waist collisions in DAΦNE and SuperB design", in Proc. of Europ. Particle Accelerator Conf. (EPAC'08), Genoa, Italy, WEXG02, pp. 1898 – 1902, 2008. doi:accelconf.web.cern.ch/e08/papers/wexg02

[15] M. Zobov, "Crab waist collision scheme: a novel approach for particle colliders", in Journal of Physics: Conference Series 747, pp. 012090, 2016. doi:10.1088/1742-6596/747/1/012090

[16] M. Zobov *et al.*, "Test of crab-waist collisions at the DAΦNE Φ-factory", Phys. Rev. Let. 104, pp. 174801, 2010. doi:10.1103/PhysRevLett.104.174801

[17] M. Koratzinos *et al.*, "Status Update of the FCC-ee IR Magnet Design", presented at the 65th ICFA Advanced Beam Dynamics Workshop on High Luminosity Circular e+e- Colliders (eeFACT22), Frascati (RM), Italy, Sept. 2022, this workshop.

[18] M. Boscolo *et al.*, "FCC-ee MDI design", presented at the 65th ICFA Advanced Beam Dynamics Workshop on High Luminosity Circular e+e- Colliders (eeFACT22), Frascati (RM), Italy, Sept. 2022, this workshop.

[19] FCC-ee collaboration, "Machine detector interface workpackage", Accessed 12th October 2022. indico.cern.ch/category/5665/

[20] FCC-ee collaboration, "FCC-EIC Joint & MDI Workshop 2022", 17th to 28th October 2022. indico.cern.ch/event/1186798/

[21] R. Ramjiawan, *et al.*,"FCCee e+/e- injection and RCS booster", presented at the 65th ICFA Advanced Beam Dynamics Workshop on High Luminosity Circular e+e- Colliders (eeFACT22), Frascati (RM), Italy, Sept. 2022, this workshop.

[22] P. Hunchak, "Studies on top-up injection into the FCC-ee collider ring", in Proc. 13th Int. Part. Accel. Conf (IPAC'22), Bangkok, Thailand, WEPOST011, SUSPMF006, pp. 1699-1702, 2022. doi:10.18429/JACoW-IPAC2022-WEPOST011

[23] M. Aiba *et al.*, "Top-up injection schemes for future circular lepton collider", Nucl. Instr. Methods in Phys. Res. Sec. A, vol. **880**, pp. 98–106, 2018. doi:10.1016/j.nima.2017.10.075

[24] J. Keintzel, "Energy sawtooth due to SR and CM energy", presented at the 2nd EPOL Workshop, 19th to 30th September 2022. indico.cern.ch/event/1181966/contributions/5047163/

[25] A. Abramov *et al.*, "Development of collimation simulations for the FCC-ee", in Proc. 13th Int. Part. Accel. Conf (IPAC'22), Bangkok, Thailand, WEPOST016, pp. 1718–1721, 2022. doi:10.18429/JACoW-IPAC2022-WEPOST016

[26] M. Hofer *et al.*, "Design of a collimation section for the FCC-ee", in Proc. 13th Int. Part. Accel. Conf (IPAC'22), Bangkok, Thailand, WEPOST017, pp. 1712–1725, 2022. doi:10.18429/JACoW-IPAC2022-WEPOST017

[27] M. Moudgalya, "First studies of the halo collimation needs in the FCC-ee", Master's thesis, Department of Physics, Imperial College London, 2021.

ISBN: 978-3-95450-236-3 ISSN: 2673-7027 doi:10.18429/JACoW-eeFACT2022-TUYAT0102

[28] F. Peauger *et al.*, "Baseline & Cavity options for FCC-ee", presented at the 65th ICFA Advanced Beam Dynamics Workshop on High Luminosity Circular e+e- Colliders (eeFACT22), Frascati (RM), Italy, Sept. 2022, this workshop.

[29] J. Keintzel, A. Blondel, T.H.B. Persson, D. Shatilov, R. Tomás, F. Zimmermann, "Centre-of-Mass Energy in FCC-ee", in Proc. IPAC'22, WEPOST007, pp. 1683–1886, 2022. doi:10.18429/JACoW-IPAC2022-WEPOST007

[30] The FCC-ee collaboration, "FCC-ee energy calibration, polarization and monochromatization (EPOL) working group", Accessed 3rd October 2022. indico.cern.ch/category/8678/

[31] J. Keintzel *et al.*, "FCC-ee Energy Calibration and Polarization", submitted to Proc. of Science, Int. Conf. on High Energy Physics (ICHEP), Bologna, Italy, paper 048, 2022.

[32] The FCC-ee collaboration, "2d FCC Polarization Workshop", 19th to 30th September 2022. indico.cern.ch/e/EPOL2022

[33] J.M. Jowett and T.M. Taylor, "Wigglers for control of beam characteristics in LEP", IEEE Trans. Nucl. Sci. **30**, pp. 2581–2583, 1983.

[34] M. Hofer, "FCC-ee optics and integration of polarimeter and wigglers", presented at the 2nd FCC EPOL Workshop, 19th to 30th September 2022. indico.cern.ch/event/1181966/contributions/5041448

[35] N. Muchnoi, "Update on polarimeter precision", presented at the 5th FCC-FS EPOL group meeting, 27th January 2022. indico.cern.ch/event/1119730/contributions/4701833

[36] A. Blondel, "Summary first week and outlook for the second", presented at the 2nd FCC EPOL Workshop, 19th to 30th September 2022. indico.cern.ch/event/1181966/contributions/5041348

[37] The FCC-ee collaboration, "FCC-ee tuning WG meeting", 22nd September 2022. indico.cern.ch/event/1201405/

[38] L. van Riesen-Haupt, H. Burkhardt, R. Tomás and T.H.B. Persson, "Comparison of accelerator codes for simulation of lepton colliders", in Proc. 12th Int. Part. Accel. Conf (IPAC'21), Campinas, SP, Brazil, TUPAB004, pp. 1334–1337, 2022. doi:10.18429/JACoW-IPAC2021-TUPAB004

[39] T.K. Charles, B. Holzer, K. Oide and F. Zimmermann, "Update on the low emittance tuning of the e+/e- Future Circular Collider", in Proc. 12th Int. Part. Accel. Conf (IPAC'21), Campinas, SP, Brazil, WEPAB011, pp. 2601–2604, 2021. doi:10.18429/JACoW-IPAC2021-WEPAB011

[40] R. Tomás *et al.*, "Correction and tuning", presented at the FCC week 2022, Paris.

[41] Y. Ohnishi, "SuperKEKB optics tuning", FCC-ee tuning meeting, Aug 25th, 2022. indico.cern.ch/event/1192040/

[42] Y. Wang *et al.*, "CEPC colliding lattice design", presented at the 65th ICFA Advanced Beam Dynamics Workshop on High Luminosity Circular e+e- Colliders (eeFACT22), Frascati (RM), Italy, Sept. 2022, this workshop.

[43] J. Keintzel, R. Tomás, F. Zimmermann, "Prospects for Optics Measurements in FCC-ee", in Proc. IPAC'22, TUOZSP1, pp. 827–830, 2022. doi:10.18429/JACoW-IPAC2022-TUOZSP1

[44] R. Tomás, *et al.*, "Record low β beating in the LHC", Phys. Rev. ST Accel. Beams **15**, pp. 091001, 2012.

[45] T. Persson, F. Carlier, J. Coello de Portugal, A. Garcia-Tabares Valdivieso, A. Langner, E. H. Maclean, L. Malina, P. Skowronski, B. Salvant, R. Tomás, and A. C. Garcia Bonilla, "LHC optics commissioning: A journey towards 1% optics control", Phys. Rev. Accel. Beams, **20**, pp. 061002, 2017.

[46] J. Keintzel *et al.*, "SuperKEKB Optics Measurements Using Turn-by-Turn Beam Position Data", in Proc. 12th Int. Part. Accel. Conf (IPAC'21), Campinas, SP, Brazil, TUPAB009, pp. 1352–1355, 2021. doi:10.18429/JACoW-IPAC2021-TUPAB009

ISBN: 978-3-95450-236-3 ISSN: 2673-7027 doi:10.18429/JACoW-eeFACT2022-TUYAT0104

CEPC BOOSTER LATTICE DESIGN *

D. Wang†, D. H. Ji, Y. M. Peng, C. H. Yu[1], Y. D. Liu, Y. Zhang[1], X. H. Cui, J. Y. Zhai, M. Li[1], C. Meng, J. Gao[1], Institute of High Energy Physics, Beijing, China
[1]also at University of Chinese Academy of Sciences, Beijing, China

Abstract

The CEPC booster provides electron and positron beams to the collider at different energies. The newest booster design is consistent with the TDR higher luminosity goals for four energy modes. The emittance of booster is reduced significantly in order to match the lower emittance of collider in TDR. Both FODO structure and TME structure was studied for booster design. A lot of efforts are made to overcome the difficulty of error sensitivity for the booster and hence the dynamic aperture with errors can fulfil the requirements at all energy modes. Also, the combined magnets scheme (B+S) are proposed to minimize the cost for magnets and power supplies. The design status of CEPC booster in TDR including parameters, optics and dynamic aperture is discussed in this paper.

INTRODUCTION

CEPC booster needs to provide electron and positron beams to the collider at different energy with required injection efficiency. The injection system consists of a 30 GeV Linac, followed by a full-energy booster ring. Electron and positron beams are generated and accelerated to 30 GeV in the Linac. The beams are then accelerated to full-energy in the booster, and injected into the collider. For different beam energies of tt, Higgs, W, and Z experiments, there will be different particle bunch structures in the collider [1]. To maximize the integrated luminosity, the injection system will operate mostly in top-up mode, and also has the ability to fill the collider from empty to full charge in a reasonable length of time [2]. The lowest field of dipole magnets in booster is 90 Gauss and the tolerance for field error at 30 GeV can be realized by the ion based magnets.

After CDR, we have reduced the emittance of collider ring and beta function at the interaction point in order to get higher luminosity for Higgs energy mode [3]. With the booster design in CDR [2, 4], it is difficult to realize the injection from booster to collider for Higgs mode even with on-axis injection scheme. For TDR design, the dynamic aperture requirement of collider ring in horizontal direction due to injection process is shown in Fig. 1. From Fig. 1, we know that the booster emittance at 120 GeV should be lower than 1.7 nm, while it is 3.6 nm in CDR.

Actually, we have made a long effort to develop a lower emittance booster since the CEPC CDR was published. After careful study and comparison among different designs, the optics based on modified-TME structure is adopted as the best candidate. The progress of booster design based on TME structure has been published in 2021 [5]. After that, we found this design is so sensitive to errors that the dynamic aperture of booster cannot fulfil the requirement when we consider the real error effects. So the booster design with TME structure is updated to make a balance between error sensitivity and emittance. We also made an alternative booster design with FODO structure. After the comparison between FODO and TME lattice including error effects, we chose the modified-TME lattice as our baseline for TDR because only the TME can fulfil the dynamic aperture requirement at all energy modes.

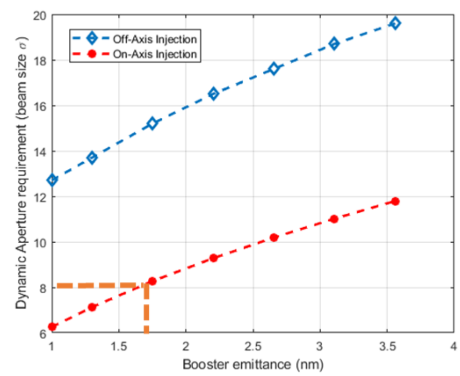

Figure 1: The dynamic aperture requirement of collider ring in horizontal direction due to injection process vs. booster emittance at 120 GeV. The horizontal emittance in collider ring at 120 GeV is 0.64 nm. The horizontal beta function at the injection point is 1800 m.

OPTICS DESIGN FOR LOWER EMITTANCE BOOSTER

New Lattice Design Based on TME

The arc is made of modified-TME cells. Figure 2 shows the optics design for the arc cell. The length of TME cell in the arc is 78 m.

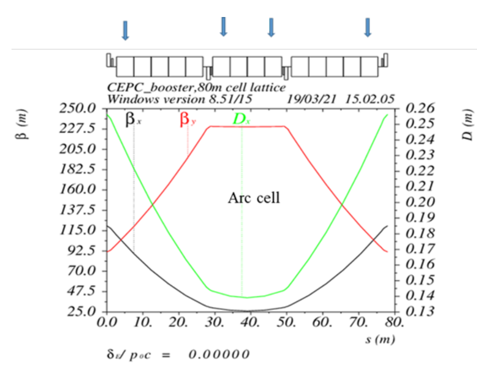

Figure 2: The Twiss functions of the TME cell in the arc region.

* Work supported by Key Research Program of Frontier Sciences, CAS (Grant No. QYZDJ-SSW-SLH004).
† wangd93@ihep.ac.cn

65th ICFA Adv. Beam Dyn. Workshop High Luminosity Circular e⁺e⁻ Colliders eeFACT2022, Frascati, Italy JACoW Publishing
ISBN: 978-3-95450-236-3 ISSN: 2673-7027 doi:10.18429/JACoW-eeFACT2022-TUYAT0104

The distribution for quadrupoles are arranged as uniform as possible to relax the error sensitivity of the lattice since the previous design. The horizontal phase advance is 100° and the vertical phase advance is 28° for each cell, which has been optimized carefully to make a balance between emittance and dynamic aperture. The emittance of booster at 120 GeV is reduced from 3.56 nm in CDR to 1.26 nm by this new design. The function of dispersion suppressor is to cancel the dispersion induced in the arc section and make a transition between arc section and straight section (shown in Fig. 3).

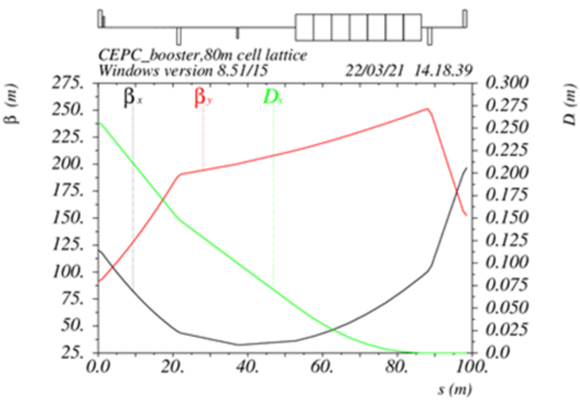

Figure 3: The Twiss functions of the dispersion suppressor.

The straight section is made of FODO cell and the length of each cell is 134 m which is shown in Fig. 4. The optimum phase advances in the arc cell and the straight FODO cell are optimized carefully in order to get the largest dynamic aperture.

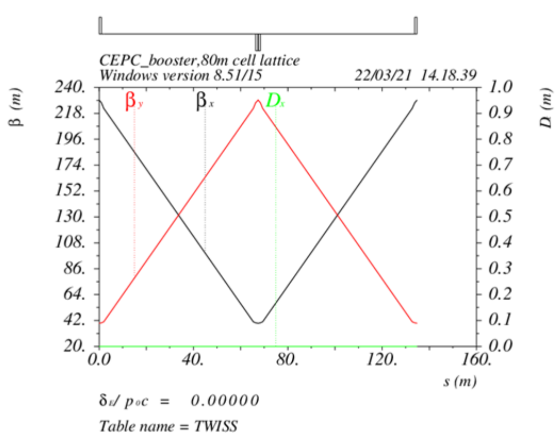

Figure 4: The Twiss functions of the FODO cell in the straight section.

New Lattice Design based on FODO

An alternative lattice design was made based on FODO structure. This is a similar structure as CDR while the cell length is decreased to 70 m. The non-interleave sextupole scheme and 90°/90° phase advance were adopted. The emittance of FODO lattice is 1.29 nm at 120 GeV. The twiss parameters of this design are shown in Figs. 5-7.

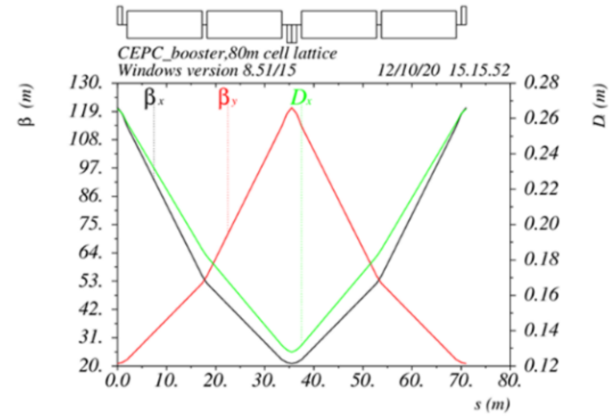

Figure 5: The Twiss functions of the FODO cell in the arc region.

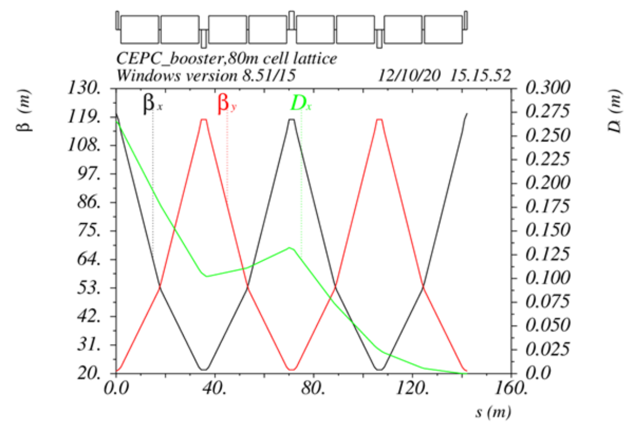

Figure 6: The Twiss functions of the dispersion suppressor.

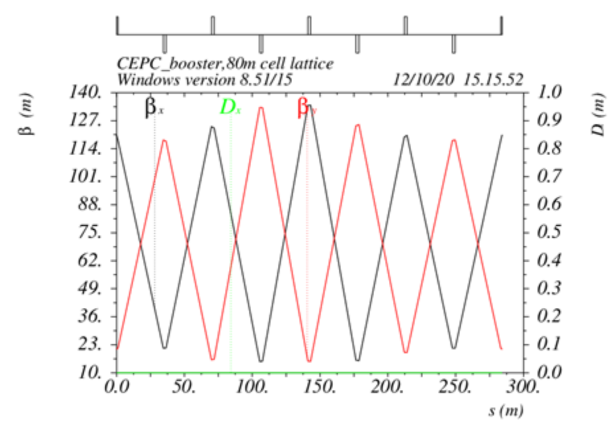

Figure 7: The Twiss functions of the straight section.

Dynamic Aperture with Error Effects

Table 1-3 list the details of the error settings. Gaussian distribution for the errors is used and is cut off at 3 σ. Both orbit correction (including horizontal dispersion correction) and optics correction has been done in AT. We have compared the two kinds of lattice while including the same errors, and only TME structure can meet the requirement of dynamic aperture. The DA results of TME lattice including SR effects are tracked by SAD which are shown in Figs. 8-10.

ISBN: 978-3-95450-236-3 ISSN: 2673-7027 doi:10.18429/JACoW-eeFACT2022-TUYAT0104

Table 1: Magnet Error Analysis Settings

Parameter	Dipole	Quad.
Transverse shift x/y (μm)	100	100
Longitudinal shift z (μm)	100	150
Tilt about x/y (mrad)	0.2	0.2
Tilt about z (mrad)	0.1	0.2
Nominal field	1×10^{-3}	2×10^{-4}

Table 2: BPM Analysis Settings

Parameter	BPM (10 Hz)
Accuracy (m)	1×10^{-7}
Tilt (mrad)	10
Gain	5%
Offset after BBA(mm)	3×10^{-2}

Table 3: Magnet Multipole Errors

Dipole	Quad.
$B1/B0 \leq 2\times10^{-4}$	
$B2/B0 \leq 5\times10^{-4}$	$B2/B1 \leq 3\times10^{-4}$
$B3/B0 \leq 2\times10^{-5}$	$B3/B1 \leq 2\times10^{-4}$
$B4/B0 \leq 8\times10^{-5}$	$B4/B1 \leq 1\times10^{-4}$
$B5/B0 \leq 2\times10^{-5}$	$B5/B1 \leq 1\times10^{-4}$
$B6/B0 \leq 8\times10^{-5}$	$B6/B1 \leq 5\times10^{-4}$
$B7/B0 \leq 2\times10^{-5}$	$B7/B1 \leq 5\times10^{-4}$
$B8/B0 \leq 8\times10^{-5}$	$B8/B1 \leq 5\times10^{-4}$
$B9/B0 \leq 2\times10^{-5}$	$B9/B1 \leq 5\times10^{-4}$
$B10/B0 \leq 8\times10^{-5}$	$B10/B1 \leq 5\times10^{-4}$

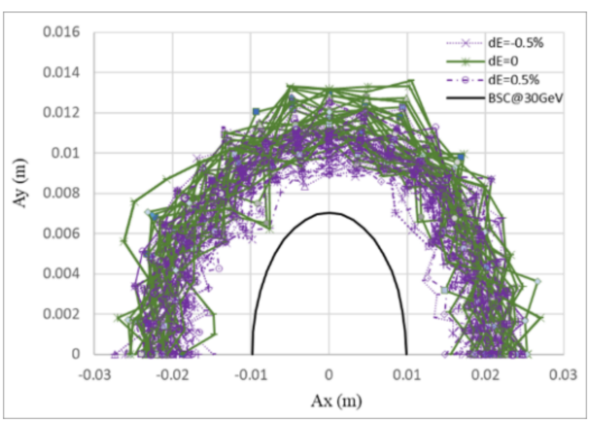

Figure 8: Dynamic aperture of booster at 30 GeV with errors and synchrotron radiation.

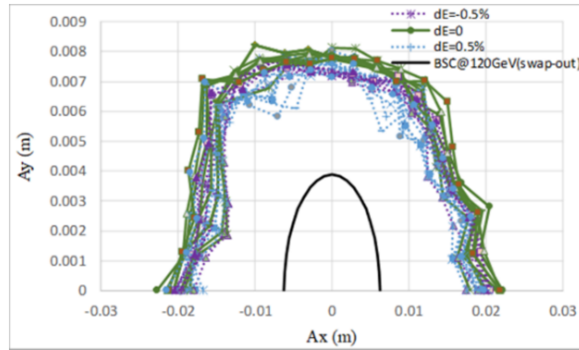

Figure 9: Dynamic aperture of booster at 120 GeV with errors and synchrotron radiation. Only the swap-out injection is considered for the BSC.

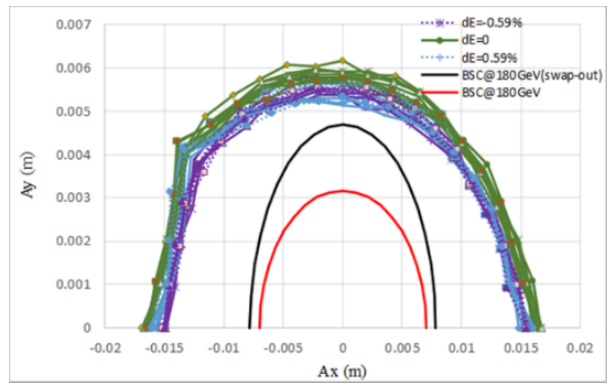

Figure 10: Dynamic aperture of booster at 180 GeV with errors and synchrotron radiation. Both the swap-out injection and off-axis injection are considered for the BSC.

NEW PARAMETERS OF BOOSTER IN TDR

The main booster parameters at injection (30 GeV) and extraction energies are listed in Table 4 and 5. Both top up injection and full injection for CEPC can be fulfilled. For the top up injection, the assumptions are 3% current decay in collider ring, including 95% transfer efficiency for booster itself. The total beam current in the booster is less than 0.3 mA for tt running, 1 mA for Higgs mode, 4 mA for W mode and 16 mA for Z which are limited by RF system for different extraction energy. The beam is injected from linac to booster by on-axis scheme and is injected from booster to collider by off-axis scheme at three different energies for tt, W and Z. Also the on-axis injection from booster to collider has been considered at 120 GeV in case the dynamic aperture of collider ring is not large enough.

ISBN: 978-3-95450-236-3 ISSN: 2673-7027 doi:10.18429/JACoW-eeFACT2022-TUYAT0104

Table 4: The Main Booster Parameters at Injection Energy

		tt	*H*	*W*	*Z*	
Beam energy	GeV	30				
Bunch number		35	268	1297	3978	5967
Threshold of single bunch current	μA	8.68	6.3	5.8		
Threshold of beam current (limited by coupled bunch instability)	mA	97	106	100	93	96
Bunch charge	nC	1.1	0.78	0.81	0.87	0.9
Single bunch current	μA	3.4	2.3	2.4	2.65	2.69
Beam current	mA	0.12	0.62	3.1	10.5	16.0
Growth time (coupled bunch instability)	ms	2530	530	100	29.1	18.7
Energy spread	%	0.025				
Synchrotron radiation loss/turn	MeV	6.5				
Momentum compaction factor	10^{-5}	1.12				
Emittance	nm	0.076				
Natural chromaticity	H/V	-372/-269				
RF voltage	MV	761.0	346.0	300.0		
Betatron tune ν_x/ν_y		321.23/117.18				
Longitudinal tune		0.14	0.0943	0.0879		
RF energy acceptance	%	5.7	3.8	3.6		
Damping time	s	3.1				
Bunch length of linac beam	mm	0.4				
Energy spread of linac beam	%	0.15				
Emittance of linac beam	nm	6.5				

Table 5: The Main Booster Parameters at Extraction Energy

		tt	*H*		*W*	*Z*	
		Off axis injection	Off axis injection	On axis injection	Off axis injection	Off axis injection	
Beam energy	GeV	180	120		80	45.5	
Bunch number		35	268	261+7	1297	3978	5967
Maximum bunch charge	nC	0.99	0.7	20.3	0.73	0.8	0.81
Maximum single bunch current	μA	3.0	2.1	61.2	2.2	2.4	2.42
Threshold of single bunch current	μA	91.5	70		22.16	9.57	
Threshold of beam current (limited by RF system)	mA	0.3	1		4	16	
Beam current	mA	0.11	0.56	0.98	2.85	9.5	14.4
Growth time (coupled bunch instability)	ms	16611	2359	1215	297.8	49.5	31.6
Bunches per pulse of Linac		1	1		1	2	
Time for ramping up	s	7.1	4.3		2.4	1.0	
Injection duration for top-up (Both beams)	s	29.2	23.1	31.8	38.1	132.4	
Injection interval for top-up	s	65	38		155	153.5	
Current decay during injection interval		3%					
Energy spread	%	0.15	0.099		0.066	0.037	
Synchrotron radiation loss/turn	GeV	8.45	1.69		0.33	0.034	
Momentum compaction factor	10^{-5}	1.12					
Emittance	nm	2.83	1.26		0.56	0.19	
Natural chromaticity	H/V	-372/-269					
Betatron tune ν_x/ν_y		321.27/117.19					
RF voltage	GV	9.7	2.17		0.87	0.46	
Longitudinal tune		0.14	0.0943		0.0879	0.0879	
RF energy acceptance	%	1.78	1.59		2.6	3.4	
Damping time	ms	14.2	47.6		160.8	879	
Natural bunch length	mm	1.8	1.85		1.3	0.75	
Full injection from empty ring	h	0.1	0.14	0.16	0.27	1.8	0.8

CONCLUSION

In the stage of TDR, a lower emittance booster has been designed in order to realize the injection for CEPC collider ring. The modified-TME structure is chosen as baseline considering all the error effects and the new design can meet the requirement for 4 energy modes. The booster parameters are updated based on the TME lattice which is consistent with CEPC TDR parameters.

REFERENCES

[1] D. Wang *et al.*, "Problems and considerations about the Injection philosophy and timing structure for CEPC", *Int. J. Mod. Phys. A*, vol. 37, p. 2246006, 2022. doi:10.1142/S0217751X2246006X

[2] The CEPC Study Group, "CEPC conceptual design report", Volume I- Accelerator, *Rep. IHEP-AC-2018-01*, Aug. 2018.

[3] CEPC Study Group, "Snowmass2021 White Paper AF3-CEPC", arXiv:2203.09451. doi:10.48550/arXiv.2203.09451

[4] D. Wang *et al.*, "Design and beam dynamics of the CEPC booster", *Int. J. Mod. Phys. A*, vol. 35, no. 15n16, p. 2041007, 2020. doi:10.1142/S0217751X20410079

[5] D. Wang *et al.*, "Design study of CEPC lower emittance booster", *Int. J. Mod. Phys. A*, vol. 36, no. 22, p. 2142014, 2021. doi:10.1142/S0217751X21420148

ISBN: 978-3-95450-236-3 ISSN: 2673-7027 doi:10.18429/JACoW-eeFACT2022-TUZAT0101

IR DESIGN ISSUES FOR HIGH LUMINOSITY AND LOW BACKGROUNDS*

M. K. Sullivan†, SLAC National Accelerator Laboratory, Menlo Park, CA, USA

Abstract

New e^+e^- collider designs use high beam currents (>1 A) to help obtain a high luminosity value. This leads to several issues that affect detector background levels. I will discuss several of these issues and indicate some of the backgrounds the detectors at these new colliders will encounter. The experience of the first two B-factories (PEP-II and KEKB) and also of the currently operating SuperKEKB accelerator will be used and the discussion will also include the new Electron-Ion Collider to be built at Brookhaven National Laboratory.

INTRODUCTION

The first e^+e^- collider was the storage ring AdA built by Bruno Touschek at the INFN laboratory at Frascati in the early 1960s. This was the first of many matter anti-matter colliders. The late 1960s and early 1970s saw the construction and commissioning of several new e^+e^- colliders. SPEAR at SLAC, Menlo Park, ADONE at INFN Frascati, DORIS at DESY, Hamburg. VEPP-2 and VEPP-2M at BINP, Novosibirsk followed in the late 1970s. The early 1980s had PEP at SLAC and PETRA at DESY. These accelerators were at the e^+e^- energy frontier for new particle searches at that time. It was thought that the PEP and PETRA storage rings with E_{cm} energies of 29 GeV for PEP and 32-48 GeV for PETRA would discover the top quark which had an expected mass at the time of about 15 GeV. Cornell University started up CESR in 1979 as a new e^+e^- collider with an E_{cm} energy range of 3.5 to 12 GeV. This machine was the first of several more accelerators to specialize in producing B mesons.

A new e^+e^- collider called TRISTAN started up in 1987 at KEK in Tsukuba, Japan with an initial beam energy of 25 GeV (50 GeV E_{cm}). In only a few years it was upgraded to a beam energy of 32 GeV. No top quark was seen but the experiments at TRISTAN confirmed the gluon first seen by PETRA experimental detectors and also measured the vacuum polarization effect of the electron. The accelerator also was a pioneer in the use of super-conducting cavities for electron storage rings along with CESR and PETRA. Shortly after TRISTAN turned on, two other e^+e^- colliders, the SLC at SLAC and LEP at CERN, Geneva, specializing in the production of the Z resonance (91.2 GeV E_{cm}) and further studies of the WW threshold (160 GeV E_{cm}) by LEP.

The 1990s saw the construction and commissioning of two new e^+e^- colliders concentrating on generating high luminosity at the Upsilon (4S) resonance (10.56 GeV) in order to produce very large samples of B mesons. The design luminosity values were 5-30 times higher than anything that had been achieved to that point.

In order to achieve these high design luminosities, both asymmetric-energy B-factory designs (PEP-II and KEKB) used a separate storage ring for each beam and then filled each ring with as many bunches as possible. This led to the first high-current (greater than 1A) collider storage rings. It should be stated that, at this time, INFN in Frascati also built and commissioned a high-current double ring collider (DAΦNE) designed for specialized studies of the φ resonance (1.02 GeV) [1-2].

HIGH-CURRENT BEAMS

The asymmetric-energy B-factories (PEP-II and KEKB) achieved and collided multi-ampere beams. The PEP-II B-factory at SLAC reached beam currents of 1.9 A for the 9 GeV electrons and 2.9 A for the 3.1 GeV positrons and the KEKB machine achieved 1.1 A in the 8 GeV electron ring and 2.6 A in the 3.5 GeV positron ring.

The B-factories encountered and solved many issues related to these high-current beams. To name a few: High-Order Mode (HOM) heating, high synchrotron power in the arcs and subsequent beam pipe outgassing, coupled bunch instabilities, synchrotron radiation backgrounds in the detector, and general beam-related backgrounds in the detector as well as the onset of backgrounds related to the collision.

The success of the B-factories has led to the design of future accelerators that implement the use of high-current storage rings as a way of achieving high luminosity design values.

NEW COLLIDER DESIGNS

Here, I touch upon some of the new collider designs that employ high-current storage rings of either electrons and/or positrons. All of the machines mentioned below are described in greater detail in presentations at this workshop. I have selected a few of the design parameters for this discussion. The first machine is an already running accelerator, SuperKEKB.

SuperKEKB

This accelerator is an upgrade of the previous B-factory machine KEKB. KEKB achieved a luminosity of $2.11 \times 10^{34}\mathrm{cm^{-2}s^{-1}}$ the world record at that time [3]. SuperKEKB is aiming to achieve a peak luminosity of $5\text{-}6 \times 10^{35}\mathrm{cm^{-2}s^{-1}}$, 30 times higher than KEKB. SuperKEKB uses a new idea called the “nanobeam” colliding scheme [4] in which the crossing angle is large, and

* Work supported by the U.S. Department of Energy, Office of Science, Office of Basic Energy Sciences, under Contract No. DE-AC02-76SF00515 and HEP.
† sullivan@slac.stanford.edu

ISBN: 978-3-95450-236-3 ISSN: 2673-7027 doi:10.18429/JACoW-eeFACT2022-TUZAT0101

the actual collision area is much shorter than the bunch length. This allows one to reduce the β_y^* value well below the bunch length and thereby gain more luminosity. The accelerator design calls for stored beam currents of 3.6 A for the 4 GeV positrons and 2.6 A for the 7 GeV electrons.

This accelerator is in the commissioning stage and has achieved a new world record luminosity of $4.65 \times 10^{34}\mathrm{cm}^{-2}\mathrm{s}^{-1}$[5]. In addition, the stored beam current of each ring is over 1 A and they have demonstrated that the nanobeam colliding scheme does work.

FCC-ee and CEPC

These two designs are very similar and hence are considered together here. The FCC-ee design is an e^+e^- collider to be built at CERN with a 91 km tunnel circumference that contains two storage rings and a booster ring. The CEPC design has a 100 km circumference tunnel. Both machines intend to run over a range of stored beam energies. They will operate with beam energies of 45.6 GeV (Z resonance), 80 GeV, (W^+W^- threshold), 120 GeV, (ZH threshold), and 182.5 GeV (ttbar threshold). The point of interest for this discussion is the Z resonance running where both machines will employ high beam currents (1.4 A for FCC-ee and 0.8 A for CEPC) in order to achieve high design luminosities of $1.8 \times 10^{36}\mathrm{cm}^{-2}\mathrm{s}^{-1}$ for the FCC-ee design and $1.2 \times 10^{36}\mathrm{cm}^{-2}\mathrm{s}^{-1}$ for the CEPC design [6, 7].

Electron Ion Collider

A new electron-ion collider (EIC) is being designed to be built at BNL using some of the infrastructure of the RHIC collider together with a new electron storage ring and an electron booster ring. This machine plans to extend the physics found at HERA concerning the structure of the proton and develop a deeper understanding of the QCD model for the proton. The electron beam will operate at three energies: 5 GeV, 10 GeV and 18 GeV. The 18 GeV running has a maximum beam current of 0.27 A limited by available RF power and by a design maximum SR power limit on the ring of 10 MW [8, 9]. Of more interest in this discussion is the 10 GeV running condition where the design beam current is 2.5 A. This will put the electron storage ring into the B-factory parameter region and will be the highest design value for this beam energy.

NON-GAUSSIAN BEAM TAILS

One of the primary issues faced by all e^+e^- collider designs is the non-gaussian or halo beam tail distribution. The non-gaussian part of the transverse beam profile is the result of beam particle interactions which impart a transverse kick to the beam particle. There are a large number of sources for this type of interaction. Here we identify a few of these sources:

Beam-gas interactions [10] This interaction which is a beam particle colliding with a residual gas molecule in the beam pipe is very important in the early running of a collider and is usually the dominant source for the non-gaussian beam tail distribution during commissioning. Collimators can be used to reduce the beam tail particle density out at high beam sigma values, but this will tend to reduce the beam lifetime to values that can be too low to maintain. Detector backgrounds are subsequently high at this time from both off-energy beam particles resulting from the collision and from excess synchrotron radiation from the beam particles with high beam sigma trajectories through the final focus magnets.

Particle-particle interactions inside a beam bunch. Touschek scattering is one, inter-beam scattering (IBS) is another [11]. Touschek scattering is generally more significant for lower energy storage rings, but it can become important if the vertical emittance and subsequently the vertical size of the beam becomes small. This interaction increases as the particle density in a single beam bunch increases. One of the primary ways used to increase luminosity is to minimize the vertical size of the beam. This technique is being used for the SuperKEKB accelerator and consequently Touschek scattering is recognized as a primary source of detector background and as a contributor to shortening the beam lifetime.

Collision interactions. Here we have several sources contributing to the beam tails. The first one is Bhabha scattering [12]. This is the cross-section used to measure the luminosity of the collision. The design luminosity of the SuperKEKB is high enough to make this the dominant term that sets the design beam lifetime at a few minutes. The second-order interaction of radiative Bhabhas [12] also contributes to the non-gaussian beam tail as well as the shortness of the beam lifetime. This interaction also produces a spectrum of high-energy gammas that travel primarily down the beam axis defined at the collision point and these photons will strike the beam pipe at or near the first major bend after the collision. Beamsstrahlung, the emission of photons from the bending of the beam particles during collision, is another beam tail contributor [13]. This process becomes much more important as the beam energy increases and as the luminosity increases.

Instabilities. If a beam happens to be close to an instability threshold, then particles in the beam can be perturbed out of the gaussian distribution and into the beam tail distributions. This is also true if the ring gets too close to a resonance in the tune plane or if the tune shift from the collision pushes beam particles onto a resonance line. If the disturbance is too strong, then the beam lifetime is severely affected, and the beam can be lost. Generally, one steers away from tune plane resonances and tries to stay below instability thresholds, but other issues, like the dynamic pressure in the storage ring can sometimes lower some instability thresholds. This is also true for the Transverse Mode Coupled Instability (TMCI) where parts of the beam pipe (like collimator jaws) are positioned too close to the beam and generate wake-fields that are strong enough to influence the next bunch in the bunch train. Electron cloud interactions can also perturb the beam particles and even if the core gaussian is relatively untouched beam particle and electron cloud interactions can push some of the beam particles into the tail distributions.

ISBN: 978-3-95450-236-3 ISSN: 2673-7027 doi:10.18429/JACoW-eeFACT2022-TUZAT0101

BEAM TAIL MODELING

We see from the above, that there are a large number of sources that can populate a non-gaussian beam tail distribution. In general, *any* perturbation of the beam particles will do this. In addition, many of these sources are time dependent making it difficult to properly model the various sources. Some sources are more important at the beginning of a fill and others can become more important as attempts are made to improve the machine performance, such as adjusting the tunes or adjusting the collimators. The B-factories pioneered the technique of continuous top-up where the ring currents are kept steady by constantly injecting (usually at a rate of tens of Hertz) bunches into the stored rings. This greatly improves the machine performance since many factors stabilize when the beam currents are steady allowing the operators to concentrate on optimizing luminosity and performance.

With all this, the realistic modelling of the non-gaussian beam tail becomes problematic. I have chosen to model the tail distributions as another gaussian distribution but with a sigma that is several times larger than the core gaussian sigma. The x and y transverse dimensions are allowed to have different tail sigma values, but the height of the tail distributions is constrained to be the same value which is typically much smaller than the core height. The integral of the total tail distribution should be less than 10% of the core integral [14] and a more typical value used for modelling is 1-5% of the core integral.

Equation (1) is the differential form of the transverse beam particle distribution used for the synchrotron radiation background calculations in the program SYNC_BKG.

$$\frac{d^2N}{dxdy} = exp\left[-\frac{x^2}{2\sigma_x^2} - \frac{y^2}{2\sigma_y^2}\right] + A_x A_y exp\left[-\frac{B_x^2 x^2}{2\sigma_x^2} - \frac{B_y^2 y^2}{2\sigma_y^2}\right] \quad (1)$$

The equation includes the non-gaussian beam tail distributions for the X and Y dimensions. The σ_x and σ_y variables are the core σ values. The A_x, A_y, B_x, and B_y values determine the beam tail distributions with respect to the core distribution. As mentioned above, A_x and A_y are constrained to have the same value by choice, and they define the height of the tail distribution with respect to the core height. The B values determine the width of the tail distribution as a divisor to the respective core sigma.

Table 1 is a list of non-gaussian beam tail distribution A and B parameters for three different cases of beam tails, used to model the backgrounds observed in the partial PXD detector of Belle II during the initial commissioning of the SuperKEKB in 2019 and right after the roll-on of Belle II. Figure 1 (top) and (bottom) show the transverse profile of the beam including the three different beam tail distributions shown in parameter list from Table 1. The tail distributions are normalized to the core distribution where the maximum of the core distribution is one.

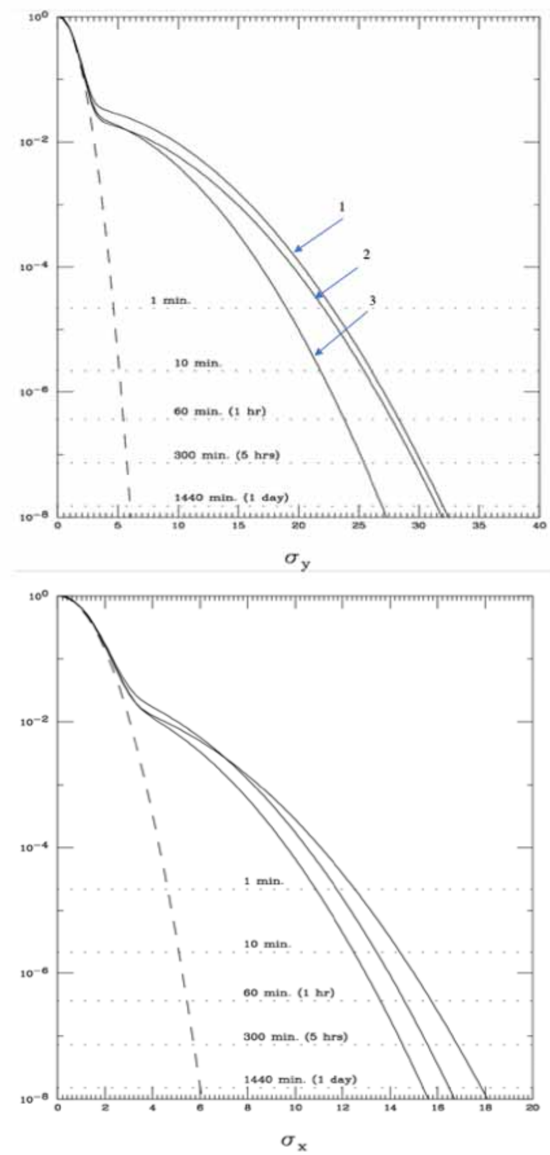

Figure 1: Top: The transverse beam profile in the X plane with the three different beam tail distributions listed in Table 1. The core gaussian distribution is shown as a dashed line and the non-gaussian beam tail distributions are shown as solid lines. Bottom: The transverse beam profile in the Y plane with the three different beam tail distributions listed in Table 1.

Table 1: List of non-gaussian beam tail distribution A and B parameters for three different cases of beam tails.

Beam Tail	A_x	B_x	A_y	B_y	%core
1	0.04	0.33	0.04	0.17	2.7
2	0.025	0.30	0.025	0.17	1.2
3	0.03	0.35	0.03	0.20	1.3

ISBN: 978-3-95450-236-3 ISSN: 2673-7027 doi:10.18429/JACoW-eeFACT2022-TUZAT0101

The modelling of the beam tail distribution can be further constrained by knowing the approximate beam lifetime and the value of the collimator settings at the time the background data was taken. This information can be used to set the particle density value at the setting of the collimator(s). Figure 1 (top) and (bottom) have dotted horizontal lines with time labels. These represent the estimated lifetime of the stored beam if a collimator setting is located at the intersection of the beam tail distribution with the dotted line. These lifetime estimates are based on a calculation for beam lifetime by M. Sands [15]. As an example, if an X collimator has a setting at 15 σ then the lifetime of the beam should be a little over 300 min for tail distribution #3, about 60 min for #1, and 10 min for #2.

Backgrounds in the detector from synchrotron radiation can come from upstream bend magnets and from upstream quadrupoles. Usually, the bend radiation can be masked away from the detector beam pipe and the backgrounds from this source can be made low. The final focus quadrupoles also generate synchrotron radiation, and this is where the beam tail distribution becomes important. The number of beam particles out at high beam sigma values determines how much background the detector will get from this source. For flat beam designs the distribution in the X plane becomes the most important as flat beam designs have the vertical focusing quadrupole as the last magnet before the Interaction Point (IP). This puts the horizontally focusing magnet outside of the vertically focusing magnet forcing the horizontal magnet to over-focus in X because the vertically focusing (horizontally defocusing) magnet will remove some of the X focusing. The focus of both magnets needs to converge at the IP.

LUMINOSITY

When the luminosity is a few × $10^{33}\,\mathrm{cm}^{-2}\mathrm{s}^{-1}$ or higher for e^+e^- colliders and eP colliders, the collision begins to add additional sources that contribute to the overall detector background level. One of these new sources is radiative Bhabha scattering where the interaction generates a high-energy (GeV) gamma ray that travels down the collision axis and an off-energy beam particle (electron or positron). The gamma rays will travel with the beam until the beam enters a dipole magnet. The gammas will then strike the beam pipe wall either inside the dipole magnet or else soon after exiting the magnet. This can be a source of neutron background as well as a source of shower debris from the showering gamma rays. The off-energy beam particle will be over-focused in the outgoing quadrupoles causing many of these particles to crash into the local beam pipe and generate shower debris in the detector. In addition, the first bend field encountered by the outgoing beam will bend many of the off-energy particles into the beam pipe wall. Both B-factories had outgoing bend fields that were relatively close to the collision point. The first PEP-II bend magnet started about 20 cm from the collision point and was one of the strongest bend fields in the entire accelerator. The first outgoing KEKB bending fields were about 2m downstream of the collision point. The close and strong bend field in the PEP-II B-factory produced a noticeable radiative Bhabha background in the detector at a lower luminosity (2-3 × 10^{33}) than for the KEKB machine which eventually began to see backgrounds from this source at a luminosity closer to 10^{34}. Figures. 2 and 3 illustrate the trajectories of these off-energy beam particles based on the energy of these beam particles after the radiative interaction and on the quadrupole and dipole fields in the interaction region.

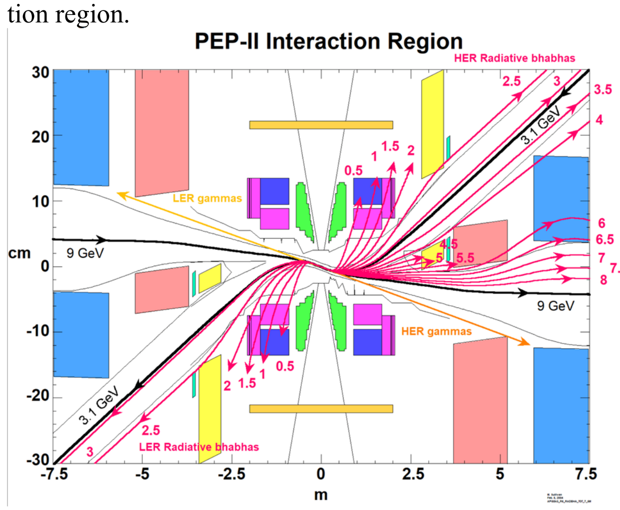

Figure 2: Layout of the PEP-II B-factory interaction region showing the trajectory of off-energy beam particles from a radiative Bhabha interaction. The gamma rays travel in a straight line away from the collision point and strike the beam pipe about 8 m downstream of the collision just outside of the blue X focusing magnet shown in the picture. The red trajectories and labels indicate the path and energy of the off-energy beam particle.

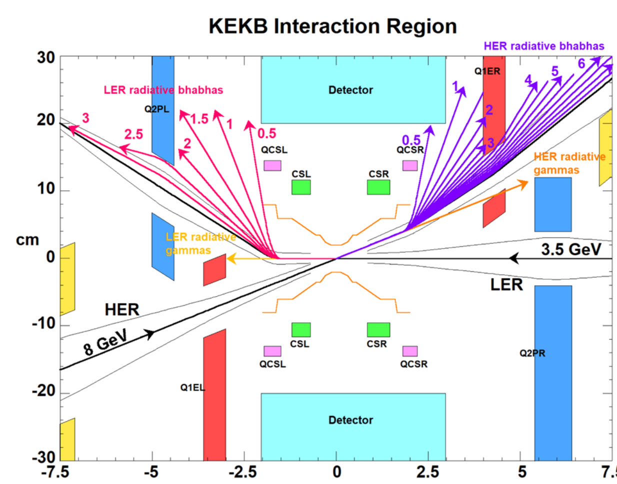

Figure 3: Layout of the KEKB B-factory interaction region showing trajectories of the off-energy beam particles after a radiative Bhabha interaction. The first strong bending fields in this design come from the outgoing beam traveling through a shared quadrupole magnetic field with a large off-axis trajectory. The incoming beams are on axis in these magnets. In the KEKB design, the gamma rays strike the beam pipe closer to the collision point than in the PEP-II design (approx. 2 m from the collision).

ISBN: 978-3-95450-236-3 ISSN: 2673-7027 doi:10.18429/JACoW-eeFACT2022-TUZAT0101

The SuperKEKB accelerator and all future collider designs discussed here have no shared quadrupole magnets. As mentioned in the figure caption, these are quadrupoles where both beams travel through the same magnetic field forcing at least one of the beams to be off axis in the quadrupole and thereby putting that beam into a strong bending field. In addition, SuperKEKB has moved the first bend magnet as far as possible from the IP as has all future collider designs. In spite of these efforts, background generated from radiative Bhabhas is still one of the highest detector backgrounds at the design luminosity of 5-6 $\times 10^{35}\mathrm{cm}^{-2}\mathrm{s}^{-1}$ for Belle II.

Two-photon Interactions

Another luminosity related interaction that can cause detector background is called the low-energy e^+e^- pair production or the two-photon process. Here two virtual photons interact to create an e^+e^- pair of low energy particles. The Feynman diagram in Fig. 4 illustrates this process.

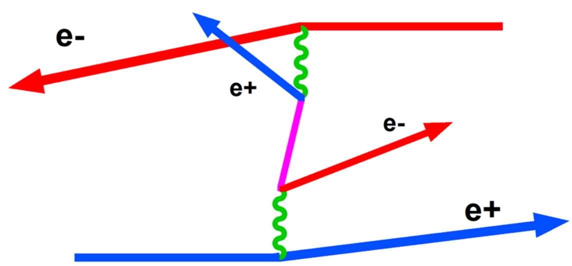

Figure 4: Feynman diagram of the interaction where an e^+e^- pair is produced. The low energy particles tend to have a trajectory that is a tight orbit around the detector axis due to the magnetic field of the detector.

Since the created particles have low energies, they will spiral around the detector magnetic field axis. As long as the particles remain inside the beam pipe this is not an issue. However, as the luminosity increases, this process will make e^+e^- pairs that have enough energy to go through the beam pipe and start spiralling through the vertex detector usually located very close to the central Be beam pipe. This generates an enormous number of hits in the vertex detector, and this can limit the detector performance. Consequently, this process can be a determining factor in how small the central beam pipe radius can be.

Beamsstrahlung

This interaction [13] is the emission of gamma rays at the collision point due to the bending of the beam particles from the entire electromagnetic fields of the other beam bunch. This was first studied for linear colliders where the collision focusing is quite intense and consequently this interaction plays an important part of the overall beam disruption parameter. Now, future collider designs also have to take this interaction into account, especially the FCC-ee and CEPC e^+e^- colliders when the accelerators are running at the Z pole (91.2 GeV) with very high beam currents. This process generates a very intense, high-power beam of gamma rays along the outgoing beam axis that must be controlled and absorbed.

SUMMARY

The new accelerator designs that use multi-ampere stored beams to attain high luminosity will move accelerator and storage ring technology farther into the new territory first touched upon by the B-factories. The heavy synchrotron radiation power loads in the arcs of these machines will require some time to fully "scrub" the vacuum chamber and reduce the dynamic vacuum pressure before the design beam currents can be reached. In addition, the high design luminosity values means that the actual beam collision will become a major source of background for the detector. The stored beam lifetime for these machines with very high luminosity goals can become dominated by the loss of beam particles due to the collision. Electron (and positron) storage rings have a very strong damping term in the synchrotron radiation losses around the ring. This powerful damping term allows beam particles to be perturbed out of the core gaussian distribution of the beam into the transverse beam tails or halo distribution in a quasi-stable manner. As the SR damping draws these beam particles back into the core the perturbing mechanisms continue to repopulate the halo distribution. Any perturbation can kick some of the core particles out onto the tail distribution.

CONCLUSION

I have tried to describe what to me will be some of the new operating conditions we will encounter in the new high-current running and in some of the future e^+e^- colliders. There are clearly many important topics not discussed here that also impact interaction region designs (i.e. High-Order Mode effects for one). I suspect that even with all of our present knowledge of colliders and also of high-current storage rings we will still encounter new and unexpected issues related to high-current stored beams and to the increased luminosity design goals in the present and new machines. But then that is what makes pushing into new territory interesting and exciting.

ACKNOWLEDGEMENTS

I wish to acknowledge the design teams from the Thomas Jefferson National Accelerator Laboratory and the Brookhaven National Laboratory for the many discussions concerning the electron high-beam current plan for the EIC. I also want to acknowledge the design teams for the FCC-ee and for the CEPC for many fruitful meetings and discussions concerning the detector backgrounds and the interaction region design. Last, but by no means least, I wish to thank the SuperKEKB and Belle II accelerator and detector background teams for their many discussions and presentations of running conditions in the process of commissioning and understanding the new accelerator and detector.

ISBN: 978-3-95450-236-3 ISSN: 2673-7027 doi:10.18429/JACoW-eeFACT2022-TUZAT0101

REFERENCES

[1] The information in the introduction came mostly from the website:
https://en.wikipedia.org/.
In particular, the links:
https://en.wikipedia.org/wiki/Particle_accelerator,
and
https://en.wikipedia.org/wiki/List_of_accelerators_in_particle_physics
as well as information concerning specific accelerators on individual web pages by the name of or the acronym for the accelerator.

[2] A.Sessler, E. Wilson, "Engines of Discovery", *World Scientific Publishing Co*., 2007.

[3] Y. Funakoshi, "Luminosity Tuning at KEKB", in *Proc. eeFACT'16*, pp. 147-150, paper TUT3BH3, 2016.

[4] SuperB Collaboration, "SuperB Conceptual Design Report", INFN/AE-07/2, arXiv:0709.0451 [hep-ex], 2007. doi:10.48550/arXiv.0709.0451

[5] Y. Funakoshi *et al.*, "The SuperKEKB has Broken the World Record of the Luminosity", in *Proc. IPAC'22*, Bangkok, Thailand, Jun. 2022, pp. 1–5. doi: 10.18429/JACoW-IPAC2022-MOPLXGD1

[6] F. Zimmermann, "FCC-ee Feasibility Study Progress", in *Proc. eeFACT'22*, Frascati, Italy, 2022, paper MOXAT0104, this workshop.

[7] Y. Li, "Towards CEPC TDR", in *Proc. eeFACT'22*, Frascati, Italy, 2022, paper MOXAT0105, this workshop.

[8] C. Montag, "eRHIC- an Electron-Ion Collider at BNL", in *Proc. SPIN'18*, Ferrara, Italy, 10-14 September, 2018. doi:10.22323/1.346.0158

[9] T. Satogata, "EIC Electron-Ion Collider," presented at *eeFACT'22*, Frascati, Italy, 2022, unpublished.

[10] A. W. Chao, K. H. Mess, M Tigner, and F. Zimmermann, Eds., *Handb. Accel. Phys. Eng.*, Sec. 3.3.9.1, pp. 287, 2nd Ed, 2013. doi:10.1142/8543

[11] A. W. Chao, K. H. Mess, M Tigner, and F. Zimmermann, Eds., *Handb. Accel. Phys. Eng.*, Sec. 2.4.12, pp. 155, 2nd Ed, 2013. doi:10.1142/8543

[12] A. W. Chao, K. H. Mess, M Tigner, and F. Zimmermann, Eds., *Handb. Accel. Phys. Eng.*, Sec. 3.3.3, pp. 273, 2nd Ed, 2013. doi:10.1142/8543

[13] A. W. Chao, K. H. Mess, M Tigner, and F. Zimmermann, Eds., *Handb. Accel. Phys. Eng.*, Sec. 2.5.3.2, pp. 177, 2nd Ed, 2013. doi:10.1142/8543

[14] E. Paterson, Private communication.

[15] M. Sands, *The Physics of Electron Storage Rings an Introduction*, SLAC-121, UC-28, 1969, pp. 141-147.

ISBN: 978-3-95450-236-3 ISSN: 2673-7027 doi:10.18429/JACoW-eeFACT2022-TUZAT0103

BEAM-INDUCED BACKGROUND SIMULATION AND MEASUREMENTS IN Belle II AT SuperKEKB*

A. Natochii†, University of Hawaii, Honolulu, Hawaii 96822, USA
on behalf of the Belle II Beam Background and Machine Detector Interface (MDI) groups

Abstract

Seeking New Physics beyond the Standard Model, the Belle II experiment at the SuperKEKB electron-positron collider has already reached a peak luminosity of about $4.7{\times}10^{34}\,\mathrm{cm^{-2}\,s^{-1}}$. Its unprecedented target luminosity of $6.3{\times}10^{35}\,\mathrm{cm^{-2}\,s^{-1}}$ requires stable machine operation and proper control of beam-induced backgrounds for safe detector operation at high beam currents. The leading background components originating from stored and colliding beams can now be predicted with reasonable accuracy. Dedicated simulations based on the particle tracking software Strategic Accelerator Design (SAD) and Geant4 are used to predict beam-induced backgrounds. These simulations are important for studying realistic collimation scenarios, estimating associated background levels at future machine optics, and making informed choices between possible machine and detector protection upgrades.

This paper reports on the Belle II beam-induced background status in 2021–2022. It overviews background simulation and measurement methodology, and discusses the expected background evolution and mitigation strategies at higher luminosity.

INTRODUCTION

The Belle II/SuperKEKB [1–3] experiment is an upgrade of Belle/KEKB [4, 5] ran between 1999 and 2010. These two projects share same goals of i) studying CP-symmetry violation in a B-meson system, and ii) searching for New Physics beyond the Standard Model. This implies a certain set of requirements for the experiments such as: i) high collision luminosity to produce a large number of $B\bar{B}$-pairs; ii) asymmetric-energy colliding beams of particles to facilitate B-meson decay time difference measurements; and iii) a high quality general-purpose spectrometer (detector) around the interaction point (IP) of two beams for precise measurements of the $B\bar{B}$-mixing rate.

Inspired by Belle/KEKB achievements, which along with BaBar/PEP-II observed large time-dependent CP-asymmetries and contributed to the 2008 Physics Nobel Prize [6], Belle II/SuperKEKB aims to collect 50 times larger data set by the 2030s. To reach this goal, an extremely high collision luminosity above $1{\times}10^{35}\,\mathrm{cm^{-2}\,s^{-1}}$ is required. Therefore, the experiment upgraded almost all detector and collider sub-systems, and implemented so-called *nano-beam* and *crab waist* collision schemes to squeeze beam sizes at the IP and improve luminosity performance [7].

Since 2019, when the detector was rolled in for comprehensive data taking, SuperKEKB has reached the world highest peak luminosity of about $4.7{\times}10^{34}\,\mathrm{cm^{-2}\,s^{-1}}$ in June 2022, while Belle II has successfully accumulated more than $0.4\,\mathrm{ab^{-1}}$ of data, which is about as large as BaBar's data set collected in almost nine years of PEP-II operation [8].

The SuperKEKB is a 3 km-long circular collider of 4 GeV positrons and 7 GeV electrons accumulated in low-energy ring (LER) and high-energy ring (HER), respectively. Its design has 40 times higher collision luminosity ($\mathcal{L} \sim I_{\pm}/\beta_{\mathrm{y}}^{*}$) than KEKB with two times higher beam currents ($I_{\pm}$) and 20 times smaller vertical beta functions at the IP (β_{y}^{*}). This causes higher beam-induced backgrounds in the Belle II detector and leads to i) a high rate of particles leaving the beam, requiring a more frequent top-up beam injection, ii) damage of sensitive detector and collider components, reducing their longevity, and iii) a high rate of beam losses in the interaction region (IR), where the Belle II locates, increasing detector hit occupancy and physics analysis noise. To reach the target luminosity of $6.3{\times}10^{35}\,\mathrm{cm^{-2}\,s^{-1}}$, a comprehensive understanding of beam-induced backgrounds and their countermeasures is essential.

In this paper, we describe main beam loss sources and their countermeasures, report on dedicated background measurements and simulation software, and discuss background estimation towards higher luminosity with a brief overview of our plans in order to facilitate stable and safe detector and machine operation.

BEAM-INDUCED BACKGROUND SOURCES

At SuperKEKB, stray particles which do not follow the nominal trajectory and hit the inner walls of the beam pipe or any other machine element are defined as lost. These particles interact with machine and detector materials producing electromagnetic (EM) showers and neutrons which may hit the detector. These losses we call a beam-induced background (BG).

Below, we define the main types of beam-induced backgrounds which contribute the most to the machine and detector performance degradation and longevity.

Touschek BG is due to a single Coulomb scattering of two particles in the same beam bunch leading to their energy change. It is one of the major backgrounds in Belle II, mainly from the LER.

Beam-gas BG is caused by Bremsstrahlung and Coulomb scatterings of a beam particle by beam pipe residual gas

* Work supported by the U.S. Department of Energy (DOE) via Award Number DE-SC0007852 and via U.S. Belle II Operations administered by Brookhaven National Laboratory (DE-SC0012704).

† natochii@hawaii.edu

ISBN: 978-3-95450-236-3 ISSN: 2673-7027 doi:10.18429/JACoW-eeFACT2022-TUZAT0103

atoms changing their energy and trajectory, respectively. Since SuperKEKB reuses the HER beam pipe from the KEKB era and the LER beam pipe is newly constructed, the LER beam-gas losses contribute the most to Belle II backgrounds due to higher vacuum pressure.

Synchrotron radiation (SR) is generated by beam particles moving through a strong magnetic field of dipole magnets and final focusing superconducting quadrupole magnets (QCS) near the IP used for beam size squeezing. The current level of the SR is of no concern in terms of occupancy for the innermost layers of the vertex detector.

Injection BG is caused by the injected beam of particles into the main ring (MR). Due to a short beam lifetime (< 1 hour), the machine operates in a so-called *top-up injection regime*. The perturbed by machine imperfections injected beam oscillates around the stored beam causing particle losses for a few milliseconds after injection. Low injection efficiency causes high injection beam losses around the MR, enlarging the DAQ dead time of the detector.

Luminosity BG is due to colliding beams at the IP. This type of backgrounds is induced by low energetic electron-positron pairs and gammas produced in two-photon and radiative Bhabha processes, respectively. At the current commissioning stage, the luminosity BG does not exceed the single-beam BG level. However, further luminosity increase will enhance this background making it dominant compared to other beam losses.

Sudden beam losses (SBLs) may occasionally occur in the LER or HER during stable machine operation at a specific location around the ring. Unfortunately, we still do not have a comprehensive explanation of such events. The potential candidates of the unexpected beam instabilities could be machine element failure, beam-dust interaction or vacuum element defects. It is a big problem for a safe and stable machine operation limiting bunch current increase above ~ 0.7 mA/bunch, while the target bunch current is about ~ 1.4 mA/bunch. Usually, only a few SBL events happen in a year. However, in 2022, we had more than 50 of them, which caused several QCS quenches and collimator damages. Figure 1 illustrates an example of the damaged collimator due to SBLs in 2021. Also, a local vacuum burst is detected in such events. Moreover, the damaged part of the collimator does not effectively collimate the beam, causing a background increase due to particle scattering off of the head protrusions. Therefore, the collimator aperture should be enlarged with further replacement of the entire jaw, leading to an extended period (weeks–months) of no beam due to radiation cooling down and replacement works.

BACKGROUND COUNTERMEASURES

To stop stray particles, a set of 11 and 20 movable masks (collimators) around LER and HER are installed [10–12]. By absorbing or strongly deviating off-trajectory particles, the collimators localize beam losses far from the IR, which significantly reduces detector backgrounds and helps to avoid QCS quenches. To minimise residual gas pressure in the

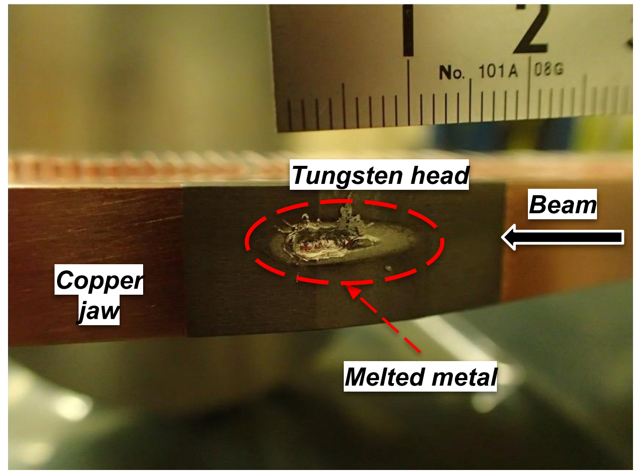

Figure 1: A severely damaged HER vertical collimator head due to sudden beam losses [9].

beam pipe, we continuously perform vacuum scrubbing and installed heavy-metal shielding around the IR beam pipe to protect the detector against EM showers. Furthermore, the IP beryllium beam pipe is coated with a gold layer to suppress the SR. To avoid direct SR hits at the detector, the internal walls of the IR beam pipe have a ridged surface, while the incoming beam pipe has varying diameters collimating most of the SR photos. Since the injection BG could be even higher than other BGs, the Belle II DAQ utilizes an injection trigger veto to not trigger on high beam losses during ~ 10 msec after each injection. This solution prevents us from taking noisy data. In addition, we continuously tune the injection chain to improve injection performances keeping the highest possible injection efficiency at the acceptable injection BG.

We use a set of diamond sensor-based detectors (Diamonds) to monitor the radiation dose rate around the IR beam pipe, see Figure 2. Four sensors highlighted in green are a part of the fast beam abort system [13]. In addition, the sCintillation Light And Waveform Sensors (CLAWS) detector system [14] monitors Belle II backgrounds in time with beam injection into the MR. Moreover, we have integrated CLAWS into the beam abort logic. The fast neutron flux in the accelerator tunnel is measured by compact Time Projection Chambers (TPCs) [15], while thermal neutron counting around Belle II is done by He^3 tubes [16].

Against SBLs, we plan i) to upgrade the abort system for fast abort signal triggering, ii) to use low-Z materials (e.g. graphite) for collimator heads, making them more robust [17], and iii) to perform vacuum system inspection, beam dynamics study and installation of additional beam loss monitors around the ring to understand the nature of SBLs better.

BACKGROUND MEASUREMENTS

When we change global machine optics settings (e.g. squeeze the beam at the IP) or install new equipment (e.g. collimators), we perform dedicated beam background mea-

ISBN: 978-3-95450-236-3 ISSN: 2673-7027 doi:10.18429/JACoW-eeFACT2022-TUZAT0103

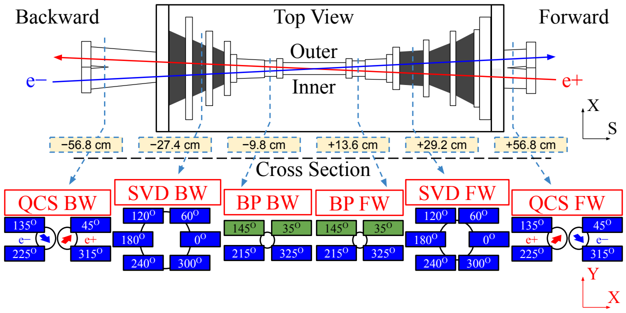

Figure 2: Diamond detector configuration in the IR. The detectors' azimuth angles are indicated in rectangles.

surements in Belle II at SuperKEKB, usually twice a year. To disentangle different background components, we run the machine in a single-beam mode, meaning that only one ring is filled with a beam at a time, and then fill both rings for luminosity background measurements. By changing the number of bunches circulating in each ring, we distinguish between Touschek and beam-gas backgrounds since the former is proportional to the beam current squared and inversely proportional to the number of bunches and bunch volume, while the latter is proportional to beam current and vacuum pressure. Since the power of the SR is proportional to the fourth power of the beam energy, we consider the SR background only for the HER beam in the Belle II pixel detector (PXD), which surrounds the IP beam pipe. At the collision operation, the single-beam fit results help estimate the contribution of the luminosity background, which is linearly proportional to the measured luminosity value.

We use our analysis results to extrapolate the measured beam-induced background toward higher beam currents assuming fixed collimator settings. Figure 3 shows an example of beam background evolution for the Time of Propagation (TOP) particle ID system as the most vulnerable Belle II sub-detector. The results are based on December-20, 2021 measurements scaling to June 2022 beam parameters and collimator settings. Wider HER collimators in 2022 significantly increase the HER beam-gas background shown in Figure 3 compared to 2021 rates listed in Table 1.

Table 1: Measured background composition in the TOP detector in June 2021 at LER and HER beam currents of about 730 mA and 650 mA, respectively, 1174 bunches, and luminosity of $2.6{\times}10^{34}$ cm^{-2} s^{-1}.

Background	Rate, MHz/PMT LER	Rate, MHz/PMT HER
Beam-gas	0.70	0.11
Touschek	0.44	0.11
Injection	0.11	0.03
Luminosity	0.45	

As demonstrated in Table 1 and Figure 3, in 2021 and 2022, Belle II did not limit beam currents since background rates were acceptable and below limits. However, it will limit SuperKEKB eventually, without further background mitigation. Therefore, to reach the target luminosity of $6.3{\times}10^{35}$ cm^{-2} s^{-1}, an upgrade of crucial detector components is foreseen. For instance, we plan to replace TOP short-lifetime conventional microchannel plate photomultiplier tubes (MCP-PMTs), which quantum efficiency strongly degrades with the background increase [19].

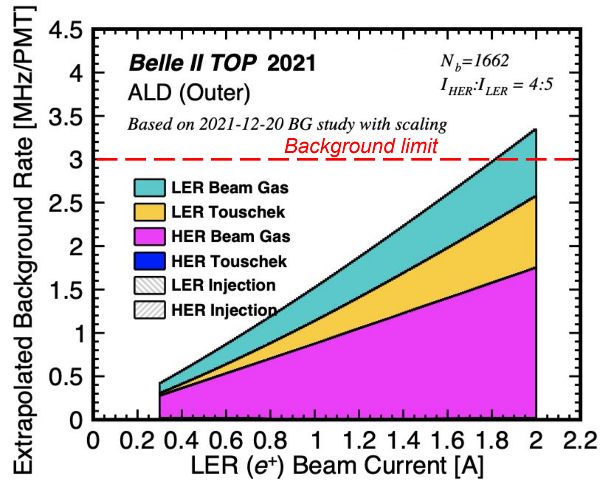

Figure 3: The extrapolated single-beam background in the TOP detector as a function of beam currents [18].

We will discuss in more detail the current Belle II background status in upcoming publications [20].

BACKGROUND SIMULATION

We developed a dedicated software for the Monte-Carlo beam-induced background simulation in Belle II. We use it for several reasons: i) to study the impact of beam optics parameters on Belle II backgrounds, ii) to develop new collimators in SuperKEKB, iii) to mitigate backgrounds better through the machine or detector adjustments and upgrades, and iv) it helps us predict background evolution at future machine settings.

We start with the multi-turn particle tracking in the machine using the Strategic Accelerator Design (SAD) software developed at KEK [21]. Beam-gas and Touschek scattered bunches of particles are tracked for 1000 machine turns, which corresponds to 10 ms of the real machine operation. The particles that reach the machine aperture (beam pipe or collimators) are defined as lost, and their coordinates are stored. Recently, we have improved the code by implementing a realist collimator profile and particle interaction with collimator materials, see Figure 4. Moreover, for the beam-gas background simulation, we use the measured vacuum pressure distribution, which is not uniformly flat around the ring. More details regarding the multi-turn particle tracking in SAD for SuperKEKB can be found in Reference [12].

Then, all lost particles within the IR, which hosts Belle II (±4 m from the IP), and accelerator tunnel (±30 m from the IP) we transfer from SAD to Geant4 [22–24] for detector

ISBN: 978-3-95450-236-3 ISSN: 2673-7027 doi:10.18429/JACoW-eeFACT2022-TUZAT0103

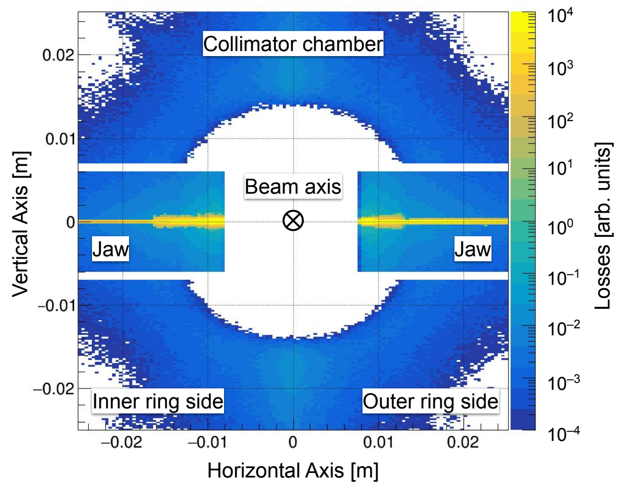

Figure 4: Simulated lost particles at the LER horizontal collimator.

response modelling. Also, we use the same Geant4 model for luminosity and SR background simulation.

In the past two years, we invested a lot of effort into improving our Geant4 model. As a result, the latest version realistically describes detector materials and accelerator tunnel, including the IP beam pipe, detector shielding, tunnel walls and machine equipment.

Validation

In 2021, we performed dedicated measurements at SuperKEKB to validate our simulation software [12]. Two collimator aperture scans were done in the LER, measuring radiation dose rates by Diamonds. First, we gradually closed the aperture of the narrowest vertical collimator, located ~ 1 km upstream of the IP. As a result, we observed a significant reduction in the IR dose rate in a single-beam mode. Then, we moved back the vertical collimator to its initial aperture and gradually closed the horizontal collimator, located about 16 m upstream of the IP. The horizontal collimator scan showed a similar trend with a noticeable reduction of IR backgrounds until a certain aperture when the particles scattered off of the collimator head, so-called tip-scatterings, started to contribute to IR beam losses increasing backgrounds at a narrower aperture. Our simulation of the collimator aperture scans reproduces the measurements with a good agreement, validating the correct implementation of collimator profiles and tip-scattering models into the particle tracking code.

Accuracy

As an accuracy check, we calculate ratios of measured (data) to simulated (MC) backgrounds based on dedicated studies conducted in 2020–2021. Due to discussed simulation improvements and the accurate Geant4 model, our current data/MC ratios are within one order of magnitude from unity. Figure 5 shows data/MC ratios for the Belle II luminosity background, which is expected to be the dominant detector background beyond 1×10^{35} cm^{-2} s^{-1}. It is a substantial improvement compared to the past measurements in 2016 [25] and 2018 [26]. It also confirms our good understanding of the main beam loss processes in SuperKEKB. In addition, we use these ratios to estimate detector backgrounds at higher luminosities [27].

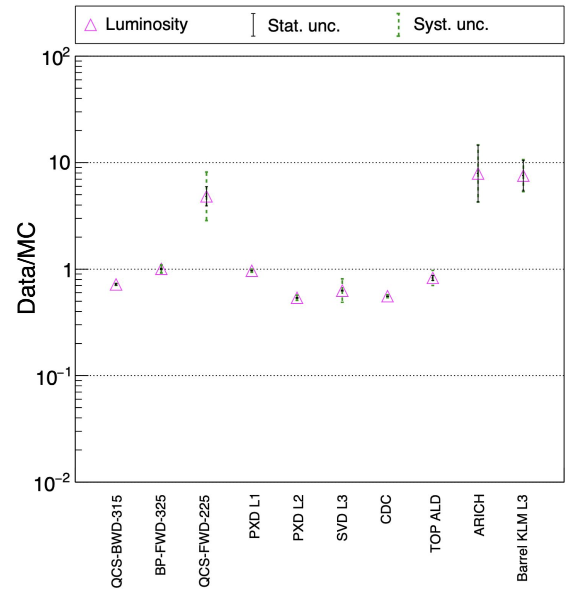

Figure 5: Calculated luminosity background data/MC ratios for Belle II sub-detectors based on dedicated background measurements at SuperKEKB in 2020–2021 [27].

FUTURE PLANS AND PROSPECTS

We use the newly improved background simulation and dedicated measurements to predict background evolution at future machine settings. According to the results presented in Reference [27], Belle II backgrounds will remain high but acceptable until a luminosity of about 2.8×10^{35} cm^{-2} s^{-1} is reached. For the target luminosity of about 6.3×10^{35} cm^{-2} s^{-1}, machine condition is very uncertain to make an accurate background prediction.

To reach the goal collecting about 50 ab^{-1} of data by the 2030s, we plan several upgrades of the machine and detector [19, 27] during future two long shutdown (LS) periods: LS1 in June 2022 – October 2023, and LS2 starting in 2027. Figure 6 schematically shows the timeline of the peak and integrated luminosity projection toward future machine parameters.

Below, we list Belle II/SuperKEKB major upgrades planned for the next decade.

- Detector upgrades are planned for LS1 and include damage sensors replacement, fully assembled PXD with two layers, and replaced short-lifetime conventional MCP-PMTs in the TOP detector. More details in Reference [19].

ISBN: 978-3-95450-236-3 ISSN: 2673-7027 doi:10.18429/JACoW-eeFACT2022-TUZAT0103

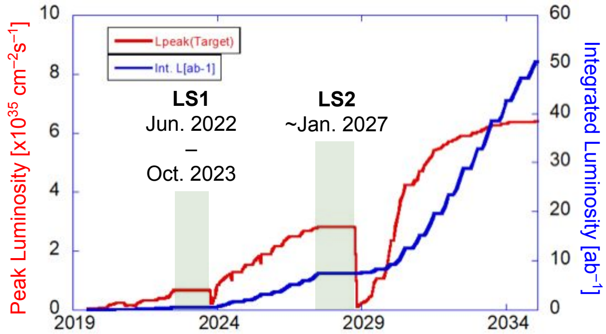

Figure 6: The Belle II/SuperKEKB luminosity projection based on the current machine achievements. Adopted from Reference [28].

- Install additional shielding during LS1 inside and outside Belle II against the SR, EM-showers and neutrons. We plan to add more polyethylene and concrete shielding on endcaps and around final focusing magnets.
- Consider a collimation system upgrade for LS1 and LS2, replacing damaged collimators with more robust collimator heads. Also, a so-called non-linear collimator (NLC) in the LER is foreseen for LS1 [27, 29, 30]. The NLC design, implementation and its impact on beam collimation will be accurately described by the Belle II/SuperKEKB team in future publications.
- To reach the target luminosity, the IR redesign during LS2 is under discussion.
- SuperKEKB beam dynamics stability, beam-beam interaction and injection performance require special attention since uncontrolled beam instabilities, beam size blow-up and high rate of injection beam losses cause machine and detector performance degradation, DAQ dead time duration increase, injection efficiency drop, and detrimental effects on the machine and detector component longevity. Therefore, the injection facility and machine feedback system upgrades, as well as accurate beam dynamics studies are under consideration.

SUMMARY

The Belle II/SuperKEKB experiment has successfully rolled in as a new generation *B*-factory searching for New Physics beyond the Standard Model. Its ultimate goal is to integrate a 50 times higher data set than its predecessor Belle/KEKB. The collider aims to reach an unprecedented luminosity of about 6.3×10^{35} cm^{-2} s^{-1} by the 2030s. Such an extreme collision rate in the interaction region surrounded by Belle II induces high beam backgrounds in the detector. A dedicated set of countermeasures was implemented to protect sensitive detector and machine components. Furthermore, we plan to install additional detector shielding during two consecutive machine stops in the next decade to reinforce the detector protection against EM showers and neutrons.

In this paper, we revisited major beam loss mechanisms, leading to high beam backgrounds in the detector, and their countermeasures. Also, we reported on the current background status in Belle II and mentioned crucial stumbling blocks limiting further beam current increase, which should be mitigated by future machine upgrades. Finally, our improved background simulation agrees with measurements and helps us predict beam-induced background evolution at higher beam currents and luminosities. Although the final machine design for the post-LS2 period is unclear, the Belle II background is expected to be acceptable at least until the luminosity of about 2.8×10^{35} cm^{-2} s^{-1}, if the assumed collimation settings are achieved.

ACKNOWLEDGMENTS

The authors are grateful to Belle II and SuperKEKB colleagues for their hard work and contribution.

REFERENCES

[1] T. Abe *et al.*, "Belle II Technical Design Report", *arXiv preprint*, KEK REPORT 2010-1, 2010. doi.org/10.48550/arXiv.1011.0352

[2] I. Adachi *et al.*, "Detectors for extreme luminosity: Belle II", *Nucl. Instrum. Methods Phys. Res., Sect. A*, vol. 907, pp. 46–59, 2018. doi.org/10.1016/j.nima.2018.03.068

[3] Y. Ohnishi *et al.*, "Accelerator design at SuperKEKB", *Prog. Theor. Exp. Phys.*, vol. 2013, p. 03A011, 2013. doi.org/10.1093/ptep/pts083

[4] J. Brodzicka *et al.*, "Physics achievements from the Belle experiment", *Prog. Theor. Exp. Phys.*, vol. 2012, p. 04D001, 2012. doi.org/10.1093/ptep/pts072

[5] T. Abe *et al.*, "Achievements of KEKB", *Prog. Theor. Exp. Phys.*, vol. 2013, p. 03A011, 2013. doi.org/10.1093/ptep/pts102

[6] "The Nobel Prize in Physics for 2008", *Press release*, https://www.nobelprize.org/prizes/physics/2008/press-release/

[7] Y. Ohnishi *et al.*, "SuperKEKB operation using crab waist collision scheme", *Eur. Phys. J. Plus*, vol. 136, p. 1023, 2021. doi.org/10.1140/epjp/s13360-021-01979-8

[8] J. Seeman, "Last Year of PEP-II B-Factory Operation", in *Proc. EPAC'08*, Genoa, Italy, Jun. 2008, paper TUXG01, pp. 946–950. https://accelconf.web.cern.ch/e08/papers/tuxg01.pdf

[9] T. Ishibashi and S. Terui (KEKB vacuum group), *private communication.*

[10] T. Ishibashi, Y. Suetsugu, and S. Terui, "Collimators for SuperKEKB Main Ring", in *Proc. IPAC'17*, Copenhagen, Denmark, May 2017, pp. 2929–2932. doi:10.18429/JACoW-IPAC2017-WEPIK009

[11] T. Ishibashi, S. Terui, Y. Suetsugu, K. Watanabe, and M. Shirai, "Movable collimator system for SuperKEKB", *Phys. Rev. Accel. Beams*, vol. 23, p. 053501, 2020. 10.1103/PhysRevAccelBeams.23.053501

ISBN: 978-3-95450-236-3 ISSN: 2673-7027 doi:10.18429/JACoW-eeFACT2022-TUZAT0103

[12] A. Natochii, S. E. Vahsen, H. Nakayama, T. Ishibashi, and S. Terui, "Improved simulation of beam backgrounds and collimation at SuperKEKB", *Phys. Rev. Accel. Beams*, vol. 24, p. 081001, 2021. doi.org/10.1103/PhysRevAccelBeams.24.081001

[13] S. Bacher *et al.*, "Performance of the diamond-based beam-loss monitor system of Belle II", *Nucl. Instrum. Methods Phys. Res., Sect. A*, vol. 997, p. 165157, 2021. doi.org/10.1016/j.nima.2021.165157

[14] M. Gabriel *et al.*, "A time resolved study of injection backgrounds during the first commissioning phase of SuperKEKB", *Eur. Phys. J. C*, vol. 81, pp. 1–19, 2021. doi.org/10.1140/epjc/s10052-021-09769-3

[15] J. Schueler *et al.*, "Application of recoil-imaging time projection chambers to directional neutron background measurements in the SuperKEKB accelerator tunnel", *Nucl. Instrum. Methods Phys. Res., Sect. A*, vol. 1040, p. 167291, 2022. doi.org/10.1016/j.nima.2022.167291

[16] S. R. de Jong, "Study of Thermal Neutron Flux from SuperKEKB in the Belle II Commissioning Detector", *PhD thesis*, BELLE2-PTHESIS-2018-002, 2017. https://docs.belle2.org/record/1066

[17] S. Terui *et al.*, "Development of Low-Z Collimator for SuperKEKB", in *Proc. IPAC'21*, Campinas, Brazil, May 2021, pp. 3537–3540. doi:10.18429/JACoW-IPAC2021-WEPAB358

[18] K. Kojima (Belle II TOP group), *private communication.*

[19] F. Forti, "Snowmass Whitepaper: The Belle II Detector Upgrade Program", *arXiv preprint*, 2022. doi.org/10.48550/arXiv.2203.11349

[20] A. Natochii *et al.*, "Measured and projected beam backgrounds in the Belle II experiment at the SuperKEKB collider", *being submitted for publication*.

[21] Strategic Accelerator Design, *SAD Home Page*. http://acc-physics.kek.jp/SAD/

[22] S. Agostinelli *et al.*, "Geant4 – a simulation toolkit", *Nucl. Instrum. Methods Phys. Res., Sect. A*, vol. 506, pp. 250–303, 2003. doi.org/10.1016/S0168-9002(03)01368-8

[23] J. Allison *et al.*, "Geant4 developments and applications", *IEEE Trans. Nucl. Sci.* , vol. 53, pp. 270–278, 2006. doi.org/10.1109/TNS.2006.869826

[24] J. Allison *et al.*, "Recent developments in Geant4", *Nucl. Instrum. Methods Phys. Res., Sect. A*, vol. 835, pp. 186–225, 2016. doi.org/10.1016/j.nima.2016.06.125

[25] P. M. Lewis *et al.*, "First measurements of beam backgrounds at SuperKEKB", *Nucl. Instrum. Methods Phys. Res., Sect. A*, vol. 914, pp. 69–144, 2019. doi.org/10.1016/j.nima.2018.05.071

[26] Z. J. Liptak *et al.*, "Measurements of beam backgrounds in SuperKEKB Phase 2", *Nucl. Instrum. Methods Phys. Res., Sect. A*, vol. 1040, p. 167168, 2022. doi.org/10.1016/j.nima.2022.167168

[27] A. Natochii *et al.*, "Beam background expectations for Belle II at SuperKEKB", *arXiv preprint*, 2022. https://arxiv.org/abs/2203.05731

[28] Belle II Luminosity, *Belle II Public WebHome*. https://confluence.desy.de/display/BI/Belle+II+Luminosity

[29] K. Oide (KEK/CERN), *private communication.*

[30] A. Faus-Golfe, J. Resta-López, and F. Zimmermann, "Non-linear Collimation in Linear and Circular Colliders", in *Proc. EPAC'06*, Edinburgh, UK, Jun. 2006, paper WEXFI03, pp. 1892–1896. https://accelconf.web.cern.ch/e06/PAPERS/WEXFI03.PDF

65th ICFA Adv. Beam Dyn. Workshop High Luminosity Circular e⁺e⁻ Colliders eeFACT2022, Frascati, Italy JACoW Publishing
ISBN: 978-3-95450-236-3 ISSN: 2673-7027 doi:10.18429/JACoW-eeFACT2022-TUZAT0201

MDI DESIGN FOR CEPC

S. Bai, H.Y. Shi, H.J. Wang, Y.W. Wang, J. Gao
Institute of High Energy Physics, Beijing, China

Abstract

The Circular Electron Positron Collider (CEPC) is a proposed Higgs factory with center of mass energy of 240 GeV to measure the properties of Higgs boson and test the standard model accurately. Machine Detector Interface (MDI) is the key research area in electron-positron colliders, especially in CEPC, it is one of the criteria to measure the accelerator and detector design performance. In this paper, we will introduce the CEPC MDI layout and (Interaction Region) IR design, IR beam pipe design, thermal analysis and injection background etc on, which are the most critical physics problem.

INTRODUCTION

With the discovery of a Higgs boson at about 125 GeV, the world high-energy physics community is investigating the feasibility of a Higgs Factory, a complement to the LHC for studying the Higgs [1]. There are two ideas now in the world to design a future Higgs factory, a linear 125×125 GeV e^+e^- collider and a circular 125 GeV e^+e^- collider. From the accelerator point of view, the circular 125 GeV e^+e^- collider, due to its low budget and mature technology, is becoming the preferred choice to the accelerator group in China. Machine Detector Interface (MDI) is one of the most challenging field in Circular Electron Positron Collider (CEPC) design, it almost covered all the common problems in accelerator and detector.

In this paper, we will introduce the critical issues of CEPC MDI, including the IR beam pipe design, thermal analysis and injection background etc on.

MDI LAYOUT AND IR DESIGN

The machine-detector interface is about ±7 m in length in the IR as can be seen in Fig. 1, where many elements need to be installed, including the detector solenoid, luminosity calorimeter, interaction region beam pipe, beryllium pipe, cryostat and bellows. The cryostat includes the final doublet superconducting magnets and anti-solenoid. The CEPC detector consists of a cylindrical drift chamber surrounded by an electromagnetic calorimeter, which is immersed in a 3 T (2 T in Z) superconducting solenoid of length 7.3 m. The accelerator components inside the detector should not interfere with the devices of the detector. The smaller the conical space occupied by accelerator components, the better will be the geometrical acceptance of the detector. From the requirement of detector, the conical space with an opening angle should not larger than 8.11 degrees. After optimization, the accelerator components inside the detector without shielding are within a conical space with an opening angle of 6.78 degrees. The crossing angle between electron and positron beams is 33 mrad in horizontal plane. The final focusing quadrupole is 1.9 m from the IP [2].

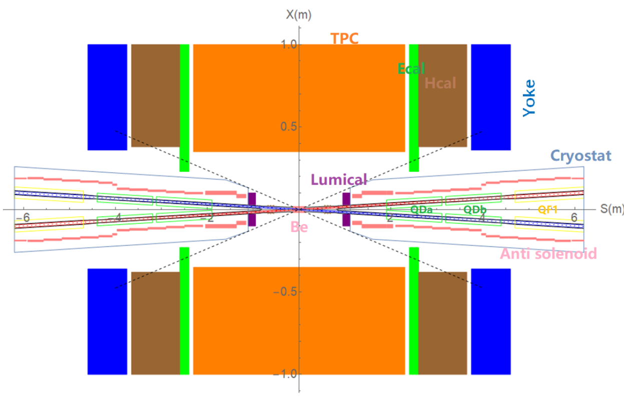

Figure 1: CPEC IR layout.

BEAM PIPE

To reduce the detector background and radiation dose from beam loss, the vacuum chamber has to accommodate the large beam stay clear region. In order to keep precise shaping, all these chambers will be manufactured with computer controlled machining and carefully welded to avoid deformation.

In the present design (Table 1 and Fig. 2), the inner diameter of the beryllium pipe was decided to be 20mm by considering both the mechanical assembly and beam background issues. The length of beryllium pipe is 85mm in longitudinal. Due to bremsstrahlung incoherent pairs, the shape of the beam pipe between 180~655 mm is selected as conic. There is a bellows for the requirements of installation in the crotch region which is located about 0.7 m away from the IP. The crotch point is at 805 mm away from the IP with slope. A race-track shape beam pipe is adopted between 805~855 mm from IP with the inner diameter 39 mm (single pipe) ~20 mm (double pipes), which is considered to control the heating problem of HOM. For the beam pipe within the final doublet quadrupoles, a room temperature beam pipe has been adopted.

Table 1: CEPC IR Central Beam Pipe Design

From IP(mm)	Shape	Inner diameter(mm)	Material	Marker
0-85	Circular	20	Be	
85~180	Circular	20	Al	
180~655	Cone	20~35	Al	Taper: 1:70
655~700	Circular	35	Al	
700~780	Circular	35	Cu	
780~805	Cone	35~39	Cu	
805~855	Race-track	39~20 double pipe	Cu	

ISBN: 978-3-95450-236-3   ISSN: 2673-7027   doi:10.18429/JACoW-eeFACT2022-TUZAT0201

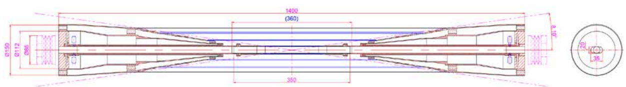

Figure 2: CEPC IR central beam pipe mechanical design.

THERMAL ANALYSIS

SR in Normal Conditions

An asymmetric lattice adopted to allow softer bends in the upstream of IP [2]. Reverse bending direction of last bends is applied to avoid synchrotron radiation hitting IP vacuum chamber. Thus, in normal conditions (Fig. 3) there is no synchrotron radiation photons hitting the central IP beam pipe, which is generated from the last bending magnet in the upstream of IP.

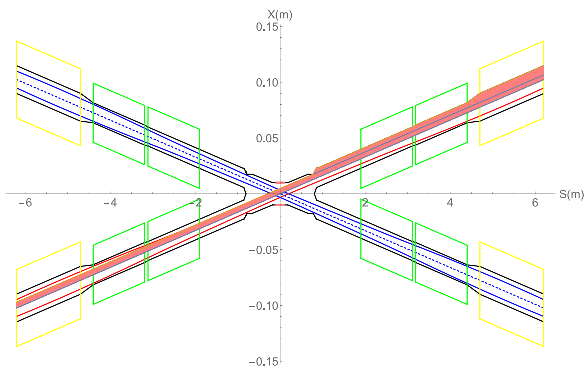

Figure 3: SR from last bending magnet in upstream of IP in normal conditions.

"Room temperature" beam pipe and conduction cooled superconducting magnet has to be adopted. For the IR beam pipe of the accelerator part beyond 700 mm away from IP, single layer beam pipe with water cooling has been adopted, and the synchrotron radiation heat load distribution is shown in Table 2.

Table 2: SR heat load distribution from last bending magnet in upstream of IP.

Region	SR heat load	SR average power density
0~780mm	0	0
780mm~805mm	23.04W	256W/cm²
805mm~855mm	53.39W	296.6W/cm²
855mm~1.9m(QDa entrance)	4.32W	1.15W/cm²
QDa	3.28W	0.75W/cm²
QDa~QDb	22.92W	79.58W/cm²
QDb	3.96W	0.91W/cm²
QDb~QF1	71.04W	65.8W/cm²
QF1	7.26W	1.34W/cm²

However, some secondaries generated within the beam pipe of QD would hit the detector beampipe, even the beryllium part. Therefore, the mitigation methods must be studied. SR photons generated from the FD magnets will hit downstream of the IR beam pipe, and the once-scattering photons will not go into the detector beam pipe but goes to even far away from the IP region.

SR in Extreme Conditions

In extreme conditions (Fig. 4) for example, if a magnet power is lost, a large distortion will appear immediately for the whole ring orbit. The beam will be lost when exceeded. In extreme cases which is about at least 10 times per day, the beam will be stopped within 0.5 ms when abnormal. The beam orbit deviation will not affect detector operation, since the high background part will be removed when data analysis is carried out.

In extreme conditions, synchrotron radiation photons will hit the bellows and Beryllium pipe in IR. There is no cooling at the bellows. Since it is a transient effect, heat load is not a problem. But the background of the detector and radiation dose should be considered under abnormal conditions.

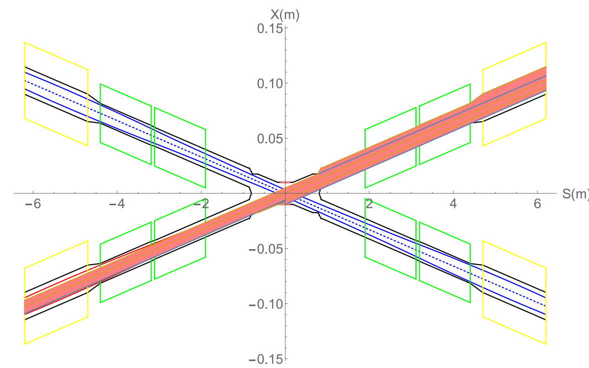

Figure 4: SR from upstream of IP in extreme conditions.

Beam Loss Backgrounds

The beam particles might abruptly lose a large fraction of energy through some scattering processes such as Radiative Bhabha scattering [3], Beamstrahlung [4], beam-gas scattering, beam-thermal photon scattering [5] and so on. According to the off-momentum dynamic aperture after optimizing the CEPC lattice, and considering the beam-beam effect and errors, the energy acceptance of CEPC is about 1.5%. If the energy loss of the beam particles are larger than 1.5% of the beam energy, these particles will be lost from the beam and might hit on the vacuum chamber. If this happens near the IR, it will cause heat load to the beam pipe. If this heat load is too large, superconducting magnet may quench. Table 3 shows the heat load distribution from beam loss backgrounds.

Table 3: Heat load distribution from beam loss backgrounds.

Region	RBB	Beamstrahlung	Beam-Gas	BTH
Berryllium pipe	6.7mW	0	0	0
Detector beam pipe	0.024W	0	4.8uW	1.2uW
Accelerator beam pipe before QDa	0.17W	0	4.2uW	1.2uW
QDa~QDb	2.13W	3.8uW	5.9uW	1.8uW
QDb~QF1	0.01W	3.8uW	0.5uW	0.6uW
QF1	0.26mW	0	3.7uW	0.66uW

Heat load in IR from beam loss backgrounds are small compared to ones generated from synchrotron radiation and HOM.

ISBN: 978-3-95450-236-3 ISSN: 2673-7027 doi:10.18429/JACoW-eeFACT2022-TUZAT0201

INJECTION BACKGROUND

When a charge is injected to a circulating beam bunch, the injected bunch is perturbed and a higher background rate is observed in the detector for few milliseconds after the injection [6]. There are two kinds of injection modes: one is the FULL injection to an empty ring; the other is the top-up injection. For the first FULL injection mode, since the detector high-voltage is off and detector measurement is off, background should not be considered. The effects from the continuous top-up injection on potential beam-loss-induced backgrounds in the IR needs to be analysed.

The effects from the continuous top-up injection on potential beam-loss-induced backgrounds in the IR are analysed (Fig. 5) using a simplified model, and radiative Bhabha scattering is considered.

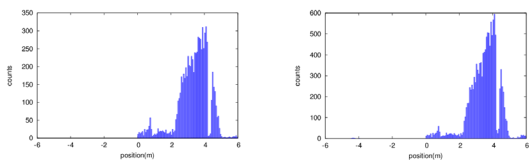

Figure 5. Beam loss background in ±6 m around IP from circular beam (left) and injection beam(right).

In addition, the presence of beam tails (Fig. 6) from the errors of the kicker (e.g. rotational error) and from imperfectly corrected X-Y coupling after the injection point should also be considered before the injection beam are damped by the radiation damping and/or transverse-feedback system.

Moreover, some tolerances such as too large emittances to imperfect beams from the Booster should be also taken into account (Fig. 7).

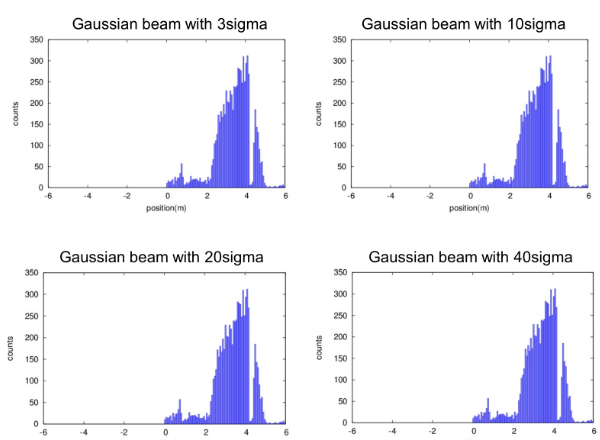

Figure 6: Beam loss background in ±6 m around IP with the presence of beam tails.

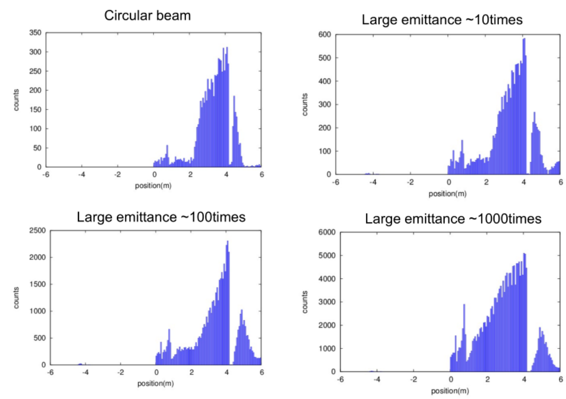

Figure 7: Beam loss background in ±6 m around IP with large emittances to imperfect beams from the Booster.

There is almost no beam loss background in the upstream of the IP which shows that the existed collimation system can well cope. However, the beam loss background in the downstream of the IP can even significantly increased. This will not have effect on the inner layer detector but the radiation background may damage the outer layer or the endcap detector, and it cannot be solved by the collimators but adding tungsten shielding may be a better choice. Furthermore, the remarkable beam loss background in the downstream of the IP can also damage the superconducting magnet coils and cause quench. In this case, the tungsten shielding is more demanded in the IR. Since the very tight space in the IP region, a tungsten-alloy beam pipe is under design in the CEPC TDR stage.

Furthermore, the beam distribution building up in the Booster and injected into the main rings is usually Gaussian distribution, but there might be non-Gaussian distribution from some interaction effects such as beam-gas scattering etc on. The beam halo occupancy in the whole beam distribution may be much larger than in the Gaussian distribution. The non-Gaussian distribution from the Booster and being injected into the main rings is evaluated (Fig. 8) by introducing a uniform and a double-Gaussian beam distribution.

The result shows that no significant increase of the beam loss background, and the existed collimation system is capable to cope.

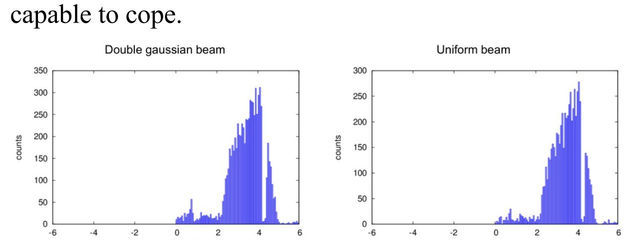

Figure 8: Beam loss background in ±6 m around IP with non-Gaussian injection beam.

ISBN: 978-3-95450-236-3 ISSN: 2673-7027 doi:10.18429/JACoW-eeFACT2022-TUZAT0201

CONCLUSION

The MDI layout has been renewed. Compatible and no interference for the design. New ϕ = 20 mm IR beam pipe is designed and renewed. The thermal analysis including synchrotron radiation and beam loss background meet the MDI requirement. The injection background result shows that no significant increase of the beam loss background, and the existed collimation system is capable to cope.

REFERENCES

[1] Accelerators for a Higgs Factory: linear vs circular (HF2012), https://indico.fnal.gov/conferenceDisplay.py?confId=5775

[2] Y. W. Wang *et al*., "A lattice design of the CEPC collider ring at Higgs energy for the high luminosity scheme", *Int. J. Mod. Phys. A*, to be published.

[3] R. Kleiss and H. Burkhardt, "BBBREM: Monte Carlo simulation of radiative Bhabha scattering in the very forward direction", *Comput. Phys. Commun.*, vol. 81, pp. 372–380, 1994. doi:10.1016/0010-4655(94)90085-X

[4] V. I. Telnov, "Restriction on the energy and luminosity of e^+e^- storage rings due to beamsstrahlung", *Phys. Rev. Lett.* vol. 110, p. 114801, 2013. doi:10.1103/PhysRevLett.110.114801

[5] H. Burkhardt, "Monte Carlo simulation of scattering of beam particles and thermal photons", CERN, Geneva, Switzerland, Rep. SL-Note-93-73-OP.

[6] P. M. Lewis *et al.*, "First measurements of beam backgrounds at SuperKEKB", *Nucl. Instrum. Methods Phys. Res. Sect. A,* vol. 914, pp. 69-144, 2019. doi:10.1016/j.nima.2018.05.071

ISBN: 978-3-95450-236-3 ISSN: 2673-7027 doi:10.18429/JACoW-eeFACT2022-TUZAT0202

FCC-ee MDI: TRAPPED MODES AND OTHER POWER LOSSES*

A. Novokhatski†, SLAC National Accelerator Laboratory, Menlo Park, CA, USA

Abstract

We discuss the beam power loss related to the heating of the vacuum beam pipe walls of the FCC-ee interaction region (IR). We analyse the excitation of trapped modes, which can accumulate electromagnetic energy and determine the locations of these modes. We study the unavoidable resistive-wall wake field, which is responsible for the direct beam pipe walls heating. We present the distribution of the heat load along the central part of IR. The results are very important for knowledge of the temperature distribution and the following cooling system design.

INTRODUCTION

It is planned that a future e+e– collider (FCC-ee) will have a very high energy, up to 375 in the center of mass and unprecedented luminosities [1]. To achieve high luminosity, currents of the electron and positron beams must be more than 1.2 A. High current beams will produce an additional heating of the beam pipe in both rings and in the interaction region. The heating of the beam pipe happens when a beam excites electromagnetic fields due to diffraction of the beam self-field from the inhomogeneous beam pipe. In a time, the diffracted fields are absorbed in the metal walls somewhere in the beam pipe. The beam loses its kinetic energy to restore its self-field when it is deaccelerated by the diffracted fields. The diffracted fields are usually called as wake fields. The FCC IR consists of an intersection of four beam pipes and present a very complicated inhomogeneity geometry. Both beams generate electromagnetic fields in IR. Depends upon the bunch spacing frequency, this may lead to a resonant excitation of a trapped mode located in some special places. There can be several trapped higher order modes (HOMs).

Another heating effect is an excitation and diffusion of the image current inside the metal beam pipe walls. This leads to a direct heating of the beam pipe. Naturally, the beam also loses energy as it is decelerated by the longitudinal electric component of the field generated by the image current. These fields are usually called as resistive-wall wake fields.

Previously, we optimized the geometry of the FCC IR beam pipe for a minimum geometrical impedance [2-4]. We use a numerical code CST [5] for 3D electromagnetic calculations. In these calculations we assume that the beam pipe materials have infinite electrical conductivity. Now the engineering design of the IR suggests what kind of materials will be used. So now, we include the additional beam losses due to interaction of the beam electromagnetic field with conductive materials of the beam pipe. Using the correspondent conductivity of the materials we calculate the heat load distribution along IR beam pipe.

* Work supported by US DoE, Contract No. DE-AC02-76SF00515
† novo@slac.stanford.edu

In the first section of this paper, we discuss what kind of electromagnetic fields are excited in IR. Then we present our concept of a low impedance IR beam pipe and show the last CAD model. Next we present results for geometrical wake potentials and an estimate beam energy loss. Then we discuss how we calculate the heat load distribution from the circulating beams and present results for wake potentials and trapped modes. Finally, we present the heat load distribution in IR. In the conclusion section we discuss the importance of the results for a colling system and future steps.

ELECTROMAGNETIC FIELDS IN IR

We can distinguish three types of the fields excited in the FCC IR by circulating beams. The first type is the electromagnetic field, which is exciting in IR in the form of propagating waves that can leave IR and then be absorbed somewhere in the rings. During the PEP-II SLAC B-Factory operation we watch these traveling waves propagating the distance more than 100 m long [6]. The second type is the field that is excited in some trapped locations of IR and be absorbed there. These fields are usually called higher order modes HOMs. There is one mode located near the pipe connection is an unavoidable mode [2]. Under resonant conditions the amplitude of the trapped mode field can be strongly magnified. The third type is an unavoidable resistive-wall wake field, which is responsible for directly heating of the metal walls. Excitation and absorption of these fields in IR may lead to additional detector background because heating effects and high frequency waves interference.

Important parameters, which characterize the excited field are a loss factor and an impedance. The loss factor tells how much energy a bunch of particle losses passing by some beam pipe element. This is equivalent to the total amount of energy of the excited fields. The loss factor is strongly depending upon the bunch length. Smaller bunches lose more energy. The impedance is a Fourier spectrum of a wake potential. The wake potential is an integral of the longitudinal electrical component of the excited fields along the bunch trajectory. The impedance shows possible trapped modes as resonate spikes in the frequency spectrum.

CONCEPT OF A LOW IMPEDANCE IR BEAM PIPE AND CAD MODEL

The main idea to decrease the wake field radiation or minimize the impedance of the chamber is naturally to use a very smooth transition from one pipe to a conjunction of two pipes. One of possibilities how to make it, is demonstrated in Fig. 1. Starting with a round pipe we make a smooth transition to a pipe with a cross section of a half of ellipse. Then we combine two half-ellipses in one full ellipse making one pipe from two pipes. It is important the

ISBN: 978-3-95450-236-3 ISSN: 2673-7027 doi:10.18429/JACoW-eeFACT2022-TUZAT0202

inner part at the conjunction location must be rounded. Finally, we make a smooth transition from a pipe with an elliptical cross section to a round pipe, which is the main central part of the interaction region. In the center of this pipe is the interaction point (IP), where electron and positron beams collide.

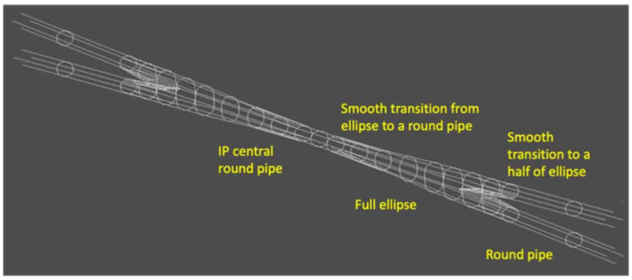

Figure 1: Smooth transitions in IR.

We use this approach to design the FCC IR beam pipe. The last geometry of the FCC IR beam pipe [3, 7] is shown in Fig. 2. Two symmetric beam pipes with radius of 15 mm are merged at 1.2 m from the IP. The central part has a 10 mm radius for ± 9 cm from the IP. There are two synchrotron radiation (SR) 7 mm masks [7] in incoming beam pipes at the distance of ±2.1 m from IP. The shape of the mask and dimensions are also shown in Fig. 2.

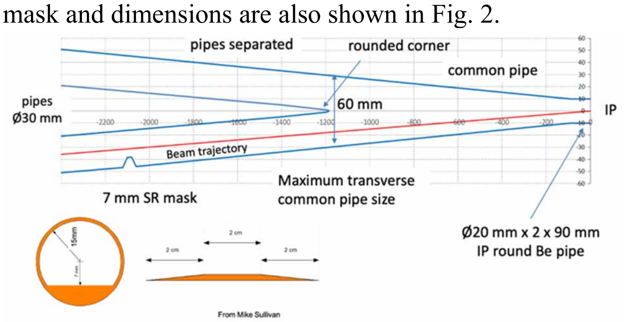

Figure 2: Last FCC IR geometry and SR mask shape.

This new geometry differs from the previous geometry described in FCC-ee CDR [1], mainly by the size of the central pipe. In previous geometry the radius of the central beam pipe was larger -15 mm. Decreasing the size of a central part gives a possibility for the FCC detector to make more precise tracking [8]. On the other as it will be shown later smaller size of a central pipe decreases the geometrical impedance and moves the unavoidable trapped mode to higher frequency, in this way making less the interaction of trapped mode with the beam.

Based on this geometry a special CAD model was developed for the wake field calculations. The difference with a real engineering CAD model is that the CAD model for the calculation does not contains small elements with dimensions less than 1 mm. The reason for this is a long length of the model: 8-10 m and a correspondent number of mesh points during calculations will reach several hundred million. The IR beam pipe CAD model designed by Luigi Pellegrino (INFN) is shown in Fig. 3. We can see smooth transitions, rounded corners where pipes merge into a single pipe and SR masks. A line with blue and orange balls shows a single beam trajectory. Presented in Fig. 3 a special view of the beam pipe does not show real dimensions. A more realistic view of the shape of a SR mask is shown on Fig. 4.

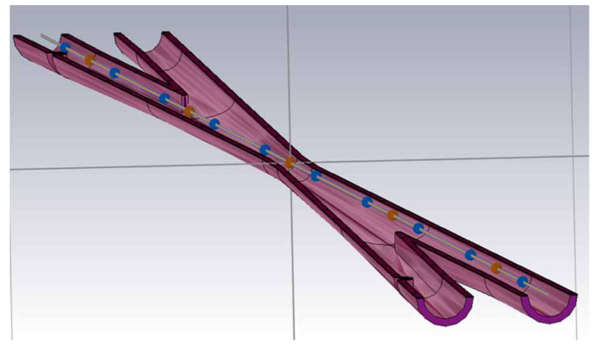

Figure 3: CAD model for the wake field calculations.

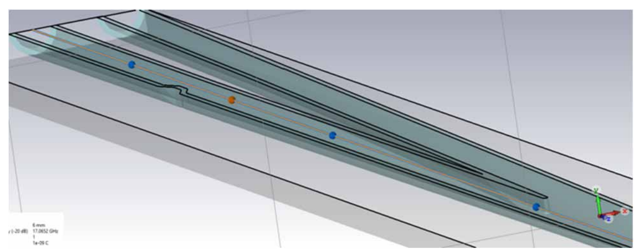

Figure 4: A more realistic view of the shape of the SR mask.

WAKE POTENTIALS AND TRAPPED MODES

Using this CAD model, we did wake field calculations giving all wall materials an infinite conductivity. This approach is usually used for calculation of the so called "geometrical" wake potentials. The result for the wake potential of a 12-mm bunch is shown in Fig. 5 by a red line. The shape of a bunch charge distribution is also shown there by a blue line.

Wake potential plot shows that addionally to the bunch looses (the region in the bunch region) we have two beating oscilations with a smaller amplidude. The distance between maximums is aproximatelly 48.1 mm that corresponds to the the frequency of 6.2 GHz. We may conclude that there are two trapped modes with close frequencies. Furier spectrum (Fig. 6) of the wake potential confirms this statement. Later, we found out that the CAD model was not exacly symmetrical relative to IP. That was the reason why the trapped modes at different sides of IP have different frequencies.

We did a special eigen mode calculation (that is also possible to do using the CST code) for this geometry to find a trapped mode field distribution and its frequency. One of the results, the electric force line distribution is shown in Fig. 7. The trapped mode is concentrated near the

ISBN: 978-3-95450-236-3 ISSN: 2673-7027 doi:10.18429/JACoW-eeFACT2022-TUZAT0202

conjunction of two pipes, in a region with maximum transverse size. This mode has a longitudinal electric component in the common pipe. Due to this component the beam with a longitudinal velocity can easily excite this mode. We call this mode by an unavoidable trapped mode in IR [2].

There are several other trapped modes due to SR masks. These modes are distributed alone large distance (Fig. 8) and ,in average, do not interact with a beam

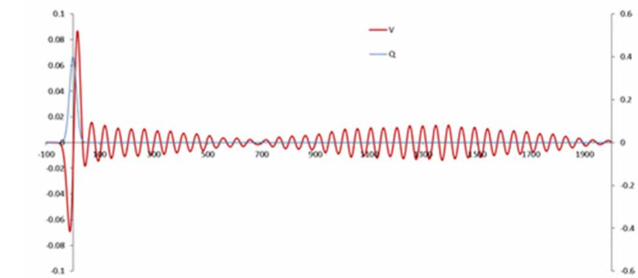

Figure 5: Wake potential of a 12-mm bunch passing the 10-m long beam pipe of the FCC IR.

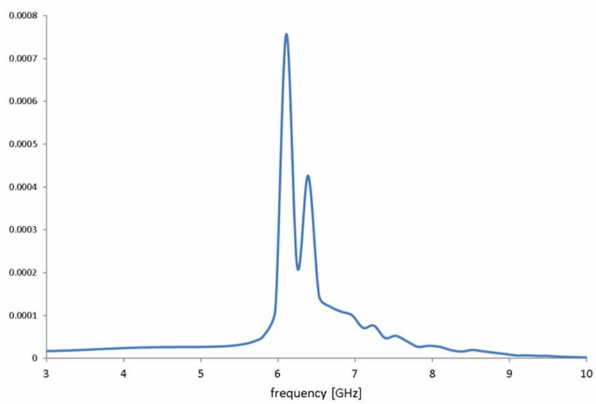

Figure 6: Spectrum of the wake potential

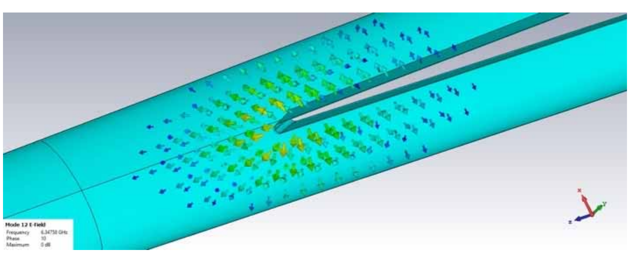

Figure 7: Unavoidable trapped mode. Electric force lines.

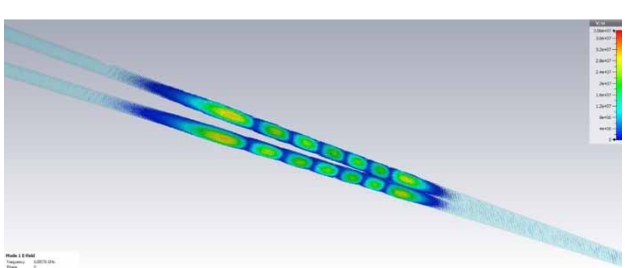

Figure 8: Another trapped mode.

The double effect of smoothing the geometry and a smaller central pipe reduces the local heating power by a factor ten with respect to the CDR design. Due to a smaller central part the unavoidable trapped mode was shifted to a higher frequency, that considerably decrease the interaction with a beam. For a bunch length of 12 mm, the nominal value with beams in collision at the Z-pole energy, the loss factor is 0.0035 V/pC per beam and the most part of the radiated power will travel out away from the IP.

However, the decrease of the the central beam pipe leads to more image current losses due to the conductivity of the metal pipe walls. To remove this heat, we will use a liquid coolant that will flow within the room temperature solutions. We plan to use paraffin in the central chamber and water outside. We plan to use an allow AlBeMet, like a beryllium as a light material for the central part and in the transition up to Lumi Monitor. Additionally, a few microns of gold coating will reduce heat load and help to protect the detector from SR photons.

The first estimate of heat load in the central gives approximately 150 W/m for a 12 mm bunch. However, to calculate more realistic number we developed a new CAD mode.

THE METHOD OF CALCULATIONS OF HEAT LOAD DISTRIBUTION

We use specially designed CAD model as an input for the wake filed calculations using the CST code. This CAD model consists of different elements, which have different materials. The CAD model, which was developed by Francesco Fransesi (INFN) is shown in Fig. 9. The model contains five parts. The central part is made from AlBeMet but coated with a gold. The allow AlBeMet has a conductivity of $2.842*10^{-7}$ S/m, a little bit higher than conductivity of a pure beryllium. The gold has conductivity of $4.561*10^{-7}$ S/m. Two transition parts are also made from AlBeMet. And other two parts are made from copper, which conductivity is $5.8*10^{-7}$ S/m

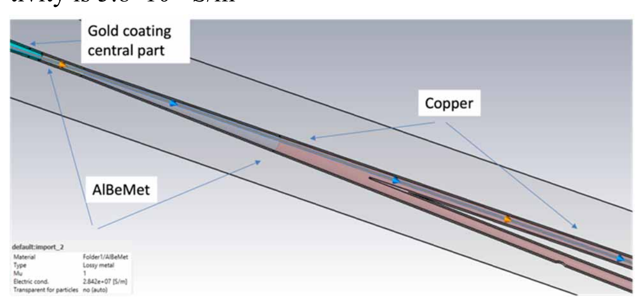

Figure 9: CAD model with different materials.

Using this model, we calculate the local heat load in following way. At first, we do wake field calculations, assuming that all materials have infinite conductivity. Then we do wake filed calculations, still assuming that all materials have infinite conductivity, except the interested part, which is given the correspondent material. And finally, we take the difference, which shows how much power is lost in this part. Naturally, it needs a lot of calculations, but the result

ISBN: 978-3-95450-236-3 ISSN: 2673-7027 doi:10.18429/JACoW-eeFACT2022-TUZAT0202

is important for the cooling system design. After calculating the wake potentials, we calculate the loss factor and the heat load power using the following formula:

$$P = k\tau I^2$$

Power = Loss factor * bunch spacing * Current**2.

The required parameters are determined by the FCC-ee beam parameters, which are presented in Table 1. This table is based on the beam optics parameters, presented at the FCC Week in Paris in 2022 [8].

Table 1: Important Beam Parameters

Parameter	**Value**
beam energy [GeV]	45
circumfarences [km]	91.2
beam current [mA]	1280
bunch intensity $[10^{11}]$	2.43
number bunches/beam	1000
rms bunch length with SR / BS [mm]	4.38 / 14.5
bunch spacing [ns]	32

HEAT LOAD DISTRIBUTION IN IR

In Fig. 10 we present the distribution of the heat load along the central part of IR (+- 4.5 m). These results are very important for the temperature distribution and correspondent cooling system design.

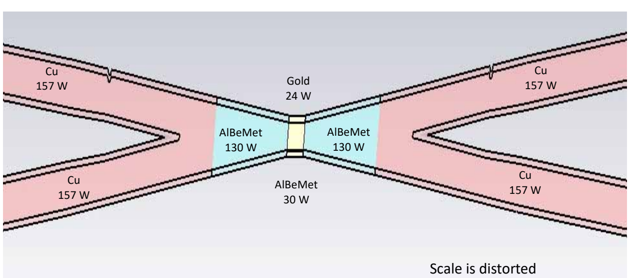

Figure 10: Heat load distribution in the FCC IR.

CONCLUSION

Calculations showed that in the IR region (±4 m) approximately 1 kW power is dissipated in the pipe wall. Necessary cooling is needed. No sing of the strong trapped modes because of the special shape of the IR chamber. However almost 3 kW power, which is generated in IR will go out in 4 pipes and will be dissipated somewhere in the rings. For the next steps it is very important to include all necessary details of the real IR chamber design in the CAD model.

ACKNOWLEDGEMENTS

Without a professionally designed CAD files I could not do accurate wake field calculations. Very appreciate the work of Miguel Gil Costa (CERN), Luigi Pellegrino, Francesco Fransesi and Stefano Lauciani (INFN). I would like to thank Frank Zimmermann, and Michael Benedikt (CERN) for their great support of this work. I would like also to thank Timothy Maxwell and John Seeman (SLAC National Accelerator Laboratory) for the real support of this activity from the SLAC side. Many thanks to Oide Katsunobu (CERN), Michael Sullivan (SLAC), Manuela Boscolo (INFN) and the entire FCC MDI team for many useful discussions.

REFERENCES

[1] A. Abada *et al.*, [FCC], “FCC-ee: The Lepton Collider: Future Circular Collider Conceptual Design Report Volume 2”, *Euro. Phys. J. Spec. Top.*, vol. 228, no. 2, pp. 261-623, 2019. doi:10.1140/epjst/e2019-9000454

[2] A. Novokhatski, M. Sullivan, E. Belli, M. G. Costa, and R. Kersevan, “Unavoidable trapped mode in the interaction region of colliding beams”, *Phys. Rev. Accel. Beams*, vol. 20, p. 111005, 2017. doi:10.1103/PhysRevAccelBeams.20. 111005

[3] A. Novokhatski, “A new low impedance IR FCC ee beam chamber”, presented at the 4th FCC Physics and Experiments Workshop - FCC November Week 2020, Nov. 2020, https://indico.cern.ch/event/932973/ contributions/4075893/.

[4] M. Boscolo *et al.*, “Challenges for the interaction region design of the Future Circular Collider FCC-ee”, in *Proc. IPAC'21*, Campinas, Brazil, May 2021, pp. 2668-2671. doi:10.18429/JACoW-IPAC2021-WEPAB029

[5] User Guide, https://www.cst.com

[6] A. Novokhatski, J. Seeman, M. Sullivan, “Radiolocation of a HOM Source in the PEP-II Rings”, in *Proc. EPAC’08,* Genoa, Italy, 2008, paper TUPP053, p. 1664.

[7] M. K. Sullivan, “SR backgrounds including the effect for a 1 cm Radius Beam Pipe”, presented at the 4th FCC Physics and Experiments Workshop - FCC November Week 2020, Nov. 2020, https://indico.cern.ch/event/932973/

[8] Michael Benedikt, “FCC Feasibility Study Overview- presented at FCC Week 2022, Sorbonne Université, Paris, France, May-Jun. 2022, https://indico.cern.ch/ event/1064327/contributions/4891236

ISBN: 978-3-95450-236-3 ISSN: 2673-7027 doi:10.18429/JACoW-eeFACT2022-TUZAT0203

MACHINE INDUCED BACKGROUNDS IN THE FCC-ee MDI REGION AND BEAMSTRAHLUNG RADIATION

A. Ciarma*, E. Perez, G. Ganis, CERN, Geneve, Switzerland
M. Boscolo, INFN-LNF, Frascati, Italy

Abstract

The design of the Machine Detector Interface area (MDI) for the Future Circular Collider (FCC) is particularly challenging. Initial studies published in 2018 in the FCC Concept Design Report (CDR) are now being enhanced in the context of the ongoing FCC Feasibility Study. With respect to the CDR, a new design for the beam-pipe central chamber of the e+e- collider (FCC-ee), featuring a smaller radius and shorter length, is being considered. The new design allows for an inner layer of the Vertex Detector Barrel to be placed closer to the interaction point. The effect of the background induced occupancy due to Incoherent Pairs Creation (IPC), beam losses in the MDI area and Synchrotron Radiation have been investigated for the CLD detector, one of the detector concepts considered for FCC-ee. The characterisation of the intense Beamstrahlung radiation produced at FCC-ee is also presented.

INTRODUCTION

Machine induced background studies were performed for the FCC-ee Conceptual Design Report (CDR) [1], including the beam losses in the Interaction Region (IR), pairs production and the development of Synchrotron Radiation (SR) masks and shieldings. After the CDR, the design of the beam pipe central chamber has changed to a reduced radius of R=10 mm and length of L=18 cm (originally R=15 mm and length of L=25 cm), allowing to have the inner layer of the Vertex Detector Barrel closer to the Interacion Point (IP).

The Vertex Detector (VXD) geometry description of the CLIC-Like Detector concept (CLD) [3] has been modified in order to fit the new FCC-ee MDI region and to study the effects of several beam induced backgrounds. In particular, the first and the second layers of the barrel have been reduced both in radius to keep the same distance from the beam pipe, and in length in order to to preserve the angular acceptance of the original design. Also, the number of sectors in the innermost layer has been reduced from 16 to 12 because the staves' width is constrained by the manufacturing process. A sketch of the new version of the CLD VXD barrel is shown in Fig. 1. To the same purpose, a re-design of the IDEA [4] Vertex Detector is currently work in progress.

In addition to the design of the 10 mm radius central part of the beam pipe and consequent modifications to the detectors, also the design of the lattice has progressed since the CDR. The current instance of the collider has 4 IPs and different beam parameters. The parameters considered for the studies presented in this work are reported in Table 1.

* Corresponding Author, andrea.ciarma@cern.ch

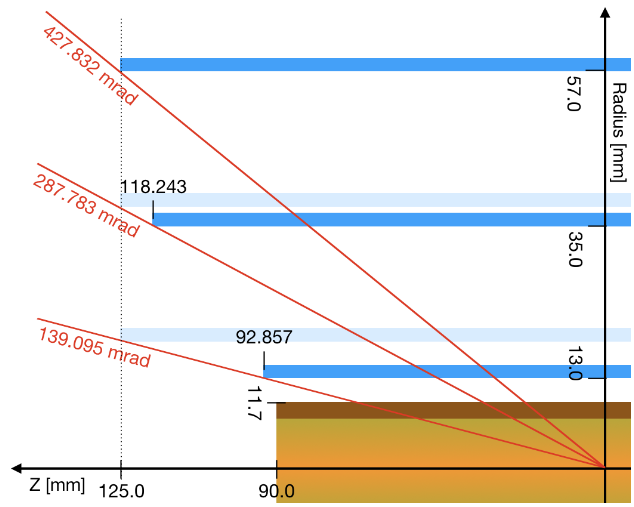

Figure 1: Sketch of the new design of the CLD VXD barrel. The blue shapes represent the dimensions of the layers in the new version, the light blue shapes refer to the CDR version. The gold shape is the beam pipe central chamber.

These modifications, together with the migration to the turnkey software Key4HEP [2], make it is necessary to repeat and extend the studies performed for the CDR. In this manuscript I present the status of the studies on the beam induced backgrounds due to the Incoherent Pairs Creation (IPC), beam losses due to failure scenarios, and synchrotron radiation on the CLD vertex detector and tracker. I also give the characterization of the beamstrahlung radiation produced at the IP at the four working points of FCC-ee.

INCOHERENT PAIRS CREATION

Secondary e^+e^- pairs can be produced via the interaction of the beamstrahlung photons with real or virtual photons

Table 1: FCC-ee beam parameters for the 4 IPs lattice

		Z	WW	ZH	$t\bar{t}$
GeV	E	45.6	80.0	120.0	182.5
nm rad	ϵ_x	71	2.16	64	1.49
pm rad	ϵ_y	1.42	4.32	1.29	2.98
mm	β_x/β_y	100/0.8	200/1	300/1	1000/1.6
µm	σ_x	8.426	20.78	13.86	38.60
nm	σ_y	33.70	65.73	35.92	69.05
mm	σ_z	15.4	8.01	6.0	2.8
10^{11}	N_e	2.43	2.91	2.04	2.37
1	N_{bunch}	10000	880	248	40

65th ICFA Adv. Beam Dyn. Workshop High Luminosity Circular e$^+$e$^-$ Colliders eeFACT2022, Frascati, Italy JACoW Publishing
ISBN: 978-3-95450-236-3 ISSN: 2673-7027 doi:10.18429/JACoW-eeFACT2022-TUZAT0203

emitted by each particle of the beams during the bunch crossing. Some of the so produced particles will pass through the detector generating background. The occupancy O induced by a bunch crossing in a subdetector is defined as:

$$O = h \cdot A_{sensor} \cdot S_{cluster} \cdot S_f$$

where h is the hit density per bunch crossing in each subdetector, A_{sensor} is the surface area of the sensors, $S_{cluster}$ is the cluster size, and S_f is a safety factor. The VXD uses silicon pixels of A_{sensor} = 25 µm × 25 µm, while the tracker (TRK) uses silicon strips of 1 mm × 0.05 mm. The cluster sizes considered for the VXD and the TRK are $S_{cluster}$=5 and $S_{cluster}$=2.5 respectively. For this study, a safety factor of S_f = 3 has been considered.

The generator used to produce the primaries for this study is GuineaPig++ [6], and the particles have been tracked in the CLD design using Key4HEP. Table 2 shows the number of pairs produced per bunch crossing and the maximum occupancy measured in each detector.

Table 2: Number of pairs produced per bunch crossing (BX) at the four working points, and maximum occupancy measured in the barrel and endcaps of the vertex detector and tracker (respectively VXDB, VXDE, TRKB, TRKE).

		Z	**WW**	**ZH**	**$t\bar{t}$**
1	Pairs/BX	1300	1800	2700	3300
10^{-6}	O_{max}(VXDB)	70	280	410	1150
10^{-6}	O_{max}(VXDE)	23	95	140	220
10^{-6}	O_{max}(TRKB)	9	20	38	40
10^{-6}	O_{max}(TRKE)	110	150	230	290

The induced occupancy increases with the beams energy. This is due to two factors: the pair production cross-section is enhanced [6], and due to the kinematics of the process more particles will enter the detector acceptance region as shown in Fig. 2.

The occupancies reported in Table 2 are all well below the percent, but depending on the electronics readout time the sensors may integrate signal over several bunch crossing. The estimate for the occupancy pile-up considering a bunch spacing Δt and readout window W_r can be obtained according to:

$$O(W_r) = O(BX)\frac{W_r}{\Delta t}$$

As shown in Table 3, even considering a readout window of W_r=10 µs - which is a conservative value - the maximum occupancy remains below the percent almost everywhere, except for the VXD barrel and TRK endcaps at the Z working point where it reaches values up to 2∼3%. While the pileup of the detectors has not been defined yet, it will be important to overlay this background to physics events in order to verify the reconstruction efficiency as a function of the readout window.

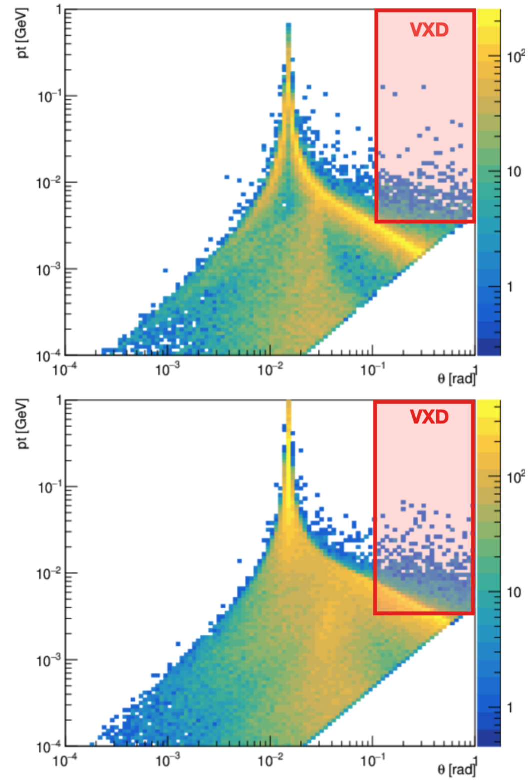

Figure 2: Production kinematics of the IPC at the Z (top) and $t\bar{t}$ (bottom) working points. The red area indicates the acceptance of the VXDB first layer.

BEAM LOSSES DUE TO FAILURE SCENARIOS

Several effects can lead to an increase of the beam emittance and consequent losses due to these particles impacting on the main collimator. This can be defined as a failure scenario. The deflected particles travel through the machine and a fraction will hit the beam pipe in the MDI region. The considered scenario is a drop of the beam lifetime down to 5 minutes due to halo losses on the primary collimator (located in point-F of the FCC-ee ring). The halo particles of a 182.5 GeV beam scattered by the primary collimator have been tracked for 700 turns in the latest lattice using X-Track [7], and the particles hitting the beam pipe in the ±7 m from the Interaction Point A have been tracked in the

Table 3: Average bunch spacing at the four working points, and maximum occupancy in the VXD and TRK considering a readout window (RW) of 1 µs and 10 µs.

		Z	**WW**	**ZH**	**$t\bar{t}$**
ns	average bunch spacing	30	345	1225	7598
10^{-3}	O_{max}(VXD), RW=1 µs	2.33	0.81	0.05	0.18
10^{-3}	O_{max}(VXD), RW=10 µs	23.3	8.12	3.34	1.51
10^{-3}	O_{max}(TRK), RW=1 µs	3.66	0.43	0.12	0.13
10^{-3}	O_{max}(TRK), RW=10 µs	36.6	4.35	1.88	0.38

ISBN: 978-3-95450-236-3 ISSN: 2673-7027 doi:10.18429/JACoW-eeFACT2022-TUZAT0203

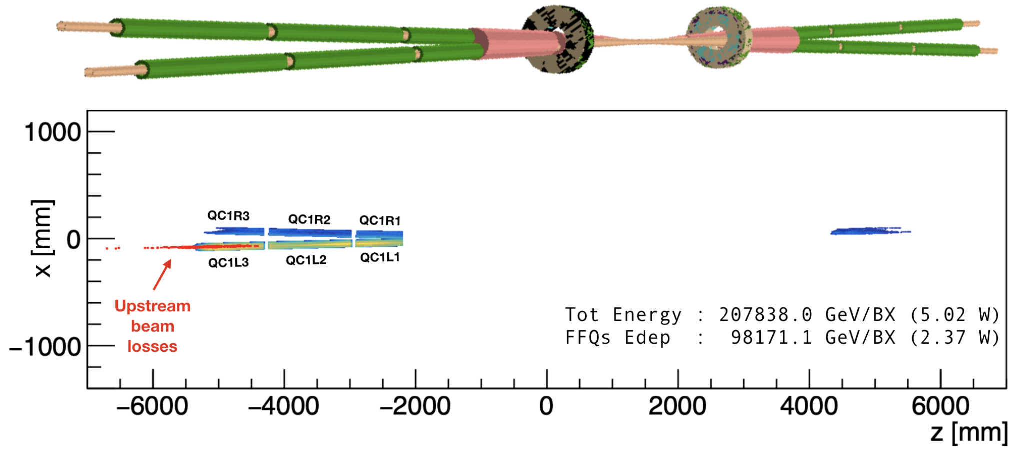

Figure 3: Top: FCCee MDI region model used in Key4HEP simulations, QC1 elements in green. Bottom: power deposited on the FFQs due to the considered failure scenario at IPA for $t\bar{t}$ energy.

CLD model of Key4HEP. The estimated loss rate in the IPA MDI area for this specific case is 1.5×10^8 Hz.

The primary beam losses are localised at 4~5 m from the IP, in correspondence of the magnetic elements of the innermost Final Focusing Quadrupole (FFQ) QC1. In order to study the deposited power on these magnets, simple cylindrical models composed of the equivalent material of the current design [8] have been introduced in the Key4HEP simulation as shown in the top of Fig. 3. The plot in the bottom part of Fig. 3 shows how the energy deposition in the FFQs due to the beam losses is mostly localised in the upstream elements (the closest to the losses) and accounts for about 2.5 W, which is about half of the total power carried by the losses. While the performance of the cryogenic system are yet to be defined, preliminary calculations show that this value should be below the quench limit of the superconductive quadrupoles. Dedicated studies on the power density deposition are currently in progress.

In terms of background, the induced occupancy in the CLD vertex detector and tracker is shown in Fig 4. The acronyms in the legends refer to: Vertex Detector barrel and endcaps (VXDB, VXDE), Inner and Outer Tracker barrel and endcaps (ITB, ITE, OTB, OTE). The particle from the beam hitting the beam pipe will produce a shower of secondaries, causing the occupancy to rise up to several percent points in particular in the IT. Please note that these plots refer to the occupancy due to a single beam, as it can be seen by the asymmetric distribution along the z-axis in the IT occupancy. Since the background level is higher than the rule-of-thumb value of 1%, further studies are needed to understand the impact on tracking efficiency and devise appropriate mitigation strategies.

SYNCHROTRON RADIATION MASK AND SHIELDINGS

The Synchrotron radiation produced by the last upstream dipole and by the final focusing quadrupoles can be a major source of background. In order to protect the detectors and mitigate the backgrounds, the use of a set of Tantalum masks internal to the beam pipe placed at the exit of the final focus quadrupole QC1 have been proposed in the CDR [1]. For the feasibility study the height of the mask has been increased from 5 mm to 8 mm in order to account for the reduced central chamber radius. Also, Tungsten shieldings have been designed to further minimise the number of photons which may scatter off the tip of the mask and produce showers in the detector.

A preliminary study has started to assess the efficiency of both masks and shieldings with the new lattice and IR. The shieldings in particular in their current design weight 180 kg per arm which should be supported by the beam pipe itself, so the possibility to reduce it while keeping sufficient protection for the detectors should be explored. Synchrotron radiation photons produced by the last downstream dipole at the $t\bar{t}$ working point have been generated using the Geant4 based toolkit BDSim [9], and have been tracked in the CLD model using Key4HEP. The energy distribution of the photons just before the Tantalum mask is shown in the left of Fig. 5. Due to the critical energy of O(100 keV) the interaction of these photons with the Tantalum mask is dominated by photoelectric effect, as shown in the right of Fig. 5.

From preliminary tracking, most of the secondaries produced by the photons impacting on the mask are efficiently absorbed by the mask itself. Anyway special attention should be given to the photons which interact with the very tip of the mask. The photoelectrons emitted near the surface of the mask can escape and reach the detector causing background. As a first approach, a monochromatic pointlike 1MeV photon beam has been simulated impinging 50 µm from the edge of the mask, and tracking in the CLD detector showed a large number of hits in particular in the tracker endcaps.

More detailed studies are currently in progress in order to understand better the impact of this potential source of background, and the effect of the Tungsten shieldings.

ISBN: 978-3-95450-236-3 ISSN: 2673-7027 doi:10.18429/JACoW-eeFACT2022-TUZAT0203

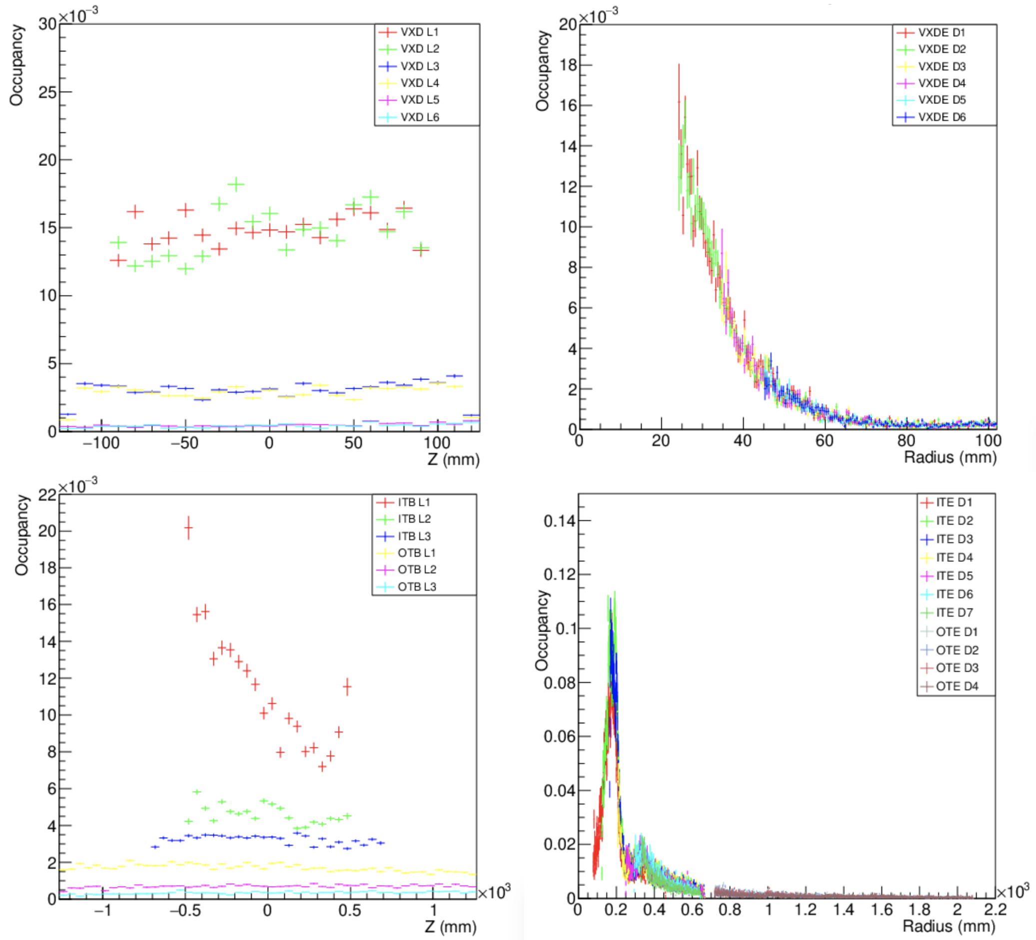

Figure 4: Occupancy induced by the beam losses in the VXD and IT/OT barrel layers (L) and endcap disks (D).

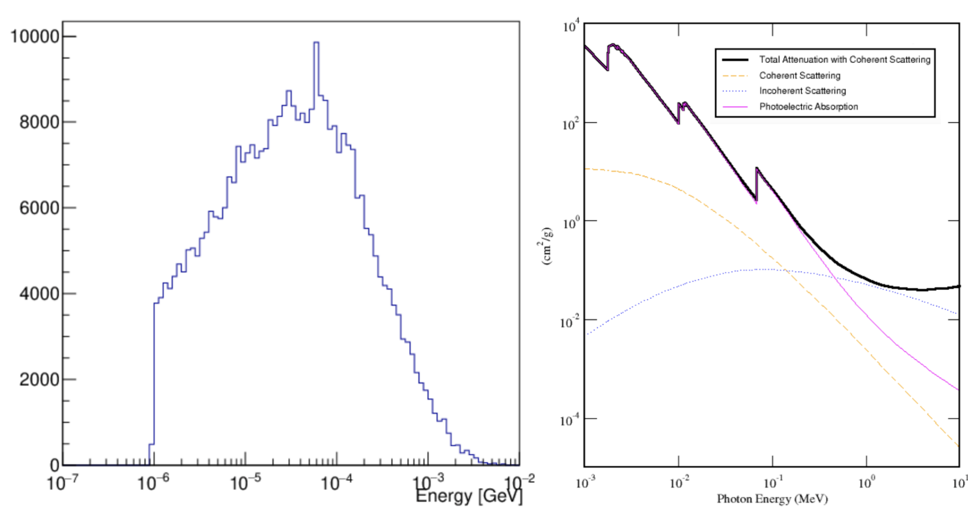

Figure 5: Left: energy spectrum of the SR photons just before the tantalum mask. Right: cross section for the interaction of photons with Tantalum [10].

BEAMSTRAHLUNG RADIATION CHARACTERIZATION

During bunch crossing each particle experiences the field generated by the charges of the opposing bunch and can be deflected, therefore emitting radiation in a similar way to Synchrotron Radiation. This process is called Beamstrahlung. The radiation is characterised by the dimensionless beamstrahlung parameter Υ [11], defined for gaussian beams as:

ISBN: 978-3-95450-236-3 ISSN: 2673-7027 doi:10.18429/JACoW-eeFACT2022-TUZAT0203

$$\Upsilon \sim \frac{5}{6} \frac{r_e^2 \gamma N_e}{\alpha \sigma_z (\sigma_x + \sigma_y)}$$

The beamstrahlung parameter depends on the beams energy E and population N_e, and on the bunch shape at collision σ_x, σ_y and σ_z. Due to the very small bunch size and high population, at FCC-ee the main driver for the bunch length and energy spread is beamstrahlung. At FCCee this parameter is in the region $\Upsilon << 1$, where the average number of photons emitted per particle n_γ, and their average energy $< E_\gamma >$ can be evaluated according to:

$$< E_\gamma > \sim E \times 0.462 \Upsilon$$

$$n_\gamma \sim 2.54 \left[\frac{\alpha^2 \sigma_z}{r_e \gamma} \Upsilon \right] \frac{1}{[1 + \Upsilon^{2/3}]^{1/2}}$$

The beamstrahlung radiation produced at FCC-ee has been simulated using the generator GuineaPig++. Due to the high bunch population and small beam size the radiation produced by each beam at the IP is extremely intense, up to several hundreds of kilowatts, as shown in Fig. 6.

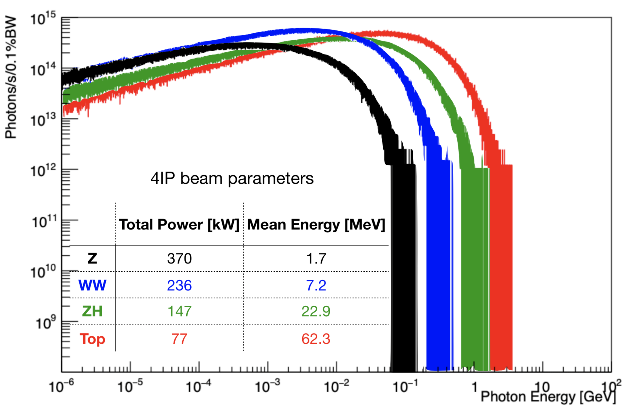

Figure 6: Energy spectrum of the beamstrahlung radiation produced at FCC-ee by each beam during bunch crossing for the four working points.

The photons are emitted collinear to the beam in a very narrow cone proportional to the inverse of their energy. As shown in Table 4, the dominant contribution to the photon beam divergence $\sigma^\gamma_{px,py}$ is the divergence of the lepton beam which produced it $\sigma^e_{px,py}$, resulting in values in the order of O(50~100).

The photons will travel from the IP and hit the beam pipe at the first bending magnet. Tracking the photons in the GDML model of the downstream beam pipe show that the hits will be centred about 50 m from the IP, as shown in Fig 7 for the Z working point (similar scenarios apply for the other working points).

Due to the very high power carried by the radiation O(100 kW) it is necessary to have a beamstrahlung photon beam dump for each downstream side of each IP. The design of a dedicated photon extraction line leading to the dump needs to fulfil several constraints.

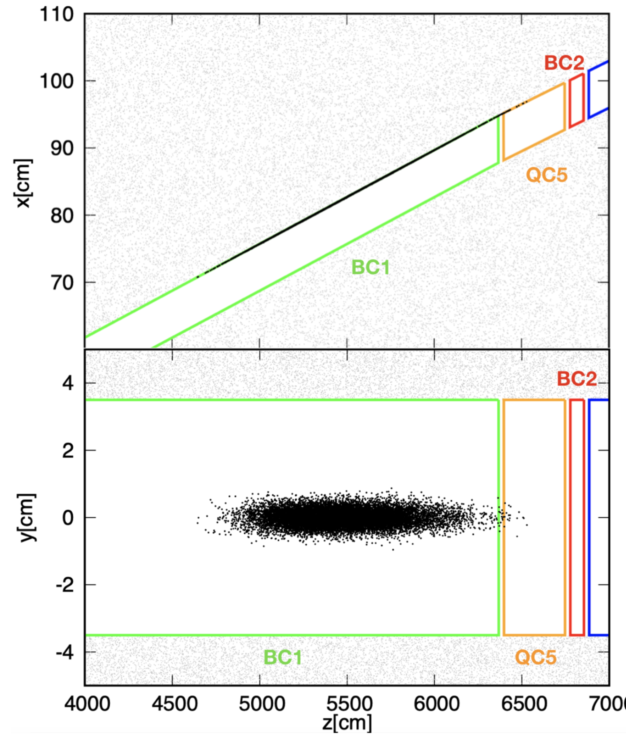

Figure 7: Location of the beamstrahlung photons hits on the beam pipe, for the Z working point.

First of all, while the transverse spot size of the photons at 50 m from the IP is well contained in a few cm^2 (see Table 4), because of the very low impinging angle the shadow of photons on the beam pipe wall is several meters long. Therefore the photon extraction window should be sufficiently large, as shown in the top of Fig. 8.

Also, in order to protect the beam pipe from secondary particles which could escape the beam dump, it is necessary to extend the extraction line to make space for sufficient shielding material. The bottom of Fig. 8 shows the separation between the lepton beam line and the beamstrahlung photon beam as a function of the distance from the IP. To obtain a separation of 1 m the beam dump should be placed at about 250 m from the IP. The integration of such line with the current design of the cavern (also with the possibility to have a dedicated tunnel) is currently under study.

Table 4: Divergence at the IP of the beamstrahlung radiation and the electron beam, photon spot size 50 m from the IP.

		Z	WW	ZH	$t\bar{t}$
σ^γ_{px}	[μrad]	91.8	110.0	51.7	44.6
σ^γ_{py}	[μrad]	49.2	73.0	41.3	50.3
σ^e_{px}	[μrad]	84.3	103.4	46.2	38.6
σ^e_{py}	[μrad]	42.1	65.7	35.9	43.2
σ^γ_x @50 m	[mm]	4.59	5.50	2.58	2.23
σ^γ_y @50 m	[mm]	2.46	3.65	2.06	2.51

ISBN: 978-3-95450-236-3 ISSN: 2673-7027 doi:10.18429/JACoW-eeFACT2022-TUZAT0203

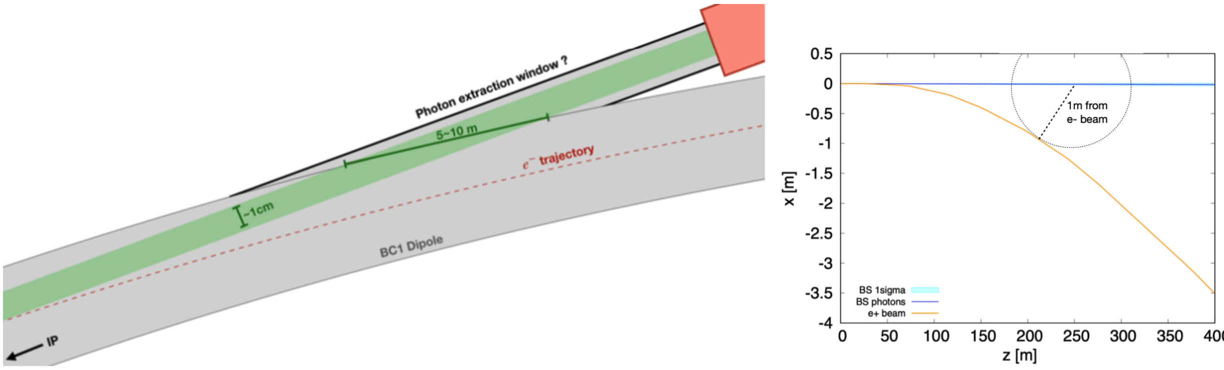

Figure 8: Left: sketch of the dedicated photon extraction line (not to scale). Right: separation between the beamstrahlung photons and the lepton beam.

CONCLUSIONS AND NEXT STEPS

The status of the beam induced background studies at FCC-ee, and the characterization of the beamstrahlung radiation produced at the IPs have been presented.

The occupancy in the CLD vertex detector due to the Incoherent Pairs Creation is below the 1% for all working points, also assuming conservative values for the sensors readout time.

The occupancy induced by a reduction of the beam lifetime down to 5 minutes at the $t\bar{t}$ energy can rise up to 10%. Further studies will cover the other working points, as well as different failure scenarios.

Preliminary studies on the Synchrotron Radiation induced background started. The absorption efficiency of the Tantalum mask on the radiation produced by the last upstream dipole at the $t\bar{t}$ working point showed that while most of the radiation is absorbed, the secondary electrons emitted near the tip of the mask can escape and generate background in the detector. Dedicated studies are currently going on to focus on this potential source of background and on the effect of the Tungsten shieldings.

The beamstrahlung radiation carries up to several hundreds of kilowatts, and hits the beam pipe at the first downstream dipole, an about 50 m from the IP. A dedicated photon extraction line and beam dump must be designed to deal with the extremely high power. The possibility to instrument the beam dump in order to measure properties of the colliding beams is also under investigation.

ACKNOWLEDGEMENTS

The authors want to akcnowledge Andrey Abramov and Kevin André for producing the primaries used respectively for the beam losses and Synchrotron Radiation studies.

REFERENCES

[1] A. Abada *et al.*, "FCC-ee: The Lepton Collider", *Eur. Phys. J. Spec. Topics*, vol. 228, no. 2, pp. 261–623, 2019. doi:10.1140/epjst/e2019-900045-4

[2] G. Ganis, C. Helsen, and V. Völkl, "Key4hep, a framework for future HEP experiments and its use in FCC", *arXiv:2111.09874*. doi:10.48550/arXiv.2111.09874

[3] N. Bacchetta *et al.*, "CLD – A Detector Concept for the FCC-ee", *arXiv:1911.12230*. doi:10.48550/arXiv.1911.12230

[4] M. Antonello, "IDEA: A detector concept for future leptonic colliders", *Nuovo Cimento C*, vol. 43, p. 27, 2020. doi:10.1393/ncc/i2020-20027-2

[5] C. Rimbault, P. Bambade, K. Mönig, and D. Schulte, "Incoherent pair generation in a beam-beam interaction simulation", *Phys. Rev. Spec. Top. Accel Beams*, vol. 9, p. 034402. doi:10.1103/PhysRevSTAB.9.034402

[6] D. Schulte, Ph.D. thesis, University of Hamburg, *Report No. TESLA-97-08*, 1996.

[7] Online Available: https://xsuite.readthedocs.io/en/latest/

[8] M. Koratzinos, private communications.

[9] L. J. Nevay *et al.*, "BDSIM: An accelerator tracking code with particle–matter interactions", *Comput. Phys. Commun.*, vol. 252, p. 107200, 2020. doi:10.1016/j.cpc.2020.107200

[10] M. J. Berger *et al.*, "XCOM: Photon Cross Section Database (version 1.5)". Online Available: http://physics.nist.gov/xcom. National Institute of Standards and Technology, Gaithersburg, MD., 2010. doi:10.18434/T48G6X

[11] K. Yokoya, P. Chen, "Beam-Beam Phenomena in Linear Colliders", *Lect. Notes Phys.*, vol. 400, pp. 415-445, 1996 (and online 2005). doi:10.1007/3-540-55250-2_37

ISBN: 978-3-95450-236-3 ISSN: 2673-7027 doi:10.18429/JACoW-eeFACT2022-TUZAT0205

FAST LUMINOSITY MONITOR FOR FCC-ee BASED ON THE LEP EXPERIENCE

A. Di Domenico*, Sapienza University and INFN Rome, Rome, Italy

Abstract

The measurement of luminosity and beam divergence performed by the LEP-5 experiment at CERN based on the detection of photons from the single breamsstrahlung process $e^+e^- \to e^+e^-\gamma$ at the LEP interaction point 1 is briefly reviewed. A possible implementation of the same methodology for a very fast luminosity monitor at FCC-ee is preliminarily discussed.

INTRODUCTION

The measurement of luminosity at colliders is essential in view of two different objectives: (i) for cross section measurements, where an accurate knowledge of the integrated luminosity is required, and (ii) for machine performance optimization and operation, where a quick feedback from a fast luminosity monitor is desirable.

The luminosity at electron-positron colliders is commonly measured and monitored by detecting the QED Bhabha scattering (BS) process $e^+e^- \to e^+e^-$. An intense R&D program is on-going for the FCC-ee collider project to reach the ambitious goal of a precision of 10^{-4} on the absolute luminosity measurement around the Z pole by detecting BS events at very small angles [1]. It is worth reminding that at the Large Electron Positron collider (LEP), the second-generation of Bhabha luminosity monitor achieved on the absolute luminosity an experimental precision of 3.4×10^{-4} [2].

Before LEP, the idea to measure the luminosity using the QED process $e^+e^- \to e^+e^-\gamma$, i.e. the single bremsstrahlung (SB), also called radiative Bhabha scattering, was first exploited at ADONE in Frascati in the '70 [3], and then at VEPP in Novosibirsk [4]. The main feature of this process is that its cross-section slightly increases with energy, $\sigma_{SB} \sim \ln s$, unlike for the BS, whose cross-section decreases as $1/s$. Moreover the BS cross-section depends on the $e^\pm$ scattering angle θ as θ^{-4}, while almost all SB photons are extremely collimated with an angular distribution in a narrow cone in the forward direction $\theta_\gamma \simeq m_e/E$. This makes SB especially convenient at high energy machines as a faster *monitor process* than BS for the easily reachable high rates, as for instance at LEP and in all four beam energy configurations foreseen at FCC-ee, namely Z, WW, HZ and $t\bar{t}$, as shown in Table 1 (for the complete set of parameters used for the present study see Refs. [5, 6]).

In the following, the measurement of luminosity and beam divergence performed by the LEP-5 experiment at the LEP interaction point 1 is briefly reviewed [7, 8]. Finally, a possible implementation of this methodology for a fast luminosity monitor at FCC-ee is considered and its feasibility briefly discussed.

* antonio.didomenico@roma1.infn.it

Table 1: Expected BS rate (for $10 < \theta < 20$ mrad) and SB rate (for $E_\gamma > 0.5$ GeV) in the four beam energy configurations of FCC-ee

	Beam energy (GeV)	BS rate (Hz)	SB rate (Hz)
Z	45	$2\cdot10^6$	$6\cdot10^{11}$
WW	80	$5\cdot10^4$	$6\cdot10^{10}$
HZ	120	$8\cdot10^3$	$2\cdot10^{10}$
$t\bar{t}$	182.5	$6\cdot10^2$	$9\cdot10^9$

THE LEP-5 EXPERIMENT

At LEP with a luminosity $L \simeq 10^{31}$ cm^{-2} s^{-1} the expected SB photon rate is of the order of 3 MHz, which means about 100 Single Bremsstrahlung photons per bunch-crossing, 5-6 orders of magnitude greater than the Bhabha Scattering rate at small angles. Another important feature is the extremely collimated angular distribution of SB photons, the typical emission angle being $\theta_\gamma \simeq \frac{m_e}{E} \simeq 10$ µrad at LEP. In Fig. 1 a sketch of the LEP straight section 1 is shown: the photons travelling with the beams escape the beam-pipe at the beginning of the arc, reaching a detector placed at the end of the straight section, about 350 m far apart from the Interaction Point (IP).

The high SB photon rate implies to work in a multi-photon regime, in which the luminosity is obtained from a measurement of the integrated energy on the detector in a certain time interval, rather than from photon counting:

$$E_{meas} - E_{bckg} = AL\int_0^{E_{beam}} \epsilon(k)k\frac{d\sigma_{SB}}{dk}dk \qquad (1)$$

where k is the photon energy, L the integrated luminosity, E_{meas} the total measured energy in the time interval, E_{bckg} the background measured energy, E_{beam} the beam energy, A the acceptance, $\epsilon(k)$ the energy detection efficiency and threshold function, and $\frac{d\sigma_{SB}}{dk}$ the differential SB cross section. E_{meas} is the measured amount of energy deposited in the detector. E_{bckg} represents the background energy to be subtracted, and which is measured under the condition of no beam crossing in IP-1, with dominant contributions from the beam-gas bremsstrahlung and Compton scattered thermal photons. In Fig. 2 the expected spatial distribution of the deposited energy on the detector is shown, compared with the angular distribution of the SB. From a two dimensional fit of this distribution, the acceptance A is evaluated, obtaining in this way a measurement of the beam position in the transverse plane, and of the beam divergence at the IP.

The SB differential cross section $d\sigma_{SB}/dk$ in eq.(1) has to be evaluated taking into account the finite transverse sizes

ISBN: 978-3-95450-236-3 ISSN: 2673-7027 doi:10.18429/JACoW-eeFACT2022-TUZAT0205

of the beams σ_x and σ_y, due to the large value of the impact parameter for the emission of SB photons at the LEP energy [4, 9–11]. The total SB cross section reduction with respect to the standard QED calculations due to the finite beam transverse sizes is ~ 25%. Finally, in the case of LEP, the radiative corrections to the cross-section are less than 1%.

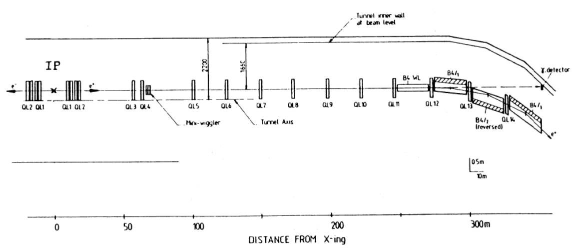

Figure 1: Sketch of the LEP straight section from the IP to the photon detector [7].

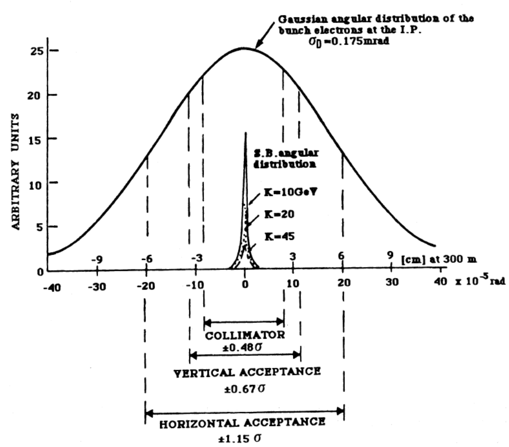

Figure 2: Angular distribution of the Single Bremsstrahlung photons due to the beam divergence [7].

Experimental Set-up

The LEP-5 experiment was approved by CERN in 1989 as a test experiment to be performed in IP-1[1], an interaction region without detectors since the four LEP experiments were installed in the even IPs. In normal conditions the beams were separated in order not to affect the beam lifetime. They were put into collisions in IP-1 only in the final 2 - 3 hours of a LEP fill, which used to last 10 - 12 hours. Moreover, also with colliding beams, the experimental conditions were different from even IPs. Since the beams were not optimized for collisions, the luminosity was lower by about one order of magnitude and the beam divergence smaller. The apparatus is sketched in Fig. 3: at the end of the straight section there was a thin aluminum window (2×5 cm^2) on the beam-pipe to allow photons to escape and to reach the photon detector placed about 350 m from the IP. The acceptance in IP-1 was only A ~ 41% due to the limited size of the window (it would have been larger in even IPs). The detector was an

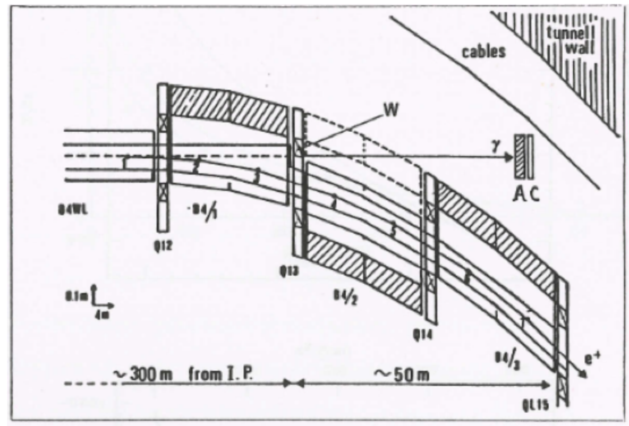

Figure 3: Sketch of the LEP-5 apparatus at the end of the straight section in IP-1.

electromagnetic calorimeter made of lead with embedded scintillating fibers as active medium [12]. In front of the calorimeter there was a 2 X_0 long absorber made of LiH, a low Z material to strongly suppress the synchrotron radiation (SR) background with respect to SB. The calorimeter consisted of a matrix of 7×6 modules each of $2.5 \times 2.5 \times 35$ cm^3 volume. The modules were built with a melting technique: molten lead was poured into a mould with spacers holding 144 steel tubes to accommodate the scintillating fibers of 1 mm diameter. The fibers were almost parallel to the flight direction of the incoming photons. From the read-out point of view each of the 6 central modules was divided into 4 separate channels to increase the spatial resolution in the central region of the calorimeter. Each readout channel was connected through a light guide to a photomultiplier.

Table 2 shows the overall reduction of the expected SR spectrum at LEP [13] with respect to SB photons, at the level of the detected energy in the calorimeter, as resulted from a detailed MC simulation including the LiH absorber and the calorimeter materials [7].

The calorimeter was installed in IP-1 during spring 1990, and data were taken during the following summer, in June - August 1990.

Lumininosity Measurement

In the following the best results, obtained during Fill 409 of LEP, are shown [7]. With separate beams in IP-1 the background from single beam radiation, due to the beam-gas bremsstrahlung and to the Compton scattered thermal photons, was measured. The beam-gas contribution was expected to be proportional to the beam current (of the positrons in this case), and to the density of residual gas in the beam-pipe, which is again proportional to the circulating currents. Also the Compton scattering of thermal photons was expected to be proportional to the beam current. Those two effects combined to produce the parabolic

[1] This is the site where now is installed the ATLAS detector at the LHC.

ISBN: 978-3-95450-236-3 ISSN: 2673-7027 doi:10.18429/JACoW-eeFACT2022-TUZAT0205

Table 2: Expected photon energy spectrum – in GeV per bunch crossing (GeV/bx) – for SR exiting from the 2×5 cm^2 window on the beam-pipe at IP-1 of LEP [13] and upstream the LiH absorber, deposited energy in the active material of the calorimeter (scintillating fibers), and total attenuation factor, compared with the corresponding quantities evaluated for the global SB energy spectrum.

Photon energy	Upstream LiH abs. (GeV/bx)	Deposited in in the fibers (GeV/bx)	Attenuation factor
20 keV	$2.2 \cdot 10^6$	-	$< 10^{-9}$
100 keV	$1.8 \cdot 10^6$	-	$< 10^{-9}$
500 keV	$4.5 \cdot 10^5$	$2.1 \cdot 10^{-3}$	$4.7 \cdot 10^{-9}$
1 MeV	$4.8 \cdot 10^4$	$5.2 \cdot 10^{-3}$	$1.1 \cdot 10^{-7}$
2 MeV	$9.1 \cdot 10^2$	$7.2 \cdot 10^{-4}$	$7.9 \cdot 10^{-7}$
SB spect.	$1.7 \cdot 10^2$	2.2	$1.3 \cdot 10^{-2}$

behaviour shown in Fig. 4. When the beams were put into collisions a sudden signal increase was observed (Fig. 5), clearly showing the additional contribution of the SB photons. At the end of the collision regime, the last three points of Fig. 5, the integrated energy went back to the background level extrapolated as a function of the beam current. In

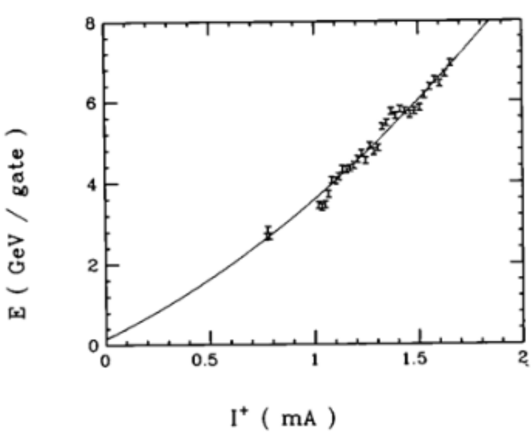

Figure 4: Deposited energy in the calorimeter with separate beams in IP-1 [7].

order to determine the absolute luminosity, the acceptance had to be evaluated from the spatial distribution of the energy on the calorimeter (Fig. 6). Finally, in Fig. 7 the result of the measurement is reported: each point corresponded to 10 minutes of data-taking, the statistical uncertainty was of the order of 1%. The *oscillating* behaviour of the luminosity in Fig. 7 was due to a β-waist scan during collisions. The systematic uncertainties were due to the background subtraction procedure (2%), the uncertainty in the evaluation of acceptance A (1.5%), the uncertainty in the SB cross section evaluation due to radiative corrections (< 1%), limited knowledge of the beam sizes (1%) and of the low energy effective threshold $E_{threshold}$ (efficiency) (1%). The total systematic uncertainty on the luminosity measurement

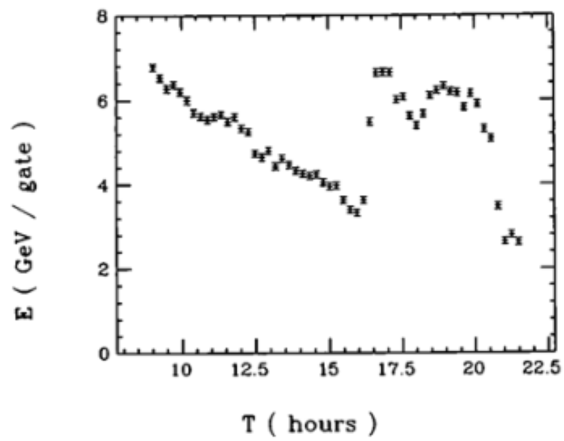

Figure 5: Signal of the Bremsstrahlung photons, collisions starts at about 16:00 hrs [7].

was $\sim 3.2\%$. This could have been reduced to the $1-2\%$ level in different experimental conditions with higher luminosity and larger acceptance (e.g. at the LEP IP-even).

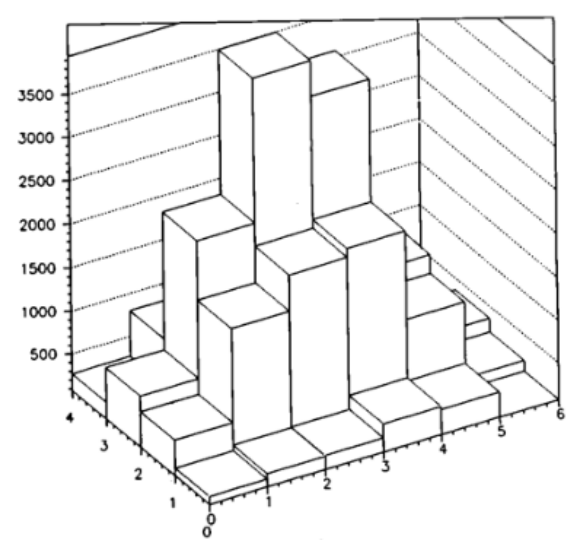

Figure 6: Spatial distribution of the deposited energy in the central modules of the calorimeter [7].

Compton Scattering of Thermal Photons

The LEP-5 experiment [14] (and independently another experiment at LEP [15]) measured for the first time the Compton scattering of the thermal photons present in the LEP beam-pipe against the high energy electrons. The LEP vacuum pipe could be considered as a black body at about 300 K temperature, hence filled with electromagnetic radiation with an energy distribution following the Planck law with a peak at $k_{max} \simeq 0.07$ eV. In the rest frame of the LEP electrons, a photon with energy k_{max} incident at an angle of 180° appears to have an energy $K^\star \simeq 2\gamma K_{max} \simeq 13.7$ keV due to the Lorentz boost. After a Compton back-scattering the photon gains another factor 2γ, then in the laboratory

ISBN: 978-3-95450-236-3 ISSN: 2673-7027 doi:10.18429/JACoW-eeFACT2022-TUZAT0205

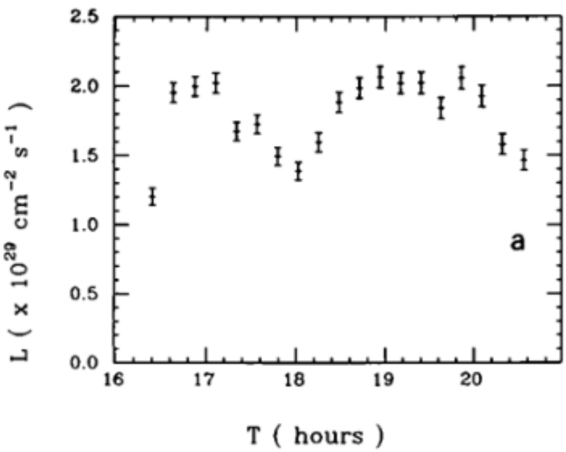

Figure 7: Luminosity as a function of time [7].

frame its energy will be $k \simeq 4\gamma^2 k_{max} \simeq 2.8$ GeV, well inside the energy range of the SB photons. Hence the Compton back-scattered photons constituted a relevant source of background for the measurement of the luminosity, of the same order of magnitude of the beam-gas bremsstrahlung, due to the extremely low vacuum pressure of LEP (of the order of 10^{-10} torr). The total background was measured with separate beams in IP-1, and in Fig. 8 the experimental spectrum of the integrated energy on the calorimeter is shown, compared with the Monte Carlo expectations for beam-gas bremsstrahlung and beam gas plus Compton backscattering [16]. The best agreement was found for an average number of beam-gas photons per bunch crossing of $\mu_{BG} = 0.44$ and of thermal photons $\mu_{TP} = 1.47$, and an effective detection energy threshold $E_{threshold} = 200$ MeV. It is worth noting that the threshold effect is clearly visible in the low energy end of the measured spectrum (Fig. 8), confirming the results of the MC simulation of the LiH absorber and the calorimeter response (Table 2). From these values an estimate of the temperature of the beam-pipe and the pressure of the residual gas in the pipe was obtained: $T \simeq 291$ K and $P \simeq 2.2 \times 10^{-10}$ torr, respectively.

Compton scattering of thermal photon could in principle decrease the beam lifetime; however the conclusion was that it could not degrade significantly the LEP performance [16].

Upgraded Set-up

During 1991 an upgrade of the experiment was performed in order to fully exploit the high rate capability of the luminosity measurement method [8]. In doing that, the possibility to measure the luminosity of the four bunches separately was also tested. This last feature would have been very important in case of polarization of LEP beams, since schemes with different polarization bunch per bunch were proposed [17]. A faster readout electronics was employed, able to process and store the signals from the calorimeter acquiring all the bunch crossings. Data were taken with this new readout on October-November 1991, but unfortunately beams were

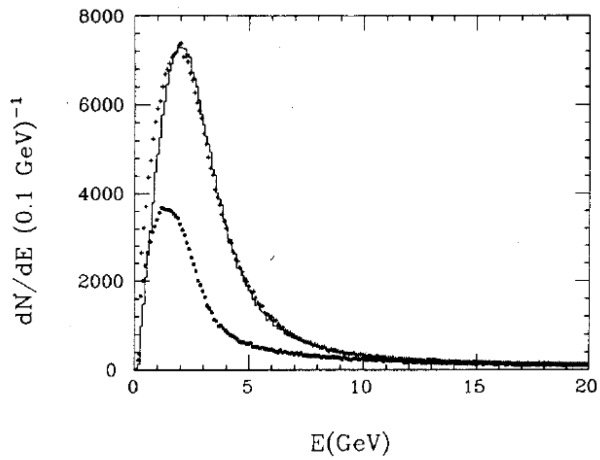

Figure 8: Spectrum of the deposited energy(histogram) compared with Monte Carlo simulation of beam gas (black points) and with beam gas plus Compton scattering (crosses) [14].

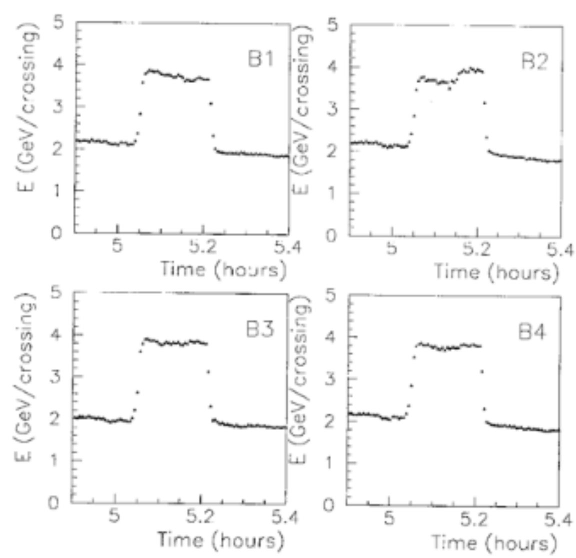

Figure 9: Deposited energy in the calorimeter for the four bunches separately [8].

unstable when put in collisions in IP-1 due to a modified optics. However only few minutes of collisions were sufficient to prove the feasibility of the measurement (see Fig. 9), despite the beam optics was not optimized and the photons distribution was centered out of the window, causing a larger systematic uncertainty due to the evaluation of the geometrical acceptance from a tail of the distribution. Anyhow the collected data showed that the bunch per bunch luminosity could be measured with a statistical uncertainty of 0.2% in only 20 seconds.

ISBN: 978-3-95450-236-3 ISSN: 2673-7027 doi:10.18429/JACoW-eeFACT2022-TUZAT0205

SOME CONSIDERATIONS ON THE FEASIBILITY AT FCC-ee

A luminosity monitor based on the detection of SB photons can reach very high rates at FCC-ee, as shown in Table 1, and could be very fast. The goal to reach $\sim 1\%$ precision on the absolute luminosity measurement for each single bunch would seem achievable, in principle, just adapting the methodology adopted at LEP and described above. It would require a good control of beam sizes and low energy effective threshold for the cross-section determination. Theoretical calculations could be improved implementing the radiative corrections. At FCC-ee the narrow angular collimation of SB photons is similar to LEP in all energy configurations, ranging from 10 to 3 μrad, with a beam divergence at IP approximately in the range $10 \div 100$ μrad. In case of a photon exit window at 50 m from IP, the beam spot can be only few mm wide, greatly improving the acceptance, and reducing the correlated systematic uncertainty. On the other hand the beam divergence and position at IP would be more difficult to be measured, requiring very good space resolution of the detector and to take into account the e.m. shower transverse sizes.

Preliminary results from detailed simulation studies to evaluate the various background sources at FCC-ee [18] show an overwhelming contribution concentrated in the forward direction, similarly to SB photons, from the beamstrahlung process [19, 20], in constrast with the LEP case, where it was fully negligible. Table 3 reports the expected total power and mean photon energy for the beamstrahlung [18] compared to SB.

Table 3: Expected total power and mean photon energy for the beamstrahlung process [18], compared to the SB process, and in the four beam energy configurations of FCC-ee.

	Beamstr. mean energy (MeV)	**Beamstr. Total power (kW)**	**SB Total power (W)**
Z	1.7	370	425
WW	7.2	236	60
HZ	22.9	147	40
$t\bar{t}$	62.3	77	2

In addition, the SR background will require a low-Z material absorber for the attenuation, whose length, shape, and material has to be carefully chosen (see e.g. Table 2) according to the simulation studies [18]. The impact of the corresponding worsening of the energy resolution and linearity of the downstream detector has to be carefully studied. The expected background contribution from the beam-gas bremsstrahlung and Compton scattering of thermal photons amounts to a fraction less than 10^{-4} of the SB signal [18], and can be neglected in all four energy configurations of FCC-ee.

In general the huge SB and background energy flux will require a very robust and radiation hard detector.

The main concern about the feasibility of a fast SB luminosity monitor at FCC-ee comes from the intense beamstrahlung background. On one hand, the signal-over-background power ratio is very unfavourable (0.1% at the Z pole) and the energy flux from beamstrahlung must be attenuated and rejected in some way. On the other hand, due to its very high power, it is anyhow necessary to have a beam dump for the beamstrahlung photons, in order for the machine to operate. The design of the overall layout of the beam dump would need to harmonize these two different requirements. The possibility of using special absorbers as in the case of SR must be judiciously studied. The huge rates of the high energy and penetrating SB photons might still allow the use of a calorimeter downstream a beam dump of several radiation lenghts, especially in the case of the softer beamstrahlung in the case of the Z pole energy configuration. The use of sweeping magnetic fields, or magnetized materials for additional background suppression, combined with possible discrimination based on the very different longitudinal e.m. shower profile of signal and background inside the calorimeter might be also exploited.

CONCLUSION

The luminosity measurement at LEP based on the SB process has been reviewed. A similar methodology could be implemented at FCC-ee. However in this case the huge background from beamstrahlung represents a major concern. Nonetheless a possible strong reduction of this background with respect to the SB signal might be achieved with the judicious exploitation of different attenuation and rejection techniques.

These solutions have to be carefully investigated and studied to understand the feasibility of a SB luminosity monitor at FCC-ee. Its main advantage would consist in a very fast and precise tool for machine operations, reaching the percent precision level on the absolute luminosity measurement, and separately for each bunch, therefore complementing the more precise but slower monitor based on BS.

ACKNOWLEDGEMENTS

The author is grateful to Manuela Boscolo for the invitation to the workshop and stimulating discussions on the subject. Thanks are due to Andrea Ciarma for providing useful information and results on background simulations in the FCC-ee environment.

REFERENCES

[1] Mogens Dam, "Challenges for FCC-ee luminosity monitor design", *Eur. Phys. J. Plus*, vol. 137, p. 81, 2022.

[2] G. Abbiendi *et al.*, "Precision luminosity for Z_0 lineshape measurements with a silicon-tungsten calorimeter", *Eur. Phys. J. C*, vol. 14, p. 373, 2000.

[3] H. Dehne, M. Preger, S. Tazzari and G. Vignola, "Luminosity measurement at ADONE by single and double bremsstrahlung", *Nucl. Instrum. Meth.*, vol. 116, pp. 345–359, 1974.

ISBN: 978-3-95450-236-3 ISSN: 2673-7027 doi:10.18429/JACoW-eeFACT2022-TUZAT0205

[4] A. Blinov *et al.*, "Luminosity measurement with the MD-1 detector at VEPP-4", *Nucl. Instrum. Meth. A*, vol. 273, pp. 31–39, 1988.

[5] A. Abada *et al.*, "FCC-ee: The Lepton Collider: Future Circular Collider Conceptual Design Report Volume 2", *Eur. Phys. J. Special Topics*, vol. 228, pp. 261–623, 2019.

[6] T. Raubenheimer, "Accelerator overview", presented at *FCC Week 2022*, Paris, France, May 2022.

[7] C. Bini *et al.*, "Fast measurement of luminosity at LEP by detecting the single bremsstrahlung photons", *Nucl. Instrum. Meth. A*, vol. 306, pp. 467–473, 1991.

[8] C. Bini *et al.*, "Fast luminosity monitor at LEP", *Nucl. Instrum. Meth. A*, vol. 349, pp. 27–31, 1994.

[9] A. Blinov *et al*., "Large impact parameter cut-off in the process $e^+e^- \to e^+e^-\gamma$" *Phys. Lett. B*, vol. 113, p. 423,1982.

[10] G. L. Kotkin, V. G. Serbo, "Beam-size effect and particle losses at B-factories KEKB and PEP-II", *Phys. Lett. B*, vol. 227, p. 137, 2005.

[11] G. L. Kotkin and V. G. Serbo, "Beam-size effect and particle losses at SuperB factory developed in Italy", *JINST*, vol. 4, p. 06015, 2009.

[12] M. Bertino *et al*, "Space resolution obtained with a highly segmented SCIFI e.m.calorimeter", *Nucl. Instrum. Meth. A*, vol. 315, pp. 27-331, 1992.

[13] C. Fischer and G. von Holtey, *LEP Note 618*, 1989.

[14] C. Bini, *et al.*,"Scattering of thermal photons by a 46 GeV positron beam at LEP", *Phys. Lett. B*, vol. 262, pp. 135–138, 1991.

[15] B. Dehning, A. Melissinos, F. Perrone, C. Rizzo and G. von Holtey, "Scattering of high energy electrons off thermal photons", *Phys. Lett. B*, vol. 249, pp. 145–148, 1990.

[16] A. Di Domenico, "Inverse Compton scattering of thermal radiation at LEP and LEP-200", *Part. Accel.*, vol. 39, pp. 137–146, 1992.

[17] G. Alexander *et al.*, "Polarization at LEP", *CERN 88-06*, 1989.

[18] A. Ciarma, "Machine induced backgrounds in the FCC-ee MDI region and beamstrahlung radiation", in *Proc. eeFACT'22*, Sept. 12-15, 2022, Frascati, Italy.

[19] K. Yokoya and P. Chen, "Frontiers of Particle Beams: Intensity Limitations", in *Proc. Topical Course Joint US-CERN School on Particle Accelerators*, Hilton Head Island, SC, US, 7-14 November 1990, *Lect. Notes Phys.*, vol. 400, p. 415, 1992.

[20] V. I. Telnov, "Restriction on the energy and luminosity of e^+e^- storage rings due to beamstrahlung", *Phys. Rev. Lett.*, vol. 110, p. 114801, 2013.

ISBN: 978-3-95450-236-3 ISSN: 2673-7027 doi:10.18429/JACoW-eeFACT2022-TUZAS0101

LONGITUDINALLY POLARIZED COLLIDING BEAMS AT THE CEPC*

Z. Duan†, T. Chen[1], W. H. Xia[1], J. Gao[1], D. H. Ji, X. P. Li, D. Wang, Y. W. Wang, J. Q. Wang[1]
Key Laboratory of Particle Acceleration Physics and Technology,
Institute of High Energy Physics, Chinese Academy of Sciences, Beijing, China
[1]also at University of Chinese Academy of Sciences, Beijing, China

Abstract

This paper reports the recent progress in the design studies of longitudinally polarized colliding beams for the Circular Electron Positron Collider (CEPC). The overall design concept is outlined, followed by more detailed descriptions of the polarized beam generation, polarization maintenance in the booster, and spin rotators in the collider rings.

INTRODUCTION

The Circular Electron Positron Collider (CEPC) [1, 2] is a next generation electron-positron circular collider, working at center-of-mass energies of 91 GeV (Z-factory), 160 GeV (W- factory), 240 GeV (Higgs-factory), upgradable to 360 GeV (ttbar energy), and aiming at ultra-high precision measurements and probe into new physics beyond Standard Model. The resonant depolarization technique (RD) [3] is essential for precision measurements of the mass of Z and W bosons, this requires transversely polarized e^+ and e^- beams with at least 5% to 10% beam polarization. Meanwhile, probing the spin dimension with longitudinally polarized colliding beams can be very beneficial to enhance particular channels, reduce background and facilitate searches for beyond Standard Model chiral new physics. This application requires 50% or more longitudinal polarization (for e- beam alone, or for both beams) at the Interaction Points (IPs) as well as a high luminosity. These applications demand a careful study of the polarized beam generation and maintenance as well as spin manipulation in the collider rings.

Top-up injection will be adopted in the CEPC collider rings, to maximize the integrated luminosity. In this operation mode, the time-averaged beam polarization P_{avg} of the colliding beams contains two different contributions, one is from the Sokolov-Ternov effect [4] in the storage ring, characterized by the equilibrium beam polarization P_{DK}, the other is from the injected beam polarization P_{inj},

$$P_{\text{avg}} = \frac{P_{\text{DK}}}{1 + \tau_{\text{DK}}/\tau_{\text{b}}} + \frac{P_{\text{inj}}}{1 + \tau_{\text{b}}/\tau_{\text{DK}}} \tag{1}$$

where τ_{b} is the beam lifetime, which is mainly limited by the radiative Bhabha effect and is correlated to the luminosity. τ_{DK} is the polarization build-up time, $\tau_{\text{DK}}^{-1} = \tau_{\text{BSK}}^{-1} + \tau_{\text{dep}}^{-1}$, where τ_{BSK} and τ_{dep} are the time constants characterizing the Sokolov-Ternov effect and the radiative depolarization effect [5], respectively. The equilibrium beam polarization P_{DK} [6] can be approximated by

$$P_{\text{DK}} \approx \frac{P_{\infty}}{1 + \frac{\tau_{\text{BKS}}}{\tau_{\text{DK}}}} \tag{2}$$

where P_{∞} is the equilibrium beam polarization taking into the orbital imperfections, but disregarding the radiative depolarization effect, $P_{\infty} = 92.4\%$ in an ideal planar ring, and is generally lower in an imperfect ring.

If a highly polarized beam is injected into the collider ring, and in the case of $\tau_{\text{b}} \ll \tau_{\text{DK}}$, the time-averaged beam polarization of the colliding beams can be evaluated by

$$P_{\text{avg}} \approx \frac{P_{\text{inj}}}{1 + \frac{\tau_{\text{b}}}{\tau_{\text{BKS}}} \frac{P_{\infty}}{P_{\text{DK}}}} \tag{3}$$

this indicates that a very low level of P_{DK} would reduce P_{avg}. In Table 1, we assume $P_{\text{inj}} = 80\%$, and calculate the required minimum P_{DK} to reach $P_{\text{avg}} \geq 50\%$. Given the relative ratio between τ_{b} and τ_{BKS}, a larger P_{DK} is required at a higher beam energy, which poses a greater challenge in the mitigation of the radiative depolarization effect in the collider rings. Nevertheless, injection of highly polarized beams into the collider rings, has the potential of reaching a high level of P_{avg} besides a high luminosity, and is essential to realize longitudinally polarized colliding beams.

Table 1: CEPC Beam Parameters Related to P_{avg}

Beam energy	**45.6 GeV Z**	**80 GeV W**	**120 GeV Higgs**
τ_{b}(hour)	2.5	1.4	0.43
τ_{BKS}(hour)	256	15.2	2.0
$P_{\text{DK,min}}$	0.6%	5%	11%

In addition, pilot non-colliding bunches might be necessary for RD measurements, since the beamstruhlung of colliding bunches substantially increases the rms beam energy spread and could limit the achievable accuracy of RD measurements. These pilot bunches operate in the decay mode, and the Sokolov-Ternov effect [4] can be used to generate the required polarization for RD measurements, where asymmetric wigglers [7] are required to boost the self-polarization process at Z-pole [8]. Nevertheless, injection of highly polarized beams into these pilot bunches could be a viable alternative approach for RD measurements as well.

Figure 1 shows the envisaged modification of the CEPC accelerator complex to implement polarized beams. Electron beam with over 80% polarization can be generated from

* Work supported by National Natural Science Foundation of China (Grant No. 11975252); National Key Program for S&T Research and Development (Grant No. 2016YFA0400400 and 2018YFA0404300); Key Research Program of Frontier Sciences, CAS (Grant No. QYZDJ-SSW-SLH004); Youth Innovation Promotion Association CAS (No. 2021012)
† zhe.duan@ihep.ac.cn

ISBN: 978-3-95450-236-3 ISSN: 2673-7027 doi:10.18429/JACoW-eeFACT2022-TUZAS0101

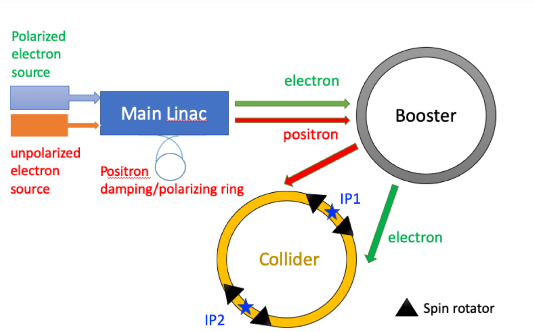

Figure 1: The envisaged modification of the CEPC accelerator complex to implement polarized beams.

the polarized electron source [9], while polarized positron source is more technically challenging [10]. We propose to implement asymmetric wigglers [7] in the positron damping ring, this would generate over 20% beam polarization within 10 minutes, sufficient for RD measurements. Then, the polarized beams are transferred through the injection chain, though it is worried that severe depolarization could occur in the booster where many spin resonances are crossed during the acceleration process, our study shows that the highly periodic lattice structure features weaker spin resonances than expected, and the depolarization could be manageable. We've also implemented a pair of spin rotators around each IP in the CEPC collider ring for the Z-pole energies, which is essential for longitudinally polarized colliding beams.

POSITRON DAMPING/POLARIZING RING

In the injector design in the CEPC CDR [1], 3 nC unpolarized positron bunches are converted from the interaction of a 4 GeV, 10 nC unpolarized primary electron bunch with a target, after pre-acceleration, they are injected into a positron damping ring to reach the desired beam quality for later transportation. By default, 4 positron bunches will stay in the positron damping ring for 20 ms, to satisfy the needs to fill the colliding bunches, In this case, the extracted bunches are unpolarized. The possibility to polarize the positron bunches using the Sokolov-Ternov effect [4] in the positron damping ring [11] or another dedicated ring of similar size [12] have been considered before. This requires very strong asymmetric wigglers to polarize all the positron bunches and satisfy the timing needs to fill all colliding bunches, which is very challenging. However, it is more feasible to generate polarized positron bunches to satisfy the needs of RD measurements. Assume we store one or two positron bunches in the positron damping ring for a longer time, say 10 min, in addition to the other bunches that supply the top-up injection. If we aim at generation of over 20% beam polarization, we need to achieve a self-polarization build-up time $\tau_{\rm DK}$ of about 30 min.

Figure 2 shows the layout of a candidate lattice of the positron damping ring. In this design, the blue region represents the lattice sections that can hold up to 24 m total

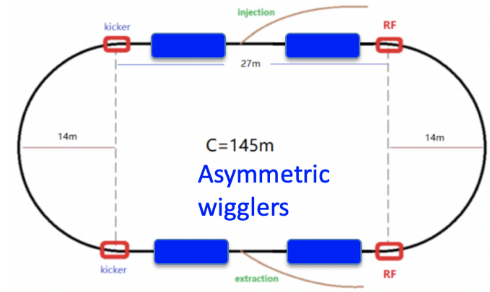

Figure 2: A schematic plot of a candidate lattice of the positron damping ring.

length of asymmetric wigglers. Some tentative parameters are summarized in Table 2. The magnetic fields of the inner and outer parts of an asymmetric wiggler are 1.8 T and -0.36 T, respectively. More detailed evaluation of the influence of the wigglers to the lattice performance is under way. This scheme is compatible with the top-up injection timing needs for the injector, and could supply one or two polarized positron bunches every 10 min for RD measurements in the positron collider ring.

Table 2: Beam Parameters of Positron Damping Ring

Parameter	Value
Beam energy, $G\gamma$	1.542 GeV, 3.5
Circumference	145 m
Wiggler magnetic field B_+/B_-	1.8 T/0.36 T
Wiggler total length	24 m
P_∞ w/ wigglers	90%
$\tau_{\rm BKS}$ w/o wigglers	52 min
$\tau_{\rm BKS}$ w/ wigglers	34 min
Store time	10 min
Polarization of extracted beam	22%

POLARIZED BEAM ACCELERATION

As the beam energy ramps in an electron (positron) booster ring, so is the closed orbit spin tune ν_0 and the amplitude-dependent spin tune ν_s among beam particles since $\nu_s \approx \nu_0 \approx a\gamma$, $a = 0.00115965$ for electron and positron, γ is the Lorentz factor. This leads to crossing of the underlying spin resonances and could lead to beam depolarization. The polarization loss during crossing of a single, isolated spin resonance can be estimated with the Froissart-Stora formula [13]: $P_f/P_i = 2e^{-\frac{\pi|\epsilon|^2}{2\alpha}} - 1$, where P_i and P_f are the beam vertical polarization before and after crossing the resonance, ϵ is the spin resonance strength, $\alpha = \frac{da\gamma}{d\theta}$ is related to the energy ramping rate. There are three parameter regimes of $|\epsilon|/\sqrt{\alpha}$: the "adiabatic crossing" regime, if $|\epsilon|/\sqrt{\alpha} > 1.84$, then the depolarization is less than 1% but with a "spin-flip"; the "fast crossing" regime, if $|\epsilon|/\sqrt{\alpha} < 0.056$ then the depolarization is also less than 1%; the "intermediate" regime, $0.056 < |\epsilon|/\sqrt{\alpha} < 1.84$, a

ISBN: 978-3-95450-236-3 ISSN: 2673-7027 doi:10.18429/JACoW-eeFACT2022-TUZAS0101

stronger depolarization occurs. There are two families of important spin resonances in this context: the imperfect resonances $\nu_0 = k, k \in Z$, mainly driven by horizontal magnetic fields due to vertical orbit offsets in quadrupoles and dipole roll errors, and the intrinsic resonances $\nu_0 = k \pm \nu_y, k \in Z$ with ν_y the vertical betatron tune, driven by the horizontal magnetic field due to vertical betatron oscillations in quadrupoles. Adjacent imperfection resonances are spaced by 440 MeV, and it is clear hundreds of spin resonances of these two families will be crossed in the acceleration of CEPC booster from injection energy at 10 GeV to extraction energies of 45.6 GeV, 80 GeV and 120 GeV.

Previous studies suggested using Siberian snakes [12, 14] in these 100 km electron boosters to mitigate the depolarization. However, the practical implementations of snakes using either bending magnets or solenoids are cumbersome in size and costs. A concept of "spin-resonance free electron ring injector" [15] was proposed in the study of the Electron Ion Collider [16]. A booster lattice with a high effective periodicity of 96 was designed, so that supper strong spin resonances are all beyond the top energy at 18 GeV, while the other spin resonances are generally weak, well within the "fast crossing" regime and severe depolarization is thus avoided. This work emphasizes on the importance of the spin resonance structure.

We carefully examined the spin resonance structure of the CEPC CDR booster lattice. It features a super-periodicity of $P = 8$ with interleaved arc and straight sections. Each arc section contains $M = 99$ FODO cells with 90 degree betatron phase advances, the vertical betatron tune is $\nu_y = 261.2$, and the total contribution from all arc sections to the vertical betatron tune is $\nu_B = 198$. A similar model ring lattice was studied in Ref. [17], where analytical estimations of the spin resonance strengths and their structure were obtained. It was shown that the contributions from all arc FODO cells add up near super strong spin resonances. The super strong imperfection resonances are located at $\nu_0 = nPM \pm [\nu_B]$, while the super strong intrinsic resonances are located at $\nu_0 = nP \pm \nu_y$ near $nPM \pm [\nu_B]$, where $[x]$ denotes the integer part of x. However, regular spin resonances away from these conditions are generally weak due to cancellation. Application of this theory to the CEPC booster lattice indicates that it has effectively a very large super-periodicity of $PM = 792$, and the first super strong resonances are located near $\nu_0 = [\nu_B] = 198$, other super strong resonances are well beyond the working beam energies of the CEPC booster.

To verify this analysis, we calculated the spin resonance spectrum of the CEPC booster lattice in the working beam energy range, as shown in Fig. 3. The DEPOL code was employed to calculate the intrinsic spin resonance strengths at a vertical normalized emittance of $10\pi\text{mm}\cdot\text{mrad}$. The super strong intrinsic resonances are near $G\gamma = 198$, between the working energies for W and Higgs, other resonances are much weaker. To evaluate the imperfection spin resonance spectrum, we introduced magnetic field errors and misalignment errors to dipoles, quadrupoles and sextupoles. The main contribution of closed orbit distortion is from the 100 μm rms misalignment error in quadrupoles, we then implemented closed orbit corrections and betatron tune corrections. For this study, we use a imperfect lattice seed after correction with a vertical rms closed orbit distortion of about 100μm. We numerically evaluated the strength of the imperfection resonance $\nu_0 = k$ via $\epsilon_k \approx \frac{1+k}{2\pi}\sum_{h=1}^{M}[p_{y,0}(s_{h,2}) - p_{y,0}(s_{h,1})]e^{ik\Phi(s_{h,1})}$, where we replace the integral by a sum over M magnet elements in the lattice, $s_{h,1}$ and $s_{h,2}$ are the longitudinal positions of the entrance and the exit of the h-th magnet, respectively, $p_{y,0}$ is the vertical canonical momentum on the closed orbit, $\Phi(s) = \frac{1}{\nu_y}\int_0^s \frac{1}{\beta_y(s)}ds$. The imperfection resonance strengths generally increase with energy besides the super strong resonance near $a\gamma = 198$. Apart from the super strong intrinsic resonance and a few imperfection resonances at higher energies, the resonance crossings of most spin resonances are well within the "fast-crossing" regime so that depolarization is very small.

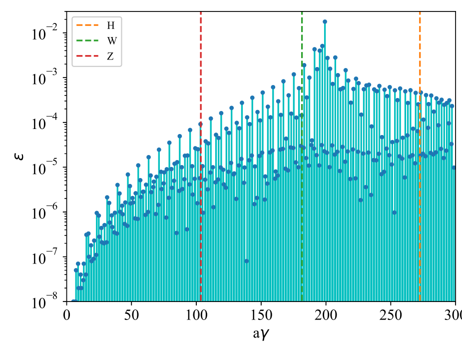

(a) Intrinsic resonances

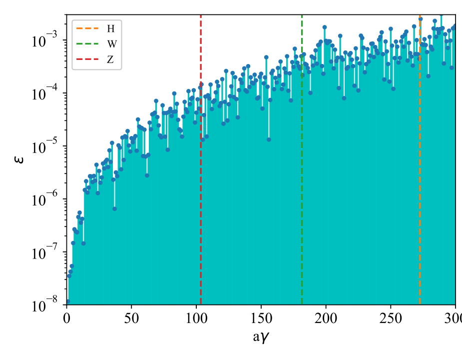

(b) Imperfection resonances

Figure 3: The spectra of intrinsic (upper) and imperfection (lower) spin resonances of an imperfect seed of the CEPC CDR booster lattice. The intrinsic resonances are calculated for a vertical normalized emittance of $10\pi\text{mm}\cdot\text{mrad}$. The three vertical dashed lines indicate the three extraction energies.

We launched simulations of the beam polarization transmission in the energy ramping process using the long term tracking capability of Bmad [18]. A cosine shape energy

ISBN: 978-3-95450-236-3 ISSN: 2673-7027 doi:10.18429/JACoW-eeFACT2022-TUZAS0101

ramping curve was adopted, $E(t) = E_{\mathrm{inj}} + \frac{(E_{\mathrm{ext}} - E_{\mathrm{inj}})}{2}(1 - \cos(\frac{\pi t}{t_{\mathrm{ramp}}}))$. The booster injection energy was fixed to 10 GeV, and the ramping time t_{ramp} was set to 1.9 s, 3.3 s and 5.0 s for the acceleration to the extraction energy 45.6 GeV (Z), 80 GeV (W) and 120 GeV (H), respectively. The RF voltages and phases are set to compensate for the synchrotron radiation energy loss, as well as maintain a fixed synchrotron tune of 0.1, 0.1, and 0.13 for the three extraction energies, respectively. The injected beam is modeled with 1000 particles in a 6D Gaussian distribution. Following the CEPC CDR parameters [1], the rms horizontal and vertical emittances are set to 80 nm and 40 nm, respectively. The rms energy spread and bunch length are set to 0.16% and 1 mm, respectively. The beam particles are initialized with a 100% vertical polarization, during the tracking the vertical polarization of the beam is calculated as the ensemble average of the vertical spins of the particles. Fig. 4 shows the evolution of the vertical beam polarization in the acceleration to the three different extraction energies. In both the cases of Z and W energies, the polarization loss is less than 5%. In contrast, in the case of Higgs energy, there is almost 40% polarization loss when crossing the super strong intrinsic resonance near $\nu_0 = 198$, and another 10% polarization loss due to resonance crossings at even higher beam energies. In principle, the impact of the super strong intrinsic resonance can be partially mitigated by a dedicated correction of the vertical equilibrium emittance, or improve the lattice design so that the first super strong resonances are beyond the whole working energy range.

These preliminary studies suggest it is possible to largely maintain the beam polarization in the acceleration process to 45.6 GeV and 80 GeV, without Siberian snakes. More detailed study of the influence of machine imperfections is under way.

SPIN ROTATORS IN THE COLLIDER RING

To realize the longitudinal polarization at IPs in the electron collider ring, a pair of spin rotators need to be inserted around each of the two IPs. This helps maintain vertical polarization in most part of the collider ring, and thus avoids significant depolarization. The detailed design of the spin rotators is reported elsewhere [19]. Here, we'll summarize the main results, and focus on the case that the spin rotator is only implemented in the electron collider ring.

Each spin rotator consists of a bending magnet section and a solenoid magnet section. The total spin rotation angle in each bending magnet section from the IP to each solenoid section needs to be an odd multiple k of $\pi/2$ to rotate the spins from the longitudinal to the radial direction, which corresponds to an orbital bending angle of at least 15.18 mrad at 45.6 GeV. Then, the solenoid section need to rotate the spin from the radial to vertical direction. The required solenoid integral strength is about 240 T·m to rotate the spin vector by $\pi/2$ at a beam energy of 45.6 GeV. This corresponds to a total length of 30 m for superconducting solenoid magnets

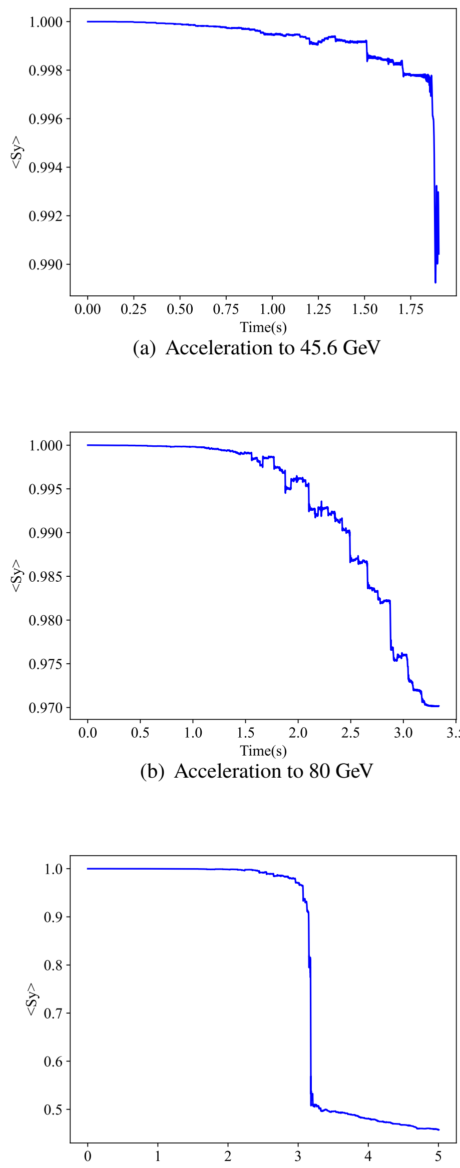

(a) Acceleration to 45.6 GeV

(b) Acceleration to 80 GeV

(c) Acceleration to 120 GeV

Figure 4: Simulated evolution of the vertical beam polarization in the acceleration to Z (upper), W (middle) and Higgs (lower) energies.

of 8 T. The solenoid magnets are interleaved by quadrupoles to compensate for the transverse coupling [20]. The layout of a pair of spin rotators around one IP is illustrated in Fig. 5. The S-shape geometry in the interaction region is utilized in the arrangement of the spin rotators, which are just placed out of the interaction region [14, 21]. The half crossing angle at the IP is 16.5 mrad, addition bending magnet sections ($\Delta\theta_1$ and $\Delta\theta_2$) are required in both spin rotators, next to the solenoid sections. In the counterpart region of the positron collider ring, the solenoid sections are replaced by straight sections with quadrupoles to match the optics. The circumference increases by about 2 km, the betatron

ISBN: 978-3-95450-236-3 ISSN: 2673-7027 doi:10.18429/JACoW-eeFACT2022-TUZAS0101

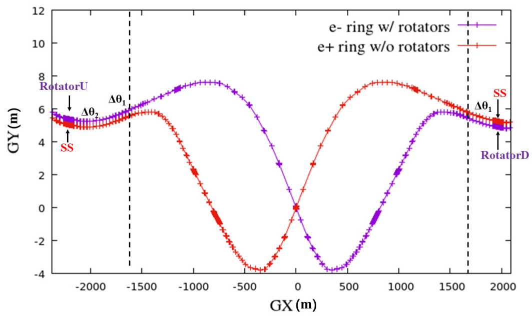

Figure 5: Geometry of the electron and positron collider rings near one interaction region [19], with solenoid spin rotators (RotatorU and RotatorD) for the electron beam, and compensating straight sections (SS) for the positron beam.

tunes increase by 10 units, while other beam parameters almost remain unchanged. Simulations also indicate there is only a moderate shrink of dynamic aperture, which can be recovered via dedicated optimizations.

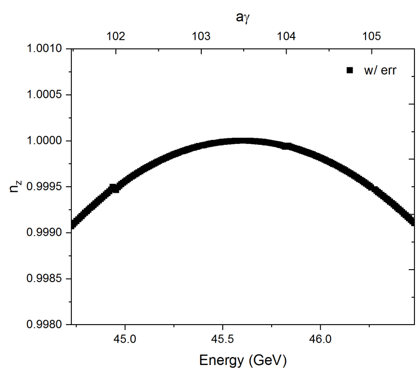

Figure 6: Longitudinal projection of $\mathbf{n_0}$ at the IP for different beam energies, for the lattice with magnet errors.

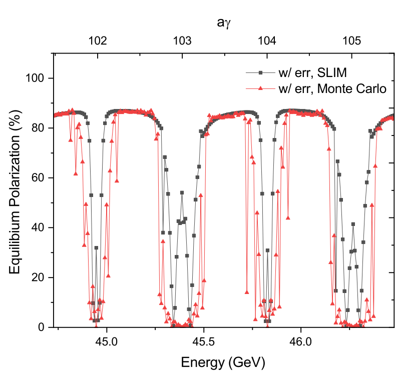

Figure 7: Comparsion of the equilibrium beam polarization for the lattice with spin rotators in the presence of magnet errors, simulated using the SLIM algorithm in Bmad and the Monte Carlo simulation in PTC, respectively. The step size $\Delta a\gamma = 0.02$.

We also numerically evaluated the performance of the spin motion using the BMAD/PTC code [18, 22]. In a realistic storage ring, the solenoid magnetic field may be not perfectly compensated due to magnets' errors. These magnet errors also drive spin resonances and lead to a reduced equilibrium beam polarization. We introduced in the solenoid sections relative field errors for solenoids and quadrupoles with a root-mean-squared value of 0.05%, and relative roll errors for quadrupoles with a root-mean-squared value of 0.01%. Fig. 6 shows the simulated longitudinal projection of the $\vec{n}_0$-axis at one IP, for different beam energies. Such an "anti-symmetric" spin rotator design is not very sensitive to a variation of the beam energy. Fig. 7 shows the simulated equilibrium beam polarization using the SLIM algorithm [23] in BMAD [18], and Monte-Carlo simulations implemented in PTC [24]. These simulations show clear depolarization near major spin resonances, the Monte-Carlo simulations also indicate the influence of higher-order synchrotron sideband spin resonances, absent from the SLIM simulations. Nevertheless, there are still sufficient safe space with fractional part of $a\gamma$ near 0.5, where the equilibrium beam polarization is very high. These simulations shows the robustness of the "anti-symmetric" spin rotator design against machine imperfections.

Next, we'll introduce other kinds of machine imperfections into the lattice with spin rotators, and evaluate the influence on the performance of the orbital and spin motion.

CONCLUSION

This paper summarizes the recent progress in the design studies of longitudinally polarized colliding beams at the CEPC. Generation of polarized beams from the source and injection into the collider rings are studied. It is proposed that positron bunches with over 20% polarization can be generated in the positron damping ring, to fit the needs of resonant depolarization. Our studies suggest beam polarization could be well preserved in the booster up to 45.6 GeV and even higher energies, without Siberian snakes. Spin rotators have also been implemented in the collider rings at Z-pole with promising performance. More technical aspects of these studies and potential extension to higher beam energies are under way.

Note that injected polarized electron and positron beams could also benefit RD measurements. Compared to the approach using self-polarization [8] with the help of asymmetric wigglers, the polarization level can be much higher, there is no initial dead time for physics, RD measurements can be conducted more frequently for at least the electron beam. It is also possible to carry out RD measurements on colliding bunches, especially at lower bunch charge. More quantitative evaluation of these aspects is planned.

ACKNOWLEDGEMENTS

The authors are grateful to D. P. Barber and S. Nikitin for helpful discussions, and D. Sagan and E. Forest for the kind help with simulation codes Bmad/PTC.

ISBN: 978-3-95450-236-3 ISSN: 2673-7027 doi:10.18429/JACoW-eeFACT2022-TUZAS0101

REFERENCES

[1] The CEPC Study Group, "CEPC Conceptual Design Report Volume I-Accelerator," *arXiv:1809.00285v1 [physics.acc-ph]*, 2018, doi:10.48550/arXiv.1809.00285

[2] The CEPC Accelerator Study Group, "Snowmass2021 White Paper AF3-CEPC," *arXiv:2203.09451*, 2022, doi:10.48550/arXiv.2203.09451

[3] Y. S. Derbenev, A. M. Kondratenko, S. I. Serednyakov, *et al.*, "Accurate calibration of the beam energy in a storage ring based on measurement of spin precession frequency of polarized particles," *Part. Accel.*, vol. 10, p. 177, 1980.

[4] A. A. Sokolov and I. M. Ternov, "On polarization and spin effects in the theory of synchrotron radiation," *Sov. Phys. Dokl.*, vol. 8, p. 1203, 1964.

[5] V. N. Baier and Y. F. Orlov, "Quantum depolarization of electrons in a magnetic field," *Sov. Phys. Dokl.*, vol. 10, p. 1145, 1966.

[6] Y. S. Derbenev and A. M. Kondratenko, "Diffusion of Particle Spin in Storage Rings," *Sov. Phys. JETP*, vol. 35, pp. 230–236, 1972.

[7] A. Blondel and J. M. Jowett, "Wigglers for polarization," *Conf. Proc. C8711093*, vol. 216, 1987.

[8] A. Blondel, P. Janot, J. Wenninger, *et al.*, "Polarization and Centre-of-mass Energy Calibration at FCC-ee," *arXiv:1909.12245 [hep-ex, physics:physics]*, 2019, doi:10.48550/arXiv.1909.12245

[9] A. Brachmann *et al.*, "The polarized electron source for the international collider (ILC) project," in *AIP Conference Proceedings*, vol. 915, 2007, pp. 1091–1094, doi:10.1063/1.2750959

[10] P. Musumeci, *et al.*, "Positron sources for future high energy physics colliders," *arXiv:2204.13245 [physics]*, 27, 2022, doi:10.48550/arXiv.2204.13245

[11] Z. Duan *et al.*, "Concepts of longitudinally polarized electron and positron colliding beams in the Circular Electron Positron Collider," *in Proc. of IPAC'19,*, Melbourne, Australia, May 2019, pp. 445-448., doi:10.18429/JACoW-IPAC2019-MOPMP012

[12] I. A. Koop, A. V. Otboev, and Y. M. Shatunov, "Ideas for longitudinal polarization at the Z/W/H/top factory," *Proc. eeFACT 2018, WEXAA04*, p. 190, 2018, doi:10.18429/JACoW-eeFACT2018-WEXAA04

[13] M. Froissart and R. Stora, "Depolarisation d'un faisceau de protons polarises dans un synchrotron," *Nucl. Instrum. Methods*, vol. 7, no. 3, pp. 297–305, 1960, doi:10.1016/0029-554X(60)90033-1

[14] S. A. Nikitin, "Polarization issues in circular electron–positron super-colliders," *Int. J. Mod. Phys. A*, vol. 35, no. 15&16, 2020, doi:10.1142/S0217751X20410018

[15] V. H. Ranjbar *et al.*, "Spin resonance free electron ring injector," *Phys. Rev. Accel. Beams*, vol. 21, p. 111 003, 2018, doi:10.1103/PhysRevAccelBeams.21.111003

[16] F. Willeke and J. Beebe-Wang, "Electron Ion Collider Conceptual Design Report 2021," Tech. Rep. BNL-221006–2021-FORE, 1765663, 2021, doi:10.2172/1765663

[17] S. Y. Lee, *Spin dynamics and snakes in synchrotrons*. World Scientific, 1997, doi:10.1142/3233

[18] D. Sagan *et al.*, "The Bmad Reference Manual," https://www.classe.cornell.edu/bmad/manual.html.

[19] W. Xia, Z. Duan, J. Gao, and Y. Wang, "Investigation of spin rotators in CEPC at the Z-pole," *Radiat. Detect. Technol. Methods*, vol. 6, no. 4, pp. 490–501, 2022, doi:10.1007/s41605-022-00344-2

[20] D. P. Barber, J. Kewisch, G. Ripken *et al.*, "A solenoid spin rotator for large electron storage rings," *Part. Accel.*, vol. 17, pp. 243–262, 1985.

[21] S. A. Nikitin, "Opportunities to obtain polarization at CEPC," *Int. J. Mod. Phys. A*, vol. 34, no. 13&14, p. 1 940 004, 2019, doi:10.1142/S0217751X19400049

[22] E. Forest, F. Schmidt, and E. McIntosh, "Introduction to the Polymorphic Tracking Code," *CERN-SL-2002-044 (AP), and KEK-Report 2002-3*, 2002.

[23] A. Chao, "Evaluation of radiative spin polarization in an electron storage ring," *Nucl. Instrum. Methods Phys. Res.*, vol. 180, p. 29, 1981.

[24] Z. Duan, M. Bai, D. P. Barber, and Q. Qin, " A Monte-Carlo simulation of the equilibrium beam polarization in ultra-high energy electron (positron) storage rings," *Nucl. Instrum. Methods Phys. Res., Sect. A*, vol. 793, pp. 81–91, 2015, doi:10.1142/S0217751X19400049

ISBN: 978-3-95450-236-3 ISSN: 2673-7027 doi:10.18429/JACoW-eeFACT2022-TUZAS0104

SPIN POLARIZATION SIMULATIONS FOR THE FUTURE CIRCULAR COLLIDER e+e- USING BMAD*

Y. Wu[1,†], F. Carlier[2], L. Van Riesen-Haupt[1], T. Pieloni[1]
[1]École Polytechnique Fédérale de Lausanne (EPFL), Lausanne, Switzerland
[2]European Organization for Nuclear Research (CERN), Geneva, Switzerland

Abstract

Measurements of particle properties with unprecedented accuracy in the Future Circular Collider e+e- (FCC-ee) are reliant on the high precision center-of-mass energy calibration, which could be realized via resonant depolarization measurements. The obtainable equilibrium spin polarization levels under the influence of lattice imperfections should be estimated via spin polarization simulations. An early-stage exploration of spin simulations in the FCC-ee has been conducted using Bmad. An effective model has been used to generate residual errors for the simulation of realistic orbits after lattice corrections. The influences of depolarization effects near the first-order spin-orbit resonances are displayed in linear polarization simulations, highlighting the demand for good closed orbit control. Furthermore, the first attempts at performing nonlinear spin tracking simulations in the FCC-ee reveals the full impact of lattice perturbations.

INTRODUCTION

The Future Circular Collider (FCC) was proposed to push both the energy and intensity frontiers of particle physics [1]. The FCC-ee, which is an electron-positron collider, as the first step of the FCC project, is designed to operate on multiple center-of-mass collision energies $\sqrt{s}$ between 88 GeV and 365 GeV for the production of Z^0 bosons ($\sqrt{s} \sim 91$ GeV), WW pairs ($\sqrt{s} \sim 160$ GeV), Higgs bosons ($\sqrt{s} \sim 240$ GeV) and top quark pairs ($\sqrt{s} \sim 350 - 365$ GeV) [1, 2].

The current precision requirements at Z mass and W mass are 4 keV and 250 keV respectively [3]. Resonant depolarization is a high precision energy calibration method that has been used in previous lepton machines such as the Large Electron–Positron Collider (LEP) [4], and is the proposed method in the FCC-ee to reach the unprecedented precision target at the Z and W pair threshold [2]. Spin polarization simulations are required to validate this energy calibration method in the FCC-ee by investigating the effects of lattice perturbations on spins. A minimum of 10% transverse polarization level at equilibrium should be guaranteed under various possible lattice conditions in order to ensure accurate energy calibration measurements [5].

Basics of Spin Dynamics

The spin precession motion in electromagnetic fields can be described by the Thomas-Bargmann-Michel-Telegdi (T-BMT) equation [6, 7],

$$\frac{\mathrm{d}\vec{S}}{\mathrm{d}t} = \vec{\Omega}_{\mathrm{BMT}} \times \vec{S}, \tag{1}$$

where $\vec{S}$ is the spin expectation and the precession vector $\vec{\Omega}_{\mathrm{BMT}}$ is in the form of [8]

$$\vec{\Omega}_{\mathrm{BMT}} = -\frac{e}{m}\left[\left(a + \frac{1}{\gamma}\right)\vec{B} - \frac{a\gamma}{\gamma+1}\vec{\beta}(\vec{\beta}\cdot\vec{B}) - \left(a + \frac{1}{\gamma+1}\right)\vec{\beta}\times\vec{E}\right], \tag{2}$$

where e and m are the particle charge and mass respectively, $\vec{\beta}$ and γ are the relativistic factors, $\vec{B}$ and $\vec{E}$ are the magnetic and electric fields, and the gyromagnetic anomaly a is approximately 0.0011597 for electrons and positrons. The precession vector can be decomposed into the periodic closed orbit term $\vec{\Omega}^{c.o}(s)$ and the other term brought by synchro-betatron motions $\vec{\omega}^{s.b}(\vec{u};s)$

$$\vec{\Omega}_{\mathrm{BMT}}(\vec{u};s) = \vec{\Omega}^{c.o}(s) + \vec{\omega}^{s.b}(\vec{u};s), \tag{3}$$

where s is the azimuthal position and vector $\vec{u} \equiv (x, x', y, y', z, \delta)$ denotes the phase space position of a particle with δ being the relative energy deviation $\delta = \Delta E/E_0$ [8]. The unit length one-turn periodic solution of the T-BMT equation on the closed orbit is denoted as $\hat{n}_0$, which is the stable spin direction on the closed orbit [9, 10]. In a perfectly aligned flat machine, arbitrary spins on the closed orbit will perform $a\gamma$ precessions around $\hat{n}_0$ during one orbital revolution, which is the closed orbit spin tune ν_0. Nevertheless, ν_0 will experience a slight deviation from $a\gamma$ when there are errors and misalignments in the machine [10].

The emission of synchrotron radiation when electrons and positrons are moving in the ring can enable spin flip which switches the spin direction between spin up and down, through the Sokolov-Ternov effect [11]. The slight difference in the transition rates between two spin states allows an accumulation of polarization along the opposite direction of the magnetic field for electrons. An equilibrium polarization level of $P_{ST} \simeq 92.38\%$ can be reached in uniform magnetic fields, while in arbitrary fields it can be estimated with the following equation [12, 13]

$$\vec{P}_{bks} = -\frac{8}{5\sqrt{3}}\hat{n}_0\frac{\oint \mathrm{d}s\frac{\hat{n}_0(s)\cdot\hat{b}(s)}{|\rho(s)|^3}}{\oint \mathrm{d}s\frac{\left[1-\frac{2}{9}(\hat{n}_0\cdot\hat{s})^2\right]}{|\rho(s)|^3}}, \tag{4}$$

where ρ represents the instantaneous bending radius, $\hat{b} = (\hat{s}\times\dot{\hat{s}})/|\dot{\hat{s}}|$ is the magnetic field direction, and $\hat{s}$ is the unit

* Work supported by the Swiss Accelerator Research and Technology (CHART)
† yi.wu@epfl.ch

ISBN: 978-3-95450-236-3 ISSN: 2673-7027 doi:10.18429/JACoW-eeFACT2022-TUZAS0104

vector of motion direction. The polarization is accumulated at a rate of

$$\tau_{bks}^{-1} = \frac{5\sqrt{3}}{8}\frac{r_e\gamma^5\hbar}{m_e}\frac{1}{C}\oint \mathrm{d}s\frac{\left[1-\frac{2}{9}\left(\hat{n}_0\cdot\hat{s}\right)^2\right]}{|\rho(s)|^3}, \tag{5}$$

where m_e is the electron mass and C is the machine circumference.

The spin diffusion caused by stochastic photon emissions during synchrotron radiation results in radiative depolarization, which competes with polarization accumulation, bringing an equilibrium polarization level that can be estimated via the Derbenev–Kondratenko–Mane (DKM) formula [14, 15],

$$P_{dk} = -\frac{8}{5\sqrt{3}} \times \frac{\oint \mathrm{d}s\left\langle \frac{1}{|\rho(s)|^3}\hat{b}\cdot\left(\hat{n}-\frac{\partial\hat{n}}{\partial\delta}\right)\right\rangle_s}{\oint \mathrm{d}s\left\langle \frac{1}{|\rho(s)|^3}\left(1-\frac{2}{9}\left(\hat{n}\cdot\hat{s}\right)^2+\frac{11}{18}\left(\frac{\partial\hat{n}}{\partial\delta}\right)^2\right)\right\rangle_s}, \tag{6}$$

where $\hat{n}(\vec{u};s)$ is the equilibrium polarization direction at each phase space and azimuthal position, and $\langle\,\rangle_s$ denotes the average over phase space at position s. Radiative depolarization is quantified by the spin-orbit coupling function $\partial\hat{n}/\partial\delta$, with the depolarization rate being

$$\tau_{dep}^{-1} = \frac{5\sqrt{3}}{8}\frac{r_e\gamma^5\hbar}{m_e}\frac{1}{C}\oint \mathrm{d}s\left\langle\frac{\frac{11}{18}\left(\frac{\partial\hat{n}}{\partial\delta}\right)^2}{|\rho(s)|^3}\right\rangle_s. \tag{7}$$

Spin-orbit resonances happen when spin precession is coherent with the disturbances experienced during synchro-betatron motions. The closed orbit spin tune satisfies the relation [9, 12]

$$\nu_0 = k + k_xQ_x + k_yQ_y + k_zQ_z, \tag{8}$$

at spin-orbit resonances, where k, k_x, k_y, k_z are integers, and Q_x, Q_y, Q_z are tunes of synchro-betatron motions. The equilibrium polarization level will be lower near spin-orbit resonances due to the particularly strong spin diffusion.

POLARIZATION SIMULATIONS

The spin polarization simulations in the FCC-ee at Z energy have been explored using Bmad, to evaluate the effects of machine imperfections on the achievable polarization level. Bmad [16] is an accelerator simulation toolkit that includes modules for spin-orbit simulations. The Tao module [17] in Bmad is based on the SLIM formalism [8, 18] and allows simulations of linearized orbital and spin motions, while the Long-Term Tracking module [19] uses Monte-Carlo spin tracking which reveals the full impact of lattice perturbations on spin polarization.

The FCC-ee lattice of version 217 at Z energy without solenoid has been used in this study, with nominal energy being 45.6 GeV. The numbers of integration steps within different types of elements in spin-orbit tracking have been determined using convergence tests [20]. An effective model as shown in Table 1 was created to generate small residual errors for different groups of elements in order to simulate the realistic orbits after lattice corrections. Misalignments of elements in three directions Δx, Δy, Δs, and angular misalignments around three axes $\Delta\theta$ (around $+y$ axis), $\Delta\phi$ (around $-x$ axis), $\Delta\psi$ (in $x-y$ plane) have been considered in the model. The values of misalignments are randomly generated, obeying truncated Gaussian distributions, truncated at $2.5\,\sigma$.

Linear Polarization Simulations

The influences of orbit distortions on equilibrium polarization in linear regime have been investigated via energy scans using the Tao module in Bmad. Figures 1 and 2 show the polarization levels at different energies using two error seeds generated from the effective model in Table 1. With the rms vertical orbit distortions of 43.7 µm and 148 µm at the nominal energy created by two seeds, equilibrium polarization levels of 91.56% and 83% can be achieved at 45.6 GeV respectively. A significant decrease of polarization can be observed when the machine operates near the first-order spin-orbit resonances $\nu_0 = k \pm Q_{x,y,z}$, where k is an integer and $Q_{x,y,z}$ represents synchro-betatron tunes.

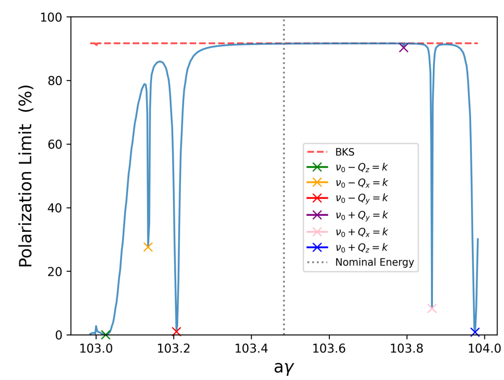

Figure 1: Energy scan using error seeds with $(\Delta y)_{\mathrm{rms}}$ = 43.7 µm

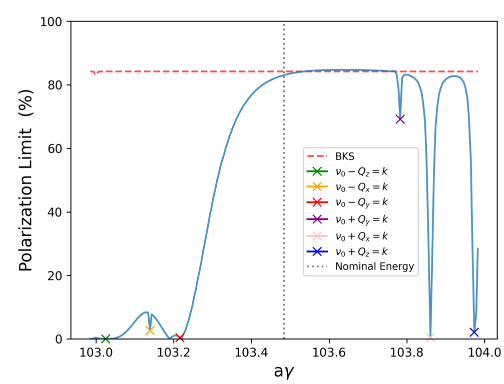

Figure 2: Energy scan using error seeds with $(\Delta y)_{\mathrm{rms}}$ = 148 µm

Compared with asymptotic polarization P_{eq}, the ratio between polarization accumulation time and depolarization

ISBN: 978-3-95450-236-3 ISSN: 2673-7027 doi:10.18429/JACoW-eeFACT2022-TUZAS0104

Table 1: An effective model for residual errors generation used in the spin-orbit simulations.

Type	$\sigma_{\Delta x}$ [μm]	$\sigma_{\Delta y}$ [μm]	$\sigma_{\Delta s}$ [μm]	$\sigma_{\Delta\psi}$ [μrad]	$\sigma_{\Delta\theta}$ [μrad]	$\sigma_{\Delta\phi}$ [μrad]
Arc quadrupole	0.1	0.1	0.1	2	2	2
Arc sextupole	0.1	0.1	0.1	2	2	2
Dipoles	0.1	0.1	0.1	2	0	0
IR quadrupole	0.1	0.1	0.1	2	2	2
IR sextupole	0.1	0.1	0.1	2	2	2

time τ_{bks}/τ_{dep} better reveals the depolarizing strength. It is related to the equilibrium polarization as

$$P_{eq} \simeq P_{bks}\frac{1}{1+\tau_{bks}/\tau_{dep}}. \tag{9}$$

Figures 3 and 4 show the depolarizing strengths at different energies using the same two error seeds as in Figure 1 and 2. It can be clearly seen that larger vertical orbit distortion results in a more significant depolarization effect at first-order spin-orbit resonances. The resonances are stronger near $a\gamma = 103$ compared to $a\gamma = 104$ due to periodic lattice structure and machine imperfections.

The energy scans of linear equilibrium spin polarization offer an illustration of the basic spin dynamics theory to first order, revealing the sensitivity of polarization curves to the orbits.

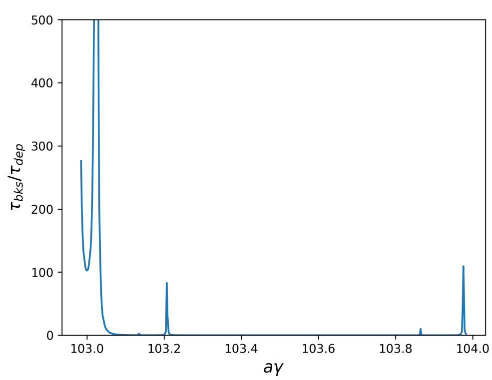

Figure 3: Depolarizing strength using error seeds with $(\Delta y)_{\mathrm{rms}} = 43.7$ μm

Nonlinear Spin Tracking Simulations

Linear spin simulations help to estimate the influence of first-order resonances. However, higher order spin resonances could be prominent at high energies and jeopardize the achievable polarization level. Nonlinear spin tracking simulations are therefore critical to evaluate the full impact of lattice imperfections on spins. The Long-Term Tracking module in Bmad has been used for Monte-Carlo spin tracking [19]. Starting from an initial level of P_0, the polarization build-up with time can be approximated as [9, 21]

$$\begin{aligned} P(t) &= P_{dk}\left[1-e^{-t/\tau_{dk}}\right] + P_0 e^{-t/\tau_{dk}} \\ &\simeq P_0 e^{-t/\tau_{dep}}. \end{aligned} \tag{10}$$

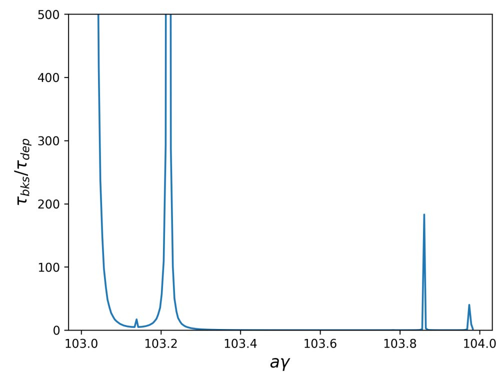

Figure 4: Depolarizing strength using error seeds with $(\Delta y)_{\mathrm{rms}} = 148$ μm

By tracking the polarization evolution of the initially polarized beam by turns, the depolarization rate τ_{dep} can be extracted by fitting the polarization build-up curve using Eq. (10). The equilibrium level can be estimated via Eq. (9), where P_{bks} and τ_{bks} can be computed in linear simulations.

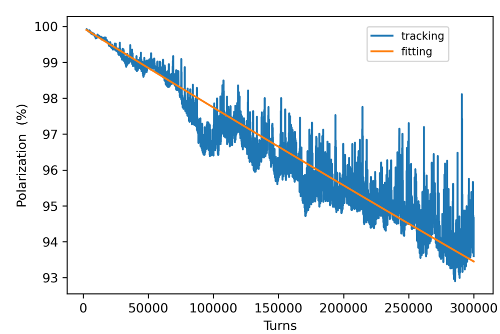

Figure 5: Polarization evolution of 10 electrons at $\nu_0 = k + Q_y - Q_z$

Figures 5 and 6 present two examples of polarization evolutions using 10 and 500 electrons respectively in nonlinear spin tracking simulations with PTC Bmad at one synchrotron sideband of the first-order vertical spin resonance $\nu_0 = k + Q_y - Q_z$. The equilibrium levels obtained from estimation are 0.15% and 0.099% respectively. Large fluctuations during evolution occur when using smaller amounts of particles as in Figure 5, resulting in R-squared value for data fitting evaluation being $R^2 \sim 0.89$, which indicates that the estimation accuracy is influenced in this case. The

ISBN: 978-3-95450-236-3 ISSN: 2673-7027 doi:10.18429/JACoW-eeFACT2022-TUZAS0104

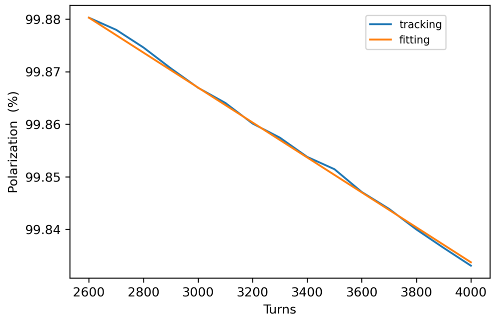

Figure 6: Polarization evolution of 500 electrons at $\nu_0 = k + Q_y - Q_z$

fitting precision is largely improved in the 500-electron case with $R^2 \sim 1$. Using a larger number of particles in nonlinear tracking enhances the estimation accuracy, while it also leads to a significant increase in the simulation time. Efforts will be made to overcome the challenges in simulation speed.

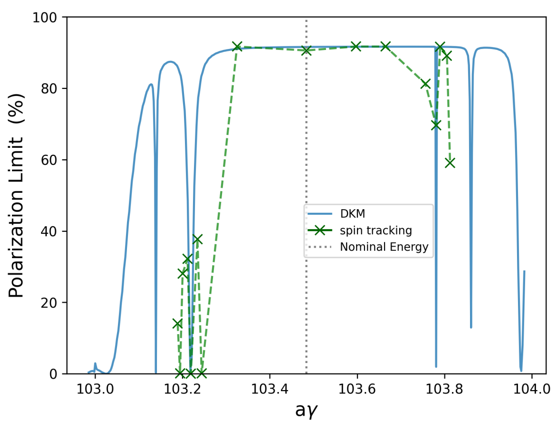

Figure 7: Polarization levels from linear and nonlinear spin simulations using the same error seed

A preliminary nonlinear spin tracking simulation has been conducted at several energies using 1000 particles tracked for 7000 turns via PTC Bmad. As shown in Figure 7, the nonlinear polarization is in good agreement with linear results. The first-order vertical resonances can be observed in both linear and nonlinear simulations, while higher order resonances such as two sidebands $\nu_0 = k + Q_y \pm Q_z$ can only be reflected in nonlinear spin tracking simulations. The equilibrium polarization near nominal energy remains sufficient for energy calibration.

CONCLUSION

High precision measurements are required in the FCC-ee to make the observation of new physics possible. Resonant depolarization is a promising method for the precise center-of-mass energy calibration in the FCC-ee at Z and W energies. A sufficient equilibrium polarization level should be guaranteed for this energy calibration method.

The early-stage explorations of the spin simulations in the FCC-ee using Bmad have been presented. The linear spin simulations reveal the depolarization effects near first-order spin-orbit resonances, while nonlinear spin trackings reflect all impacts of lattice perturbations. The sensitivity of spin polarization to lattice imperfections has been verified, which highlights the demand for a good closed orbit control. This work offers a promising outlook for the spin polarization studies in the FCC-ee.

REFERENCES

[1] A. Abada *et al.*, "FCC Physics Opportunities: Future Circular Collider Conceptual Design Report Volume 1," *European Physical Journal C*, vol. 79, no. 6, p. 474, 2019.

[2] A. Abada *et al.*, "FCC-ee: The Lepton Collider: Future Circular Collider Conceptual Design Report Volume 2," *European Physical Journal: Special Topics*, vol. 228, no. 2, pp. 261–623, 2019.

[3] A. Blondel, "PED Overview: Centre-of-mass energy calibration." https://indico.cern.ch/event/1064327/contributions/4893236/attachments/2452727/4203106/EPOL%202022-05-30.pdf.

[4] R. Assmann *et al.*, "The energy calibration of LEP in the 1993 scan," *Zeitschrift für Physik C Particles and Fields*, vol. 66, no. 4, pp. 567–582, 1995.

[5] A. Blondel *et al.*, "Polarization and Centre-of-mass Energy Calibration at FCC-ee," *arXiv preprint arXiv:1909.12245*, 2019.

[6] L. H. Thomas, "The kinematics of an electron with an axis," *The London, Edinburgh, and Dublin Philosophical Magazine and Journal of Science*, vol. 3, no. 13, pp. 1–22, 1927.

[7] V. Bargmann, L. Michel, and V. Telegdi, "Precession of the polarization of particles moving in a homogeneous electromagnetic field," *Physical Review Letters*, vol. 2, no. 10, p. 435, 1959.

[8] A. W. Chao, *Special Topics in Accelerator Physics*. World Scientific, 2022.

[9] A. W. Chao *et al.*, *Handbook of accelerator physics and engineering*. World scientific, 2013.

[10] D. P. Barber, "An Introduction to Spin Polarisation in Accelerators and Storage Rings." https://www.desy.de/~mpybar/CI-lectures-2014.pdf.

[11] A. Sokolov and M. Ternov, "On polarization and spin effects in the theory of synchrotron radiation," in *Sov. Phys.-Dokl.*, vol. 8, pp. 1203–1205, 1964.

ISBN: 978-3-95450-236-3 ISSN: 2673-7027 doi:10.18429/JACoW-eeFACT2022-TUZAS0104

[12] D. P. Barber, "Spin Dynamics and Simulation of Spin Motion in Storage Rings," in *AIP Conference Proceedings*, vol. 1008, pp. 82–90, American Institute of Physics, 2008.

[13] V. Baier, V. Katkov, and V. Strakhovenko, "Kinetics of Radiative Polarization," *Sov. Phys. JETP*, vol. 31, p. 908, 1970.

[14] Y. S. Derbenev and A. Kondratenko, "Polarization kinetics of particles in storage rings," *Sov. Phys. JETP*, vol. 37, no. 6, pp. 968–973, 1973.

[15] S. R. Mane, "Derivation of the equilibrium degree of polarization in high-energy electron storage rings," *Physical Review Letters*, vol. 57, no. 1, p. 78, 1986.

[16] D. Sagan, "Bmad, a subroutine library for relativistic charged-particle dynamics." https://www.classe.cornell.edu/bmad.

[17] D. Sagan, "The Tao Manual." https://www.classe.cornell.edu/bmad/tao.html.

[18] A. W. Chao, "Evaluation of Radiative Spin Polarization in an Electron Storage Ring," *Nuclear Instruments and Methods*, vol. 180, no. 1, pp. 29–36, 1981.

[19] D. Sagan, "Long Term Tracking Program." https://www.classe.cornell.edu/bmad/other_manuals.html, 2021.

[20] Y. Wu, "First Exploration of Spin Dynamics Simulations in FCC-ee for Depolarization Based Energy Calibration." presented at FCC Week May-June 2022, Sorbonne Université, Paris, France, https://indico.cern.ch/event/923801/contributions/4893334/.

[21] E. Gianfelice-Wendt, "The polarization code challenge." presented at FCC Week Nov. 2020, https://indico.cern.ch/event/923801/contributions/4044076/.

ISBN: 978-3-95450-236-3 ISSN: 2673-7027 doi:10.18429/JACoW-eeFACT2022-TUZAS0105

PROGRESS IN EIC POLARIZATION STUDIES FOR THE INJECTORS AND STORAGE RING

V. H. Ranjbar*, Brookhaven National Laboratory, Upton NY, USA
E. Gianfelice, Fermilab, Batavia, IL, USA

Abstract

We present recent progress in simulations and studies for the EIC's Electron Storage RING (ESR) and the EIC's polarized injector the Rapid Cycling Synchrotron.

INTRODUCTION

The Electron Ion Collider (EIC) to be built will collide polarized electrons and ions up to 140 GeV center of mass with a time averaged polarization of 70% and luminosity up to 10^{34} cm^{-2} s^{-1} (see Fig. 1). The EIC's Rapid Cycling Synchrotron (RCS) will accelerate 2 polarized electrons bunches from 400 MeV to energies of 5, 10 and 18 GeV and inject them into the EIC's Electron Storage Ring (ESR).These bunches will be stored between 4-6 minutes at 18 GeV in bunches parallel and anti-parallel to the dipole guide field. The time in store is determined by the polarization lifetime and the requirement to maintain average polarization at 70%. In this paper we study the impact of misalignments on polarization lifetime and approaches to correct and counter act their effects on lifetime.

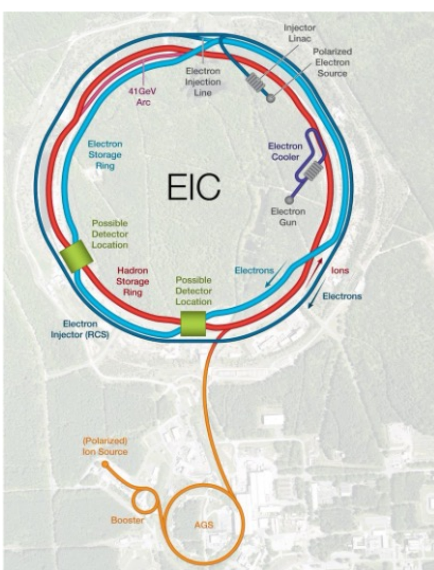

Figure 1: EIC Complex

The RCS injector is designed to accelerate polarized electrons maintaining 85% polarization. This is accomplished due to the special lattice design which avoids and minimizes the spin resonances in the acceleration range. We present progress on development of this lattice and studies of the impact of misalignments and approaches to correct for their effects on polarization.

* vranjbar@bnl.gov

POLARIZATION IN THE ESR

EIC experiments require an average polarization of at least 70% oriented in the longitudinal plane, using both helicities within the same store. The electrons will be stored in the ESR at energies of 5, 10 and 18 GeV. The radiative effects on polarization in an electron storage ring is given by the Sokolov-Ternov effect. In an ideal planar ring with out spin rotators, the periodic solution to the Thomas-BMT equation, $\hat{n}_0$, is vertical and electron polarization builds up anti-parallel wrt the dipole guide field. The asymptotic polarization is P_∞= 92.4%. The rate at which the polarization is built up is given by,

$$\tau_p^{-1} = \frac{5\sqrt{3}}{8}\frac{r_e\hbar\gamma^5}{m_0C}\oint\frac{ds}{|\rho|^3}\,. \qquad (1)$$

Asymptotic Polarization in ESR

In an actual ring, $\hat{n}_0(s)$ is not vertical and the beam has a finite vertical size, thus photon emission leads to spin diffusion that lowers the asymptotic polarization. Because experiments require the simultaneous storage of electron bunches with both spin helicity, Sokolov-Ternov effect cannot be used to self-polarize the beam. Thus a full energy electron injector is needed and the EIC will use the RCS to inject with 85% polarization in the desired spin orientation. As well in the ESR since longitudinal polarization is required, the spin will be brought into the longitudinal direction at the interaction point (IP) using a combination of solenoids and dipoles to the left and right of the IP.

Depending on the actual equilibrium polarization, the Sokolov-Ternov effect can cause the rapid decay of a highly polarized beam. This decay is described using,

$$P(t) = P_\infty(1-e^{t/\tau_P}) + P(0)e^{-t/\tau_P}\,. \qquad (2)$$

Here the polarization time constant can be estimated using,

$$\frac{1}{\tau_p} \approx \frac{1}{\tau_{BKS}} + \frac{1}{\tau_d}$$
$$P_\infty \approx \frac{\tau_p}{\tau_{BKS}}P_{BKS}\,. \qquad (3)$$

Here P_{BKS} and τ_{BKS} are the Baier-Katkov-Strakhovenko generalization of the Sokolov-Ternov quantities when $\hat{n}_0$ is not everywhere perpendicular to the velocity. These values can be calculated for a given lattice. Thus τ_d and P_∞ depends on the actual machine. While τ_d is the spin diffusion time for a given lattice, this is determined using direct spin-orbit tracking. We use MADX to manage the optics and misalignments together with the spin tracking codes: SITF

ISBN: 978-3-95450-236-3 ISSN: 2673-7027 doi:10.18429/JACoW-eeFACT2022-TUZAS0105

(part of SITROS package) for computing polarization in linear spin motion approximation (as SLIM, but it digests thick lenses) and SITROS Monte Carlo tracking of particles with stochastic photons emission at user chosen dipoles. First $\hat{n}_0$ is calculated and then spins are initialized parallel to it and tracked for several thousand turns. From this the diffusion time τ_d and the asymptotic polarization P_∞ is determined.

The decay profiles for 85% polarized bunches with initial spin oriented up and down are shown for different asymptotic polarization values in Fig. 2.

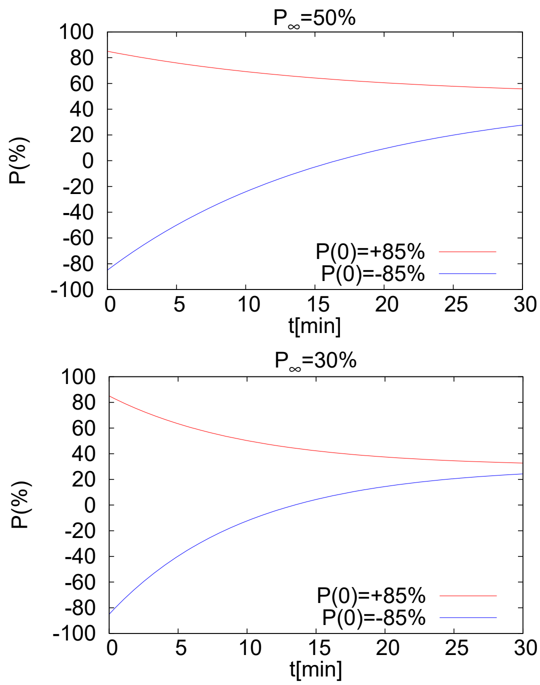

Figure 2: Polarization versus time for two different P_∞.

To maintain an average polarization of 70% we show the run time as a function of P_∞ for spin up and spin down bunches in Fig. 3

Misalignment and Correction for ESR

Since 2017 the ESR optics have been undergoing adjustments, as such we have considered 2 different iterations of the ESR optics for the 18 GeV case. We first considered optics developed in 2019 (version 5.2) with one collision IP and a beta minimum of 0.048m. For this optics $P_{BKS} \approx$ 82.7% and $\tau_{BKS} \approx 35.5$ minutes. We next considered optics from 2022 (version 5.5) with one collision IP and a beta minimum of 0.057m. For this optics $P_{BKS} \approx 86.5\%$ and $\tau_{BKS} \approx 36.8$ minutes. In both cases the fractional tunes are $q_x = 0.12$ and $q_y = 0.10$ close to the integer and the difference linear coupling resonances. The required vertical beam size at the IP should be $\sigma_y^* \approx 12\,\mu\text{m}$ so that it can match the proton beam size.

We applied random misalignments to the quadrupoles in the lattice using an RMS of 200 µm for the horizontal and vertical displacement and a roll angle of 200 µrad. A generous correction scheme was adopted consisting of a double plane reading BPM and a horizontal and a vertical

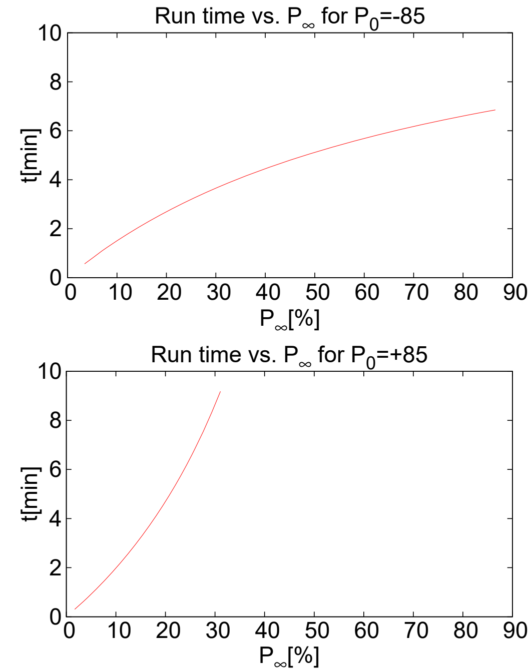

Figure 3: Run time versus P_∞ necessary to maintain average polarization of 70%.

corrector close to each quadrupole. This yielded RMS orbit distortions of 4.80 and 11.6 mm in the horizontal and vertical plane respectively. Then correcting this orbit down to 0.4 to 0.2 mm RMS was not sufficient to recover decent average polarization as you can see in Fig. 4. No sizable improvement was observed by correcting betatron coupling and $\delta\hat{n}_0$.

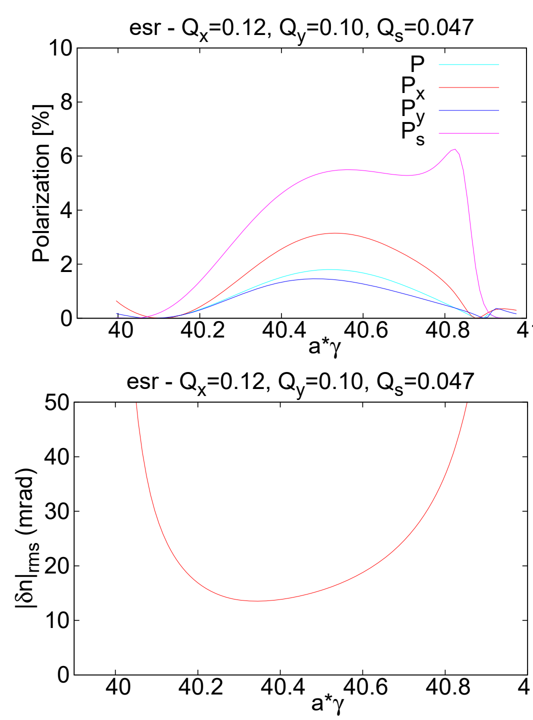

Figure 4: Expected polarization from linear calculation (top) and $\delta\hat{n}_0$ (bottom) for ESR optics 5.2 in presence of misalignments and loose orbit correction.

ISBN: 978-3-95450-236-3 ISSN: 2673-7027 doi:10.18429/JACoW-eeFACT2022-TUZAS0105

Next correcting down to 0.04 mm RMS along with the betatron coupling restored the 40% level of asymptotic polarization (see Figs. 5 and 6). However the beam size remained about 6 times too small for the matching proton beam.

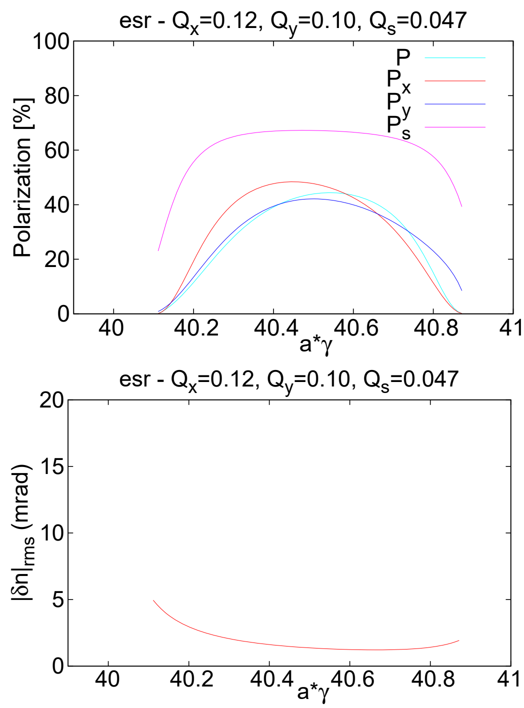

Figure 5: Expected polarization from linear calculation (top) and $\delta\hat{n}_0$ (bottom) for ESR optics 5.2 in presence of misalignments and tighten orbit correction.

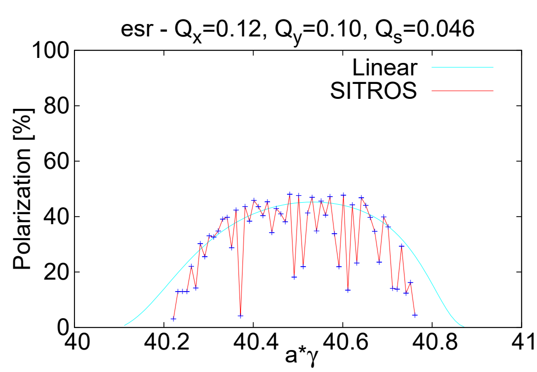

Figure 6: Expected polarization from tracking, 5.2 optics. The cyan line refers to the linear calculation. With respect to Fig. 5 the correction of $\delta\hat{n}_0$ was added.

There are several approaches to increase the vertical beam size at the colliding IP. Local coupling was initially considered, however beam-beam simulation studies have shown that this approach has too negative an impact on the luminosity. Another approach is to use a long vertical bump through the arc sextupoles exciting betatron coupling. This however had a very bad impact on polarization performance for the ESR 5.2. Finally a vertical orbit bump in a straight section without quadrupoles was explored. This could work if this vertical dispersion section is spin-matched. Alternatively a convenient location for the 5.2 lattice was found at 2528 m from IP6. Using this bump the vertical emittance could be increased to 3 nm with acceptable loss of polarization (see Fig. 7).

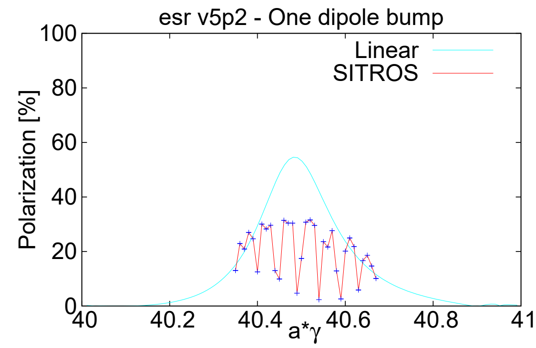

Figure 7: Expected polarization from tracking in presence of a vertical dipole bump at 2528 m in the 5.2 optics, aiming to $\epsilon_y \approx 3$ nm.

In the 5.5 optics version the rotator scheme was changed leading to an asymptotic peak polarization of 34% at $a\gamma = 40.5$ even for the machine without misalignments. The same rms misalignments as for the 5.2 optics were introduced. For this optics the somewhat loose correction was sufficient in restoring large polarization, without need of betatron coupling correction (see Fig. 8). The vertical beam size obtained by SITROS tracking is 10.2 µm at the IP, in agreement with the analytical value of 11.1 µm, and about what needed for matching the proton beam vertical size, without using any extra emittance knob.

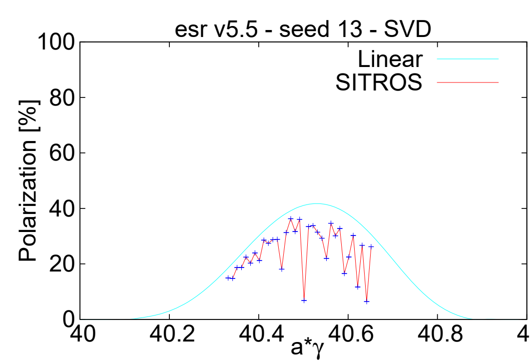

Figure 8: Expected polarization from tracking, 5.5 optics. The cyan line refers to the linear calculation.

POLARIZATION IN THE RCS

A Rapid Cycling Synchrotron (RCS) will be used to accelerate, accumulate and inject up two 28 nC polarized electron bunches into the EIC electron storage ring (ESR) per second [1]. In the peak current regimes, the RCS will take two trains of four 7 nC bunches for a total of 8 bunches injected from the LINAC. These will be injected at 400 MeV at a rate of two 7 nC bunches per LINAC cycle. Each LINAC cycle should take 100 Hz requiring at least 40 msecs to fill the RCS. We have budgeted 54 msecs for the whole injection process as shown in Fig. 9 [2]. These bunches will be injected into

ISBN: 978-3-95450-236-3 ISSN: 2673-7027 doi:10.18429/JACoW-eeFACT2022-TUZAS0105

two trains of four adjacent 591 MHz buckets. Since a rise time of 1.69 ns is necessary to inject into neighboring buckets a special system of RF-crab like cavity kickers will be used to generate the necessary kick profile [3]. The two bunch trains will then be merged into two 28 nC bunches. These will then be accelerated at a maximum ramp rate of 0.176 GeV/ms to their final energy of 5, or 10 GeV and extracted on a 20 msec flattop. In the case of 18 GeV only two lower charge bunches will be injected and merged per train. These yield two 11.7 nC merged bunches which will be accelerated and extracted at 18 GeV. The dipole power supply profile is illustrated in Fig. 10 and the main parameters of the RCS are summarized in Table 1.

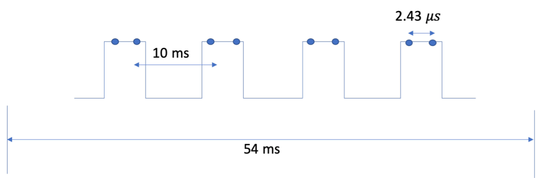

Figure 9: RCS injection pulse structure.

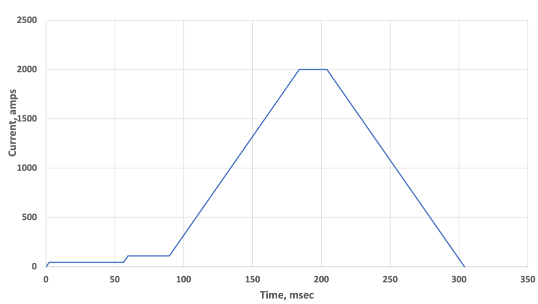

Figure 10: Power supply profile of RCS Ramp

RCS SPIN RESONANCE-FREE DESIGN

A spin resonance-free design has been proposed in Ref. [4]. In a typical circular lattice where the field is dominated by the guide dipole field, the rate of spin precession per turn, or spin tune (ν_s), is determined by the energy and conveniently expressed as $a\gamma$, where $a = \frac{g-2}{2}$ is the anomalous magnetic moment coefficient for an electron (0.001159), and γ is the relativistic factor. For the case of a depolarizing intrinsic spin resonance this occurs whenever the spin tune $a\gamma = nP \pm Q_y$. Here n is an arbitrary integer, P is the periodicity of the lattice, and Q_y is the vertical betatron tune.

Thus the first two important intrinsic spin resonances that an accelerating electron will encounter occur at $a\gamma = Q_y$ and at $a\gamma = P - Q_y$ (for $P > Q_y$) . If we now ensure that both Q_y and $P - Q_y$ are greater than the maximum $a\gamma$ value, (or Q_y is greater and $P - Q_y$ is less than the lowest $a\gamma$ value), then all the important intrinsic spin depolarizing resonances will be avoided.

We chose $P = 96$, constraining the integer part of the vertical betatron tune to be $41 < [Q_y] < 55$, since we accelerate to energies less than $a\gamma = 41$. Here $[Q_y]$ indicates the nearest integer of the vertical betatron tune. We chose $[Q_y] = 50$. As a result, the two first intrinsic resonances will occur near $a\gamma = 50$, and $a\gamma = 96 - 50 = 46$.

A side benefit is that in addition to the intrinsic resonances, the imperfection resonances are also minimized due to the design of this lattice. This is because the strongest imperfection resonances, like the intrinsic resonances for a pure ring, will be at $nP \pm [Q_y]$.

RCS Geometry

The RCS geometry has to fit inside the RHIC tunnel which resembles a hexagon with rounded corners rather than a circle, and therefore has a natural periodicity of 6 which spoils the 96 periodicity we want to accomplish. However the spin precession, advances by $a\gamma$, only in the dipoles, so one can maintain the periodicity of 96 from the point of view of $a\gamma$ precession. This can be accomplished by designing the straight sections such that each has a betatron phase advance equal to 2π. In this way the straight sections will not contribute to the integral that defines the strength of the spin resonance (see Fig. 11). Thus we can maintain the 96 super-periodicity from the point of view of the spin precession.

The lattice incorporates the existing RHIC straight sections that do not contribute to the intrinsic spin resonance strength, thus preserving the 96 periodicity from a spin precession point of view. The proposed layout for the RCS places it at a radius outside of the existing RHIC beam line but within the tunnel.

RCS Spin Transparent Arc Connecting Region

Experiments are located at interaction regions IP6 and IP8. At these locations the RCS beamline needs to bypass the detector achieving greater than 5 m displacement from the center of the IP based on the current sPHENIX and eSTAR detector design. This displacement is achieved by moving the last three and first three dipoles from the arcs around IP6 and IP8 towards the center of the IP and to two other symmetric locations in the straight section. In this

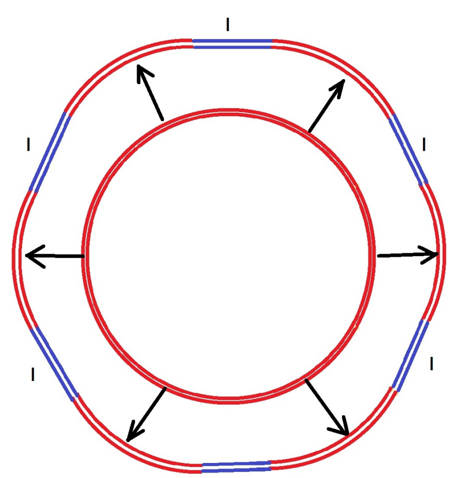

Figure 11: Projecting the pure ring lattice with 96 superperiodicity onto the RHIC six fold periodic ring.

ISBN: 978-3-95450-236-3 ISSN: 2673-7027 doi:10.18429/JACoW-eeFACT2022-TUZAS0105

Table 1: RCS injector Parameters

Parameter	5 GeV	10 GeV	18 GeV
Injection energy [MeV]		400	
Momentum compaction α_c		0.000219	
Max relative pol. loss		5%	
Circumference [m]		3846.17	
Ramping repetition rate [Hz]		1	
Acceleration time [ms], [turns]		100, 8000	
Total number of "spin effective" superperiods		96	
Horizontal tune		58.8	
Vertical tune		64.2	
Round beam pipe inner diameter [mm]		32.9	
Number of bunches injected	8	8	2
Charge per bunch at injection [nC]	7	7	5.5
Number of bunches at extraction		2	
Radio frequency [MHz]		591	
Total Cavity peak Voltage [MV]		60	
Bunching Cavity 1 [MHz]		295.5	
Bunching Cavity 2 [MHz]		147.8	
Bunch length injection [ps]		40	
Bunch length extraction [ps]	23.3	23.3	30
Hor. and Ver. emittance normalized (inj.) [mm-mrad]		40, 40	
Emittances at RCS extraction $\varepsilon_x/\varepsilon_y$ [nm]	20/2	20/1.2	24/2
RMS energy deviation at injection dp/p [10^{-3}]		2.5	
RMS energy deviation at extraction dp/p [10^-3]	0.68	0.58	1.09

configuration the RCS beam trajectory misses the detector center by 3.86 m and avoids the other potential obstructions in the tunnel. In the remaining IP2, IP4, IP10 and IP12 a geometry is adopted which yields an 153 m long straight section at the center of the IP. This geometry is accomplished also by moving three dipoles from the arcs on either end. The long straight is necessary to accommodate the RF system modules located at IP10, but we maintain this geometry through the remaining IP's.

Since original design, the RCS lattice has undergone two major revisions to avoid obstructions of walls, other beamlines and to remove all RCS magnets from the detector hall. This has resulted in the maximum beta function increasing from 70m to 120m. We have managed to maintain the zero polarization losses on ramp due to intrinsic spin resonances. As well the off-momentum dynamic aperture has been increased from 1% to 1.5% [5].

In this paper we focus on the aspects of the polarization transmission for the new design. In particular we study the impact of misalignment and field errors.

Impact of Misalignments

Initial efforts with the new RCS lattice layout yielded optics which had very little beta-beat and a large off-momentum aperture. The estimated polarization loss at the level of 5 sigma also yielded polarization losses due to intrinsics less than 1%. In the past we would use an arbitrary metric of polarization transmission for a 1000 mm-mrad rms emittance beam distribution. This of course was orders of magnitude higher than our physical aperture would permit. Previous lattices yielded intrinsic spin resonance induced polarization loss as estimated by DEPOL of under 5% at 1000 mm-mrad. This initial lattice yielded transmissions of 15% at 1000 mm-mrad, yet at the relevant operating emittances (40 mm-mrad) we shouldn't have seen any polarization loss. However studying the effect of imperfection spin resonances driven by closed orbit distortions showed a lower threshold in terms of RMS orbit distortion for polarization loss. This of course is to be expected since it is well understood that the strength of both imperfection and intrinsic spin resonances are correlated due to their shared harmonic structure. Thus reducing the strength of the intrinsic spin resonances has the added benefit of reducing the strength of the average imperfection spin resonances. We revisited the RCS optics design and further pushed the intrinsic induced polarization losses to 8%, this did introduce some level of beta-beating however the overall off-momentum dynamic aperture was recovered and the sensitivity of the imperfections spin resonances to RMS orbit distortions was reduced as can be seen in Fig. 12

These results were confirmed using direct spin-orbit tracking in Zgoubi [6, 7] considering misalignments on the level of 0.6 mm RMS in the vertical plane and 0.3 mm RMS in the horizontal plane.

Intrinsic resonance as calculated by DEPOL yield no cumulative depolarization loss for a beam with a vertical emittance of 40 mm-mrad rms normalized emittance (RCS's emittance at injection which falls to near zero by 18 GeV).

ISBN: 978-3-95450-236-3 ISSN: 2673-7027 doi:10.18429/JACoW-eeFACT2022-TUZAS0105

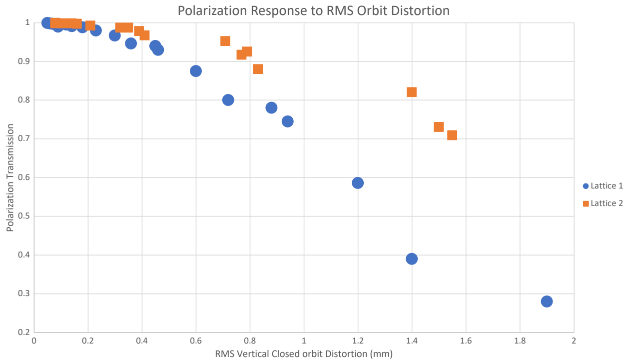

Figure 12: Comparison of polarization transmission due to imperfection spin resonances as function of RMS orbit distortion. Lattice 1, was our first RCS optics attempt with 15% intrinsic resonance induced losses at RMS emittance of 1000 mm-mrad. Lattice 2 was our second and last RCS optics configuration with 8% losses at the same RMS emittance. This reduced imperfection spin resonance sensitivity as can be seen in the plot.

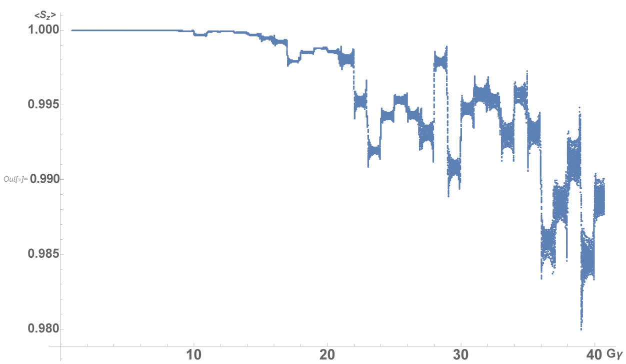

Figure 13: 13 particle tracking with 0.6 mm RMS vertical and 0.3 mm RMS horizontal closed orbit distortion.

Imperfections could however potentially cause greater than 5% losses during ramp. Due primarily to quadrupole misalignment and dipole rolls. But these effects can be controlled to bring our losses below 5% on ramp. Orbit Smoothing and Imperfection bumps

CONCLUSION

ESR studies show that the sensitivity to errors for different optics are a function of different $\gamma\frac{d\hat{n}}{d\gamma}$. Using the current rotator scheme the unperturbed polarization is much lower yet since the machine being less sensitive to errors it does not need an aggressive correction approach which may challenge the ability of our orbit correction resolution. Thus we can employ a correction approach similar to what was used in HERAe. Additionally this new lattice may be not require an intervention to increase the vertical beam size at the collision point. For the RCS, studies show that Polarization losses in this lattice are driven by imperfections. Intrinsic resonances are so weak that even large field distortions should be tolerable. It is projected that corrections down to < 0.5 mm rms should be sufficient to keep losses < 5% during the 18 GeV Ramp.

ACKNOWLEDGEMENTS

Work supported by Brookhaven Science Associates, LLC under Contract No. DE-SC0012704 and by Fermi Research Alliance, LLC under Contract No. DE-AC02-07CH11359 with the U.S. Department of Energy, Office of Science, Office of High Energy Physics. This research used resources of the National Energy Research Scientific Computing Center (NERSC), a U.S. Department of Energy Office of Science User Facility located at Lawrence Berkeley National Laboratory, operated under Contract No. DE-AC02-05CH11231 using NERSC award ERCAP0017154.

REFERENCES

[1] C. Montag *et al.*, "Electron-ion collider design status," in *Proc. 13th Int. Particle Accelerator Conf. (IPAC'22)*, Bangkok, Thailand, Jun. 2022, pp. 1954–1957. doi:10.18429/JACoW-IPAC2022-WEPOPT044

[2] E. Wang *et al.*, "The design of a high charge polarized preinjector for the electron-ion collider," in *Proc. 12th Int. Particle Accelerator Conf. (IPAC'21)*, Campinas, Brazil, May 2021, pp. 1428–1430. doi:10.18429/JACoW-IPAC2021-TUPAB037

[3] G. T. Park *et al.*, "RF harmonic kicker R&D demonstration and its application to the RCS injection of the EIC," in *Proc. 12th Int. Particle Accelerator Conf. (IPAC'21)*, Campinas, Brazil, May 2021, pp. 2632–2635. doi:10.18429/JACoW-IPAC2021-WEPAB019

[4] V. H. Ranjbar *et al.*, "Spin resonance free electron ring injector," *Phys. Rev. Accel. Beams*, vol. 21, no. 11, p. 111003, 2018. doi:10.1103/PhysRevAccelBeams.21.111003

[5] H. Lovelace III, F. Lin, C. Montag, and V. Ranjbar, "The EIC rapid cycling synchrotron dynamic aperture optimization," in *Proc. 13th Int. Particle Accelerator Conf. (IPAC'22)*, Bangkok, Thailand, Jun. 2022, pp. 210–213. doi:10.18429/JACoW-IPAC2022-MOPOST055

[6] F. Méot, "The ray-tracing code Zgoubi - Status," *Nucl. Instrum. Methods Sect. A*, vol. 767, p. 112125, 2014. doi:10.1016/j.nima.2014.07.022

[7] F. Méot, Zgoubi users guide, http://www.osti.gov/scitech/biblio/1062013

ISBN: 978-3-95450-236-3 ISSN: 2673-7027 doi:10.18429/JACoW-eeFACT2022-WEXAT0101

BEAM-BEAM INTERACTION IN SuperKEKB: SIMULATIONS AND EXPERIMENTAL RESULTS

D. Zhou*, K. Ohmi, Y. Funakoshi, Y. Ohnishi, KEK, Tsukuba, Japan
Y. Zhang, IHEP, Beijing, China

Abstract

The beam-beam interaction is one of the most critical factors determining the luminosity performance of SuperKEKB. Simulations and experimental results from SuperKEKB have shown that a complete understanding of the beam-beam effects demands reliable models of 1) the nonlinear beam-beam interaction at the interaction point, 2) the one-turn lattice transfer map with machine imperfections, and 3) other intensity-dependent collective effects. The interplay of these factors makes it difficult to predict the luminosity performance of SuperKEKB via simulations.

INTRODUCTION

This paper continues the authors' previous work to discuss the beam-beam effects on luminosity in SuperKEKB [1]. SuperKEKB commissioning had three phases: Phase-1 [2, 3] (February - June 2016, without installation of the final focusing superconducting QCS magnets and roll-in of Belle II detector), Phase-2 [4] (February - July 2018, with QCS and Belle II, but without the vertex detector), and Phase-3 [5] (from March 2019 until present with the full Belle II detector). Beam commissioning without collisions in Phase-1 achieved small vertical emittances of less than 10 pm for both beams, which is essential for high luminosity. Machine tuning with collisions in Phase-2 confirmed the nano-beam collision scheme [6], i.e., collision with a large crossing angle and vertical beta function β_y^* at the IP much smaller than bunch length σ_z. However, without the CW, the beam-beam (BB) driven vertical emittance blowup was severe, causing degradation of specific luminosity (L_{sp}) as bunch currents increased.

The uncontrollable blowup in vertical emittances sets a severe limit on the luminosity performance and motivated the installation of the CW in SuperKEKB [7]. Beam commissioning with the CW at SuperKEKB has been successful with $\beta_y^* = 1$ and 0.8 mm [7]. Experiments have shown that the CW effectively suppresses vertical blowup and allows larger beam currents to be stored in the rings [8]. On Jun. 22, 2022, a luminosity record of 4.71×10^{34} cm^{-2}s^{-1} was achieved at SuperKEKB with $\beta_y^* = 1$ mm and total beam currents $I_+/I_- = 1.46/1.145$ A [9].

LUMINOSITY PERFORMANCE WITH CRAB WAIST

Since April 2020, the crab waist (CW) has been implemented at SuperKEKB to suppress beam-beam resonances [10, 11]. Luminosity performance has been improving with the following observations (see Refs. [7, 8] for reviews): 1) Luminosity performance became closer to the predictions of simulations; 2) Balanced collision (i.e., $\sigma_{y+}^* \approx \sigma_{y-}^*$, the vertical beam sizes at the IP are close to each other) was achieved with careful tuning knobs; 3) The fractional working point could be set around the design values (.53, .57); 4) The total beam currents were not limited by BB blowup, but by injection power and by machine failures of sudden beam losses (SBLs, their sources are unclear so far); 5) There still exists an unexpected degradation of L_sp vs. product of bunch currents (see Figs. 1 and 4). In particular, increasing the beam current does not give large increases in luminosity.

Figures 1, 2 and 3 compare the L_{sp} and transverse beam sizes at the IP from strong-strong BB simulations and measurements using X-ray monitors (XRMs). The machine parameters of 2022.04.05 in Table 1 are used for BB simulations. Optics functions at the IP and the XRMs calculated from a lattice model are used to estimate the beam sizes at the IP in measurements. In both simulations and experiments, the luminosity is sensitive to the vertical beam sizes at the IP. With the standard settings of 40% and 80% CW strengths in the experiments, respectively, for HER and LER (40% CW strength was set for HER due to a technical constraint), the decrease of L_{sp} in strong-strong BB simulation is mainly attributed to bunch lengthening due to the longitudinal wakefields and weak vertical blowup of HER beam due to insufficient CW strength. However, experimental results showed a much faster L_{sp} decrease as bunch currents increase. The sources of luminosity degradation are discussed in the next section. The plots also show simulations with the CW strengths varied. It is seen that the L_{sp} drop in simulations correlates with BB-driven blowup in the positron beam because its vertical fractional tune .589 is close to the 5th-order BB resonances.

Figures 4, 5 and 6 show a comparison of simulations and measurements with machine conditions of 2021. One can see that the machine operation after April of 2022 showed gradual beam-size blowup as the bunch currents were increased (see Figs. 2 and 3); while in 2021, the beam-size blowup was severe for both e+ and e- beams. At that time, it was difficult to achieve a balanced collision (i.e., $\sigma_{y+}^* \approx \sigma_{y-}^*$). A "flip-flop" blowup appeared when the bunch-current product $I_{b+}I_{b-} \gtrsim 0.4$ mA^2: When one beam was tuned to have a small vertical beam size at IP, another beam blew up severely. This severe blowup at high bunch currents was believed to be related to the "-1 mode instability" of the positron beam, which was driven by the interplay of vertical impedance (dominated by small-gap collimators) and the bunch-by-bunch (BxB) feedback (FB) system as discussed in detail in

* dmzhou@post.kek.jp

ISBN: 978-3-95450-236-3 ISSN: 2673-7027 doi:10.18429/JACoW-eeFACT2022-WEXAT0101

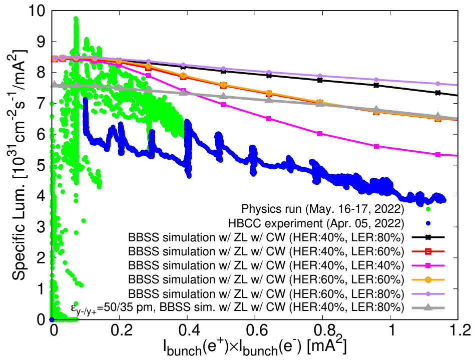

Figure 1: L_{sp} predicted by BBSS [12] simulations with the inclusion of longitudinal impedances and from experiments of high-bunch current collision (HBCC) machine study (blue dots) and physics run (green dots) in 2022. During the HBCC machine study, the collision for $I_{b+}I_{b-} < 0.4$ mA^2 was not optimized, resulting in lower L_{sp} than the physics run.

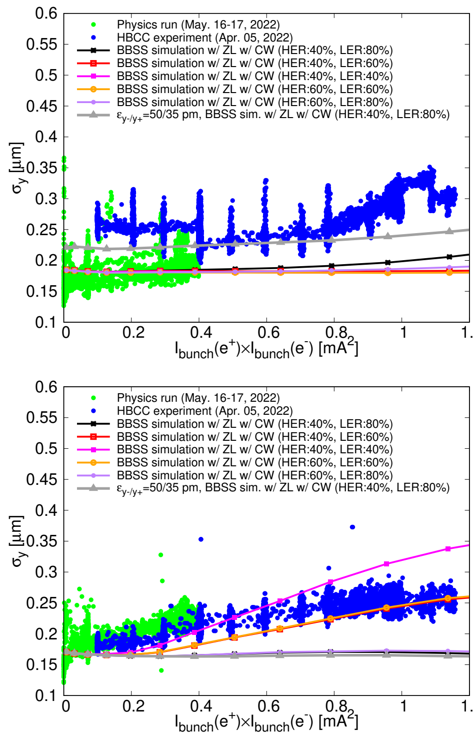

Figure 2: Vertical beam sizes of electron (upper) and positron (lower) beams at the IP (corresponding to Fig. 1) predicted by BBSS simulations compared with experiments. The dots and lines with the same colors in the upper and lower plots correspond to the same machine conditions.

Ref. [13]. After fine-tuning the BxB FB system in March of 2022, the "-1 mode instability" was suppressed significantly, and the beam-size blowup became less severe as shown in Figs. 2 and 3.

During physics runs or machine studies, the horizontal blowup in both beams has been observed in qualitative agreement with BB simulations. Machine tunings showed the horizontal blowup was sensitive to the horizontal tune and affected the injection efficiency. This can be explained as

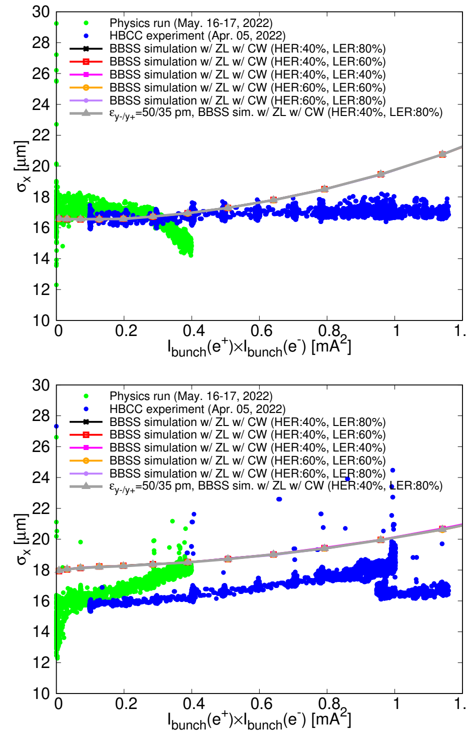

Figure 3: Horizontal beam sizes of electron (upper) and positron (lower) beams at the IP (corresponding to Fig. 1) predicted by BBSS simulations compared with experiments. The dots and lines with the same colors in the upper and lower plots correspond to the same machine conditions. The green dots in the upper figure are unreliable because of failure in the XRM. The horizontal tune of the e+ beam was changed during the HBCC study, resulting in a decrease of σ_x for $I_{b+}I_{b-} > 0.95$ mA^2.

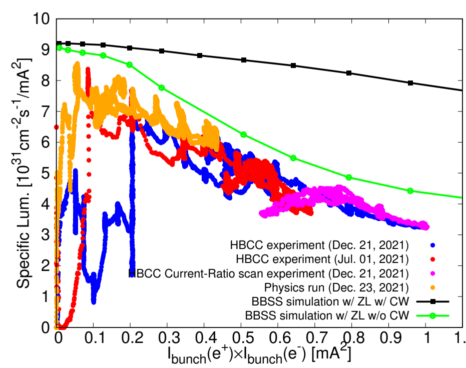

Figure 4: L_{sp} predicted by BBSS simulations with the inclusion of longitudinal impedances and from experiments of HBCC machine studies (blue, red, and magenta dots) and physics run (orange dots) in 2021.

follows: After installing the CW, both LER and HER have been operated with the horizontal tunes between the synchro-betatron resonances $\nu_x - \nu_s = N/2$ and $\nu_x - 2\nu_s = N/2$ (see Table 1). The beams' footprints spread in the tune space because of beam-beam, impedance effects, and lattice nonlinearity. When the tune footprint touches the resonance lines, the beam lifetime reduces, and extra beam losses appear in the injected bunches.

ISBN: 978-3-95450-236-3 ISSN: 2673-7027 doi:10.18429/JACoW-eeFACT2022-WEXAT0101

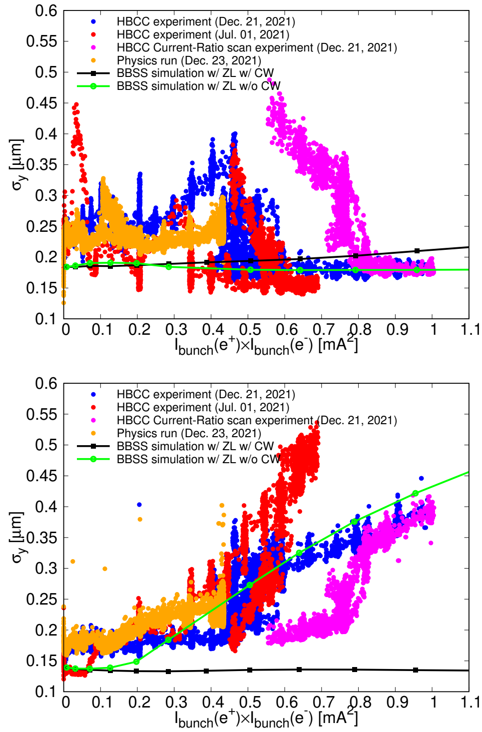

Figure 5: Vertical beam sizes of electron (upper) and positron (lower) beams at the IP (corresponding to Fig. 4) predicted by BBSS simulations compared with experiments. The dots and lines with the same colors in the upper and lower plots correspond to the same machine conditions.

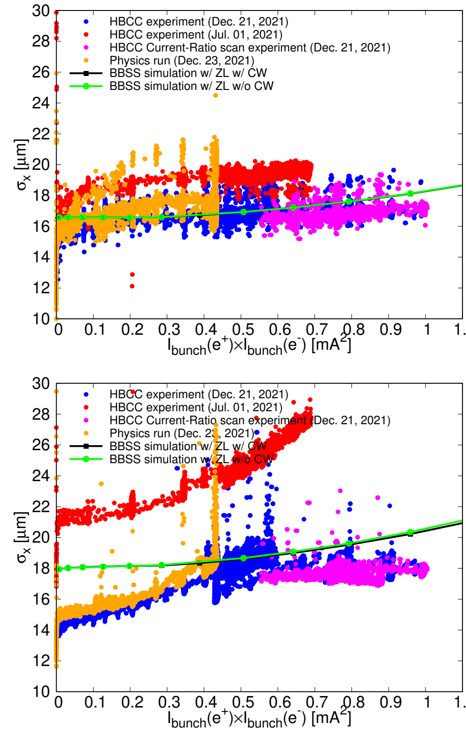

Figure 6: Horizontal beam sizes of electron (upper) and positron (lower) beams at the IP (corresponding to Fig. 4) predicted by BBSS simulations compared with experiments. The dots and lines with the same colors in the upper and lower plots correspond to the same machine conditions. For $I_{b+}I_{b-} \geq 0.4$ mA^2, the horizontal tune of the positron beam was tuned to suppress the horizontal blowup, which helped improve the injection efficiency.

Table 1: SuperKEKB machine parameters for machine operation on Dec. 21, 2021, and on Apr. 5, 2022, respectively. The vertical emittances are values measured by X-ray monitors without collisions.

Parameter	2021.12.21		2022.04.05	
	LER	HER	LER	HER
I_b (mA)	1.0	0.8	0.71	0.57
ϵ_x (nm)	4.0	4.6	4.0	4.6
ϵ_y (pm)	20	35	30	35
β_x (mm)	80	60	80	60
β_y (mm)	1	1	1	1
σ_{z0} (mm)	4.6	5.0	4.6	5.1
ν_x	44.524	45.53	44.524	45.532
ν_y	46.589	43.572	46.589	43.572
ν_s	0.023	0.027	0.023	0.027
Crab waist ratio	80%	40%	80%	40%
N_b	393		1174	

SOURCES OF LUMINOSITY DEGRADATION

Known Sources

Simulations and experiments have identified the known sources of luminosity degradation: 1) Bunch lengthening driven by longitudinal impedance. The scaling law of specific luminosity shows $L_{sp} \propto 1/\sqrt{\sigma_{z+}^2 + \sigma_{z-}^2}$. Simulations using impedance models predict $\sigma_z(I_b) = \sigma_{z0} + A \cdot I_b$ with I_b the bunch current and A about 1 mm/mA for both rings, while measurements using streak cameras showed A to be about 2 mm/mA. The sources of discrepancy in simulated and measured bunch lengthening are under investigation. Nevertheless, the bunch lengthening is expected to cause a loss of geometric luminosity by order of 10% at the bunch current product of $I_{b+}I_{b-} = 1$ mA^2. 2) Chromatic couplings. Their effects on luminosity were recognized at KEKB [14]. For SuperKEKB, rotatable skew-sextupoles are installed in LER, and dedicated skew-sextupoles are installed in HER to control the global chromatic coupling (see Ref. [15]). Simulations showed that chromatic couplings from the nonlinear IR can cause remarkable loss if they are not well suppressed in the case of $\beta^*_{y+}/\beta^*_{y-} = 0.27/0.3$ mm (final design configuration of SuperKEKB). For the case of $\beta^*_y = 1$ mm (This is the achieved β^*_y in 2021 and 2022), simulations with measured chromatic couplings showed a few percent of luminosity loss. 3) Beam oscillation excited by the injection kickers of LER. It was found that the injection kickers in the LER were not perfectly balanced. This causes a leakage kick to the beam in the horizontal direction during the injection. Due to the global coupling of the lattice, the vertical oscillation is also excited. From the waveform of the kickers' field, roughly 20% of the stored

ISBN: 978-3-95450-236-3 ISSN: 2673-7027 doi:10.18429/JACoW-eeFACT2022-WEXAT0101

beam will be excited. The BxB FB system can damp the dipole oscillations in less than 200 turns (Compared with the radiation damping time of about 4500 turns). A simple estimate shows it will cause a loss rate of about 1% to the luminosity. 4) Vertical blowup in the LER driven by the interplay of vertical impedance and feedback system. The problem was well suppressed by fine-tuning the feedback system (see Ref. [13, 16]). But this interplay can remain a source of vertical blowup, especially when the vertical small-gap collimators were severely damaged [17], generating extra vertical impedances. 5) Injection background. The

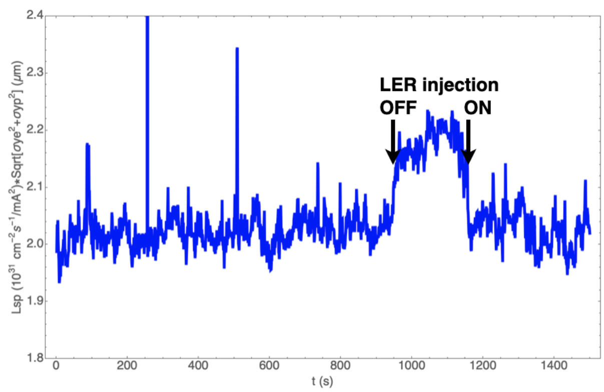

Figure 7: The weighted luminosity $L_{sp}\sqrt{\sigma_{y+}^{*2}+\sigma_{y-}^{*2}}$ synchronized with LER injection during the physics run on Jun. 2, 2022.

electromagnetic calorimeter (ECL) [18] has been used to measure the online luminosity at Belle II. The luminosity data provided by ECL is the most important reference for machine tunings and online optimizations. In this paper, the beam-beam simulations are compared only with the luminosity of ECL. It was identified that the ECL luminosity had a clear correlation with the LER injection [19]. Figure 7 shows an example of this correlation. When the LER injection was intentionally turned off or on, a sudden change in L_{sp} was observed. The following investigations showed that the luminosity measurement by ECL was affected by the injection background during the LER's beam injection [20]. Quantitatively, the luminosity measured by ECL dropped by <5% during LER injection while luminosity measured by ZDLM (Zero Degree Luminosity Monitor [21]) did not [20]. Further investigations are ongoing to understand the correlation between ECL luminosity and the background from LER injection.

Sources to be Investigated

There are sources of luminosity degradation to be investigated through simulations and experiments: 1) Imperfect CW and insufficient CW strengths. The nonlinear optics and optics distortion (its sources include machine errors, current-dependent orbit drift, etc.) around the IR might reduce the effectiveness of CW in suppressing BB resonances. In 2022, it was identified that the synchrotron radiation (SR) heating caused drift of closed orbit (COD) at SuperKEKB [9]. The small horizontal offset at the strong sextupoles for local chromaticity correction generates a significant beta-beat in the rings. Figures 1 and 4 show luminosity degradation by insufficient CW strengths. The CW strength of HER has been 40% due to technical constraints. Beam-beam simulations showed that this is insufficient to suppress the 5th-order BB resonances and can be a source of vertical blowup in the e- beam and consequent luminosity degradation. 2) BB-driven incoherent synchro-betatron resonances. Currently, the working point of SuperKEKB is between $\nu_x-\nu_s=N/2$ and $\nu_x-2\nu_s=N/2$, which are strong due to the BB interaction [10] and nonlinear chromatic optics. The tune space in this region might not be large enough to hold the footprint of the beams. Note that collective effects and machine nonlinearity stretch the tune footprint. 3) Interplay of BB, longitudinal and transverse impedances, and BxB FB system. The interplay of transverse impedances and BxB FB system is discussed in Refs. [13, 16]. To simulate the interplay of all these three factors, it is necessary to construct a realistic model of FB system, taking into account the realistic settings of the FB parameters, the environment noises, etc. 4) Interplay of BB and nonlinear lattices. This was identified as important for the final design of SuperKEKB configurations but should not be for the case of β_y^* =1 mm [22]. On this issue, the machine errors are unknown sources of lattice nonlinearity. The CW, which was not counted in the final design, introduces additional nonlinearity to the lattices. 5) Coupled bunch instabilities (CBI) with large bunch numbers and high total currents. With 2151 bunches and total beam currents of 1.4/1.12 A achieved in LER/HER, L_{sp} degradation due to CBI has not been seen. As shown in Fig. 8, machine tunings with different numbers of bunches for collisions led to the same best luminosity. This indicates that CBI, which is always suppressed by the BxB FB system, should not be a source of L_{sp} degradation in the current phase. Furthermore, the ZDLM luminosity data showed flat BxB luminosity [23], and CBI driven by electron cloud was not observed for the cases shown in Fig. 8.

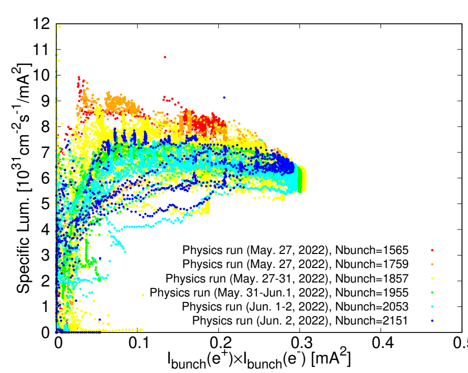

Figure 8: Measured L_{sp} as a function of bunch current product with the different numbers of bunches during the physics runs in 2022. Machine tunings were routinely done to achieve the best luminosity performance around $I_{b+}I_{b-}\approx$ 0.3 mA^2.

ISBN: 978-3-95450-236-3 ISSN: 2673-7027 doi:10.18429/JACoW-eeFACT2022-WEXAT0101

SUMMARY

Since April 2020, the CW has been incorporated with the nano-beam collision scheme at SuperKEKB and has proved decisive in suppressing nonlinear BB effects. The interplay between beam-beam and single-bunch impedance effects is critical at SuperKEKB. Especially the longitudinal monopole and vertical dipole impedances are essential in affecting machine performance. The intense interplay of bunch-by-bunch feedback and vertical impedance in LER has been a strong limit of luminosity performance until April 2022. After fine-tuning the feedback system, this problem was relaxed but remained a possible source of mild vertical emittance blowup.

ACKNOWLEDGEMENTS

We thank the SuperKEKB team and the Belle II team for their constant support of our work. The author D.Z. thanks S. Uehara and K. Matsuoka for fruitful discussions on luminosity measurements at Belle II.

REFERENCES

[1] D. Zhou, Y. Funakoshi, K. Ohmi, Y. Ohnishi, and Y. Zhang, "Simulations and Measurements of Luminosity at SuperKEKB", in *Proc. 13th Int. Particle Accelerator Conf. (IPAC'22)*, Bangkok, Thailand, Jun. 2022, pp. 2011-2014. doi:10.18429/JACoW-IPAC2022-WEPOPT064

[2] Y. Ohnishi *et al.*, "Commissioning of the Phase-I SuperKEKB B-Factory and Update on the Overall Status", in *Proc. 2nd North American Particle Accelerator Conf. (NAPAC'16)*, Chicago, IL, USA, Oct. 2016, pp. 32-36. doi:10.18429/JACoW-NAPAC2016-MOB3IO01

[3] Y. Funakoshi *et al.*, "Beam Commissioning of SuperKEKB", in *Proc. 7th Int. Particle Accelerator Conf. (IPAC'16)*, Busan, Korea, May 2016, pp. 1019-1021. doi:10.18429/JACoW-IPAC2016-TUOBA01

[4] Y. Ohnishi, "Highlights from SuperKEKB Phase 2 Commissioning", in *Proc. 62nd ICFA Advanced Beam Dynamics Workshop on High Luminosity Circular e^+e^- Colliders (eeFACT'18)*, Hong Kong, China, Sep. 2018, pp. 1-6. doi:10.18429/JACoW-eeFACT2018-MOXAA02

[5] A. Morita *et al.*, "Status of Early SuperKEKB Phase-3 Commissioning", in *Proc. 10th Int. Particle Accelerator Conf. (IPAC'19)*, Melbourne, Australia, May 2019. doi:10.18429/JACoW-IPAC2019-WEYYPLM1

[6] Y. Ohnishi *et al.*, "Accelerator design at SuperKEKB", *Progress of Theoretical and Experimental Physics*, vol. 2013, no. 3, p. 03A011, Mar. 2013. doi:10.1093/ptep/pts083

[7] Y. Ohnishi *et al.*, "SuperKEKB operation using crab waist collision scheme", *Euro. Phys. J. Plus*, vol. 136, p. 1023, 2021. doi:10.1140/epjp/s13360-021-01979-8

[8] Y. Funakoshi *et al.*, "The SuperKEKB Has Broken the World Record of the Luminosity", in *Proc. 13th Int. Particle Accelerator Conf. (IPAC'22)*, Bangkok, Thailand, Jun. 2022, pp. 1–5. doi:10.18429/JACoW-IPAC2022-MOPLXGD1

[9] Y. Ohnishi, "SuperKEKB luminosity quest", in *Proc. 65th ICFA Advanced Beam Dynamics Workshop on High Luminosity Circular e^+e^- Colliders (eeFACT'22)*, Frascati, Italy, Sep. 2022, paper MOXAT0103, this workshop.

[10] P. Raimondi *et al.*, "Beam-Beam Issues for Colliding Schemes with Large Piwinski Angle and Crabbed Waist", arXiv:physics/0702033, 2007.

[11] M. Zobov *et al.*, "Test of "Crab-Waist" Collisions at the DAΦNE Φ Factory", *Phys. Rev. Lett.*, vol. 104, p. 174801, 2010. doi:10.1103/PhysRevLett.104.174801

[12] K. Ohmi, "Simulation of beam-beam effects in a circular e^+e^- collider", *Phys. Rev. E*, vol. 62, p. 7287, 2000. doi:10.1103/PhysRevE.62.7287

[13] K. Ohmi *et al.*, "Study for -1 mode instability in SuperKEKB low energy ring", in *Proc. 65th ICFA Advanced Beam Dynamics Workshop on High Luminosity Circular e^+e^- Colliders (eeFACT'22)*, Frascati, Italy, Sep. 2022, paper WEXAT0102, this workshop.

[14] D. Zhou *et al.*, "Simulations of beam-beam effect in the presence of general chromaticity", *Phys. Rev. Spec. Top. Accel. Beams*, vol. 13, p. 021001, 2010. doi:10.1103/PhysRevSTAB.13.021001

[15] M. Masuzawa *et al.*, "Chromatic X-Y Coupling Correction by Tilting Sextupole Magnets in the SuperKEKB Positron Ring", presented at the 13th Int. Particle Accelerator Conf. (IPAC'22), Bangkok, Thailand, Jun. 2022, paper TUOZSP2, unpublished.

[16] S. Terui *et al.*, "The Report of Machine Studies Related to the Vertical Beam Size Blow-Up in SuperKEKB LER", in *Proc. 13th Int. Particle Accelerator Conf. (IPAC'22)*, Bangkok, Thailand, Jun. 2022, pp. 2169–2172. doi:10.18429/JACoW-IPAC2022-WEPOTK050

[17] T. Ishibashi *et al.*, "Status and Experiences of the vacuum system in the SuperKEKB main ring", in *Proc. 65th ICFA Advanced Beam Dynamics Workshop on High Luminosity Circular e^+e^- Colliders (eeFACT'22)*, Frascati, Italy, Sep. 2022, paper THXAS0102, this workshop.

[18] F. Abudinen *et al.*, "Measurement of the integrated luminosity of the Phase 2 data of the Belle II experiment", *Chin. Phys. C*, vol. 44, no. 2, p. 021001, 2020. doi:10.1088/1674-1137/44/2/021001

[19] D. Zhou, "Specific-luminosity degradation correlated with LER injection", presented at the 6th SuperKEKB commissioning meeting, Jun. 17, 2022.

[20] K. Matsuoka, "Luminosity degradation by the beam injection", presented at the 12th SuperKEKB commissioning meeting, Oct. 14, 2022.

[21] T. Hirai *et al.*, "Real-time luminosity monitor for a b-factory experiment", *Nucl. Instrum. Methods Phys. Res. A*, vol. 458, pp. 670-676, 2001.

[22] D. Zhou *et al.*, "Interplay of Beam-Beam, Lattice Nonlinearity, and Space Charge Effects in the SuperKEKB Collider", in *Proc. 6th Int. Particle Accelerator Conf. (IPAC'15)*, Richmond, VA, USA, May 2015, pp. 2413-2417. doi:10.18429/JACoW-IPAC2015-WEYB3

[23] S. Uehara, Private communication.

ISBN: 978-3-95450-236-3 ISSN: 2673-7027 doi:10.18429/JACoW-eeFACT2022-WEXAT0102

STUDY FOR -1 MODE INSTABILITY IN SuperKEKB LOW ENERGY RING

K. Ohmi, H. Fukuma, T. Ishibashi, S. Terui, M. Tobiyama, D. Zhou
KEK, Tsukuba, Ibaraki, Japan

Abstract

A beam size blow-up has been observed in increasing beam current in superKEKB Low Energy Ring (LER). The blow-up is a single bunch effect, which appears at high bunch current $I_b \approx 1$ mA. -1 mode ($\nu_y - \nu_s$) signal was detected in a beam position monitor at the appearance of the blow-up. The blow up is suppressed at vertical tune $\nu_y > 0.59$, while the beam injection is hard at the tune. The blow-up disappeared at turning off a bunch-by-bunch feedback. The luminosity performance of SuperKEKB is limited by the blowup, because it depends on the feedback tuning, operating point and collimator conditions Measurements and simulations for the blow-up are presented to explain the phenomenon.

INTRODUCTION

SuperKEKB consists of Low Energy Ring (LER) and High Energy Ring (HER), which store 4 GeV positron beam and 7 GeV electron beam, respectively. In physics operation, lower vertical tune in LER has tended to have lower luminosity and beam instability. We began to measure LER beam size without collision to make clear the reason. A beam size blow-up has been observed increasing beam current ∼ 1 A in LER since 2021 spring.

Several times of measurements have been performed since 2021. The blow-up has been seen in single beam operation of LER. The blow-up was independent of the number of bunch stored: i.e. it was seen at I = 90 mA in 99 bunches storage, while at around 1 A in 1000-1500 bunches storage in physics run. The beam size depended only on the bunch current. Therefore this phenomenon was concluded as single beam and single bunch effect.

The blow-up also depended on the collimator aperture. In LER, a few number of collimators contributes dominantly as impedance sources. Narrower aperture of the collimators resulted in larger beam size blow-up. The phenomenon was concluded as an impedance related effect. - 1 mode ($\nu_y - \nu_s$) signal was detected in a beam position monitor at the appearance of the blow-up. The separation of ν_y and $\nu_y - \nu_s$ signals was sufficient to exclude the possibility of TMCI.

The blow-up depends on bunch-by-bunch feedback system. The bunch-by-bunch feedback is essential for multi-bunch and high-current operation. The feedback could be turned off in accelerator experiments with a very small number of bunches (∼ 30) and beam current I=30mA. The blow-up disappeared when turn off the feedback.

We call this beam-size blow-up -1 mode instability. This paper shows the experimental results and discussions for mechanism of the beam-size blow up or -1 mode instability.

MEASUREMENTS OF LER

The beam size blow-up is related to the vertical impedance. Amplitude of the vertical impedance is evaluated by measurement of current dependent tune shift, which is expressed by the well known formula,

$$\Delta\nu_y = \frac{Ne^2}{4\pi E}\sum_i \beta_{y,i}k_{y,i} \quad (1)$$

$$= 2\times 10^{-19}\sum_i \beta_{y,i}k_{y,i}[V/C]I[mA]. \quad (2)$$

where LER parameters are substituted into Eq. (1) on Eq.(2). The vertical kick factor (k_y) is express by the vertical wake field and/or impedance

$$k_y = \iint_{-\infty}^{\infty} W_y(z-z')\rho(z)\rho(z')dzdz' \quad (3)$$

$$= -\frac{i}{2\pi}\int_{-\infty}^{\infty} d\omega Z_y(\omega)e^{-\omega^2\sigma_z^2/c^2} \quad (4)$$

where Gaussian density distribution $\rho(z) = e^{-z^2/(2\sigma_z^2)}/(\sqrt{2\pi}\sigma_z)$ is assumed in Eq. (4).

Four vertical collimators D2V1,V2 (s =1800 m), D3V1 (s =2714 m) and D6V1 (s =1800 m) are installed to protect the physics detector Bell-II from beam background, where s is position from the Interaction Point. The collimators, especially D2V1 and D6V1, are dominant source of the vertical impedance.

Electro-magnetic filed simulations using GdFidl citeGDFDL and ECHO3D [2] gave $\sum\beta_y k_y = 3.3\times10^{16}$ V/C for collimators and 1.8×10^{16} V/C for the beam chamber in Interaction Region and others: i.e., 5.1×10^{16} V/C in total [3]. The impedance corresponds to a collimator aperture setting used in the measurements presented in this paper. The collimators are slightly opened in physics run: i.e., the collimator impedance is 2.9×10^{16} V/C.

The current dependent tune shift was measured in a single bunch operation. Figure 1 shows vertical tune shifts for $\nu_{y,0}$ =0.614 and 0.592 as functions of bunch current. Tune shift is linear for the bunch current. The linear coefficients are fitted as seen in the figure. The tune shift was determined as $\Delta\nu_y/I = 1.1$ mA^{-1}. Corresponding impedance/ kick factor is $\sum\beta_y k_y = 5.5\times10^{16}$ V/C. The difference between the measurement and simulations is within 10%.

Vertical beam size has been measured by Xray monitor using coded aperture mask [5] in SuperKEKB. Figure 2 shows the beam size as a function of the bunch current. Beam sizes for the two collimator apertures of D6V1 are plotted by blue and orange points. Corresponding collimator

ISBN: 978-3-95450-236-3 ISSN: 2673-7027 doi:10.18429/JACoW-eeFACT2022-WEXAT0102

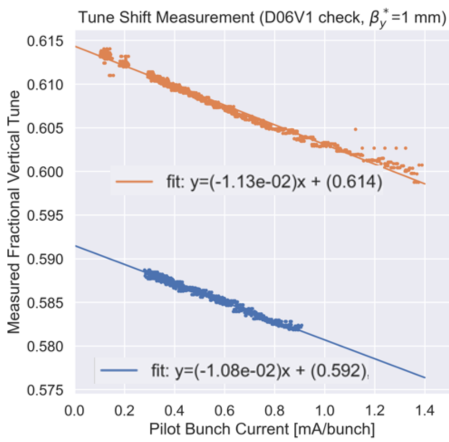

Figure 1: Vertical tune as functions of bunch current for $\nu_{y,0}$ =0.614 and 0.592.

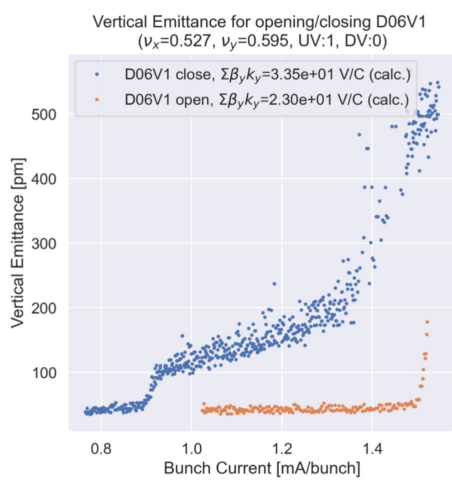

Figure 2: Beam size as function of bunch current. Blue and orange points are given for the total (collimator) impedance $\sum \beta_y k_y = 5.2(3.35)$ and $4.1(2.30) \times 10^{16}$ V/C, respectively.

impedance is $\sum \beta_y k_y = 3.35$ and 2.30×10^{16} V/C. The total impedance is 5.2 and 4.1×10^{16} V/C for blue and orange. The impedance ratio is 1.27. The products of the impedance times bunch current at $\varepsilon_y = 200$ pm are nearly equal, $1.3 \times 5.2 \approx 1.55 \times 4.1$. Scaling for the product is not perfect as shown in the figure: i.e., the lines are not coincide for scaling in the horizontal axis..

Beam size was measured for varying the vertical tune. The beam size blow-up caused by the synchro-beta resonances $\nu_x - \nu_y + n_z \nu_s$ =integer for n_z =1 and 2 has been observed at a low bunch current in KEKB and SuperKEKB [4]. In the early stage of the measurements, the beam size increased at lower tune $\nu_y < 0.6$ at high bunch current $I_b \geq 0.9$ mA. Thus we speculated that the synchro beta resonance had some effects on this beam size blow up. A machine experiment was performed to understand whether the phenomenon was related to x-y coupling. Vertical beam size was measured with scanning the vertical tune at two different horizontal tune $\nu_x = 0.5310$ (left) and 0.5935 (right) as shown in the top two plots in Fig. 3. The bottom two plots show the vertical

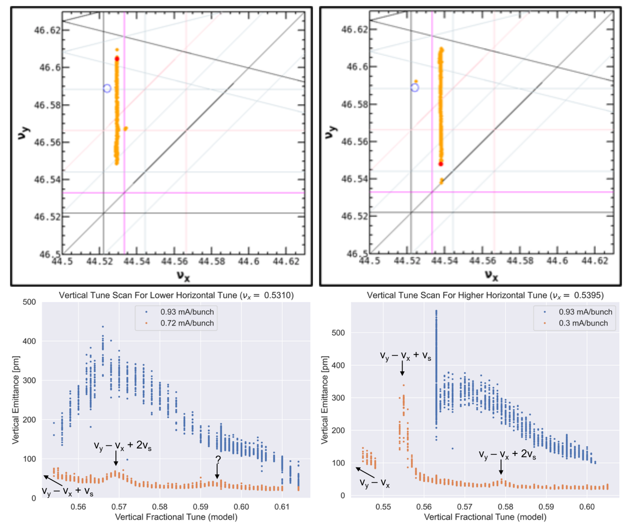

Figure 3: Beam size scanning along the vertical tune. Top plots show the history of the tune scan, and bottom left and right plots are given for $\nu_x = 0.5310$ and 0.5395 corresponding to top plots, respectively.

beam size at the corresponding horizontal tunes. Orange and blue points depicts the vertical emittance at below (0.3-0.7 mA) and above (0.9 mA) the threshold of the beam size blowup. First ($n_z = 1$) and second ($n_z = 2$) synchro-beta side bands were seen below the threshold current. On the other hand a broad peak was seen at $\nu_y < 0.61$ above the threshold current. Beam size as a function of the vertical tune is independent of ν_x at high bunch current. We concluded that the beam size blow up was irrelevant to x-y coupling.

A beam position monitor, which is used for bunch-by-bunch feedback, can record positions of all bunches in every turns (typically 2048 or 4096 turns). The device is called Bunch Oscillation Recorder. An unstable oscillation mode as single bunch instability is detected by taking Fourier analysis of the BOR data. Figure 4 shows the Fourier spectra for varying the beam current, where the number of bunches are 99. This signal means occurrence of self-excited oscillation. 5 plots (top and bottom left/center) shows Fourier amplitude of the bunch current 0.3, 0.5, 0.7, 0.9 and 1.1 mA. The last plot placed at right bottom shows amplitude at 1.1 mA after increasing feedback gain. The vertical emittance is kept to be 30 pm at I_b $\leq$0.7 mA. Increasing the bunch current, the vertical emittance increases. The sharp peak was seen around $\nu_y - \nu_s$ in the Fourier amplitude when vertical emittance begin to increase. Increasing the feedback gain, both the beam size and Fourier amplitude of -1 mode are reduced.

Stable and unstable oscillation modes are also measured by detecting a response for forced oscillation scanning the frequency. Left picture of Fig. 5 shows the frequency response in horizontal and vertical positions of the pilot bunch at $I = 1.5$ mA. Betatron and its synchrotron sideband are seen. The fact, in which betatron and its sideband are seen, means that it is below the TMCI threshold. The peak posi-

ISBN: 978-3-95450-236-3 ISSN: 2673-7027 doi:10.18429/JACoW-eeFACT2022-WEXAT0102

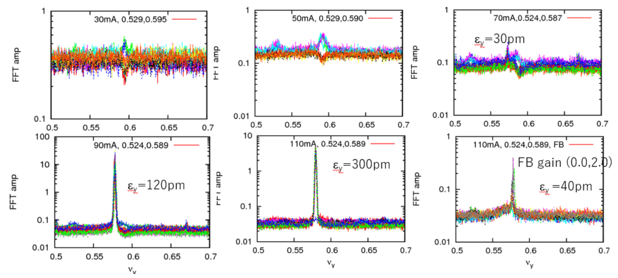

Figure 4: Fourier amplitude of the bunch oscillation recorder. Top three and bottom left and center are given for the bunch current 0.3, 0.5, 0.7, 0.9 and 1.1 mA. Bottom right plot is given for increasing feedback gain.

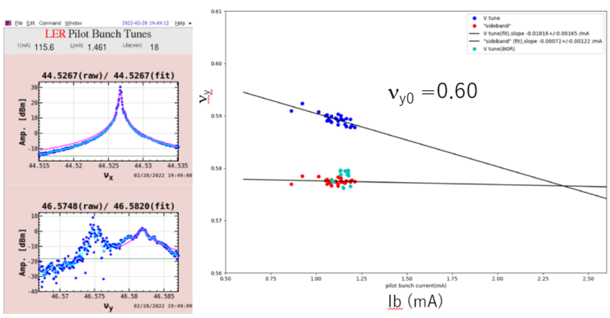

Figure 5: Left: Mode tune seen in response for frequency scanning forced oscillation. Right: Tune peak positions detected in self excitation (Fig. 4, cyan) and forced oscillation (blue and red).

tions of the self-excited signal and the response signal are plotted in Fig. 5 right. The self excited signal was coincide with the synchro-beta sideband. Changing the vertical betatron tune, the two peaks shifted simultaneously: i.e., it is clear that the lower peak is synchro-beta sideband. The beam size blowup was concluded to be caused by excitation of $\nu_y - \nu_s$ mode, and was called the -1 mode instability.

Bunch-by-bunch feedback system is necessary to suppress coupled bunch instability at total current $I > 50$ mA typically. Reducing the number of bunches to 30 bunch and total current 30mA, the beam size measurement becomes possible without the bunch-by-bunch feedback. Figure 6 shows the beam size as function of bunch current for feedback ON/OFF. Orange and blue points are vertical emittance in the first trial of the feedback ON/OFF. The emittance increase disappeared completely by turning off the bunch-by-bunch feedback. Green points are that after feedback tuning as is discussed in next section.

BUNCH-BY-BUNCH FEEDBACK

In the end of previous section, we show that the bunch-by-bunch feedback system has an important role in the vertical emittance growth as shown in Fig. 6.

Feedback system equips two independent feedback loops. Each set consists of transverse strip line kicker and beam position monitor. Table 1 shows the betatron function and

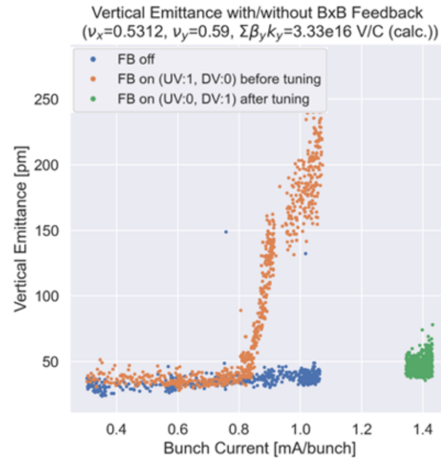

Figure 6: Beam size as functions of bunch current for feedback ON/OFF.

phase at feedback kickers, monitors and major impedance source D6V1. Another major collimator D2V1 is located at a position with an integer betatron phase difference from D6V1.

Figure 7 shows schematic view of the feedback system configuration. Beam is kicked by the kickers 1 and 2 based on the beam positions measured by the monitors 1 and 2 in previous turns.

Kicker strength is determined by the measured beam positions using Finite Impulse Response filter as follows,

$$\Delta P_K(n) = \sum_{k=1}^{N_{tap}} c(k) X(n-k) \qquad (5)$$

where $X(n)$ is vertical position measured by the monitor at n-th turn, and $\Delta P_K(n)$ is momentum kick applied at kicker. X and P are normalized as $X(n) = y(n)/\sqrt{\beta_y}$ and $P(n) = \sqrt{\beta_y} p_y(n) + \alpha_y y(n)/\sqrt{\beta_y}$ for measured $y(n)$ and $p_y(n)$, respectively. N_{tap} is called the tap number. Position data

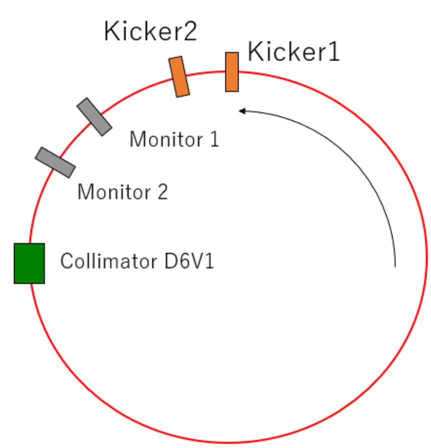

Figure 7: Schematic view of the feedback system configuration.

ISBN: 978-3-95450-236-3 ISSN: 2673-7027 doi:10.18429/JACoW-eeFACT2022-WEXAT0102

Table 1: Position, beta function, and phase at the feedback kickers, monitors and the collimator D6V1.

Element	α_x	β_x	$\phi_x/2\pi$	s(m)	α_x	β_x	$\phi_y/2\pi$
Kicker 1	.68	19.6	21.9781	1489.30	-1.14	6.3	22.7721
Kicker 2	.56	17.6	21.9913	1490.84	-1.70	10.7	22.8020
Mon. 1	.50	23.9	22.0432	1499.91	.85	19.4	22.9117
Mon. 2	-.50	23.9	22.1906	1519.07	-.85	19.4	23.1355
D6V1	1.71	14.6	27.4756	1870.27	-10.1	67.3	28.8574
IP	0.00	.080	44.5250	3016.30	0.00	.001	46.5870

up to N_{tap} turns before are used for the feedback. Beam positions at the monitor are transferred to those at the kicker,

$$X(n) = X_K(n)\cos(k\mu + \Delta\phi) - P_K(n)\sin(k\mu + \Delta\phi), \quad (6)$$

where $\Delta\phi = \phi_K - \phi_M$ is vertical betatron phase difference from the monitor to kicker. $\Delta\phi/2\pi = -0.1396$ and -0.3335 for the first and second feedback loops as shown in Table 1. $\mu = 2\pi\nu_y$ is (angular) tune of an oscillation mode. Tune is changed in arc section outside of Kicker-Monitor system.

Resistive and reactive components of the feedback are expressed by

$$\Delta P_K(n) = -2d_P P_K(n) - 2d_X X_K(n). \quad (7)$$

The components are given by

$$d_P = \frac{1}{2}\sum_{k=1}^{N_{tap}} c(k)\sin(k\mu + \Delta\phi) \quad (8)$$

$$d_X = -\frac{1}{2}\sum_{k=1}^{N_{tap}} c(k)\cos(k\mu + \Delta\phi). \quad (9)$$

The coefficients are used before March 11, 2022 as

$$\begin{aligned} c_1 &= \{21623, -5530, -11430, 25925, -32767, 31362, \\ &\quad -20832, 5288, 12317, -25956\}; \\ c_2 &= \{26781, -26182, 7149, 2479, -22777, 25564, \\ &\quad -32767, 19752\}; \end{aligned} \quad (10)$$

N_{tap} are 10 and 8 for the 1-st and 2-nd feedback loops.

They are changed at March 12 as

$$\begin{aligned} c_1 &= \{29144, -32767, -16328, 19950\}; \quad (11) \\ c_2 &= \{10883, -32767, 28452, -20750, -7342, 21524\}; \end{aligned}$$

N_{tap}'s are reduced to be 4 and 6.

Using Eqs. (8) and (9), resistive and reactive components as a function of mode tune are evaluated. Figure 8 shows resistive and reactive components of the filter coefficients of Eq. (10). Blue and orange points are given for 1-st and 2-nd feedback loops. The feedback gain is maximum at around $\nu_y = 0.58$. While the gain is poor for synchro-beta side band ($\nu < 0.54$) at $\nu_y \approx 0.56$. The reactive component change the sign at the peak of resistive component.

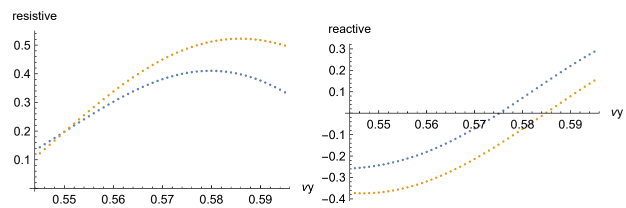

Figure 8: Resistive and reactive components for the FIR filter in Eq. (10) (before Mar. 11).

Figure 9 shows resistive and reactive components of the filter coefficients of Eq. (11). The resistive component is kept a sufficient level at low frequency.

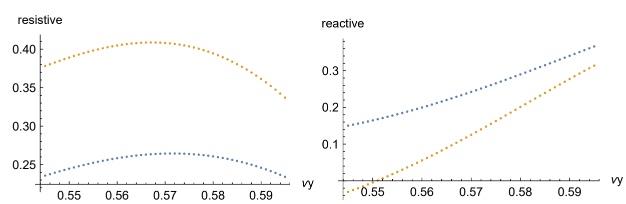

Figure 9: Resistive and reactive components for the FIR filter in Eq. (11) (Mar. 12).

SIMULATION OF HEAD-TAIL INSTABILITY CONSIDERING THE BUNCH-BY-BUNCH FEEDBACK

Multi-particle tracking simulation is performed with considering the wake field and the bunch-by-bunch feedback system. The total wake field of every accelerator component evaluated by ECHO3D [2] (collimators), GDFidl [1] (cavities and other vacuum components) and analytic formula(resistivity) is shown in Fig. 10. $W(z)$ is calculated by using a virtual short bunch with the length of 0.5 mm. Red and magenta lines are dipole field induced by dipole moment and quadrupole field induced by monopole (density) component. The kick factor k_y is given by -4.7×10^{16} and -1.0×10^{16} V/C. Corresponding vertical tune shift is 0.011 mA^{-1}. Quadrupole and dipole kick are almost cancelled in horizontal. The vertical quadrupole component is similar and opposite sign with the horizontal quadrupole component. These are characteristics of vertical collimator, which has translational symmetry in horizontal.

ISBN: 978-3-95450-236-3 ISSN: 2673-7027 doi:10.18429/JACoW-eeFACT2022-WEXAT0102

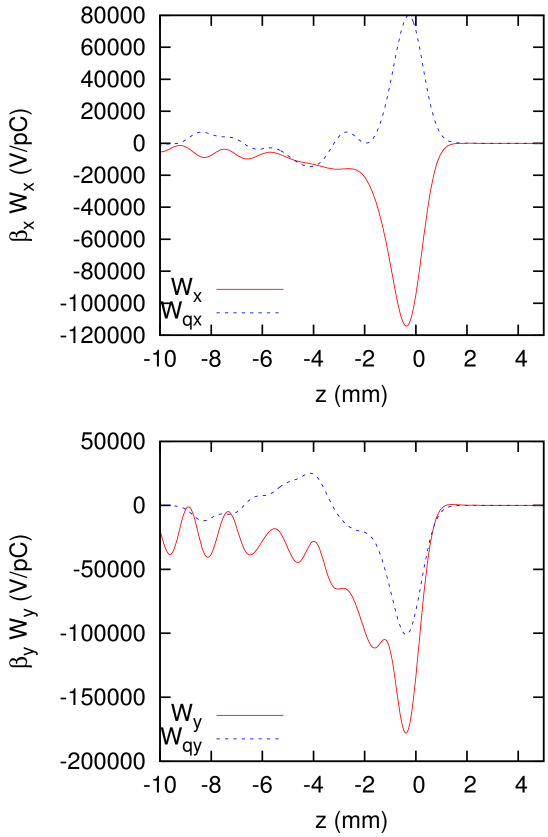

Figure 10: Transverse wake field. Red and blue lines are dipole field induced by dipole moment and quadrupole field induced by monopole component, respectively.

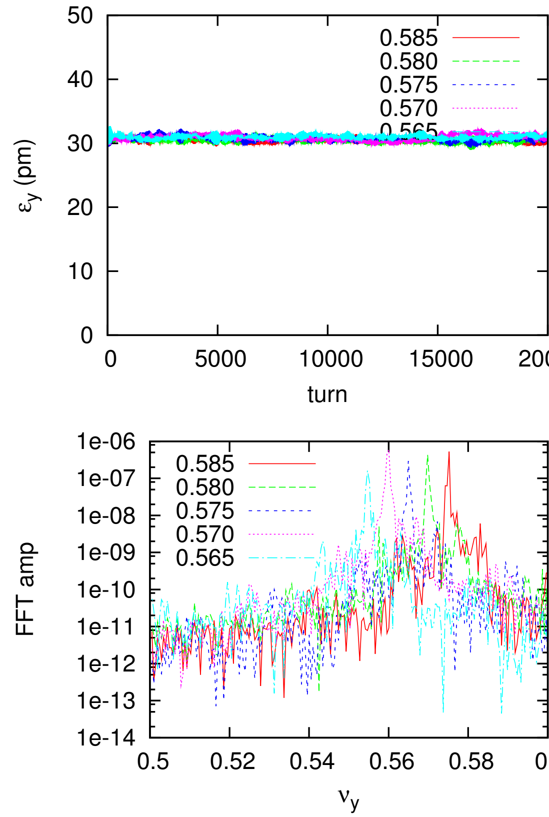

Figure 11: Evolution of vertical emittance and Fourier coefficients for the dipole motion, where thefeedback was turning off.

The particle tracking simulation was performed by momentum kick given by convolution of the dipole-quadrupole wake fields and dipole-monopole moments.

$$\Delta p_y = -\frac{Ne^2}{E}\int_{-\infty}^{\infty}[W_y(z-z')\rho_y(z')+W_{Q,y}(z-z')\rho(z')]dz', \tag{12}$$

where $\rho(z)$ is the bunch density (monopole moment) and $\rho_y(z) = \rho(z)\langle y(z)\rangle$ is dipole moment as a function of z. Macro-particles of 100,000 are used in the simulation. Bunch current is set to be 1 mA, $N = 6.25 \times 10^{10}$.

Figure 11 shows vertical emittance and Fourier spectra for the vertical dipole motion $\langle y\rangle = \int \rho_y(z)dz$, where the feedback was turning off. The vertical tune was scanned between 0.565-0.585 in steps of 0.005. There was no emittance growth in every tune. Betatron tune is seen in the peak of Fourier coefficient. Tune shift around 0.01 is seen.

Figure 12 shows vertical emittance and Fourier coefficient for the vertical dipole motion using bunch-by-bunch feedback system. where FIR filter of Eq. (10) with the damping rate 0.1 is used. Strong emittance growth is seen in lower betatron tune $\nu_y = 0.570, 0.565$. In Fourier spectrum, -1 mode signal is seen around $\nu_y - \nu_s$ in every tune, while the betatron signal is suppressed. These behaviors are consistent with the experimental results seen in Figs. 3-6.

Figure 13 shows the results at the bunch current of 0.5 mA. Other conditions are the same as in Fig. 12. There was no emittance growth in every tune. -1 mode is seen in the peak of Fourier spectra.

Simulations for a weak feedback strength with the damping rates of 0.04, 0.06 and 0.08 were performed. Emittance growth was seen at 0.08. The feedback damping time is estimated around 0.01-0.02 in the measurement for damping of injected beam. The blow-up was also not seen in a simple single tap feedback with only resistive component with the damping rate of 0.1.

SUMMARY

We have studied a beam size blow-up observed in superKEKB Low Energy Ring (LER). The experimental results are summarized as follows:

- The blowup is single bunch effect.
- It is irrelevant to x-y coupling.
- It is impedance phenomenon. As far as the tune shift was concerned, the threshold is about half that of TMCI.
- -1 mode signal ($\nu_y - \nu_s$) is seen with the appearance of the blow-up.
- Turning off the bunch-by-bunch feedback results in disappearance of the blow up.

ISBN: 978-3-95450-236-3 ISSN: 2673-7027 doi:10.18429/JACoW-eeFACT2022-WEXAT0102

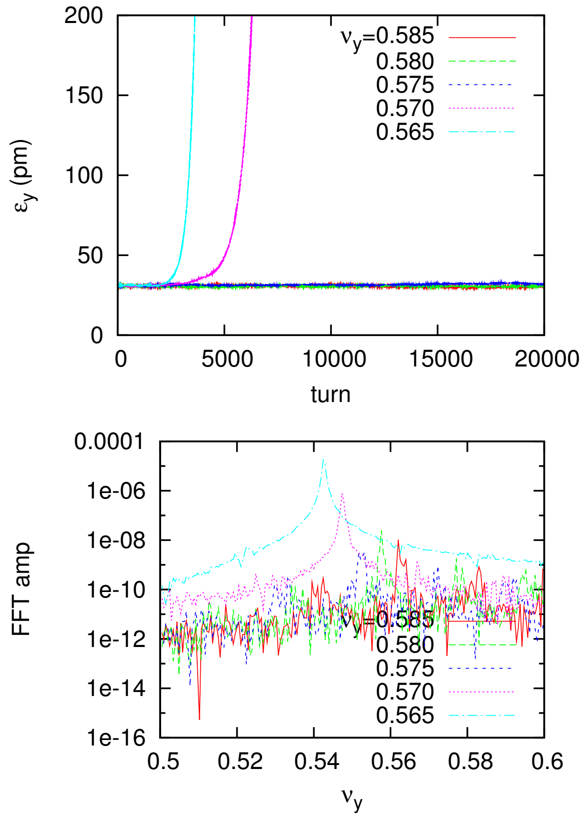

Figure 12: Evolution of vertical emittance and Fourier coefficients for the dipole motion at the bunch current 1 mA, where the feedback is turned on with FIR filter of Eq. (10) and the damping rate of 0.1.

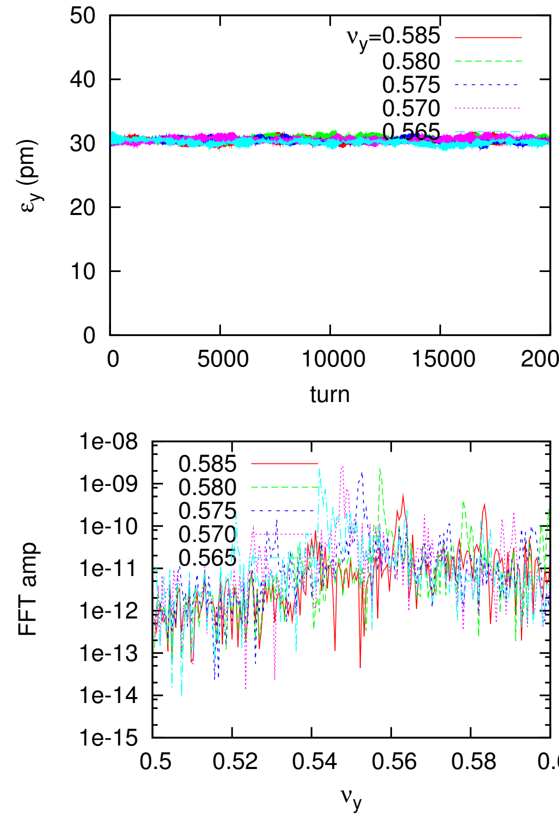

Figure 13: Evolution of vertical emittance and Fourier coefficients for the dipole motion at the bunch current 0.5 mA, where the feedback is turned on with FIR filter of Eq. (10) and the damping rate of 0.1.

The bunch-by-bunch feedback system in SuperKEKB adopted multitap scheme with a digital FIR filter. Resistive and reactive component of the feedback depends on the filter parameters and the frequency of unstable mode. Multi-particle tracking simulation has been done considering the impedance and feedback. Using the filter parameters and high damping rate 0.1, -1 mode instability was reproduced in the simulation. Emittance growth appeared at low vertical tune $\nu_y \leq 0.57$. There was no instability in lower bunch current, lower impedance, simple single tap feedback nor filter parameter change as was done in the experiment.

The assumed feedback gain 0.1 in the simulation is higher than the actual setting, 0.01-0.02. It seems that we have not yet reached perfect understanding of the -1 mode instability. Digital noise/step of the monitor and kicker is studied in the future.

REFERENCES

[1] The GDFIDL electromagnetic field simulator, `http://www.gdfidl.de`

[2] I. Zagorodnov, Code ECHO, `http://www.desy.de/~zagor`

[3] T. Ishibashi *et al.*, `https://kds.kek.jp/event/40318/`

[4] Y. Seimiya, K. Ohmi, D. Zhou, J. W. Flanagan, and Y. Ohnishi, “Symplectic expression for chromatic aberrations”, *Prog. Theor. Phys.*, vol. 127, no. 6, p. 1099–1119, 2012. `doi:10.1143/PTP.127.1099`

[5] J. W. Flanagan *et al.*, “X-ray monitor based on coded-aperature imaging for KEKB upgrade and ILC damping ring” in *Proc. EPAC’08*, Genoa, Italy, Jun. 2008, paper TUOCM02, pp. 1029–1031.

ISBN: 978-3-95450-236-3 ISSN: 2673-7027 doi:10.18429/JACoW-eeFACT2022-WEXAS0101

CAVITY AND CRYOMODULE DEVELOPMENTS FOR EIC *

R. A. Rimmer[†], E. Daly, J. Guo, J. Henry, J. Matalevich, H. Wang, JLab, Newport News, VA, USA
D. Holmes, K. Smith, W. Xu, A. Zaltsman, B. Xiao, BNL, Upton, NY, USA
S. De Silva, J. Delayen, Old Dominion University, Norfolk, VA, USA

Abstract

The EIC is a major new project under construction at BNL in partnership with JLab. It relies upon a number of new SRF cavities at 197 MHz, 394 MHz, 591 MHz and 1773 MHz to pre-bunch, accelerate, cool and crab the stored beams. R&D is focusing on the 591 MHz elliptical cavity and 197 MHz crab cavity first as these are the most challenging. Preliminary designs of these cavities are presented along with an R&D status report. To avoid developing multiple different cryostats a modular approach is adopted using a high degree of commonality of parts and systems. This approach may be easily adapted to other frequencies and applications.

OVERVIEW OF SRF SYSTEMS FOR EIC

The electron ion collider (EIC) [1], is a complex machine incorporating many of the challenges of e+e- factories, hadron-hadron colliders and even light sources. The complex consists of a hadron injector complex and storage ring based on upgrades to the RHIC facility, a new high-current electron storage ring and an RCS as a full energy injector. Most of the existing RF systems for RHIC will be retained or repurposed however new 591 MHz SRF bunching systems will be needed in both collider rings to attain the short bunches needed for high luminosity. In the high-current ESR these will be heavily HOM-damped single-cell cavities similar to those used in the B-factories, with high power beam line absorbers (BLAs). Table 1 lists the high level parameters for the ESR. Dual 400 kW fundamental power couplers will be used on each cavity. In the HSR the current is 0.75 A so multi-cell cavities can be used and the required voltage is about 20 MV. One or two 5-cell cavities can fulfil these requirements. Although HOM power will be lower than the ESR good damping is still required and the impedance of same-passband modes must be carefully managed. In the CDR a scaled version of a previous 5-cell cavity was assumed. Similar 5-cell cavities can be used in the RCS and in the ERL for strong hadron cooling (SHC). 1773 MHz harmonic cavities are needed to linearize the cooler linac and 197 MHz buncher cavities are needed in the injector. A low energy pre-cooler ERL is also proposed that would use 197 MHz accelerating cavities. The other major SRF system in EIC is the crabbing cavities for the interaction point (IP). Because of the large crossing angle a high crabbing voltage is needed. Due to the long bunch length in the hadron ring 197 MHz cavities are chosen with 394 MHz harmonic cavities to maintain a linear crab kick along the bunch length. The shorter bunch length in the ESR allows single 394 MHz crabbing systems to be used. Given the large number of systems to be developed a modular cryostat approach with a high degree of commonality of components is being followed to minimize design effort and speed up development.

* Work supported by Brookhaven Science Associates, LLC under U.S.DOE contract No. DE-AC02-98CH10886, and by Jefferson Science Associates, LLC under U.S. DOE Contract No. DE-AC05-06OR23177.
† rarimmer@jlab.org

R&D PRIORITIES

Four items were chosen for early R&D based on risk; the 591 MHz ESR single cell, the 197 MHz crab cavity, the 400 kW FPC and the high power BLA. One prototype of each cavity will be built and tested and small batches of FPC's and BLA's will be built and evaluated. The other cavity types are assumed to be lower risk or can be developed by extrapolating from these designs, e.g. the 394 MHz crab cavity can be developed using lessons learned from the 197 MHz prototype and the 5-cell 591 MHz cavities can be developed from the single cell.

591 MHz ESR 1-CELL CAVITY

The CDR describes a symmetric 1-cell cavity using two large beam pipe absorbers, developed from an earlier 2-cell design in the pre-CDR. see Fig. 1. The number of cavities is determined by the peak voltage needed to maintain adequate bucket height at 18 GeV and the amount of coupler power needed to replace synchrotron radiation and other losses, see Table 1.

The high average current and naturally short bunch length lead to high HOM power of >40 kW per cavity. Up to 10 MW of beam power must be supplied and symmetric dual 400 kW FPC's will be fitted to each of the 17 single-cell cavities.

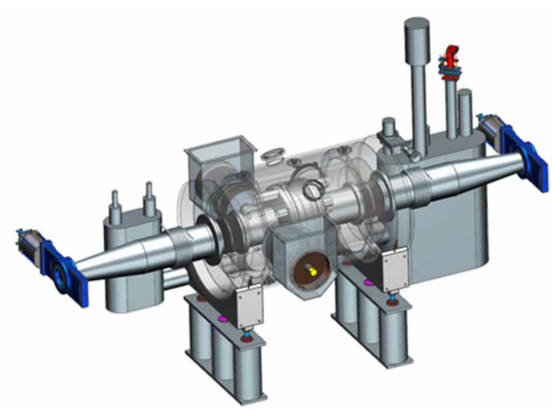

Figure 1: Symmetric single cell 591 MHz SRF cryomodule with two large warm BLA's and tapers in the CDR.

ISBN: 978-3-95450-236-3 ISSN: 2673-7027 doi:10.18429/JACoW-eeFACT2022-WEXAS0101

Table 1: ESR RF Requirements

V (MV)	I (A)	No. cavities	Beam Power (MW)	Coup. power (kW)	HOM power (kW)
68	2.5	17	10	400	>40

RF Design

The cavity is a low R/Q design to minimize beam gap transients and overall impedance. The large beam pipes needed for HOM damping must be tapered down to fit through the straight section quadrupole magnets. 150mm ID shielded gate valves are chosen to isolate each module. The CDR assumes one cavity per cryomodule as in KEK-B and other rings. Since the CDR a more compact design with one large and one small beam pipe has been developed, Fig. 2, eliminating one taper and one large BLA. This asymmetric design is about 25% shorter, and has 11% lower loss factor, although the power in the one remaining large BLA is increased by 13%. A comparison of the two designs is given in Table 2. Both cavities meet the requirements for longitudinal impedance less than 1.53 kΩ-GHz and transverse impedance less than 0.71 MΩ/m per cavity for 17 cavities.

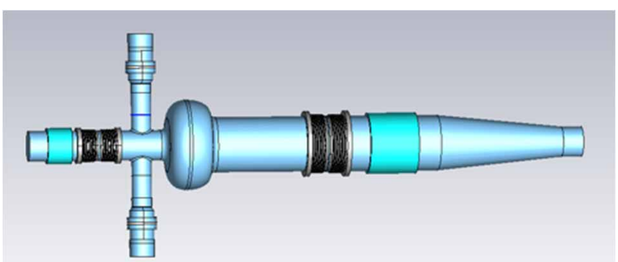

Figure 2: New asymmetric 591 MHz 1-cell SRF cavity with one large and one small BLA. About 64% of the HOM power goes to the large BLA, 28% to the small one and 8% exits the beam pipes.

Table 2: Basic ESR Cavity Design Parameters

Parameter	Sym.	Asym.
R/Q (circuit definition, Ω)	37	38
Epk/Eacc	2.13	2.01
Bpk/Eacc (mT/MV/m)	4.87	4.87
G (Ohms)	293	307
FPC tip penetration at Qext=3.5E5	1mm	3mm
Approx. total length (Gate valve to gate valve)	3.75m	2.8m

Figures 3 and 4 show the longitudinal and transverse impedance spectra of the asymmetric cavity. Coupled-bunch feedback systems will give additional margin on top of this.

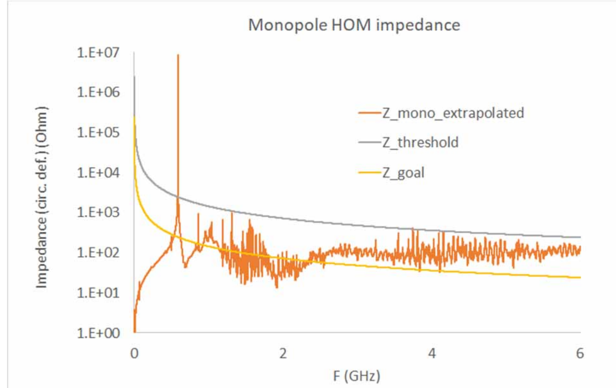

Figure 3: Monopole impedance of asymmetric 591 MHz SRF cavity.

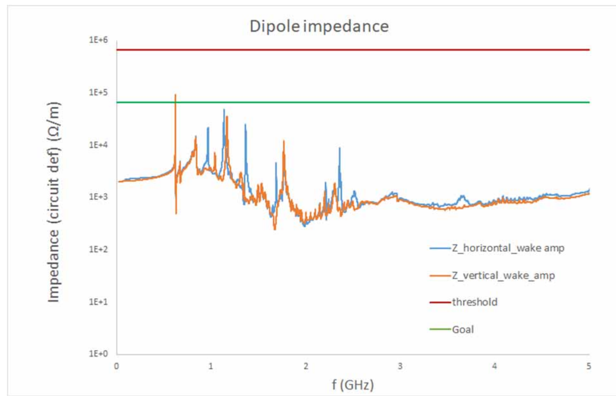

Figure 4: Dipole impedance of asymmetric 591 MHz SRF cavity.

Mechanical Design

Although large the ESR cavity can withstand atmospheric pressure without external support and once in the helium vessel with tuner fitted will be able to withstand maximum over-pressure of 2.2 atmospheres warm. Tables 2 and 3 show the mechanical properties of the bare cavity. Figures 5 and 6 show ANSYS simulations of the tuning force and pressure analysis, as shown also in Table 4. Stiffeners will be added to control Lorentz force detuning and pressure sensitivity as needed. Vertical test results will be available in time to influence the first article cavity and cryostat.

Table 3: Mechanical Properties of Bare 591 MHz cavity

Tuning Sensitivity (KHz/mm)	Stiffness (N/mm)	Elastic tuning range (mm)	Force to Yield (N)
447.05	14,258	0.435	6,200

ISBN: 978-3-95450-236-3 ISSN: 2673-7027 doi:10.18429/JACoW-eeFACT2022-WEXAS0101

Table 4: Pressure sensitivity of warm cavity with both ends constrained, no stiffeners.

Pressure (atm), 295.15K	Pressure sensitivity (Hz/atm)	Stress (MPa)	Safe?
1	12,028	19.97	Yes
2	12,003	39.94	Yes
3	11,979	59.91	No

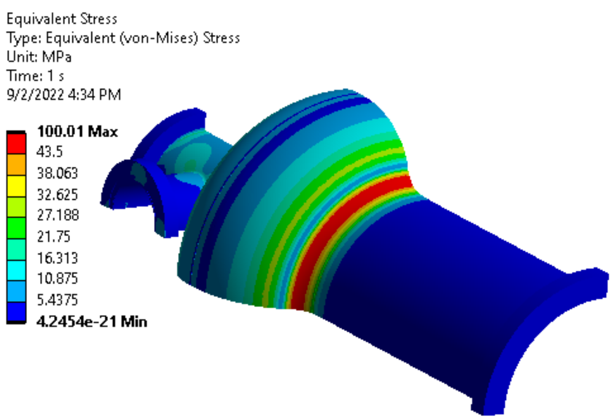

Figure 5. Tuning deformation of 591 MHz 1-cell cavity.

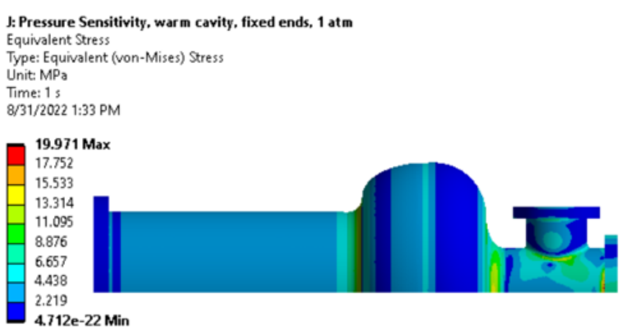

Figure 6. Pressure sensitivity of warm cavity with both ends constrained, no stiffeners.

Thermal Design

Initial thermal analysis, Fig. 7, shows that the 400 kW FPC can be integrated into the cryostat using a helium gas cooled connection similar to the SNS cryostat. The coupler port location is chosen to allow the lowest Q_{ext} foreseen in any operating scenario to be achieved. The FPC will be fixed but will have a range of Q_{ext} adjustment by stub tuners in the external circuit. Fig. 8 shows the proposed fabrication scheme which follows conventional SRF construction practices. Subject to final design review it is intended to start prototyping the bare cavity in the near future.

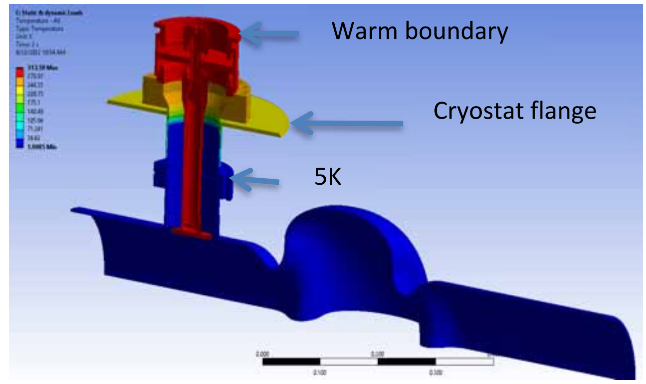

Figure 7: Preliminary thermal analysis of FPC cold to warm transition.

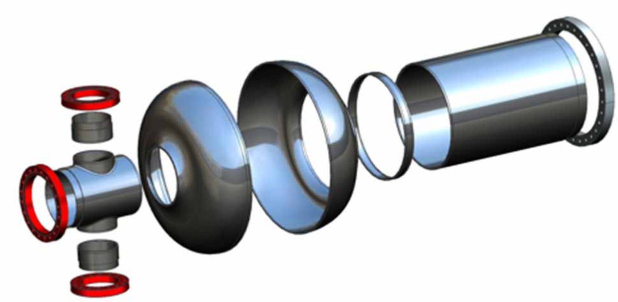

Figure 8: Fabrication model of the 591 MHz 1-cell SRF prototype cavity.

197 MHz CRAB CAVITY

The crab cavity systems for EIC are very challenging, combining low frequency, high gradient and high HOM power. Hence the 197 MHz crab was chosen for early R&D and prototyping. Both RFD and DQW designs were evaluated based on prior experience with the cavities for LHC. Both designs met requirements. The RFD design was selected for EIC as the fabrication plan was slightly further advanced. Table 5 shows the high level parameters. Because of the high hadron energy and the large crossing angle almost 34 MV of installed voltage is needed, with four cavities each side of each IP. The cavity qualification will include margin to be able to run with one cavity off. Second harmonic 394 MHz cavities are needed to linearize the crab kick over the long hadron bunches. The ESR having lower energy electrons can get by with a single 394 MHz cavity each side of each IP, but the higher current makes the HOM damping even more demanding. The impedance budget allows for a future second IP.

ISBN: 978-3-95450-236-3 ISSN: 2673-7027 doi:10.18429/JACoW-eeFACT2022-WEXAS0101

Table 5: Crab Cavity RF Requirements

	V_t (MV)		No. Cavities per IP	
system	HSR	ESR	HSR	ESR
197 MHz	33.8	-	8	-
394 MHz	4.75	2.9	4	2

RF Design

The 197 MHz RFD cavity is optimized to minimize peak surface fields and most multipacting barriers by careful choice of dimensions. The poles will be held fixed in operation to avoid variability in multipole components and tuning will be made via the side walls. The cavity will have compact “dog-bone” waveguide HOM dampers on the end caps to un-trap all harmful HOMs. Four identical ports will be used, two vertical and two horizontal, to maintain symmetry, see Fig. 9. In the 197 MHz cavity one vertical and one horizontal port will be terminated by broad-band HOM absorbers. The other horizontal port will accommodate the FPC and the remaining vertical port will house the field probe. Two options are under consideration for the absorbers, internal waveguide types, Fig. 10 and external loads with a cold coax to waveguide transition inside the module, Fig. 11. Both options meet the stringent HOM damping requirements and the module length is the same in each case. A selection will be made at a later date based on cost and manufacturability. The choice is independent of the cavity prototyping since the ports are the same in either case. Figures 12 and 13 show the transverse and longitudinal impedances of the cavity and Figs. 14 and 15 show the two module options. Figure 16 shows an early concept of the 394 MHz crab cavity that must handle the higher HOM power of the ESR. In this concept all four ports are terminated to share the HOM power between more loads.

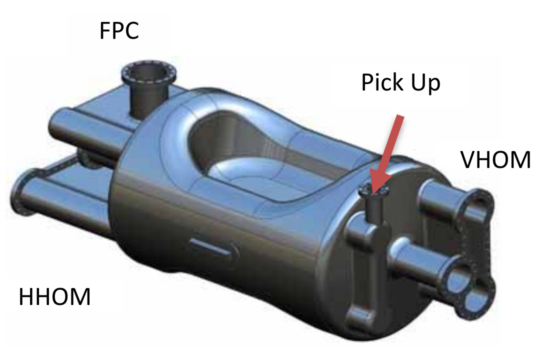

Figure 9: 197 MHz RFD type crab cavity.

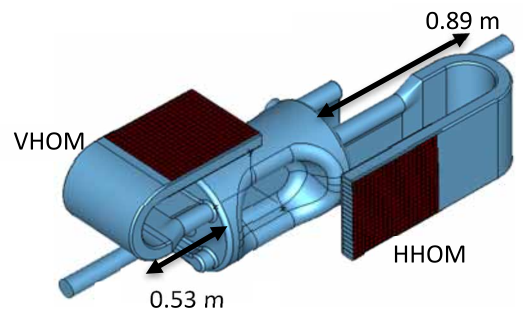

Figure 10: RFD with waveguide HOM absorbers.

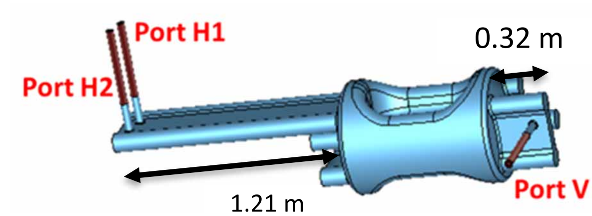

Figure 11: Crab cavity with coaxial HOMs.

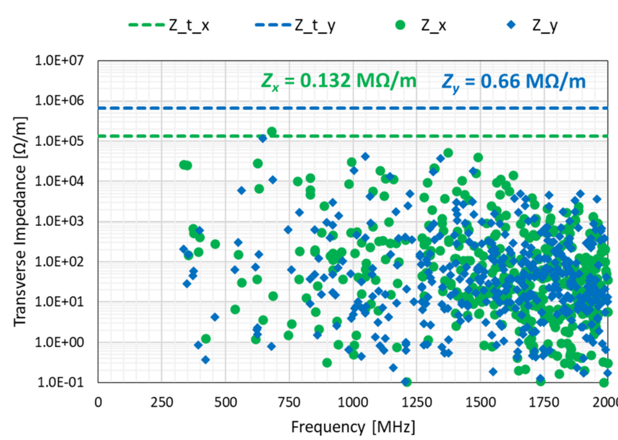

Figure 12: Transverse impedance of modes in the 197 MHz crab cavity.

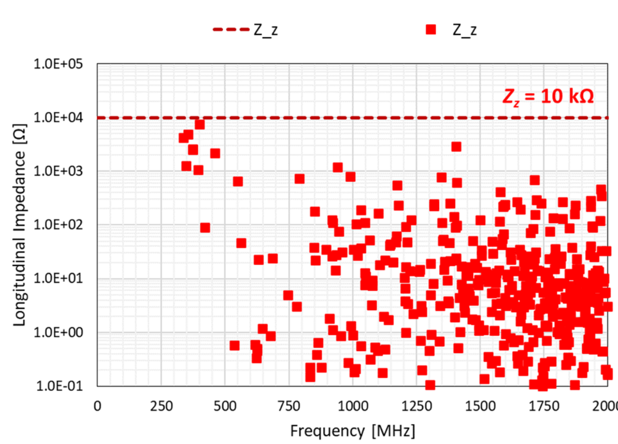

Figure 13: Longitudinal impedance of modes in the 197 MHz crab cavity.

ISBN: 978-3-95450-236-3 ISSN: 2673-7027 doi:10.18429/JACoW-eeFACT2022-WEXAS0101

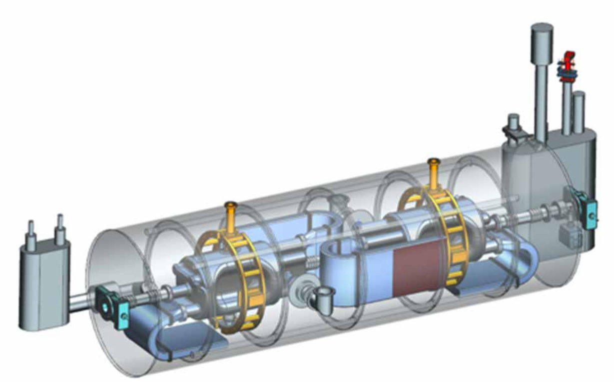

Figure 14: 197 MHz crab cavity cryomodule with internal waveguide HOM loads.

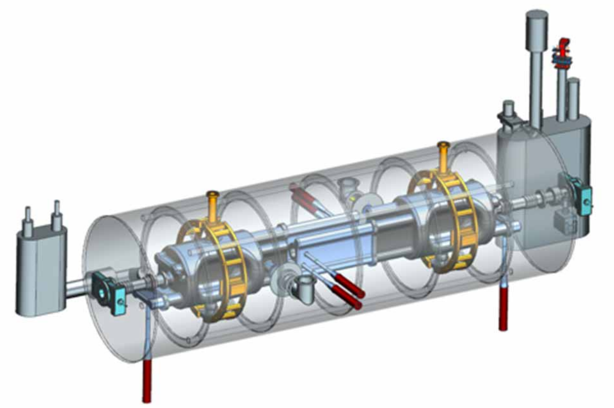

Figure 15: 197 MHz crab cavity cryomodule with exteral coaxial HOM loads.

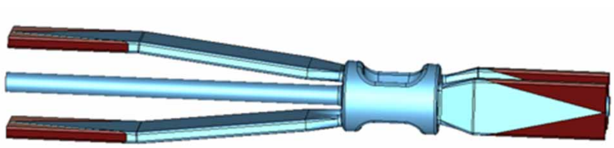

Figure 16: Simulation model of 394 MHz crab cavity concept with 4 HOM absorbers to handle the increased power of the ESR. In practice the waveguides would be folded similarly to the 197 MHz cavity.

Mechanical Design

The 197 MHz crab cavity is very large and cannot withstand significant external pressure without additional support. An external frame will be used to maintain the pole separation and fix the tuner mounts during handling and leak checking and the end caps will be constrained longitudinally against external pressure. For the bare cavity prototype this cage will also support the cavity during processing and vertical testing. For the production cavities this function will be incorporated into the helium vessel design. Detailed mechanical analysis of the cavity and cage are ongoing.

The fabrication of the cavity is complicated by the shape and size of the parts. It will not be possible to deep draw the poles in one step so the poles will be fabricated from sub-assemblies and joined to the "saddle" part of the body by e-beam welding. Side plates that also incorporate the tuner mounts will join the poles together to form the central barrel of the cavity. The end caps will be assembled from pressed dishes, dog bone waveguides and beam tubes. At this stage all surfaces are accessible for trimming and mechanical polishing if needed. The final joins will be circumferential full-penetration e-beam welds between the end caps and the body. Figure 17 shows the high level assemblies. Details of the sub-assembly fabrications are still being developed. Subject to design review, fabrication of the prototype 197 MHz crab cavity will begin in the near future.

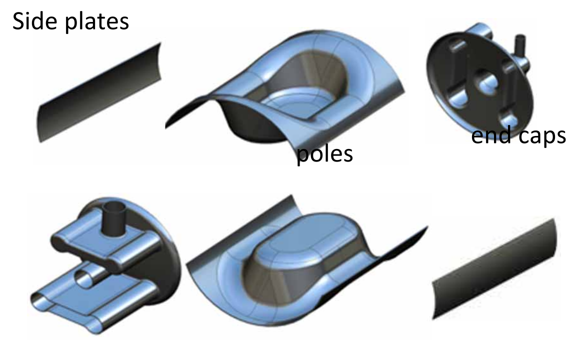

Figure 17. Major high-level subassemblies of the 197 MHz crab cavity prototype. Each assembly will be made from several smaller parts.

FPC AND BLA

The 400 kW FPC and high power beamline absorbers are critical components and therefore chosen for early R&D. The FPC [3], has gone through one design iteration already based on early testing experience. The design features a robust high purity alumina ceramic, water-cooled inner and warm outer conductors, a choke design for low surface fields on the ceramic and triple joints and mechanical design capable of withstanding 10G shock loads, see figure 18 . Six next-generation couplers will now be fabricated and tested with two being aimed at the first article cryomodule. The cold to warn outer conductor transition will have helium gas cooling to minimize dynamic load to the cryogenic system.

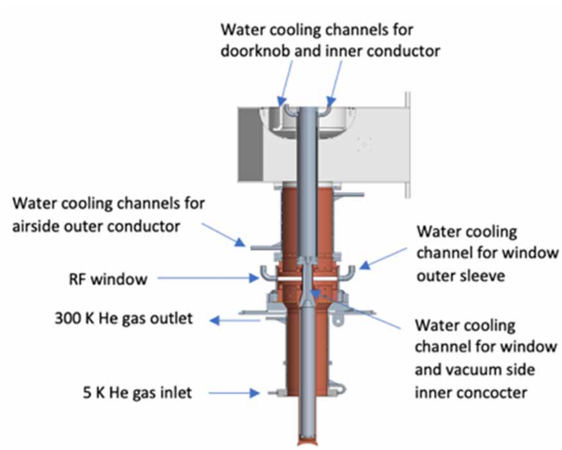

Figure18. High power FPC with water-cooled antenna and helium gas cooled cold outer conductor.

ISBN: 978-3-95450-236-3 ISSN: 2673-7027 doi:10.18429/JACoW-eeFACT2022-WEXAS0101

The high power beam line absorber [4], follows the "shrink fit" approach used by Argonne National lab for the APS upgrade. A one-piece cylinder of silicon carbide loaded dielectric absorber is fitted inside a water cooled jacket with no water to vacuum braze joints, see figure 19. Although the HOM power is high the power density in the large ceramic is within already demonstrated limits. Two prototypes have already been successfully completed and passed outgassing and low power RF tests. High power tests using a klystron RF source are planned soon.

Figure 19. Dielectric beam line absorber with shrink-fit cooling jacket.

5-CELL AND OTHER CAVITIES

In addition to the cavities selected for early R&D several other important designs are needed. The HSR, RCS and cooler ERL all require 591 MHz 5-cell cavities. These are assumed to be developed from the ESR 1-cell and are the same in all applications, using two high power BLA's with tapers, see figure 20. While this design will likely meet all requirements for beam voltage, HOM damping etc, the BLA end groups are sized for the high current HSR and may be more than what is required in the other applications. The long end groups drive the size of the cooler ERL and in the future more compact HOM end groups could be considered for the RCS and ERL.

Other cavities needed include a 1773 MHz 5-cell cavity for linearization in the cooler. This can be similar to CEBAF multi-cell designs or scaled from the 591 MHz 5-cell cavity. The cooler injector and proposed low energy precooler will need 197 MHz quarter wave accelerating cavities. These can be conventional SRF designs except for the high power couplers and strong HOM damping needed. These cavities are not part of the early R&D program, but basic concepts are being developed for layouts, costing etc. as needed.

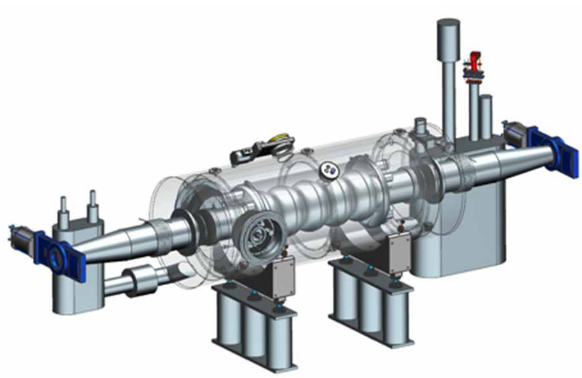

Figure 20: 5-cell cavity module for use in the HSR, RCS and cooler developed from ESR 1-cell.

MODULAR CRYOSTAT

In order to reduce costs, speed up development and provide for ease of support and maintenance a modular approach is being taken in developing the various cryomodules needed for EIC. Using standardized dimensions for vacuum vessels, helium vessels, end cans, couplers, valves etc. ensures a high degree of commonality between the modules. Differences are kept to a minimum and only when driven by requirements, such as the 197 MHz crab cavity, which is significantly bigger than all the other cavities. Even then many common components and subassemblies can be used. For simplicity and ease of integration the cryostat dimensions used for the SNS PPU, which is currently in production at JLab, were taken as the starting point. While the details of the 2 K cryogenic distribution for EIC have not been finalized we have used the SNS end cans with bayonet fittings as a basis, however these are literally "bolt-on" and can be replaced by a different interconnect scheme if necessary.

CONCLUSIONS

A variety of challenging cavities, cryomodules and ancillary components are needed for EIC. The designs from the CDR are being further developed to be ready for the TDR and CD2. The ESR 591 MHz single cell and the HSR 197 MHz crab cavities were selected for early R&D and good progress has been made on these designs. The high power FPC and BLA, which are critical components, have similarly progressed to prototyping and testing. More designs are needed but these will be developed from and informed by the early R&D models. The modular cryostat approach will speed up development, minimize total cost and design effort and allow common spares and easier support of the machine in operation.

REFERENCES

[1] EIC Conceptual Design Report, 2021,`https://www.bnl.gov/ec/files/EIC_CDR_Final.pdf`

[2] J. Guo *et. al.*, "Design of the Electron Ion Collider Electron Storage Ring SRF cavity", in *Proc. IPAC22*, Bangkok, Thailand, Jun. 2022, pp. 1307-13010. `doi:10.18429/JACoW-IPAC2022`

[3] W. Xu, Z.A. Conway, J.M. Fite, D. Holmes, K.S. Smith, and A. Zaltsman, "High Power Coupler Devepment for EIC", in *Proc. SRF'21*, East Lansing, MI, USA, Jun.-Jul. 2021, pp. 632-636. `doi:10.18429/JACoW-SRF2021-WEPTEV002`

[4] B.P. Xiao *et al.*, "HOM Damper Design for BNL EIC 197 MHz Crab Cavity", in *Proc. SRF'21*, East Lansing, MI, USA, Jun.-Jul. 2021, pp. 624-626. `doi:10.18429/JACoW-SRF2021-WEPCAV014`

ISBN: 978-3-95450-236-3 ISSN: 2673-7027 doi:10.18429/JACoW-eeFACT2022-WEXAS0102

SuperKEKB OPERATING EXPERIENCE OF RF SYSTEM AT HIGH CURRENT

M. Nishiwaki*, T. Abe, K. Akai, S. Enomoto, T. Furuya, A. Kabe, T. Kageyama, T. Kobayashi, K. Marutsuka, S. Mitsunobu, Y. Morita, K. Nakanishi, S. Ogasawara, T. Okada, M. Ono, H. Sakai, Y. Takeuchi, K. Watanabe, M. Yoshida, S. Yoshimoto and K. Yoshino
High Energy Accelerator Research Organization (KEK), Tsukuba, Japan

Abstract

SuperKEKB aims for high luminosity on the order of 10^{35} /cm^2/s with high beam currents of 2.6 A for electron and 3.6 A for positron to search a new physics beyond the Standard Model in the B meson regime. In recent operations, we achieved new record of the luminosity of 4.7×10^{34} /cm^2/s with 1.1 A for electron and 1.3 A for positron. The RF system that is basically reused from KEKB is operating stably in the high current operation owing to the measures against to large beam power and HOM power. To cope with the large beam power, it has been increased the number of klystrons that drive only one normal conducting cavity (ARES) and reinforced the input couplers of ARES. As a measure against HOM power, the additional HOM dampers have been installed to superconducting cavities. One-third of LLRF control systems have been replaced with newly developed digital system to improve accuracy and flexibility. New damper system for coupled bunch instability expected in high current has been installed to new digital system. In this report, operation status of RF system under the high current operation will be presented.

INTRODUCTION

The SuperKEKB accelerator that is an electron-positron asymmetric energy collider is an upgrade machine from KEKB accelerator aiming for a significant increase of luminosity. SuperKEKB main ring consists of a 7 GeV electron ring (high energy ring, HER) and a 4 GeV positron ring (low energy ring, LER). To achieve high luminosity, the beam currents are designed as 2.6 A for HER and 3.6 A for LER [1]. The first commissioning beam operation without collision was performed in 2016 as Phase-1. After the Belle II detector rolled in, Phase-2 beam operation started and the first beam collision event was observed at Belle II in 2018. A full-scale collision experiment (Phase-3) has been continued since 2019. In recent operation, the achieved beam currents are 1.14 A for HER and 1.46 A for LER, and the peak luminosity of 4.65×10^{34} /cm^2/s was recorded [2, 3].

The RF-related operation parameters in KEKB (achieved) and SuperKEKB (design) are shown in Table 1. The design beam current is nearly twice as high as the KEKB achieved, and the beam power becomes large accordingly [4–6]. The RF system consisting both of normal-conducting cavities (ARES) [7–9] and superconducting cavities (SCC) [10, 11] has been reused from KEKB with reinforcement to handle the high beam current and the large beam power. The ARES stations have 1:2 configuration in which one klystron drives two ARESs, and 1:1 configuration in which one klystron drives one ARES. The SCC station has one cavity driven by one klystron.

The main upgrade items are as follows:

- Increasing the number of RF klystron stations of ARES 1:1 configuration.
- In ARES, changing input coupling factor β from 3 (1:2 configuration) to 5 (1:1 configuration).
- In SCC, installation of additional higher-order-mode (HOM) dampers.
- In High-Power RF (HPRF) system, replacement of deteriorated klystrons with higher gain and more stable ones.
- In Low-Level RF (LLRF) system, replacing with new digital LLRF system in a part of ARES 1:1 stations and development of new damper system for coupled instability.

The addition of klystron to upgrade from ARES 1:2 to 1:1 configuration and the increase of input coupling factor of ARES are essential to provide the large beam power. The HOM power excited in the SCC module at the design current is estimated to be more than double the power achieved in KEKB, and to exceed the allowable power of the existing ferrite dampers. Then, additional dampers are necessary to reduce the load of ferrite dampers. The replacement of the old HPRF and LLRF systems with new systems increases the stability and accuracy of beam operation.

The layout of RF stations in SuperKEKB at present is shown in Fig. 1. There are a total of 30 RF klystron stations consisting 16 ARES (22 cavities) stations in LER and 6 ARES (8 cavities) and 8 SCC stations in HER. To date, the number of ARES 1:1 station is partially increased to 10 (LER) and 4 (HER) stations. In addition, countermeasures against RF-related instabilities in LLRF are essential for the high beam current operation. These measures have been completed partially. Remaining update items will be performed in the future to achieve the target beam current and luminosity. The details of upgrade of each component are described in Refs. [9, 13–18]. In this report, the operation status of RF system and the high beam current-related issues in RF system are described.

OPERATION STATUS OF RF SYSTEM

In the recent beam operation, the RF system is operating stably without any troubles requiring long shutdown.

* michiru.nishiwaki@kek.jp

ISBN: 978-3-95450-236-3 ISSN: 2673-7027 doi:10.18429/JACoW-eeFACT2022-WEXAS0102

Table 1: RF-related machine parameters achieved at KEKB [12] and those of the design values in SuperKEKB [6].

		KEKB (achieved)				**SuperKEKB (design)**			
Parameters	**Unit**	**LER**	**HER**			**LER**		**HER**	
Beam energy	GeV	3.5	8.0			4.0		7.0	
Beam current	A	2.0	1.4			3.6		2.6	
Bunch length	mm	6–7	6–7			6		5	
Number of bunch		1585	1585			2500		2500	
Total RF voltage	MV	8	13–15			10–11		15	
Energy loss/turn	MV	1.6	3.5			1.76		2.43	
Total beam power	MW	3.3	5.0			~8		~8	
RF frequency	MHz	508.9				508.9			
Revolution frequency	kHz	99.4				99.4			
Cavity type		ARES	ARES		SCC	ARES		ARES	SCC
No. of cavities		20	10	2	8	8	14	8	8
Klystron : cavities		1:2	1:2	1:1	1:1	1:2	1:1	1:1	1:1
No. of klystron stations		10	5	2	8	4	14	8	8
RF voltage/cavity	MV	0.4	0.31	0.31	1.24	~0.5	~0.5	~0.5	1.3–1.5
Beam poser/cavity	kW	200	200	550	400	200	600	600	400
R/Q of cavity	Ω	15	15	15	93	15	15	15	93
Loaded Q (Q_L)	$\times 10^4$	3	3	1.7	~5	3	1.7	1.7	~5

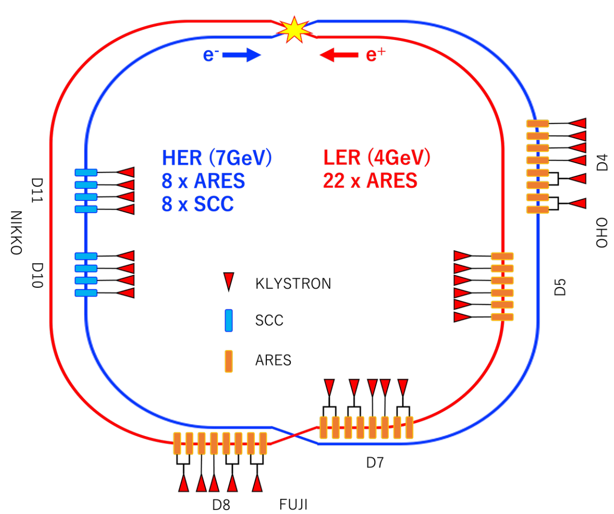

Figure 1: Layout of RF system of SuperKEKB. There are a total of 30 RF stations consisting both of normal-conducting cavity (ARES) and superconducting cavity (SCC) stations.

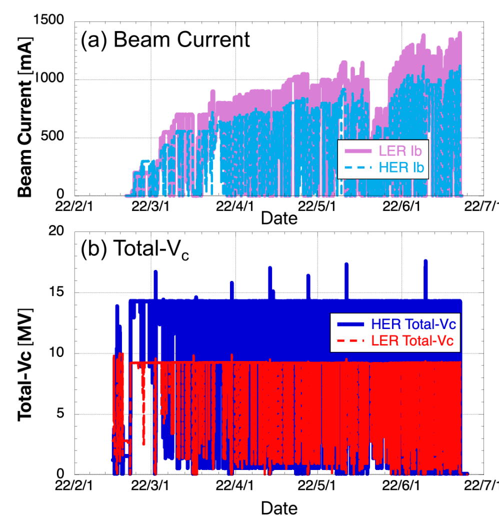

Figure 2: Operation history of 2022ab run. (a) shows beam current of LER (pink) and HER (cyan). (b) indicates total-V_c of LER (red) and HER (blue). The spikes in total-V_c are correspond to cavity aging in regular maintenance day.

Figure 2 shows the history of the beam current and total-V_c for both rings in the run of 2022ab (from Feb. to June 2022). In this run, the beam current was gradually increased while increasing the number of bunches, finally achieved up to 1.46 A for LER and 1.14 A for HER with 2346 bunches. The total-V_c for both rings were kept as 9.12 MV for LER and 14.2 MV for HER through this run. After middle of April, although one of ARES 1:1 stations (D07C) in LER was detuned (parked) due to a problem with the control system of the klystron power supply, the total-V_c was able to be maintained by increasing the voltage of other cavities. The voltage of each ARES cavity was 0.40–0.45 MV/cavity. In SCC, the cavity voltage was 1.35 MV/cavity. The spikes of total-V_c shown in Fig. 2(b) are correspond to cavity aging in regular maintenance days. The drop downs of total-V_c are the results of beam aborts. When the beam higher than 300 mA is aborted (dumped instantaneously), the RF is turned off by the interlock of the reflection power from the cavity in almost all RF stations. Conversely, if the interlock works even at one RF station and the RF is turned off, the beam of the corresponding ring is aborted.

Figure 3 shows the power delivered to beam by each cavity as a function of the stored beam current. For the maximum

ISBN: 978-3-95450-236-3 ISSN: 2673-7027 doi:10.18429/JACoW-eeFACT2022-WEXAS0102

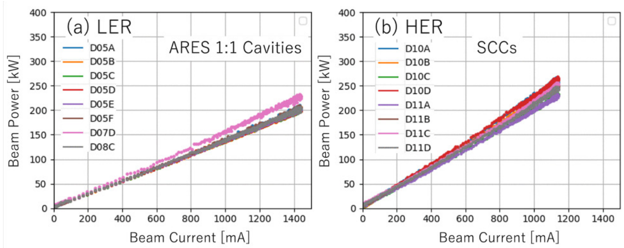

Figure 3: Beam power of each cavity as a function of the stored beam current. (a) shows ARES 1:1 cavities in LER. (b) shows SCCs in HER. The beam power is obtained by subtracting the reflected power from the cavity and the cavity wall loss from the klystron output or cavity input power.

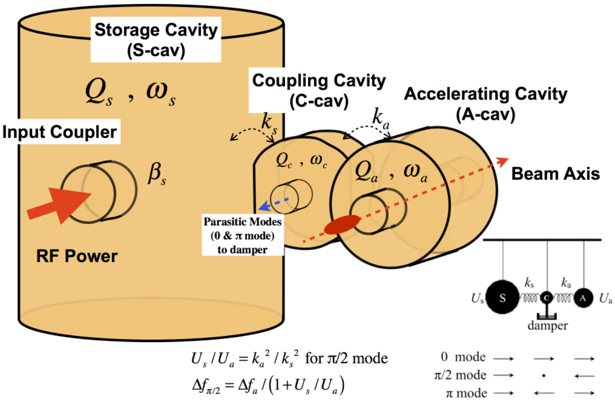

Figure 4: Illustration of the ARES cavity structure.

beam current, the beam power was reached to ~230 kW in an 1:1 ARES cavity in LER (Fig. 3(a)) and ~260 kW in a SCC in HER (Fig. 3(b)). In higher beam current operation, the optimization of the beam loading balance among the RF stations will be essential for stable and efficient beam operation. The optimization tool has been established and used in the actual beam operation [19].

All beam aborts are analyzed by recording the RF and beam signals to find the cause of trip. In particular, in ARES stations with digital LLRF system, all RF signals are recorded with a resolution of around 0.1 µs in maximum before and after events such as abort and RF off [16]. The fast-signal monitor is very useful as a diagnosis tool for the RF system. The number of beam aborts caused by the RF system was ~10% of all aborts (725 aborts in 2022ab), excluding manual and low current (<50 mA) aborts. The ~35% of the RF aborts were due to breakdown of ARES cavities and SCCs. In the 2022ab operation, the trip rates due to breakdown were ~0.5/cavity for the 30 ARES cavities and ~0.9/cavity for the 8 SCCs in four months operation. The trip rates of cavities are not changed significantly since KEKB operation. The ~40% of the RF aborts were due to HPRF system including incorrect operation of the interlock system of the klystron power supply system. As mentioned above, in 2022ab run, one klystron station was disconnected from the beam operation because the heater power supply of the klystron was broken due to a control board failure. One of the causes of problems on the HPRF system is the deterioration of the devices and infrastructure due to aging. Also in LLRF system, the aging of analog control modules is main cause of the failures. For stable operation, regular inspections and updating of devices are being carried out throughout the RF system.

ARES CAVITY

The ARES is a unique cavity, which is specialized for KEKB [7, 8]. It consists of a three-cavity system operated in the $\pi/2$ mode: the accelerating (A-) cavity is coupled to a storage (S-) cavity via a coupling (C-) cavity as shown in Figure 4 [9]. The A-cavity is structured to damp HOM. The S-cavity with a large stored energy plays a role in suppressing the optimum detuning of accelerating $\pi/2$ mode ($f_{\pi/2}$). Corresponding to the stored energy ratio of $U_s/U_a = 9$, where U_s and U_a are stored energies of S- and A-cavities, the detuning of $\pi/2$ mode ($\Delta f_{\pi/2}$) is one tenth that of A-cavity (Δf_a). As a result, the coupled bunch instabilities driven by the accelerating mode is suppressed. The C-cavity is equipped with a damper to damp parasitic 0 and π-modes. The $\pi/2$ mode has a high Q value of ~110,000 and a low R/Q value of 15 Ω.

The high-power input coupler has been upgraded to cope with the large beam power of SuperKEKB. At the design beam current, the beam power of 1:1 ARES is estimated as 600 kW in a cavity and the input power become to be 800 kW including the cavity wall loss of around 150 kW. In order to increase the input power from 400 to 800 kW, the coupling factor β of the input coupler has been increased from 3 to 5 [6, 14]. In addition, to suppress multipactoring problem in the coaxial lines of the couplers, the fine groove structure is adopted for the outer conductor surface (Fig. 5) [13]. 14 of the 32 input couplers have been upgraded with an increased coupling factor β of 5 and the fine groove structure. Those new input couplers have no multipactoring and other problems in SuperKEKB beam operation so far.

At higher beam current operation, diagnostic tools will become more important. In the ARES system, all input couplers are monitored with TV or network cameras attached to the viewport of S-cavity on the opposite side of the input coupler. A few seconds of video of the camera before and after the RF is turned off is automatically recorded on mass storage devices. Figure 6 shows examples of the recorded videos with the cameras. This diagnostic tool can isolate the problem; it is related to the input coupler or not. Another diagnostic tool is fast-signal recording by the digital LLRF. Figure 7 shows examples of the fast signals with a microsecond resolution. When the RF switch is turned off due to a reason other than the cavity, the field falls with a tail determined from the fill time (~10 µs) as seen in Fig. 7(a). On the other hand, as seen in Fig. 7(b), the field drops in a much shorter time than the fill time, which can be understood as an occurrence of cavity breakdown due to vacuum arc.

65th ICFA Adv. Beam Dyn. Workshop High Luminosity Circular e+e− Colliders eeFACT2022, Frascati, Italy JACoW Publishing
ISBN: 978-3-95450-236-3 ISSN: 2673-7027 doi:10.18429/JACoW-eeFACT2022-WEXAS0102

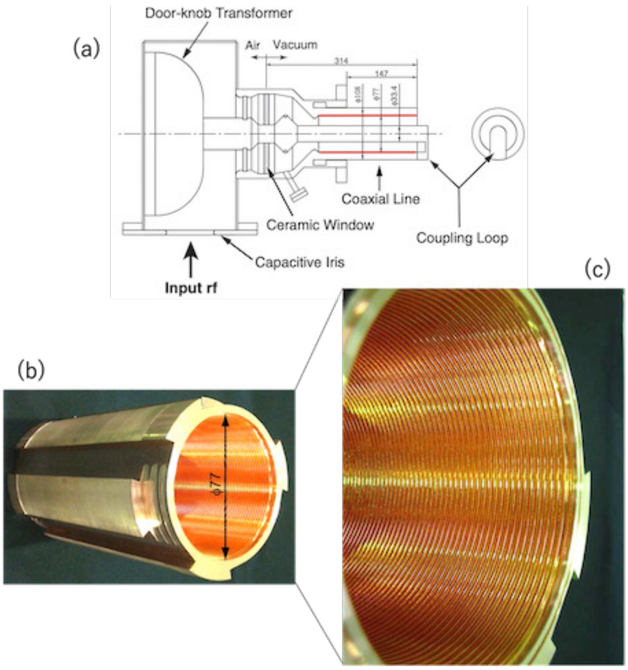

Figure 5: Schematic view of input coupler for the ARES(a), outer conductor with fine grooving (b) and zoom of fine grooving(c). The red line in (a) indicate the fine grooving structure.

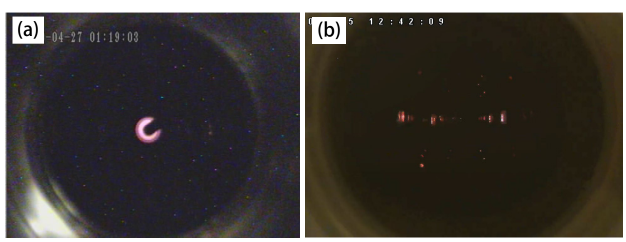

Figure 6: Examples of the recorded videos with the cameras attached to the viewport of S-cavity on the side opposite the input coupler at the moment of cavity trips. (a) Clear discharge from multipactoring on the RF window in the input coupler was observed. (b) Lights came not from the input coupler but some other place with scattered reflection.

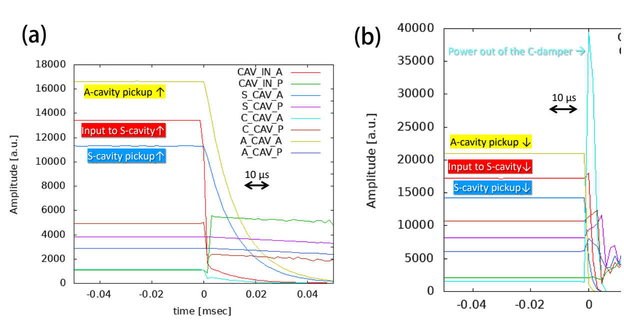

Figure 7: Examples of the fast signals recorded by the digital LLRF; (a) when the RF switch was turned off manually, (b) cavity breakdown event.

SCC MODULE

The SCC modules (Fig. 8) [10] and cryogenic system [20] are also reused from KEKB. The SCC module was designed for KEKB with HOM damped structure equipped with a pair of ferrite HOM dampers on both small beam pipe (SBP) and large beam pipe (LBP) [21]. The beam power and accelerating voltage are kept by sharing with ARES cavities by giving phase-offset.

The handling large HOM powers induced by the high beam current is one of the main issues. According to the power flow simulation in one cavity module, the load of the existing a pair of ferrite dampers is around 20 kW, which is not much increased from the maximum absorbed power of 16 kW in KEKB operation [11]. But large HOM power is emitted through the downstream beam duct and the power becomes additional load of the dampers of downstream cavity [22]. To reduce the emission power, two sets of additional HOM dampers made by SiC have been installed to the downstream of two SCC modules [17, 23]. In the beam operation, the HOM power absorbed by the ferrite dampers of downstream cavities were reduced by more than 10% by the additional SiC dampers as shown in Fig. 9. The absorbed HOM power by a pair of ferrite dampers in one SCC module were ~8 kW at the maximum beam current in 2022ab. To achieve design beam current, SiC dampers will be installed to downstream of all cavities.

Another issue is degradation of the cavity performance of Q_0. In the long-term operation since 1998, SCCs experienced several vacuum works and troubles. As a result, performance of several cavities degraded with strong field emission. To recover the cavity performance, we developed horizontal high-pressure rinse (HHPR) method [24]. By HHPR, the performance of three cavities have been success-

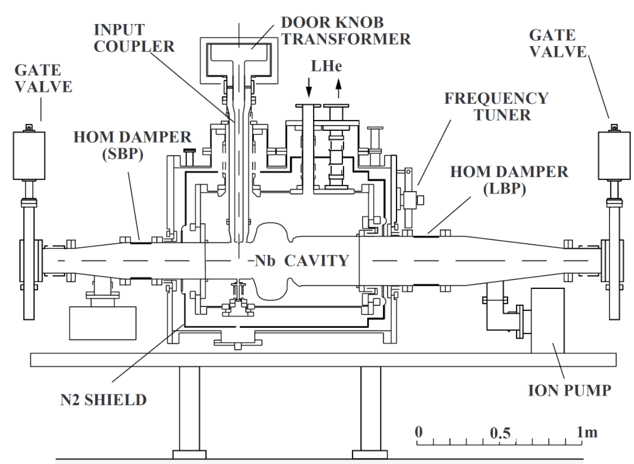

Figure 8: Cross-sectional view of HOM damped SCC designed for KEKB. This cavity is used for SuperKEKB. Ferrite HOM dampers are equipped on both SBP and LBP. The SBP and LBP diameters are 220 mm and 300 mm, respectively.

ISBN: 978-3-95450-236-3 ISSN: 2673-7027 doi:10.18429/JACoW-eeFACT2022-WEXAS0102

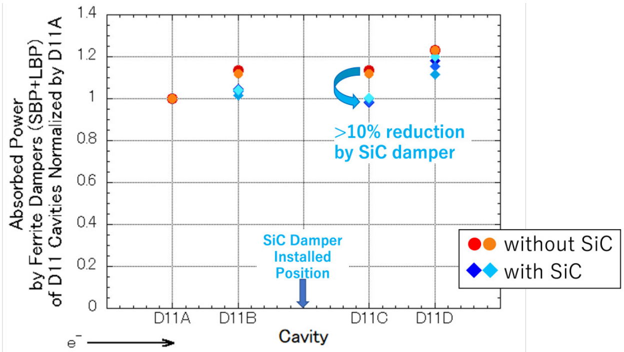

Figure 9: Ratio of absorbed HOM power by ferrite dampers of SCC cavities in D11 section.

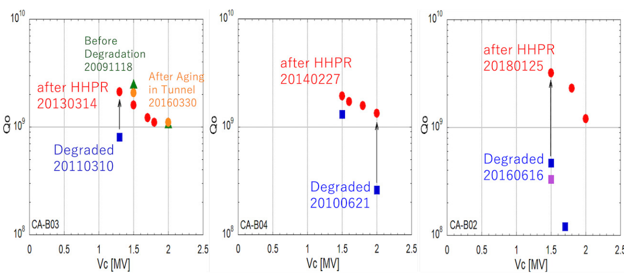

Figure 10: Q_0 values as a function of V_c before and after HHPR for three degraded cavities.

fully recovered as shown in Fig. 10 and those cavities are operating stably in SuperKEKB.

In the beam operation, the RF signals are monitored by oscilloscopes every beam aborts to analyze the cause of trip. Figure 11 shows an example of a trip by multipacting in cavity. The spike of V_c (cavity pickup) signal was found ~40 ms before RF turned off by the interlock from the breakdown detector (Fig. 11(a)). It is supposed that the multipacting occurred and disappeared in a few tens of microseconds (Fig. 11(b)), and the local normal conducting region generated by the multipacting gradually propagated, increasing the cavity wall loss. Finally, an increase in klystron output power was observed as a result of feedback control to keep V_c constant (Fig. 11(c)). It is important to detect malfunctions of SRF system quickly by the diagnostic system in order to continue stable operation at high beam currents.

HIGH BEAM CURRENT-RELATED ISSUES IN RF SYSTEM

The RF issues to be considered for the high beam current are summarized in Ref. [25]. In SuperKEKB, coupled bunch instability (CBI) excited by accelerating mode and an effect of bunch gap transient is estimated to be problem in high beam current operation. The countermeasures in SuperKEKB are introduced below. For CBI due to HOM, the ARES and SCC are designed as HOM dumped structures and equipped with HOM dampers [7, 10]. Additionally the bunch-by-bunch feedback system is effective for damping the instability.

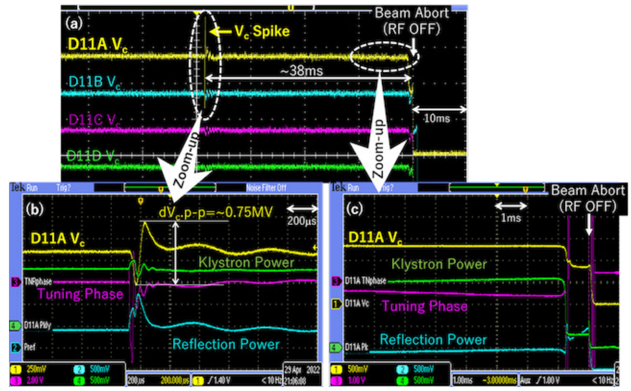

Figure 11: Example of RF signals of a trip event of D11A cavity monitored by oscilloscopes; (a) long-range monitor of V_c of 4 cavities, (b) focused on V_c spike event, (c) focused on just before beam abort. The V_c (yellow), klystron output power (green), cavity reflection power (cyan) and cavity tuning phase (magenta) are indicated in (b) and (c).

CBI due to $\mu = -1$, -2 and -3 Mode [18, 26]

The growth rates of CBI due to accelerating mode are estimated as shown in Figure 12 for SuperKEKB LER (upper) and HER (lower side) [18]. The threshold of beam currents for $\mu = -1$ mode are less than the design currents in both of LER and HER. The dashed lines show the damping rates with a parked (detuned) cavity. In that case, the thresholds of $\mu = -2$ mode are also below the design currents for both ring. In HER operation, CBI of $\mu = -1$ mode is excited at lower beam current than expected, but the cause is still not clear. Though it is necessary to investigate the cause, CBI damper is essential in order to continuing beam operation.

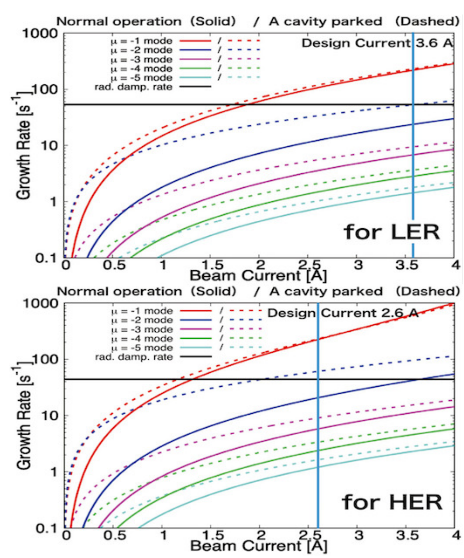

Figure 12: Estimation of the growth rate of the coupled bunch instability due to accelerating mode of $\mu = -1$, -2 and -3. Upper and lower side indicate for LER and HER, respectively.

ISBN: 978-3-95450-236-3 ISSN: 2673-7027 doi:10.18429/JACoW-eeFACT2022-WEXAS0102

In LLRF system of SuperKEKB, new damper system with new digital filters for CBI has been developed [18]. The damper system is installed to ARES station with digital LLRF system. The damper system can correspond to $\mu = -1, -2$ and -3 modes in parallel as shown in Fig. 13 [26]. Figure 14 shows examples of beam spectra without (upper side) and with (lower side) CBI damper [18]. In that case, $\mu = -2$ mode was excited intentionally by detuning one SCC of −200 kHz in HER. One can see a peak in upper spectra at frequency of $f_{rf} - 2f_0 + f_s$, where f_{rf} is RF frequency of 508.876 MHz, f_0 is revolution frequency of 99.4 kHz and f_s is synchrotron frequency of 2.78 kHz in design [6]. After tuning of phase and amplitude of the CBI damper, the peak is disappeared in lower spectra. The new CBI damper has been operating from Phase-2 operation (2019) in both rings. The CBI is not a problem with this damper systems up to 1.46 A for LER and 1.14 A for HER.

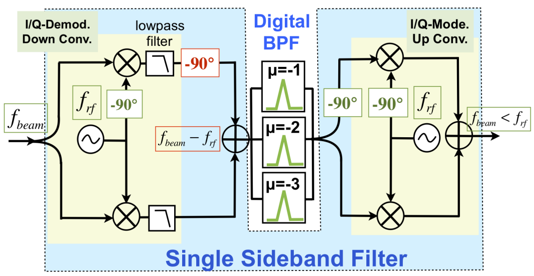

Figure 13: Block diagram of new digital filter with single sideband filter for CBI damper. The digital filter is available for the $\mu = -1, -2$ and -3 modes in parallel.

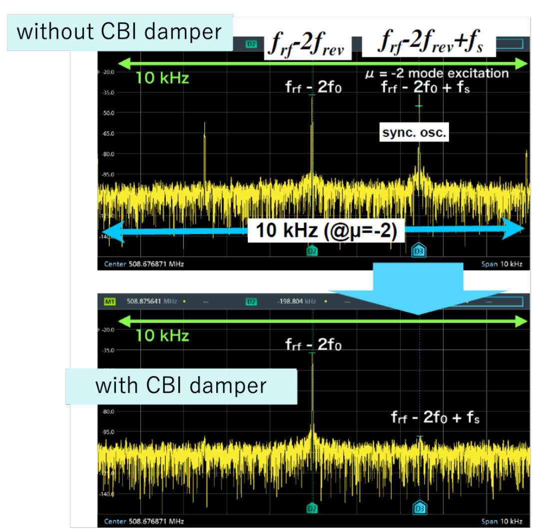

Figure 14: Example of beam spectra without (up) and with (bottom) CBI damper for $\mu = -2$ mode.

Stability of the Zero Mode under heavy beam loading [27, 28]

In SuperKEKB high-current beam operation, achieving the stability of the zero mode associated with the accelerating mode of the RF system is an important concern because of heavy beam loading. The stability criterion can be more severe compared to the Robinson's one [29] by the effects of control functions in the LLRF system including amplitude and phase control loops for the cavity field. The issue is a more serious problem in the HER compared to the LER because of high impedance of superconducting cavities operating in the HER.

As a countermeasure, the RF system is equipped with a direct RF feedback system (DRFB) to effectively reduce the impedance of the cavities and a zero mode oscillation damper (ZMD). Although the DRFB and ZMD were also used at KEKB to mitigate the beam loading [30], they have more significant roles in SuperKEKB because of higher beam current. Figure 15 shows a schematic view of the LLRF system, highlighting an SCC station (D11-A). Because the bandwidths of the amplitude and phase control loops are much less than the revolution frequency, 99.4 kHz, these loops do not interact with the beam at the higher coupled modes such as −1, −2, −3 modes, but are intertwined with the beam, DRFB, and ZMD in the zero mode.

The stability of the zero mode for the system was quantitatively analyzed with heavy beam loading, taking these loops into account [28]. Two different approaches were used in the analysis: One was based on the characteristic equation (CE) and the other using a simulation in the time domain. First, the consistency between both methods was confirmed by applying them to typical cases. Next, the simulation results were compared to measurements performed in a machine study conducted in 2019 [27] during SuperKEKB beam operation. Figure 16 shows the zero-mode coherent synchrotron frequency f_s as a function of the beam current at different DRFB gains obtained from the simulation (blue and black marks), as well as the measured values in the machine study (red marks). In both the simulation and measurement, f_s

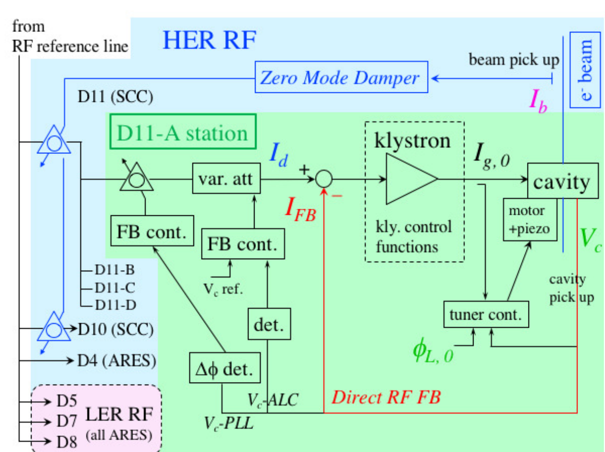

Figure 15: Schematic view of LLRF system for SuperKEKB, highlighting an SCC station (D11-A) in green colored part. In addition to the amplitude and phase control loops for the cavity field, the DRFB and ZMD are implemented. Cavity tuning is performed based on the relative phase between the klystron output and cavity voltage.

ISBN: 978-3-95450-236-3 ISSN: 2673-7027 doi:10.18429/JACoW-eeFACT2022-WEXAS0102

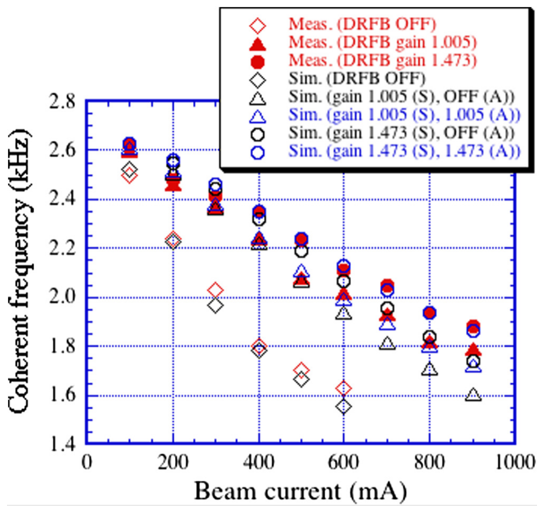

Figure 16: Calculated and measured frequencies of the zero-mode coherent synchrotron oscillation f_s with SCC and ARES in the HER as a function of the stored beam current. The blue (black) marks correspond to the DRFB for ARES on (off) in the simulation. The red marks show measured values in the beam study [27]. The circle (triangle) marks indicate the DRFB gain of 1.473 (1.005). The diamond marks indicate DRFB off (from [28]).

decreased as the beam current increased owing to beam loading and the effect of the DRFB on reducing the f_s shift was clearly observed. The simulation and measurement results were in good agreement.

Having confirmed the validity of these methods, analysis using the CE and simulation were comprehensively conducted for future high-current beam operations in SuperKEKB. The results showed the effectiveness of DRFB and ZMD, which played an important role in ensuring the zero mode stability. In beam operations, maximum achievable stored current may be considerably lower than the threshold current obtained from the analysis for different reasons such as: scattering the cavity performance or operating conditions, nonlinearities of klystrons and other RF components, and fluctuations caused by unknown jitters and machine errors. Because it is difficult to accurately predict these uncertain effects, we searched parameter sets that provided sufficient high threshold currents compared to the design currents. Here, as reference guideline, a threshold current target value of 4 A (5 A) in the HER (LER) was set because it was considered to be a good margin for the design current of 2.6 A (3.6 A), although it had not yet been validated for the operation. Efforts to obtain more reliable confirmation on this would be continued in the beam operation with increasing beam current step by step. Thus, different operational parameter sets as well as possible system modifications were investigated, thereby creating a considerably good margin to compensate for the possible deficiencies at higher beam currents. The results could be used as guidelines for future beam operation by increasing the beam current step by step. For more details, see Ref. [28].

Bunch Gap Transient [31, 32]

In a multi-bunch storage ring, bunch trains have an empty-bucket gap to ensure the rise time of the beam abort kicker. However, the gap modulates the amplitude and phase of an accelerating cavity field. As a result, the longitudinal synchronous position is shifted bunch by bunch along the train. For colliders such as SuperKEKB, the collision point shift is causing a loss of luminosity. Figure 17 shows an example of RF phase modulation of the accelerating cavity of ARES (D05A) measured with digital LLRF system in the beam current of 1 A in LER. The blue solid line is measured and red dashed line is simulated results. The horizontal axis is time in microseconds. The time interval of 10 μs is the revolution period. In recent operation, we have two abort gaps in one revolution to be short the wait time for abort. The rapid phase change was observed at the leading part of train. From the results of new simulation studies for the bunch gap transient [31], the rapid phase change at the leading part is caused by a transient loading in the three-cavity system of ARES (Fig. 4). In other words, the rapid phase change is due to the parasitic (0 and π) modes of ARES.

The collision point shift can be estimated from a phase difference between LER and HER. Figure 18 shows the phase difference between LER and HER ($\Delta\phi_{HER} - \Delta\phi_{LER}$) of the gap region, obtained from the simulation with the SuperKEKB design parameters (the gap length of 2%). The red solid line indicates the relative phase. As one can see, the maximum phase difference will be 5.5° (pk-pk) at the leading part of collision bunches. The phase shift of 5.5° corresponds to a longitudinal displacement of $0.44\sigma_z$ at the collision point, where the bunch length (σ_z) is 5 mm (rms). Except the leading part, the phase difference along the train is not so large ($< 1°$).

Because, in SuperKEKB, the crossing angle between the two beams at the collision point is larger and the vertical beta

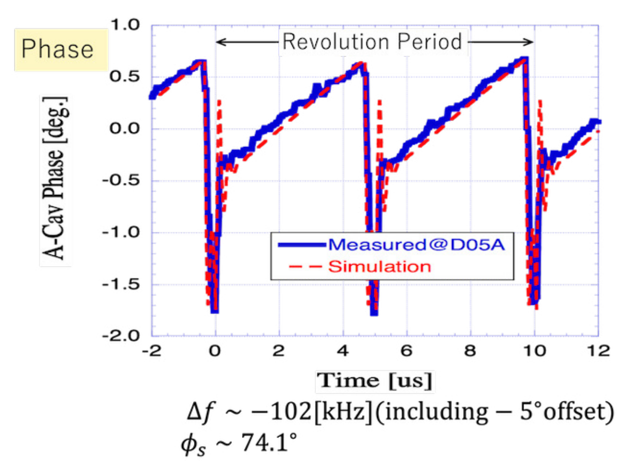

Figure 17: RF phase modulation in the accelerating (A-) cavity of ARES in LER. Blue solid line is measured and red dashed line is simulated results. The beam current was around 1 A. There are two abort gaps i.e. two trains in the revolution period of 10 μs.

ISBN: 978-3-95450-236-3 ISSN: 2673-7027 doi:10.18429/JACoW-eeFACT2022-WEXAS0102

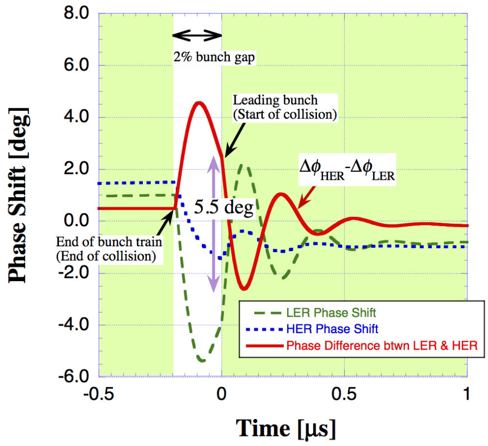

Figure 18: Phase difference between LER and HER (red solid line = $\Delta\phi_{HER} - \Delta\phi_{LER}$). Zoomed the gap region.

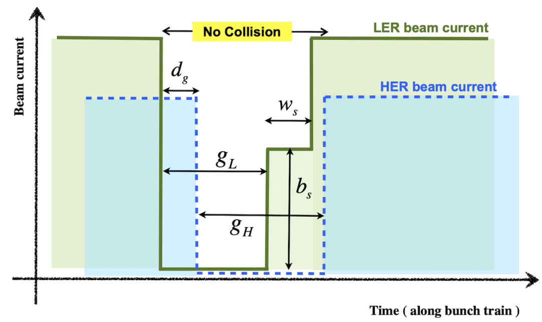

Figure 19: Illustration of a bunch fill pattern for more effective mitigation. HER gap is delayed by d_g. The bunch current in the leading part of LER is increased in two steps with a time interval w_s with the step height of b_s. g_L and g_H are the gap length of LER and HER, respectively.

function is much smaller than those of KEKB, the effect of the large phase difference might be crucial issue to achieve high luminosity. Unfortunately, the feed-forward control cannot be available in our RF system to mitigate the phase modulation due to the gap transient, because the klystron performance (the bandwidth of ~100 kHz and the output power) is not enough to cancel the rapid phase modulation.

We have proposed the method to mitigate the phase difference [31]. The first point of the mitigation method is making a delay of the HER gap timing with respect to the LER gap. The second point is to increase the bunch current in the leading part of LER in a step-like manner as shown in Fig. 19. The HER gap is delayed by d_g. The bunch current in the leading part of LER is increased in two steps with a time interval w_s with the step height of b_s. g_L and g_H are the gap lengths of LER and HER, respectively, and are set to 2% ($g_L = g_H = 200$ ns), which is the minimum length required from the rise time of the abort kicker. b_s is set to half of the nominal bunch current for simplicity. The simulation was performed by changing the parameters d_g and w_s. The best result was obtained with $d_g = 160$ ns and $w_s = 140$ ns. The result is shown in Fig. 20. The phase difference between LER and HER is reduced to 0.4° at the leading part of the collision as shown in Fig. 20(b), while the phase difference along the train is kept small as shown in Fig. 20(a). From the simulation, it is found that the fill pattern change of LER in addition to the HER delay gives more effective mitigation. For more details, see Ref. [31]. In actual operation, it is necessary to optimize the fill pattern and gap delay while observing the luminosity.

SUMMARY

SuperKEKB is steadily increasing the beam current and continues to update own luminosity record. The RF system of SuperKEKB is operating stably at large beam current of 1.14 A for HER and 1.46 A for LER in 2022ab operation. The cavities are operating stably with low trip rates. The ARES and SCC systems have been upgraded to handle the

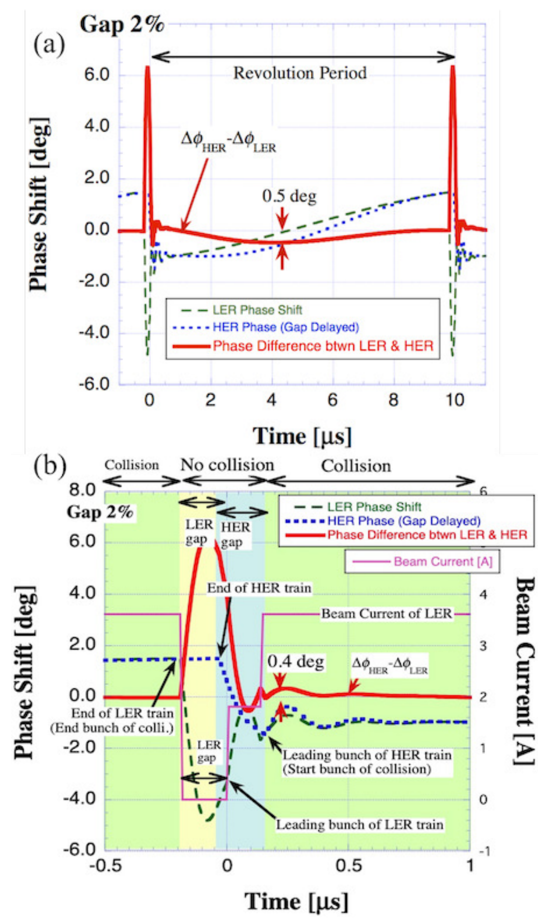

Figure 20: Phase difference between LER and HER with the mitigation method of Fig. 19. The HER delay $d_g = 160$ ns and the LER step height $w_s = 140$ ns. Bottom plot (b) is zoom of the gap region of upside plot (a).

ISBN: 978-3-95450-236-3 ISSN: 2673-7027 doi:10.18429/JACoW-eeFACT2022-WEXAS0102

high beam current and the large beam power. For ARES, the input coupler has been upgraded with increasing coupling factor and the fine grooving structure. The couplers have no problems in the beam operation. It is confirmed that the additional SiC HOM dampers for SCC reduce HOM load of ferrite dampers of downstream cavities. In the future, SiC dampers will be installed to downstream of all cavities. To control instabilities, such as CBI and coherent oscillation due to large beam current, CBI damper, DRFB and ZMD are established and working well. Comprehensive analysis using the CE and simulations showed the effectiveness of DRFB and ZMD in ensuring zero-mode stability, as well as guidelines for future beam operations by increasing the beam current step by step. The mitigation method of the beam phase difference between LER and HER due to the bunch gap transient effect is proposed: the relative phase change at IP can be reduced by optimization of the gap delay and bunch fill pattern.

REFERENCES

[1] Y. Ohnishi *et al.*, "Accelerator Design at SuperKEKB", Prog. Theor. Exp. Phys., vol. 2013, no. 3, p. 03A011, 2013. https://doi.org/10.1093/ptep/pts083

[2] Y. Funakoshi *et al.*, "The SuperKEKB Has Broken the World Record of the Luminosity", in *Proc. IPAC'22*, Bangkok, Thailand, Jun. 2022, pp. 1–5. doi:10.18429/JACoW-IPAC2022-MOPLXGD1

[3] Y. Ohnishi, "SuperKEKB Luminosity Quest", presented at the 65th ICFA Advanced Beam Dynamics Workshop on High Luminosity Circular e+e- Colliders (eeFACT22), Frascati (RM), Italy, Sept. 2022, this workshop.

[4] K. Akai *et al.*, "RF Systems for the KEK B-Factory", Nucl. Instrum. Methods Phys. Res., Sect. A499, 45 (2003). https://doi.org/10.1016/S0168-9002(02)01773-4

[5] K. Akai *et al.*, "RF System for SuperKEKB", in *Proc. of the 7th Annual Meeting of Particle Accelerator Society of Japan*, Himeji, Japan, Aug. 4-6, 2010, pp. 177–181. https://www.pasj.jp/web_publish/pasj7/proceedings/SH_4PM_2/WESH05.pdf

[6] SuperKEKB Design Report, RF System, 2014. https://www-linac.kek.jp/linac-com/report/skb-tdr/6_RF_190131b_pp149-215Akai.pdf

[7] Y. Yamazaki and T. Kageyama, "A Three-Cavity System which Suppresses the Coupled-Bunch Instability Associated with the Accelerating Mode", Part. Accel., 44, 107 (1993).

[8] T. Kageyama *et al.*, "The ARES Cavity for KEKB", in *Proc. APAC'98*, Tsukuba, Japan, Mar. 1998, pp. 773-775 (1998). https://accelconf.web.cern.ch/a98/APAC98/6D039.PDF

[9] T. Kageyama, T. Abe, H. Sakai, Y. Takeuchi and K. Yoshino, "ARES Cavity System for SuperKEKB", in *Proc. of the 8th Annual Meeting of Particle Accelerator Society of Japan*, Tsukuba, Japan, Aug. 1-3, 2011, pp. 1245–1249. https://www.pasj.jp/web_publish/pasj8/proceedings/poster/TUPS126.pdf

[10] T. Furuya *et al.*, "Recent Status of the Superconducting Cavities for KEKB", in *Proc. SRF'99*, Santa Fe, NM, USA, Nov. 1999, paper MOP001, pp. 31–36. https://accelconf.web.cern.ch/SRF99/papers/mop001.pdf

[11] Y. Morita *et al.*, "Status of KEKB Superconducting Cavities and Study for Future SKEKB", in *Proc. SRF'09*, Berlin, Germany, Sep. 2009, paper TUPPO022, pp. 236–238. https://accelconf.web.cern.ch/SRF2009/papers/tuppo022.pdf

[12] T. Abe *et al.*, "Performance and Operation Results of the RF Systems at the KEK B-Factory", Prog. Theor. Exp. Phys. 2013, 03A006 (2013). https://doi.org/10.1093/ptep/ptt020

[13] T. Abe, T. Kageyama, H. Sakai, Y. Takeuchi and K. Yoshino "Multipactoring Suppression by Fine Grooving of Conductor Surfaces of Coaxial-line Input Couplers for High Beam Current Storage Rings", Phys. Rev. Accel. Beams 13, 102001 (2010). https://link.aps.org/doi/10.1103/PhysRevSTAB.13.102001

[14] T. Kageyama, K. Yoshino, H. Sakai, T. Abe and Y. Takeuchi, "Input Coupler for the ARES Cavity in SuperKEKB", in *Proc. of the 11th Annual Meeting of Particle Accelerator Society of Japan*, Aomori, Japan, Aug. 9-11, 2014, pp. 590–594. https://www.pasj.jp/web_publish/pasj2014/proceedings/PDF/SAP0/SAP044.pdf

[15] K. Watanabe, M. Yoshida, S. Yoshimoto, K. Marutsuka and M. Ono, "Current Status of the High-Power RF Systems in MR for Super-KEKB", in *Proc. of the 12th Annual Meeting of Particle Accelerator Society of Japan*, Tsuruga, Japan, Aug. 5-7, 2015, pp. 630–633. https://www.pasj.jp/web_publish/pasj2015/proceedings/PDF/WEP0/WEP065.pdf

[16] T. Kobayashi *et al.*, "Development and Construction Status of New LLRF Control System for SuperKEKB", in *Proc. IPAC'14*, Dresden, Germany, Jun. 2014, pp. 2444–2446. doi:10.18429/JACoW-IPAC2014-WEPME071

[17] M. Nishiwaki, K. Akai, T. Furuya, A. Kabe, S. Mitsunobu and Y. Morita, "Operation Status of Superconducting Accelerating Cavity and Development of SiC Damper for SuperKEKB", in *Proc. of the 14th Annual Meeting of Particle Accelerator Society of Japan*, Sapporo, Japan, Aug. 1-3, 2017, pp. 914-918. https://www.pasj.jp/web_publish/pasj2017/proceedings/PDF/WEP0/WEP037.pdf

[18] K. Hirosawa, K. Akai, E. Ezura, T. Kobayashi, K. Nakanishi and S. Yoshimoto, "Advanced Damper System with a Flexible and Fine-tunable Filter for Longitudinal Coupled-bunch Instabilities Caused by the Accelerating Mode in SuperKEKB", Nuclear Inst. and Methods in Physics Research, A 953 (2020) 163007. https://doi.org/10.1016/j.nima.2019.163007

[19] S. Ogasawara, K. Akai, T. Kobayashi, K. Nakanishi and M. Nishiwaki, "Optimization of RF Phase and Beam Loading Distribution among RF Stations in SuperKEKB", presented at the The Low Level RF Workshop 2022 (LLRF22), Brugg-Windisch, Switzerland, Sept. 2022.

[20] K. Nakanishi *et al.*, "KEKB/SuperKEKB Cryogenics Operation", in *Proc. eeFACT'18*, Hong Kong, China, Sep. 2018, pp. 276. doi:10.18429/JACoW-eeFACT2018-WEPAB04

[21] T. Tajima, "Development of Higher-Order-Mode (HOM) Absorbers for KEKB Superconducting Cavities", KEK

ISBN: 978-3-95450-236-3 ISSN: 2673-7027 doi:10.18429/JACoW-eeFACT2022-WEXAS0102

Report 2000-10 (2000). https://lib-extopc.kek.jp/preprints/PDF/2000/0024/0024010.pdf

[22] M. Nishiwaki, K. Akai, T. Furuya, A. Kabe, S. Mitsunobu and Y. Morita, "Developments of SiC Damper for SuperKEKB Superconducting Cavity", in *Proc. SRF'15*, Whistler, Canada, Sep. 2015, paper THPB071, pp. 1289–1292. http://srf2015.vrws.de/papers/thpb071.pdf

[23] M. Nishiwaki, K. Akai, T. Furuya,S. Mitsunobu and Y. Morita, "Status of Superconducting Accelerating Cavity at SuperKEKB Phase-2 Operation", in *Proc. of the 15th Annual Meeting of Particle Accelerator Society of Japan*, Nagaoka, Japan, Aug. 7-10, 2018, pp. 428-432. https://www.pasj.jp/web_publish/pasj2018/proceedings/PDF/WEP0/WEP049.pdf

[24] Y. Morita, K. Akai, T. Furuya, A. Kabe, S. Mitsunobu and M. Nishiwaki, "Developments of Horizontal High Pressure Rinsing for SuperKEKB SRF Cavities", in *Proc. SRF'15*, Whistler, Canada, Sep. 2015, paper MOPB116, pp. 443–447. https://jacow.org/SRF2015/papers/MOPB116.pdf

[25] K. Akai, "RF Issues for High Intensity Factories", in *Proc. EPAC'96*, Sitges, Spain, Jun. 1996, paper TUX03A, pp. 205-209 (1996). https://accelconf.web.cern.ch/e96/PAPERS/ORALS/TUX03A.PDF

[26] T. Kobayashi, "RF system (2)", OHO'19 (2019).

[27] K. Akai, A. Kabe, T. Kobayashi, K. Nakanishi and M. Nishiwaki, "Verification of RF Feedback to Suppress Longitudinal Instability due to Beam Loading in SuperKEKB", in *Proc. of the 10th Annual Meeting of Particle Accelerator Society of Japan, 2020*, p.320. https://www.pasj.jp/web_publish/pasj2020/proceedings/PDF/WEPP/WEPP35.pdf

[28] K. Akai, "Stability Analysis of RF Accelerating Mode with Feedback Loops under Heavy Beam Loading in SuperKEKB", Phys. Rev. Accel. Beams 25, 102002 (2022). https://doi.org/10.1103/PhysRevAccelBeams.25.102002

[29] K. W. Robinson, "Stability of beam in radiofrequency system, Cambridge Electron Accelerator", Report No. CEAL-1010 (1964).

[30] K. Akai, N. Akasaka, K. Ebihara, E. Ezura, M. Suetake and S. Yoshimoto, "The Low-Level RF System for KEKB", in *Proc. EPAC'98*, Stockholm, Sweden, Jun. 1998, paper TUP10G, pp. 1749–1751. https://jacow.org/e98/papers/TUP10G.pdf

[31] T. Kobayashi and K.Akai, "Advanced Simulation Study on Bunch Gap Transient Effect", Phys. Rev. Accel. Beams 19, 062001 (2016). https://link.aps.org/doi/10.1103/PhysRevAccelBeams.19.062001

[32] T. Kobayashi and K. Akai, "LLRF Controls Including Gap Transients at KEKB and Plans for SuperKEKB", in *Proc. eeFACT'16*, Daresbury, UK, Oct. 2016, pp. 177–184. doi:10.18429/JACoW-eeFACT2016-WET2H7

ISBN: 978-3-95450-236-3 ISSN: 2673-7027 doi:10.18429/JACoW-eeFACT2022-WEYAT0101

COLLECTIVE EFFECTS STUDIES FOR CEPC

Na Wang[1†], Yuan Zhang[1, 2], Haisheng Xu[1], Saike Tian[1], Yudong Liu[1], Chuntao Lin[3]
[1]Institute of High Energy Physics, CAS, Beijing, 100049, China
[2] University of Chinese Academy of Sciences, CAS, Beijing, 100049, China
[3]Institute of Advanced Science Facilities, Shenzhen, China

Abstract

The impedance model of the Circular Electron Positron Collider (CEPC) storage ring is updated according to the development of the vacuum components based on the circular beam pipe. With the impedance model, the single bunch and coupled bunch instabilities for different operation scenarios are investigated. Particularly, the key instability issues driven by the beam coupling impedance in the Z operation mode are discussed. The influence of the longitudinal impedance on the transverse mode coupling instability is analysed both numerically and analytically. In addition, trapped ions can induce bunch centroid oscillation and emittance growth. The possibility of ion trapping and fast beam ion instability in the CEPC storage ring are also investigated.

INTRODUCTION

The Circular Electron Positron Collider (CEPC) is a double ring lepton collider covers a wide beam energy range from 45 GeV (Z-pole) to 180 GeV (tt-bar) [1,2]. Since the Z mode has the lowest beam energy, as well as highest beam current and slowest synchrotron radiation damping, normally it shows the most critical requirements on the collective effects. In order to estimate the influence of these effects, the impedance model of the CEPC collider has been evolving since the start of the project [3-6]. Based on the impedance, systematic studies on the beam instability issues and their mitigations have been performed. In this paper, the resistive wall impedance and its induced coupled bunch instability are updated by considering more detailed vacuum chamber designs. In addition, macro particle simulations are performed for the single bunch effect and beam ion instabilities. The perturbation of longitudinal impedance on the transverse mode coupling instability is investigated analytically.

IMPEDANCE MODELING

The impedance model is developed considering both resistive wall and geometrical impedances. The main vacuum chamber has a circular cross section with radius of 28 mm, which is made of copper and has a layer of NEG coating on its inner surface to reduce the secondary electron yield as well as for the vacuum pumping. In order to evaluate the resistive wall impedance, multi-layer analytical formula from field matching is used [7].

Meanwhile, simplified formulas are derived for longitudinal and transverse resistive wall impedance of the coated metallic chambers:

$$Z_{||}^{\mathrm{RW}}(\omega) = \frac{Z_0\delta_1\mu_1 k_0[\mathrm{sgn}(\omega)-i]}{4\pi b\mu_0} \times \frac{\alpha\tanh(x_1)+\tanh(x_2)}{\alpha+\tanh(x_1)\tanh(x_2)} \tag{1}$$

$$Z_{\perp}^{\mathrm{RW}}(\omega) = \frac{4-k_r^2 b^2}{\sqrt{k_0^2+k_r^2}}\frac{1-i\mathrm{sgn}(\omega)}{4\pi b^3\delta_1\sigma_1} \times \frac{1+\alpha\tanh(x_1)\tanh(x_2)}{\alpha\tanh(x_2)+\tanh(x_1)} \tag{2}$$

where b is the beam pipe aperture, $\alpha=\delta_1\mu_1/\delta_2\mu_2$, $x_i=\lambda_i d_i$, $\lambda_i \simeq \sqrt{-2i}/\delta_i$, δ_i, d_i and μ_i are the skin depth, thickness and conductivity of the i'th layer, respectively. The numerical results are benchmarked with ImpedanceWake2D [8] and excellent agreements have been reached in the frequency range of interest.

Except the typical NEG coated vacuum chambers, the resistive wall impedance contributed by the MDI chambers, collimators in the interaction region and stainless steel chambers for flanges, bellows and BPMs are also considered. Since the Machine Detector Interface (MDI) and collimators may contribute large impedances, either due to the smaller beam pipe aperture or large local beta functions, the resistive wall impedance of the tapers are considered in more detail. Assuming the longitudinal and transverse resistive wall impedance is inverse proportional to the radius r or cubic of r, by integrating the impedance along the taper, we get the longitudinal and transverse resistive wall impedance of a taper is the impedance of a cylinder of unit length with the smaller aperture r_1 of the taper multiplied by the following factors

$$f_{||}^{RW} = \frac{r_1}{\tan\theta}\log\left(1 + L/r_1\tan\theta\right), \tag{3}$$

$$f_{T}^{RW} = \frac{r_1}{2}\frac{2r_1/L+\tan\theta}{(r_1/L+\tan\theta)^2}, \tag{4}$$

where L and θ are the length and angle of the taper, respectively.

The longitudinal and transverse resistive wall impedance contributed from different vacuum components is summarized in Fig. 1 and Fig. 2, respectively. Here, the transverse impedance has been normalized by the local beta functions. In addition, geometrical form factors [9] are considered for the resistive wall impedance of the vacuum chambers with non-axial symmetry. We can see that the impedance contributed by the typical vacuum chamber dominates both the longitudinal and transverse resistive wall impedance. The contributions from the MDI and collimators are considerably small.

† wangn@ihep.ac.cn

65th ICFA Adv. Beam Dyn. Workshop High Luminosity Circular e^+e^- Colliders eeFACT2022, Frascati, Italy JACoW Publishing
ISBN: 978-3-95450-236-3 ISSN: 2673-7027 doi:10.18429/JACoW-eeFACT2022-WEYAT0101

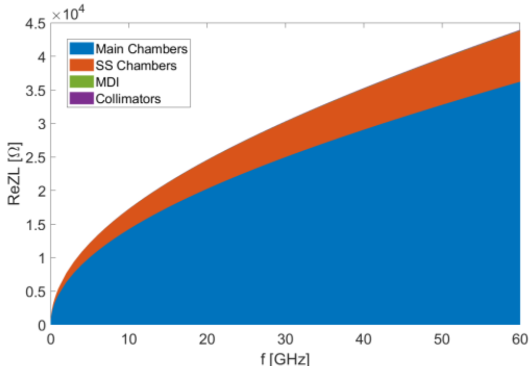

Figure 1: Real part of the longitudinal resistive wall impedance contributed from different type of vacuum chambers.

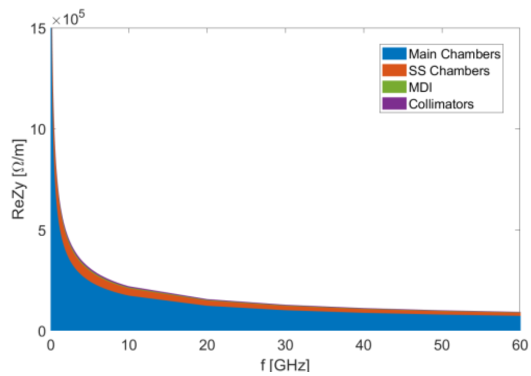

Figure 2: Real part of the transverse resistive wall impedance contributed from different type of vacuum chambers.

On the other hand, the geometrical impedances are simulated by CST [10] and ABCI [11] codes. The impedance generated by the RF cavities, flanges, bellows, gate valves, pumping ports, BPMs, collimators in the interaction region, and the electro separators, are included in the impedance model. Figures 2 and 3 show the total longitudinal and transverse impedances by summing up all the impedance contributors. The results show that both longitudinal and transverse broadband impedance are dominated by the resistive wall, flanges and bellows. Here, we should note that the impedance contributed by the injection and extraction elements, feedback kickers, absorbers, as well as masks and collimators outside the interaction region are not included yet. The impedance model will be continuously updated along with the development of the hardware designs.

The impedance budget calculated with an rms bunch length of 3mm gives the total longitudinal broadband impedance of 15.8 mΩ and transverse kick factor of 25.0 kV/pC/m. The results are more or less consistent with the CDR budget. The main difference is due to revision of the chamber cross section, more detailed number of elements, and more contributors included.

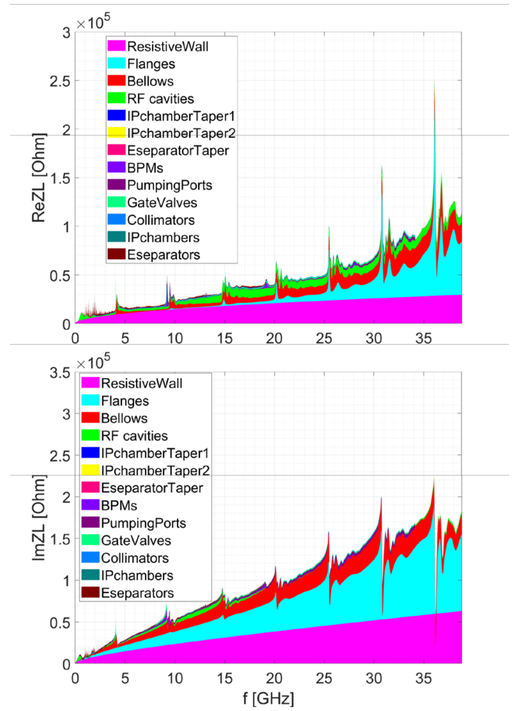

Figure 3: Real (top) and imaginary (bottom) part of the longitudinal impedance contributed from different vacuum components.

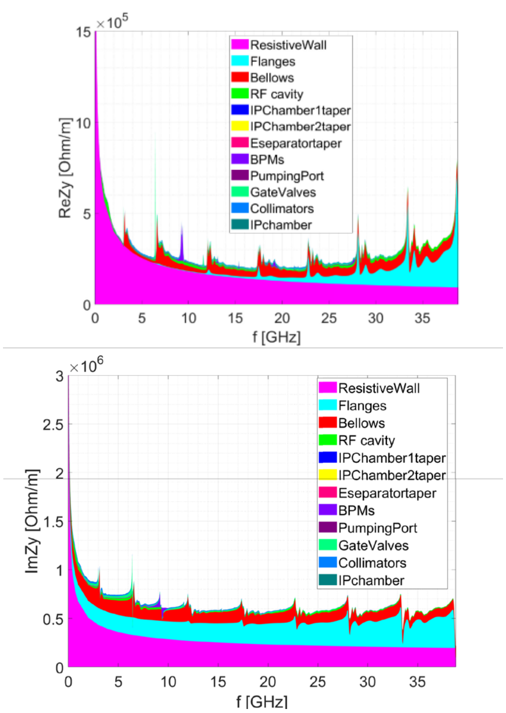

Figure 4: Real (top) and imaginary (bottom) part of the transverse impedance contributed from different vacuum components.

IMPEDANCE EFFECTS

Based on the impedance model, the collective effects are estimated by both analytical estimation and numerical simulations. Preliminary estimations on the instability

ISBN: 978-3-95450-236-3 ISSN: 2673-7027 doi:10.18429/JACoW-eeFACT2022-WEYAT0101

threshold for different operation scenarios are first given based on the analytical criterions. For the single bunch effect, the longitudinal impedance is above the threshold of Higgs, W and Z. This will induce bunch lengthening, energy spread increase, as well as synchrotron tune shift and spread. Although the criterion usually underestimates the instability threshold, we do observe its influence on the beam-beam interactions, which forced the optimization on the lattice design [12, 13]. In the transverse case, the impedance is above the threshold only for the Z operation mode, which will induce transverse mode coupling instability. This is a fast instability and normally with beam losses. For the multi-bunch case, there are also tight requirements on the narrowband impedance for Z. The thresholds on the narrowband impedance are at least two orders lower than the other energies. Therefore, the high order modes need to be well controlled to meet the requirements. In the following, the detailed analysis on instability issues driven by the impedance for Z will be discussed. The main beam parameters used in the following studies are listed in Table 1.

Table 1: Main beam parameters of CEPC Z

Parameter	**Symbol**	**Value**
Beam energy	E [GeV]	45.5
Circumference	C [km]	100
Beam current	I_0 [mA]	803.5
Bunch number	n_b	11934
Mom. compaction	α_p	1.43×10^{-5}
Betatron tune	ν_x/ν_y	317.1/317.22
Synchrotron tune	ν_s	0.035
Radiation damping	$\tau_x/\tau_y/\tau_z$ [ms]	850/850/425

Microwave Instability

In the longitudinal case, the threshold current of the microwave instability is approximately half of the design bunch intensity at 22.4 nC, as shown in Fig. 5. At the same time, we can also found apparent bunch lengthening and synchrotron tune shift and spread, even below the threshold, as shown in Figs. 5 and 6. The above effects will further influence the beam-beam interaction according to more consistent studies including both beam-beam and impedance [12, 13] due to the X-Z coupling [14]. On the other hand, we can expect additional bunch lengthening and energy spread increase due to the beamstrahlung, which will mitigate the perturbation induced by the impedance in the longitudinal plane.

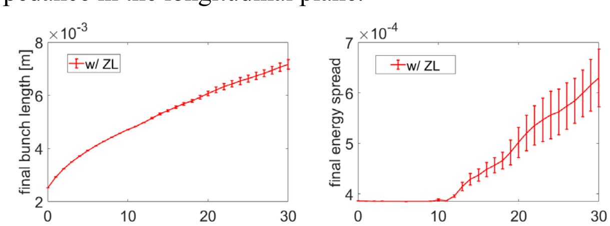

Figure 5: Variation of bunch length and incoherent synchrotron tune shift with bunch intensity.

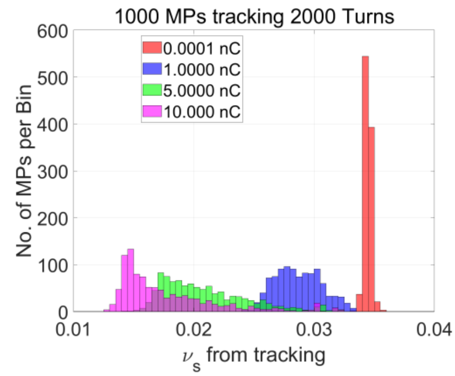

Figure 6: Histogram of the incoherent synchrotron tune at different bunch intensity.

Transverse Mode Coupling Instability

The transverse mode coupling instability is the main constraint on the single bunch current. The instability has been investigated in three different ways.

Analytical Estimations with Classical Vlasov Solver Mode analysis with and without impedance induced bunch lengthening are calculated. The results are shown in Fig. 7. Without bunch lengthening, the TMCI threshold is around 60% of the design value. When consider the impedance bunch lengthening, the analytical estimations show that threshold current will be increased by approximately a factor of two. The instability is supposed to be further detuned when consider bunch lengthening due to the beamstrahlung.

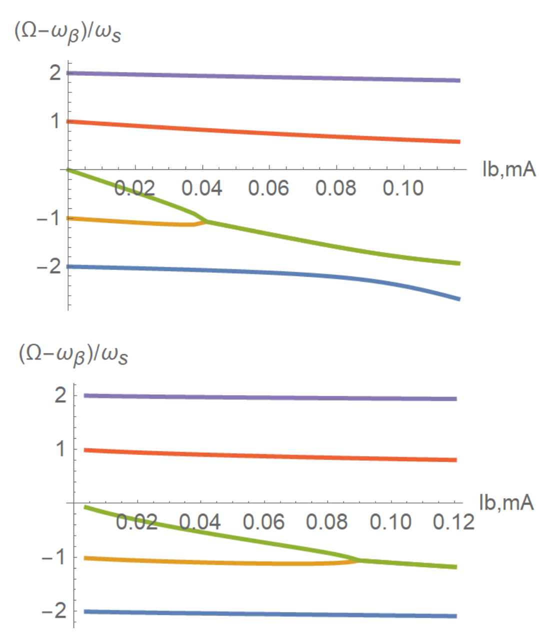

Figure 7: Dependence of the transverse mode frequency shift on the bunch current, without impedance induced bunch lengthening (up) and when the bunch lengthening at different bunch current been taken into account (bottom).

Micro particle simulations Particle tracking simulations including the longitudinal and transverse impedance

ISBN: 978-3-95450-236-3 ISSN: 2673-7027 doi:10.18429/JACoW-eeFACT2022-WEYAT0101

consistently are performed with the code Elegant [15]. The results are shown in Fig. 8, and compared with the case without longitudinal impedance. Without longitudinal impedance, the instability threshold is around 14 nC, which is consistent with the analytical estimation of the same case as given in Fig. 7. However, when include the longitudinal impedance, the instability gets more unstable and the threshold decreased to 10 nC, which is much lower than the analytical estimation only with bunch lengthening. Above the threshold, apparent beam losses and transverse centroid oscillations are observed. On the other hand, the shift of mode 0 below the threshold is still consistent with the analytical results. The instability is suspected to be induced by the enhanced mode coupling due to the smaller incoherent synchrotron tune. To mitigate the instability, dependence of the threshold beam current on the chromaticity is checked. The results show that the threshold current even decreases with increase of the chromaticity. Here, it should be noted that the nonlinear effects due to the variation of the transverse tune with amplitude is not included yet, which is expected to help in damping the instability.

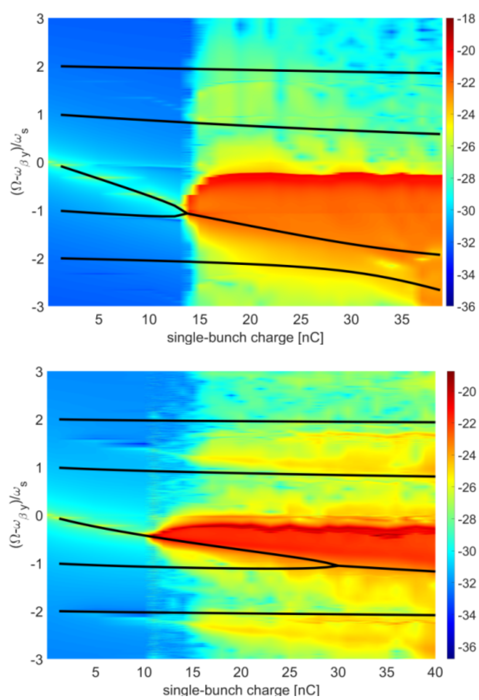

Figure 8: Variation of the transverse mode frequency shift with bunch intensity obtained from macro particle simulations, without (up) and with (bottom) longitudinal impedance. Different colour represents the amplitude of the FFT of the bunch centroid oscillation, and the black lines shows the analytical estimation on the mode frequency shift.

Analytical estimation considering the longitudinal perturbations Mode analysis considering perturbations from longitudinal impedance, as well as lengthened bunch from beamstrahlung, is performed using the method in Ref. [16]. Both longitudinal phase space distribution and synchrotron tune are projected into different action and angles. Considering the bunch lengthening from beamstrahlung, we get the instability threshold with longitudinal impedance as shown in Fig. 9. Including the longitudinal impedance, the higher order modes shift to mode 0 with wider bandwidth, and the instability threshold is decreased from 36 nC to 30 nC.

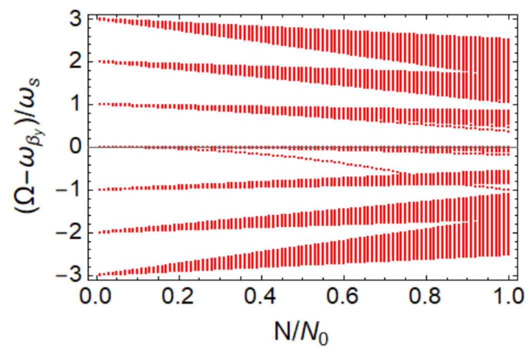

Figure 9: Variation of the transverse mode frequency shift with bunch intensity by considering the longitudinal impedance consistently.

Transverse Resistive Wall Instability

For the multi-bunch effects, coupled bunch instability driven by the resonance at zero frequency of the transverse resistive wall impedance gives extremely fast instability growth rate in the order of several turns. The transverse resistive wall impedance around zero frequency contributed by different vacuum components is shown in Fig. 10. The most dangerous mode is at frequency of –2.338 kHz, and the growth rate is dominated by the typical vacuum chamber. The instability is much faster than the synchrotron radiation damping and gives tough requirements on the feedback system. A combination of broadband feedback and mode feedback is proposed to damp the instability.

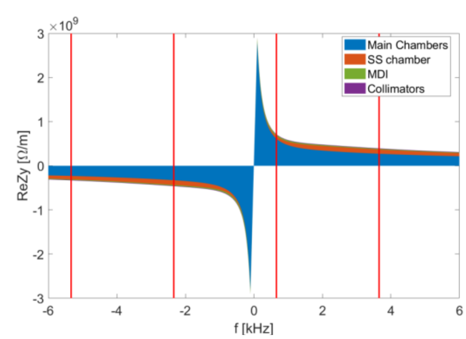

Figure 10: Transverse resistive wall impedance contributed by different type of vacuum chambers.

FAST BEAM ION INSTABILITY

Trapped ions can induce bunch centroid oscillation and emittance growth. The possible of ion trapping and fast beam ion instability are investigated. With vacuum pressure of 1 nTorr, and CO as the ion species, analytical estimations show that the instability growth for W and Z

ISBN: 978-3-95450-236-3 ISSN: 2673-7027 doi:10.18429/JACoW-eeFACT2022-WEYAT0101

are faster than synchrotron radiation damping, even considering multi bunch train filling pattern.

Particle tracking simulations are also performed with Elegant for different betatron functions. Multi-train filling pattern is effective in mitigating the beam ion instability. However, except the case with very low betatron functions at the interaction point, both horizontal and veritcal beam centroid oscillation amplitude increased to larger than 10% of the transverse beam size, and then saturate at around the scale of the beam size. Beam emittance growth is also foreseen. One example with ring average betatron functions is shown in Fig 11. Therefore, bunch by bunch feedback is needed to damp the instability.

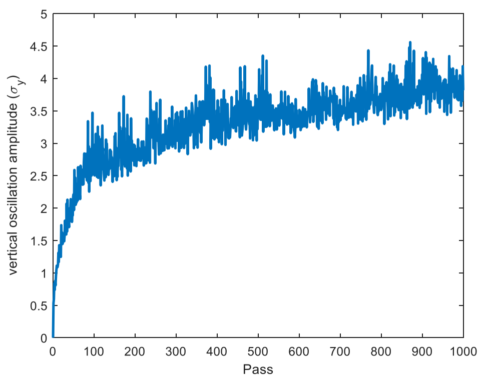

Figure 11: Variation of the vertical bunch centroid oscillation with number of turns under the influence of ions.

CONCLUSION

The collective beam instabilities are potential restrictions in CEPC to achieve high luminosity performance. Systematic studies have been performed to investigate the influence from the collective effects. The results show no apparent showstoppers from collective effects for the high energy operation modes, except for Z. The main constraint for the single bunch current is from the transverse mode coupling instability. The instability threshold is below the design current when including both longitudinal and transverse impedance consistently. The possible mitigations are investigated. The total beam current is mainly constraint by the transverse resistive wall instability, which gives tough requirements on the bunch-by-bunch feedback designs. In addition, the beam ion effects also show influence on the beam stability even considering a multi-train filling pattern, and feedback is required. Besides, consistent studies also show crosstalk between the transverse impedance and the beam-beam interaction. Therefore, collective effects studies need to get more involved with beam-beam and hardware designs.

REFERENCES

[1] CEPC Study Group, "CEPC Conceptual Design Report: Volume 1 – Accelerator," arXiv:1809.00285 [physics.acc-ph], 2018. doi:10.48550/arXiv.1809.00285

[2] Y.W. Wang *et al.*, "Lattice design of the CEPC collider ring for a high luminosity scheme", in *Proc. IPAC'21*, Campinas, Brazil, May 2021, pp. 2679-2682. doi:10.18429/JACoW-IPAC2021-WEPAB033

[3] N. Wang *et al*, "Impedance and collective effects studies in CEPC", in *Proc. HF'14*, Beijing, China, Oct. 2014, paper SAT4B1, pp. 218-222.

[4] N. Wang *et al.*, "Instability issues in CEPC", in *Proc. eeFACT'16*, Daresbury, UK, Oct. 2016, pp. 108-111. doi:10.18429/JACoW-eeFACT2016-TUT3AH2.

[5] N. Wang, Y. D. Liu, H.J. Zheng, D.J. Gong and J. He, "Collective effects in CEPC", in *ICFA Beam Dynamics Newsletter* no. 72, p. 55, 2017.

[6] Na Wang *et al.*, "Mitigation of Coherent Beam Instabilities in CEPC", in *Proc. of ICFA mini-Workshop on Mitigation of Coherent Beam Instabilities in Particle Accelerators* (MCBI 2019), Zermatt, Switzerland, Sep. 2019, CERN-2020-009 (2020), p. 286. doi:10.23732/CYRCP-2020-009.286.

[7] N. Wang and Q. Qin, "Resistive-wall impedance of two-layer tube", *Phys. Rev. Spec. Top. Accel Beams*, vol. 10, 111003, 2007. doi:10.1103/PhysRevSTAB.10.111003

[8] N. Mounet, "The LHC Transverse Coupled-Bunch Instability (Ph.D. thesis)", Ecole Polytechnique, Lausanne, 2012.

[9] Y.T. Wang, N. Wang, H.S. Xu and G. Xu, "Tune shift due to the quadrupolar resistive-wall impedance of an elliptical beam pipe", *Nucl. Instrum. Methods Phys. Res., Sect. A*, vol. 1029, p. 166414, 2022. doi:10.1016/j.nima.2022.166414

[10] CST Particle Studio, http://www.3ds.com.

[11] Yong Ho Chin, http://abci.kek.jp/abci.htm.

[12] Y. Zhang *et al.*, "Self-consistent simulations of beam-beam interaction in future e⁺e⁻ circular colliders including beamstrahlung and longitudinal coupling impedance", *Phys. Rev. Spec. Top. Accel Beams*, vol. 23, p. 104402, 2020. doi:10.1103/PhysRevAccelBeams.23.104402

[13] C. Lin, K. Ohmi, and Y. Zhang, "Coupling effects of beam-beam interaction and longitudinal impedance", *Phys. Rev. Accel. Beams*, vol. 25, p. 011001, 2022. doi:10.1103/PhysRevAccelBeams.25.011001

[14] K. Ohmi, N. Kuroo, K. Oide, D. Zhou, and F. Zimmermann, "Coherent Beam-Beam Instability in Collisions with a Large Crossing Angle", *Phys. Rev. Lett.*, vol. 119, p. 134801, 2017. doi:10.1103/PhysRevLett.119.134801

[15] M. Borland, "elegant: A Flexible SDDS-Compliant Code for Accelerator Simulation", Advanced Photon Source LS-287, 2000.

[16] Y. Wang and M. Borland, "Pelegant: A Parallel Accelerator Simulation Code for Electron Generation and Tracking", in *Proc. of the 12th Advanced Accelerator Concepts Workshop*, AIP Conf. Proc., vol. 877, p. 241, 2006.

ISBN: 978-3-95450-236-3 ISSN: 2673-7027 doi:10.18429/JACoW-eeFACT2022-WEYAT0102

MITIGATION OF ELECTRON CLOUD EFFECT IN THE SuperKEKB POSITRON RING

Y. Suetsugu[1,†], H. Fukuma, K. Ohmi, M. Tobiyama[1], H. Ikeda[1], K. Shibata[1], T. Ishibashi[1], M. Shirai, S. Terui, K. Kanazawa, H. Hisamatsu, M. L. Yao[1], KEK, Tsukuba, Japan
[1]also at SOKENDAI, Hayama, Japan

Abstract

A critical issue for SuperKEKB is the electron cloud effect (ECE) in the positron ring. Various countermeasures, such as ante-chambers, TiN-film coatings, clearing electrodes, and grooved surfaces, were prepared before commencing commissioning. The ECE, however, was observed during Phase−1 commissioning (2016) caused by the electron cloud in Al-alloy bellows chambers and also in the beam pipes at drift spaces, although the beam pipes had antechambers and TiN-film coatings. The threshold of the current linear density for exciting the ECE was approximately 0.12 mA bunch^{-1} RF-bucket^{-1}. Permanent magnets and solenoids were attached to them to generate magnetic fields in the beam direction as additional countermeasures. Consequently, the current linear density threshold increased up to over 0.53 mA bunch^{-1} RF-bucket^{-1} in Phase−3 commissioning (2019). Currently, there is no clear evidence of ECE during a normal operation. The effectiveness of the ante-chambers and TiN-film coatings of real beam pipes and groove structures used in bending magnets were experimentally re-evaluated. This report summarises the mitigation techniques used in SuperKEKB and the results thus far.

INTRODUCTION

The SuperKEKB is an electron-positron collider with asymmetric energies in KEK that aims for an extremely high luminosity utilising a "nano-beam" collision scheme (Fig. 1) [1, 2]. The main ring (MR) consists of two rings, that is, the high-energy ring (HER) for 7 GeV electrons and the low-energy ring (LER) for 4 GeV positrons. The beam pipes in the MR tunnel are shown in Fig. 2.

Figure 1: SuperKEKB at KEK Tsukuba campus.

† yusuke.suetsugu@kek.jp

Single-bunch instability caused by the electron cloud, that is, the electron cloud effect (ECE), is a severe problem for the SuperKEKB LER [3, 4]. Therefore, more effective countermeasures are required. From simulations, the average density of electrons in the ring should be less than ~3×10^{11} m^{-3} to avoid excitation of the ECE [5]. Hence, various types of countermeasures against ECE were adopted in the SuperKEKB LER, which are summarized in Table 1, and typical views of each countermeasure are shown in Fig. 3 [6].

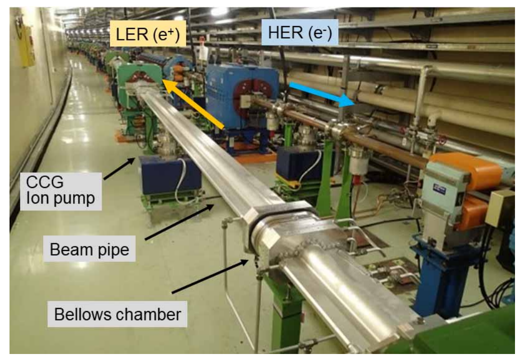

Figure 2: LER and HER in the MR tunnel.

COUNTERMEASURES IN SUPERKEKB

An antechamber helps to minimise the effects of photoelectrons because most of the synchrotron radiation (SR) is directly irradiated at its side wall (Fig. 3(a)). However, secondary electrons play a significant role in electron cloud formation in the high-bunch current regime. Most of the beam pipes for the LER were made of aluminium (Al)-alloy, and the beam channel was coated with a TiN film to reduce the secondary electron yield (SEY) (Fig. 3(b)). Clearing electrodes were installed in the beam pipes for wiggler magnets instead of TiN-film coating. A clearing electrode absorbs electrons around the beam orbit using a static electric field. These beam pipes also have antechambers and are made of copper (Fig. 3(c)). A grooved surface was adopted for the beam pipes in the bending magnets in the arc section. The grooved surface geometrically reduces the SEY. The TiN-film coating was subsequently applied to the grooved surface (Fig.3(d)). As a result, approximately 90% of the beam pipes in the ring had antechambers and TiN-film coating. A magnetic field in the beam direction (B_z) generated by solenoids or permanent magnets around the beam pipe is highly effective in suppressing the electron emissions from the inner wall. These are available only in the drift spaces (field-free regions) between electromagnets, such as quadrupole and sextupole magnets (Fig.3(e) and 3(f)). The circular dots in Table 1 indicate the

ISBN: 978-3-95450-236-3 ISSN: 2673-7027 doi:10.18429/JACoW-eeFACT2022-WEYAT0102

Table 1: Countermeasures used to minimize the ECE in the SuperKEKB LER. The circular dots indicate the countermeasures applied for each main section in the ring.

Sections	Length [m]	n_e (circular) [m^{-3}]	Countermeasures Antechamber (1/5)	TiN coating (3/5)	Solenoid (B_z) (1/50)**	Groove (1/2)	Electrode (1/100)	n_e (expected) [m^{-3}]
Drift space (arc)	1629	8×10^{12}	●	●	●			2×10^{10}
Corrector mag.	316	8×10^{12}	●	●	●			2×10^{10}
Bending mag.	519	1×10^{12}	●	●		●		6×10^{10}
Wiggler mag.	154	4×10^{12}	●	●*			●	5×10^{9}
Quadrupole and Sextupole mag.	254	4×10^{10}	●	●				5×10^{9}
RF cav. section	124	1×10^{11}		●	●			1×10^{9}
IR	20	5×10^{11}		●	●			6×10^{9}
Total	3016							
Average		5.5×10^{12}						2.4×10^{10}

*Except for beam pipes with clearing electrodes.
**Uniform magnetic field in the beam direction is assumed.
Abbreviations:
RF cav. section: Beam pipes around RF cavities, IR: Interaction region
n_e (circular): Density of electrons expected for circular beam pipe (copper)
n_e (expected): Density of electrons expected after applying countermeasures
Antechamber: Antechamber scheme, Solenoid: Solenoid winding, but actually applying a magnetic field in the beam direction (B_z)
Groove: Beam pipe with grooves, Electrode: Beam pipe with clearing electrodes

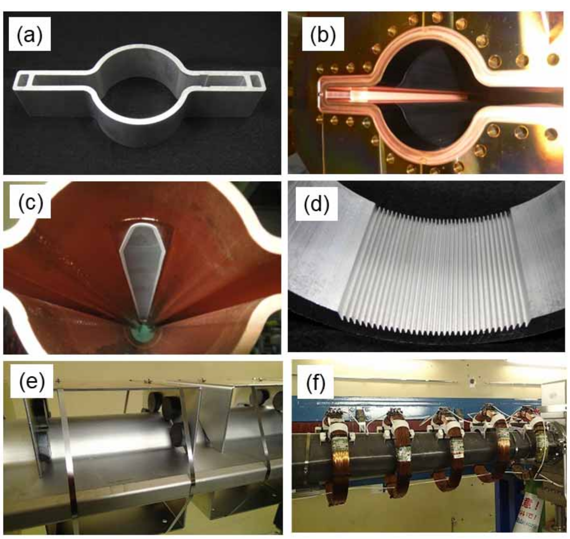

Figure 3: Typical view of countermeasures adopted to SuperKEKB LER: (a) beam pipes with ante-chambers, (b) TiN-film coating, (c) clearing electrode, (d) groove structure, magnetic fields in the beam direction by (e) permanent magnets, and (f) solenoids.

countermeasures applied to each main section of the ring. The density of electrons (n_e) expected in the case of circular beam pipes (copper) and those with the above countermeasures are also presented in the table. Here, the efficiencies in reducing n_e for the antechamber scheme, TiN-film coating, solenoid (i.e., B_z), grooved surface, and clearing electrode are assumed to be 1/5, 3/5, 1/50, 1/2, and 1/100, respectively, based on the experimental results obtained in the R&D up to that time. With these countermeasures, a n_e value of approximately 2×10^{10} m^{-3} was expected at the designed beam parameters, that is, a beam current of 3.6 A at a bunch fill pattern of one train of 2500 bunches, with a bunch spacing of two RF-buckets (referred to as 1/2500/2 RF hereafter). Here, one RF-bucket corresponds to 2 ns. This value of n_e is sufficiently lower than the threshold density of electrons (n_{e_th}) of 3×10^{11} m^{-3}. The B_z at drift spaces were not prepared before Phase–1 commissioning because the expected beam current was not very high during the Phase–1 commissioning; it was approximately a maximum of 1 A.

Several beam pipes for tests were installed in the ring to investigate ECE, and the n_e around the beam was measured via electron current monitors, which were also used in previous KEKB experiments [7]. A test beam pipe with two electron monitors is shown in Fig. 4. These monitors were set up at the bottom of the beam channel. The voltage applied to the electron collector was 100 V, whereas that applied to the grid (repeller) was typically −500 V. The test beam pipe is placed in the arc section of the ring. The line density of synchrotron radiation (SR) photons is 1×10^{15} photons s^{-1} m^{-1} mA^{-1}, which is almost the same as the average value of the arc sections. A weak magnetic field in the vertical direction (B_y) can be applied at the location of the electron monitors by the solenoids at the top and bottom sides of the beam pipe (see Fig. 4).

ECE IN PHASE–1 COMMISSIONING

First Observation

ECEs, such as a blow-up of vertical beam size and nonlinear pressure rise with beam current, were first observed during Phase–1 commissioning from a beam current (I) of approximately 600 mA at a bunch fill pattern of

ISBN: 978-3-95450-236-3 ISSN: 2673-7027 doi:10.18429/JACoW-eeFACT2022-WEYAT0102

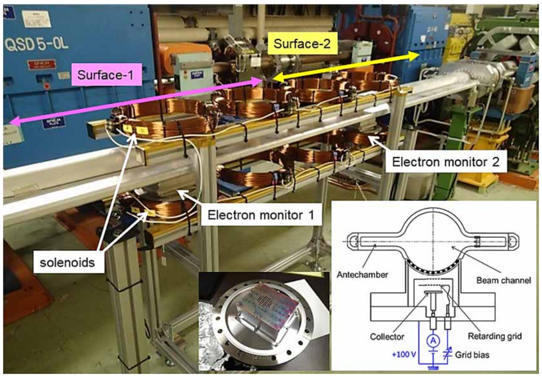

Figure 4: A test beam pipe with two electron monitors installed at a drift space of the LER.

1/1576/3.06 RF, despite the implementation of the various countermeasures described above [8, 9]. Here "3.06RF" means the average RF-bucket spacings of a pattern with a mixture of 3 and 4 RF-bucket spacings. This value of I corresponds to the current line density (I_d), i.e., the bunch current divided by the bunch spacing, of 0.12 mA bunch^{-1} RF-bucket^{-1}. The vertical beam size was measured using an X-ray beam size monitor [10]. Since B_z was not applied to the beam pipes at the drift spaces, the excitation of the ECE is an undeniable possibility. However, the threshold of the beam current for exciting the ECE was much lower than expected, that is, over 1 A with 3RF-bucket spacings.

A dedicated machine study to investigate the phenomena found that the threshold of I_d (I_{d_th} [mA bunch^{-1} RF-bucket^{-1}]) where the blow-up of the beam size begins was almost independent of the bunch fill patterns, as shown in Fig. 5(a). This is a typical characteristic of ECE. The I_{d_th} was 0.1 – 0.12 mA bunch^{-1} RF-bucket^{-1}. The modes of coupled-bunch instability were also typical for ECE because of the electrons in the drift spaces [11]. Furthermore, the n_e measured at the region "without" TiN-film coating in the test beam pipe was of the order of 10^{12} m^{-3} at an I value of 600 mA. The n_e value was over 10 times higher than n_{e_th}, ~3×10^{11} m^{-3}, as expected from the simulation. It was observed that this ECE was caused by the electrons in the Al-alloy bellows chambers without TiN-film coating (see Fig. 2), although they occupy only ~5% of the circumference of the ring.

To counteract the ECE, two units of permanent magnets (PM), where eight small (ϕ = 30 mm) PMs were attached to a C-shaped iron plate (yoke) in each unit, were placed at the top and bottom of each Al-alloy bellows chamber, as shown in Fig. 6. A B_z value of approximately 100 G was formed in most regions of the PM units, although the polarity reverses locally near the magnets.

ECE at a Higher Beam Current

After attaching the PM units to all the Al-alloy bellows chambers, the blow-up of the vertical beam size was not evident until I reached ~ 800 mA. The measurement of the vertical beam size for bunch fill patterns of 4/150/2 RF, 4/150/3 RF, 4/150/4 RF and 4/150/6 RF showed that the

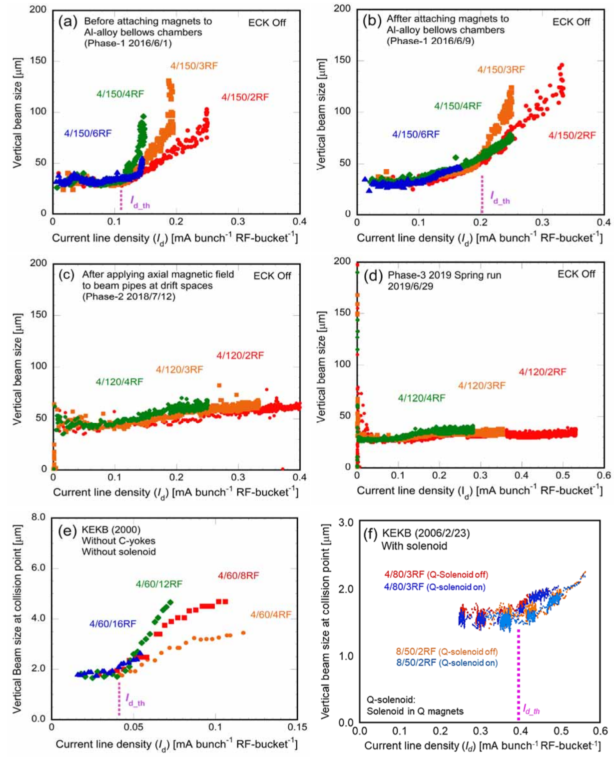

Figure 5: Vertical beam sizes as a function of the current line density (I_d) for several bunch fill patterns measured (a) before and (b) after attaching PM units to Al-alloy bellows chambers in Phase–1 commissioning, (c) in Phase–2 commissioning, (d) in Phase–3 commissioning, and in the KEKB era (e) without and (f) with solenoids, where ECK means the emittance control knob.

I_{d_th} shifted from 0.12 mA bunch^{-1} RF-bucket^{-1} to approximately 0.2 mA bunch^{-1} RF-bucket^{-1}, as shown in Fig. 5(b).

The n_e measured in the region "with" TiN-film coating in the test beam pipe approached the value of n_{e_th} at the I_d of 0.2 mA bunch^{-1} RF-bucket^{-1}. Transverse coupled bunch instabilities with modes caused by electrons in drift spaces were also detected. This means that ECE was excited by the electron cloud formed in the beam pipes with antechambers and TiN-film coating at the drift spaces.

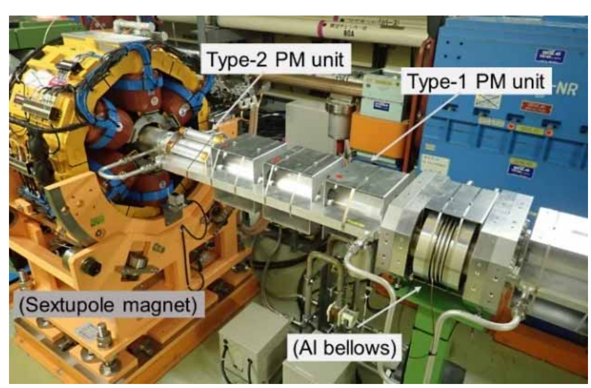

Figure 6: PM units attached to the beam pipes at drift spaces.

ISBN: 978-3-95450-236-3 ISSN: 2673-7027 doi:10.18429/JACoW-eeFACT2022-WEYAT0102

At this point, approximately 90 % of the beam pipes in the LER had antechambers and TiN-film coating. It should be noted that I_{d_th} is much higher than that in the case of the KEKB at an early stage [12], where most beam pipes were circular and made of copper (OFHC) without any coatings or solenoid windings. The I_{d_th} at that time was approximately 0.04 mA bunch^{-1} RF-bucket^{-1}, as shown in Fig. 5(e). Meanwhile, after applying PM units to only Al-alloy bellows chambers in the SuperKEKB, the I_{d_th} is 0.2 mA bunch^{-1} RF-bucket^{-1} (Fig. 5(b)), which is approximately five times that in the KEKB. This indicates that the antechambers and TiN-film coating of the beam pipes effectively suppressed the ECE.

Additional countermeasures

PM units and solenoids were attached to most of the beam pipes at drift spaces in the LER as additional countermeasures for the next Phase–2 commissioning phase. The PM units with iron yokes (Type–1unit), similar to those used for Al-alloy bellows chambers, were placed in series around the beam pipe, as shown in Fig. 6, which produced a B_z of approximately 60 G. A simulation using the CLOUDLAND code [13] showed that n_e around the beam orbit reduced to approximately 1/10th of n_{e_th} even for the designed beam parameters, as shown in Figs. 7(a) and 7(b). However, Type–1 units cannot be used near electromagnets, such as quadrupole and sextupole magnets, because the iron yokes affect their magnetic fields. Therefore, another type of PM unit (Type–2 unit), consisting of Al-alloy cylinders with permanent magnets inside and Al-alloy supports, was placed close to the electromagnets (Fig. 6). The value of B_z inside the Type–2 unit was approximately 100 G. Solenoid windings were revived for the beam pipes that had been used since the KEKB era [14]. Before starting Phase–2 commissioning, as a result, approximately 86% of the drift spaces (approximately 2 km) were covered with a B_z higher than approximately 20 G. A simulation indicated that the n_e around the beam orbit at a B_z value higher than 10 G is lower than 1×10^{11} m^{-3} even for the designed beam parameters [6].

ECE IN PHASE–2 COMMISSIONING

Figure 5(c) shows the dependence of the vertical beam size on I_d for the three bunch fill patterns in Phase–2 commissioning, 2018. The blow-up of the beam sizes was not observed until the I_d of 0.4 mA bunch^{-1} RF-bucket^{-1}. I_{d_th} increased by at least two times compared to Phase–1 commissioning (Fig. 5(b)). I_d is the maximum value that can be stably stored at that time. The pressure increased in almost proportionally with the beam current.

The modes and growth rates of the transverse coupled bunch instabilities were measured and analysed again. The modes caused by the electrons near the inner wall trapped by B_z were observed, instead of the modes caused by the electrons in the drift spaces [15]. Furthermore, the growth rates were much slower than those measured during Phase–1 commissioning. The coupled bunch instability

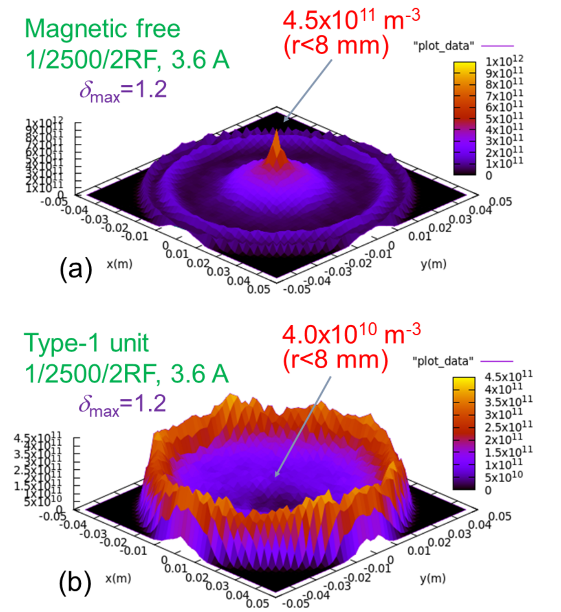

Figure 7: Density of electrons (n_e) in a beam pipe (a) without magnetic field and (b) with Type–1 PM units calculated by CLOUDLAND simulation code for a beam current of 3.6A at a bunch fill pattern of 1/2500/2RF.

was effectively suppressed by the bunch-by-bunch feedback system. The measured n_e in the test beam pipe in the region with TiN-film coating without B_z did not change from that observed in Phase–1 commissioning.

From these observations, it can be concluded that additional countermeasures, that is, a B_z generated by PM units and solenoids at drift spaces, contributed to suppressing the ECE in Phase–2 commissioning.

Re-evaluation of the Effectiveness of Antechamber and TiN-film Coating

First, as a measure of the effectiveness of a beam pipe with an antechamber in suppressing photoelectrons, the reduction rate of the number of photoelectrons in the beam channel relative to a simple circular beam pipe (α) is defined as follows:

$$\alpha \equiv \frac{p_b+\beta\times p_a}{p_b+p_a}. \quad (1)$$

Here, p_b and p_a are the numbers of photoelectrons generated in the beam channel and antechamber, respectively. Hence, the total number of photoelectrons in the beam pipe at this location is $p_b + p_a$. β is the probability that the electrons in the antechamber pass into the beam channel and is estimated to be approximately 0.05 in our case through a simulation [6]. For the case of a circular beam pipe, for example, $\alpha = 1$ because $\beta = 1$. A small value of α implies the high effectiveness of the antechamber.

Meanwhile, the maximum SEY (δ_{max}) was used as a measure of the effectiveness of TiN-film coating with regards to reducing secondary electrons. δ_{max} was estimated using the fact that the ECE was excited at an I value of

ISBN: 978-3-95450-236-3 ISSN: 2673-7027 doi:10.18429/JACoW-eeFACT2022-WEYAT0102

approximately 900 mA for a bunch fill pattern of 1/1576/3.06 RF during Phase–1 commissioning as described previously. This implies that n_e should be approximately 3×10^{11} m^{-3} for these beam parameters. The line density of photons of SR is 1×10^{15} photons s^{-1} m^{-1} mA^{-1} on average in the beam pipes at the arc sections. Under these conditions, δ_{max} was calculated as a function of the number of photoelectrons in the beam channel, that is, α, using CLOUDLAND and PyECLOUD [16] simulation codes.

If the value of α is estimated from simulations or measurements, δ_{max} of the surface can be evaluated. For example, the value of α was estimated to be 0.01 in the experiment during the KEKB commissioning, where a test beam pipe with an antechamber made of pure copper was used [17]. Using this α value, δ_{max} was estimated to be approximately 1.4. This value of δ_{max} is higher than that obtained for TiN-film coating (1.0 – 1.2) after sufficient electron bombardment in a laboratory [18]. Hence, estimating the α value for a real beam pipe is necessary.

Note that the re-evaluated values of α and δ_{max} here are the averages of those measured in the ring because the ECE is excited by the average value of n_e. However, ~90% of the beam pipes in the ring have antechambers and TiN-film coating. Beam pipes in other parts do not have antechambers but are in straight sections with weak SR intensity. The effects of these parts are small.

α and δ_{max} values were re-evaluated by several methods using simulations and experiments during Phase–2 commissioning [6]. Here, the result obtained from the measured n_e with small permanent magnets at the ends of antechambers is reported as a representative example.

If n_e is almost proportional to the number of photoelectrons in the beam channel, which holds for the n_e value of the order of 10^{11} m^{-3}, the ratio of electron density under the condition that the electrons from the antechamber can be negligible (n_{e0}) to that under the usual condition (n_e) is written as follows:

$$\frac{n_{e0}}{n_e} = \frac{p_b}{p_b+\beta\times p_a}. \tag{2}$$

If n_{e0} and n_e are measured, then the α value can be deduced using Eqs. (1) and (2).

n_{e0} was measured during Phase–2 commissioning by attaching weak permanent magnets with yokes at only the ends of the antechambers along the test beam pipe, as shown in Fig. 8. These magnets generate weak B_y along the antechamber and confine the emitted photoelectrons. The B_y value close to the permanent magnets, that is, at the end of the antechamber, was approximately 100 G, but that in the beam channel was less than 0.5 G, which is the same order as the terrestrial magnetism. In the simulation, a B_y of this order of magnitude had no effect on n_e in the beam channel. It was also experimentally found to have little effect on the measurement of n_e using our electron monitors.

The measured values of n_{e0} and n_e for a bunch fill pattern of 1/1576/3.06 RF are presented in Fig. 9. High n_e values at low I_d are not reliable because the volume used in the calculation of n_e is so small that the estimation method is no longer valid in principle [7]. The ratio n_{e0}/n_e was 1.5/3.3 at a bunch current of 0.45 mA bunch^{-1}. Assuming a β value of 0.05, the ratio p_b/p_a was calculated to be 0.04 from Eq. (2). α was then calculated as 0.08 from Eq. (1). Consequently, δ_{max} was evaluated to be approximately 0.7 – 0.8, which is close to the value obtained in the laboratory.

Although the results of the re-evaluation studies were relatively scattered, all values of α were larger than that obtained in the KEKB experiments, that is, 0.01 [6]. This difference can be explained by the following: (a) the location of the experimental setup, that is, just downstream (KEKB) and seven meters downstream (SuperKEKB) of a bending magnet, (b) the height of the antechamber, that is, 18 mm (KEKB) and 14 mm (SuperKEKB), (c) the material of the beam pipe, that is, copper (KEKB) and Al-alloy (SuperKEKB), and (d) the treatment of the innermost surface of the antechamber where the SR is directly irradiated. The most plausible cause among these is (a) and (b); that is, some portion of photons from upstream hit the beam channel owing to the vertical spread and scattering far downstream of the bending magnets in the real machine.

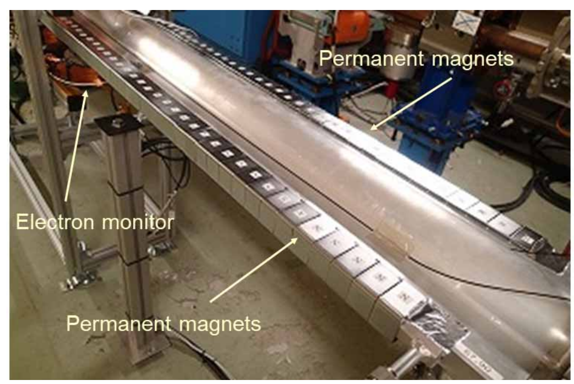

Figure 8: Weak PMs attached at the ends of antechambers of the test beam pipe with electron monitors to prevent the photoelectrons generated in the antechamber from entering the beam channel.

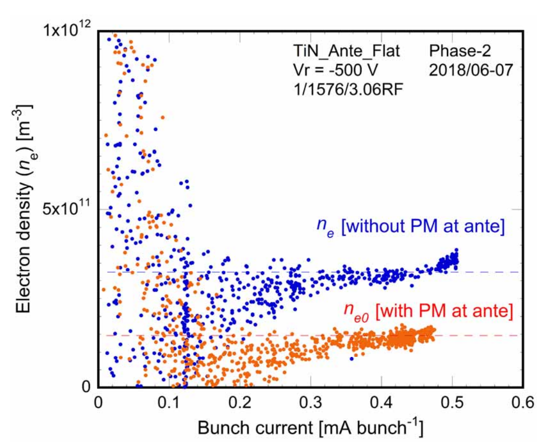

Figure 9: Measured electron density near the beam orbit for the cases with (n_{e0}) and without PMs (n_e) in the antechambers.

ISBN: 978-3-95450-236-3 ISSN: 2673-7027 doi:10.18429/JACoW-eeFACT2022-WEYAT0102

Conversely, for the δ_{max} of the TiN-film coating, the values are closer to or are somewhat lower than those obtained in the laboratory. The TiN-film coating seems to work well as expected, with regards to reducing the emission of secondary electrons.

ECE IN PHASE-3 COMMISSIONING

Before starting Phase–3 commissioning, the PM units were further added to the drift spaces, up to approximately 91% of the drift spaces. During Phase–3 commissioning in June 2019, the vertical beam sizes and modes of instabilities were again measured by changing the bunch fill patterns. The changes in the vertical beam sizes with respect to I_d for the bunch fill patterns of 4/120/2 RF, 4/120/3 RF and 4/120/4 RF are shown in Fig. 5(d). No beam-size blow-up was observed until the I_d of 0.53 mA bunch^{-1} RF-bucket^{-1}, which was approximately 2.6 times higher than that in Phase–1 commissioning. Note again that I_d is the maximum value that can be stably stored at that time. Furthermore, coupled-bunch instabilities related to the electron cloud in the drift spaces were not observed. The pressure increased almost proportionally to the beam current, and no abnormal pressure increases were observed. The B_z produced by the PMs works effectively to suppress ECE. The I_d of 0.53 mA bunch^{-1} RF-bucket^{-1} corresponds to approximately 2.5 A for the bunch fill pattern of 1/2400/2 RF.

As a reference, the changes in vertical beam sizes against I_d for the bunch fill patterns of 4/80/3 RF and 8/50/2 RF after setting solenoids in the KEKB era (2006) are shown in Fig. 5(f) [19], where most of the drift spaces and the beam pipes in quadrupole magnets were covered with solenoids. The condition regarding the magnetic fields in the beam direction is similar to that in Phase–3 of SuperKEKB. The I_{d_th} was approximately 0.4 mA bunch^{-1} RF-bucket^{-1} at that time. After this measurement, the B_z of approximately 1500 solenoids was increased by a factor of 1.7 with new power supplies, and the I_{d_th} should have somewhat improved [20]. A measurement showed that the value of I_{d_th} was 0.44 mA bunch^{-1} RF-bucket^{-1} at a bunch fill pattern of 8/100/2 RF in June 2009.

The effectiveness of the groove structure on the top and bottom sides of the beam channel was also re-evaluated. As for the groove structure, the effects on the reduction of SEY were examined in the KEKB era at a wiggler section by changing the shape and materials of the groove structures [21]. The effectiveness was evaluated using a test chamber with the same groove structure used for the beam pipes in the bending magnets of SuperKEKB [22]. Figure 10(a) and 10(b) show the dependence of the measured electron current (I_e) on the beam current (I) for the bunch fill pattern of 1/1576/3.05 RF at $B_y = 0$ in the test chamber. The value of I_{e_Al} (without groove and TiN-film coating) was much higher than that of the $I_{e\_Al+groove}$ (with groove but without TiN-film coating), and the effectiveness of the groove structure was evident. However, the values of I_{e_TiN} (without groove but with TiN-film coating) and $I_{e\_TiN+groove}$ (with both groove and TiN-film coating) are almost identical. The possible reasons for this are as follows. The value of

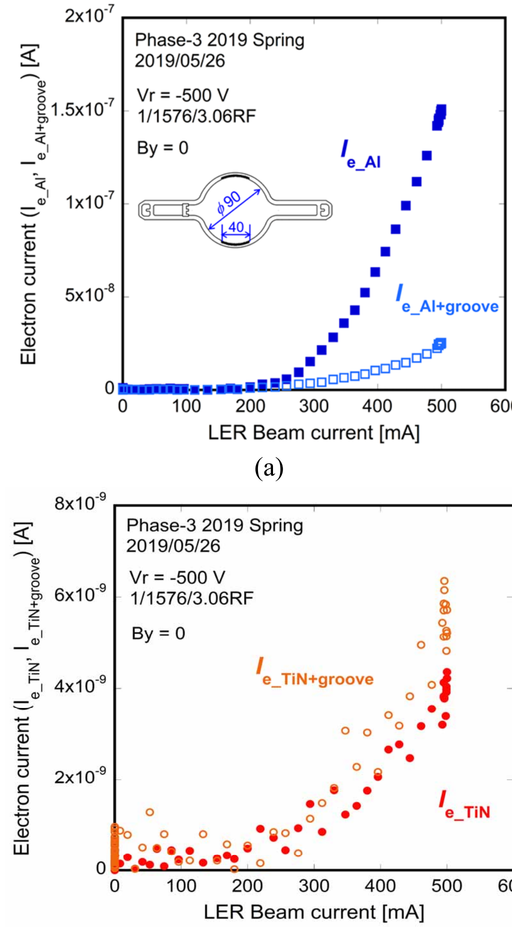

Figure 10: Electron currents of Al-alloy beams pipes (a) without and (b) with TiN-film coating for without (I_{e_Al}, I_{e_TiN}) and with ($I_{e\_Al+groove}$, $I_{e\_TiN+groove}$) groove structure in each case ($B_y = 0$).

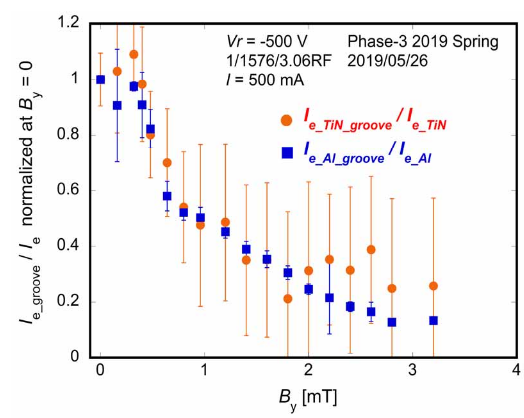

Figure 11: Changes of $I_{e\_TiN+groove}$ / I_{e_TiN} and $I_{e\_Al+groove}$ / I_{e_Al} against B_y, where the values are normalized at $B_y = 0$.

n_e in the beam pipe with the TiN-film coating (low SEY) was of the order of 10^{11} m^{-3}, and the effect of photoelectrons was larger than that of secondary electrons. Therefore, I_e, is almost the same regardless of the presence or absence of groove structures. In contrast, for the case without the

ISBN: 978-3-95450-236-3 ISSN: 2673-7027 doi:10.18429/JACoW-eeFACT2022-WEYAT0102

TiN-film coating (high SEY), the value of n_e is of the order of 10^{12} m^{-3}, and the SEY plays a large role. The effect of the groove structure with a low SEY was clearly observed.

Considering the positions of the groove structures, that is, the top and bottom of the beam channel, as shown in Fig. 10(a), I_e was measured by applying a weak B_y at the location of the electron monitors. It is expected that the effect of the groove structure becomes prominent when restricting the movement of electrons in the vertical direction by applying B_y. Furthermore, photoelectrons from the side of the beam pipes are suppressed. However, estimating n_e becomes impossible using the method used so far. The dependences of $I_{e\_Al+groove}$ / I_{e_Al} and $I_{e\_TiN+groove}$ / I_{e_TiN} on B_y at I = 500 mA are plotted in Fig. 11. Here, the measured values were normalised tp the values of $B_y = 0$ to observe qualitative changes. Despite the scattering of the measured values for the case of the TiN-film coating, the measured I_e with the groove structure ($I_{e\_Al+groove}$ and $I_{e\_TiN+groove}$) became smaller than those without it (I_{e_Al} and I_{e_TiN}) with B_y. This means that the SEY of the groove structure is smaller than that of the smooth surfaces, regardless of the presence or absence of TiN-film coating. Beam pipes with a groove structure are used in bending magnets, and the results obtained here also hold in the real case.

Since the experiment in 2019, we have had little chance to conduct dedicated experiments on ECE using a single beam. As a piece of supporting evidence that the ECE causes no beam size blow-up during the physics run (colliding beams), the luminosity of each bunch at a bunch fill

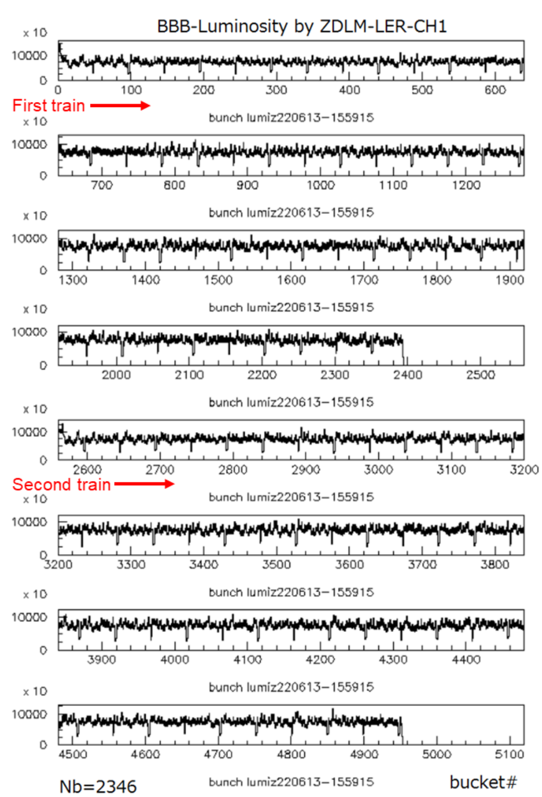

Figure 12: Bunch-by-bunch luminosity for a bunch fill pattern of 2/1173/2.04RF on 13th June, 2022. The vertical axis shows the number of hits at the ZDLM channel.

pattern of 2/1173/2.04 RF measured by the zero-degree luminosity monitor (ZDLM) [23] at a beam current of 1250 mA in June 2022 is shown in Fig. 12 (corresponding to the I_d of approximately 0.26 mA bunch^{-1} RF-bucket^{-1}). Currently, almost all the parts of the trains are two RF-bucket spacings. As seen in the figure, the bunch luminosity seems to be flat along the train, and there is no apparent "long-term" change for each train. The reasons for the high hit rate at the beginning of each bunch train (i.e., bunch number of 1–15 and 2561–2575 in Fig. 12) are the effects of the dead time and pile-up of the detector, non-uniformity of the bunch current, and beam-beam effects, although further analysis is required [24]. As indicated in this figure, there is no degradation in the luminosity along the train, which is a result of the beam-size blow-up caused by the ECE.

In the recent single-beam operation, a vertical beam-size blow-up was observed at a bunch current of approximately 0.6 mA bunch^{-1}, independent of bunch fill patterns [2]. A coherent oscillation at the frequency corresponding to $\nu_y - \nu_s$ was observed, and this instability was called "–1 mode instability", where ν_y and ν_s are the vertical betatron and synchrotron tunes, respectively. The instability is not caused by ECE, but is related to the impedance, especially that of the beam collimators. Further investigation is required to understand the instability mechanism.

As a part of R&D, to search for a surface with a lower SEY than before, a surface with thermal-sprayed copper has been investigated in the laboratory [25]. The rough surface geometrically decreases the SEY. The δ_{max} was approximately 0.7, even without TiN-film coatings, after sufficient electron bombardment. During Phase–3 commissioning, a test beam pipe with this surface was first installed in the ring, and its properties were studied using beams. The measured n_e value was lower than that of the surface with the TiN-film coating (2/1124/2.13 RF). Further analysis of these results is underway.

SUMMARY

ECE was observed in the SuperKEKB LER during Phase–1 commissioning. The ECE due to the Al-alloy bellows chambers and the beam pipes at drift spaces was successfully suppressed by applying PM units which produced a B_z of ~60 G. The antechambers and TiN-film coating seemed to function to some extent, but the experiment during Phase–2 commissioning found that the effectiveness of the antechambers of the real beam pipe in suppressing the photoelectron was lower than expected. The importance of suppressing photoelectrons was recognized. In the experiment in Phase–3 commissioning, no beam size bow-up was observed until the I_d of 0.53 mA bunch^{-1} RF-bucket^{-1}. The effectiveness of the groove structure adopted in the real ring in decreasing the SEY was also confirmed. It is deduced from the bunch-by-bunch luminosity measurement that there is no beam-size blow-up in the usual operation condition until a beam current of 1250 mA with a bunch fill pattern of 2/1173/2.04 RF in June, 2022.

ISBN: 978-3-95450-236-3 ISSN: 2673-7027 doi:10.18429/JACoW-eeFACT2022-WEYAT0102

SuperKEKB continues the physics experiment. The luminosity has been increasing annually, breaking the world record since 2021. No indication of ECE has been observed, and the various countermeasures against ECE seem to be working as expected. However, the design beam current (corresponding to an I_d of 0.73 mA bunch^{-1} RF-bucket^{-1}) has not yet been achieved. Careful observations of the ECE will continue during Phase–3 commissioning and beyond.

ACKNOWLEDGEMENTS

The authors would like to thank all the staff of the KEKB accelerator division for their cooperation and continuous encouragement during the commissioning phase.

REFERENCES

[1] SuperKEKB, https://www-superkekb.kek.jp/.

[2] Y. Funakoshi *et al.*, "The SuperKEKB has Broken the World Record of the Luminosity", in *Proc. IPAC'22*, Bangkok, Thailand, Jun. 2022, pp. 1–5. doi: 10.18429/JACoW-IPAC2022-MOPLXGD1

[3] K. Ohmi and F. Zimmermann, "Head-Tail Instability Caused by Electron Clouds in Positron Storage Rings", *Phys. Rev. Lett.*, vol. 85, p. 3821, 2000. doi:10.1103/PhysRevLett.85.3821

[4] F. Zimmermann, "Review of single-bunch instabilities driven by an electron cloud", *Phys. Rev. ST Accel. Beams*, vol. 7, p. 124801, 2004. doi:10.1103/PhysRevSTAB.7.124801

[5] Y. Susaki and K. Ohmi, "Electron cloud instability in SuperKEKB low energy ring," in *Proc. IPAC'10*, Kyoto, May 2010, pp.1545–1547, https://accelconf.web.cern.ch/IPAC10/papers/tupeb014.pdf

[6] Y. Suetsugu *et al.*, "Mitigating the electron cloud effect in the SuperKEKB positron ring", *Phys. Rev. Accel. Beams*, vol. 22, p. 023201, 2019. doi:10.1103/PhysRevAccelBeams.22.023201

[7] K. Kanazawa *et al.*, "Measurement of the electron cloud density around the beam", in *Proc. PAC'05*, Knoxville, USA, May 1995, pp. 1054–1056, https://accelconf.web.cern.ch/p05/PAPERS/FPAP007.PDF

[8] Y. Suetsugu *et al.*, "Achievements and problems in the first commissioning of SuperKEKB vacuum system", *J. Vac. Sci. Technol. A*, vol. 35, p. 03E103, 2017. doi:10.1116/1.4977764

[9] Y. Suetsugu *et al.*, "First Commissioning of the SupeKEKB Vacuum System", *Phys. Rev. Accel. Beams*, vol. 19, p. 121001, 2016. doi:10.1103/PhysRevAccelBeams.19.121001

[10] E. Mulyani, *et al.*, "Image Reconstruction Techniques Based on Coded Aperture Imaging for SuperKEKB X-Ray Beam Size Monitor", in *Proc. IPAC'18*, Vancouver, Canada, Apr.–May 2018, pp. 4819–4822. doi:10.18429/JACoW-IPAC2018-THPML074

[11] K. Ohmi, *et al.*, "Electron Cloud Studies in SuperKEKB Phase I Commissioning", in *Proc. IPAC'17*, Copenhagen, Denmark, May 2017, pp. 3104–3106. doi:10.18429/JACoW-IPAC2017-WEPIK075

[12] H. Fukuma *et al.*, "Observation of vertical beam blow-up in KEKB low energy ring", in *Proc. of EPAC'00*, Vienna, Austria, Jun. 2000, pp. 1122–1124, https://accelconf.web.cern.ch/e00/PAPERS/WEP5A12.pdf

[13] L. Wang *et al.*, "Numerical study of the photoelectrons cloud in KEKB low energy ring with a three-dimensional particle in cell method", *Phys. Rev. ST Accel. Beams*, vol. 5, p. 124402, 2002. doi:10.1103/PhysRevSTAB.5.124402

[14] H. Fukuma *et al.*, "Status of Solenoid System to Suppress the Electron Cloud Effects at the KEKB", in *AIP Conference Proceedings 642*, *ICFA-HB2002*, Batavia, USA, Apr. 2002, pp.357–359. doi:10.1063/1.1522668

[15] S. S. Win *et al.*, "Numerical study of coupled-bunch instability caused by an electron cloud", *Phys. Rev. ST Accel. Beams*, vol, 8, p. 094401, 2005. doi:10.1103/PhysRevSTAB.8.094401

[16] G. Iadarola and G. Rumolo, "PyECLOUD and build-up simulations at CERN", in *Proc. ECLOUD'12*, Isola d'Elba, Italy, Jun. 2012, CERN, Yellow Report No. CERN-2013-002, pp. 189–194., https://ecloud12.web.cern.ch/Proceedings/Edited/Iadarola-edited.pdf

[17] Y. Suetsugu *et al.*, "R&D of copper beam duct with antechamber scheme for high current accelerators", *Nucl. Instrum. Methods Phys. Res. A*, vol. 538, p. 206, 2005. doi:10.1016/j.nima.2004.09.015

[18] K. Shibata *et al.*, "Development of TiN coating system for beam ducts of KEK B-factory", in *Proc. EPAC'08*, Genoa, Italy, Jun. 2008, pp. 1700–1702, https://accelconf.web.cern.ch/e08/papers/tupp071.pdf

[19] H. Fukuma, "Effect of Solenoid in Quadrupole Magnet on Electron Cloud Instability", presented in *11th KEKB Review Committee*, KEK, Tsukuba, Japan, Mar. 2006, https://www-kekb.kek.jp/MAC/2006/Report/

[20] H. Fukuma, private communication, Aug. 2022.

[21] Y. Suetsugu *et al.*, "Continuing study on electron-cloud clearing techniques in high intensity positron ring: Mitigation by using groove surface in vertical magnetic field", *Nucl. Instrum. Methods Phys. Res. A*, vol. 604, p. 449, 2009. doi:10.1016/j.nima.2009.03.011

[22] Y. Suetsugu *et al.*, "Construction status of the SuperKEKB vacuum system", *Vacuum*, vol. 121, p. 238, 2015. doi:10.1016/j.vacuum.2014.12.010

[23] T. Hirai *et al.*, "Real-time luminosity monitor for a B-factory experiment", *Nucl. Instrum. Methods Phys. Res. A*, vol. 458, p. 670, 2001. doi:10.1016/S0168-9002(00)00766-X

[24] S. Uehara, private communication, July. 2022.

[25] M. Yao *et al.*, "Study on copper thermal spray coating to mitigate electron cloud effect", in *Proc. PASJ2021*, Online, Japan, Aug. 2021, paper TUP010, pp. 427–431. https://www.pasj.jp/web_publish/pasj2021/proceedings/PDF/TUPO/TUP010.pdf

ISBN: 978-3-95450-236-3 ISSN: 2673-7027 doi:10.18429/JACoW-eeFACT2022-WEYAT0103

STUDIES AND POSSIBLE MITIGATION OF ELECTRON CLOUD EFFECTS IN FCC-ee

F. Yaman*,[1], İzmir Institute of Technology, İzmir, Türkiye
F. Zimmermann, CERN, Geneva, Switzerland
[1]also at STFC, Sci-Tech Daresbury, UK

Abstract

In this work, we present numerical results for the electron cloud build-up and mitigation studies considering Arc Dipole and Drift sections of the FCC-ee collider. We report the central electron density that could be reached by minimising secondary electron contributions and the photoelectron generation rates in order to achieve e^- densities lower than the single-bunch instability threshold, considering the baseline beam parameters. Additionally, simulation results revealing the behavior of electron-cloud formations for various SEY values, photoemission rates, vacuum chamber radii, and bunch spacings are included. In the last section, we discuss initial investigations to clean residual electrons after the beam pass.

INTRODUCTION

The FCC-ee, which is designed for performing precision measurements at each of several different collision energies between 88 and 365 GeV, is the first stage of the FCC project hosted by CERN [1,2]. The design achieves a high luminosity with an e^+e^- circular collider of circumference ≈ 90 km, for the arcs of which we shall analyze electron cloud build-up scenarios. The exponential generation of electrons which may occur when the primary e^- hit the pipe walls, could cause beam loss, emittance growth, trajectory change, and wakefields [3,4]. The primary sources of the electrons in the accelerators and storage rings are photoemission, ionization of residual gases, and strikes of strayed beam particles to the beam pipes. For detailed investigations of the electron cloud mechanism, we employ PyECLOUD [5] to perform two-dimensional electrostatic particle in cell simulations. In the computations, the Furman-Pivi secondary electron yield model for copper, see Refs. [6,7] and ECLOUD model based on laboratory measurements at CERN for the copper surface of the LHC [8,9] are used.

MACHINE & SIMULATION PARAMETERS

We consider the machine and beam parameters which are given in Table 1 for the build-up simulations. Additionally, also the drift region, circular beam pipe radius 30 mm and 35 mm, bunch spacings 25 ns, 30 ns and 32 ns, total secondary emission parameter SEY = $\{1.1, 1.2, 1.3, 1.4\}$, the number of primary electrons generated by a single positively-charged particle per unit length $n'_\gamma = \{10^{-3}, 10^{-4}, 10^{-5}, 10^{-6}\}$ m^{-1} are scanned for the FCC-ee collider arcs. As a result, we obtain electron densities at the center of the vacuum chamber during 150 bunch passes where an average of all minimum density values is calculated to compare with the single-bunch instability threshold. The latter can be estimated as [12, 13]

$$\rho_{\mathrm{thr}} = \frac{2\gamma Q_s \omega_e \sigma_z / c}{\sqrt{3} K Q r_e \beta_y C}, \tag{1}$$

where

$$\omega_e = \left(\frac{N_b r_e c^2}{\sqrt{2\pi}\sigma_z \sigma_y (\sigma_x + \sigma_y)} \right)^{1/2}, \tag{2}$$

$K = \omega_e \sigma_z / c$, $Q = \min(\omega_e \sigma_z / c, 7)$, see Ref. [11].

Table 1: Simulation parameters for the simulations of electron-cloud evolution in an arc dipole, corresponding to collisions at 4 interaction points [10, 11].

Parameter	**FCC-ee Collider Arc Dipole**
beam energy [GeV]	45.6
bunches per train	150
trains per beam	1
r.m.s. bunch length [mm]	4.32
hor. r.m.s. beam size [µm]	207
vert. r.m.s. beam size [µm]	12.1
external magnetic field [T]	0.01415
bunch population N_b [10^{11}]	2.76
circumference C [km]	91.2
chamber radius r_0 [mm]	35
momentum compaction factor α_C [10^{-4}]	0.285
synchrotron tune Q_s	0.037
average beta function β_y [m]	50
threshold density ρ_{thr} [10^{12} m^{-3}]	0.043

NUMERICAL RESULTS

Firstly, Figure 1 displays minimum electron densities for a case without any secondary emission (SEY ≈ 0) and for a more realistic scenario (SEY = 1.1), considering a photoelectron rate of $n'_\gamma = 10^{-6}$ m^{-1}/e$^+$ and 32 ns bunch spacing. The former results for the arc dipoles reported in Ref. [11], even though the longitudinal rms bunch length, bunch population, and transverse beam sizes) had different

* fatihyaman@iyte.edu.tr

ISBN: 978-3-95450-236-3 ISSN: 2673-7027 doi:10.18429/JACoW-eeFACT2022-WEYAT0103

values (namely 3.5 mm, 2.8×10^{11}, 120 µm and 7 µm, respectively), still resemble those for the current parameters. For instance, in both old and new simulations, the minimum center density is $\approx 2\times10^{7}$ m^{-3} for SEY $\approx$ 0, and the maximum value $\approx 5\times10^{8}$ m^{-3} for SEY=1.1, for both SEY models.

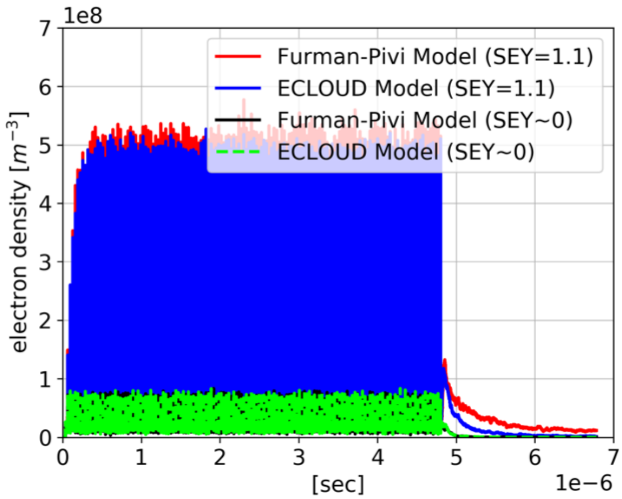

(a) e^- densities at the center of the vacuum chamber

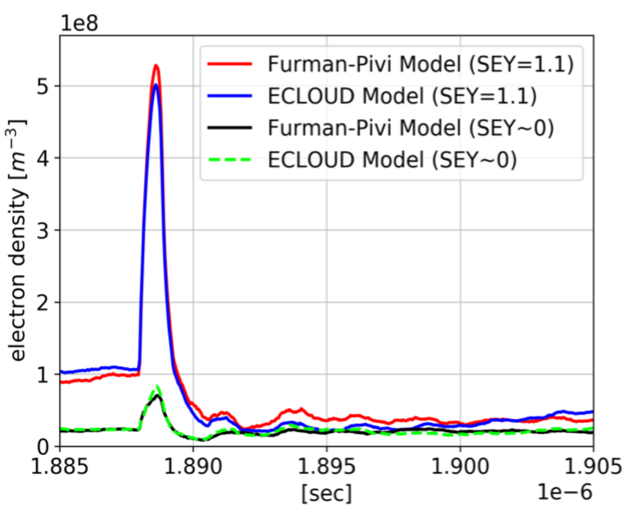

(b) variations of e^- densities during and after a bunch pass

Figure 1: Electron density for $n'_\gamma = 10^{-6}$ m^{-1} as a function of time, in the FCC-ee positron arc dipoles for Z pole operation.

For SEY=1.1, the Furman-Pivi and ECLOUD models for the secondary emission also yield similar results for the field-free regions, as is shown in Fig. 2, which was prepared by keeping the same parameters used for the previous example except for the external magnetic field, which is set to zero. However, a slight increase in the maxima of the oscillations can be noticed for the Furman-Pivi SEY model result. This behavior is expected according to our experience from past numerical experiments, since the Furman-Pivi model tends to yield higher electron density values. Furthermore, by comparing Figs. 1 and 2, we conclude that 0.01415 T an external magnetic field of 142 G, results in $\approx$ 2.5 times lower electron densities, for SEY=1.1 and $n'_\gamma = 10^{-6}$ m^{-1}.

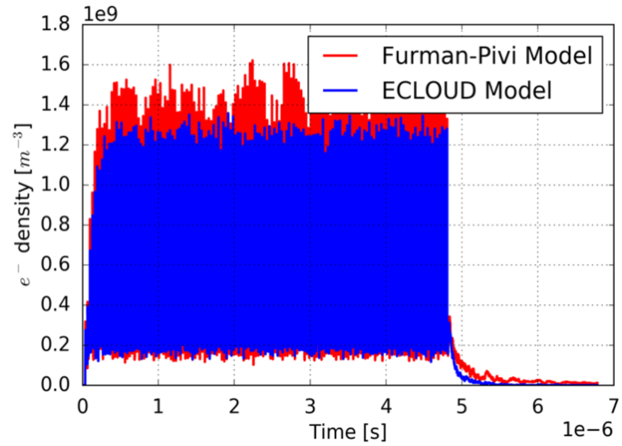

Figure 2: Electron density at the pipe center, as a function of time, for a bunch spacing of 32 ns, SEY=1.1, $n'_\gamma = 10^{-6}$ m^{-1}, without magnetic field.

Next, we examine the dependence of electron cloud buildup for a smaller beam pipe radius of 30 mm (instead of 35 mm), for 25 ns bunch spacing in the arc dipoles. Accordingly, in Fig. 3, the first row corresponds to the simulations with 30 mm pipe radius while the second row indicates results for 35 mm radius. For low SEY, the electron cloud is dominated by photoelectrons; therefore, a larger chamber reduces the average e- density, as can be seen from this figure. On the other hand, for SEY = 1.3 and SEY = 1.4, the multipacting dominates; in this case a larger chamber increases the multipacting and hence the maximum electron density. However, this behavior of the density maxima is now always followed by the more relevant density minima.

To compare the center densities with the threshold density $\rho_{thr} = 4.3\times10^{10}$ m^{-3} calculated via Eq. (1), the average of the minimum center-density values in the dipoles for the simulations with 25 ns bunches and two different radii is computed. Such average results obtained for various SEY values and photoelectron generation rates by employing both secondary emission yield models are depicted in Fig. 4. According to our simulation, the Furman-Pivi SEY model combined with the parameter $n'_\gamma = 10^{-3}$ m^{-1}, yields an electron density at the pipe center which exceed the threshold for both chamber radii. However, we obtain electron densities lower than the threshold by employing $n'_\gamma = 10^{-4}$ m^{-1} for all SEY values in the explored parameter range, up to SEY=1.4, although the density value for SEY = 1.4 with the Furman-Pivi model is still close to the threshold density, see Fig. 4 (b), so that the safety margin is small.

Our last numerical experiment is devoted to clearing the residual electrons with a single satellite bunch following a regular bunch train. In Ref. [14], Ruggiero and Zhang reported that a significant reduction of the beam-induced heat load can be obtained, for the case of the LHC, by choosing an optimum satellite bunch intensity and distance from the

ISBN: 978-3-95450-236-3 ISSN: 2673-7027 doi:10.18429/JACoW-eeFACT2022-WEYAT0103

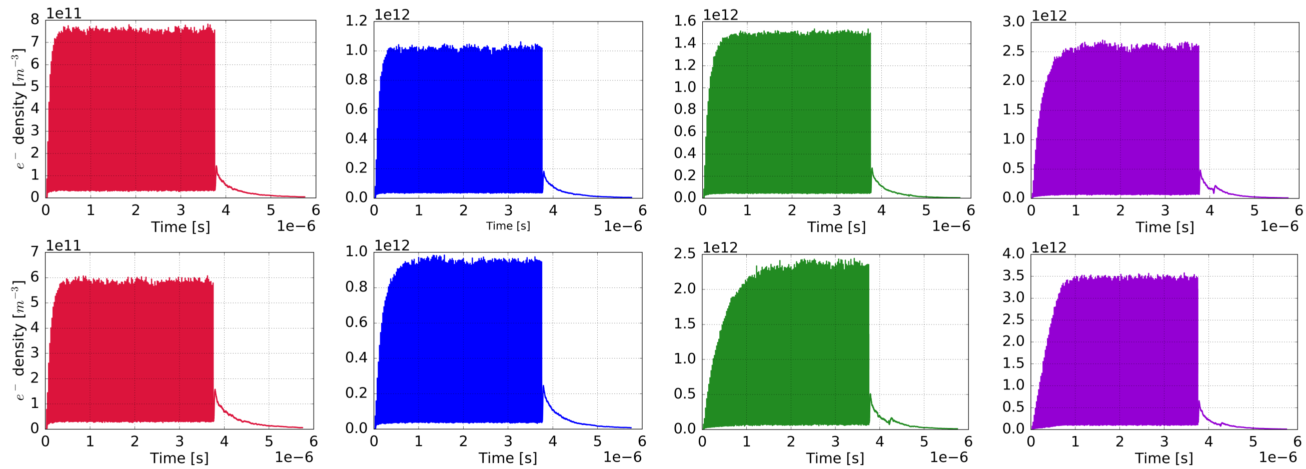

(a) SEY=1.1 (b) SEY=1.2 (c) SEY=1.3 (d) SEY=1.4

Figure 3: Electron density in the arc dipoles for bunch spacing:25 ns, SEY model:Furman-Pivi, $n'_\gamma = 10^{-3}$ m^{-1}, comparing chamber radii of 30 mm (top), and 35 mm (bottom)
.

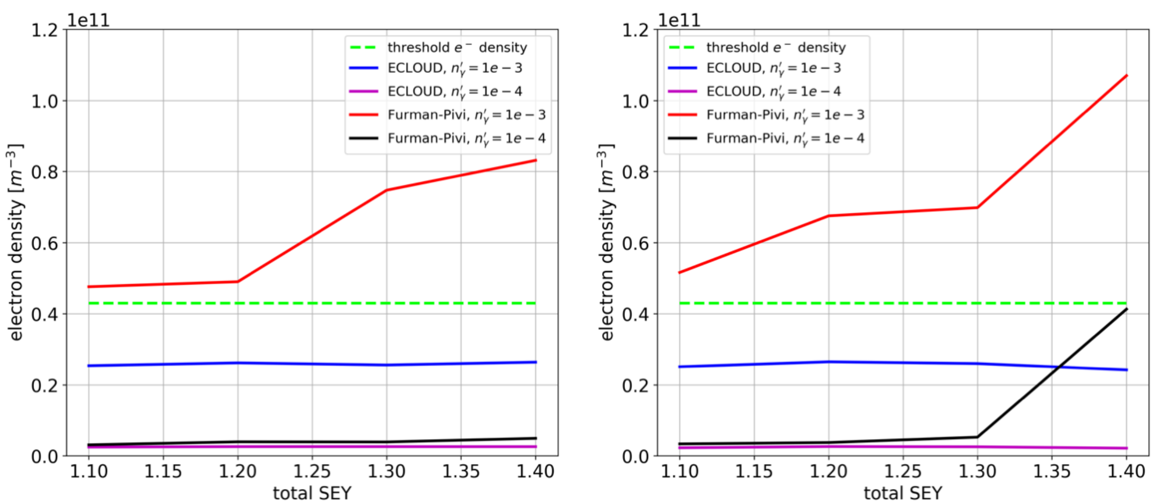

(a) chamber radius:30 mm (b) chamber radius:35 mm

Figure 4: Effect of the vacuum chamber radius for 25 ns spacing in the arc dipoles.

preceding nominal bunches. For the FCC-ee, we consider bunches at 30 ns spacing bunches with a bunch population of $N_b = 2.76 \times 10^{11}$ and the strongest secondary and photoemission parameters, namely SEY = 1.4 $n'_\gamma = 10^{-3}$ m^{-1} in addition to the Furman-Pivi model in the drift region. With this set of parameters, electron densities reach $\approx 1.75 \times 10^{13}$ m^{-3} during the bunch passes and sustain a electron density at the level of $\approx 10^7$ m^{-3} at the center of the beam pipe.

In Fig. 5, we examine the possibility of clearing the electrons left behind after the last bunch passes, in the drift region via an additional satellite bunch, whose populations is varied in between $10^4 - 10^{12}$ positrons. The satellite bunch was placed 15.45 ns behind the latest bunch in the train. At the distance of 15.45 ns the central electron density assumes a local minimum value. A significant increase of the electron density occurs for the largest satellite bunch population $N_b = 10^{12}$, in the parametric scan [15]. Otherwise, all other satellite bunches with different populations help to reduce the residual electron density. Trailing bunches with lower charges accomplish a more significant clearing of electrons [16] at the beginning. However, after a sufficiently long time, the center densities all converge to similar values, e.g., to $\approx 10^7$ m^{-3} about 20 µs after the train passage, including for the case without any trailing bunch.

CONCLUSION

In this study, we have reported results of electron-cloud build-up simulations with various combinations of SEY and photoelectron generation rates for the FCC-ee collider arc dipole beam pipe. The minimum attainabble electron density with negligible secondary emission in the dipole region is obtained as $\approx 2 \times 10^7$ m^{-3}. Furthermore, the evolution of the center electron density levels as a function of time

ISBN: 978-3-95450-236-3 ISSN: 2673-7027 doi:10.18429/JACoW-eeFACT2022-WEYAT0103

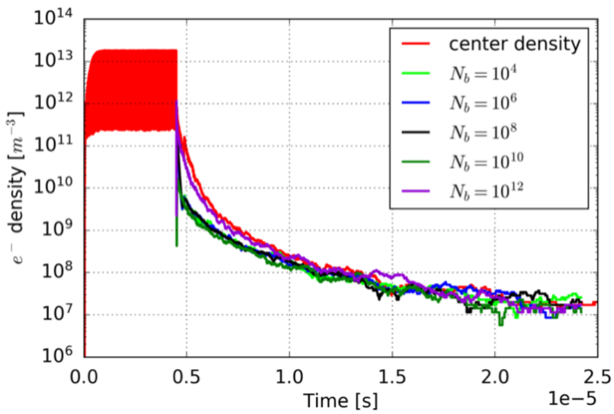

Figure 5: Mitigation tests via single trailing bunch in Drift

during several bunch passafes agree well, using either the ECLOUD or the Furman-Pivi model for the second amission yield, when considering the longest bunch spacing (32 ns) with the lowest SEY (1.1) and photoemission (10^{-6} m^{-1}), in our parameter scan for dipole and drift regions. The effect of the circular beam pipe radius is presented for 25 ns bunches. Reducing the vacuum chamber radius from 35 to 30 mm can helps suppress the electron-cloud formation.

Combining the results of Refs. [11, 15, 17], we conclude that, in order to keep minimum center electron densities lower than the single bunch instability threshold for both dipole and field-free regions, the condition $n'_\gamma < 10^{-3}$ m^{-1} should be satisfied independently of the SEY model, within the entire range of scanned beam and machine parameters, total SEY values, bunch spacings and pipe radii.

More specifically, for the dipole region, only $n'_\gamma = 10^{-3}$ m^{-1} combined with total SEY starting from 1.1 up to 1.4 of the Furman-Pivi model yields central densities larger than the threshold considering 30 mm or 35 mm circular beam pipe radius and any of 25 ns, 30 ns and 32 ns bunch spacings.

On the other hand, e^- density values at center of the vacuum chamber obtained with either ECLOUD or Furman-Pivi SEY models in the range of total SEY = 1.1–1.4 for $n'_\gamma = 10^{-3}$ m^{-1}, exceed the threshold level in the drift region. Additionally, as a particular case, for 35 mm pipe radius, the combination of $n'_\gamma = 10^{-4}$ m^{-1} with the total SEY = 1.4 of the Furman-Pivi model also leads to a density above the threshold.

It is worth noting that preliminary simulation results indicate the possibility of reaching $n'_\gamma \leq 10^{-4}$ m^{-1} by adding winglets and the photon absorbers to the vacuum chamber, see Ref. [18].

In the last part of the numerical section we presented initial results for clearing the residual electrons after the passage of a bunch train with a special single trailing bunch, demonstrating that such low-charge satellite bunches reduce the electron density, during several μs. This is of practical interest, since the separation of bunch trains for the FCC-ee Z running mode, will be of order 1–2 μs. For distances larger than about 5 μs the simulated density value converges to the one obtained without satellite bunch.

REFERENCES

[1] A. Abada *et al.* (edited by M. Benedikt *et al.*), “FCC-ee: the lepton collider, future circular collider conceptual design report volume 2”, *Eur. Phys. J. Spec. Top.*, vol. 228, p. 261, 2019. 10.1140/epjst/e2019-900045-4

[2] A. Abada *et al.* (edited by M. Mangano *et al.*), “FCC physics opportunities, future circular collider conceptual design report volume 1”, *Eur. Phys. J. C.*, vol. 79, p. 474, 2019. 10.1140/epjc/s10052-019-6904-3

[3] M. A. Furman and G. R. Lambertson, “The electron cloud effect in the arcs of the PEP-II Positron Ring”, Report Nos. LBNL- 41123/CBP Note-246 and KEK Proc. 97-17, p. 170, 1997.

[4] F. Zimmermann, “A simulation study of electron-cloud instability and beam induced multipacting in the LHC”, LHC-Project-Report vol. 95, 1997.

[5] PyECLOUD, https://github.com/PyCOMPLETE/PyECLOUD

[6] M. A. Furman and M. T. F. Pivi, “Probabilistic model for the simulation of secondary electron emission”, Abbreviation Title *Phys. Rev. Spec. Top. Accel. Beam*, vol. 5, p. 124404, 2002. 10.1103/PhysRevSTAB.5.124404

[7] E. G. T. Wulff and G. Iadarola, “Implementation and benchmarking of the Furman-Pivi model for Secondary Electron Emission in the PyECLOUD simulation code”, CERN, Geneva, Switzerland, Rep. No. CERN-ACC-2019-0029, 2019.

[8] B. Henrist, N. Hilleret, M. Jimenez, C. Scheuerlein, M. Taborelli, and G. Vorlaufer, “Secondary electron emission data for the simulation of electron cloud”, in *Proc. ECLOUD’02*, CERN, Geneva, Switzerland, Apr. 2001, pp.75–78. doi:10.5170/CERN-2002-001.75

[9] G. Iadarola, “Electron cloud studies for CERN particle accelerators and simulation code development”, PhD Thesis, Univ. Naples, CERN-THESIS-2014-047, 2014.

[10] K. Oide, D. Shatilov, *et al.*, “Collider performance, beam optics and design considerations baseline”, FCCIS Deliverable Report FCCIS-P1-WP2-D2.1

[11] F. Yaman *et al.*, “Mitigation of electron cloud effects in the FCC-ee collider”, *Eur. Phys. J. Tech. Instrum.*, vol. 9, p. 9, 2002. doi:0.1140/epjti/s40485-022-00085-y

[12] K. Ohmi, “Beam-beam and electron cloud effects in CEPC/FCC-ee”, *Int. J. Mod. Phys. A*, vol. 31, no. 33, p. 1644014, 2016. doi:10.1142/S0217751X16440140.

[13] K. Ohmi, F. Zimmermann, and E. Perevedentsev, “Wake-field and fast head-tail instability caused by an electron cloud”, *Phys. Rev. E*, vol. 65, p. 016502, 2001. 10.1103/PhysRevE.65.016502

[14] F. Ruggiero and X. Zhang, “Collective instabilities in the LHC: Electron cloud and satellite bunches”, *AIP Conf. Proc.*, vol. 496, pp. 40–48, 1999.

[15] F. Yaman and F. Zimmermann, “Studies and possible mitigation of electron cloud effects in FCC-ee”, in *Proc. 65th*

ISBN: 978-3-95450-236-3 ISSN: 2673-7027 doi:10.18429/JACoW-eeFACT2022-WEYAT0103

ICFA Advanced Beam Dynamics Workshop on High Luminosity Circular e+e- Colliders (eeFACT'22), Frascati, Italy, Sep. 2022, accompanying slides to paper WEYAT0103, this workshop.

[16] S. Veitzer (Tech-X), private communication, 2021.

[17] F. Yaman and F. Zimmermann, "Updates on the electron cloud build-up results for the FCC-ee", presented at the 159th FCC-ee Optics Design Meeting", 2022, https://indico.cern.ch/event/1205924/.

[18] F. Yaman, "Electron cloud densities at the center of the FCC-ee dipoles", presented at the 130th FCC-ee Optics Design Meeting, 2020, https://indico.cern.ch/event/982651/.

ISBN: 978-3-95450-236-3 ISSN: 2673-7027 doi:10.18429/JACoW-eeFACT2022-WEYAS0104

THIN FILMS ACTIVITIES IN THE IFAST PROGRAM

C.Z. Antoine†, S. Berry, Y. Kalboussi, T. Proslier, Université Paris-Saclay, CEA, Département des Accélérateurs, de la Cryogénie et du Magnétisme, Gif-sur-Yvette, France
O. Hryhorenko, D. Longuevergne, Thierry Pépin-Donat, Université Paris-Saclay, CNRS/IN2P3, IJCLab, Paris, France
R. Ries, E. Seiler, Institute of Electrical Engineering, SAS, Bratislava, Slovakia
S. Keckert, J. Knobloch[1], O. Kugeler, D. Tikhonov, Helmholtz-Zentrum Berlin für Materialien und Energie GmbH, Berlin, Germany
S. Prucnal, S. Zhou, Helmholtz-Zentrum Dresden-Rossendorf (HZDR), Institute of Ion Beam Physics and Materials Research, Dresden, Germany
O. Azzolini, E. Chyhyrynets, D. Ford, V. Garcia, G. Keppel, C. Pira, A. Salmaso, F. Stivanello, INFN Laboratori Nazionali di Legnaro, Legnaro (PD), Italy
M. Bertucci,R. Paparella, INFN LASA, Segrate (MI), Italy
G. Burt[2], D. Turner[2], D. Seal[2], H. Marks[2], Lancaster University, Lancaster, UK
J. W. Bradley[2], F. Walk[2], F. Lockwood-Estrin[2], Liverpool University, Liverpool UK
R. Berton, D. Piccoli, F. Piccoli, G. Squizzato, F. Telatin
PICCOLI s.r.l., Noale (VE), Italy
A. Medvids, A. Mychko, Laboratory of Semiconductor Physics,
Riga Technical University, Riga, Latvia
O. Malyshev[2], R. Valizadeh[2], A. Hannah[2], J. Conlon[2], T. Sian[2], L. Smith[2], A. Vick[2]
STFC Daresbury Laboratory, Warrington, UK
Ö. Sezgin, M. Vogel, A. Zubtsovskii, X. Jiang, Institute of Materials Engineering, University of Siegen, Siegen, Germany
[1] also at Universität Siegen, 57072 Siegen
[2] also at Cockcroft Institute, Warrington, UK

Abstract

Now that bulk Nb technology has reached it full maturity, improving SRF technology demands that new materials need to be developed. For reasons explained in the talk, all next generation SRF materials will be in the form of thin films. The IFAST project has the ambition to coordinate European activities on that topic, not only throughout its own program (that will be presented here), but also by keeping in touch with all actors worldwide, with the hope of developing a more efficient collaborative actions in a limited funding context. In this paper, we will present the challenges presented by the development of new thin films materials, each developed for tailored applications and the main research direction proposed by the thin film community.

* Work supported by the European Union's IFAST collaboration H2020 Research and Innovation Programme under Grant Agreement no. 101004730
† claire.antoine@cea.fr

TAILORED MATERIAL FOR SRF

The SRF technology is mostly based on ultra pure bulk niobium, which is not optimized to maximize its superconducting properties (surface resistance), but rather to maximize thermal stabilization of dissipating defects. By separating each functions (mechanical structure, thermal transfer, surface resistance, surface protection…), one can achieve superconducting cavities with enhanced performance (Fig. 1). One can even hope to tune their performances for specific applications.

This process is already "en marche". For instance, the "doping procedure" proposed by FNAL [1] consist in diffusing interstitial atoms in a shallow part of the surface.

ISBN: 978-3-95450-236-3 ISSN: 2673-7027 doi:10.18429/JACoW-eeFACT2022-WEYAS0104

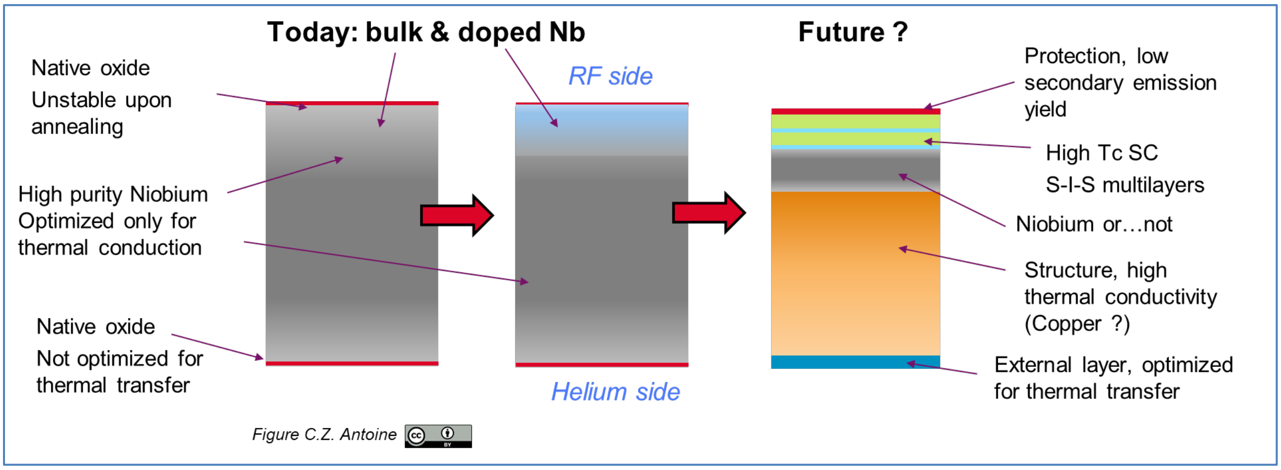

Figure 1: Expected evolution of the functionalization of SRF materials.

It is sufficient to tune the superconducting properties of the cavities' inner surface without affecting the bulk thermal conductivity. Replacing the external part of the cavity by a copper, as a highly thermally conducting and mechanical support, keeping only a thin niobium layer at the inner surface has been tried for decades, but it is only recently, with new deposition processes that dense enough films have been achieved, which exhibit improved performances.

Technological Challenges

Improving RF technology presents huge challenges in material science. Indeed, when one deals with classical copper cavities, the main requirements on the material are based on metallurgy, a science that started to be explored by humanity 6000 years ago. When one switches to niobium, still a pure metal, one has to face new challenges. The main one arises from the fact that the penetration depth of the field is ~ 40 nm, hence everything that happens on surface starts to become of paramount importance. Surface science, especially at the nm level was much more recently mastered.

Then higher Tc materials are all compounds, so it also requires mastering the chemical aspects in order to get the proper superconducting phase. Most of these materials are brittle and cannot be considered to build bulk cavities. They have to be deposited in "thick" (µm) or "thin" (nm) films. Here again, Physical Vapor deposition (PVD) techniques or Chemical Vapor deposition (CVD) techniques have been mainly developed in the course of XXth century and are still in development.

The parameter space to be explored is vast, and needs a substantial investment in material science, as has been done in the superconducting magnet community over the past 70 years.

The understanding of the physics of superconductors for magnet applications has led to tremendous progresses and opened a large domain of applications.

Unfortunately, the requirement for SRF materials are literally opposite to the requirement for magnets applications, and somehow the exploration has to be started over, but in a very different direction.

Type II Superconductors, Domains of Application

Actually thousands of superconductors (SC) have been listed but only a dozen have found applications. They are all type II. In short, magnets use type II superconductors in the mixed state. Defects are voluntarily introduced to enhance the critical current density, which in turn decreases the transition between the Meissner and mixed state (Fig. 2) by reducing the lower critical magnetic field, H_{C1}.

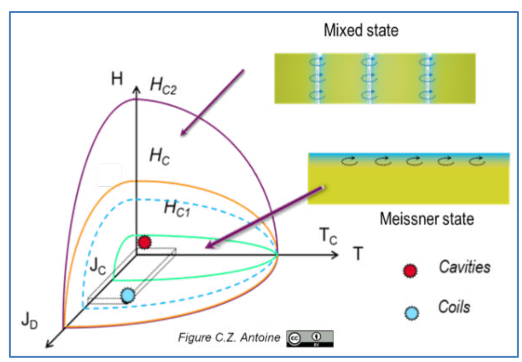

Figure 2: Meissner and mixed state. At low magnetic field, supercurrents screen the external magnetic field and the SC is in the Meissner state. Above H_{C1}, it is energetically favourable for the magnetic field lines to enter the SC as normal conducting zones surrounded by screening currents, while the rest of the material remains fully superconducting; this is the mixed state.

In RF, the mixed state is too dissipative, and cavities must be kept in the Meissner state. It means reducing the density of defects that could promote early entry of the field lines (vortex), characteristic of mixed state. Niobium it the material with the highest first critical field H_{C1}, which explain why it has become the material of choice for SRF applications [2].

ISBN: 978-3-95450-236-3 ISSN: 2673-7027 doi:10.18429/JACoW-eeFACT2022-WEYAS0104

Superheating Field and Multilayer Concept

In fact, in RF cavities, where the magnetic field is parallel to the surface, it is difficult to nucleate a vortex. This configuration helps to maintain the Meissner state as a metastable state above H_{C1} up to the “superheating field” in theory (Fig. 3). This rationale is used to predict the maximum accelerating field in cavities.

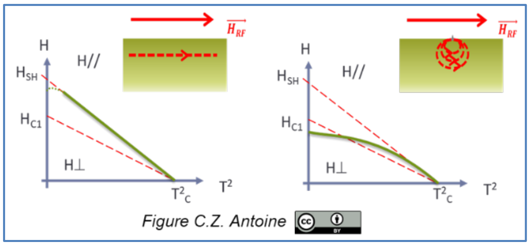

Figure 3. Vortex penetration in parallel field, without (left) or with (right) defects. The green curves are the actual transition field in the projection of the phase diagram from Figure 2 in the H vs T^2 dimensions.

In realistic condition, complex materials tend to exhibit many defects which can prevent the superheated state to be maintained.

In 2006, A. Gurevich proposed a new multi-layered structure that could overcome that issue [3]. If one places a dielectric layer a few 10s of nm below the surface, it will break any vortex loop in a vortex plus antivortex that coalesce together within a few RF periods (see Fig. 4). Moreover, if the top layer is a superconductor with a higher T_C than Nb, the surface resistance will be lower. Limiting its thickness to a few 10s of nm (i.e. below its field penetration depth λ) it a way to artificially enhance its transition field [4]. With this structure, one becomes less sensitive to defects [5], and it is one of the ways that are explored to get higher performances, as described below.

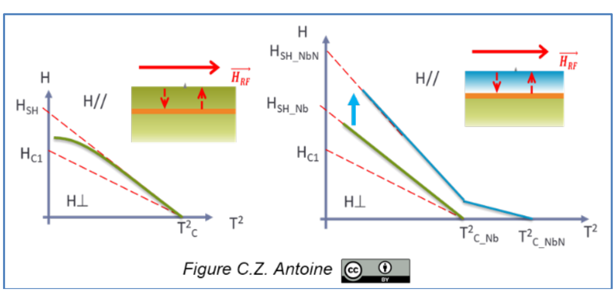

Figure 4: Effect of a dielectric layer and multilayer concept. With multilayers, one can both gain on the quality factor and the accelerating field.

IFAST THIN FILM ACTIVITIES

The WP9 from IFAST, “Innovative superconducting cavities”, is focused on improving performance and reduce cost of SRF acceleration systems based mostly on the use of thin films. It comes after several European projects on the topics (WP12.2 within Eucard2, WP15 within Aries) that helped bringing together the few teams working on that topic in Europe and keep in touch with the international community [6-8].

The European members are from France (CEA, CNRS), from Germany (HZB, USI), from Italy (INFN, PICCOLI srl), from Latvia (RTU), from Slovakia (IEE), and from United Kingdom (UKRI), but we have also external collaborators, both formal (JALB, PTI, MEPHI) and informal (CERN, DESY).

One part of the job (task 9.1) is contributing at building together a global strategy to be able to produce Superconducting RF (SRF) cavities coated with a superconducting films, and participating to the corresponding chapters (thin films) initiatives like e.g. the Snowmass propositions [9] or the European Accelerator R&D Roadmap Implementation [10].

Functionalizing SRF material requires 4 main actions:

- Mastering thin film deposition techniques in terms of final composition and structure.
- Adapting known deposition techniques to the internal complex shape of the cavities (not always compatible with standard techniques).
- Mastering interfaces quality (substrate preparation, interlayers).
- Finding the proper compromise between optimum superconducting quality and fabrication cost (choice of the superconducting material).

Past projects have shown promising results at least on flat samples. The objective of IFAST is to pass from developments on samples to the first RF prototypes and merge all the developments that have been mastered over the last years.

Among the recent achievements, here are the most compelling steps:

- Nb thin film layers with performance close to bulk Nb (mitigation of the Q-slope, high transition field) were observed at CERN [11, 12] and at JLab [13, 14]. It opens the route to Cu cavities deposited with functionalized layers on the top of a thick Nb film. The quality of the substrate (Cu) appears to have a paramount importance on these performances [15-17].
- Bulk niobium cavities deposited with high Tc material like Nb_3Sn start to exhibit very high Q_0 opening the route to operation at higher temperature and alternate cooling schemes. These higher Tc materials are very sensitive to defects and do not reach high fields yet [18, 19]. Successful alternative fabrication routes have been explored on samples (direct deposition on copper [19-22], bronze route…).
- The multilayers concept has proven to be effective both in increasing the penetration field of vortices (which drives the maximum accelerating field), and reducing the surface resistance [5]. Moreover, the “protective” effect of such structures opens the route to more realistic materials and less sensitivity to defects, including Nb_3Sn or NbTiN multilayers.

General Strategy

The general strategy (Task 9.1 of WP9) consist into pursuing the optimization and the industrialization of key steps:

ISBN: 978-3-95450-236-3 ISSN: 2673-7027 doi:10.18429/JACoW-eeFACT2022-WEYAS0104

- Substrates preparation (Nb, Cu), e.g. Plasma Electropolishing (PEP) developed at INFN, metallographic polishing(developed at CNRS), pre-and post-treatment (laser at RTU, flash annealing at HZDR).
- Production of seamless copper cavities as the risk of poor film deposition at welding has been assessed [16]
- Optimization of deposition techniques: Energetic deposition techniques, atomic layer deposition (ALD)… to get Nb, NbN, Nb_3Sn, V_3Si… thick films (µm) and/or SIS Multilayers (nm)
- Firstly producing and RF testing prototypes of SRF cavities at 6 GHz. These cavities are easier to fabricate, handle, and dissect… so that fast feedback can be provided.
- Finally producing accelerator type 1.3 GHz cavities (as a feasibility assessment). 1.3 GHz cavities present the advantage that they allow evaluating both residual and BCS resistance.

There is also a strong necessity to develop advanced characterizations tools to be able to measure superconducting properties in condition close to cavity operation, a condition which is not available with conventional techniques.

Seamless Elliptical Cavities (Task 9.2)

Producing seamless copper substrate is mandatory. Many 6 GHz cavities are required for destructible tests during the optimization stage; automated production of 1.3 GHz cavities will be necessary at the prototyping stage. In the task 9.2, the goal is to switch from a semi-automatic to a fully automatic process using a CNC machine. The work is developed in collaboration between INFN and the company Piccoli. The process is now assessed, including the optimization of the annealing temperature. Up to now, twenty 6 GHz cavities and three 1.3 GHz cavities have been produced and distributed among collaborators for further deposition. Further improvement of the automation is regarded [23, 24]. Surface treatment of copper is also an important part of the process [15, 25]

From Samples to Cavities (Task 9.3)

Thick Nb layers on copper. As mentioned earlier, getting bulk like performance on Nb films is an important step. Activities have been conducted at UKRI, INFN and USI [6, 8, 12, 17, 26-28].

Higher Tc materials. Because the material of choice will combine enhanced superconducting properties with relative easiness to produce it, several higher Tc materials are still in the optimization process: Nb_3Sn, NbTiN, NbN, MgB_2… They are complex (compound) materials, composition needs to be adjusted to get best SRF performance, and then the optimized recipes need to be adapted for complex geometries [29]. Deposition set-ups for 6 GHz cavities have been designed, build and commissioned at INFN, STFC and USI [30], along with specific developments on sputtering targets [31].

First attempts of deposition in 6 GHz cavities are undergoing [22][32].

In between, the work on flat sample allow assessing their structures and evaluate their RF properties on QPR flat samples (see below). A specific deposition set-up was built in Legnaro, while the existing set-up was used at USI .

Deposition of thick films and multilayers structures are studied in parallel. Nb/AlN/NbN have been deposited on bulk and copper QPR supports.

Surface Engineering with ALD (Task 9.4)

Atomic Layer Deposition is a particular technique based on chemical reaction of precursors adsorbed on the reactor surface (which is the cavity itself). It is a highly conformational technique particularly well adapted to complex shapes encountered in our domain, and it is easily scalable to industrial production.

A wide range of compounds are manageable in the same deposition set-up so that in situ composite fabrication is achievable.

A 1.3 GHz deposition set-up has been constructed so that results obtained on samples can be now tested on actual cavities.

Three types of functionalized layers are being explored:

- SIS multilayers: good quality NbTiN/AlN mulitlayers have been deposited on Nb samples with a Tc between 14 and 15.5 K after a final annealing. A first 1.3 GHz has been deposited with the same recipe [33].
- Dielectric surface engineering and doping. The native oxide on Nb is defective. It can be replaced by e.g. Al_2O_3 deposited by ALD followed by an annealing. The process has been tested on 2 1.3 GHz cavities with an observed increase of the quality factor [34].
- Low secondary yield cap layer. The secondary electron yield (SEY) is at the origin of the multipacting phenomena. Depositing a thin capping layer by ALD (~10 nm) proved to decrease the SEY on both samples [35] and cavities [36].

Surface Engineering with Heat (Task 9.5)

Among the pre- and post- treatments of substrates as well as films, laser and flash lamp annealing are being explored. Both treatment are very superficial, which is a plus since copper has a very low melting point and some of the films require higher temperature treatments. Only surface is affected, and these heat treatments are liable to smooth the surfaces [37-39], help to recrystallize, improve films adhesion and decrease porosities [27]. Such surface treatment could also be used to stabilize the high temperature phase of A15 compound (with the highest Tc) or built specific alloys [40]. Here also set-ups adapted to cavities treatments are under development at RTU and HZDR.

QPR Cavity: RF Evaluation (Task 9.6)

Material characterization techniques, even the most advanced ones, are still not predictive of future RF behaviour. The development of a QPR cavity at HZB [41, 42] has permitted to start to explore RF behaviour at 3 different frequencies on flat samples, small enough to be easy to handle,

ISBN: 978-3-95450-236-3 ISSN: 2673-7027 doi:10.18429/JACoW-eeFACT2022-WEYAS0104

It has allowed the measurements of Nb, NbN and NbN multilayers developed by HiPIMS at USI [43-48]; Nb and Nb_3Sn and multilayer structures prepared by DCMS or HiPIMS at STFC, and Nb and Nb_3Sn thick films prepared by DCMS at INFN. Preparation of bulk Niobium like PEP (developed at INFN) or metallographic polishing (developed at CNRS [49]) are also under study [43, 44, 50].

Material Characterization

The development of complex material requires thorough characterization tools. Classical material characterization: optical and confocal microscopy, SEM, EDX and EBSD, Ion beam miller for cross-section, X-Ray, TEM, and basic superconducting properties are measured: Tc, RRR, DC magnetometry, AC susceptibility.

In addition, specific original characterization tools have been developed to measure the superconducting samples behaviour in condition closest to the operating cavities condition: Tunnelling microscopy (Superconducting gap, density of superconducting states cartography), flux penetration measurement set-ups (at UKRI [51] and CEA [52]), Surface resistance on small sample (7.8 GHz cavity at UKRI).

CONCLUSION

Thin films SRF activities are still conducted in a few small groups, with few resources. Coordination and exchanges help to derive maximum benefit of the vast space parameter to be explored.

The next generation of SRF material is "en route" with already very nice results on samples, and early progress on R&D cavities. We hope IFAST WP9 (and collaborators) will bridge the gap between lab R&D and 1rst prototypes development. If successful this step will prove that a full change of technology is possible after more than 50 years of bulk Nb domination.

If accelerator community wants SRF technology to evolve in that direction, strong investments are needed in the near future.

To end on a positive note, several of the techniques underdevelopment are liable to be applied on bulk Nb cavities, opening the route to future up-grades of existing machines.

ACKNOWLEDGEMENTS

This work forms part of the European Union's IFAST collaboration H2020 Research Infrastructures Programme under Grant Agreement no. 101004730.

REFERENCES

[1] A. Grassellino *et al.*, "N doping: progress in development and understanding", in *Proc. SRF'2015*, 2015, p. 48-54.

[2] For the reader interested by details, more can be learnt e.g. in the master lecture "Superconductivity in accelerators", https://irfu.cea.fr/Cours/claire.antoine/

[3] A. Gurevich, "Enhancement of RF breakdown field of SC by multilayer coating", *Appl. Phys. Lett.*, vol. 88, p. 012511, 2006.

[4] A. Gurevich, "Maximum screening fields of superconducting multilayer structures". *AIP Advances*, 2015. 5(1), p. 017112.

[5] C.Z. Antoine *et al.*, "Optimization of tailored multilayer superconductors for RF application and protection against premature vortex penetration", *Superconductor Science and Technology*, 32(8), 2019.

[6] R. Valizadeh *et al.*, "Synthesis of Nb and Alternative Superconducting Film to Nb for SRF Cavity as Single Layer", *Proc. SRF'21*, 2021, East Lansing, MI, USA, p. 893-898.

[7] O.B. Malyshev *et al.*, "Main Highlights of ARIES WP15 Collaboration", in *Proc. SRF'21*, 2021, East Lansing, MI, USA.

[8] D.A. Turner *et al.*, "Magnetic Field Penetration of Niobium Thin Films Produced by the Aries Collaboration", in *Proc. SRF'21*, 2021, East Lansing, MI, USA.

[9] A.- M. Valente-Feliciano *et al.*, "Next-Generation Superconducting RF Technology based on Advanced Thin Film Technologies and Innovative Materials for Accelerator Enhanced Performance & Energy Reach", in *Letter of interest Snowmass 21*. 2021.

[10] C. Adolphsen *et al.*, "European Strategy for Particle Physics--Accelerator R&D; Roadmap", CERN Yellow Reports, monographs, 2022.

[11] S. Aull *et al.*, "On the understanding of Q-Slope of niobium thin films", in *Proc. SRF'15*, 2015, Whistler, BC, Canada.

[12] M. Arzeo *et al.*, "Enhanced radio-frequency performance of niobium films on copper substrates deposited by high power impulse magnetron sputtering". *Superconductor Science and Technology*, 2022. 35(5): p. 054008.

[13] A.-M. Valente-Feliciano, "Superconducting RF materials other than bulk niobium: a review". *Superconductor Science and Technology*, 2016. 29(11): p. 113002.

[14] M.C. Burton *et al.*, "RF Results of Nb Coated SRF Accelerator Cavities via HiPIMS". 2019, Thomas Jefferson National Accelerator Facility (TJNAF), Newport News, VA

[15] C. Pira *et al.* ,"Impact of the Cu substrate surface preparation on the morphological, superconductive and rf properties of the Nb RF Superconductivity", in *Proc. SRF'19*, Dresden, Germany, 30 June-05 July 2019.

[16] S.T. López *et al.*, "A seamless quarter-wave resonator for hie-Isolde", in *Proc. SRF*, 2017.

[17] R. Ries *et al.*, "Superconducting properties and surface roughness of thin Nb samples fabricated for SRF applications". in *Journal of Physics*: Conference Series. 2020: IOP Publishing.

[18] R. Porter *et al.*, "Next generation Nb3Sn SRF cavities for linear accelerators". in *Proc. LINAC'18*, Beijing, China, 16-21 September 2018. 2019: JACOW Publishing, Geneva, Switzerland.

[19] M.N. Sayeed *et al.*, "Deposition of Nb_3Sn Films by Multilayer Sequential Sputtering for SRF Cavity Application". in *Proc. SRF'19*, 2019. Dresden, Germany.

[20] W. Tan *et al.*, "Nb3Sn Thin Film Deposition On Copper By DC Magnetron Sputtering". 2018.

[21] E. Ilyina *et al.*, "Development of sputtered Nb3Sn films on copper substrates for superconducting radiofrequency applications". *Superconductor Science and Technology*, 2019. 32(3): p. 035002.

ISBN: 978-3-95450-236-3 ISSN: 2673-7027 doi:10.18429/JACoW-eeFACT2022-WEYAS0104

[22] R. Valizadeh *et al.*, "PVD Depostion of Nb3Sn thin film on copper substrate from an alloy Nb3Sn target". *Proc. IPAC'19*, 2019, pp. 2818-2821.

[23] F. Sciarrabba *et al.*, "1.3 GHz Seamless Copper Cavities via CNC Spinning Technique", in *Proc. SRF'21*, East Lansing, MI, USA, Jun.-Jul. 2021, pp. 440-444. doi:10.18429/JACoW-SRF2021-TUPCAV003

[24] S.B. Leith *et al.*, "Initial Results from Investigations into Different Surface Peparation Techniques of OFHC Copper for SRF Applications", in *Proc. SRF'19*, 2019, Dresden, Germany.

[25] C. Pira *et al.*, "Plasma Electrolytic Polishing as a Promising Treatment Replacement of Electropolishing in the Copper and Niobium Substrate Preparation for SRF", in *Proc. SRF'21*, Jun.-Jul. 2021, East Lansing, MI, USA, pp. 718-724.

[26] S. Aliasghari *et al.*, "X-ray computed tomographic and focused ion beam/electron microscopic investigation of coating defects in niobium-coated copper superconducting radio-frequency cavities". *Materials Chemistry and Physics*, 2021. 273: p. 125062.

[27] R. Ries *et al.*, "Improvement of the first flux entry field by laser post-treatment of the thin Nb film on Cu". *Superconductor Science and Technology*, 2021. 34(6): p. 065001.

[28] V. Palmieri *et al., "*The Way of Thick Films toward a Flat Q-curve in Sputtered Cavities". in *Proc. SRF'17*, 2017. doi:10.18429/JACoW-SRF2017-TUYBA03.

[29] M. Zanierato *et al.*, "Nb_3Sn Films Depositions from Targets Synthesized via Liquid Tin Diffusion", in Proc. SRF'21, East Lansing, MI, USA, Jun.-Jul. 2021, pp. 452-456. doi:10.18429/JACoW-SRF2021-TUPCAV006. V.A. Garcia Diaz *et al.*, "Thick Film Morphology and SC Characterizations of 6 GHz Nb/Cu Cavities", in *Proc. SRF'21*, East Lansing, MI, USA, Jun.-Jul. 2021, pp. 18-22. doi:10.18429/JACoW-SRF2021-SUPCAV007

[30] X.J. M. Vogel, A.O. Sezgin. "New Sputtering Coating Facility for Nb-Based Thin Films in 1.3 GHz Cavities", in *Proc. IPAC'22*, Bangkok, Thailand, 2022.

[31] M. Zanierato *et al.*, Nb_3Sn Films Depositions from Targets Synthesized via Liquid Tin Diffusion, in Proc. SRF'21, East Lansing, MI, USA, Jun.-Jul. 2021, pp. 452-456. doi:10.18429/JACoW-SRF2021-TUPCAV006

[32] A. Hannah, "First 6 ghz cavity deposition with b1 superconducting thin film at ASTEC", in *Proc. IPAC'22*, Bangkok, Thailand, 2022.

[33] "Optimization of the superconducting properties of NbTiN thin films synthesized by ALD" Y. Kalboussi, F. Miserque, T. Proslier. TBS. APL.

[34] "Atomic layer deposition engineering of Oxide interface in SRF cavities" Y. Kalboussi, F. Miserque, T. Proslier. TBS. PRSTAB

[35] S. Bira, D. Longuevergne, Y. Kalboussi, S. Keckert, J. Knobloch, O. Kugeler, T. Proslier, "Multipacting Analysis of the Quadripolar Resonator (QPR) at HZB", SRF2021. doi:10.18429/JACoW-SRF2021-SUPCAV013.

[36] Y. Kalboussi *et al.*, "Multipacting suppression by Atomic Layer Deposition of TiN in SRF cavities", TBS PRSTA

[37] Rastislav Ries *et al.*, "Correlation between first flux entry field and surface roughness of Nb samples", in *Proc. EUCAS 2019*. 2019, Glasgow, UK.

[38] N.A. Vainos, "Laser growth and processing of photonic devices". 2012: Elsevier.

[39] L. Rebohle, S. Prucnal, and W. Skorupa, "A review of thermal processing in the subsecond range: semiconductors and beyond". *Semiconductor Science and Technology*, 2016. 31(10): p. 103001.

[40] Z. Li *et al.*, "Phase Selection in Mn–Si Alloys by Fast Solid-State Reaction with Enhanced Skyrmion Stability", *Advanced Functional Materials*, 2021. 31(15): p. 2009723.

[41] S. Keckert *et al.*, "Characterizing materials for superconducting radiofrequency applications—A comprehensive overview of the quadrupole resonator design and measurement capabilities". *Review of Scientific Instruments,* 2021. 92(6): p. 064710.

[42] R.K. S. Keckert *et al.*, "Mitigation of Parasitic Losses in the Quadrupole Resonator Enabling Direct Measurements of Low Residual Resistances of SRF Samples". in *Proc. IPAC'22*, Bangkok, Thailand.

[43] A. Sezgin *et al., "*HiPIMS-coated novel S (I) S multilayers for srf cavities". in *Proc. IPAC'22*, Bangkok, Thailand, 2022.

[44] A. Sezgin *et al., "*Investigation of HiPIMS-coated S (I) S structures for srf cavities". in *Proc. LINAC'22*, Liverpool, UK. 2022.

[45] S. Leith *et al.*, "Superconducting NbN thin films for use in superconducting radio f*requency cavities".* Superconductor Science and Technology, 2021. 34(025006).

[46] S. Leith *et al.,* "The Development of HiPIMS Multilayer SIS film coatings on Copper for SRF Applications". in *9th International Workshop on Thin Films and New Ideas for Pushing the Limits of RF Superconductivity*. 2021.

[47] M.V. S. Leith, B. Bai, X. Jiang, E. Seiler, and R. Ries, "HiPIMS NbN Thin Film Development for use in Multilayer SIS films", in *Proc. SRF2021*. 2021.

[48] A.Ö. Sezgin *et al., "*NbN Thin Film-Based Multilayer (S-(I)-S) Structures for SRF Cavities". in *9th International Workshop on Thin Films and New Ideas for Pushing the Limits of RF Superconductivity*. 2021.

[49] O. Hryhorenko *et al.*, "Metallographic Polishing Pathway to the Future of Large Scale SRF Facilities". in *Proc. SRF'19*, Dresden, Germany, 30 June-05 July 2019.

[50] S. Keckert *et al.*, "Mitigation of parasitic losses in the quadrupole resonator enabling direct measurements of low residual resistances of SRF samples". *AIP Advances*, 2021. 11(12): p. 125326.

[51] D.A. Turner *et al.*, "A facility for the characterisation of planar multilayer structures with preliminary niobium results". *Superconductor Science and Technology*, 2022. 35(9): p. 095004.

[52] M. Aburas, C.Z. Antoine, and A. Four. "Local magnetometer: First critical field measurement of multilayer superconductors", in *Proc. SRF'17*, Lanzhou, China, 2017.

ISBN: 978-3-95450-236-3 ISSN: 2673-7027 doi:10.18429/JACoW-eeFACT2022-WEZAT0102

TOWARDS BEAM-BEAM SIMULATIONS FOR FCC-ee*

P. Kicsiny†,1,2, X. Buffat[1], G. Iadarola[1], T. Pieloni[2], D. Schulte[1], M. Seidel[2,3]
[1]CERN, Geneva, Switzerland
[2]École Polytechnique Fédérale de Lausanne (EPFL), Lausanne, Switzerland
[3]Paul Scherrer Institut, 5232 Villigen PSI, Switzerland

Abstract

The FCC-ee (Future Circular Collider) lepton collider is currently the most favored next generation research infrastructure project at CERN, aimed at studying properties of standard model particles with the highest precision ever. The chosen parameters of the machine yield unprecedented conditions which give rise to previously unseen dynamical effects during collisions. The exploration and understanding of these beam-beam effects is of crucial importance for the success of the FCC-ee feasibility study. To address this challenge, a new general purpose software framework for beam dynamics simulations is currently under development at CERN. This presentation will discuss the contributions to the software development related to beam-beam effects with benchmark studies and applications.

INTRODUCTION

The FCC-ee feasibility study [1] aims at verifying the possibility to build a near 100 km long circular collider in the Geneva area. The study would be the first stage towards a 100 TeV hadron collider, termed FCC-hh. These colliders aim notably to search for new physics beyond the standard model. During beam-beam collisions the particles in the two colliding beams experience an electromagnetic (EM) force by the presence of the opposite beam. This nonlinear beam-beam "kick" perturbs the particle trajectories resulting in long term changes in the dynamical behavior of the beams, collectively referred to as beam-beam effects [2]. Due to the nonlinear nature of the interaction, a purely analytical treatment of these effects is excluded. Instead, numerical multiparticle simulations are commonly used where the dynamical variables of the particles are tracked. The difficulty in simulating this dynamics lies in the complexity of the FCC-ee machine and the interplay of the different dynamical effects.

The collider infrastructure is designed to maximize achievable luminosity. To this end, a setup called the crab-waist scheme [3] has been proposed, which mitigates the nonlinear effect of beam-beam collisions and achieves extremely small, nanometer sized beams at the interaction points (IPs) by colliding beams with a crossing angle of 30 mrad and by using special purpose, so called crab-sextupoles. Another setup, commonly used in synchrotron light sources, is the top-up injection scheme [4], which means that new, low intensity beam bunches are injected with a high frequency to maintain high bunch intensities in the beams. This helps to maintain high luminosity, which decreases due to the reduced beam lifetime caused mainly by the emission of radiation during the collision.

Beamstrahlung

Arguably one of the most important beam-beam effects in the FCC-ee is beamstrahlung, i.e., the emission of high energy (up to GeV order) photons relative to the particle energy during collision. The photon emission happens due to the local bending of the particle trajectories in the collective EM field of the opposite bunch. Beamstrahlung has deteriorating impact on the bunch quality. The quantum nature of photon emission increases the energy spread of the beam, which is converted to an increase of the bunch length [5]. It also reduces the luminosity and leads to an increased loss rate of particles due to the reduction of the dynamic aperture [6].

SIMULATION OF FCC-ee BEAM-BEAM EFFECTS

The FCC-ee is a highly complex machine, where many dynamical effects interplay with each other. Therefore a simulation that aims to model the beam dynamics has to be self-consistent, i.e., not relying on any other external input or modification of intermediate variables during the simulation. Currently there exist several toolkits to model beam dynamics in high energy colliders. Some of the most well known codes are `MAD-X` [7], `SixTrack` [8], `PyHEADTAIL` [9] and `COMBIp` [10]. Each of these codes have been developed aiming for different studies, each having different features. There are other codes which were developed specifically for studying beam-beam effects in colliders. Some of the most well known are `BBWS` [11] and `BBSS` [12], `LIFETRAC` [13] and `GUINEA-PIG` [14]. Each of these codes uses different approximations to boost performance or numerical precision for certain types of studies. The main challenge that limits simulation capabilities is to interface such codes when we want to study the interplay of different mechanisms, crucial for the FCC-ee feasibility study. Hence the need for a single, self-consistent and open source simulation tool following mainstream computing paradigms, i.e., modern programming languages and compatibility with multiple platforms such as CPU or GPU from different vendors and which incorporates all elements of a complex accelerator, necessary for studying FCC-ee beam dynamics. A new simulation tool, called `xsuite` [15], targets the above outlined demanding

* This work was performed under the auspices and with support from the Swiss Accelerator Research and Technology program (CHART, www.chart.ch).
† peter.kicsiny@cern.ch

ISBN: 978-3-95450-236-3 ISSN: 2673-7027 doi:10.18429/JACoW-eeFACT2022-WEZAT0102

criteria. This contribution will present recent progress on the development of this framework, related to beam-beam collision modelling, and first studies, performed using the tool.

Beam-beam Models

In the following we describe how beam-beam interactions in high energy colliders are most commonly modelled in a multiparticle tracking code, such as `xsuite`. We model the interaction of two bunches at a time, each of which consists of a number of macroparticles, usually $10^4 - 10^6$. The macroparticles each have their own 6D dynamical variables (x, p_x, y, p_y, z, p_z). During a collision the two bunches move across each other and the particles receive a kick by the collective EM field of the opposite bunch, which corresponds to a change in their momentum variables. Our approach follows [16], in which the two bunches are first rotated and Lorentz-boosted into a frame where the initially large crossing angle is eliminated and the collision is head-on. In this new reference frame the EM fields are purely transversal due to the ultra-relativistic nature of the collision ($\gamma = \frac{E}{E_0} >> 1$), which makes the computation of the beam-beam kick easier. The bunches are longitudinally sliced to preserve symplecticity, to account for the transverse offset of the particles due to the rotation as well as the beam size variation due to the hourglass effect. Then they are moved across each other by one slice at a time, where each particle in each slice will now receive a separate kick from each slice of the opposite bunch. In general, the higher the number of slices, the more accurate is the model as more slices can better model the transverse geometry of the bunch, which is important for configurations with a large crossing angle, such as the FCC-ee. The sufficient amount of slices for a given beam can be estimated as

$$N_s = 10 \cdot \frac{\sigma_z}{\min(L_i, \beta_y^*)}, \tag{1}$$

where N_s is the number of slices, σ_z is the equilibrium RMS bunch length, β_y^* is the optical beta function at the IP and L_i is the interaction length, i.e., the overlap area between the two bunches at collision, as described in [17]. The ratio of bunch length to waist or collision length is a measure for the variation of the bunch cross section during collision, with a high ratio indicating that more slices are required for accurate simulation.

In `xsuite` the beam-beam kick is computed in the soft-Gaussian approximation, using the Bassetti-Erskine formula [18], which is a computationally cheap approximation assuming and valid for Gaussian beam profiles. The formula computes the kick using the statistical moments of the slices of the opposite bunch, with which a given particle is interacting. The collision is simulated by sliding the sliced bunches across each other in discrete steps where in each step there are a number of slices of bunch 1 overlapping with slices of bunch 2. In each step the overlapping slice pairs are interacting, whereby the particles in one slice experience the kick from the opposite slice. This process is illustrated on Fig. 1.

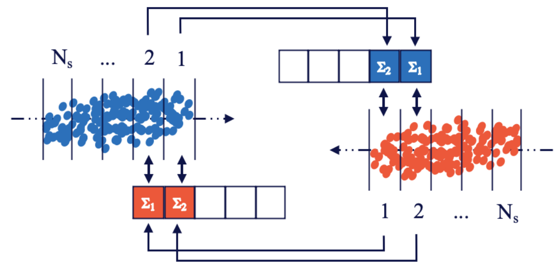

Figure 1: Modelling of beam-beam collision in a numerical tracking code, using the Lorentz-boost approach. Note the difference in the transverse offset between the head and the tail of the bunches.

In this model there is a trade-off between computational efficiency (speed) and accuracy, depending on the update frequency of the beam-beam kick strength. On one end, we can model the collision by only tracking one (called weak) bunch and freezing the other (called strong) bunch. This is called the weak-strong approximation. In this case the strong bunch slices represent a constant EM lens each of which the strength is precomputed and never changed. This model is not self-consistent because it does not follow the evolution of the strong bunch, but it is optimal for studying multi-turn single-particle effects, e.g., the evolution of the weak bunch sizes and emittances over many tracking turns. It is the computationally cheapest but the least accurate beam-beam model.

In the so called quasi strong-strong approximation both bunches are tracked and the beam-beam kicks are periodically recomputed using the up-to-date statistical moments of the bunch slices. This model is more accurate than the weak-strong but computationally more expensive because we have to recompute the statistical moments periodically. The quasi strong-strong approach is a good approximation if we want to study slow instabilities such as the 3D flip-flop instability [17], and configurations with a low disruption parameter, where the bunch profile does not change significantly within one collision. Recomputing the statistical moments every turn allows to simulate fast instabilities, e.g., the recently discovered coherent head-tail instability [19]

At the other end of the trade-off spectrum is the full strong-strong approach, where the statistical moments of each slice of both bunches are recomputed after each slice pair interaction. This is the computationally most expensive but the most realistic and the only self-consistent approach. With this we can more accurately simulate fast instabilities and the disruption of the bunch profile within the same collision (meaning a high disruption parameter).

The beam-beam model of `xsuite` is being developed in a way that the choice of the approximation is flexible and uses the same code. The model is planned to be extended by the capability to simulate background generating pro-

ISBN: 978-3-95450-236-3 ISSN: 2673-7027 doi:10.18429/JACoW-eeFACT2022-WEZAT0102

cesses, such as beamstrahlung (first implementation already exists, benchmark shown in Sec. 4.) and Bhabha scattering (implementation ongoing), as well as to use a numerical field-solver for general, non-Gaussian profiles, which is to be tested in the future. Such field solvers are already implemented in `xsuite` for other purposes but not yet linked to the beam-beam model.

PERFORMANCE OF THE XSUITE BEAM-BEAM MODEL

We have chosen to benchmark the performance of the `xsuite` beam-beam model in the strong-strong approach, that being the computationally heaviest. We have chosen `COMBIp` as our benchmark code, which is a well established tracking tool optimized for strong-strong simulations at the LHC. In the study we have performed a single beam-beam collision followed by a linear tracking through the LHC arc and we tracked for 10 turns with both codes in the exact same setting. The computation time needed for the tracking with the linear transfer map (being a simple matrix multiplication) is negligible compared to that needed for the simulation of the strong-strong beam-beam collision, therefore the measured wall times are characteristic of the beam-beam model. We have opted for a configuration featuring the HL-LHC, with no crossing angle and round Gaussian beams for simplicity. We have initialised 10^6 macroparticles and performed a scan in the number of longitudinal slices in the beam-beam model. Figure 2 shows a comparison of the wall times averaged per turn for `COMBIp` (blue) and for `xsuite` (red).

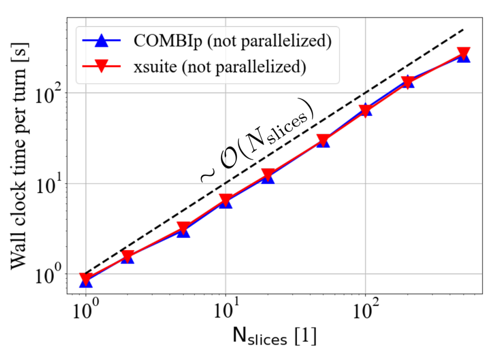

Figure 2: Simulated average wall clock time per turn of the strong-strong beam-beam model as a function of the number of longitudinal slices for `xsuite` (red) and the reference code `COMBIp` (blue).

The study shows that the runtimes scale approximately linear to the number of slices. In addition, it can be seen that `xsuite` could be optimised to have similar runtimes to `COMBIp`. Note that these simulations did not use any parallelisation. In `xsuite` it is possible to use OpenMP for multi-threading, which has been tested with an example study, scanning the number of threads and measuring the wall time, using the FCC-ee Z parameters, and tracking for 100 collisions corresponding to 100 half turns, with 10^6 macroparticles and 300 slices, which is the optimal setting for this configuration. The parallelisation is done on the loop over the macroparticles inside the beam-beam model. The obtained scaling is shown on Fig. 3. The displayed wall times are normalised to that with only one thread requested. The scaling up to 4 threads is ideal, with a factor 4 speedup. Afterwards it saturates at about a factor 5 speedup compared to the sequential case. The saturation is likely caused by the relatively low number of macroparticles per slice (3333). After a given thread count, the time needed to communicate between the C kernel and the python interface becomes comparable to the time spent, per thread, looping over the particles. This could be improved by using a higher number of macroparticles.

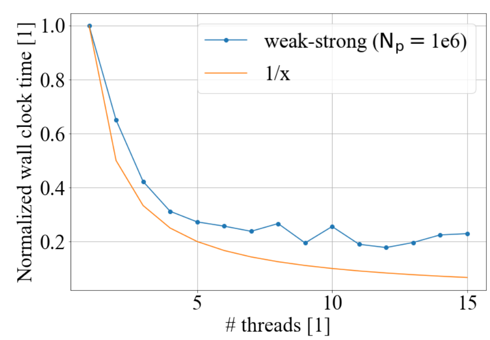

Figure 3: Integrated wall clock time as a function of the number of compute threads for a set of weak-strong simulations (including a linear half-arc) with the FCC-ee Z parameters, each tracked for 100 half turns.

Full scale simulations using an element by element model of the collider ring and the strong-strong collision model with many macroparticles will likely require a better parallelisation scheme. `xsuite` is designed to be a multiplatform software, and for beam-beam simulations the performance on GPUs is planned to be tested in the near future.

BEAMSTRAHLUNG BENCHMARK

As mentioned in the previous section, a first model of the beamstrahlung photon emission has been implemented in `xsuite`. The implementation is based on `GUINEA-PIG`, which is considered to be a state of the art tool for beamstrahlung simulation. It is capable of modelling a single beam-beam collision and generating background radiation of different kinds. It uses a particle in cell (PIC) solver, which corresponds to a fully self-consistent strong-strong model. In the following benchmark study we have compared the energy spectrum of the emitted beamstrahlung photons in a flat beam configuration ($\varepsilon_x = 2.7 \cdot 10^{-10}$ m, $\varepsilon_x = 2.7 \cdot 10^{-12}$ m, $\beta_x = \beta_y = 0.15$ m) with the nominal FCC-ee crossing angle (30 mrad) between `GUINEA-PIG` and `xsuite`, using the weak-strong approximation in the latter, with 100 slices having a uniform bin width. With both codes,

ISBN: 978-3-95450-236-3 ISSN: 2673-7027 doi:10.18429/JACoW-eeFACT2022-WEZAT0102

we have performed a single collision (without tracking in the arc) using 10^5 macroparticles and recorded the photon spectrum, which is shown in Fig. 4. The plot shows the absolute energy spectrum of the emitted beamstrahlung photons against the normalised photon count, which shows a good qualitative agreement between the two codes.

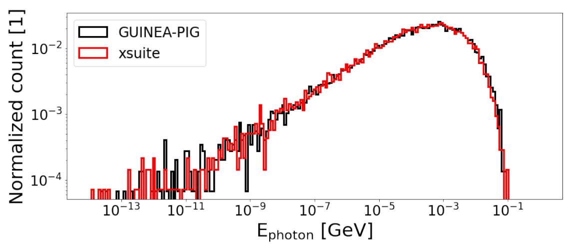

Figure 4: Energy spectrum of emitted beamstrahlung photons using `GUINEA-PIG` (black) and `xsuite` (red). Photon counts are normalised to 1.

A next step in this direction is to implement an event generator for the Bhabha-scattering process, which is useful for simulating the beam lifetime, beam losses as well as photons used for luminosity calibration.

SIMPLIFIED TRACKING SIMULATIONS

After benchmarking the beam-beam element's performance and the beamstrahlung photon generation, the next step is to perform simplified tracking simulations with `xsuite`. For these studies we exploit the superperiodicity of the FCC-ee ring, namely we only simulate half a turn in one iteration, using the half tunes. Our simulations consist of an IP, including beamstrahlung, plus a simplified tracking over the half arc with a linear transfer matrix. Furthermore, the arc is split into 3 segments and we insert 2 crab-sextupoles between them to implement the crab waist scheme. We start each (half) turn in front of the right sextupole, where our observation point for the emittances is located. Our observation point for the RMS beam sizes is located in front of the IP. We implement an effective model for synchrotron radiation, by using a simplified exponential damping and Gaussian noise excitation. In the following studies we use 300 bins for the longitudinal slicing of the bunches, each containing an equal amount of charge. Our setup is sketched on Fig. 5.

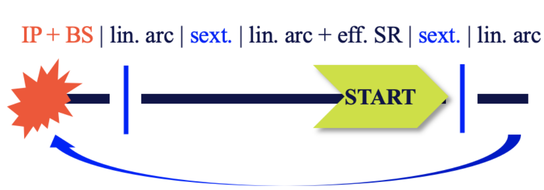

Figure 5: Simplified tracking model used for our simulations presented in this contribution.

Equilibrium Bunch Length

First we have looked at the evolution of the weak bunch length, which blows up as a direct consequence of beamstrahlung, in the weak-strong approximation. We initialise the length of the weak bunch to the equilibrium value without beamstrahlung, but with synchrotron radiation. The length of the strong bunch, a constant EM lens in this case, but computed from an actual Gaussian distribution of 10^6 macroparticles, is initialised with the equilibrium bunch length with beamstrahlung. We have performed tracking for 10^4 turns in all FCC-ee configurations using 10^4 macroparticles in the weak bunch. Figure 6 shows the bunch length evolution in units of the equilibrium length with beamstrahlung.

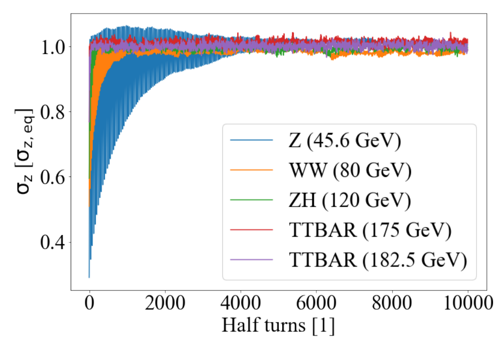

Figure 6: Evolution of weak bunch length for all FCC-ee energies. The values are always normalised to the nominal equilibrium bunch length, taken from [1].

It can be seen that the bunch length converges to the equilibrium value in all configurations. The rate of damping increases with increasing energy which corresponds to our expectations.

Crab Waist and Transverse Blowup

In the following study, using the same tracking model as outlined earlier, we have investigated the equilibrium transverse bunch sizes. These blow up due to the nonlinear kick received from the beam-beam interaction, even without beamstrahlung. In general the crab-waist scheme improves the nonlinear dynamics at the collision and mitigates this transverse blowup. With the crab-sextupoles implemented in our model, we expect no blowup in either transverse size. Since the geometrical magnet strength k_2 of the crab-sextupoles is a free parameter which affects the final blowup, we have performed an optimisation study where we scanned this parameter and observed the equilibrium bunch sizes. In each setting we have performed tracking for $3 \cdot 10^4$ turns, otherwise identical parameters to the previous study. Note that the previous study has been performed using the optimal crab-sextupole strength. Figure 7 shows the equilibrium bunch sizes (of the weak bunch) as a function of the k_2 geometrical sextupole strength. The values on the y axis are normalised to the initial bunch size, which is also the expected final size since we expect no blowup.

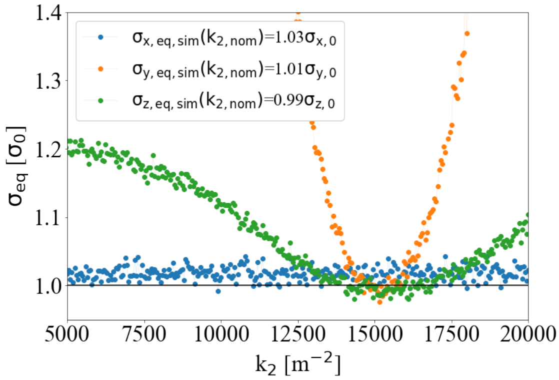

Figure 7: Simulated equilibrium weak bunch sizes as a function of the geometrical crab-sextupole strength k_2 at the FCC-ee Z resonance. The values are always normalised to the nominal equilibrium (=initial in this case) bunch sizes.

The statistical uncertainty on the presented values is around 1%. The results verify that the minimum of the blowup occurs with the sextupole strength set to its nominal value, reported in [1].

In case of strong-strong simulations with the same settings, we observed a transverse blowup. In this case, both the horizontal and vertical bunch size blows up for both bunches. The reason for this could be an insufficient statistics in the bunch slices to compute the beam-beam kick. Since we have used 10^4 macroparticles per bunch with 300 slices, it equals to about 33-34 macroparticles per slice. Alternatively, the blowup could be a sign of the recently observed coherent head-tail instability [19]. The understanding of this blowup in strong-strong simulations requires further investigation, which is currently ongoing.

SUMMARY AND CONCLUSIONS

We have developed a flexible beam-beam collision model in the `xsuite` beam dynamics simulation framework and performed several benchmark studies. A first implementation of Beamstrahlung is available [15] for further studies, such as collimation. We have experienced a rapid transverse blowup in strong-strong simulations, which is likely linked to insufficient statistics. There is ongoing work to investigate the source of this blowup using further parameter scans (e.g., tune scans) as well as frequency map analysis (FMA) [20].

After a sufficient benchmark of the `xsuite` beam-beam model, we are planning to perform studies related to the 3D flip-flop instability which can result from an initial asymmetry in the colliding bunch intensities. This scenario will be relevant during the FCC-ee top-up injection and can efficiently be simulated using `xsuite`, since the injection and the beam-beam collision can be treated self-consistently within the same framework. Another priority is to implement an efficient event generator for the Bhabha scattering process which will enable us to estimate luminosity, study beam lifetime and better understand the consequences of beam background on the infrastructure.

Once the necessary ingredients are finalised, `xsuite` will have a large potential for complex beam-dynamics studies in the context of the FCC-ee, such as the study of lattice imperfections, the interplay with a real lattice model or with wakefields, multiple IP configurations, monochromation and much more.

ACKNOWLEDGEMENTS

The authors would like to thank F. Carlier, M. Hofer, K. Oide, D. Shatilov and D. Zhou for their useful input and feedback on the project.

REFERENCES

[1] M. Benedikt, *et al.*, “FCC-ee: The lepton collider: future circular collider conceptual design report volume 2”, *Eur. Phys. J. Spec. Top.*, vol. 228, pp. 261–623, 2019. doi:10.1140/epjst/e2019-900045-4

[2] W. Herr and T. Pieloni, “Beam-beam effects”, in *CAS - CERN Accelerator School: Advanced Accelerator Physics*, Trondheim, Norway, Aug. 2013, pp. 431–459. doi:10.5170/CERN-2014-009.431

[3] M. Zobov, “Crab Waist collision scheme: a novel approach for particle colliders”, *J. Phys. Conf. Ser.*, vol. 747, p. 012090, 2016. doi:10.1088/1742-6596/747/1/012090

[4] M. Aiba *et al.*, “Top-up injection schemes for future circular lepton collider”, *Nucl. Instrum. Methods Phys. Res., A*, vol. 880 pp. 98–106, 2018. doi:10.1016/j.nima.2017.10.075

[5] M. A. Valdivia García and F. Zimmermann, “Beam blow up due to beamstrahlung in circular e⁺e⁻ colliders”, *Eur. Phys. J. Plus*, vol. 36 p. 501, (18 pages) 2021. 10.1140/epjp/s13360-021-01485-x

[6] F. Zimmermann *et al.*, “Beam dynamics challenges for FCC-ee”, *ICFA Beam Dynanics Newsletter*, vol. 67 pp. 93–100, 2015.

[7] MAD-X, https://mad.web.cern.ch/mad

[8] SixTrack, http://sixtrack.web.cern.ch/SixTrack

[9] PyHEADTAIL, https://github.com/PyCOMPLETE/PyHEADTAIL

[10] COMBIp, https://combi.web.cern.ch/parallelization

[11] K. Ohmi and D. Shatilov, ”Status of benchmark of Lifetrack and BBWS”, *FCC-ee Meeting*, CERN, 31 Aug. 2015.

[12] BBSS, https://oraweb.cern.ch/pls/hhh/code_website.disp_code?code_name=BBSS

[13] A. Valishev, Y. Alexahin, V. Lebedev, and D. Shatilov, “LIFETRAC code for the weak-strong simulation of the beam-beam effect in Tevatron”, in *Proc. 21st IEEE Particle Accelerator Conf. (IPAC’05)*, Knoxville, TN, USA, May 2005, p. 4138.

[14] GUINEA-PIG, https://abpcomputing.web.cern.ch/codes/codes_pages/Guinea-Pig

[15] xsuite, https://github.com/xsuite

ISBN: 978-3-95450-236-3 ISSN: 2673-7027 doi:10.18429/JACoW-eeFACT2022-WEZAT0102

[16] K. Hirata, "Analysis of beam-beam interactions with a large crossing angle", *Phys. Rev. Lett.*, vol. 74, no.12, pp. 2228-2231. doi:10.1103/PhysRevLett.74.2228

[17] D. Shatilov, "FCC-ee Parameter Optimization", *ICFA Beam Dynamics Newsletter*, vol. 72, pp. 30–41, 2017, https://cds.cern.ch/record/2816655

[18] M. Bassetti and G. Erskine, "Closed expression for the electrical field of a two-dimensional Gaussian charge", CERN, Geneva, Switzerland, Rep. No. CERN-ISR-TH-80-06, 1980, https://cds.cern.ch/record/122227

[19] K. Ohmi, N. Kuroo, K. Oide, D. Zhou, and F. Zimmermann, "Coherent beam-beam instability in collisions with a large crossing angle", *Phys. Rev. Lett.*, vol. 119, p. 134801, Sep. 2017. doi:10.1103/PhysRevLett.119.134801

[20] J. Laskar, "Frequency analysis of a dynamical system", *Celestial Mech. Dyn. Astron*, vol. 56, pp. 191-196, May 1993. doi:10.1007/BF00699731

ISBN: 978-3-95450-236-3 ISSN: 2673-7027 doi:10.18429/JACoW-eeFACT2022-WEZAS0101

OVERVIEW AND PROSPECTS OF THE SuperKEKB COMMISSIONING

Y. Funakoshi* on behalf of the SuperKEKB commissioning group
KEK, Tsukuba, Ibaraki 305-0801, Japan

Abstract

The Phase 3 beam commissioning of SuperKEKB is summarized. As for the prospects of SuperKEKB commissioning, we focus on critical issues toward the next mile stone of the luminosity of $1 \times 10^{35}\text{cm}^{-2}\text{s}^{-1}$.

INTRODUCTION

The purpose of SuperKEKB is to search for a new physics beyond the standard model of the particle physics in the B meson regime. SuperKEKB consists of the injector linac, a damping ring for the positron beam, two main rings; *i.e.* the low energy ring (LER) for positrons and the high energy ring (HER) for electrons and the physics detector named Belle II. The beam energies of LER and HER are 4 GeV and 7 GeV, respectively. The design beam currents of LER and HER are 3.6 A and 2.6 A, respectively. The design luminosity is $8 \times 10^{35}\text{cm}^{-2}\text{s}^{-1}$. More detailed design parameters of SuperKEKB is described elsewhere [1]. The Phase 1 beam commissioning was done from Feb. 2016 to June 2016. In this phase, the machine operation was done without the IR (Interaction Region) devises nor the Belle II detector. The purposes of the operation in Phase 1 were vacuum scrubbing, low emittance tuning and beam background study using specially designed background detectors. The Phase 2 beam commissioning was done from March 2018 to July 2018. In this phase, a pilot run of SuperKEKB and the Belle II detector was performed. Although most of the Belle II detector was installed, the most sensitive detectors to the beam background, *i.e.* the pixel vertex detectors and the silicon vertex detectors were not installed in this phase. The purposes of the operation in Phase 2 were demonstration of "nano-beam collision scheme" and the study on beam background with much lower beta functions at the IP than those in KEKB. The achieved luminosity in Phase 2 was 5.6×10^{33} cm^{-2}s^{-1} with $^*_y$ of 3 mm. The Phase 3 beam operation started in March 2019 and has continued until now. An initial report on the Phase 3 operation is shown elsewhere [2]. In this report, we summarize the progress of SuperKEKB in Phase 3. The machine operation of SuperKEKB was halted on June 22nd 2022 for a long shutdown (LS1: Long Shutdown 1). During LS1, we will do several upgrade works as is shown below. After LS1, the machine operation will be resumed in autumn 2023 or later. Also discussed in this report are critical issues on luminosity improvement after LS1. We focus on the most critical issues and more comprehensive discussions are given elsewhere [3,4].

OVERVIEW OF PHASE 3 OPERATION

The history of machine operation in Phase 3 is shown in Fig. 1. In the figure shown are the history of the HER beam current, the LER beam current, the peak luminosity and the total integrated luminosity (delivered and recorded values) from the top to the bottom, respectively. Both in the beam currents and the luminosity, there has been a great progress since IPAC2020 held in May 2020. Table 1 shows a comparison of machine parameters in 4 cases. The highest peak luminosity so far achieved is 4.65×10^{34} cm^{-2}s^{-1} as is shown in Fig. 1. This is the official record on the peak luminosity at SuperKEKB. A higher value of 4.71×10^{34} cm^{-2}s^{-1} was achieved in a test run with the Belle II detector HV off. The recorded and delivered total integrated luminosity so far are 424 and 491 fb^{-1}, respectively. In comparison between the parameters at present with those achieved by KEKB, the peak luminosity at present is more than twice higher than the achieved value at KEKB. But comparing the present beam performance with the design of SuperKEKB, we are still at an early stage of the project. In the following, we summarized progress in Phase 3 on the three parameters related to the luminosity; *i.e.* vertical beta function at the IP (β_y^*), the beam currents and the vertical beam-beam parameter (ξ_y).

Squeezing β_y^*

In Phase 2, we successfully squeezed β_y^* down to 3 mm. This value was already a half of the value achieved at KEKB and demonstrated effectiveness of the nano-beam scheme. Progress in squeezing β_y^* in Phase 3 is also shown in Fig. 1. The physics run in Phase 3 started with β_y^* of 3 mm in 2019. At the end of 2019, we successfully reached β_y^* of 1 mm. In the process of squeezing β_y^*, we found that minimising the x–y coupling parameters at the IP is essentially important to get a high luminosity. Roughly speaking, the achieved luminosity has been inversely proportional to β_y^* with the x–y coupling tuning in the range of β_y^* from 3 mm to 1 mm. In 2020 and 2022, we tried to squeeze β_y^* down to 0.8 mm as is seen in Fig. 1. The operations with β_y^* of 0.8 mm were short time trials. In both trials, we could not store the same beam currents as the case of β_y^* of 1 mm mainly due to poor injection efficiency. As a result, an achieved luminosity with β_y^* of 0.8 mm so far is much lower than that with β_y^*

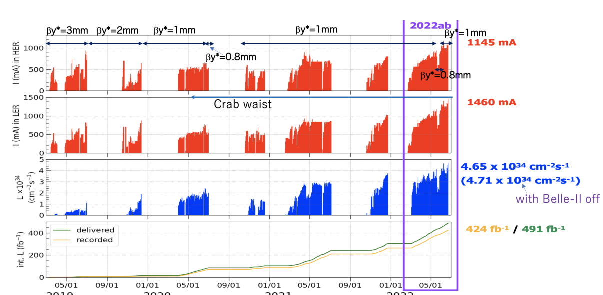

Figure 1: Operation history in Phase 3.

* email: yoshihiro.funakoshi@kek.jp

ISBN: 978-3-95450-236-3 ISSN: 2673-7027 doi:10.18429/JACoW-eeFACT2022-WEZAS0101

Table 1: Comparison of Machine Parameters

	KEKB Achieved		**SuperKEKB** 2020 May 1st		**SuperKEKB** 2022 June 8th		**SuperKEKB** Design	
	LER	**HER**	**LER**	**HER**	**LER**	**HER**	**LER**	**HER**
I_{beam}[A]	1.637	1.188	0.438	0.517	1.321	1.099	3.6	2.6
# of bunches	1585		783		2249		2500	
I_{bunch}[mA]	1.033	0.7495	0.5593	0.6603	0.5873	0.4887	1.440	1.040
β_y^* [mm]	5.9	5.9	1.0	1.0	1.0	1.0	0.27	0.30
ξ_y	0.129	0.090	0.0236	0.0219	0.0407	0.0279	0.0881	0.0807
					0.0565*	0.0434*		
Luminosity [10^{34} cm^{-2}s^{-1}]	2.11		1.57		4.65		80	
Integrate luminosity [ab^{-1}]	1.04		0.03		0.41		50	

* values in high bunch current study

of 1 mm. This seems a serious problem to be solved for a higher luminosity in future. This issue is discussed in more details later in this report.

Increasing Beam Currents

Increasing the beam currents has been one of the main ways of the luminosity improvement. As shown in Fig. 1, we have been increasing beam currents gradually with fighting with several obstacles which are listed in the following.

- Hardware damages due to sudden beam losses
- Detector beam background
- Beam injection
- Beam instability

Of those obstacles, the sudden beam loss has put us the most serious restriction. As is addressed in the following section, frequent hardware troubles on collimators (and Belle II sub-detectors) happened when the bunch current in LER is larger than 0.7 mA. In comparison between the parameters at present (June 8th 2022) with those on May 1st 2020, the total beam currents increased by a factor 2 or 3. However, the increases in the bunch currents are small. The increases in the beam currents were done mainly by increasing the number of bunches. This is due to the sudden beam loss problem as is described in the next section.

Current beam background (BG) rates in Belle II are acceptable and well below limits and Belle II did not limit beam currents in 2021 and 2022. It will limit SuperKEKB beam currents eventually, without further background mitigation. To reach the design luminosity, an upgrade of crucial detector components is foreseen (e.g. short lifetime conventional PMTs for TOP (Time of Propagation) counter). The beam gas BG in LER is expected to be lowered in the process of vacuum scrubbing. We also expect that BG will be lowered by IR radiation shield reinforcement to be done in LS1. On the other hand, the luminosity related BG will increase with a higher luminosity. Issues related to beam injection are discussed in the next section.

In SuperKEKB, the apertures of vertical collimators are set very close to the beams. The half aperture of the vertical collimators is set at about 2 mm or narrower and its impedance would cause the TMCI (Transverse Mode Coupling Instability) particularly in LER. We have intensively studies their effects. We have observed vertical beam-size blow-ups around 0.8 mA/bunch in LER with single-beam operations, and this value is about 50 % or more lower than an expected TMCI threshold. When the beam-size blow-ups have been observed, a peak corresponding to $\nu_y - \nu_s$ appears and so we call this "-1 mode instability". The impedance in vertical collimators contributes to this instability and opening apertures of them can raise the threshold. The vertical bunch-by-bunch feedback system with a standard setting enhances this instability and its tunings can suppress the instability. The mechanism of the -1 mode instability has been investigated by K. Ohmi [5]. Impedance dependence of the -1 mode instability is one of motivations to introduce the nonlinear collimator. Since the apertures of vertical collimators scale as β_y^*, TMCI would set a limit on the bunch current at smaller values of β_y^*. Results of the machine study on TMCI in LER are summarized below. With the use of 2 vertical collimators and taking into account the impedance from the high-β region around final focus quadrupoles, the TMCI threshold will be lower than the design bunch current of 1.44 mA when $\beta_y^* < 0.6$ mm. By introducing a nonlinear collimator, we can raise the threshold or use more vertical collimators and meanwhile reduce Belle II BG. Coupled bunch instability from the resistive wall impedance and from the electron clouds has been well suppressed by the bunch-by-bunch feedback so far. The longitudinal coupled bunch instability caused by fundamental mode impedance of RF cavities has been well suppressed by -1 mode dampers in both rings. In the current beam condition (4 or 6 ns bunch spacing, < 0.7 mA/bunch), no significant beam size blowup due to the electron clouds effects has been observed in LER.

Beam-beam Parameters

Improving the beam-beam performance, which usually means suppression of the beam-beam blowup, is one of the most important ways to improve the luminosity. The in-

65th ICFA Adv. Beam Dyn. Workshop High Luminosity Circular e⁺e⁻ Colliders eeFACT2022, Frascati, Italy JACoW Publishing
ISBN: 978-3-95450-236-3 ISSN: 2673-7027 doi:10.18429/JACoW-eeFACT2022-WEZAS0101

dexes to show the beam-beam performance are the specific luminosity or the vertical beam-beam parameter. In the following, our efforts to improve the beam-beam performance in Phase 3 are summarized. The following three subjects are discussed in this report.

- Introduction of crab waist scheme
- Tuning on the IP parameters
- Tuning on the bunch-by-bunch feedback system

Crab Waist In March 2020, we decided to introduce the crab waist scheme, which was an option in the design of SuperKEKB. The motivations of the introduction were in the following. The beam-beam performance was poor in spite of all of knob tunings for improving it and it was limited by beam-beam resonances which can be suppressed by the crab waist. This is the second application of the crab waist scheme following DAΦNE [6] for actual collider machines. The crab waist scheme was realized by making an intentional imbalance of strength of paired sextupole magnets in the vertical local chromaticity correction section. The crab waist scheme was introduced by the following steps:

- 2020 March 16th : LER crab waist (40 %)
- 2020 March 24th : LER crab waist (60 %)
- 2020 April 24th : HER crab waist (40 %)
- 2020 June 1st : LER crab waist (80 %)

Here, the strength of the crab waist (crab waist ratio) is also shown. The strength (imbalance) of the crab waist sextupoles which brings the complete crab waist is 100 %. The lower crab waist ratio means the weaker crab waist sextupoles (weaker imbalance). Since the setting in the final step on June 1st 2020, the same setting of the crab waist sextupoles has been used up to now.

Effectiveness of the crab waist is shown in Fig. 2. In the figure, the green dots show the specific luminosity without the crab waist. The others show that with crab waist and the pink dots correspond to that after the final step. Here, the specific luminosity is defined as the total luminosity divided by the number of bunches and by the bunch current product. As is seen in the comparison between the green dots (w/o crab waist) and the pink dots (w/ crab waist), the specific luminosity was improved with the crab waist and the improvement is higher as the bunch currents increase. In addition, the bunch currents could be increased with the crab waist. Without the crab waist, the bunch current product was limited at around 0.38 mA^2 due to the beam-beam blowup. With the crab waist, we could increase the bunch current product up to over 0.5 mA^2. This is also a benefit of the crab waist. As a side effect of the crab waist, it was expected that dynamic aperture shrinks and the beam lifetime decreases. In the case of $^*_y$ = 1 mm, however, no lifetime decrease was observed in both LER and HER. This was because the narrow physical apertures at collimators determine the lifetime. In the case of lower $^*_y$, simulations showed the lifetime with crab waist will set a strong limit. The experimental result that the crab waist improves the specific luminosity is supported by the beam-beam simulations as is shown in Fig. 3.

While the green line in the graph shows the result of the strong-strong beam-beam simulation without the crab waist, the black line shows that with crab waist (LER:80 % and HER:40 %). In both cases, the longitudinal impedance was considered in the simulations. Effectiveness of the crab waist scheme is clearly demonstrated in the figure. Other data in the figure are experimental data taken in 2021 with the crab waist. If the simulation reproduced the experimental data correctly, the experimental data would agree with the black line. In reality, however, there is a large discrepancy.

Knob Tuning on IP Parameters Like at KEKB, tuning on beam parameters such as the local x–y coupling, the chromatic x–y coupling, the vertical dispersion at the IP are very important for increasing the luminosity. We do tuning to adjust these parameters by using skew-Q windings on sextupole magnets. As for the chromatic coupling at IP, we also use rotatable sextupole magnets installed in LER.

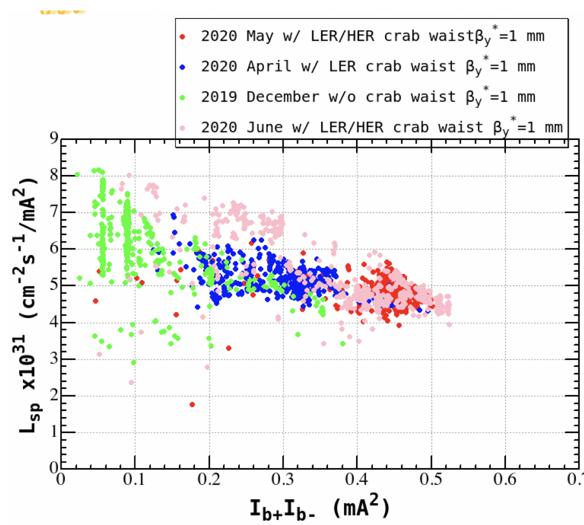

Figure 2: Comparison of specific luminosity of different crab waist settings.

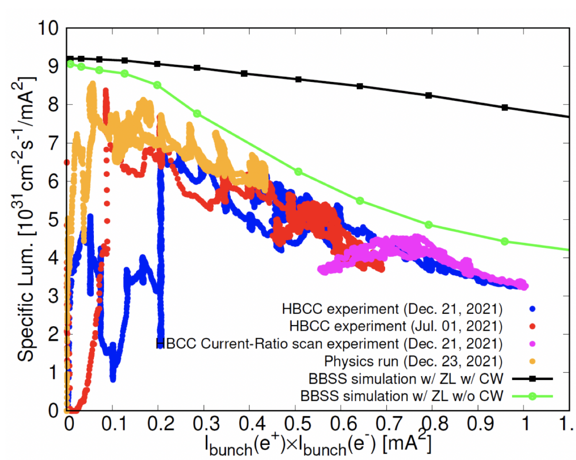

Figure 3: Beam-beam simulations without the crab waist and with the crab waist. Experimental data taken in 2021 are also shown.

ISBN: 978-3-95450-236-3 ISSN: 2673-7027 doi:10.18429/JACoW-eeFACT2022-WEZAS0101

Also like at KEKB, the standard method of tuning on those parameters is to scan the parameters one by one so that the luminosity is maximized, although we also take the smaller vertical beam sizes in some cases. As is mentioned above, in the process of squeezing β_y^* from 3 mm to 1 mm, we found that minimising the x–y coupling parameters at the IP is essentially important to get a high luminosity.

Bunch-by-bunch Feedback Gain In May 2021, the luminosity increased by lowering gain of the bunch-by-bunch feedback (FB) system in HER. The FB system has two loops and the feedback gains of the both loops in the vertical direction were lowered by 4 dB. As a result of this gain change, the luminosity increased by ~ 25 %. Noise mixed in the FB system affected the luminosity. The noise was caused by a troubled module in the FB circuits. Since the noise frequency was near the betatron tune, its effect was large.

CRITICAL ISSUES AT PRESENT AND AFTER LS1 (LONG-SHUTDOWN 1)

Machine Parameters for Luminosity of $1 \times 10^{35}\,\mathrm{cm^{-2}s^{-1}}$

The next target of the luminosity at SuperKEKB is $1 \times 10^{35}\,\mathrm{cm^{-2}s^{-1}}$. We will aim at the luminosity within 1 or 2 years after LS1. In the following, examples of parameter sets with which the target luminosity would be achieved are shown. The maximum number of bunches with 2 RF bucket spacing, which is the design bucket spacing, is 2346. This number is smaller than the design value of 2500. This is because we currently use two abort gaps for faster beam abort. In the following, this number is assumed. As shown in Table 1, the achieved number of bunches is already not far from this number and we will have to increase bunch currents for a higher luminosity. The basis of the following estimation is the specific luminosity shown in Fig. 4. In the graph,

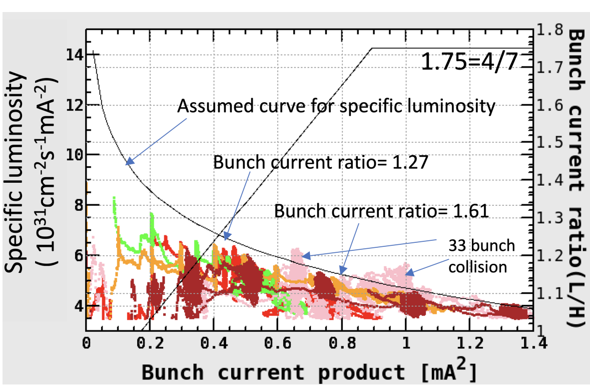

Figure 4: Specific luminosity as function of bunch current product in the case of $_y^*$ of 1mm. Assumed values of the ratio of bunch currents between LER and HER are also shown.

dots in several colors are shown. The dots in green show the specific luminosity achieved during physic experiment and dots in other colors are those achieved in high-bunch-current machine studies with fewer number of bunches. In all data, $_y^*$ was 1mm. An assumed curve for the luminosity estimation is also shown in the figure. The assumed curve of the specific luminosity is rather high compared with achieved values except for the 33 bunch collision cases. If this high specific luminosity with the smallest number of bunches (33) is reproduced in the 2346 bunches case, we could expect a higher luminosity. In the high-bunch-current machine study in 2021, the beam current ratio of LER and HER has to be increase as the function of the bunch current product as is shown in the figure. In the following, we assume that the beam current ratio increases linearly as the function of the bunch current product up to the inverse of the beam current (1.75) as is shown in the figure. With the above assumptions, the beam currents needed to achieve the luminosity of $1 \times 10^{35}\,\mathrm{cm^{-2}s^{-1}}$ can be estimated and are shown in Table 2. In the table, parameters in the case of $_y^*$ of 0.8 mm is also shown. In this case, the specific luminosity is assumed to be 25 % higher than the case of $_y^*$ of 1 mm. In the table, the number of bunches includes one special bunch called "pilot bunch" which is used for tune monitoring and has no collision partner bunch.

Sudden Beam Loss Events

To achieve beam parameters in Table 2, a serious obstacle is very fast beam loss events which we call as "sudden beam loss". As is shown below, those events limit the bunch current mainly in LER seriously and will be a serious obstacle to achieve the bunch currents in Table 2.

We have encountered frequently events where the beam is lost very fast and largely. The events occur in both rings but the LER beam loss is more serious. Figure 5 shows a typical data of the large beam loss event. As is seen in the figure, more than a half of the beam current was lost within 3 turns. Almost no beam oscillations were observed in both horizontal and vertical directions before the beam loss, although some vertical oscillation was observed in some other events. No beam size blowup was observed using the turn-by-turn beam size monitor before the beam loss. The large losses often cause damages of the vertical collimators and the damage brought increase of detector beam background. In some

Table 2: Parameters for Luminosity $1 \times 10^{35}\,\mathrm{cm^{-2}s^{-1}}$

Parameter	LER	HER	LER	HER
# of bunches	2345+1*)		2345+1*)	
Luminosity	$1 \times 10^{35}\,\mathrm{cm^{-2}s^{-1}}$		$1 \times 10^{35}\,\mathrm{cm^{-2}s^{-1}}$	
I_{total} [A]	2.08	1.48	2.78	1.65
I_{bunch} [mA]	0.89	0.63	1.18	0.70
$_y^*$ [mm]	0.8	0.8	1	1
$_y^*$ [m]	0.154	0.154	0.211	0.211
$_z$ [mm]	6.49	6.35	7.26	6.51
Beam life-time [min.]	3.4	14.8	4.7	16.9

* including a pilot bunch w/o collision partner bunch

ISBN: 978-3-95450-236-3 ISSN: 2673-7027 doi:10.18429/JACoW-eeFACT2022-WEZAS0101

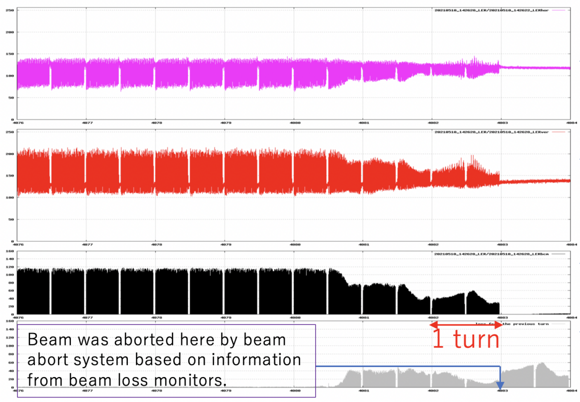

Figure 5: An observed event of an LER large and fast beam loss as function of time. The top row: horizontal oscillation from Bunch Oscillation Recorder (BOR). The second row: vertical oscillation from BOR. The third row: data of bunch current monitor (BCM). The bottom row: amount of beam loss (from BCM). The BOR amplitude is the product of oscillation amplitudes and bunch currents.

cases, the loss causes a QCS (superconducting magnets near IP) quench. In other cases, the loss causes a damage of Belle II sub-detectors. The frequency of these events has been increasing as the total beam current increases. Based on experiences of the events which occurred during the period from March to mid-May 2022, we worked out an empirical rule to prevent the events that the bunch current must not exceed 0.7 mA per bunch. The recent increase in beam currents was achieved by increasing the number of bunches while respecting this rule. It is very important to achieve the bunch currents particularly in LER shown in Table 2 to solve this serious issue.

The mechanism of the sudden beam loss has not been understood well. A hypothesis was proposed to try to explain the event in our team [7]. In the hypothesis, a microparticle heated by the beam-induced field causes a macroscopic vacuum arc and the beam is kicked by the vacuum arc. We will continue to study this hypothesis. A joint Belle II-SuperKEKB team has been working to identify the original places of the fast beam losses. Recent progress shows collimators near the injection region are the most possible candidates. Investigations are ongoing to fully understand this issue and countermeasures are being sought.

Beam Injection Issues

Currently, we conduct physics experiment with $^*_y$ of 1 mm. We tried to squeeze $^*_y$ down to 0.8 mm in June 2020 and in May 2022. The luminosity with $^*_y$ of 0.8 mm did not reach that with $^*_y$ of 1 mm both times, since the total beam currents particularly in LER was much lower than those with $^*_y$ of 1 mm due to mainly poorer injection efficiency. This means that the maximum beam currents in the rings were limited by the balance between the charge injected to the rings and the charge loss due to beam lifetime. Although he beam lifetime with $^*_y$ of 0.8 mm is somewhat shorter than that with $^*_y$ of 1 mm, the poor injection efficiency is more serious problem. The beam injection efficiency in LER as the function of the bunch currents stored in the ring is shown in Fig. 6. We observe strong beam current dependence. Here, we plot the dependence as the bunch current dependence. The reason for the beam current dependence has not been understood well. A possible reason is that the effective feedback gain for each bunch depends on the bunch current in the ring. Injection efficiency seems to be affected by beam-beam effects. We need more simulations and machine study on those issues.

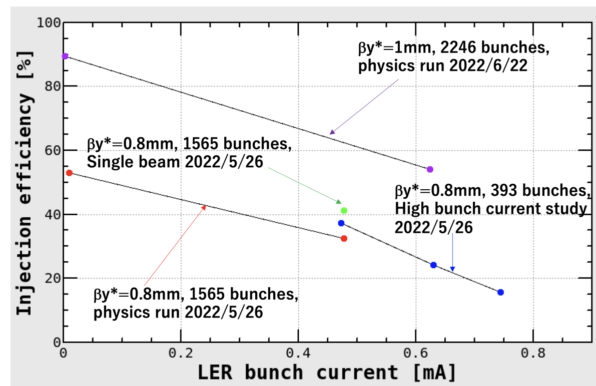

Figure 6: The injection efficiency as function of the bunch current in LER. Both cases of β_y^* of 0.8 mm and 1 mm are shown. There is strong beam current dependence. We have not yet understood the reason for the beam current dependence. Here, we plot the dependence as the bunch current dependence.

In the following, we estimate necessary injection efficiency to store the beam currents shown in Table 2. To compensate the beam loss due to beam lifetime, the following injection charge is required.

$$I_{inj,eff} \equiv I_{inj}E_{inj} = \frac{1}{f_{rev}}\frac{I_{total}}{Life}$$

Here, $I_{inj,eff}$[C/s], I_{inj}[C/s], E_{inj}, f_{rev}[Hz], I_{total}[A] and $Life$[s] denote the effective injection charge, the injection charge at the entrance of the ring, injection efficiency, the revolution frequency, the total beam current in the ring and the beam lifetime, respectively. As for the beam lifetime, the Touschek lifetime and the vacuum lifetime are considered and the luminosity lifetime from the radiative Bhabha scattering is ignored. We assume the following equations for the beam lifetimes. The Touschek beam lifetime is expressed as

$$\tau_{Touschek} = C_T \frac{n_b}{I_{total}} \sqrt{\varepsilon_x \varepsilon_y} \sigma_z .$$

Here, n_b, ε_x, ε_y and σ_z denote the number of bunches, the horizontal emittance, the vertical emittance and the bunch length, respectively. The vacuum beam lifetime is expressed as

$$\tau_{Vacuum} = C_V \frac{1}{I_{total}} .$$

In those equations, C_T and C_V are coefficients which depend on the physical and/or dynamic aperture in the rings and

ISBN: 978-3-95450-236-3 ISSN: 2673-7027 doi:10.18429/JACoW-eeFACT2022-WEZAS0101

are determined experimentally. As for the vacuum beam lifetime, the effect of the Coulomb scattering is dominant and the that of Bremsstrahlung can be ignored. The ratio between the Touschek and vacuum lifetime is determined experimentally by changing the number of bunches. The Touschek liftetime is dominates over the vacuum lifetime in both rings, although the vacuum effect still plays some role in LER. In the equation of the Touschek lifetime, the data of the streak camera are used for σ_z which is dependent on the bunch currents. The value of ε_y is estimated by using the specific luminosity assumed in Fig. 4 with an assumption that the the vertical emittances of both rings are equal. As for the value of ε_x, the measured data during the physics experiment are used. With those assumptions, required injection charges as the function of the total beam currents are plotted in Figs. 7 and 8.

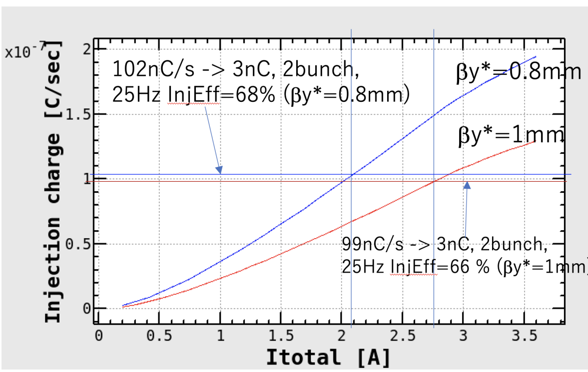

Figure 7: The required effective injection charge as the function of the total beam current in LER. The number of bunches is assumed to be 2346. Both cases of $^*_y$ = 0.8 mm and $^*_y$ = 1 mm are shown.

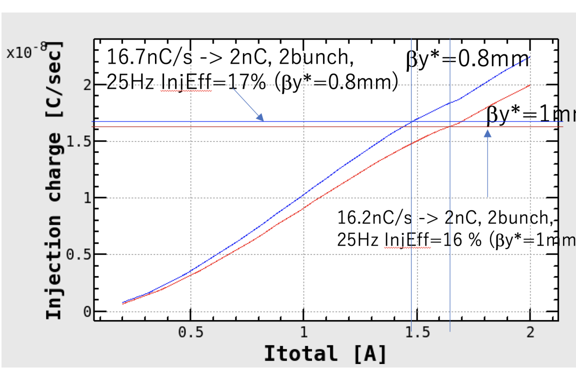

Figure 8: The required effective injection charge as the function of the total beam current in HER. The number of bunches is assumed to be 2346. Both cases of $^*_y$ = 0.8 mm and $^*_y$ = 1mm are shown.

As is seen in Fig. 7, to accumulate the beam currents of LER shown in Table 2 in the case of $^*_y$ = 0.8 mm (1 mm), we need at least the effective injection charge of 102 nC/s (99 nC/s). Those effective injection charges correspond to 3 nC injection charge at 25 Hz with 2-bunch injection and 68 % (66 %) injection efficiency. At SuperKEKB, the maximum repetition rate of the injector linac is 50 Hz which is shared by LER, HER, PF and PR-AR. The 2-bunch injection means that the 2 bunches from the injector are injected to the ring simultaneously. Due to the constraint of synchronizaiton between the injector and the rings, more number of bunches can not be injected simultaneously. In comparison between the above required injection efficiency and the achieved values shown in Fig. 6, we need improvement in the injection efficiency. Particularly in the case of $^*_y$ = 0.8 mm, we need drastic improvement such as drastic improvement in the dynamic aperture. It is important to solve the problem of the strong bunch current dependence of the injection efficiency. As for the injection charge, 3 nC per bunch has been already achieved. Since the design value of the positron charge is 4 nC per bunch, there is some room for improvement. Improvement in the beam lifetime is also helpful. As is seen in Fig. 8, to accumulate the beam currents of HER shown in Table 2 in the case of $^*_y$ = 0.8 mm (1 mm), we need at least the effective injection charge of 16.7nC/s (16.2 nC/s). Those effective injection charges correspond to 2 nC injection charge at 25Hz with 2-bunch injection and 17 % (16 %) injection efficiency. In the actual operation, the injection charge of 1.5 nC per bunch is achieved. The beam injection with the injection charge of 2 nC per bunch and the 2-bunch injection will be possible with some efforts. The design injection charge of HER is also 4 nC. With consideration of achieved injection efficiency, a typical value of which in the physics run is 50% in both $^*_y$ = 0.8 mm and 1 mm, we can be rather optimistic in the HER injection. As for the repetition rate, those of PF and PF-AR are less than 1 Hz in the top-up injection. If we can reduce the repetition rate of HER down to less than 25 Hz, we may increase the injection rate of LER from 25 Hz to some extent to mitigate difficulty of the LER injection.

WORKS IN LS1 AND BEAM OPERATION AFTER LS1

SuperKEKB will be shut down from July 2022 to September 2023. We call this shutdown as Long-Shutdown 1 (LS1). The main purpose of LS1 is to install additional VXD's (vertex detectors) and to replace a vulnerable part of PMTs of the TOP counters. In this opportunity, the following works will also be done on the accelerator side.

- IR radiation shield reinforcement for BG reduction
- Installation of a nonlinear collimator for impedance and BG reduction
- Replace collimator heads with robust ones in LER
- New beam pipes with wider aperture at HER injection point for improvement of injection efficiency
- others

Within 1 or 2 years after LS1, we will aim at the luminosity of 1×10^{35} cm^{-2}s^{-1} with $\beta^*_y = 0.8$ mm. We will also try to squeeze β^*_y down to 0.6 mm.

ISBN: 978-3-95450-236-3 ISSN: 2673-7027 doi:10.18429/JACoW-eeFACT2022-WEZAS0101

REFERENCES

[1] T. Abe *et al.*, "Technical Design Report of SuperKEKB", `https://kds.kek.jp/indico/event/15914/`.

[2] A. Morita, "Status of early SuperKEKB Phase-3 commissioning", in *Proc. IPAC'19*, Melbourne, Australia, May 2019, pp. 2255–2257. doi:10.18429/JACoW-IPAC2019-WEYYPLM1

[3] Y. Ohnishi *et al.*, "SuperKEKB Luminosity Quest", in *Proc. eeFACT'22*, Frascati, Italy, Sep. 2022, paper MOXAT0103, this conference.

[4] Y. Funakoshi *et al.*, "THE SuperKEKB has broken the world record of the luminosity", in *Proc. IPAC'22*, Bangkok, Thailand, Jun. 2022, pp. 1–5. doi:10.18429/JACoW-IPAC2022-MOPLXGD1

[5] K. Ohmi *et al.*, "Study for 1-mode instability in SuperKEKB low energy ring", in *Proc. eeFACT'22*, Frascati, Italy, Sep. 2022, paper WEAXT0102, this conference.

[6] C. Milardi, "DAΦNE setup and operation with the crab-waist collision", in *Proc. EPAC'08*, Genoa, Italy, Jun. 2008, pp. 2599-2601.

[7] Y. Lui *et al.*, "Sudden beam losses at SuperKEKB", `https://kds.kek.jp/event/43499/`.

ISBN: 978-3-95450-236-3 ISSN: 2673-7027 doi:10.18429/JACoW-eeFACT2022-WEZAS0105

FCC-ee CIVIL ENGINEERING AND INFRASTRUCTURE STUDIES

L. Bromiley, J. Osborne, CERN, Geneva, Switzerland

Abstract

The European Organisation for Nuclear Research (CERN) is planning a Future Circular Collider (FCC), to be the successor of the current Large Hadron Collider (LHC). Significant civil engineering is required to accommodate the physics experiments and associated infrastructure. The 91.2 km, 5.5 m diameter tunnel will be situated in the Geneva region, straddling the Swiss-French border. Civil engineering studies are to incorporate the needs of both the FCC lepton collider (FCC-ee) and the FCC hadron collider (FCC-hh), as the tunnel will host both machines consecutively.

INTRODUCTION

At completion, the FCC tunnel will house the world's largest particle accelerator. The study, currently in the feasibility stage, officially commenced in 2013 following recommendations made by the European Strategy for Particle Physics Update (ESPPU). To support the physics requirements, the CERN civil engineering team has been studying the feasibility of constructing a 91.2 km circumference tunnel project beneath the Geneva region.

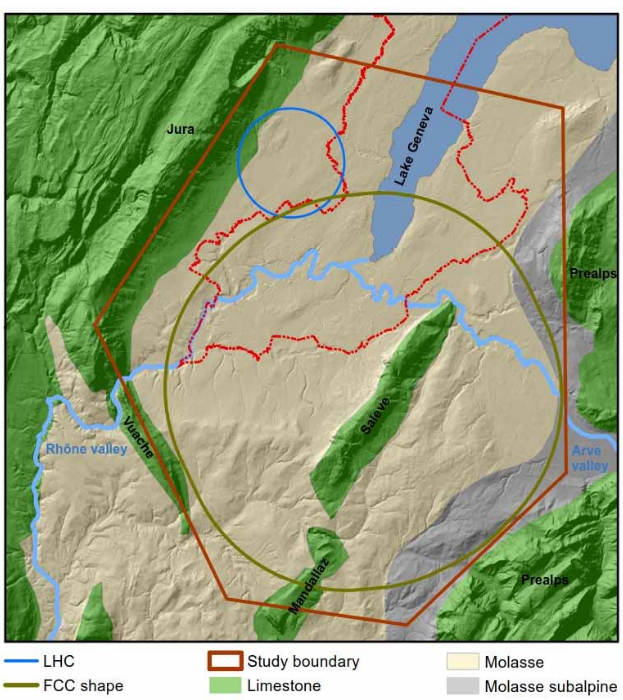

Figure 1: FCC study area (CERN).

CERN has a history of completing large civil engineering works to facilitate physics research. When CERN completed construction of the LEP (Large Electron-Positron) in 1989 [1], it was the largest physics facility ever built. This made Europe a worldwide leader in science and technology [2].

To validate the physics case of FCC, the tunnelling studies must satisfy requirements for both a lepton (ee) and a hadron (hh) machine, as well as reuse the existing LEP/LHC infrastructure.

Like the LHC before it, the FCC will extend into the territories of both France and Switzerland. As a result, the main challenges encountered by the civil engineers will be the geological features, local stakeholders, environmental constraints, and project costs.

Geological site investigations are therefore required to validate the geological assumptions made at the conceptual design stage. An initial site investigation campaign is planned to start in 2023 in the areas of highest geological uncertainty.

This paper describes the present state of the civil engineering feasibility studies for the FCC tunnel.

FEASIBILITY STUDY

Project Description

Following studies of various locations and geometries of the accelerator machine, the conceptual design of the FCC considers a quasi-circular tunnel, with a circumference of 91.2 km situated in the Geneva basin. The tunnel will be buried underground at an average elevation of 300 m ASL.

In addition to the main tunnel, approximately 10 km of transfer tunnels, 4 km of beam dump tunnels, 6 km of bypass tunnels, 14 shafts, 12 large caverns and 8 surface sites are required.

The primary objective of the civil engineering studies so far has been to locate the tunnel within the topographical and geological boundaries of the Geneva basin. While also ensuring adequate connection to existing LHC infrastructure.

The locations of the surface sites have been selected to match the machine's layout, for example the predefined experimental points, but also considering surface access and local environment factors.

Approximately 9 million cubic metres of spoil will result from the excavations of FCC tunnels and structures [3]. Around 95% of this will be molasse, the reuse potential of which – although it has proved to be a good rock for tunnelling – is not obvious. Research is currently being undertaken to investigate opportunities to reuse or recycle tunnel spoil rather than resorting to typical landfill disposal.

Summary of Main Structures

- 1 machine tunnel of 91.2 km length, 5.5 m diameter
- 14 vertical shafts of 12 – 18 m diameter, 140 – 400 m depth
- 8 service caverns, 100 to 150 m length, 15 m high, 25 m wide

ISBN: 978-3-95450-236-3 ISSN: 2673-7027 doi:10.18429/JACoW-eeFACT2022-WEZAS0105

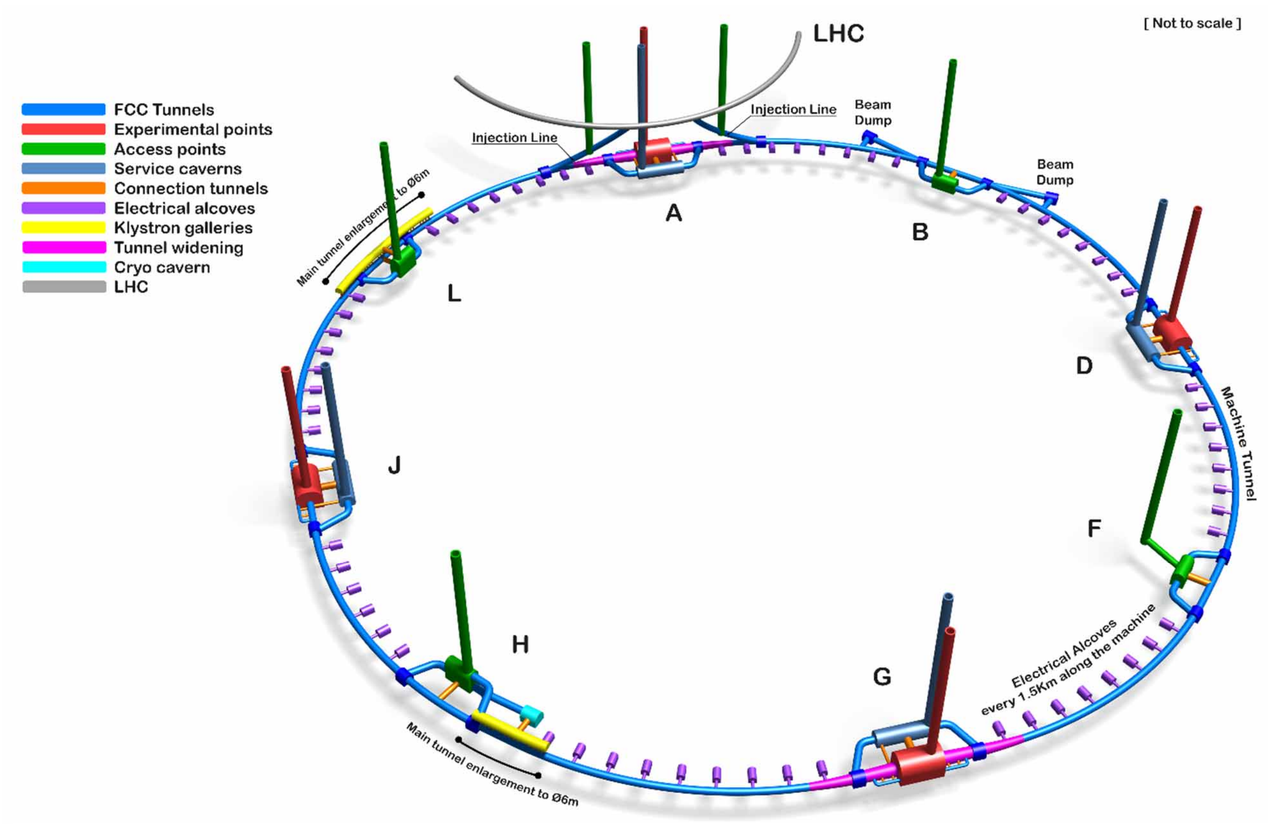

Figure 2: FCC schematic diagram. (Angel Navascues Cornago, CERN).

- 4 experiment caverns, 66 m length, 30 m high, 30 m wide
- 2 beam transfer tunnels from the LHC, 4.1 and 6.1 km in length, 5.5 m diameter
- 2 beam dump tunnels, 2 km length, 5.5 m diameter
- Several 5.5 m diameter bypass tunnels, totalling approximately 5 km
- 18 junction caverns of varying dimensions
- 2 Klystron Galleries, one at point H, 1078 m length and one at point L, 1990 m length. Both galleries with a span of 9.8 m and a height of 5.4 m
- 60 electrical alcoves, at 1.5 km spacing around the ring, 25 m length and 6 m diameter

The structures listed above form the 'Baseline Design', which is the infrastructure required for a hadron or 'FCC-hh' accelerator. However, the tunnel will also accommodate a lepton collider 'FCC-ee' prior to the hadron machine installation. To meet the lepton machine requirements the tunnel will require widening at the two experimental sites, A and G. This widening will be to a maximum span of 11 m and for a length of 1000 m each side of the experimental caverns at the two points. The FCC-ee will also require beam injection from the existing CERN Super Proton Synchrotron (SPS) housed in beam transfer tunnels. Exact layouts of these transfer tunnels are to be confirmed.

The eight underground sites (A to L) require large surface works that will accommodate the necessary infrastructure such as transformers, helium tanks, and cryogenic plants, as well as offices for operations and management. The four experimental sites will be roughly 6 Ha in surface area and the technical sites will be roughly 4 Ha in area. Exact layouts of the surface sites are being developed and final layouts will depend on machine requirements as well as local constraints.

Geology

The Geneva basin has three main ground types: moraines, molasse and limestone. The variable sedimentary rock, called molasse, is overlaid by low-strength glacial deposits, called moraines. The depth of the moraines varies from only a few metres up to 100 metres. Limestone features in the form of the Jura Mountains, the Alpine foothills, the Vuache and Saleve chains border and intersect the layers of molasse. The molasse is composed of horizontally bedded layers of marls and sandstones. The term sandstone refers to cemented sandy or silty rocks and the term marl refers to clayey rocks [4]. These layers can vary considerably in strength. The molasse is considered a suitable rock type for tunnel boring machine (TBM) excavation, as it is stable and dry; however, the heterogeneity of the rock leads to some uncertainty. Therefore, it is essential that the large span caverns are constructed in stronger sandstone.

ISBN: 978-3-95450-236-3 ISSN: 2673-7027 doi:10.18429/JACoW-eeFACT2022-WEZAS0105

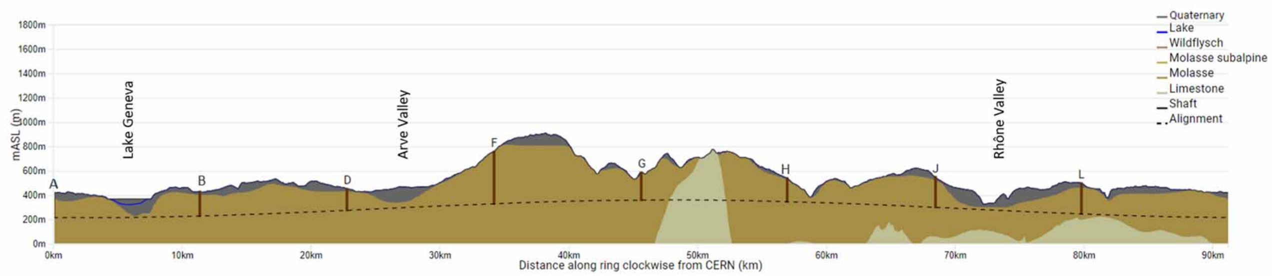

Figure 3: FCC Long section. (CERN).

Directly under the lakebed, there are very soft deposits which have been identified in previous site investigation campaigns along the proposed alignment. These have been identified as very soft lacustrine clayey silts and glacial-lacustrine silts and clays with elastic modulus between 2 MPa and 10 MPa, extending from the lakebed to a level of 260 m [3]. Despite little available information for the Arve Valley and Rhône Valley, it is expected that soft deposits, alluvial and alluvio-glacial moraines are to be encountered at depths of up to approximately 100 m below ground level. To avoid construction challenges and the risk of water inflow, the alignment of the tunnel has been lowered by a further 30 m to allow the tunnel to pass through the stronger rock.

There are some known faults within the molasse that will bisect the alignment of the tunnel. The LEP, and before that the Super Proton Synchrotron (SPS), passed through the significant fault of the Allondon near Meyrin, without encountering significant problems during construction. Though for the LEP and LHC, the faults have posed greater problems regarding long-term stability.

The Jura and Vuache limestone are challenging for excavation due to karstic features formed by chemical weathering of the rock. It is common for the karsts to be filled with water and sediment, which can lead to water inflow and instability during excavation. In comparison to the molasse, CERN has experienced significant issues with excavating in the limestone of the Geneva region. During the construction of the LEP, sector 3 to 4 was excavated in the Jura limestone where there were major issues with water ingress at the tunnel face [2].

Horizontal Alignment

Since the FCC study was launched in 2012 various shapes and sizes for the machine ring have been considered, these have ranged from 47 km to 100 km circumference rings in addition to less conventional “racetrack” shapes. The smallest options were ruled out early-on, even though they carried the lowest risk for civil engineering, as the accelerator would not be able to reach adequate energies. By 2016, an approximately 100 km diameter ring had been adopted by the project team. This ring was initially considered in two distinct positions, one under the Jura, and the other in the molasse basin passing below Lake Geneva. The Jura option was excluded due to the high risk of tunnelling through the karstic limestone with very high overburden.

From 2016 onwards small variations on the chosen position have been evaluated. In the Geneva basin there is limited scope to place a 30 km diameter ring with adequate connections to the existing particle accelerator, whilst avoiding the undesirable ground conditions. Therefore, the strategy for placement has been to avoid the limestone of the Jura and Pre-Alps, whilst also aiming to minimise tunnelling in the water-bearing moraine layer and keeping overburden to a minimum. This has led to the current position that fits tightly within the natural boundaries of the limestone formations, and the lake whose depth increases to the north-east.

Vertical Alignment

A key objective of the study so far has been to develop a vertical alignment that places all cavern excavations in rock and the remaining structures and connections in adequate ground conditions. These conditions tend to be met by deepening the vertical alignment. However, operation of the FCC and connections to the existing LHC are more efficient with a shallow alignment, so a compromise must be made.

Based on the available information, the vertical alignment has been chosen so that both conditions are satisfied in the best way. This has resulted in an alignment with tunnel ground covers of between 50 m and 650 m.

Shaft

A total number of 14 shafts are required to provide access to the subsurface tunnels. The two transfer tunnels between the LHC and FCC will each require a temporary construction shaft. The 12 permanent shafts will be situated at each of the 8 FCC surface sites, with two shafts (one to the service cavern and one to the experiment cavern) at each of the experimental locations (A, D, G, and L) and one shaft at each of the technical sites (B, F, H, and L).

The vertical shafts will be of various dimensions, from 12 to 18 m diameter. At the time of writing, the specific diameter of each shaft is to be confirmed following confirmation of the machine layout and access requirements.

Due to existing surface constraints, three of the service cavern access shafts are likely to require offset from the centre points of the machine straight sections. The point B service shaft requires a 440 m clockwise offset around the FCC ring, to reduce environmental impact at the surface in a sensitive area. Point F requires the shaft to be offset both 430 m anticlockwise and 400 m inside the ring, to avoid

ISBN: 978-3-95450-236-3 ISSN: 2673-7027 doi:10.18429/JACoW-eeFACT2022-WEZAS0105

residential constraints at the surface. Whilst at point H the service shaft will be offset 800 m around the ring due to environmental and residential constraints.

Caverns

Sub-surface caverns are required at each of the FCC points, to accommodate the detectors, maintenance equipment, transport vehicles, service infrastructure and access. The experiment sites have both an experiment cavern and a service cavern, spaced 50 m apart. Initial design proposals had the two caverns side by side, with a concrete pillar as support, like the existing cavern arrangement at the LHC point 5. However, to provide shielding from stray magnetic fields, the caverns need to be spaced further apart. Consequently, construction risks will also be reduced because of the increased spacing.

At the four technical sites only service caverns are required, connected to the machine tunnel via bypass tunnels. Where tunnels intersect, junction caverns are also proposed, to help the TBM excavate from the bypass tunnels to the machine tunnel.

Tunnels

As well as the 91.2 km length main machine tunnel, there will be an additional 25 km of tunnels in the form of bypass, injection, beam dump and service tunnels connecting to the main tunnel. Most of the tunnels will be 5.5 m internal diameter, however, in certain places such as the Klystron galleries at Points H and L, the machine tunnel requires widening to 6 m to accommodate the extra machine infrastructure.

Figure 4 shows the typical tunnel cross section, with the tunnel floor arrangement, ventilation and smoke extraction

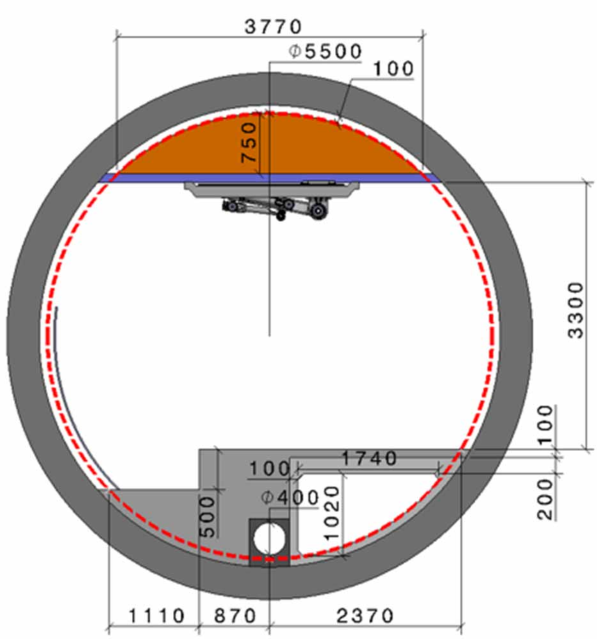

Figure 4: Typical FCC tunnel cross section. (Fani Valchkova-Georgieva, CERN).

ducts, and the position of the rail mounted maintenance robot at the tunnel ceiling

Safety partitions are to be provided every 440 m along the tunnel, in the form of fire walls and doors, so that individual sections of tunnel can be isolated in the event of an emergency. This allows incidents themselves to be contained within tunnel compartments to restrict further spread, as well as providing safe compartments for evacuees to shelter in whilst awaiting rescue.

Construction

TBMs will be used for most of the FCC tunnel excavations. These utilise an integrated full-face excavation and support system that is available for various ground conditions. The head of the TBM is equipped with modern systems of excavation which allow high rates of advance while ensuring full support of the surrounding ground. A shield or tail skin provides initial support to the ground and protection to construction personnel [3].

The tunnelling method is driven by the ground characteristics and more importantly, the stand-up time. Soft ground has very limited stand-up time which makes it imperative that the excavation is supported immediately. In comparison, hard rocks allow the excavations to be done in advances up to 4 m, before supporting the excavated void. Choosing between a gripper TBM or a shielded TBM is dictated by controlling the stability of the ground during construction and the expected amount of water ingress [5].

For shorter runs of tunnelling, caverns, alcoves and areas of high geological risk (i.e. areas of limestone), more traditional methods of excavation are employed. Drill and blast is one such method where holes are drilled in the rock face and charged with explosives, which are then detonated and the fallen rock removed. Whilst this method of excavation does not match the speed of a TBM, it allows the rock face to be more closely surveyed and controlled. This is important in areas of geological risk such as the limestone, where encountering karst formations can result in water inflow. Furthermore, drill and blast is essential in excavating irregular tunnel shapes such as for the caverns, junctions, klystron galleries and tunnel widenings where a non-circular tunnel is required.

Thermal Heat Recovery

Engineering consultancy Arup recently completed a feasibility study into tunnel heat recovery from future CERN tunnels [6]. The study focused on the implementation of a heat recovery system into the tunnel lining of the Compact Linear Collider (CLIC). Whilst CLIC is a separate project to the FCC, the study can be deemed applicable, as FCC and CLIC share similar tunnel geometries and geological properties.

Ambient temperature increases with depth below the earth's surface. As a result, it is possible to extract heat from the ground to provide heating for residential and commercial properties. The study investigated the potential heat extraction available from the machine tunnel, considering the geothermal properties of the region and an estimate of the residential heating demand at the surface.

ISBN: 978-3-95450-236-3 ISSN: 2673-7027 doi:10.18429/JACoW-eeFACT2022-WEZAS0105

The study concluded that heat recovery systems could be implemented in the tunnel lining, to provide 10-30 W/m2 of output, so long as energy balancing is provided by heat rejection during summer.

Costs

Total civil engineering costs were calculated to be around CHF 6 billion by the consulting engineers ILF when the FCC design included 12 points and a machine tunnel length of 97 km [3]. Since then, the FCC layout has been reduced to 8 surface sites and 91.2 km length as described above. Whilst this reduction in scope will reduce costs, a full assessment of the scheme is yet to be undertaken by the consultant ILF, so an accurate cost schedule for the updated design is not yet available.

The original cost estimate produced by ILF included direct costs (materials, equipment, and personnel) and indirect costs (management, support personnel, site preparation and dismantling). However, it did not include costs for land procurement or spoil disposal.

Material and labour costs were derived from previous project data, equipment costs were taken from the BGL Construction Equipment Register and building costs were calculated in accordance with the BKI Construction Costs [3]. ILF cross checked these estimated costs with the HL-LHC (High-Luminosity LHC) project and other tunnelling projects across Europe.

For the updated 8-point FCC, civil engineering costs are currently being updated as the design progresses.

CONCLUSION

The conceptual design for the FCC underground infrastructure ensures compatibility for hosting both the FCC-ee and FCC-hh consecutively. The geometry of the tunnel is strictly dictated by defined parameters of the machine and experiments. The project has been set out at the optimum location to achieve the best connections to the existing CERN accelerator complex, within the most favourable ground conditions. Some degree of change will be expected following the results from the planned site investigations, which will commence in 2024. The FCC location, alignment and construction methods will then be further refined.

REFERENCES

[1] CERN Press Release, “The LEP Story”, available at `https://home.cern/news/press-release/cern/lep-story`
Accessed on 29 July 2022.

[2] H. Schopper, *LEP – The Lord of the Colliders Rings at CERN 1980–2000*. Geneva. Springer, 2009.

[3] ILF, “FCC Cost and Schedule Study”, CERB, Geneva, Switzerland, Internal Rep. EDMS 2050504 v.1, 2017.

[4] E. J. Fern,·V. Di Murro, K. Soga, Z. Li, L. Scibile, and J. A. Osborne, “Geotechnical characterisation of a weak sedimentary rock mass at CERN, Geneva”, *J. Tunnelling and Underground Space Technol.,* Geneva, 2018, `https://www.sciencedirect.com/science/artcle/am/pii/S0886779817310349`

[5] D. Chapman, N. Metje, and A Stark, *Introduction to Tunnel Construction*, 2nd Edition, Dec. 2017, CRC Press, Taylor & Francis Group, ISBN 9781498766241.

[6] CLIC, “Geothermal use of tunnels”, CERN, Geneva, Switzerland, Tech. Rep. ARUP_202204_CERN, May 2022.

ISBN: 978-3-95450-236-3 ISSN: 2673-7027 doi:10.18429/JACoW-eeFACT2022-WEZAS0106

METHODS AND EXPERIENCES OF AUTOMATED TUNING OF ACCELERATORS*

Xiaobiao Huang†, SLAC National Accelerator Laboratory, Menlo Park, CA, USA

Abstract

Automated tuning, or beam-based optimization, is a general approach to improve accelerator performances. The approach is different from the other common approach of beam-based correction. The differences between these two approaches and the advantages of the optimization approach are discussed. Two online optimization methods, the robust conjugate direction search (RCDS) and the multi-generation Gaussian process optimizer (MG-GPO), are described. Experiences of apply the methods to storage ring nonlinear dynamics optimization at SPEAR3 and APS storage rings, as well as application to other machines, are presented.

INTRODUCTION

An accelerator typically has many error sources that cause its behavior to differ from the ideal design. The performance of the machine can be substantially degraded due to the errors. The machine also has many control parameters (i.e., knobs) that can be used to change its behavior, which could compensate the effects of the errors and restore the machine performance. Accelerator physicists use beam-based measurements to determine the desired knob adjustments. The methods employed to find the accelerator setting based on beam-based measurements could be classified into two categories: beam-based correction and beam-based optimization [1].

In this paper, we will first discuss the characteristics of these two approaches. This is followed by discussions on the methods and application of beam-based optimization. The methods to be focused on are the robust conjugate direction search (RCDS) method [2] and the multi-generation Gaussian process optimizer (MG-GPO) [3]. Considerations on application of the methods to real-life accelerator tuning problems are discussed. Some important applications, such as minimization of the vertical emittance in storage rings, tuning of linac front end, and optimization of nonlinear beam dynamics of storage rings, are described.

BEAM-BASED CORRECTION AND OPTIMIZATION

The performance of an accelerator can be characterized by various metrics, such as beam intensity, beam size, beam lifetime, beam loss, transmission efficiency, injection efficiency, and beam stability. These metrics could be constantly monitored, or in some cases, are measured on demand. Depending on the purpose of the machine, each accelerator may have a different set of performance metrics of importance. In many cases, a set of knobs can target one performance metric without affecting the others. However, in some cases, the same set of knobs that are used to tune one metric can simultaneously impact the other metrics.

The diagnostic system of the accelerator measure and monitor many signals that represent the state of the machine or the beam. For example, the orbit of the beam throughout the accelerator is typically monitored with beam position monitors (BPMs). The transverse beam profile and in turn the transverse beam size can be measured at some locations. In circular accelerators, the betatron tunes can be constantly monitored. Some machine state variables can be derived from the monitor signals. In some cases, the beam or the machine are intentionally perturbed in order to perform an observation of the machine state. For example, the betatron phase advances can be measured from turn-by-turn BPM data when the beam is kicked. The closed orbit response, measured by making a small change to an orbit corrector, is another example.

The machine state as characterized by the diagnostic system could be directly correlated with the performance metrics, such that restoring the machine state automatically also restores the performance. In other cases, the correlation is not as strong; yet, it is still generally preferred to operate under certain machine states. In those cases, a "golden" machine state can be defined as the target configuration. For example, a golden beam orbit is usually defined for a storage ring. Desired values of betatron tunes and chromaticities are also specified. In a linac or transport line, the desired orbit and beam distribution is often specified at some strategically important locations, for example, at the end of the transport line for injection to another accelerator or at the entrance of the undulators in a free electron laser.

Often times, a known set of knobs can be used to change a certain aspect of the machine state. If there are enough effective knobs, it may be possible to move the machine into any reasonable state with those knobs. Because usually each knob has a definitive and predictable effect to the machine state, given the current machine state, the current knob setting, and the target machine state, one could work out the required adjustment to the knobs in a deterministic fashion. As not everything is perfectly known, it may take several iterations to reach the target state. The process of of bringing the machine state as measured by the beam diagnostic system to a target state with control knobs via a deterministic procedure is called beam-based correction.

Beam-based correction requires beam diagnostics that can sufficiently characterize the machine states, a known target machine state, knobs that can effectively change the machine state, and a deterministic procedure to determine the required knob changes toward the target. Reaching the

* Work supported by DOE Contract No. DE-AC02-76SF00515
† xiahuang@slac.stanford.edu

ISBN: 978-3-95450-236-3 ISSN: 2673-7027 doi:10.18429/JACoW-eeFACT2022-WEZAS0106

target state does not necessarily leads to the highest machine performance, as the correlation between the machine state and the performance metrics is not always strong and the optimal target state could change with other controlled or uncontrolled machine conditions (e.g., drift w/ ambient temperature).

Beam-based optimization is another category of beam-based methods to tune knobs for improving accelerator performances. This approach is also referred to as automated tuning. Manual tuning is common in accelerator control. As accelerators adopted computerized control early on, there have been various attempts to automate the tuning process [2, 4].

Beam-based optimization aims at improving the performance metrics directly by changing the tuning knobs, using the measured performance metrics as the guide. It is the same as mathematical optimization - the performance metrics are the objective functions and the tuning knobs are the optimization variables. The objective functions are evaluated by performing a measurement on the machine, after the tuning knobs are dialed in. The accelerator can be considered a black box; the main requirements for the machine are that the knobs are effective in changing the performance and that it can reproduce the performance for the same knob setting. No measurement of the machine state is necessary, unless certain features of the machine state are part of the performance metrics.

The optimization approach has some advantages over the correction approach. It does not have high requirements for diagnostics, as measurements for the performance metrics are usually available. It does not need a target state. This would be important in the commissioning phase of an accelerator as the target state, needed by the correction approach, may be still undetermined. Nor does it require enough a prior knowledge about the system to relate the target to the knobs. Therefore, it is relatively easy to set up and perform beam-based optimization (see Fig. 1).

The key to beam-based optimization is robust, efficient optimization algorithms. The requirements for online optimization algorithms may differ from that for usual mathematical optimization. In the next section we will discuss the considerations and requirements for online optimization algorithms, as well as discuss some specific options.

BEAM-BASED OPTIMIZATION ALGORITHMS

Considerations

Mathematical optimization is a well-researched area. There are numerous optimization algorithms. However, online optimization has special requirements and not all algorithms are suitable for online application [2].

One important difference is that the objective function in online optimization is impacted by measurement errors. For the same machine configuration, corresponding to the same set of optimization variables, the objective function evaluated on the machine will have slightly different value

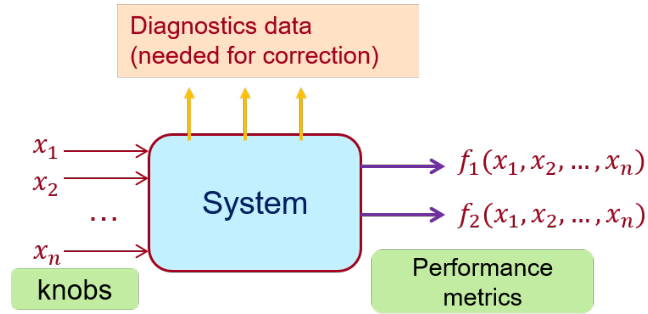

Figure 1: An illustration of the accelerator system for beam-based correction or optimization.

every time. The difference comes from the measurement errors of the parameters that come into the definition of the objective function. These errors could be due to the diagnostic system involved in the measurements. They could also be due to fluctuations of the machine condition that cause the parameter to actually change. Errors in the objective function can severely impact the performance of some algorithms, sometimes causing them to fail completely. For example, in the Nelder-Mead simplex method [5], the operations of the algorithm depend on the comparison results of the function values. When the comparison results are altered by measurement errors, the algorithm takes wrong paths, which could slow down or even prevent the convergence to the optimum.

The measurement errors also cause difficulties to gradient-based optimization algorithms. These algorithms require the first-order or second-order derivatives of the objective function. Ordinarily, the derivatives can be approximated with numerical differences. However, when there are errors in function evaluations, the derivatives will have large errors as usually the step size used in numerical differential is small. The errors to second order derivatives are even larger. The alternative of using an accelerator model to compute the derivatives may not work as the model is inaccurate - otherwise online tuning would be unnecessary. Therefore, gradient-based algorithms, such as Newton's method or pseudo-Newton methods, are typically not used in online applications.

High efficiency is especially important for online optimization. This is because evaluation of the objective function takes time, and the overall time available for machine study is usually limited. The evaluation time include the time needed to change the machine setting until it settles in the new state and the time to measure the performance metrics. The time for a magnet to change to a new setpoint may be up to a few seconds, depending on the type of magnet and power supply. The measurement of performance metrics could vary from nearly instantaneous, seconds to tens of seconds, or even longer. An optimization session on the machine is usually up to a few hours in duration. Therefore, the number of function evaluations in one session can be

ISBN: 978-3-95450-236-3 ISSN: 2673-7027 doi:10.18429/JACoW-eeFACT2022-WEZAS0106

between tens to a few hundreds, with which the algorithm has to locate the optimum.

Special consideration is also needed on ensuring the safety of the machine. Safety caution could be implemented in the control system, for example, by setting software limit to the knob ranges. It can also be implemented in the objective function, in which more complex conditions or measures can be programmed. For example, a corner in the parameter space can be excluded; a "not an number" (NaN) value could be returned for an invalid beam condition; or the optimization can be paused if a certain beam condition is detected. The implementation of the algorithm should be aware of the scenarios that could occur during the evaluation of the objective function on the machine. By properly handling the scenarios, the optimization can be made safer, more efficient, and more reliable.

Algorithms

We discuss a few useful algorithms for online optimization, including Nelder-Mead simplex, robust conjugate direction search (RCDS), and multi-generation Gaussian process optimizer (MG-GPO).

The simplex algorithm is an efficient, gradient-free method. It converges to a minimum by morphing a simplex, a geometric body in the N-dimensional parameter space defined by $N+1$ vertices, through a number of operations, including reflection, expansion, and contraction. In online application, the biggest challenge is that comparison of function values on the vertices can be altered by measurement noise, as the simplex size is reduced. The robust simplex (RSimplex) method can alleviate the issue by using extra sampling to reduce noise when necessary [6]. However, an accurate noise model is needed for it to be the most efficient. Using a large initial simplex size could also help reduce the impact the noise.

The RCDS method combines the power of conjugate direction searches and a robust, noise-aware 1-dimensional optimizer and is ideal for locating the optimum from a point in its vicinity. Search along one conjugate direction is independent of the search along another, which gives the method high efficiency. The conjugate direction set could be derived from a model by calculating the Hessian matrix of the objective function. The key of RCDS for its effectiveness comes from its ability to optimize under noise. During the step of bracketing the minimum, instead of merely comparing the function values between two points, the robust 1-D optimizer requires the end points to be higher than the lowest point (for a minimization problem) inside the bracket by 2 or 3 sigma. It also uses parabolic fitting to improve the accuracy in determining the minimum. The RCDS method has been successfully applied to many real-life accelerator optimization problems.

Many optimization algorithms, including simplex and RCDS, are inclined to converge to a local minimum. In many accelerator optimization problems, the true challenge is to find the global optimum in a high dimensional parameter space. Stochastic algorithms, such as random search, simulated annealing, genetic algorithms (GA) [7], and particle swarm optimization (PSO) [8, 9], are often used for global optimization. By using random operations to generate new candidate solutions, or a random decision process, these algorithms can break out from the attraction of local minima. However, these algorithms are typically not very efficient.

The MG-GPO method is a stochastic optimization algorithm with relatively high efficiency, which is enabled by machine learning. Similar to GA and PSO, it is population based and generates new solutions with random optimizations. However, it makes better use of the information contained in the solutions previously evaluated. A Gaussian process (GP) regression model is constructed for each objective function, using the existing solutions and a prior model characterized by the kernel matrix. The models can predict the performance of a trial solution. Instead of evaluating all trial solutions, MG-GPO uses the GP models to predict the performance of a large set of trial solutions and select only the ones expected to have good performance for evaluation. The algorithm has been benchmarked against many advanced stochastic algorithms and it was demonstrated it has superior convergence speed. It has also been tested in simulation and online problems. The MG-GPO algorithm is suitable for global optimization of complex, large parameter spaces.

Bayesian optimization (BO), also based on Gaussian process regression, has been adopted for accelerator tuning [10–12]. Bayesian optimization can be very efficient. Compared to BO, MG-GPO may be more robust and less dependent on the starting point and fine tuning of hyperparameters in the algorithm, for example, as experienced in the linac front-end tuning at APS [13].

APPLICATION EXAMPLES

There have been many successful applications of online optimization of accelerator performances. We will only discuss a few selected examples.

Storage Ring Vertical Emittance Minimization

In electron storage rings, the vertical emittance can come from the horizontal-vertical linear coupling and the vertical dispersion. Both effects are primarily due to random errors in the real machine, for example, misalignment of quadrupole (rolls) and sextupole magnets. Skew quadrupoles are effective knobs for controlling the vertical emittance as they can compensate both linear coupling and vertical dispersion. In storage ring light sources, a small vertical emittance corresponds to photon beam high brightness. In some cases the vertical emittance is set to a relative high level to achieve a reasonable Touschek lifetime. Even for these cases, it is preferable to first minimize the vertical emittance and then adjust the dispersion wave knob to increase it to the desired level.

At the SPEAR3 storage ring, the vertical emittance minimization problem has been used to test optimization algo-

ISBN: 978-3-95450-236-3 ISSN: 2673-7027 doi:10.18429/JACoW-eeFACT2022-WEZAS0106

rithms [2,12,14,15]. The ring has 13 free skew quadrupoles, which are used as tuning knobs. The beam loss rate, in a Touschek loss dominated parameter regime, normalized by the single bunch current, can be used as the objective function. A small vertical emittance corresponds to high beam loss rate. The beam loss rate can be measured by observing the beam current change over a fixed duration, or with beam loss monitors. In the latter case, it may be desirable to concentrate beam loss at where the loss monitor is located or use loss monitors distributed around the ring.

The RCDS method has been used to minimize the SPEAR3 vertical emittance [2]. The conjugate direction set is obtained with the Jacobian matrix of the off-diagonal blocks of the orbit response matrix with respect to the skew quadrupole knobs - it corresponds to the singular value decomposition (SVD) of the Jacobian matrix. In the experiments, all of the skew quadrupoles are initially set to zero strength. With about 200 function evaluations, the beam loss rate is increased to the maximum level. The skew quadrupole setting for the maximum beam loss rate is similar to the setting found with LOCO (correction with orbit response matrix) [16,17], while the maximum loss rate was higher than that of LOCO. The MG-GPO method has also been successfully applied to the SPEAR3 vertical emittance minimization problem [15].

Linac Transmission

Online optimization has been successfully used to tune the machine for optimal beam transmission in the linacs of both SPEAR3 and APS.

Some recent results for APS linac are reported in [13]. In the APS experiments, the goal is improve the transmission from the gun, around the alpha magnet, and in the first section of the linac. The objective function is the the charge measured in the L3 section. The tuning knobs are steering magnets and quadrupole magnets before and immediately after the alpha magnet. There are 12 tuning knobs. Several algorithms have been tested, including the simplex method, RCDS, PSO, and MG-GPO. Simplex works in many cases and converges fast, although it can also fail to make any improvement. For RCDS, it is important to correctly set the noise sigma parameter. For the MG-GPO algorithm, different population size of 8, 12, 20, and 30 was tried and was found to be robust. It converges faster than the PSO method and can find better solutions. The online tuning has been very helpful when a new gun was installed and it has been routinely used for linac front-end tuning.

Storage Ring Nonlinear Dynamics Optimization

Storage ring nonlinear dynamics tuning is extremely important for the commissioning of low emittance storage rings since these rings tend to have small dynamic aperture and momentum aperture, while there is no other reliable methods to compensate the inevitable errors in the real machine [18].

Online optimization of dynamic aperture with the RCDS method has been successively applied at several storage rings, including SPEAR3, MAX-IV [19], and NSLS-II [20]. Typically, the injection efficiency can be used as the objective function. If the initial injection efficiency is high, a reduced kicker bump or kicker bump mismatch may be used to decrease the injection efficiency and thus allow room for improvement. The sextupole and octupole (if available) magnets are used as tuning knobs. In the SPEAR3 case, a substantial improvement of more than 30% was achieved for DA; similarly large improvement was seen on MAX-IV and NSLS-II. PSO and MG-GPO have also been successfully used for DA optimization at SPEAR3.

At ESRF, sextupole knobs were used to maximize the Touschek lifetime [21]. The objective is lifetime normalized with beam current and the measured vertical beam size. In an experiment, the lifetime was improved from 11 h to 17 h.

In a recent study [22], simultaneous optimization of the dynamic aperture and Touschek lifetime was demonstrated on the APS storage ring, using MG-GPO, a multi-objective optimization method. The same 5 sextupole knobs are used for both objectives. These knobs are constructed from the 280 sextupole magnets, each with individual power supply, with symmetry considerations. A population size of 15 was used. To evaluate the objective functions without frequently dumping beam, for each generation, the injection efficiency was first measured for all solutions, which is followed by the lifetime measurements. Substantial improvements to both the dynamic aperture and the Touschek lifetime objectives were made.

SUMMARY

We discussed characteristics of the two beam-based approaches for improving accelerator performance: correction and optimization, in particular, the need for beam-based optimization and the special considerations for its implementation. Several online optimization algorithms, such as simplex, RCDS, and MG-GPO, are discussed. Their application to a few important real-life accelerator problems are described.

REFERENCES

[1] X. Huang, "Development and application of online optimization algorithms," in *Proceedings of NAPAC2016*, Chicago, IL, 2016, pp. 1287–1291.

[2] X. Huang, J. Corbett, J. Safranek, and J. Wu, "An algorithm for online optimization of accelerators," *Nucl. Instrum. Methods Phys. Res, Section A*, vol. 726, pp. 77 – 83, 2013. [Online]. Available: http://www.sciencedirect.com/science/article/pii/S0168900213006347

[3] X. Huang, M. Song, and Z. Zhang, "Multi-objective multi-generation gaussian process optimizer for design optimization," *CoRR*, vol. abs/1907.00250, 2019. [Online]. Available: http://arxiv.org/abs/1907.00250

[4] L. Emery, M. Borland, and H. Shang, "Use of a general-purpose optimization module in accelerator control," in *Proceedings of the PAC'03*, 2003, pp. 2330–2332.

[5] J. A. Nelder and R. Mead, "A simplex method for function minimization," *The Computer Journal*, vol. 7,

ISBN: 978-3-95450-236-3 ISSN: 2673-7027 doi:10.18429/JACoW-eeFACT2022-WEZAS0106

no. 4, pp. 308–313, 01 1965. [Online]. Available: https://doi.org/10.1093/comjnl/7.4.308

[6] X. Huang, "Robust simplex algorithm for online optimization," *Phys. Rev. Accel. Beams*, vol. 21, p. 104601, Oct 2018. [Online]. Available: https://link.aps.org/doi/10.1103/PhysRevAccelBeams.21.104601

[7] K. Deb, A. Pratap, S. Agarwal, and T. Meyarivan, "A fast and elitist multiobjective genetic algorithm: NSGA-II," *Trans. Evol. Comp*, vol. 6, no. 2, pp. 182–197, Apr. 2002. [Online]. Available: http://dx.doi.org/10.1109/4235.996017

[8] J. Kennedy and R. Eberhart, "Particle swarm optimization," in *Proceedings of ICNN'95 - International Conference on Neural Networks*, vol. 4, Nov 1995, pp. 1942–1948 vol.4.

[9] X. Pang and L. Rybarcyk, "Multi-objective particle swarm and genetic algorithm for the optimization of the LANSCE linac operation," *Nucl. Instrum. Methods Phys. Res, Section A*, vol. 741, pp. 124 – 129, 2014. [Online]. Available: http://www.sciencedirect.com/science/article/pii/S0168900213017464

[10] M. McIntire, T. Cope, and D. Ratner, "Bayesian optimization of FEL performance at LCLS," in *Proceedings of IPAC2016*, Busan, Korea, 2016, pp. 2972–2975.

[11] J. Duris, D. Kennedy, A. Hanuka, J. Shtalenkova, A. Edelen, P. Baxevanis, A. Egger, T. Cope, M. McIntire, S. Ermon, and D. Ratner, "Bayesian optimization of a free-electron laser," *Phys. Rev. Lett.*, vol. 124, p. 124801, Mar 2020. [Online]. Available: https://link.aps.org/doi/10.1103/PhysRevLett.124.124801

[12] A. Hanuka, X. Huang, J. Shtalenkova, D. Kennedy, A. Edelen, Z. Zhang, V. R. Lalchand, D. Ratner, and J. Duris, "Physics model-informed gaussian process for online optimization of particle accelerators," *Phys. Rev. Accel. Beams*, vol. 24, p. 072802, Jul 2021. [Online]. Available: https://link.aps.org/doi/10.1103/PhysRevAccelBeams.24.072802

[13] H. Shang, Y. Sun, X. Huang, M. Song, and Z. Zhang, "Experience with on-line optimizers for APS linac front end optimization," in *Proceedings of the IPAC'21*, 2021, pp. 2151–2154.

[14] K. Tian, J. Safranek, and Y. Yan, "Machine based optimization using genetic algorithms in a storage ring," *Phys. Rev. ST Accel. Beams*, vol. 17, p. 020703, Feb 2014. [Online]. Available: https://link.aps.org/doi/10.1103/PhysRevSTAB.17.020703

[15] Z. Zhang, M. Song, and X. Huang, "Online accelerator optimization with a machine learning-based stochastic algorithm," *Machine Learning: Science and Technology*, vol. 2, no. 1, p. 015014, Dec 2020. [Online]. Available: https://dx.doi.org/10.1088/2632-2153/abc81e

[16] J. Safranek, "Experimental determination of storage ring optics using orbit response measurements," *Nucl. Instrum. Methods Phys. Res, Section A*, vol. 388, no. 1, pp. 27 – 36, 1997. [Online]. Available: http://www.sciencedirect.com/science/article/pii/S0168900297003094

[17] J. Safranek, G. Portmann, and A. Terebilo, "Matlab-based LOCO," in *Proceedings of EPAC'02*, 2002, pp. 1184–1186.

[18] X. Huang and J. Safranek, "Online optimization of storage ring nonlinear beam dynamics," *Phys. Rev. ST Accel. Beams*, vol. 18, p. 084001, Aug 2015. [Online]. Available: https://link.aps.org/doi/10.1103/PhysRevSTAB.18.084001

[19] D. K. Olsson, "Online optimisation of the MAX-IV 3 Gev ring dynamic aperture," in *Proceedings of IPAC2018*, Vancouver, BC, Canada, 2018, pp. 2281–2283.

[20] X. Yang *et al.*, "Online optimization of NSLS-II dynamic aperture and injection transient," in *Proceedings of IPAC2022*, Bangkok, Thailand, 2022, pp. 1159–1162.

[21] S. Liuzzo, N. Carmignani, L. Farvacque, B. Nash, T. Perron, P. Raimondi, R. Versteegen, and S. M. White, "RCDS optimizations for the ESRF storage ring," in *Proceedings of IPAC2016*, Busan, Korea, 2016, pp. 3420–3422.

[22] L. Emery, H. Shang, Y. Sun, and X. Huang, "Application of a machine learning based algorithm to online optimization of the nonlinear beam dynamics of the argonne advanced photon source," *Phys. Rev. Accel. Beams*, vol. 24, p. 082802, Aug 2021. [Online]. Available: https://link.aps.org/doi/10.1103/PhysRevAccelBeams.24.082802

ISBN: 978-3-95450-236-3 ISSN: 2673-7027 doi:10.18429/JACoW-eeFACT2022-WEZAT0202

LESSONS LEARNED FROM OPERATIONAL EXPERIENCE OF SuperKEKB IR MAGNETS AND UPGRADE PLANS FOR THE FUTURE

Y. Arimoto*, K. Aoki, M. Kawai, T. Kawamoto, M. Maszawa, S. Nakamura, Y. Ohsawa, N. Ohuichi, T. Oki, R. Ueki, X. Wang, H. Yamaoka, Z. Zong, KEK, Tsukuba, Japan

Abstract

SuperKEKB is an upgraded accelerator from KEKB, aiming at a luminosity of $6 \times 10^{35}\,\mathrm{cm^{-2}\,s^{-1}}$. It is currently in operation, setting new luminosity records. We have completely redesigned the final-focus-magnet system to achieve the target luminosity by upgrading from KEKB to SuperKEKB. After the completion of the system, it started its practical operation in 2018 after measuring the magnetic field in IR. The operation is generally stable, but some troubles have occurred. One of them is a quench. Radiation related to stored beam deposit energy on the superconducting coil. And then, we experienced the tune variations in LER, which suggested fluctuations in the main quadrupole magnetic field, and measurements using the R & D magnet demonstrated this phenomenon. In addition, we are seeking a plan to upgrade the QCS for the long shutdown around 2027.

INTRODUCTION

KEKB is a B-Factory and is an e^+/e^- collider operated from 1998 to 2010 [1]. It achieved a peak luminosity of $2.11 \times 10^{34}\,\mathrm{cm^{-2}\,s^{-1}}$ and an integrated luminosity of $1040\,\mathrm{fb^{-1}}$. The Belle experiment using KEKB has achieved many physics results. To make precise measurements of weak interaction parameters and find new physics beyond the Standard Model, the KEKB has been upgraded to the SuperKEKB [2]. It aims at a peak luminosity of $6 \times 10^{35}\,\mathrm{cm^{-2}\,s^{-1}}$ and the integrated luminosity of $50\,\mathrm{ab^{-1}}$. The operation of the SuperKEKB started from 2018 and achieved the peak luminosity of $4.7 \times 10^{34}\,\mathrm{cm^{-2}\,s^{-1}}$ up to 2022 [3].

FINAL FOCUS SYSTEM OF KEKB AND SUPERKEKB

One of the critical components for the accelerator upgrade from KEKB to SuperKEKB is a final focus system with superconducting (SC) magnets called QCS. At an interaction point (IP), a design vertical-beam size, σ_y^* of SuperKEKB is 50 nm and is 20 times smaller than KEKB.

To achieve this, the QCS system designed for SuperKEKB has independent quadrupole doublets for each ring. For the KEKB-QCS (in this section, we denote this as K-QCS), the electron and positron beam went through the same quadrupole magnets of the QCS. So, the SuperKEKB-QCS (in this section, we denote this as SK-QCS) consists of eight quadrupole doublets; on the other hand, the K-QCS has two quadrupole magnets [4, 5]. Figures 1 and 2 show schematic layouts of the QCS of KEKB and SuperKEKB, respectively. The SK-QCS also has the leak field cancel magnets; they cancel the leak field from QC1LP and QC1RP to HER. The four solenoids of the SK-QCS compensate for the integral solenoid field of Belle II detector , while the K-QCS has two compensation solenoids.

Table 1: KEKB and SuperKEKB Main Parameters

	KEKB		SuperKEKB	
	LER	HER	LER	HER
E [GeV]	3.5	8.0	4.0	7.0
θ_{cross} [mrad]	22		83	
β_y^* [mm]	5.9	5.9	0.27	0.30
σ_y^* [nm]	900	900	48	62

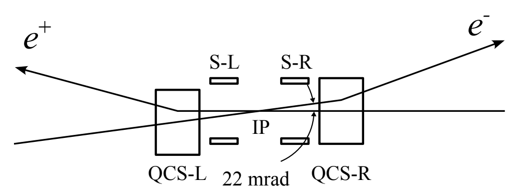

Figure 1: The schematic layout of the KEKB-QCS. S-L and S-R are the compensation solenoids, and the QCS-L and QCS-R are the SC quarupole magnets.

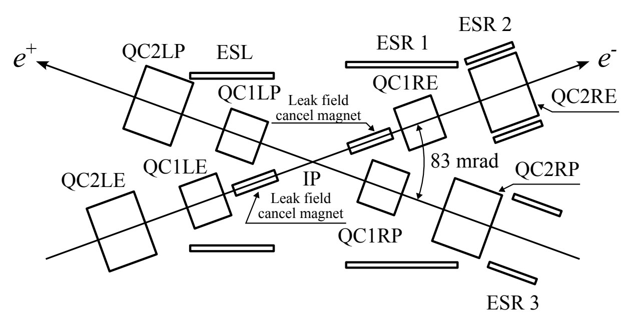

Figure 2: Schematic layout of SuperKEKB-QCS. The magnets representing with "QC" at beginning are the superconducting quadrupole magnets. The leak field cancel magnets are canceling the leak field from QC1RP and QC1LP quads. ESL, ESR1, ESR2, and ESR3 are the compensation solenoids.

Tables 2 and 3 show the main parameters for the quadrupole magnets of KEK and SuperKEKB, respectively. The letter "L" or "R" in all magnet names indicates the magnet on the left or right side of the IP, viewing the IP from the center of the accelerator ring, respectively. The QCS-L and QCS-R magnets are the vertical-focusing quadrupole magnets for KEKB in Table 2. The vertical-focusing quadrupole

* yasushi.arimoto@kek.jp

ISBN: 978-3-95450-236-3 ISSN: 2673-7027 doi:10.18429/JACoW-eeFACT2022-WEZAT0202

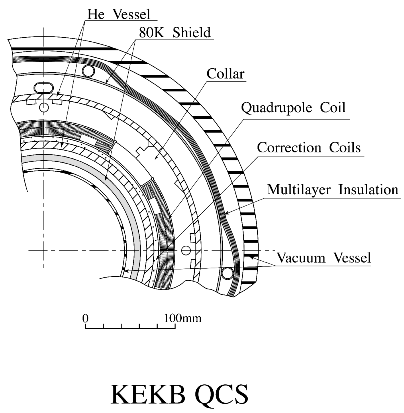

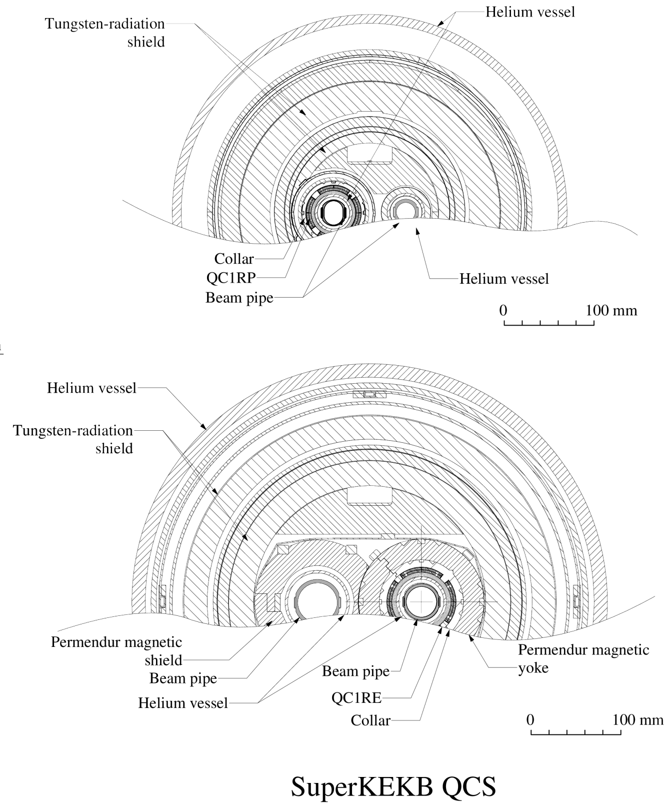

Figure 3: The cross sections of KEKB-QCS [4] and QC1RP and QC1RE for SuperKEKB QCS.

magnets of SuperKEKB are the QC1LP(RP) magnet and the QC1LE(RE) magnet. The QC1LP(RP) and QC1LE(RE) magnets have a B-field gradient of around 70 T/m, and they are three times larger than the QCS-L(R) magnet. Figure 3 shows the cross sections of K-QCS and SK-QCS. The aperture of the QC1LP(RP) and QC1LE(RE) magnets are ten times smaller than QCS-L(-R) magnet.

The SK-QCS has two-refrigerator units whose power is 250 kW at 4.4 K for one unit. We repurposed these refrigerators from TRISTAN and KEKB [6]. The K-QCS has one refrigerator unit repurposed from TRISTAN [4].

The SK-QCS is a more complex system with more SC magnets than K-QCS. Figure 4 shows the entire layout of the SK-QCS magnet and the Belle II solenoid magnet.

Table 2: The main parameters of the QCS quadrupole magnets for KEKB [4]. Here, G is a B-field gradient, I is an operation current. r_{in} is the inner radius of the SC conductor, and L_{eff} is the effective length of the quadrupole field.

Magnet Name	G [T/m]	I [A]	r_{in} [mm]	L_{eff} [mm]
QCS-L	21.66	2963	260	483
QCS-R	21.73	2963	260	385

Table 3: The main parameters of the QCS quadrupole magnets for SuperKEKB. Here, G is a B-field gradient at the operation current, I on April 11th, 2020 [6].

Magnet Name	G	I	r_{in}	L_{eff}
QC1LP	67.8	1598	25.0	334
QC1RP	67.8	1599	25.0	334
QC2LP	28.1	879	53.8	410
QC2RP	28.2	882	53.8	410
QC1LE	72.4	1581	33.0	373
QC1RE	68.6	1499	33.0	373
QC2LE	29.1	1001	59.3	537
QC2RE	30.8	1249	59.3	419

MAGNETIC MEASUREMENTS

We performed several magnetic measurements at the interaction region (IR). The solenoid field generates the electromagnetic force of 52.5 kN and 33.7 kN on the ESL and ESR1, respectively; as a result, the magnets would move [6]. Moreover, the magnet yoke would exhibit magnetic saturation. Since it is not easy to calculate these effects precisely, we performed the in-sites measurement despite taking time and effort.

We had three types of magnetic measurements, a measurement of B-field multipole with harmonic coils, a measurement of the magnet centers with a single stretched wire

ISBN: 978-3-95450-236-3 ISSN: 2673-7027 doi:10.18429/JACoW-eeFACT2022-WEZAT0202

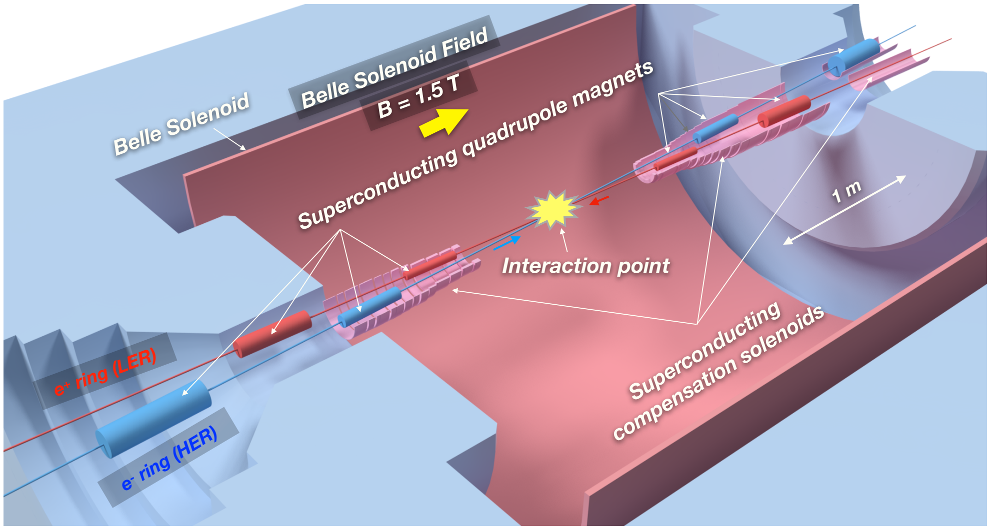

Figure 4: The entire layout of the QCS in the Belle II detector.

(SSW) method, and a measurement of solenoid field with a Hall probe [6].

Measurement of Higher Order Harmonics with Harmonic Coils

The *B*-field of the quadrupole magnet is expanded in multipoles;

$$B(x,y) = 10^{-4} B_2 \sum_{n=1}^{\infty} (b_n + i a_n) \left(\frac{x+iy}{R_{\mathrm{ref}}} \right)^{n-1} \tag{1}$$

here, B_2 is the amplitude of the quadrupole field at the reference radius, R_{ref}, and b_n and a_n are the normal and skew multipoles, respectively. Here, although b_n and a_n are non-dimensional values, we use the "units" as a unit of them. The target higher order multipoles is less than one unit.

Our harmonic coil system has long-winding coils to measure integral *B*-field and short-winding coils to measure axial profiles. We have several kinds of winding radii for each coil. The length of the short coil is 20 mm, and that of long coils is 595-795 mm and longer than the length of the magnets.

The measured integral field with the long coils exhibits slightly larger error fields for allowed components; the other components less than 1-2 units except for the QC2RE quadrupole magnet [6]]. The QC2RE quadrupole magnet exhibit the skew sextupole component of 20 units and 8 units for skew octupole components when the Belle II and the compensation solenoids are turned on. The axial solenoid field has a maximum distance of the IP of 2620 mm. The asymmetric shape of the iron frame causes this.

The QC2RE, ESR2, and ESR3 are contained in an iron structure to shield the solenoid field. The frame is asymmetrical in shape to extract SC wires. Figure 5 shows a perse view of a 3D CAD drawing of the iron structure. The left figure is the iron structure view from the non-IP side. As can be seen from this figure, the shape is asymmetrical at the end. In order to quantitatively investigate the effect of the field quality and to compare it with the measured values, we modeled the iron structure shape on the IP side and calculated it with Opera3D. For simplicity, the model has top-bottom symmetry, and the shape on the non-IP side is a circle. Figure 6 shows an axial profile of the QC2RE quadrupole obtained by energizing all the solenoids. The horizontal axis is the HER beam axis, and the origin is the IP. The measurement and calculation results are solid lines and dashed lines, respectively. Figure 6-(a),-(b), and -(c) are the profiles of skew quadrupole, sextupole, and octupole components at $R_{\mathrm{ref}} = 35$ mm, respectively. At the bottom of these plots, the top view of the QC2RE magnet and the iron structure is illustrated with the same scale and position. At both ends of the iron structure, the plots for all components show a sharp peak error field, and the calculation represents good agreement with the measurement at the IP side. Since the model reproduces the actual geometry only on the IP side, the non-IP side does not reproduce the measurement result.

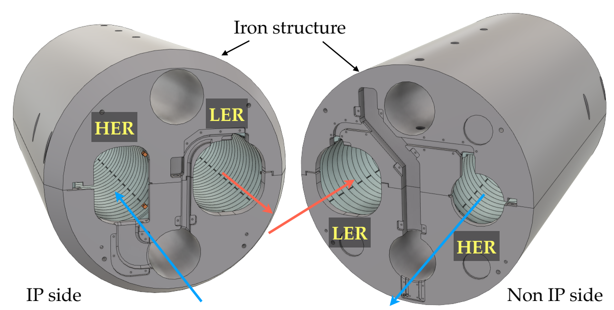

Figure 5: The perse view of the iron structure of the QC2RE. The left is the view from the IP side, and the right is the view from the non-IP side. The QC2RE locates at the HER axis.

Measurement of Magnet Center

We measured the magnet centers of the quadrupole magnets with the single stretched wire (SSW) method [7]. A

ISBN: 978-3-95450-236-3 ISSN: 2673-7027 doi:10.18429/JACoW-eeFACT2022-WEZAT0202

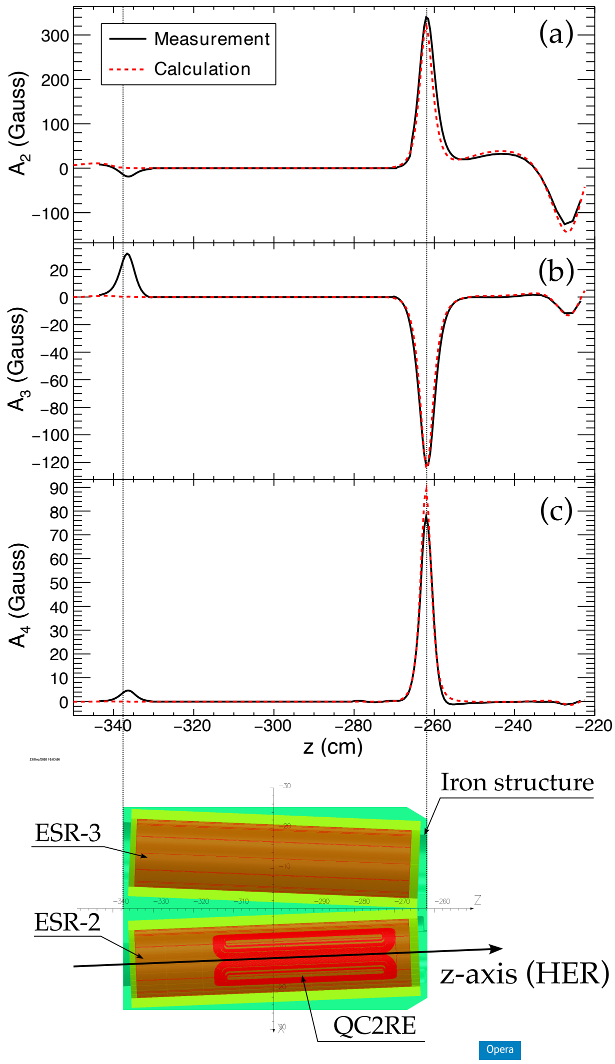

Figure 6: The axial profile of QC2RE. (a) The profile of skew quad, (b) the profile of skew sextupole, (c) the profile of skew octupole. The reference radius for these components is 35 mm. The horizontal axis is axial distance along HER axis and the origin is the IP. Solid lines are measurement result with the harmonic coil and the dashed curves are calculation results with Opera3D/TOSCA.

wire made of BeCu stretched from the end of the QCS cryostat through the beam pipe via the IP to the end of the other QCS cryostat. Both ends of the wire are fixed on precise x-y stages of the SSW units. The stretched wire's diameter and length are 0.1 mm and 9 m, respectively. We performed the SSW measurement with AC mode to separate the DC solenoid fields; we energized a quadrupole magnet with AC at 7.8125 Hz. Figure 7 shows the measured magnet center for the quadrupole field. The top two plots are x-direction offsets, and the bottom one is the vertical (y-) direction offsets of the magnet center. The left (right) plots are the HER (LER) magnet center. Black circles are the obtained offsets when the all-solenoid field is off, and the red squares are the offsets when the all-solenoids are on. Magnet positions varied with the solenoid fields turned on/off by $dx \sim 0.1$ mm, $dy \sim 0.3$ mm. The maximum horizontal (x-) offset is 0.7 mm for the QC1RP, and the maximum y-offset is -0.6 mm for the QC2LP. We can correct these quadrupole offsets with the dipole correctors and beam orbit tuning.

OPERATIONAL EXPERIENCE

Current Stability

The power supplies for QCS are IGBT type [8]. They supply stabilized current by the digital and analog feedback and achieved stability of 2 ppm a week. Figure 8 shows the one-week stability of the power supply for each main quadrupole magnet, and the red and blue lines are output current and correction voltage by digital feedback, respectively.

Failures

From 2018 to 2022, the QCS system experienced 62 power shutdown events by failures, such as magnet quench, the troubles of the power supplies, etc. Figure 9 shows the summary of failures from the start of SuperKEKB operation (Phase 3) to the long-shutdown 1. The gray, green, and blue bars are events caused by the troubles of the cooling water or the power supplies, the earthquake, and the beams, respectively.

The quench mechanism associated with the beam is not well understood, but from the fact that there was a sudden (about one μs)increase in coil voltage and background at Belle II detector, we deduce that the radiation originating from the beam deposited enough energy to cause the superconducting wire to quench.

At the early stage of the operation (2018), the magnet-quench related to the beam frequently happened, adjustment collimators or implementation of the fast abort system by Belle II detector significantly reduced the frequency of beam related quench event. The mechanism of the QCS failure by the earthquake is inferred as follows; when the earthquake happened, the relative distance varied between QCS solenoids and Belle II solenoid. And then, Faraday's induced voltage exceeds the threshold of the quench detector; as a result, the power supply moves to the shutdown process. The recovery time is typically one hour when the quadrupole magnet quenched, in the case of the compensation solenoids, ESL, or ESR1, it takes three to six hours.

Time Variation of Quadrupole Field

SuperKEKB is constant energy, so the quadrupole magnets in the QCS operate in dc mode. However, LER's vertical setting (model) tune varied after powering off/on the quadrupole magnet by 2×10^{-2} in a few hours.

Here, the model tune is a calculation tune from the lattice model with the operation current of the quadrupole magnets. The tune itself is kept constant by a tune feedback system. So, the drift of the model tune indicates some quadrupole magnetic field varies while the operation current is constant.

ISBN: 978-3-95450-236-3 ISSN: 2673-7027 doi:10.18429/JACoW-eeFACT2022-WEZAT0202

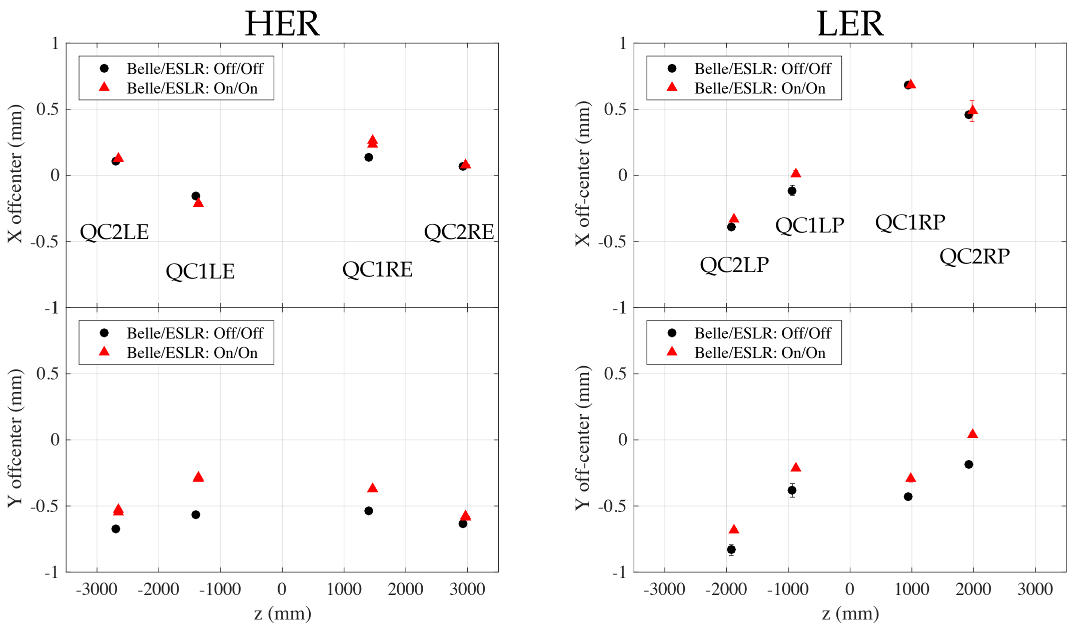

Figure 7: The offsets of magnet center from the target alignment position.

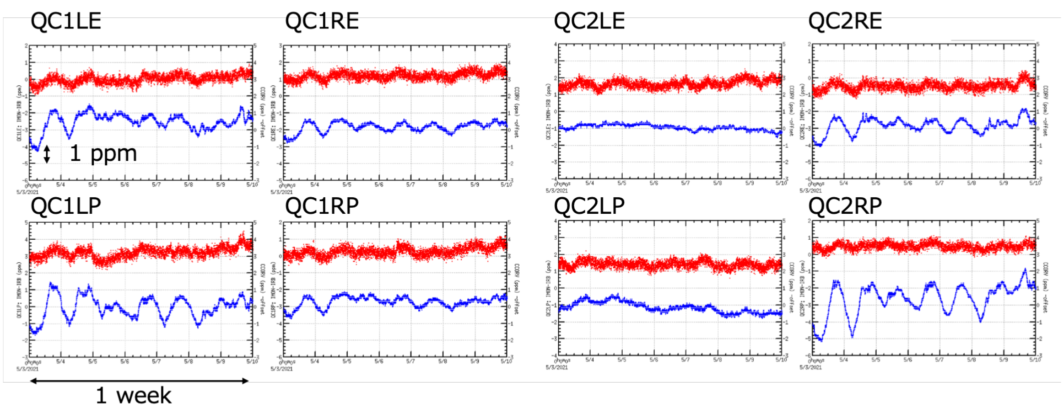

Figure 8: One week stability of power supply for each quadrupole magnets. The red and blue lines are output current and correction voltage by digital feedback, respectively.

Assuming the QCS quadrupole magnet caused this, the value of tune variation corresponds to the quadrupole field variation of ~2×10^{-4} on the QC1P.

Therefore, we performed measurements with the QC1P R&D magnet with the harmonic coil to confirm whether the magnetic field varies. Figure 10 shows the measured quadrupole components as a function of time. The black open and closed circles are obtained data by an energizing magnet current from 0 A to 1600 A. The red squares are the data by setting the current from 1638.3 A to 1600 A. The vertical axis is a ratio of the quadrupole variation, and is defined as follows;

$$\Delta R = \frac{C_2(t) - C_{20}}{C_{20}}. \qquad (2)$$

Here, $C_2(t)$ is the amplitude of the quadrupole field at the time of t. The origin of the time is the setting time to the target magnet current. Furthermore, C_{20} is the quadrupole amplitude at $t \sim 2 \times 10^4$ at the down ramp. Figure 11 shows the recycling and ramping pattern. The plot exhibit that the quadrupole field varies by 3×10^{-4} in 7 hours as a function of $\log t$. This field variation is in the same order as the observed vertical-model tunes. We deduce that the flux creep in the superconductor cable cause this variation. Other accelerator facilities, such as Tevatron, DESY, and RHIC reported this phenomenon [9–11].

It depends on the ramping pattern of the magnet, and the optimized pattern suppresses the time variation. The obtained time variation energized after the optimized ramping is the red squares and is about 0.2×10^{-4}.

FUTURE UPGRADE OPTION

The SuperKEKB aims to achieve an integrated luminosity of 50 ab^{-1} around 2030. To achieve this, we need a luminosity of 6×10^{35} $\mathrm{cm}^{-2}\,\mathrm{s}^{-1}$. We have issues such as transverse-mode-coupling-instability, short-beam lifetime,

ISBN: 978-3-95450-236-3 ISSN: 2673-7027 doi:10.18429/JACoW-eeFACT2022-WEZAT0202

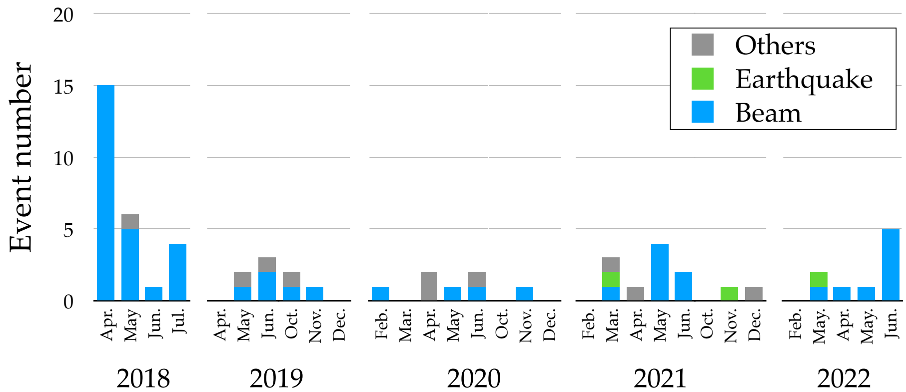

Figure 9: Summary of QCS failures.

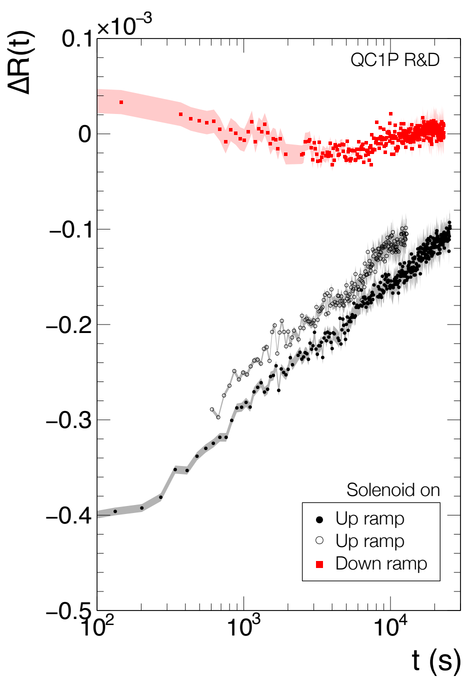

Figure 10: Time variation of quadrupole field of QC1P R&D magnet. The shaded areas are the uncertainties from the uncertainty of a thermal expansion of the harmonic-coil bobbin made of G10.

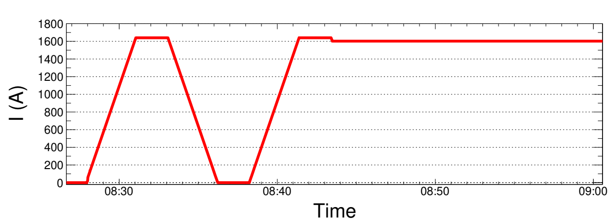

Figure 11: The optimized ramping pettern for QC1P magnet.

low-injection efficiency, and so on to increase the current luminosity. The QCS can contribute to improving beam lifetime. So we are investigating several upgrade options for the QCS. The upgrade is scheduled at long-shutdown-2 (LS2) period, which starts around 2027.

Although we are investigating the upgrade options, have yet to reach a final solution. The examples of the options which we have investigated so far are shown below;

- Moving the QC1P and QC1E away from the IP by 250 mm and 100 mm, respectively, and separating the compensation solenoid field and the main quadrupole field.
- Reducing the detector solenoid field from 1.5 T to 1.2 T.
- Increasing the inner radius of the corrector and setting the outer side of the main quadrupole magnet of QC1P.
- Getting QC1P and the compensation solenoid closer to IP by 300 mm.

After a detailed study, the options to move the magnets away from the IP and reduce the detector-solenoid field do not improve the luminosity.

Increasing the corrector's inner radius enables setting the corrector outside the main quadrupole magnet. As a result, we can enlarge the inner radius of the beam pipes at QC1P from 13.5 mm to 18.0 mm vertically and from 10.5 mm to 14.9 mm horizontally. Although this modification does not improve the beam lifetime, it is still open for discussion because it is expected that this reduces the beam background at the Belle II detector.

Moving the QC1P to the IP side by 300 mm is expected to increase the Touschek lifetime by ~ 2 times in calculation based on a simple lattice model. However, the option requires drastic modification at the IR, including the Belle II detector. Therefore, we need not only the design of the QCS but multifaceted investigation, such as how to install the detector and the QCS, impact on no BPM in the vicinity of the IP, further precise beam simulation, and the required time for the modification.

SUMMARY

On the upgrade from KEKB to SuperKEKB, we newly designed and constructed the QCS system for SuperKEKB. SuperKEKB requires the individual SC quadrupole magnets on the both ring, while KEKB had a common SC quadrupole magnet. As a result, the system is more complex than KEKB.

We performed the in-sites three kinds of magnetic measurements; the *B*-field multipole measurement, the magnet

ISBN: 978-3-95450-236-3 ISSN: 2673-7027 doi:10.18429/JACoW-eeFACT2022-WEZAT0202

center measurement, and the solenoid *B*-filed profile measurement. The field-multipole measurement results showed good qualities (less than 1-2 units) for all the quadrupole magnets except for the QC2RE magnet. When applying all the solenoid fields, the QC2RE magnet showed large multipole errors of 20 units for A_3 and 8 units for A_4. It is caused by the irregular shape at the iron structure end. The 3D magnetic analysis also represents this. The measured offsets of the magnet center were 0.7 mm at maximum, which is within range of a correction with the dipole correctors and the beam orbit tuning. The magnet center moved by 0.3 mm vertically by energizing the solenoid fields.

In the operation of SuperKEKB, the power supplies for the QCS are stable within 2 ppm a week. During the operation, we had many quenches associated with the beam. The typical recovery time was one hour and it is an acceptable time. We experienced shutdown by earthquake three times, because the induced voltage by earthquakes is sometimes over the threshold of the quench detector.

We are investigating upgrade options for the QCS to increase luminosity.

ACKNOWLEDGEMENTS

The authors are grateful to all the members of SuperKEKB accelerator and Belle II. The authors appreciate the engineers of Hitachi Technologies and Services. Finally, the authors express gratitude to the Mitsubishi Electric System & Service Co. engineers.

REFERENCES

[1] T. Abe *et al.*, "Achievements of KEKB," *Prog. Theor. Exp. Phys.*, vol. 2013, no. 3, p. 03A001, 2013. doi:10.1093/ptep/pts102

[2] Y. Ohnishi *et al.*, "Accelerator design at SuperKEKB," *Progr. Theor. Exp. Phys.*, vol. 2013, no. 3, p. 03A011, 2013. doi:10.1093/ptep/pts083

[3] Y. Onishi, "SuperKEKB luminosity quest," in *Proc. eeFACT'22*, Frascati, Italy, Sep. 2022, paper MOXAT0103, this conference.

[4] K. Tsuchiya, N. Ohuchi, T. Ogitsu, T. Ozaki, and R. Sugahara, "Superconducting final focusing system for KEKB," in in *PACS2001. Proc. 2001 Particle Accelerator Conf. (Cat. No.01CH37268)*, Chicago, IL, USA, Jun. 2001, pp. 3633-3635. doi:10.1109/PAC.2001.988202

[5] K. Tsuchiya, T. Ogitsu, N. Ohuchi, T. Ozaki, N. Toge, and H. Sakurabata, "Superconducting magnets for the interaction region of KEKB," *IEEE Trans. Appl. Supercond.*, vol. 9, no. 2, pp. 1045–1048, 1999. doi:10.1109/77.783476

[6] N. Ohuchi *et al.*, "SuperKEKB beam final focus superconducting magnet system," *Nucl. Instrum. Methods Phys. Res. Sect. A*, vol. 1021, p. 165930, 2022. doi:10.1016/j.nima.2021.165930

[7] Y. Arimoto *et al.*, "Magnetic measurement with single stretched wire method on SuperKEKB final focus quadrupoles," in *Proc. IPAC'19*, Melbourne, Australia, May 2019, pp. 432-435. doi:10.18429/JACoW-IPAC2019-MOPMP006

[8] T. Oki, N. Tokuda, T. Adachi, N. Ohuchi, and S. Nakamura, "Full-scale prototype power supply for SuperKEKB final focus superconducting magnets," *IEEE Trans. Appl. Supercond.*, vol. 26, no. 4, p. 0601404, 2016. doi:10.1109/TASC.2016.2523058

[9] R. Hanft, B. Brown, D. Herrup, M. Lamm, A. McInturff, and M. Syphers, "Studies of time dependence of fields in tevatron superconducting dipole magnets," *IEEE Trans. Magn.*, vol. 25, no. 2, pp. 1647–1651, 1989. doi:10.1109/20.92616

[10] H. Brück *et al.*, "Time dependence of persistent current effects in the superconducting hera magnets," in *11th Int. Conf. on Magnet Technology (MT-11)*, vol. 1, 1990, pp. 141–146. doi:10.1007/978-94-009-0769-0_24

[11] C. Liu, D. Bruno, A. Marusic, M. Minty, P. Thieberger, and X. Wang, "Mitigation of persistent current effects in the rhic superconducting magnets," *Phys. Rev. Accel. Beams*, vol. 22, p. 111003, 2019. doi:10.1103/PhysRevAccelBeams.22.111003

ISBN: 978-3-95450-236-3 ISSN: 2673-7027 doi:10.18429/JACoW-eeFACT2022-WEZAT0204

STATUS OF INTERACTION REGION MAGNETS FOR CEPC*

Chuang Shen[1,2], Yingshun Zhu[†,1,2], Xiangchen Yang[1], Ran Liang[1], Fusan Chen[1,2], Wei Zou[3], Yi Wan[3], Xinlian Wu[3]
[1] Key Laboratory of Particle Acceleration Physics and Technology, Institute of High Energy Physics, Chinese Academy of Science, Beijing, China
[2] University of Chinese Academy of Sciences, Beijing, China
[3] Hefei Keye Electrical Physical Equipment Manufacturing Co., Ltd, Hefei, China

Abstract

High gradient quadrupole magnets are required on both sides of the interaction points in the proposed Circular Electron Positron Collider (CEPC). There are three double aperture superconducting quadrupoles with a crossing angle between two aperture centerlines of 33 mrad. It is challenging to meet stringent design requirements, including limited space, magnetic field crosstalk between two apertures, magnetic field gradients up to 142 T/m, etc. In this paper, status of superconducting magnets in CEPC interaction region in the technical design stage is described. Magnetic design of superconducting quadrupole magnet with three kinds of quadrupole coil structures, including cos2θ coil, CCT coil, and Serpentine coil is presented and compared. In addition, the development status of a single aperture short model quadrupole magnet with a magnetic length of 0.5 m is presented.

INTRODUCTION

To further study Higgs particles, Chinese physicists put forward a plan to build a Circular Electron Positron Collider (CEPC). Since the publication of CEPC conceptual design report (CDR) in 2018 [1], related research is going on. To pursue higher collision luminosity, accelerator physicists proposed a CEPC technical design report (TDR) based on the CEPC CDR study [2]. The superconducting quadrupole magnet QD0 is divided into two superconducting quadrupole magnets Q1a and Q1b. As shown in Fig. 1, compact high gradient quadrupole Q1a, Q1b and Q2 are required on both sides of the collision points. Q1a, Q1b and Q2 are double aperture quadrupoles and are operated fully inside the solenoid field of the detector magnet which has a central field of 3.0 T. To minimize the effect of the longitudinal solenoid field on the accelerator beam, anti-solenoids before Q1a and compensating solenoid outside Q1a, Q1b and Q2 are needed [3]. Their magnetic field direction is opposite to the detector solenoid, and the total integral longitudinal field generated by the detector solenoid and anti-solenoid coils is zero. It is also required that the total solenoid field inside the Q1a, Q1b and Q2 magnet aperture be close to zero.

*Work supported by the National Natural Science Foundation of China under contract 11875272.
† yszhu@ihep.ac.cn

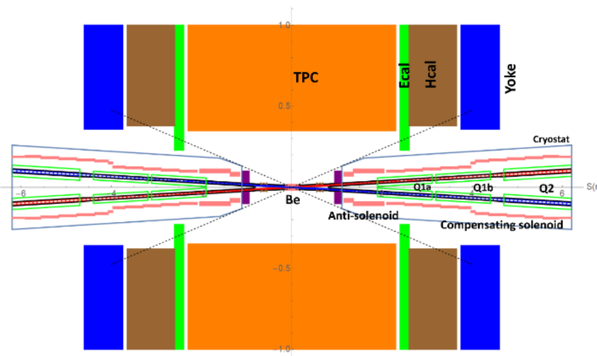

Figure 1: Layout of CEPC TDR interaction region (TPC = Time Projection Chamber, Ecal = Electromagnetic Calorimeter, Hcal = Hadronic Calorimeter, Be = beam tube near the IP. The dotted line refers to the included angle of the outer contour of cryostat).

SUPERCONDUCTING MAGNET ELECTROMAGNETIC DESIGN

Quadrupole Magnet Q1a Design

The first double-aperture quadrupole magnet Q1a was moved forward to a position 1.9 m from the interaction point (IP). The minimum distance between two aperture centerlines is only 62.71 mm, so a very limited radial space is available. The gradient of superconducting magnet Q1a is required to be 142 T/m, and the magnetic length is 1.21 m. The magnetic field harmonics in the good field region are required to be less than 5×10^{-4}. The field crosstalk of the two apertures in Q1a with such a small aperture separation distance is serious, and the dipole field at the center of each aperture is required to be less than 3 mT. The design requirements of the double aperture superconducting quadrupole magnet Q1a are listed in Table 1.

Table 1: Design requirements of the double aperture superconducting quadrupole magnet Q1a.

Item	Value	Unit
Field gradient	142.3	T/m
Magnetic length	1210	mm
Reference radius	7.46	mm
Minimum distance between two aperture centerlines	62.71	mm
High order field harmonics	$\leq5\times10^{-4}$	
Dipole field at the center of each aperture	≤3	mT

ISBN: 978-3-95450-236-3 ISSN: 2673-7027 doi:10.18429/JACoW-eeFACT2022-WEZAT0204

In the layout of CEPC TDR interaction region, the combined superconducting magnet is placed on a cantilever support, and then goes deep into the Detector. Such a magnet fixing method places strict requirements on the weight of superconducting magnets. It is most desirable to remove all iron yoke and keep only coils, so that the weight of the superconducting magnet can be minimized. Two electromagnetic design schemes are studied, one is a pure coil magnet structure without iron yoke, and the other is a magnet structure with iron yoke outside the coil.

Cos2θ Quadrupole Coil

In the cos2θ quadrupole coil, Rutherford cable made of 0.5 mm NbTi strand is used. The establishment of the 2D model and the magnetic field calculation are performed by ROXIE [4]. The design of magnet Q1a is based on two-layer cos2θ quadrupole coil and the two blocks in each layer are separated by wedge. The Rutherford cable with a trapezoidal angle of 2.1 degrees is twisted by 10 NbTi strands. The two-dimensional simulation model of the single-aperture model Q1a is shown in Fig. 2. The inner and outer radius of the coil are 20 mm and 25.65 mm, and the distance between the two layers is 0.35mm. The design current in Rutherford cable is 2650 pA and the peak field in coil is 3.572 T.

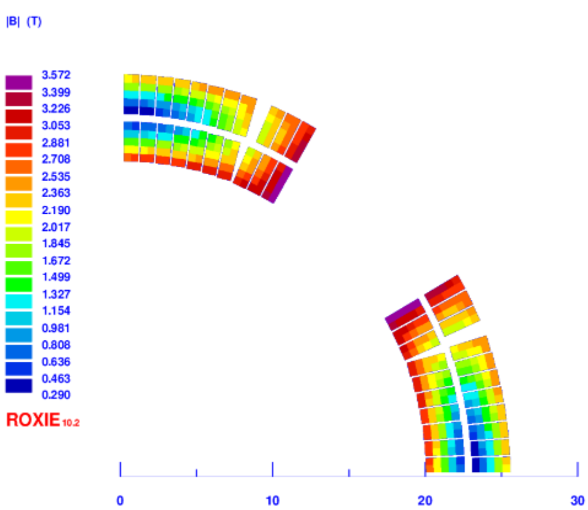

Figure 2: Layout of 2D cos2θ quadrupole coils without iron yoke.

As shown in Fig. 3, under the condition that the coil layout is unchanged, the iron yoke made of FeCoV is added outside the coil to enhance the field gradient, reduce the coil excitation current, and shield the field crosstalk. The inner and outer radius of the iron yoke are 30.5 mm and 44 mm. After adding the iron yoke, the exciting current in Rutherford cable is 2020 A and the peak field in coil is 3.413 T.

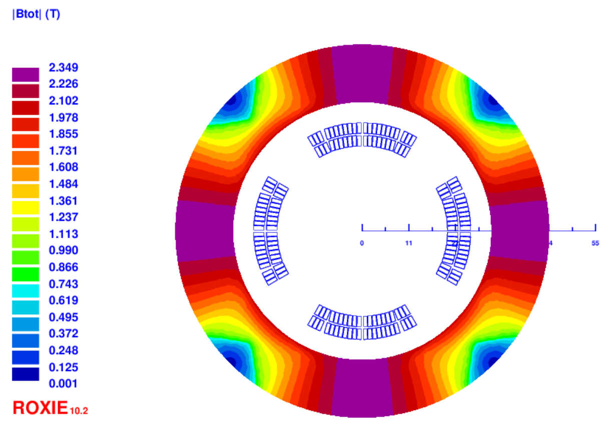

Figure 3: Layout of 2D cos2θ quadrupole coils with iron yoke.

CCT Quadrupole Coil

In CCT quadrupole coil option, the coil is wound by 10 NbTi strands in the form of 2×5, and the diameter of a single NbTi strand is 0.5 mm. In order to save the calculation time in 3D, the model is simplified, and one rectangular conductor is used instead of 10 strands. The cross-sectional size of the coil is 1 mm × 2.5 mm, and the electrical characteristic parameter is the average effect of 10 strands on the cross-section [5]. The inner radius of first layer coil is 22 mm and the inner radius of second layer coil is 25.5 mm. The single-aperture magnet consists of two layers of coils and its OPERA coil simulation results is shown in Fig. 4 [8]. The design current in each strand is 472.5 A and the peak field in the coil is 4.25 T.

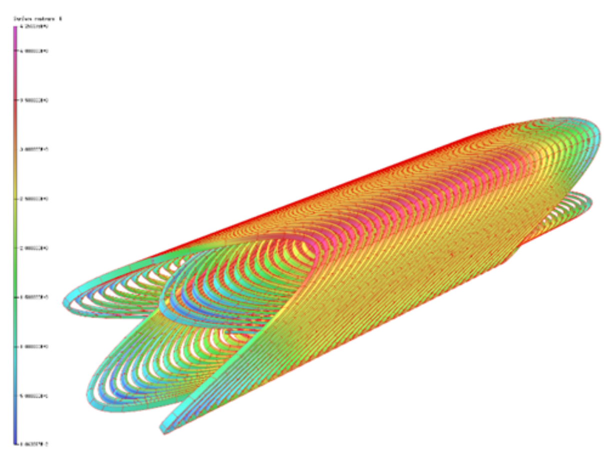

Figure 4: Simulation model of CCT quadrupole coil without iron yoke.

As shown in Fig. 5, the iron yoke made of FeCoV is added outside the coil. The inner radius and outer radius of the iron yoke are 30.5 mm and 44 mm, respectively. The exciting current in each strand drops to 324 A and the peak field in the coil is 3.783 T.

65th ICFA Adv. Beam Dyn. Workshop High Luminosity Circular e⁺e⁻ Colliders eeFACT2022, Frascati, Italy JACoW Publishing
ISBN: 978-3-95450-236-3 ISSN: 2673-7027 doi:10.18429/JACoW-eeFACT2022-WEZAT0204

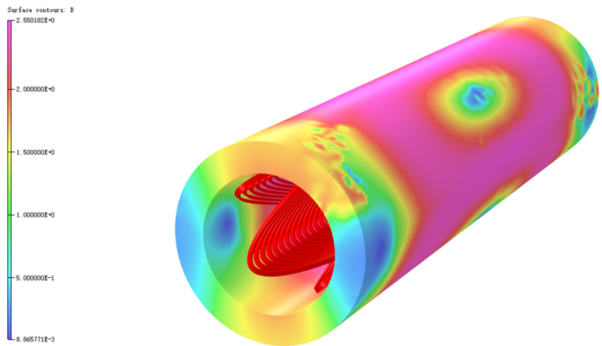

Figure 5: Simulation model of CCT coil with iron yoke.

Serpentine Quadrupole Coil

The serpentine quadrupole coil consists of eight layers of coils. The coil is directly wound by superconducting NbTi strands with a diameter of 0.5 mm [7]. The coil section arrangement is shown in Fig. 6. The design current in each strand is 480 A and the peak field in the coil is 4.2 T.

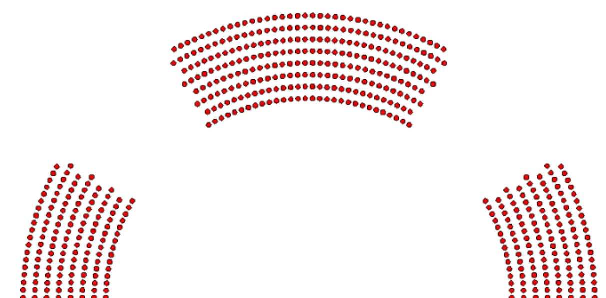

Figure 6: Layout of serpentine coil without iron yoke.

As shown in Fig. 7, the iron yoke made of FeCoV is added outside the coil. The inner radius and outer radius of the iron yoke are 30.5 mm and 44 mm. The exciting current in each strand drops to 334 A and the peak field in the coil is 3.8 T.

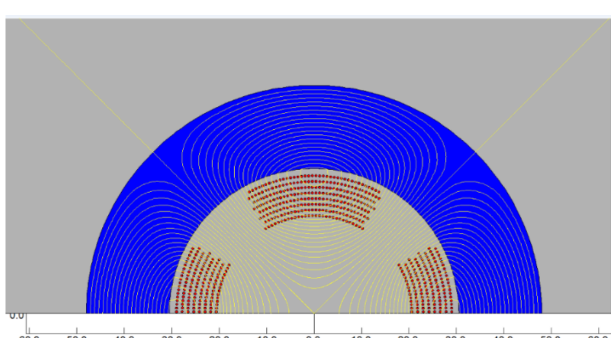

Figure 7: Layout of serpentine coil with iron yoke.

Table 2 lists the key performance parameters of the three coils. Based on the physical requirements of Q1a, all three coil structures were designed using 0.5 mm diameter NbTi strand. Under the same physical requirements, the operation current in the strand of cos2θ quadrupole coil is the smallest and the peak field in the cos2θ coil is the smallest. Therefore, cos2θ quadrupole coil is used as the baseline scheme of superconducting quadrupole magnet in CEPC interaction region, while racetrack coil and CCT coil are two alternative schemes.

Table 2: Electromagnetic performance comparison of three kinds of quadrupole coils

Coil type	Cos2θ coil	CCT coil	Serpentine coil
Gradient (T/m)	142.17	142.75	142.5
I_strand (A)	265	472.5	480
Peak field in coil (T)	3.572	4.251	4.2
After adding FeCoV iron yoke outside coil:			
Gradient (T/m)	142.4	140.8	142.3
I_strand (A)	202	324	334
Peak field in coil (T)	3.413	3.783	3.8

Crosstalk Between Two Apertures

Two single aperture quadrupole magnets are distributed at an angle of 33 mrad, 1.9 meters away from the interaction point. The field crosstalk between the two apertures will introduce a dipole field at the center of each aperture, which is far greater than 3 mT, reaching about 100 mT. The dipole field at the center of the aperture along the longitudinal direction is shown in Fig. 8. Not only cos2θ quadrupole coil has cross talk problems, but also CCT quadrupole coil and serpentine quadrupole coil have similar situation.

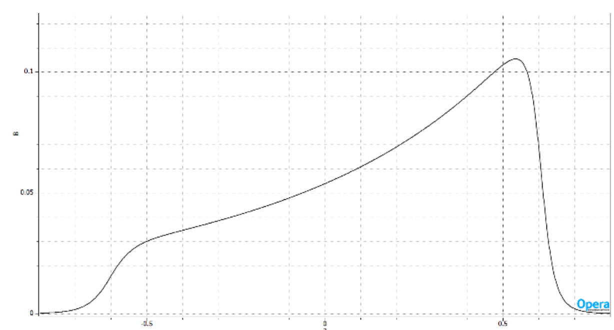

Figure 8: Dipole field along the centerline of each aperture in 3D calculation.

Therefore, in our baseline design, iron yoke is added outside the coil to enhance the field gradient, reduce the coil excitation current, and shield the field crosstalk. The two apertures of Q1a magnet are designed according to the same polarity, magnetic field gradient and field quality requirements in each aperture. There is not enough space to place two single apertures side by side, so a compact double aperture magnet design is adopted in Fig. 9. The two single apertures intersect in the middle part and the iron yoke made of FeCoV is shared by the two apertures. At the end closed to IP of magnet Q1a, the maximum dipole field at the center of each aperture is 2 mT, which meets the design requirement.

ISBN: 978-3-95450-236-3 ISSN: 2673-7027 doi:10.18429/JACoW-eeFACT2022-WEZAT0204

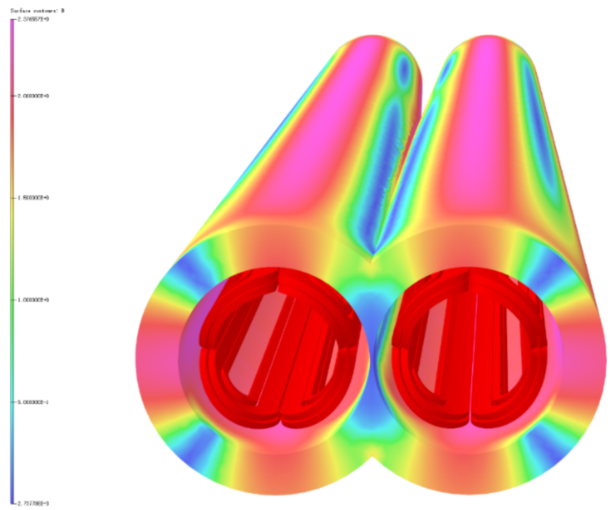

Figure 9: Simulation model of double aperture magnet Q1a.

The important design parameters including the mechanical size parameters, the electromagnetic parameters and the force analysis of the double aperture magnet Q1a are listed in Table 3.

Table 3: Electromagnetic design results of the double aperture superconducting quadrupole magnet Q1a

Magnet name	Q1a-double aperture
Field gradient (T/m)	142.41
Magnetic length (m)	1211.80
Coil turns per pole	21
Excitation current (A）	2020
Coil layers	2
Conductor	Rutherford Cable, width 2.5 mm, mid thickness 0.93 mm, keystone angle 2.1 deg, Cu:Sc=1.3, 10 strands
Maximum dipole field at the center of each aperture (mT)	2.497
Stored energy (KJ) (double aperture)	11.5
Inductance (mH）	5.64
Peak field in coil (T)	3.413
Load line	78.79%
Integrated field harmonics	b_6 = -0.61 b_{10} = -0.24
Coil inner diameter (mm)	40
Coil outer diameter (mm)	51.3
Yoke outer diameter (mm)	88
X direction Lorentz force/octant (kN)	62.33
Y direction Lorentz force/octant (kN)	-58.59
Net weight (kg)	93

Quadrupole Magnet Q1b Design

The double-aperture quadrupole magnet Q1b was moved forward to a position 3.19 m from the interaction point (IP). The minimum distance between the centerlines of two apertures is 105.28 mm. The gradient of superconducting magnet Q1b is required to be 85.4 T/m, and the magnetic length is 1.21 m. The magnetic field harmonics in the good field region are required to be less than 5×10^{-4}. The dipole field at the center of each aperture is required to be less than 3 mT. The design requirements of the double aperture superconducting quadrupole magnet Q1b are list in Table 4.

Table 4: Design requirements of the double aperture superconducting quadrupole magnet Q1b

Item	Value	Unit
Field gradient	85.4	T/m
Magnetic length	1210	mm
Reference radius	9.085	mm
Minimum distance between two aperture centerlines	105.28	mm
High order field harmonics	≤5×10^{-4}	
Dipole field at the center of each aperture	≤3	mT

In the cos2θ quadrupole coil structure, Rutherford cable made of 0.5 mm NbTi strand is used. The baseline design of magnet Q1b is based on two-layer cos2θ quadrupole coil. The first layer coil consists of one block and the two blocks of second layer are separated by wedge. The Rutherford cable with a trapezoidal angle of 1.9 degrees is twisted by 12 NbTi strands. The two-dimensional simulation model of the single-aperture model Q1b is shown in Fig. 10. The inner and outer radius of the coil are 26 mm and 32.15 mm, and the distance between the two layers is 0.35 mm. The design current of Rutherford cable is 1590 A and the peak field in coil is 2.675 T. The iron yoke made of FeCoV is added outside the collar to enhance the field gradient, reduce the coil excitation current and shield the field crosstalk. The inner and outer radius of iron yoke are 39 mm and 51.7 mm.

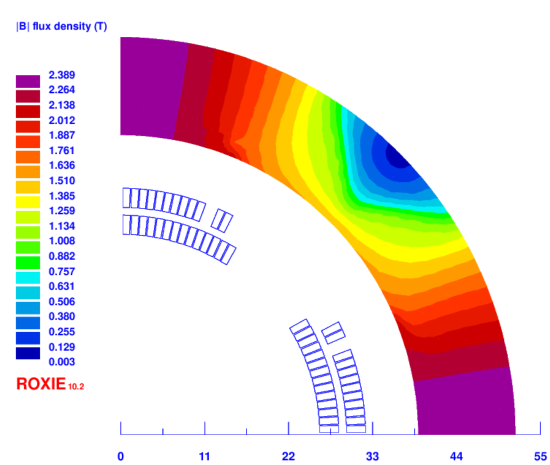

Figure 10: Layout of Q1b cos2θ quadrupole coils with iron yoke.

As shown in Fig. 11, the two apertures of Q1b magnet are designed according to the same polarity, magnetic field gradient and field quality requirements in each aperture. The minimum distance between the two apertures of the superconducting magnet Q1b is 105.28 mm, while the outer radius of the iron yoke is 51.7 mm, so the coils of two

ISBN: 978-3-95450-236-3 ISSN: 2673-7027 doi:10.18429/JACoW-eeFACT2022-WEZAT0204

apertures do not need to share the iron yoke like Q1a. The maximum dipole magnetic field at the center of each aperture is 2.3 mT.

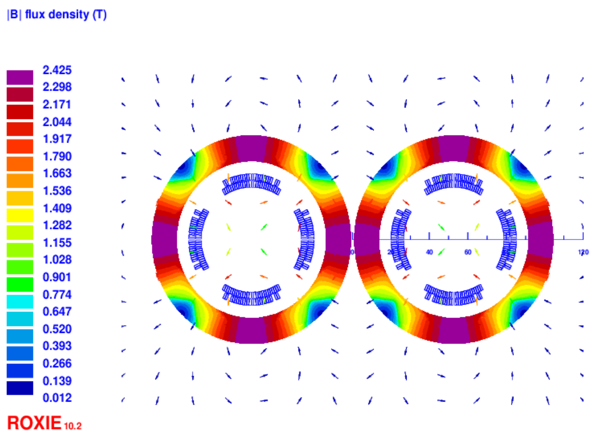

Figure 11: 2D layout of double aperture magnet Q1b near IP side.

The important design parameters including the mechanical size parameters, the electromagnetic parameters and the force analysis of the double aperture magnet Q1b are listed in Table 5.

Table 5: Electromagnetic design results of the double aperture superconducting quadrupole magnet Q1b

Magnet name	**Q1b-double aperture**
Field gradient (T/m)	85.5
Magnetic length (m)	1211.84
Coil turns per pole	26
Excitation current (A)	1590
Coil layers	2
Conductor	Rutherford Cable, width 3 mm, mid thickness 0.93 mm, keystone angle 1.9 deg, Cu:Sc=1.3, 12 strands
Maximum dipole field at the center of each aperture (mT)	2.301
Stored energy (KJ) (double aperture)	11.03
Inductance (mH)	8.75
Peak field in coil (T)	2.675
Load line	55.93%
Integrated field harmonics	$b_6 = 0.25$ $b_{10} = -0.14$
Coil inner diameter (mm)	52
Coil outer diameter (mm)	64.3
Yoke outer diameter (mm)	104
X direction Lorentz force/octant (kN)	45.86
Y direction Lorentz force/octant (kN)	-44.69
Net weight (kg)	124

Quadrupole Magnet Q2 Design

The double-aperture quadrupole magnet Q2 was moved forward to a position 4.7 m from the interaction point (IP). The minimum distance between two aperture centerlines is 155.11 mm. The gradient of superconducting magnet Q2 is required to be 96.7 T/m and the magnetic length is 1.5 m. The magnetic field harmonics in the good field region are required to be less than 5×10^{-4}. Considering the field crosstalk of the two apertures, the dipole field at the center of each aperture is required to be less than 3 mT. The design requirements of the double aperture superconducting quadrupole magnet Q2 are list in Table 6.

Table 6: Design requirements of the double aperture superconducting quadrupole magnet Q2

Item	**Value**	**Unit**
Field gradient	96.7	T/m
Magnetic length	1500	mm
Reference radius	12.24	mm
Minimum distance between two aperture centerlines	155.11	mm
High order field harmonics	$\leq5\times10^{-4}$	
Dipole field at the center of each aperture	≤3	mT

In the cos2θ quadrupole coil structure, Rutherford cable made of 0.5 mm NbTi strand is used. The design of magnet Q2 is based on two-layer cos2θ quadrupole coil. Each layer of coil has only one block. The Rutherford cable with a trapezoidal angle of 1.9 degrees is twisted by 12 NbTi strands. The two-dimensional simulation model of the single-aperture model Q2 is shown in Fig. 12. The inner and outer radius of the coil are 31 mm and 37.65 mm, and the distance between the two layers is 0.35mm. The design current in Rutherford cable is 1925 A and the peak field in coil is 3.656 T. The iron yoke made of FeCoV is added outside the collar to enhance the field gradient, reduce the coil excitation current, and shield the field crosstalk. The inner radius and outer radius of iron yoke are 44 mm and 63.2 mm.

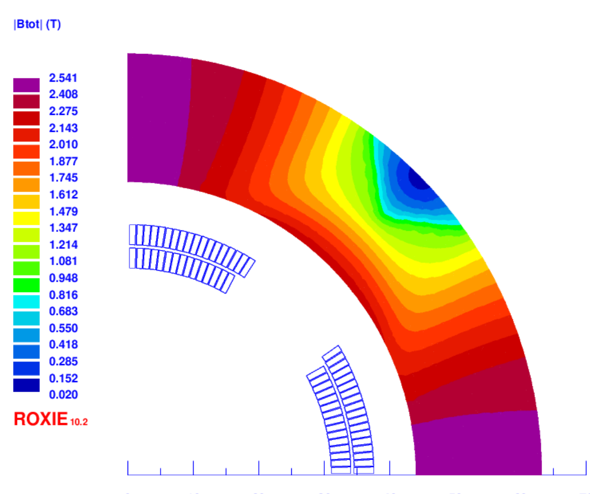

Figure 12: Layout of Q2 cos2θ quadrupole coil with iron yoke.

As shown in Fig. 13, the two apertures of Q2 magnet are designed according to the same polarity, magnetic field gradient and field quality requirements in each aperture. The minimum distance between the two apertures of the

ISBN: 978-3-95450-236-3 ISSN: 2673-7027 doi:10.18429/JACoW-eeFACT2022-WEZAT0204

superconducting magnet Q2 is 155.11mm, while the outer radius of the iron yoke is 63.2 mm, so the coils of two apertures do not need to share the iron yoke. The maximum dipole field at the center of each aperture is 2.54 mT.

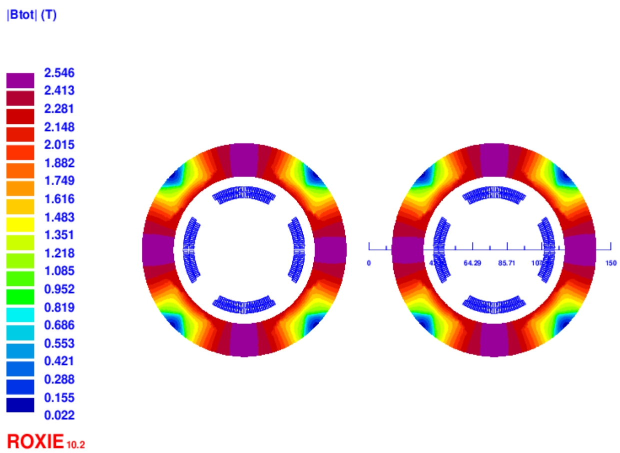

Figure 13: 2D Layout of double aperture magnet Q1b near IP side.

The important design parameters including the mechanical size parameters, the electromagnetic parameters and the force analysis of the double aperture magnet Q1b are listed in Table 7.

Table 7: Electromagnetic design results of the double aperture superconducting quadrupole magnet Q2

Magnet name	Q2-double aperture
Field gradient (T/m)	97.7
Magnetic length (m)	1502.08
Coil turns per pole	33
Excitation current (A）	1925
Coil layers	2
Conductor	Rutherford Cable, width 3 mm, mid thickness 0.93 mm, keystone angle 1.9 deg, Cu:Sc=1.3, 12 strands
Maximum dipole field at the center of each aperture (mT)	2.5401
Stored energy (KJ) (double aperture)	33.28
Inductance (mH）	18.19
Peak field in coil (T)	3.656
Load line	72.05 %
Integrated field harmonics	b_6 = -0.52 b_{10} = -0.49
Coil inner diameter (mm)	62
Coil outer diameter (mm)	75.30
Yoke outer diameter (mm)	126.4
X direction Lorentz force/octant (kN)	126.94
Y direction Lorentz force/octant (kN)	-112.68
Net weight (kg)	235

Anti-solenoid Design

The design of anti-solenoid is basically the same as in CDR [1]. The anti-solenoid is divided into a total of 29 sections with different inner coil diameters. The central field of the first section anti-solenoid is the strongest, with a peak value of 6.8 T. The net solenoid field inside quadrupole at each longitudinal position is smaller than 300 Gs [9]. As shown in Fig. 14, the total integral solenoid field generated by the detector solenoid and anti- solenoid coils is zero.

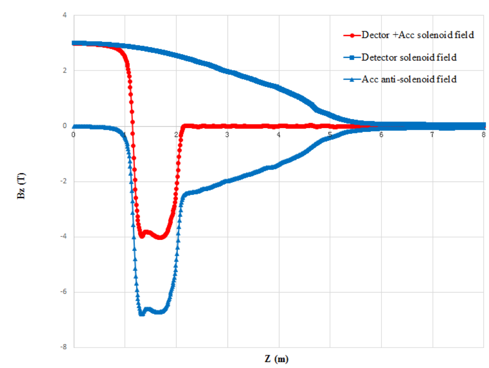

Figure 14: Magnetic field distribution of solenoid field.

Status of 0.5 m Single Aperture Short Model Quadrupole

In the R&D, the first step is to study and master main key technologies of superconducting quadrupole magnet by developing a short model magnet with 0.5 m length (near IP side). Research on main key technologies of 0.5 m single aperture quadrupole model has started (NbTi, 136 T/m), in collaboration with HeFei KEYE Company, including quadrupole coil winding technology, fabrication of quadrupole coil with small diameter, stress control, quadrupole magnet assembly, cryogenics vertical test and field measurement technology, etc.

Manufacture of 0.5 m single aperture short model quadrupole has been completed in HeFei KEYE in August 2022. Then, the magnet has been transported to IHEP. Rotating coil magnetic field measurement has been done with 4 A current at room temperature. Cryogenic excitation test at 4.2 K in the vertical Dewar will be performed in future, to verify whether high magnetic field gradient can be achieved.

Figure 15: 0.5 m single aperture short model magnet.

ISBN: 978-3-95450-236-3 ISSN: 2673-7027 doi:10.18429/JACoW-eeFACT2022-WEZAT0204

CONCLUSION

Superconducting magnets in interaction region are key devices for CEPC. Despite of limited space and high field gradient, field crosstalk effect between two apertures is negligible using iron yoke. According to the physical design requirements of double aperture superconducting magnet Q1a, the electromagnetic design of three alternative coil schemes is completed. Under the condition that the superconducting strands are identical, the electromagnetic performances of cos2θ coil, CCT coil and serpentine coil are compared. From the comparison results, cos2θ quadrupole coil has a lower excitation current and a smaller peak field in the coil. Therefore, the superconducting quadrupole magnets in CEPC TDR interaction region adopt cos2θ coil with iron yoke as the baseline. The high-order field harmonics in superconducting quadrupole magnets Q1a, Q1b and Q2 are less than 5×10^{-4}. The calculated dipole field at the center of the aperture is less than 3 mT. Manufacture of 0.5 m single aperture short model quadrupole has been completed, and cryogenic excitation test will be performed in the future.

REFERENCES

[1] The CEPC Study Group, "CEPC Conceptual Design Report: Voume 1 - Accelerator," *arxiv:1809.00285*, 2018. doi:10.48550/arxiv.1809.00285

[2] Gao Jie, "CEPC and SppC Status—From the completion of CDR towards TDR," *Int. J. Mod. Phys. A*, vol. 36, no. 22, p. 2142005, 2021. doi:10.1142/S0217751X21420057

[3] C. Shen, Y. Zhu, and F. Chen, "Design and Optimization of the Superconducting Quadrupole Magnet Q1a in CEPC Interaction Region", *IEEE Trans. Appl. Supercond.*, vol. 30, no. 6, p. 4004804, 2022. doi:10.1109/TASC.2022.3163684

[4] B. Auchmann, "ROXIE 10.2," 2010. https://espace.cern.ch/roxie/Lists/New%20in%20Version%2010/AllItems.aspx

[5] S. Caspi *et al.*, "Canted–Cosine–Theta Magnet (CCT) - A Concept for High Field Accelerator Magnets," *IEEE Trans. Appl. Supercond.*, vol. 24, no. 3, p. 4001804, 2014. doi:10.1109/TASC.2013.2284722

[6] W. Wu *et al.*, "Multipole magnets for the HIAF fragment separator using the Canted-Cosine-Theta (CCT) geometry," *Journal of Physics: Conference Series*, vol. 1401, no. 1, p. 012015, 2020. doi:10.1088/1742-6596/1401/1/012015

[7] B. Parker and J. Escallier, "Serpentine Coil Topology for BNL Direct Wind Superconducting Magnets," in *Proc. of PAC'05*, pp. 737-739, 2005. doi:10.1109/PAC.2005.1590546

[8] Dassault systems, "Opera 2020," 2020. https://www.3ds.com/products-services/simulia/products/opera/

[9] Y. Zhu *et al.*, "Final Focus Superconducting Magnets for CEPC," *IEEE Trans. Appl. Supercond.*, vol. 30, no. 4, p. 4002105, 2020. doi:10.1109/TASC.2020.2973110

ISBN: 978-3-95450-236-3 ISSN: 2673-7027 doi:10.18429/JACoW-eeFACT2022-WEZAS0202

SuperKEKB BEAM INSTABILITIES CHALLENGES AND EXPERIENCE

H. Ikeda*[1,2], H. Fukuma[1], T. Kobayashi[1,2], T. Mimashi[1,2], T. Mitsuhashi[1], G. Mitsuka[1,2], S. Sasaki[1], M. Tobiyama[1,2]
[1] High Energy Accelerator Research Organization (KEK), Tsukuba, Japan
[2] SOKENDAI, Tsukuba, Japan

Abstract

KEKB was upgraded from 2011 over 5 years in order to increase the luminosity and started SuperKEKB commissioning in 2018 after the test operation. In order to cope with large beam currents and small beam sizes, various updates have been applied to the beam instrumentation system. This talk summarizes the performance of beam instrumentation in SuperKEKB Phase-III and challenges to it.

INTRODUCTION

SuperKEKB is a collider with 7 GeV electrons (HER) and 4 GeV positrons (LER). The circumference of the ring is 3 km and many beam instrumentation system are installed as shown in Table 1 [1]. Aiming at the world's highest luminosity, we adopted the nanobeam method. Therefore, as design values, we adopted a squeeze of βy^* by 20 and a beam current by 2 relative to KEKB ones, and recorded a peak luminosity two times larger than KEKB [2]. Among various improvements related to beam monitors to get higher luminosity, we will focus on improvements related to synchrotron radiation monitors (SRM) and beam loss monitors (LM) in this paper.

SYNCHROTRON RADIATION MONITOR

We use emission-light from the bending magnet that located last part of the arc section of electron and positron rings. An extraction chamber is set at 23 m downstream of the source bending magnet. A diamond mirror is inserted in the chamber as shown in Fig.1. The emission-light is sent through an optical window and several transfer mirrors to an optical hut for various measurements.

We replaced the extraction mirrors for better measurements, and introduced a coronagraph for beam halo measurements and an injection beam measurement system using the same optics system as the coronagraph.

Diamond Mirror

An extraction mirror of visible light is made of diamond to suppress the thermal deformation. We developed a single crystal diamond mirror and made efforts to suppress the current dependence of thermal deformation, but the mirror had not only the current dependence of the deformation at high currents, but also some deformations made during manufacturing process at the beginning of SuperKEKB [3]. We made a new thick polycrystalline diamond mirror that is not easily deformed by heat, then installed it in 2020 [4].

Resistance to thermal deformation of the new mirror is similar to single crystal and its reflectance is high because the coating is changed from gold to platinum. As the result, we succeeded to obtain a sufficient amount of light for beam profile measurement of each bunch, and it became possible to measure the beam halo and injection beam for each turn.

Table 1: SuperKEKB Beam Instrumentation System

System	Quantity HER	LER	DR
Beam position monitor (BPM)	466	444	83
Displacement sensor	110	108	0
Transverse bunch feedback system	2	2	1
Longitudinal bunch feedback system	0	1	0
Visible SR size monitor	1	1	1
X-ray size monitor	1	1	0
Beamstrahlung monitor	1	1	0
Betatron tune monitor	2	2	1
Beam loss monitor		207	34
DCCT	1	1	1
CT	1	1	0
Bunch current monitor	1	1	1

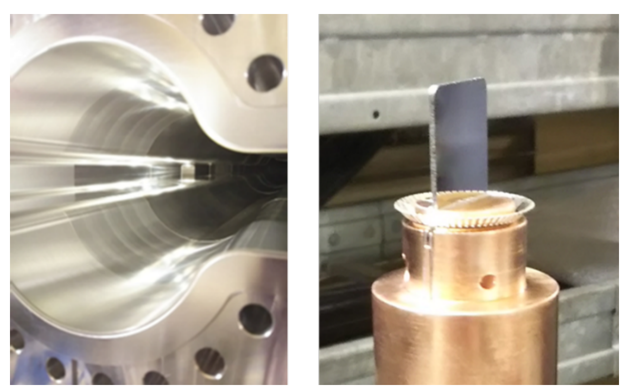

Figure 1: Extraction chamber (left) and Diamond mirror (right).

Coronagraph

Beam halo may cause unexpected beam loss or long-term irradiation leading to luminosity degradation and damage to accelerator components. Understanding and hopefully lowering beam halos have been attempted in

* hitomi.ikeda@kek.jp

ISBN: 978-3-95450-236-3 ISSN: 2673-7027 doi:10.18429/JACoW-eeFACT2022-WEZAS0202

high-power and/or high-luminosity accelerators. Our challenge is non-invasive measurements of beam halo with sensitivity better than 1e-5. Thus the coronagraph was introduced to SRM for that purpose [5]. Figure 2 shows the schematic view of the coronagraph. In order to eliminate chromatic aberration, the objective lens system adopts a reflective mirror system rather than a refractive lens system. An opaque disk was inserted to hide beam core and second stage was set as re-diffraction. Diffraction fringes of objective lens aperture is shown in Fig. 3. After blocking the diffraction fringes by the Lyot stop, we can observe the beam halo. Figure 4 shows the image of beam core, diffraction fringes and the re-diffraction fringes blocked by Lyot stop measured by a gated camera. Figure 5 shows the bunch current dependence of HER beam. Some parts look particularly bright because the center of the opaque disk and the center of the beam are not aligned due to changes of the beam orbit. Diffraction fringes made by the optics after the Lyot stop and leakage of diffraction fringes by the diamond mirror also remain. Figure 6 shows a comparison of halos between HER and LER with beam core shown overlapping. The halos look different although the measured beam current is a similar value.

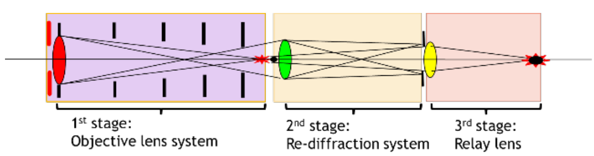

Figure 2: Schematic view of Coronagraph.

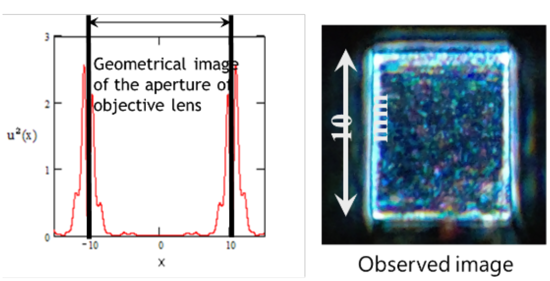

Figure 3: Left: Calculation of diffraction patterns. Right: The aperture images of the re-diffraction system.

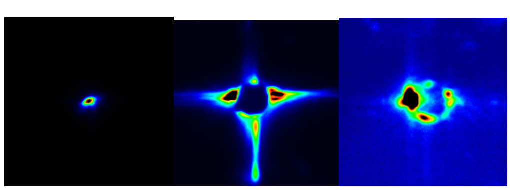

Figure 4 : Image of beam core (left), core blocked by a Φ 3 mm disk (center) and re-diffraction fringes blocked by the Lyot stop (right).

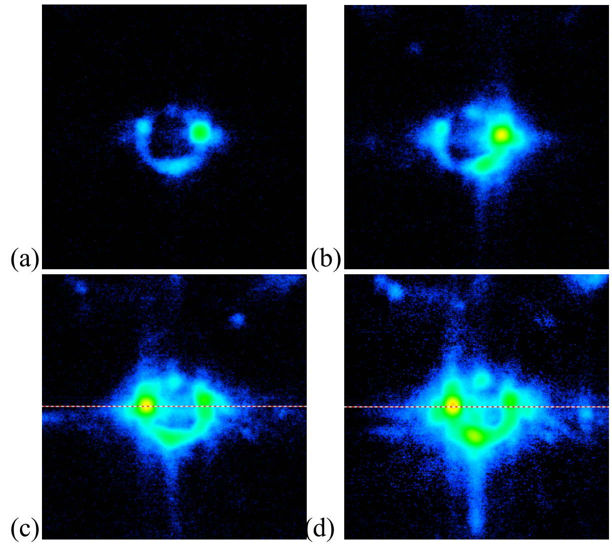

Figure 5: Bunch current dependence of re-diffraction image ((a) 0.055 mA/bunch, (b) 0.15 mA/bunch, (c) 0.28 mA/bunch and (d) 0.55 mA/bunch).

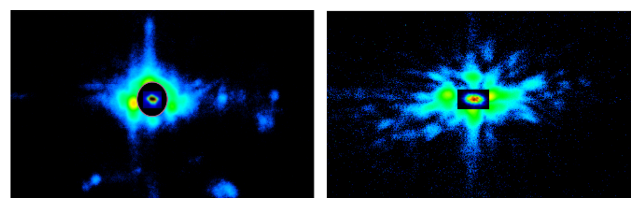

Figure 6: Comparison of halos between HER (left) and LER (right) with overlapped beam core.

The sensitivity in beam halo measurement was estimated to be order of 10^{-6} by measuring the brightness of the beam core and beam tail and scaling them with the current value used for the measurement.

Injection Beam Measurement

When the injection efficiency becomes unstable, it becomes difficult to accumulate the beam and the background to the Belle II detector increases, which interferes with physics experiments. It is important to observe how the injection beam circulates the ring usually and prepare for the measurement of difference with worth efficiency injection beam. Since it became possible to measure the beam in bunch by bunch, we tried to see the state of the injection beam. Object system designed for the coronagraph was used to measure the injection beam as shown in Fig. 7. Single-turn injection was applied to the HER beam. (Each injection kicks out the previously injected bunch. Then the ring always has only one bunch). We measured the beam shape in each turn after injection by using the gated camera.

ISBN: 978-3-95450-236-3 ISSN: 2673-7027 doi:10.18429/JACoW-eeFACT2022-WEZAS0202

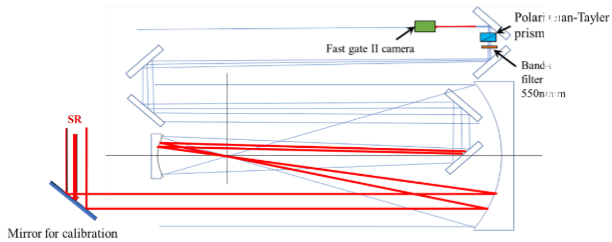

Figure 7: Gregorian objective for observation of injection beam f=7028 mm.

Calibration was performed using a stored beam reducing gate width of the gated camera when the beam was stable. The mirror was placed on a cross roller stage equipped with a micro-meter and moved horizontally by ± 15 mm to change the position on the screen. This movement corresponds to moving the beam virtually. The result is shown in Fig. 8. The error bars due to measurement re-producibility are smaller than the circles of the plot, and the variability of circles at the same position comes from the displacement of the beam due to the difference in measurement time. No large distortion is seen on the photoelectric surface of the CCD camera.

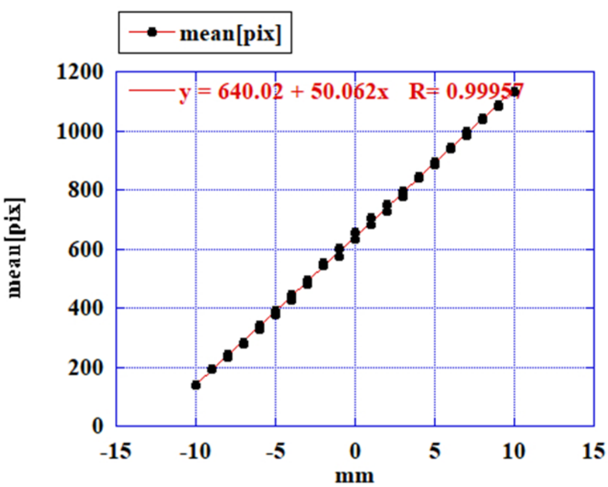

Figure 8: Calibration result of gated camera.

Horizontal beam size for each turn of the injection beam after the calibration is shown in Fig. 9 (a). The injection beam repeatedly expands and contracts and damped after 10,000 turns (10 ms). The beam size is including the diffraction effect in this measurement. Figure 9 (b), (c) show the injection beam oscillation. It can be seen that the amplitude becomes stable while oscillating with a width of about ± 4.5 mm at the maximum.

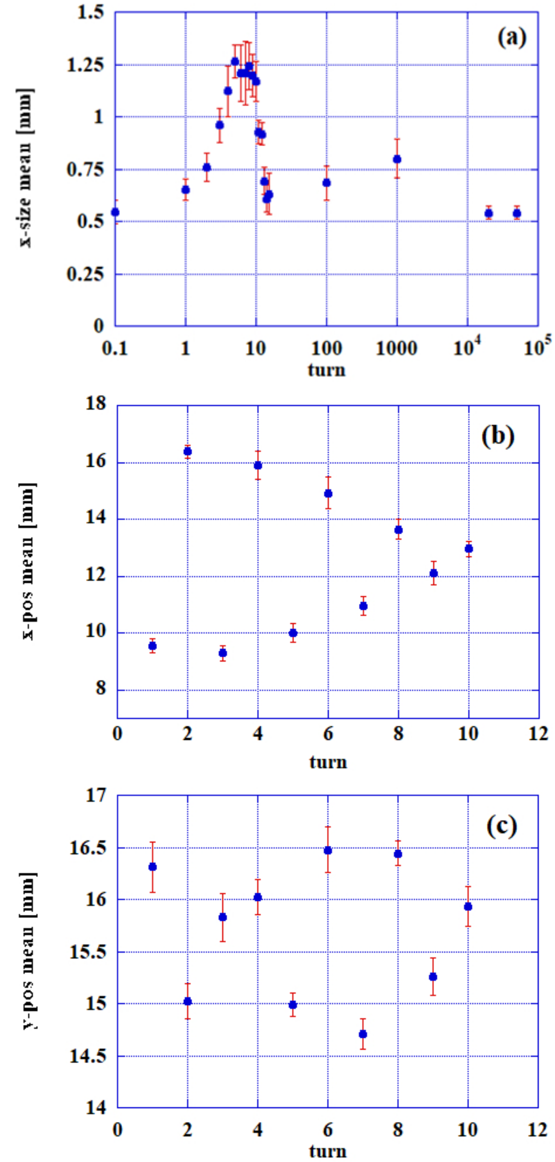

Figure 9: (a) Horizontal beam size, (b) horizontal beam position, (c) and vertical beam position for each turn after injection.

BEAM LOSS MONITOR

We have to protect the hardware components of the detector and the accelerator from the damage caused at high beam currents. The fast beam abort system is developed in the SuperKEKB in order to abort the beam as soon as possible when the abnormal situation happens. And also we need to investigate the cause of abnormalities in the beam and deal with them. In both cases, a combination of loss monitors and other monitors are important.

ISBN: 978-3-95450-236-3 ISSN: 2673-7027 doi:10.18429/JACoW-eeFACT2022-WEZAS0202

Loss Monitor System

Loss monitor (LM) measures the beam loss to be used for triggering the beam abort kicker, tuning and analysis of the beam operation [7]. We are using ion chambers (IC) and PIN photodiodes (PD) as a sensor. ICs are put to cable lacks of all over the tunnel to cover a wide range in space. PDs have fast response and can identify the ring in which the beam loss occurred. The PDs are mainly located downstream of collimators which have narrow apertures in the ring. LM signals from the whole ring are collected at five local control rooms (LCRs). Abort trigger signal is generated in integrators at LCRs and the generation time for beam abort is faster than 2 µs.

We have introduced optical fibers as a new loss monitor in order to deal with "sudden beam loss" which will be described later. Since the LM signal is sent to 5 LCRs around the ring, the cable length is not minimised. In order to send abort signals at the minimum distance, the optical fibers were laid in the power supply building closest to the downstream side of the collimator where beam loss is most often detected as shown in Fig. 10. The fiber is input to a PMT module and light is converted to electrical signals which generate an abort trigger signal. Figure 11 shows the signals from the fiber when the sudden beam loss occurred.

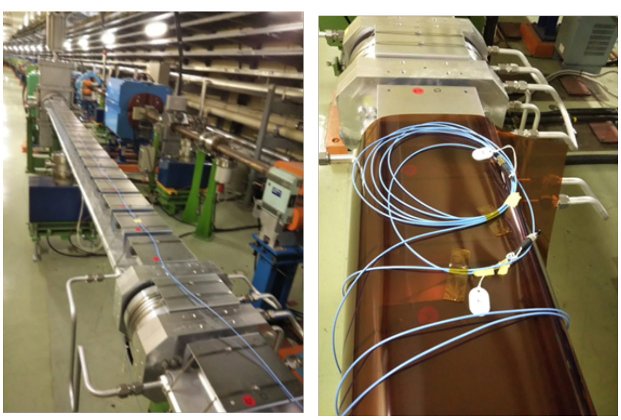
Figure 10: Optical fiber setting in the ring.

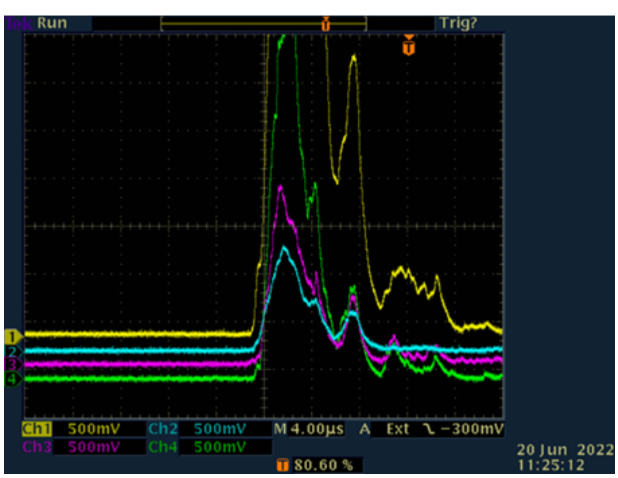

Figure 11: Signal of the optical fiber loss monitor.

Abort System

In order to protect the hardware components against the high beam currents, we installed the controlled abort system [8, 9]. The beam abort kicker consists of several magnets as shown in the Fig. 12. The beam is kicked by an abort kicker, taken out of the vacuum chamber through an abort window made of Ti, and led to a beam dump. Duration of dumped beam is 10µs which corresponds to one revolution time. Build-up time of the abort kicker magnet is 200 ns and we have to put empty bucket space (abort gap) larger than the built-up time. Synchronization of the kicker timing and the abort gap is required for the protection of hardware.

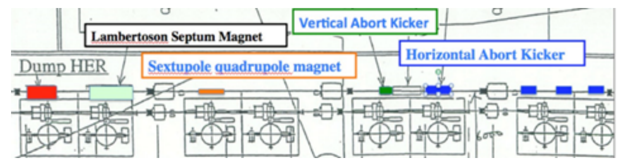

Figure 12: SuperKEKB abort kicker system.

Figure 13 shows the flow of time from the signal output of each trigger source to charging of the abort kicker and kicking all the beams out of the ring. We minimized the abort trigger time to protect the hardware damage as follows [10].

We introduced the injection veto system to PD LM to set lower threshold and for the abort trigger to be issued quickly. Also we changed the signal route of the LM installed at the downstream of one collimator that frequently issues abort triggers so as to send the abort trigger signal earlier. Since new fiber LM mentioned above is close to the abort kicker, it was a great time saver. In order to minimize delay to synchronize to the abort gap, unnecessary fixed delays were removed and the number of abort gap in the beam train was increased from one to two. As a result of reducing the time required in the abort system as much as possible, the delay time, which took 21 to 39 µs at the beginning of commissioning, was reduced to 17 to 30 µs.

Sudden Beam Loss

The biggest goal of SuperKEKB is to increase luminosity, but one of the obstacles is sudden beam loss. The cause of the sudden large beam loss is unclear, but it causes collimator (and other component) damage, QCS quench, large background to Belle-II. We also cannot storage a large current since it causes beam abort. Then we started a task force to investigate and resolve the cause of the sudden beam loss.

We checked the loss monitor signals at the abort occurred, which abort was thought to be caused by beam loss. The beam loss looks started within one turn at the collimators in whole ring and the Belle II detector We checked the loss monitor signals at the abort occurred, which abort was thought to be caused by beam loss. The beam loss looks started within one turn at the collimators in whole ring and the Belle II detector.

ISBN: 978-3-95450-236-3 ISSN: 2673-7027 doi:10.18429/JACoW-eeFACT2022-WEZAS0202

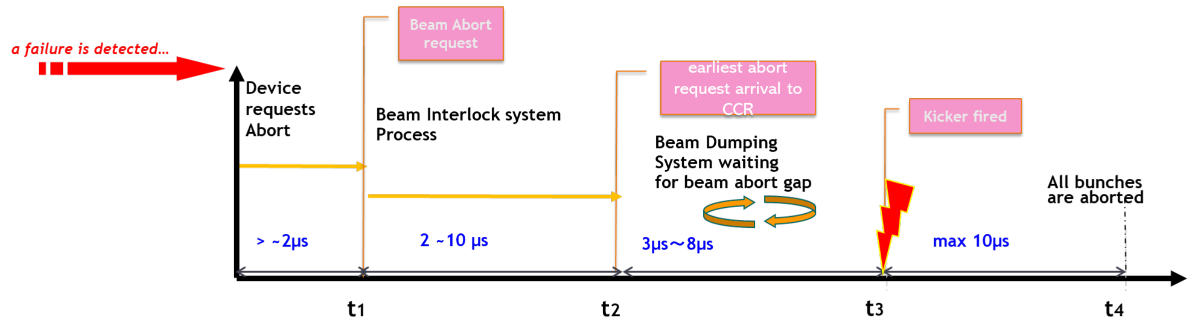

Figure 13: Time delay of the abort trigger flow.

In order to investigate where in the train the beam loss started at the moment of beam loss, we recorded the bunch current 4096 turns before the abort trigger using feedback processors [11]. Beam loss measured by the bunch current monitor (BCM) occurred suddenly on a certain turn as shown in Fig. 13. Beam loss occurs in both HER and LER, but the damage to the hardware is particularly large when loss occurs in LER. We don't know if it will happen even with a single beam operation, low current beam because we haven't operated for a long time. In order to find out where in the ring the beam loss first started, we installed loss monitors specialized for timing measurement inside the ring. Beam loss occurs in collimator and near interaction point, and where it occurs first depends on collimator tuning [12]. The Bunch oscillation is measured 4096 turns before the abort trigger using the feedback processors and the orbit is calculated from the data. The orbit changed on the order of 1mm at the feedback position. It is likely to occur when a bunch current is exceeded a level. The bunch current was around 0.7 mA at first, but after the collimator was damaged the current limit looks decrease. We checked many other monitors but there are no signs before beam loss starting such as small beam loss, beam oscillation, beam size change and it is not clear if the orbit changed significantly. Pressure bursts have been observed here and there, and it rarely occurs in the same place except in the collimator section. It may be the result of the abort, not the reason. Acoustic waves were detected at the time of collimator beam loss, but since we only measured a few events before shutdown, we will continue the measurements.

There is no evidence that the place where the beam loss first occurred is the same or close as the place where the causative phenomenon occurred. One of the causes of beam loss seen in KEKB and other accelerators is damage of vacuum component such as RF fingers in which case change of beam phase (beam energy losses) had been observed ms to hundreds of μs before aborts [13,14]. Abnormal temperature risings at bellows chambers had been observed and the catastrophic damages in the RF finger had been confirmed. It is proposed that the metal particles scattered by the arc discharge collided with the beam. Such a phenomenon could not be measured in this sudden beam loss. At the early stage of SuperKEKB, beam loss due to dust was observed [15-17]. However, after cleaning or tapping the vacuum chamber to remove as much dust as possible, the number of such events decreased. Since the growth time of conventional instabilities would be order of more than tens of turns, they do not match the cause of the current sudden beam loss.

A hypothesis that can cause the beam loss in a few turns is the "fireball" seen in RF cavities [18, 19]. A microparticle with a high sublimation point is heated by the beam-induced field and becomes fireball. Plasma is generated around the fireball after the fireball touches some metal surface with low sublimation point. The plasma grows up into a macroscopic vacuum arc, possibly leading to significant interactions with the beam particles.

We plan to continue discussions, including other possibilities and simulations.

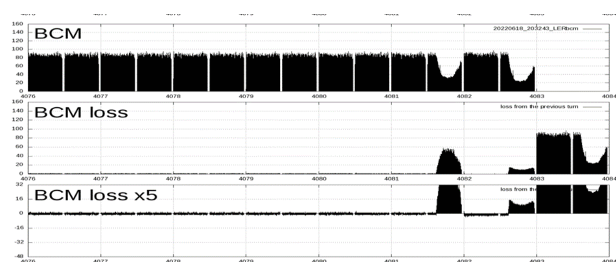

Figure 13: An example of a bunch current when a sudden beam loss occurs. First plot is a bunch current distribution, second plot is a bunch current difference from previous turn and third plot is 5 times of second plot.

CONCLUSION

By replacing the light extraction mirrors for both the electron ring and the positron ring, the image of the beam can be clearly focused, and the smaller charge beam can be measured turn by turn. We developed coronagraphs in SuperKEKB enabling non-invasive and high-sensitivity measurements for beam halo. Some beam halos are observed in both HER and LER and the sensitivity was ~O(1e-6) compared with the beam core. We also prepared a system for observing the behaviour of the injection beam in the ring when the injection efficiency becomes unstable. It was observed that the injection beam size was dumped while oscillating even when the beam condition was stable. The reference data was measured in the study mode, which can measure only the injection beam in a single turn injection and by masking the stored beam, it is

ISBN: 978-3-95450-236-3 ISSN: 2673-7027 doi:10.18429/JACoW-eeFACT2022-WEZAS0202

possible to measure some injection condition even during collision operation.

In order to protect the hardware from dangerous beam loss, we speeded up the abort trigger by increasing the number of abort gap, introducing injection veto for LM, changing the cable route and introducing new LM.

One of the obstacles for luminosity increasing is sudden beam loss and the cause of the beam loss is still unclear. We are investigating with loss monitors and other monitors, but no phenomena that clarify the cause have been found. We started the international task force to investigate and resolve the cause of the sudden beam loss.

REFERENCES

[1] "Beam Instrumentation", in SuperKEKB Design Report, 2014, `https://www-linac.kek.jp/linac-com/report/skb-tdr/9_BeamInstrumentation2020_10_19.pdf`

[2] Y. Funakoshi *et al.*, "The SuperKEKB Has Broken the World Record of the Luminosity", in *Proc. IPAC'22*, Bangkok, Thailand, Jun. 2022, pp. 1-5. `doi:10.18429/JACoW-IPAC2022-MOPLXGD1`

[3] J.W. Flanagan *et al.*, "Thermal Performance of Diamond SR Extraction Mirrors for SuperKEKB", in *Proc. IBIC'19*, Malmo, Sweden, Sep. 2019, pp. 332-335. `doi:10.18429/ JACoW-IBIC2019-TUPP01`

[4] G. Mitsuka, H. Ikeda, and T. M. Mitsuhashi, "Renovation of the SR Beam Profile Monitors with Novel Polycrystalline Diamond Mirrors at the SuperKEKB Accelerator", in *Proc. IPAC'22*, Bangkok, Thailand, Jun. 2022, pp. 313-315. `doi:10.18429/JACoW-IPAC2022-MOPOPT031`

[5] G. Mitsuka, H. Ikeda, and T. M. Mitsuhashi, "Design and Construction of Optical System of the Coronagraph for Beam Halo Observation in the SuperKEKB", in *Proc. IPAC'22,* Bangkok, Thailand, Jun. 2022, pp. 769-771. `doi:10.18429/JACoW-IPAC2022-TUOXGD1`

[6] H. Ikeda, T. M. Mitsuhashi, and G. Mitsuka, "Injection Beam Measurement Using Synchrotron Radiation Monitor at the SuperKEKB Electron Ring", in *Proc. IPAC'22*, Bangkok, Thailand, Jun. 2022, pp. 3121-3123. `doi:10.18429/JACoW-IPAC2022-FROXGD3`

[7] H. Ikeda, M. Arinaga, J. W. Flanagan, H. Fukuma, and M. Tobiyama, "Beam Loss Monitor at SuperKEKB", in *Proc. IBIC'14*, Monterey, CA, USA, Sep. 2014, paper TUPD22, pp. 459-462.

[8] T. Mimashi *et al.,* "SuperKEKB Beam abort System", in *Proc. IPAC'14*, Dresden, Germany, Jun. 2014, pp. 116-118. `doi:10.18429/JACoW-IPAC2014-MOPRO023`

[9] T. Mimashi *et al.*, "Performance of SuperKEKB High Energy Ring Beam Abort System", in *Proc. IPAC'17*, Copenhagen, Denmark, May 2017, pp. 2939-2942. `doi:10.18429/JACoW-IPAC2017-WEPIK012`

[10] H. Ikeda, T. Mimashi, S. Nakamura, T. Oki, and S. Sasaki, "Fast Trigger System for Beam Abort System in SuperKEKB", in *Proc. IPAC'22*, Bangkok, Thailand, Jun. 2022, pp. 754-756 `doi:10.18429/JACoW-IPAC2022-MOPOMS048`

[11] M. Tobiyama *et al.,* "Bunch by bunch feedback systems for SuperKEKB rings", in *Proc. of PASJ2016*, Chiba, Japan (2016), TUOM06.

[12] Y. Liu *et al.,* "Study of beam loss of SuperKEKB based on new loss monitor system for Belle II", presented at *JPS'22,* Okayama, Japan, Sep. 2022.

[13] Y. Suetsugu, "Experiences on High Current", presented at the *9th KEKB Acc. Review*, KEK, February 16-18, 2004, `https://www-kekb.kek.jp/MAC/2004/`

[14] Y. Funakoshi, "KEKB status", presented at the *11th KEKB Acc. Review*, KEK, March 21-23, 2006, `https://www-kekb.kek.jp/MAC/2006/`

[15] Y. Suetsugu *et al.*, "First commissioning of the SuperKEKB vacuum system", *Phys. Rev. Accel. Beams*, vol. 19, p. 121001, 2016. `doi:10.1103/PhysRevAccelBeams.19.121001`

[16] Y. Suetsugu *et al.,* "SuperKEKB main ring vacuum system status until the end of Phase-2 commissioning", *J. Vac. Sci. Technol., A*, vol. 37, p. 021602, 2019. `doi:10.1116/1.5083928`

[17] S. Terui *et al.*, "Observation of Pressure Bursts in the SuperKEKB Positron Ring", in *Proc. IPAC'18*, Vancouver, Canada, Apr.-May 2018, pp. 2830-2832. `doi:10.18429/JACoW-IPAC2018-WEPML058`

[18] T. Abe, "Minuscule Gremlins Cause Vacuum Breakdown in Radio-Frequency Accelerating Cavities", *KEK Accelerator Laboratory Topics* 2019-01-22, 2019, `https://www2.kek.jp/accl/eng/topics/topics190122.html`

[19] T. Abe, T. Kageyama, H. Sakai, Y. Takeuchi and K. Yoshino, "Direct observation of breakdown trigger seeds in a nor-mal-conducting rf accelerating cavity", *Phys. Rev. Accel. Beams,* vol. 21, no.12, 122002, 2018. `doi:10.1103/PhysRevAccelBeams.21.122002`

65th ICFA Adv. Beam Dyn. Workshop High Luminosity Circular e⁺e⁻ Colliders eeFACT2022, Frascati, Italy JACoW Publishing
ISBN: 978-3-95450-236-3 ISSN: 2673-7027 doi:10.18429/JACoW-eeFACT2022-WEZAS0203

BEAM INSTRUMENTATION CHALLENGES FOR FCC-ee

E. Carideo, T. Lefevre, S. Mazzoni, A. Schlögelhofer, M. Wendt*, CERN, Geneva, Switzerland
B. Härer, G. Niehues, M. Reißig, A.-S. Müller, KIT, Kalrsruhe, Germany
U. Iriso, ALBA-CELLS, Bellaterra, Spain
T. Mitsuhashi, KEK, Tsukuba, Japan
M. Siano, University of Milano, Milano, Italy

Abstract

For the accelerator-based future of high energy physics at the energy frontier, CERN started to investigate a 92 km circumference Future Circular Collider (FCC), as e^+/e^- collider the FCC-ee will operate at beam energies up to 182.5 GeV. Beside the machine operational aspects, beam instrumentation will play a key role in verifying and optimizing the machine to achieve the ambitious beam parameters and quality. This paper gives a brief overview of the various challenges to develop the required beam instruments, with focus on beam position, beam size and bunch length measurements, and well as an outline of the planned R&D activities.

INTRODUCTION

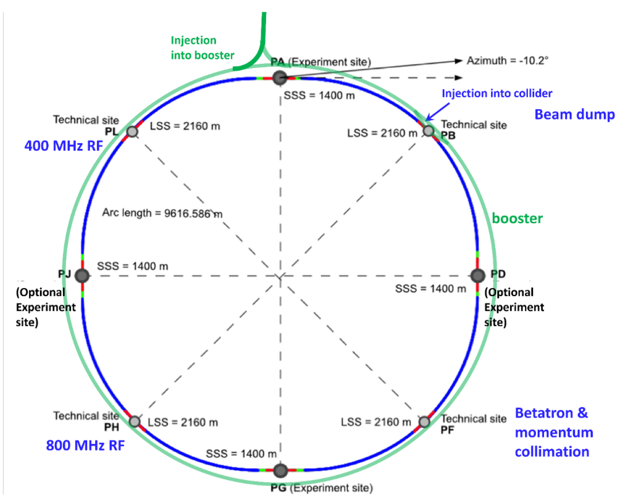

Figure 1: Layout of the main rings of FCC-ee.

The FCC-ee project [1] consists of two main rings and a booster ring in a tunnel of approximately 92 km circumference, plus the injectors and a positron source. For this discussion on the challenges and requirements of the FCC-ee beam instrumentation we focus on the main rings, see Fig. 1, which – with except of the large circumference – has many aspects in common with 4th-generation synchrotron light sources.

Table 1 lists those FCC-ee beam parameters which are particular relevant for the beam instrumentation, with the red highlighted values presenting the biggest challenges.

* manfred.wendt@cern.ch

Table 1: FCC-ee beam parameters relevant to beam instrumentation.

Parameter (4 IPs, t_{rev} = 304 μs)	Value
circumference [km]	91.18
max. beam energy [GeV]	182.5
max. beam current [mA]	1280
max. # of bunches/beam	10000
min. bunch spacing [ns]	25 (15)
max. bunch intensity [10^{11}]	2.43
min. H geometric emittance [nm]	0.71
min. V geometric emittance [pm]	1.42
min. H rms IP spot size [μm]	8
min. V rms IP spot size [nm]	34
min. rms bunch length SR/BS [mm]	1.95 / 2.75

BEAM POSITION MEASUREMENT

The two main rings and the booster ring together will need a total of approximately 7000 beam position monitors (BPM), distributed along the ~90 km FCC-ee tunnel. In the arcs, the preferred location of the button-style BPM pickups is next to the quadrupole, with the BPM body rigidly fixed to the pole shoes at one end of the magnet. An study currently investigates the integration of the BPM pickup with the quadrupole in a way that no extra space is required. While many details of the four, symmetrically arranged BPM pickup electrodes still need to be developed, a study to optimize new manufacturing processes of the the BPM body with the vacuum chamber made out of copper, together with the button RF UHV feedthrough have been initiated, see also Fig. 2.

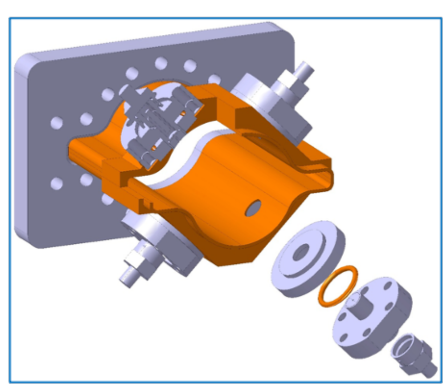

Figure 2: Manufacturing R&D for FCC-ee BPM pickups.

ISBN: 978-3-95450-236-3 ISSN: 2673-7027 doi:10.18429/JACoW-eeFACT2022-WEZAS0203

Being one of the large scale beam instrumentation systems, the FCC-ee BPM system not only needs to fulfill the core requirements like resolution and accuracy, but also has to be optimized along other aspects, such as segmentation of read-out electronics in the tunnel, costs, maintenance aspects, integration with other systems like RF, timing signals, corrector magnet power supplies, etc. The beam position data from BPM system will be used for the beam orbit feedback, therefore latency effects need to be considered.

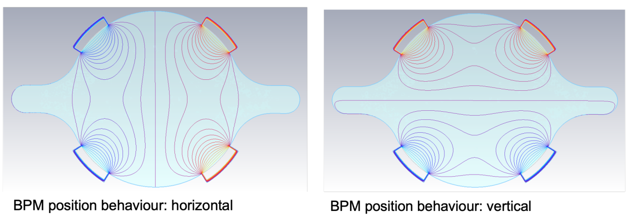

Figure 3: Lines of constant beam displacement of a button BPM, horizontal (left), vertical (right).

BPM Requirements

Some of the basic requirements for the BPM system have been discussed during the workshop and since, and of course, a formal BPM requirement document still has to be drafted. While some of those requirements are similar to those of the 4$^{\text{th}}$-generation synchrotron light sources, the 70 mm diameter of the FCC-ee vacuum chamber with it's "winglets" for the synchrotron light absorption is substantially larger, therefore results in a reduced the position sensitivity of the BPM, which is slightly below $2/R$ (with $R = 35$ mm) near the center of the vacuum chamber due to the "rotated" BPM pickup electrodes, see also Fig. 3.

Similar to the present LHC BPM system, the FCC-ee BPMs need to acquire bunch-by-bunch and turn-by-turn beam positions in a synchronized fashion, and report the beam orbit average value of the position data for all bunches in a turn over many turns. We currently assume a minimum bunch spacing of 25 ns for the FCC-ee, however, that value may be reduced down to 15 ns, see Table. 1.

Resolution A BPM orbit resolution of <1 µm is anticipated, while the turn-by-turn resolution should achieve 10 µm.

Accuracy A relative accuracy, i.e. not accounting for the BPM offset, in the range 1 . . . 10 µm seems feasible, but requires a correction of the non-linearities of the BPM pickup, see also Fig. 3.

Alignment & roll errors A stretched-wire based, electromagnetic pre-alignment of the integrated BPM-quadrupole module can substantially reduce alignment errors and allows to evaluate offset and roll-errors between the electromagnetic center of the BPM pickup and the magnetic center of the quadrupole [2–5]. Simulations indicate that alignment errors with x, y-offsets of ∼10 µm and rolls of 10 . . . 30 µrad can be tolerated.

IP BPM's

With nanometer beam size beams at the interaction point (IP), design and integration of the BPM's in the superconducting (SC) final focus quadrupoles becomes mission critical. Fortunately the e^+/e^- beam are already separated entering the final focus segmented SC quadrupole, therefore also those 3+3 BPMs pickups (per beam) can be realized as button-style. The warm bore of the quadrupole simplifies to some extend the challenges of the pickup, however, alignment, integration including cable routing and long-term stability issues need to be studied in detail as those BPMs have the tightest requirements.

Wakefield and Beam-Coupling Impedance

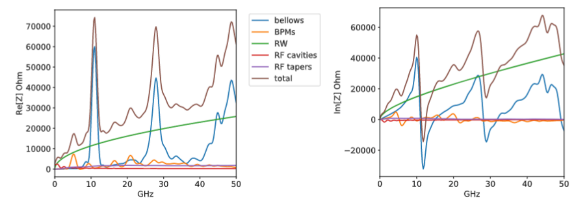

Figure 4: Real (left) and imaginary (right) part of beam-coupling impedance of different devices.
The total impedance is the sum of all the contributions.

Improving the accuracy of the beam impedance model of an accelerator is important to minimize beam instabilities and keep power losses under control. The total beam-coupling impedance for the FCC-ee, as well as the contribution of each device, is shown in Fig. 4 and in [6] the method utilised to calculate them is described.

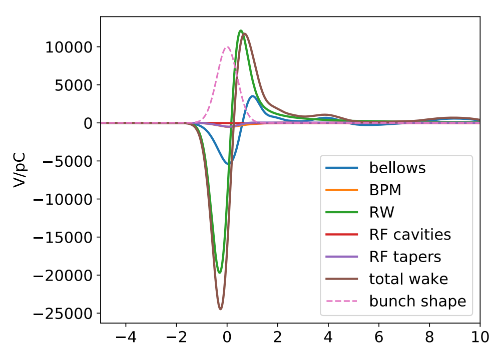

Figure 5: Wake potential of a 0.4 mm *Gaussian* bunch due to different devices and used as input for beam dynamics simulations.

We have calculated the contribution of impedance model of the machine devices that have been evaluated until now, shown in Fig 5. A mayor contributor to the total beam-coupling impedance is the resistive wall (RW) impedance of the beam pipe and bellows with the RF fingers necessary to guarantee good electrical contact between sections of the beam pipe. For the other devices, just the beam position

ISBN: 978-3-95450-236-3 ISSN: 2673-7027 doi:10.18429/JACoW-eeFACT2022-WEZAS0203

monitors show a small peak around 5 GHz, Fig.4 but we have to remind that this study is still a work in progress. For the moment, for the total contribution to the impedance budget the real number of bellows is still unknown but to be conservative we decided to overestimate the number of bellows distributed along the machine to 20000. In addition to the resistive wall and bellows, we also evaluated the contribution due to the 400 MHz RF system, consisting out of 52 single cell cavities arranged in groups of 4 for each cryomodule, which has, at each end, a 500 mm long taper section to ensure a smooth transition between the 50 mm and the 150 mm circular pipes inside the cryomodule. Finally, also the 4000 BPMs of the two main rings have been taken into account [7].

BEAM LOSS MEASUREMENT

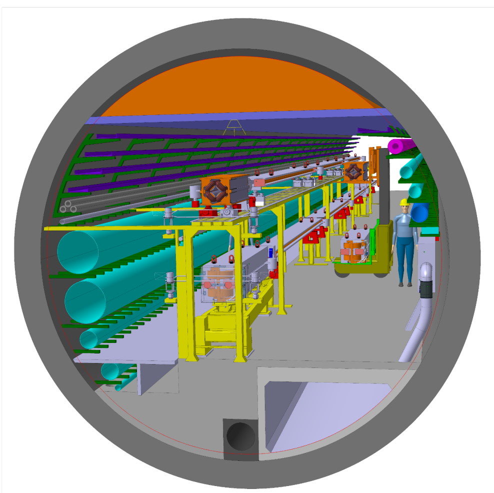

Figure 6: FCC-ee tunnel layout.

Dedicated R&D activities on the beam loss monitors (BLM) for the FCC-ee have not yet been started. However, the large energy stored in both, the two main rings and the booster ring requires a well defined machine protectino system (MPS), which needs to be supported by a BLM system. For the BLMs, several challenges need to be addressed:

- Distributed large scale system, consisting out of several thousand beam loss monitors.
- The BLMs in the FCC-ee arcs need to be insensitive to X-rays.
- The beam losses from the individual rings in the FCC-ee tunnel need to be identified. Figure 6 shows the close proximity of the three accelerator rings.

Several ideas are discussed to address the last point, to distinguish the beam losses – which expect to appear mostly near the quadrupole magnets – between the individual rings. An arc layout with the location of the booster quadrupoles longitudinally staged between the main ring quadrupoles would certainly help to address the problem.

Some of the BLM R&D done for Compact LInear Collider (CLIC) addresses the issue to disentangle losses from counter-travelling beams in close proximity [8–10], and recent studies of "optical *Cherenkov* fibers" at the CERN CLEAR beam test facility show promising results to detect particle losses with high directivity, see the principle illustrated in Fig. 7.

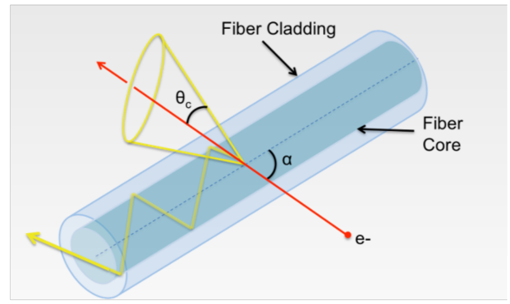

Figure 7: *Cherenkov* radiation from an optical fiber used as beam loss detector.

BEAM SIZE MEASUREMENT

A variety of R&D activities address the measurement of the small transverse beam size, which in the case of FCC-ee are as small as 5 . . . 7 µm in the vertical plane. The main challenges are then linked to the use of very high energy beams for which synchrotron radiation will suffer from diffraction effects and would require the use and detection of high energy X-rays. In addition, the small bending angle of main dipoles would make the photon extraction line particularly long and the very large beam current would also put high constrains on the impedance and heat load of the photon extraction vacuum vessel (mirrors and windows).

Beam Size Measurement R&D at KEK

Development of poly-crystal Diamond mirror for the SR monitor of FCC ee by using the SuperKEKB SR monitor The remarkable idea of a "single crystal diamond mirror" was developed as synchrotron radiation (SR) extraction mirror for SuperKEKB [11]. Diamond has an outstanding thermal conductivity, enabling to solve the biggest problem "how to suppress thermal deformation". But we still face the problem, thickness and size are limited to 0.5 mm and 10 mm × 10 mm, and due to this limit, we could not make a large mirror in the required high optical quality. Recently, an optical quality poly-crystal diamond material was developed and realized as larger and thicker bulk mirror. Using this material, a mirror of size 20 mm × 30 mm and 2 mm thickness was manufactured and tested in the SuperKEKB high energy ring (HER) SR monitor. The result of the optical testing showed a surface flatness is better than $\lambda/5$. The deformation during irradiation of SR was measured using a hole-array mask. As result, no significant deformation was observed for a beam current of 1200 mA in the storage ring. This mirror is now regularly used as SR monitor for SuperKEKB.

65th ICFA Adv. Beam Dyn. Workshop High Luminosity Circular e⁺e⁻ Colliders eeFACT2022, Frascati, Italy JACoW Publishing
ISBN: 978-3-95450-236-3 ISSN: 2673-7027 doi:10.18429/JACoW-eeFACT2022-WEZAS0203

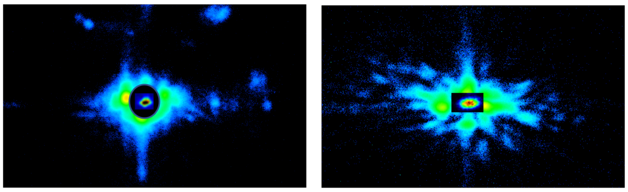

(a) HER, $I_{beam} = 0.57$ mA (b) LER, $I_{beam} = 0.61$ mA

Figure 8: Beam halo measurement at SuperKEKB, using a diamond mirror for the SR extraction.

Development of the coronagraph with long-focus *Gregorian* telephoto-objective system for beam halo observation For the observation of the beam halo a coronagraph was developed and manufactured. The coronagraph has three stages of optical systems, the objective system, the re-diffraction system and the relay system. Since the SR monitor should have a long optical path (a few hundred meter), we need an objective system with a long focal length [12]. Moreover, the entrance aperture is determined by the extraction mirror. Therefore, we must assign this aperture for the entrance pupil of the objective system. To satisfy these two conditions we developed a coronagraph with a reflective telephoto system based on the *Gregorian* telescope for the objective system to be utilized at SuperKEKB. The focal length is designed to be 7028 mm and front principal point position is designed to be at the location of the extraction mirror. As a result of this construction, the performance of the objective system has a diffraction limited quality. The re-diffraction system and relay system are designed based on the *Kepler* type telescope. As result of the optical testing using the beams in the HER and LER, we achieved a contrast better than 6-orders of magnitude betwee the beam core and the background. The observation of beam halo in the HER proofed to be rather simple, showing a smooth transition between the beam core continues to the beam tail, then to the halo, see Fig. 8a. In the LER we observed a more complicated distribution of beam halo as shown in Fig. 8b. In both Figures, 8a and 8b, the beam core image and the shadow of the opaque mask are superimposed to the halo image.

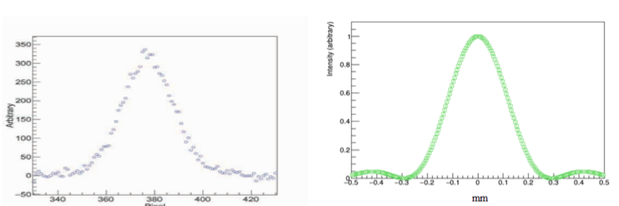

(a) Observed interferogram (hor. axis: 1 pixel ≡ 10 µm) (b) Simulation of the interferogram.

Figure 9: X-ray interferometer R&D at SuperKEKB, using an angular beam size of 2.7 µrad.

Development of a X-ray interferometer for the measurement of the apparent very small beam size in FCC-ee, using the X-ray monitor line in SuperKEKB FCC-ee is very large machine with a large bending radius, which makes a long distance between the beam source point and the observation point at the SR monitor necessary 3). The expected apparent angular beam size (the apparent angular size of the beam is defined as $\theta_s = \sigma/d$, with σ being the beam size and d the distance between the beam source point and the observation point) in FCC-ee is around 0.05 µrad. The best resolution achieved by popular instruments, such as the pinhole camera, the SR interferometer, etc. are about 0.5 µrad, still not sufficient to measure the apparent very small beam size of the FCC-ee [13]. An X-ray interferometer promises for a very high resolution due to short wavelength of the X-rays, typically 0.1 nm. We developed an X-ray interferometer utilizing the X-ray monitor line in the HER of SuperKEKB. A double slit of 15 µm in width and 30 µm in separation, realized on a 20 µm thick Au plate, was installed 10 m downstream the source point. The X-ray interferogram is observed 30 m downstream from the double slit by using a YAG fluorescence screen. The observation result of the interferogram for an angular beam size of 2.7 µrad (measured by the X-ray coded aperture) is shown in Fig. 9a. For comparison, the result of a simulation of the interferogram is shown in Fig. fig:XraySim. Since interference fringe is smeared-out by the rather large beam size, we could not observe a sign of the interference fringe in this test. In the next beam studies we will try the investigate the X-ray interferometer for a beam size <1.5 µrad.

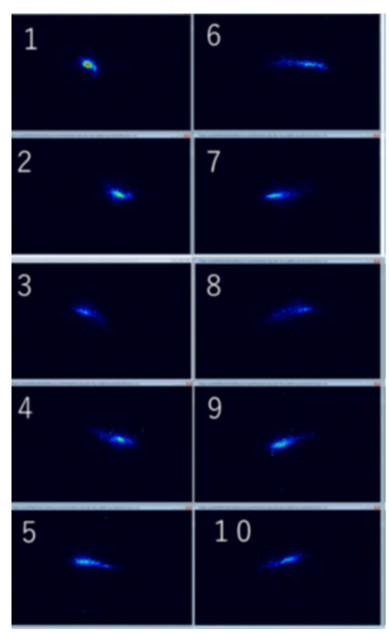

Figure 10: Profiles of the injected beam bunch for the 1st ten turns into the HER of SuperKEKB.

Fast gated camera Since the SuperKEKB operating tune is close to a half-integer, the bunches oscillate strongly

ISBN: 978-3-95450-236-3 ISSN: 2673-7027 doi:10.18429/JACoW-eeFACT2022-WEZAS0203

on a turn-by-turn basis. Utilizing the coronagraph, we can mask the stored beam profile. This setup enables to observe the injected beam profile in presence of stored beam. As a result of the observation of injected beam with a fast gated, image intensified camera, we now can measure the turn-by-turn instantaneous beam profile of a selected bunch. This apparatus is particular valuable for observing the turn-by-turn injected beam profile [14, 15]. We used the *Gregorian* reflective objective system developed for the coronagraph to obtain the images of the injected beam profile at SuperKEKB [15]. Figure 10 shows the injected beam profile of turns #1 to #10 in the HER after injection. The bunch profile using the coronagraph is shown in Fig. 11. This observation is very helpful for the injection tuning.

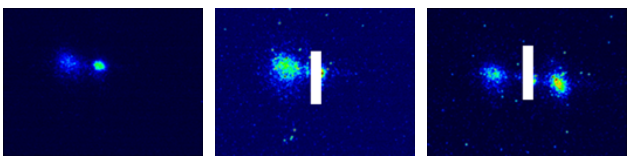

(a) Stored beam and injected 1st turn beam. (b) Masked stored beam, and injected 1st turn beam. (c) Masked stored beam, and injected 1st, 2nd turn beam.

Figure 11: Injected beam profile measured with the coronograph. In (b) and (c) the mask is indicated as white rectangle.

Beam Size Measurement R&D – 2D Heterodyne Near-Field Speckles

Recently, we have developed a novel interferometric technique to perform full 2D coherence mapping of X-ray synchrotron radiation, thus full 2D beam size measurements [16]. The method relies on Fourier analysis of the Heterodyne Near Field Speckles (HNFS) formed by interfering the weak spherical waves scattered by nanoparticles suspended in water with the intense trans-illuminating X-ray beam. This peculiar interference generates a stochastic intensity distribution known as a speckle pattern. The spatial power spectrum of such speckles exhibits peculiar oscillations, known as Talbot oscillations [17], whose envelope allows direct mapping of the full 2D coherence function of the incoming synchrotron light [16, 18, 19]. The 2D beam profile, as well as the horizontal and vertical beam sizes, is then retrieved by the Fourier transform of the measured 2D spatial coherence, under the conditions of applicability of the Van Cittert and Zernike theorem [20]. More in general, approaches based on statistical optics should be adopted [16, 21].

We have validated the technique at the NCD-SWEET undulator beamline at the ALBA synchrotron light source through a systematic measurement of the horizontal and vertical beam sizes as a function of the machine coupling parameter [16]. The experimental setup is sketched in Fig. 12(a). It is marked by simplicity, and does not require any dedicated X-ray optics. A typical example of acquired X-ray speckles is shown in Fig. 12(b), and the corresponding 2D power spectrum is reported in Fig. 12(c).

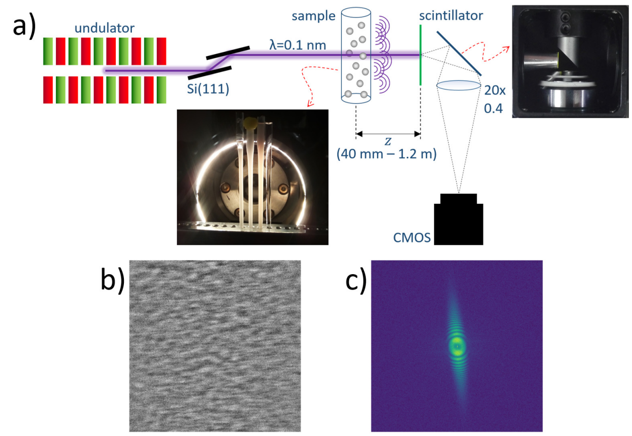

Figure 12: Sketch of the HNFS setup at the NCD-SWEET bemaline at ALBA (a). Measured X-ray speckles (b) and corresponding power spectrum (c) with 12.4 keV photons.

Thanks to the 2D mapping of the HNFS method, we can unambiguously identify and assess the horizontal and vertical beam sizes even in presence of misaligned optics, as indicated in Fig. 12(c) by the tilt of the power spectrum. Results are reported in Fig. 13 alongside with theoretical predictions, and prove that the HNFS method can be employed as a reliable technique to measure transverse beam sizes in a wide range of sizes, from a few micrometers up to more than 100 µm.

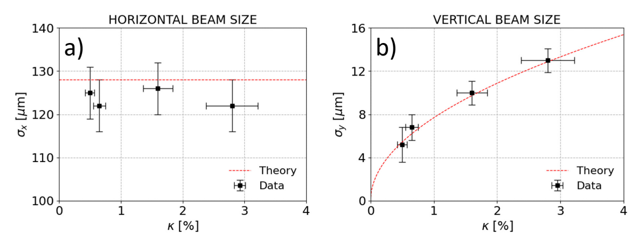

Figure 13: Measured horizontal (a) and vertical (b) beam size at the NCD-SWEET beamline as a function of the ALBA coupling parameter.

Laser Wire Scanner

Laser Wire Scanners (LWS) have already demonstrated their ability to measure micron beam sizes [22]. They use high power lasers that would interact with the primary beams and produce Compton scattered photons and electrons/positrons. LWS will be based on the same technologies, laser and detectors as the ones developed for the FCCee Compton polarimeter [23]. A different laser-beam interaction vacuum chamber would actually required for LWS and will be studied in the future.

BUNCH LENGTH MEASUREMENT

In the FCC-ee main rings, up to 10000, few mm long, bunches are colliding permanently. The amount of beam-

ISBN: 978-3-95450-236-3 ISSN: 2673-7027 doi:10.18429/JACoW-eeFACT2022-WEZAS0203

strahlung photons emitted during collision is large and generates an even larger increase in bunch length, up to 14 mm in the worse case scenario when colliding at 45 GeV beam energy. To maintain the collision rate at the highest level, a top-up injection scheme is proposed, injecting new short bunches in RF buckets populated with longer colliding bunches. To optimise this process, a precise knowledge of the longitudinal bunch profile along the ring is needed continuously. Different methods can be envisaged for that such as a photon counting techniques [24] or streak camera measurements [25] based on the measurement of visible photons emitted via Synchrotron radiation (SR) or *Cherenkov* diffraction radiation (ChDR). Techniques using electro-optical sampling and bi-refringent crystal are also discussed as well as frequency spectrum analysis using the emission of coherent radiation from short bunches at mm wavelength again using SR or ChDR [26]. In the paragraphs below, we present the status of the work being performed at the moment on Cherenkov Diffraction radiation and E-O detection in the context of FCC-ee, as well as streak camera measurements performed at KEK.

Streak camera measurements at KEK

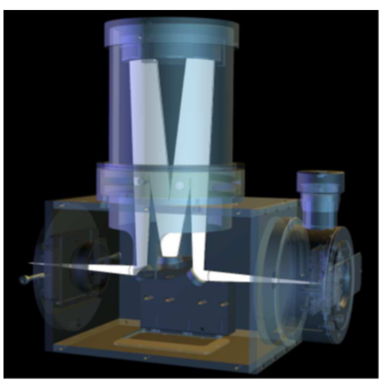

Figure 14: *Offner* relay reflective system for the streak camera reflective input optics.

The streak camera is an important tool to diagnose the temporal profile of the beam bunches in the optical diagnostic beam-line of SuperKEKB for bunches of typically 5 . . . 10 mm RMS length. The reduction of the chromatic aberration of the streak camera optics is one of the most important points in this measurement technique. For this purpose, typically a band-pass filter is used in the optical path, however, this reduces the light input intensity for low bunch intensities, which results in noisy, unreliable measurements. A different solution has been implemented using reflective optics. Therefore we have developed an *Offner* relay reflective system [27, 28]. Figure 14 shows a cutaway side view of the reflective input optics. Using this input optics, we can measure the bunch length down to low bunch intensities < 0.1 mA. A result of bunch length measurement at LER of SuperKEKB is shown in Fig. 15.

Another important application of the streak camera is the correlated spatial-temporal measurement of an electron

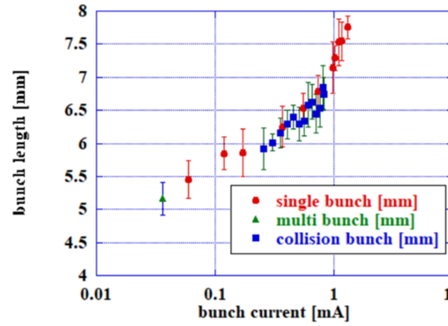

Figure 15: Bunch length measurement results at the LER of SuperKEKB.

bunch. This technique enables the observation of instabilities of the beam, such as head-tail oscillations, quadrupole oscillations, or the beam size blow-up due to the electron cloud instability, etc. [29]. Figure 16 shows the observation for quadrupole and head-tail oscillations at the KEK Photon Factory.

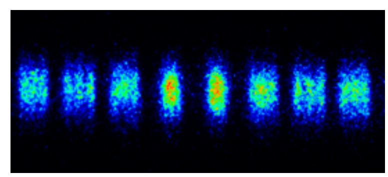

(a) Quadrupole oscillations

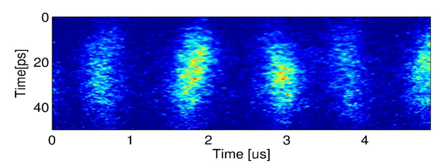

(b) Head-tail oscillations

Figure 16: Correlated spatial-temporal streak camera measurements at the KEK Photon Factory.

R&D based on Cherenkov Diffraction Radiation

A charged particle moving in close vicinity to a dielectric generates Cherenkov diffraction radiation (ChDR) if its velocity v is greater than the speed of light in the dielectric material. Figure 17 illustrates this principle. The generated radiation is emitted at a well-defined angle $\theta_{Ch} = \arccos[1/(n_1\beta)]$ which is known as *Cherenkov* angle [30] and where $n_1 = \sqrt{\epsilon_r \mu_r}$ denotes the refractive index of the dielectric and $\beta = v/c$.

The properties of ChDR are of high interest for beam diagnostic devices due to its high directivity, non-invasive characteristic and small form factor of radiators. Especially making use of the incoherent ChDR is a promising candidate for bunch-length diagnostics at FCC-ee. However, two analytical models [31, 32] predict different photon yields the higher the frequency, being far inside the incoherent part

ISBN: 978-3-95450-236-3 ISSN: 2673-7027 doi:10.18429/JACoW-eeFACT2022-WEZAS0203

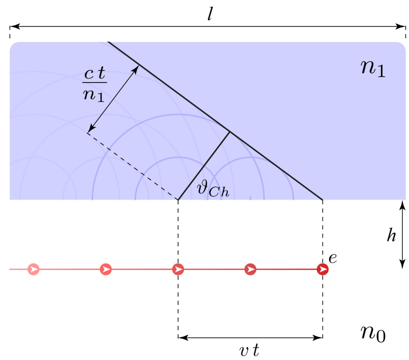

Figure 17: A particle with charge e travelling in vacuum along the boundary to a dielectric with refractive index n_1. The length of the radiator is given as l and the distance between the particle and the radiator surface is denoted h. ChDR is emitted at the *Cherenkov* angle ϑ_{Ch}.

of the spectrum. To validate the predictions there only exists very little experimental data on ChDR in the incoherent regime [33] and experiments with the coherent part of the spectrum [34] to compare the two different analytical models have not been conclusive. We herein discuss the simulation results of experiments aiming to verify the validity of the two different analytical models by calculating the energy loss of a charged particle due to ChDR.

Both models consider the dielectric as shown in Fig. 17 to be infinitely wide (perpendicular to the plane) with the particle travelling in parallel to the surface of the dielectric. The length l of the dielectric is restricted for one model, but considered infinite ($l = \infty$) for the other. The infinitely long model [31] we denote *stationary model* hereafter. The model restricted in length [32] we denote as *non-stationary model*. In all presented calculations holds $n_0 = 1$ and all results are scaled to the same radiator length of $l = 10$ mm. The variables with the greatest effect concerning photon yield are the particle energy and the impact parameter. The first approach for a possible experimental setup considers relatively high energies with a well-controlled transverse beam size. The second approach considers ultra-high energy electron beams.

At the ATF2 beamline at KEK [35] the horizontal beam size is only around 10 µm (1σ), while still providing a high particle energy above 1 GeV and a high bunch charge of more than 1 nC. In Fig. 18 the expected photon yield for the visible spectrum (400-700 nm) from the two models is shown for beam parameters resembling the ATF2 beamline. The plot shows that the expected photon yield per cm of dielectric for the non-stationary model (orange trace) is in the order of magnitude one could expect from particles in the halo [35] producing direct *Cherenkov* radiation (red trace). At distances of around 0.5 mm the non-stationary model predicts nearly 10^5 photons per bunch being emitted as ChDR. The photon yield per cm from the stationary model would be four orders of magnitude lower than that.

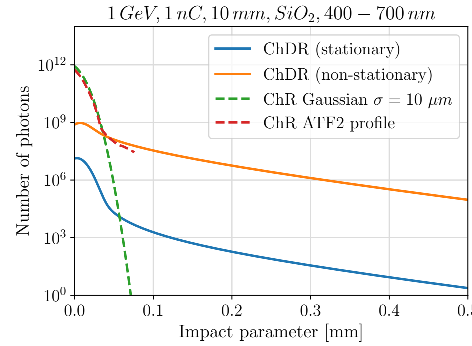

Figure 18: Expected photon yield according to the two different analytical models. The green dotted line corresponds to the photon yield from *Cherenkov* radiation of particles in a *Gaussian* beam hitting the radiator. The red dotted line corresponds to the photon yield from *Cherenkov* radiation considering the beam halo of the ATF2 beam line.

For the second approach, we consider ultra-high energy electrons delivered to the North Area at CERN. As the transverse beam size provided at the North Area is typically in the order of several millimetres the contribution from direct *Cherenkov* radiation on a radiator is too high to discriminate from ChDR. However, as electrons are delivered using a slow extraction scheme from the SPS the possibility remains to track each particle individually. We aim for the highest electron energies without reducing the number of electrons available per spill. The calculated photon yield for 40 and 100 GeV electrons is shown in Fig. 19. With 10^7 particles per spill one could expect the production of several hundred photons due to ChDR even at large distances of several millimeters. However, the photon yield predicted by the stationary model would be more than ten orders of magnitude lower than that.

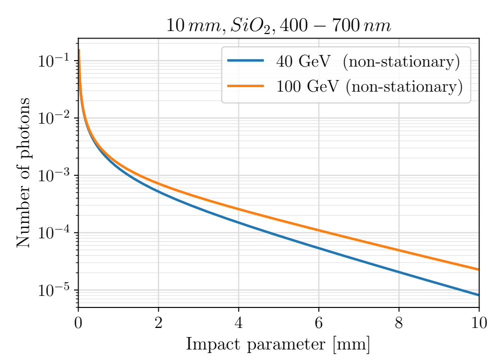

Figure 19: Expected photon yield from ChDR of a single particle calculated using the non-stationary model.

To conclude, the verification of different analytical models presents a challenge given the current test beams even under optimal conditions. We have shown that two different experimental setups might be able to verify the photon yield of ChDR as predicted by the non-stationary model. The

ISBN: 978-3-95450-236-3 ISSN: 2673-7027 doi:10.18429/JACoW-eeFACT2022-WEZAS0203

photon yield due to ChDR as predicated by the stationary model is way below that and very unlikely to be measured considering the two different test beams.

R&D based on Electro-Optical Spectral Decoding

FCC-ee requires a bunch-by-bunch bunch profile monitoring system for its top-up injection and a diagnostics tool based on electro-optical spectral decoding (EOSD) is a possible candidate to fulfill the requirements. At the electron storage ring KARA at KIT, an electro-optical (EO) near-field monitor is installed to perform single shot, turn-by-turn longitudinal bunch profile measurements [36]. It has proven to be a valuable diagnostics tool, which among high-throughput data streaming of single electron bunch profiles [37], is also used for tomography of the longitudinal phase-space [38]. Therefore, the KARA EO diagnostic tools can provide a good foundation for the development of a similar diagnostics system for FCC-ee.

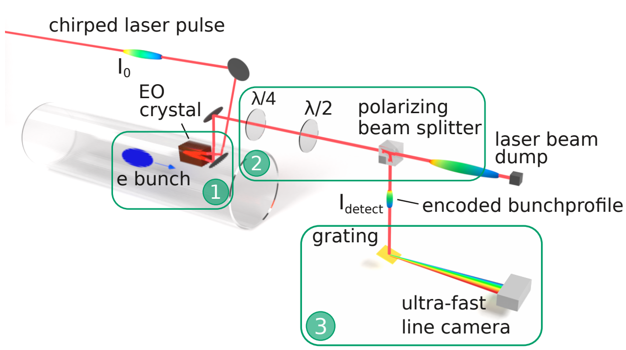

Figure 20: Principle of the EO bunch profile monitor at KARA. Adapted from [38].

Figure 20 shows the principle of the bunch profile monitor at KARA using electro-optical spectral decoding (EOSD), which is best described in three steps: In the first step, the bunch profile is encoded into the polarisation of a chirped laser pulse by sending it though an electro-optical crystal next to the electron bunch. The *Coulomb* field of the electrons change the birefringence of the crystal according to the *Pockels* effect, which modulates the polarization of the laser pulse [39]. In the second step, the modulation of the polarization is transformed into an intensity modulation by the use of two waveplates and a polarizing beam splitter in a near-crossed configuration. The third step is a spectrometer containing the KIT-build ultra-fast line camera KALYPSO with a Mfps frame rate [40], which allows turn-by-turn measurements of the spectrum of single laser pulses. Since a chirped laser pulse has been used in the beginning, the intensity modulation in the spectrum corresponds to the temporal charge density profile of a single electron bunch. At KARA, these measurements are performed with an operation mode for short bunches with one single bunch in the ring. However, KARA is also suited for future prototype tests for EOSD at FCC-ee, because the existing EO monitor can be modified and the bunch length and number of bunches can be increased to better fit the beam parameters at FCC-ee.

In order to investigate the challenges for the application of a similar EOSD diagnostic system at FCC-ee, the setup has been replicated in simulations [41]. KARA and FCC-ee machine parameters are different in many ways, but with respect to EOSD, the following particular changes have been identified that need to be addressed: Due to a higher charge density in the bunches, the *Coulomb* fields are up to 10 times stronger than at KARA, depending the operation modes of the accelerators. Strong *Coulomb* fields should be avoided, because it leads to a non-linear relation of the bunch profile and the modulation of the laser pulse. The second major challenge occurs during operation for the production of Z-bosons at an collision energy of 92 MeV, where FCC-ee will have bunch lengths of up to $\sigma_{\mathrm{FCCee\ Z}} = 15.4$ mm [42]. These bunches are much longer than the typical bunch length during measurements at KARA of around $\sigma_{\mathrm{KARA}} = 3$ mm.

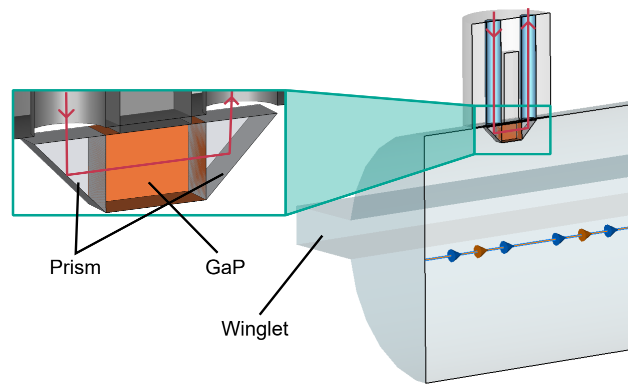

Figure 21: Concept of an adapted EO monitor design for FCC-ee [43].

Therefore, a new conceptual design of the crystal holder has been developed and tested in simulations [43]. In Fig. 21, the adapted design is presented as a 3D model installed in the FCC-ee beam pipe. Compared to the KARA setup, it has a modified laser path through the crystal, which avoids the laser pulse first travelling upstream against the direction of the electron bunch. This modification allows measurements of longer bunches, because it avoids disturbances by an overlapping upstream signal. The KARA design had a metal mirror next to the crystal to guide the laser beam, which has been replaced by prisms for the new design. This is used for the modified laser path and it helps to reduce impedance and disturbances of the *Coulomb* field. By placing the crystal at the edge of the beam pipe, the strength of the *Coulomb* field in the crystal during Z-operation is reduced to a level similar to the KARA setup.

As a result, the simulations show that single bunch EOSD measurements similar to the measurements at KARA can be achieved with the adapted design. Refining, building and testing the prototype design is currently in progress, with the goal to provide a proof-of-principle for an EOSD bunch profile monitor for FCC-ee.

ISBN: 978-3-95450-236-3 ISSN: 2673-7027 doi:10.18429/JACoW-eeFACT2022-WEZAS0203

CONCLUSIONS

An overview of the technical challenges for some of the major beam instrumentation systems for FCC-ee was presented, along with first R&D initiatives and some relevant beam studies. However, beside these technical and scientific challenges, also managerial and funding challenges lie ahead – for both, the FCC-ee BI R&D program and the final realization. It may be worth to mention, past experience show the contribution of the beam instrumentation on the total project costs for hadron colliders was typically in the range 3 . . . 5 %, while for lepton machines like 4th-generation synchrotron light sources the BI cost contribution is up to 10 %.

REFERENCES

[1] A. Abada *et al.*, "FCC-ee: The Lepton Collider: Future Circular Collider Conceptual Design Report Volume 2," *Eur. Phys. J. ST*, vol. 228, no. 2, pp. 261–623, 2019. DOI: 10.1140/epjst/e2019-900045-4.

[2] F. Brinker, A. Hagestedt, and M. Wendt, "Precision alignment of bpm's with quadrupole magnets," 1996.

[3] G. Priebe, D. Nölle, M. Wendt, and M. Werner, "Precision alignments of stripline bpm's with quadrupole magnets for ttf2," 2004.

[4] D. Noelle, G. Priebe, M. Wendt, and M. Werner, "BPMs with precise alignment for TTF2," *AIP Conf. Proc.*, vol. 732, no. 1, T. Shea and R. C. Sibley, Eds., pp. 166–173, 2004. DOI: 10.1063/1.1831144.

[5] S. Zorzetti, M. Wendt, and L. Fanucci, "Study of the Electrical Center of a Resonant Cavity Beam Position Monitor (RF-BPM) and Its Integration with the Main Beam Quadrupole for Alignment Purposes," in *2nd North American Particle Accelerator Conference*, 2017, FRA2CO03. DOI: 10.18429/JACoW-NAPAC2016-FRA2CO03.

[6] E. Carideo, M. Migliorati, D. De Arcangelis, and I. M. Zobov, "Transverse and longitudinal single bunch instabilities in fcc-ee,"

[7] M. Migliorati, C. Antuono, E. Carideo, Y. Zhang, and M. Zobov, "Impedance modelling and collective effects in the future circular e⊕ e⊖ collider with 4 ips," *arXiv preprint arXiv:2204.04616*, 2022.

[8] M. Kastriotou *et al.*, "BLM Crosstalk Studies on the CLIC Two-Beam Module," in *Proc. of International Beam Instrumentation Conference (IBIC2015), Melbourne, Australia, 13-17 September 2015*, (Melbourne, Australia), M. Boland, D. Button, K. Riches, and V. R. Schaa, Eds., ser. International Beam Instrumentation Conference, JACoW, Geneva, Switzerland: JACoW, Jan. 2016, pp. 148–151, ISBN: 978-3-95450-176-2. DOI: 10.18429/JACoW-IBIC2015-MOPB045. http://accelconf.web.cern.ch/AccelConf/IBIC2015/papers/mopb045.pdf

[9] E. Nebot Del Busto *et al.*, "Position Resolution of Optical Fibre-Based Beam Loss Monitors Using Long Electron Pulses," in *Proc. of International Beam Instrumentation Conference (IBIC2015), Melbourne, Australia, 13-17 September 2015*, (Melbourne, Australia), M. Boland, D. Button, K. Riches, and V. R. Schaa, Eds., ser. International Beam Instrumentation Conference, JACoW, Geneva, Switzerland: JACoW, Jan. 2016, pp. 580–584, ISBN: 978-3-95450-176-2. DOI: 10.18429/JACoW-IBIC2015-WEBLA03. http://accelconf.web.cern.ch/AccelConf/IBIC2015/papers/webla03.pdf

[10] M. Kastriotou *et al.*, "A Versatile Beam Loss Monitoring System for CLIC," in *Proc. of International Particle Accelerator Conference (IPAC'16), Busan, Korea, May 8-13, 2016*, (Busan, Korea), ser. International Particle Accelerator Conference, doi:10.18429/JACoW-IPAC2016-MOPMR024, Geneva, Switzerland: JACoW, Jun. 2016, pp. 286–289, ISBN: 978-3-95450-147-2. DOI: doi:10.18429/JACoW-IPAC2016-MOPMR024. http://jacow.org/ipac2016/papers/mopmr024.pdf

[11] G. Mitsuka, H. Ikeda, and T. Mitsuhashi, "Renovation of the SR Beam Profile Monitors with Novel Polycrystalline Diamond Mirrors at the SuperKEKB Accelerator," in *Proc. IPAC'22*, (Bangkok, Thailand), ser. International Particle Accelerator Conference, JACoW Publishing, Geneva, Switzerland, Jul. 2022, MOPOPT031, pp. 313–315, ISBN: 978-3-95450-227-1. DOI: 10.18429/JACoW-IPAC2022-MOPOPT031. https://jacow.org/ipac2022/papers/mopopt031.pdf

[12] G. Mitsuka, H. Ikeda, and T. Mitsuhashi, "Design and Construction of Optical System of the Coronagraph for Beam Halo Observation in the SuperKEKB," in *Proc. IPAC'22*, (Bangkok, Thailand), ser. International Particle Accelerator Conference, JACoW Publishing, Geneva, Switzerland, Jul. 2022, TUOXGD1, pp. 769–771, ISBN: 978-3-95450-227-1. DOI: 10.18429/JACoW-IPAC2022-TUOXGD1. https://jacow.org/ipac2022/papers/tuoxgd1.pdf

[13] T. Mitsuhashi, K. Oide, and F. Zimmermann, "Conceptual Design for SR Monitor in the FCC Beam Emittance (Size) Diagnostic," in *Proc. of International Particle Accelerator Conference (IPAC'16), Busan, Korea, May 8-13, 2016*, (Busan, Korea), ser. International Particle Accelerator Conference, doi:10.18429/JACoW-IPAC2016-MOPMB022, Geneva, Switzerland: JACoW, Jun. 2016, pp. 133–136, ISBN: 978-3-95450-147-2. DOI: doi:10.18429/JACoW-IPAC2016-MOPMB022. http://jacow.org/ipac2016/papers/mopmb022.pdf

[14] M. Boland, T. Mitsuhashi, and K. Wootton, "Turn-by-turn observation of the injected beam profile at the australian synchrotron storage ring," vol. IBIC2012, Geneva, Switzerland: JACoW, 2012, pp. 276–278, ISBN: 978-3-95450-119-9.

[15] H. Ikeda, T. Mitsuhashi, and G. Mitsuka, "Injection Beam Measurement Using Synchrotron Radiation Monitor at the SuperKEKB Electron Ring," in *Proc. IPAC'22*, (Bangkok, Thailand), ser. International Particle Accelerator Conference, JACoW Publishing, Geneva, Switzerland, Jul. 2022, FROXGD3, pp. 3121–3123, ISBN: 978-3-95450-227-1. DOI: 10.18429/JACoW-IPAC2022-FROXGD3. https://jacow.org/ipac2022/papers/froxgd3.pdf

[16] M. Siano *et al.*, "Two-dimensional electron beam size measurements with x-ray heterodyne near field speckles," *Phys. Rev. Accel. Beams*, vol. 25, p. 052 801, 2022.

[17] M. Siano, B. Paroli, and M. A. C. Potenza, "Heterodyne near field speckles: From laser light to x-rays," *Advances in Physics: X*, vol. 6, p. 1 891 001, 2021.

[18] M. D. Alaimo *et al.*, "Probing the transverse coherence of an undulator x-ray beam using brownian particles," *Phys. Rev. Lett.*, vol. 103, p. 194 805, 2009.

[19] M. Siano *et al.*, "Characterizing temporal coherence of visible synchrotron radiation with heterodyne near field speckles," *Phys. Rev. Accel. Beams*, vol. 20, p. 110 702, 2017.

ISBN: 978-3-95450-236-3 ISSN: 2673-7027 doi:10.18429/JACoW-eeFACT2022-WEZAS0203

[20] J. W. Goodman, *Statistical Optics*. John Wiley & Sons, Inc., New York, 2000.

[21] M. Siano *et al.*, "Focus: Fast monte carlo approach to coherence of undulator sources," *Proceedings of the 11th International Beam Instrumentation Conference IBIC 2022*, 2022.

[22] L. J. Nevay *et al.*, "Laserwire at the accelerator test facility 2 with submicrometer resolution," *Phys. Rev. ST Accel. Beams*, vol. 17, p. 072 802, 7 Jul. 2014. DOI: 10.1103/PhysRevSTAB.17.072802. https://link.aps.org/doi/10.1103/PhysRevSTAB.17.072802

[23] A. Blondel *et al.*, "Polarization and Centre-of-mass Energy Calibration at FCC-ee," Sep. 2019. arXiv: 1909.12245 [physics.acc-ph].

[24] A. Jeff *et al.*, "Longitudinal density monitor for the lhc," *Phys. Rev. ST Accel. Beams*, vol. 15, p. 032 803, 3 Mar. 2012. DOI: 10.1103/PhysRevSTAB.15.032803. https://link.aps.org/doi/10.1103/PhysRevSTAB.15.032803

[25] C. P. Welsch *et al.*, "Longitudinal beam profile measurements at ctf3 using a streak camera," *Journal of Instrumentation*, vol. 1, no. 09, P09002, Sep. 2006. DOI: 10.1088/1748-0221/1/09/P09002. https://dx.doi.org/10.1088/1748-0221/1/09/P09002

[26] A. Curcio *et al.*, "Noninvasive bunch length measurements exploiting cherenkov diffraction radiation," *Phys. Rev. Accel. Beams*, vol. 23, p. 022 802, 2 Feb. 2020. DOI: 10.1103/PhysRevAccelBeams.23.022802. https://link.aps.org/doi/10.1103/PhysRevAccelBeams.23.022802

[27] T. Obina and T. Mitsuhashi, "Measurement of bunch lengthening effects using a streak camera with reflective optics," vol. DIPAC2007, Geneva, Switzerland: JACoW, 2007, pp. 256–258, ISBN: 978-3-95450-011-6.

[28] M. Boland, T. Mitsuhashi, and Y. Tan, "Reflective Streak Camera Bunch Length Measurements at the Australian Synchrotron," in *Proc. 5th International Particle Accelerator Conference (IPAC'14), Dresden, Germany, June 15-20, 2014*, (Dresden, Germany), ser. International Particle Accelerator Conference, https://doi.org/10.18429/JACoW-IPAC2014-THPME080, Geneva, Switzerland: JACoW, Jul. 2014, pp. 3421–3423, ISBN: 978-3-95450-132-8. DOI: https://doi.org/10.18429/JACoW-IPAC2014-THPME080. http://jacow.org/ipac2014/papers/thpme080.pdf

[29] H. Obina *et al.*, "Vertical beam size measurement by streak camera under colliding and single beam conditions in kekb," vol. PAC2005, IEEE, 2005, pp. 31 294–3196, ISBN: 0-7803-8860-7.

[30] I. M. Frank and I. E. Tamm, "Coherent visible radiation of fast electrons passing through matter," *Compt. Rend. Acad. Sci. URSS*, vol. 14, no. 3, pp. 109–114, 1937. DOI: 10.3367/UFNr.0093.196710o.0388.

[31] R. Ulrich, "Zur Cerenkov-Strahlung von Elektronen dicht über einem Dielektrikum," *Zeitschrift fur Physik*, vol. 194, no. 2, Apr. 1966. DOI: 10.1007/BF01326045.

[32] A. Potylitsyn and S. Gogolev, "Radiation losses of the relativistic charge moving near a dielectric radiator," *Russian Physics Journal*, vol. 62, Apr. 2020. DOI: 10.1007/s11182-020-01965-0.

[33] R. Kieffer *et al.*, "Direct observation of incoherent cherenkov diffraction radiation in the visible range," *Phys. Rev. Lett.*, vol. 121, p. 054 802, 5 Aug. 2018. DOI: 10.1103/PhysRevLett.121.054802. https://link.aps.org/doi/10.1103/PhysRevLett.121.054802

[34] K. Łasocha *et al.*, "Experimental Verification of Several Theoretical Models for ChDR Description," in *Proc. IPAC'22*, (Bangkok, Thailand), ser. International Particle Accelerator Conference, JACoW Publishing, Geneva, Switzerland, Jul. 2022, THOYGD1, pp. 2420–2423, ISBN: 978-3-95450-227-1. DOI: 10.18429/JACoW-IPAC2022-THOYGD1. https://jacow.org/ipac2022/papers/thoygd1.pdf

[35] R. Yang *et al.*, "Evaluation of beam halo from beam-gas scattering at the kek accelerator test facility," *Phys. Rev. Accel. Beams*, vol. 21, p. 051 001, 5 May 2018. DOI: 10.1103/PhysRevAccelBeams.21.051001. https://link.aps.org/doi/10.1103/PhysRevAccelBeams.21.051001

[36] N. Hiller *et al.*, "A Setup for Single Shot Electro Optical Bunch Length Measurements at the ANKA Storage Ring," in *Proc. IPAC'11*, (San Sebastian, Spain, Sep. 2011), JACoW Publishing, Geneva, Switzerland, pp. 1206–1208. https://jacow.org/IPAC2011/papers/TUPC086.pdf

[37] S. Funkner *et al.*, "High throughput data streaming of individual longitudinal electron bunch profiles," *Physical Review Accelerators and Beams*, vol. 22, no. 2, p. 022 801, Feb. 2019. DOI: 10.1103/physrevaccelbeams.22.022801.

[38] S. Funkner *et al.*, "Revealing the dynamics of ultrarelativistic non-equilibrium many-electron systems with phase space tomography," *arXiv preprint*, DOI: 10.48550/arXiv.1912.01323.

[39] I. Wilke, A. M. MacLeod, W. A. Gillespie, G. Berden, G. M. H. Knippels, and A. F. G. van der Meer, "Single-Shot Electron-Beam Bunch Length Measurements," *Physical Review Letters*, vol. 88, no. 12, p. 124 801, Mar. 2002. DOI: 10.1103/physrevlett.88.124801.

[40] M. Patil *et al.*, "Ultra-Fast Line-Camera KALYPSO for fs-Laser-Based Electron Beam Diagnostics," *Proceedings of the 10th International Beam Instrumentation Conference*, vol. IBIC2021, Re of Korea, 2021. DOI: 10.18429/JACOW-IBIC2021-MOOB01.

[41] M. Reißig *et al.*, "Development of an Electro-Optical Longitudinal Bunch Profile Monitor at KARA Towards a Beam Diagnostics Tool for FCC-ee," in *Proc. IPAC'22*, (Bangkok, Thailand), ser. International Particle Accelerator Conference, JACoW Publishing, Geneva, Switzerland, Jul. 2022, pp. 296–299, ISBN: 978-3-95-450227-1. DOI: 10.18429/JACoW-IPAC2022-MOPOPT025.

[42] K. Oide. "$\beta_x^* = 10$ cm optics for Z," 151st FCC-ee Optics Design Meeting. (May 17, 2022), https://indico.cern.ch/event/1118299/contributions/4766789/attachments/2409541/4122785/Bx%5C%2A10cm_Oide_220317.pdf

[43] M. Reissig *et al.*, "Status of a Monitor Design for Single-Shot Electro-Optical Bunch Profile Measurements at FCC-ee," (Kraków, Poland, Sep. 2022), presented at IBIC'22, Kraków, Poland, Sep. 2022, paper WEP26, unpublished.

ISBN: 978-3-95450-236-3 ISSN: 2673-7027 doi:10.18429/JACoW-eeFACT2022-THXAT0101

P^3: A POSITRON SOURCE DEMONSTRATOR FOR FCC-ee

N. Vallis[1,*], B. Auchmann[2], P. Craievich, M. Duda, H. Garcia-Rodrigues, J. Kosse, M. Schaer, R. Zennaro, Paul Scherrer Institut, 5232 Villigen PSI, Switzerland
[1]also at EPFL, Lausanne, Switzerland
[2]also at CERN, Geneva, Switzerland

Abstract

The PSI Positron Production project (P^3 or P-cubed) is a demonstrator for a novel positron source for FCC-ee. The high current requirements of future colliders can be compromised by the extremely high positron emittance at the production target and consequent poor capture and transport to the damping ring. However, recent advances in high-temperature superconductors allow for a highly efficient matching of such an emittance through the use a solenoid around the target delivering a field over 10 T on-axis. Moreover, the emittance of the matched positron beam can be contained through large aperture RF cavities surrounded by a multi-Tesla field generated by conventional superconducting solenoids, where simulations estimate a yield higher by one order of magnitude with respect to the state-of-the-art. The goal of P^3 is to demonstrate this basic principle by implementing the aforementioned solenoids into a prototype positron source based on a 6 GeV electron beam from the SwissFEL linac, including two RF capture cavities and a beam diagnostics section.

INTRODUCTION

The Future Circular Collider (FCC) study group published in 2019 a Conceptual Design Report for an electron-positron collider (FCC-ee) with a centre-of-mass energy from 90 to 365 GeV and a beam current up to 1.4 A [1]. This high current requirement depends largely upon an injector complex (see Fig. 1) consisting of two separate sources and linacs for electrons and positrons up to 1.54 GeV, a damping ring (DR) to cool the positron emittance and a common linac up to 6 GeV [2].

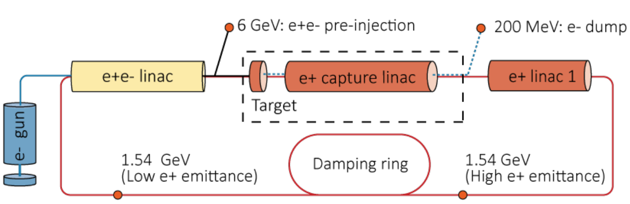

Figure 1: Latest proposal for the FCC-ee Injector Complex.

The principle method for positron production at FCC-ee is based on a 6 GeV electron beam impinging a 17.5 mm-thick (or $5X_0$) amorphous W target, which generates a positron yield around 13 N_{e+}/N_{e-} at the target exit [3]. However, the extremely high emittance and energy spread of the secondary distribution can lead to poor capture rates, compromising the yield of positrons accepted at the DR. The state-of-the art for a similar positron source is that of the SuperKEKB factory, allowing for 0.5 N_{e+}/N_{e-}, based on a 3.2 GeV electron drive beam with a bunch charge of 10 nC [4]. By contrast, the FCC-ee injection requires yield of 1 N_{e+}/N_{e-} at the DR, plus a safety factor of 2 in the design [5].

The PSI Positron Production project (P^3 or P-cubed) was proposed as a demonstrator for a novel solution for the FCC-ee positron source and capture linac. The baseline design of P^3 (see Fig. 2) consists of an adiabatic matching device (AMD) based on high-temperature superconducting (HTS) solenoids surrounding the target with a max. field on-axis of 12.7 T and two standing-wave (SW) capture RF cavities in S-band with a large iris aperture of 20 mm radius surrounded by conventional superconducting solenoids with a max. 1.5 T field on-axis. A beam diagnostics section will provide the first exprerimental estimations of the positron yield, which according to simulations is expected to improve the SuperKEKB record by one order of magnitude.

P^3 will use a 6 GeV drive electron beam generated at the SwissFEL linac. On the one hand, SwissFEL can provide the desired beam energy and transverse size with extreme precision. On the other hand, due to the radioprotection limitations at SwissFEL, the drive beams of P^3 and FCC-ee show substantial differences regarding bunch charge and time structure (see Table 1). This results in a significantly lower radiation load in the P^3 target, excluding any thermo-mechanical studies from the scope of the experiment.

Table 1: Main Drive Linac Parameters

	FCC-ee	**P^3 (SwissFEL)**
Energy [GeV]	6	
$\sigma_{x,RMS}$ [mm]	0.5 - 1.0	
Q_{bunch} [nC]	0.88 - 1.17[1]	0.20
Reptition rate [Hz]	200	1
Bunches per pulse	2	1

[1]Based on 5.0 - 5.5 nC requirements at booster ring and preliminary yield estimations of 4.7 - 5.7 N_{e+}/N_{e-}.

KEY TECHNOLOGY

HTS Adiabatic Matching Device

HTS solenoids will be used to deliver a peak on-axis field of 12.7 T around the target in order to match the extremely high positron emittance. This technology can lead to significantly higher yields with respect a conventional, normal-conducting flux concentrator (FC) [6]. The solenoids will be

* nicolas.vallis@psi.ch

ISBN: 978-3-95450-236-3 ISSN: 2673-7027 doi:10.18429/JACoW-eeFACT2022-THXAT0101

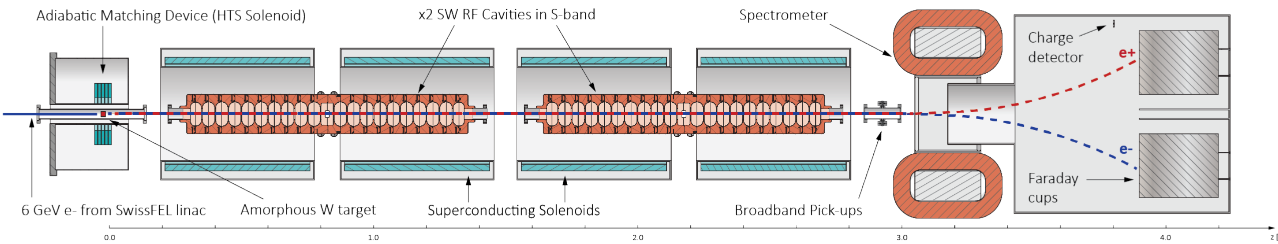

Figure 2: Baseline design of the P^3 experiment.

implemented with non-insulated ReBCO tape, which does not require a high-temperature or high-pressure treatment, and can be assembled in-house [7]. A reliable operation over 20 T in the conductor at 20 - 30 °K of a 4 ReBCO coil prototype (see Fig. 3) has been demonstrated experimentally at PSI, whithout the need of helium cooling, and showing a great self-protection against quenching. In addition, simulation studies show no critical radioprotection issues with the FCC-ee beam [8]. At this stage, major advances have been made towards a technical design of the AMD for P^3, including of 5 HTS coils and a relatively compact cryostat (see Fig. 3).

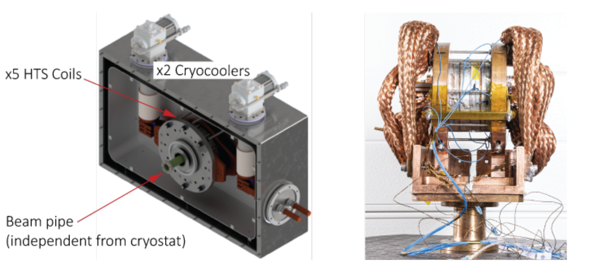

Figure 3: AMD cryostat (left) and HTS demonstrator (right).

S-band, SW Cavities

The capture of secondary positrons into stable RF buckets is provided by two SW RF cavities in S-band, the main parameters of which are shown in Table 2. The SW design allows for a large aperture of 20 mm radius and a good RF efficiency without the need of a pulse compressor. The operation in S-band was chosen based on the availability of commercial klystrons and conventional waveguide components, instead of the L-band baseline for the FCC-ee injector. A single klystron modulator can provide the required peak power and RF pulse length to fill the two cavities and reach a gradient of 18 MV/m. A waveguide coupler placed centrally is used to increase the mode separation.

Superconducting Solenoids around RF Cavities

The use of NbTi, a conventional low-temperature superconductor, remains the preferred technology the solenoids around the RF cavities. A concept design for this superconducting solution is depicted in Fig. 2, where the goal is to generate a flat, 1.5 T field on-axis, as shown in Fig. 4g. However, the feasibility and cost-effectiveness of NbTi is under study, and the use of normal-conducting solenoids providing a 0.4 T field on-axis is still under consideration.

Table 2: Main Parameters of the SW Cavities

Parameter	**Value**
Length [m]	1.2
RF frequency [GHz]	2.9988
Nominal gradient [MV/m]	18
Number of cells	21
R/L	13.9 MΩ/ m
Aperture [mm]	40
Mode separation (in π mode) [MHz]	5.3
RF Pulse length [µs]	3
Coupling factor	2

BEAM DYNAMICS

Figure 4 shows the P^3 beam simulated with ASTRA [9] according to the reference working point, where experiment parameters have been optimized to provide a maximum yield of 8 N_{e+}/N_{e-} at the DR[1]. The key techniques to obtain this high yield are elucidated below.

Emittance Matching and Containment

HTS solenoids work as an AMD, matching the positron emittance through an adiabatically decreasing B_z profile. The matching power is maximized with the remarkably high magnetic strength (12.7 T), which leads to a significantly better yield with respect to conventional solutions (see Refs. [6, 10]). In order to contain such emittance and avoid beam explosion, a strong and flat magnetic channel around the RF cavities is applied. Simulation studies show a great impact of the field strength and flatness: first, normal-conducting solenoids at 0.4 T would imply a factor 3 reduction of the capture efficiency as compared to the 1.5 T superconducting scheme; in addition, Figs. 4g and 4e show how small variations in the magnetic field profile cause significant positron losses. These losses tend to decrease after a few RF cavities as the beam energy increases, and the emittance reaches a stable value. The P^3 simulations show a capture efficiency rate of 76% and an RMS emittance around 15 000 $\pi \cdot$ mm $\cdot$ mrad after the second cavity.

[1] Yield at DR is estimated by simulating the beam to 200 MeV (10 Cavities) and applying an analytical transformation of the longitudinal plane to 1.54 GeV and a rectangular filter of ±3.8 % in energy and $\pm\lambda/2$ in z

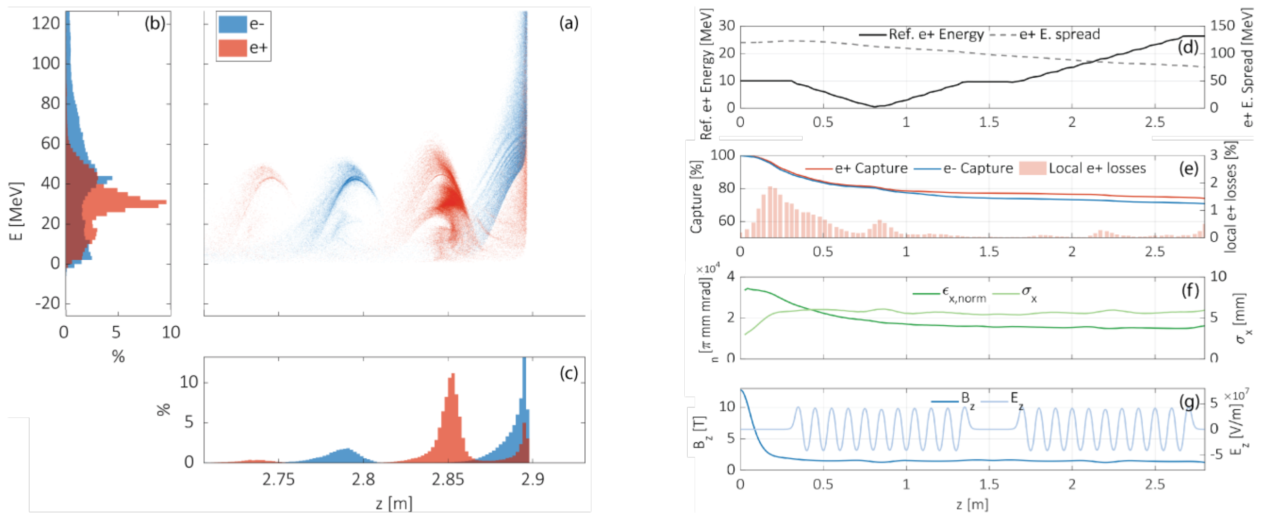

Figure 4: Longitudinal profile of P^3 beam at z = 2.85 m a to c) and evolution of main parameters (d to g).

Bunching by Deceleration

Due to the extremely high energy spread at the source, the beam is non-relativistic over the first RF cells, which allows for bunching through RF deceleration [11]. Simulations show that yield is maximized through partial deceleration over the first cavity and on-crest acceleration over the second (see Fig. 4d). This working point leads positrons to bunch around the second bucket (see Fig 4a).

BEAM DIAGNOSTICS

Broadband Pick-ups

Broadband pick-ups (BBPs) placed after the second RF cavity can provide a high resolution measurement of the time structure of the beam that would allow to distinguish consecutive electron and positron bunches [12].

Faraday Cups

As seen in Fig. 2, electrons and positrons will be separated by a spectrometer and dumped into independent Faraday cups that will provide a charge measurement integrated over many bunches. In pursuit of a compact design, these faraday cups are implemented through a 25 Ω coaxial layout, matched to the standard 50 Ω through two parallel coaxial guides. Due to the significant losses in the spectrometer walls and the rather small size of the faraday cups, only 68% and 65% of captured positrons and electrons are eventually measured.

Narrow Charge Detector

The spectrum of the longitudinal momentum (p_z) of the beam can be measured through varying the spectrometer field strength and placing a screen of narrow width within the vacuum chamber. The obtained distribution of measurements can be transformed into a histogram of p_z by applying the magnetic rigidity law. The optimum position (x = -350 mm, z = 3800 mm) of the charge detector has been determined and preliminary simulations show an accurate reconstruction of the p_z spectrum through a scan up to 0.3 T of the dipole field. The technology of the detector is still under discussion.

CONCLUSION

Major advances have been made regarding the development of P^3. On the one hand, the highly advanced design stage allows to initiate the material purchase of the RF cavities and the AMD. Regarding the latter, a reliable operation of HTS solenoids at fields above the P^3 requirements on-axis has been demonstrated and no prohibitive radiation protection issues have been found [8]. On the other hand, while the technology of the solenoids around the RF cavities is still under discussion, superconducting (1.5 T) and normal conducting (0.4 T) options have been studied, the first being the baseline option due to the outstanding capture efficiency provided. The same conclusion applies to the beam diagnostics section, where despite absence of a final technological choice, preliminary simulations show a reliable performance of the arrangement of BBPs, two faraday cups and a narrow charge detector. For all these reasons, we can conclude that the delivery of a full technical design is feasible and on-schedule for the next few months.

ACKNOWLEDGEMENTS

This work was done under the auspices of CHART Collaboration (Swiss Accelerator Research and Technology, `http://www.chart.ch`).

REFERENCES

[1] M. Benedikt *et al.*, “FCC-ee: the lepton collider”, *Eur. Phys. J. Spec. Top.*, vol. 228, pp. 261—623, 2019. doi:10.1140/epjst/e2019-900045-4

[2] P. Craievich *et al.*, “The FCCee pre-injector complex”, in *Proc. IPAC’22*, Bangkok, Thailand, Jun. 2022, pp. 2007–2010. doi:10.18429/JACoW-IPAC2022-WEPOPT063

ISBN: 978-3-95450-236-3 ISSN: 2673-7027 doi:10.18429/JACoW-eeFACT2022-THXAT0101

[3] I. Chaikovska *et al.*, "Positron source for FCC-ee", in *Proc. IPAC'19*, Melbourne, Australia, May 2019, pp. 424–427. doi:10.18429/JACoW-IPAC2019-MOPMP003

[4] K. Akai, K. Furukawa, and H. Koiso, "SuperKEKB collider", *Nucl. Instrum. Methods Phys. Res. Sect. A*, vol. 907, pp. 188-–199, 2018. doi:10.1016/j.nima.2018.08.017

[5] S. Ogur *et al.*, "Overall injection strategy for FCC-ee", in *Proc. eeFACT'18*, Hong Kong, China, Sep. 2018, p. 131. doi:10.18429/JACoW-eeFACT2018-TUPAB03

[6] Y. Zhao *et al.*, "Comparison of different matching device field profiles ofr the FCC-ee positron source", in *Proc. IPAC'21*, Campinas, Brazil, May 2021, pp. 2617–2620. doi:10.18429/JACoW-IPAC2021-WEPAB015

[7] Y. Iwasa, "HTS Magnet", in *Case Studies in Superconducting Magnets: Design and Operational Uses*, Springer, Boston 2009, ISBN 978-0-387-09799-2, pp. 587–589.

[8] B. Humann *et al.*, "Radiation load studies for the FCC-ee positron source with a superconducting matching device", in *Proc. IPAC'22*, Bangkok, Thailand, Jun. 2022, pp. 2879–2882. doi:10.18429/JACoW-IPAC2022-THPOTK048

[9] ASTRA, "A space charge tracking algorithm", v. 3.2, DESY, Hamburg, Germany, 2017.

[10] E. Bulyak *et al.*, "Theoretical investigations on the adiabatic matching device–based positron capture system', 2022. 10.48550/arXiv.2207.06126

[11] B. Aune and N. H. Miller, "New method for positron production at SLAC", in *Proc. LINAC'79*, Montauk, New York, USA, pp. 440–443.

[12] T. Suwada *et al.*, "First simultaneous detection of electron and positron bunches at the positron capture section of the SuperKEKB factory", *Sci. Rep.*, vol. 11, 2011. doi:10.1038/s41598-021-91707-0

ISBN: 978-3-95450-236-3 ISSN: 2673-7027 doi:10.18429/JACoW-eeFACT2022-THXAT0102

ISSUES RELATED TO CEPC e+/e- INJECTION*

Cai Meng†, Jie Gao, Xiaoping Li, Guoxi Pei, Dou Wang, Jingru Zhang
Key Laboratory of Particle Acceleration Physics and Technology,
Institute of High Energy Physics, Beijing, China

Abstract

Circular Electron-Positron Collider (CEPC) is a 100 km ring collider as a Higgs factory. It consists of a double ring collider, a full energy booster, a Linac and several transport lines. The Linac is a normal conducting S-band and C-band linear accelerator and provide electron and positron beam at an energy up to 30 GeV with repetition frequency of 100 Hz. After a conventional positron source, there is a 1.1 GeV damping ring to reduce the emittance of positron beam. C-band accelerating structures are adopted to accelerate electron and positron beam from 1.1 GeV to 30 GeV. For Z mode, in order to obtain higher injection speed, the Linac operates in double-bunch acceleration mode. The physics design and dynamic simulation results of the Linac will be detailed presented in this paper.

INTRODUCTION

The Higgs boson was discovery at the ATLAS and CMS experiments of the Large Hadron Collider at CERN in July 2012 [1, 2]. In Autumn 2012, Chinese scientists proposed a Circular Electron Positron Collider (CEPC) at 240 GeV centre of mass for Higgs studies [3]. The CEPC is a 100 km ring collider as a Higgs factory and it could later be used to host a Super Proton Proton Collider (SppC) as a machine for new physics and discovery. The CEPC accelerator comprises a double ring collider, a booster, a Linac and several transport lines. The booster and the collider ring are placed in the same tunnel and have the same circumference, which is about 100 m underground. In addition to the Higgs mode (120 GeV), CEPC will also run in W (80 GeV), Z (45.5 GeV), and ttbar mode (180 GeV).

From the pre-CDR stage to TDR stage, the CEPC Linac has undergone several iterations [4, 5] and evolution of parameters is shown in Fig. 1. For the 100 km booster with maximum extraction energy of 180 GeV, the dipole magnetic field is low at the injection energy and high at the maximum extraction energy. So, the design of booster dipole magnet and power supply is very difficult. In order to solve the problem, we choose the injection energy as 20 GeV and used iron-corn magnet which material is oriented silicon steel sheet. However, non-oriented silicon steel sheet is very expensive. If the Linac energy is increased from 20 GeV to 30 GeV, booster dipole magnet material can use non-oriented silicon steel sheet instead of oriented silicon steel sheet. Comprehensively considering the cost of the injector, the Linac energy was determined to be 30 GeV. Currently, for the latest scheme of Linac, the energy is 30 GeV, emittance is 6.5 nm and the bunch charge is 1.5 nC. Considering maintaining the potential to meet high requirements and future upgrades, the maximum bunch charge is 3 nC. At the Z mode with large bunch number in collider ring, the Linac run in double-bunch acceleration mode to speed up the injection speed.

Stage			PreCDR	CDR									TDR					
Parameter		Unit	V1	V2			V3								V4		
				V2.1	V2.2	V2.3	V3.1	V3.2	V3.3	V3.4	V3.5	V3.6	V3.7	V3.8	V4.1	V4.2	V4.3
Beam energy (e+/e-)	E_{e-}/E_{e+}	GeV	6	10					4	10			20	10/20	20		30
Repetition rate	f_{rep}	Hz	50					100									
Bunch number per pulse			1													1&2	
Bunch population (e+/e-)	N_{e-}/N_{e+}	$\times 10^9$	20				6.25			6.25(18.8)	9.4 (18.8)						
		nC	3.2				1			1(3)	1.5 (3)						
Energy spread (e^+/e^-)	σ_E	$\times 10^{-3}$	1				2								1.5		
e^- bunch charge at target		nC	10														
e^- beam energy at target		GeV	4						2	4							
Emittance	ε	nm	300								120		60	40	10		6.5
Damping Ring			Yes			No					Yes	Yes			Yes		
	E_{e+}	GeV	1.1								1.1	1.1			1.1		
	C	m	58.5								58.5	75.4			147		
	ε_0	mm-mrad	287								287	377			94		
Bunch compressor			No							Yes	No		Yes				
Accelerating strucutre			S-band										S-band+C-band				
RF frequency	f_{RF}	MHz	2856.75									2860	2860/5720				
Accelerating gradient		MV/m	15/27	18/27 or. 18/21			21						22 & 27/45				
Klystron-to-ACC.Struc.			1-t-2	1-t-2 or. 1-t-4			1-t-4						1-t-4 & 1-t-2(S)/1-t-2(C)				
Shared Linac Energy range		MeV	200-1100		No												
Linac tunnel length		km	600	1200					500	1200			1400				1800
Collider circumference		km	54 & 61	61			100										
Layout			shared Linac	3 layout schemes			TGB or EBTL		Pre-BST	EBTL							
Date			Apr-16	Nov-16			Dec-16	Apr-17	Aug-17	Oct-17	Dec-17	Jul-18	Mar-19	Sep-19	May-21	Mar-22	Jun-22

Figure 1: Evolution of the CEPC Linac parameters.

* Work supported by the Youth Innovation Promotion Association CAS (2019016)
† mengc@ihep.ac.cn

ISBN: 978-3-95450-236-3 ISSN: 2673-7027 doi:10.18429/JACoW-eeFACT2022-THXAT0102

LAYOUT

The CEPC Linac can provide electron and positron beams with energy up to 30 GeV. The Linac is composed of an electron source and bunching system (ESBS), a first accelerating section (FAS) where electron beam is accelerated to 4 GeV, a positron source and pre-accelerating section (PSPAS) where positron beam is produced and accelerated to 200 MeV, a second accelerating section (SAS) where positron beam is accelerated to 1.1 GeV, a third accelerating section (TAS) where electron beam and positron beam are accelerated from 1.1 GeV to 30 GeV, a 1.1 GeV electron bypass transport line (EBTL) where electron beam is bypassed in electron mode and a 1.1 GeV damping ring (DR) where positron beam is damped to reduce the emittance. In order to avoid the interference with energy analysing station, waveguide, positron source, transport lines between Linac and damping ring, and so on, the deflection direction of the EBTL is vertical and the separation distance is 1.2 m. The Linac layout is shown in Fig. 2. For the FAS, the bunch charge is about 10 nC for positron production, we use S-band accelerating structure to suppress the Wakefield effect. For the SAS, the emittance of positron beam is very large, so we use S-band accelerating structure, For the TAS, we use C-band accelerating structure to reduce Linac size and save cost. The Linac length is 1.6 km and there is about 200 m as reserved space, so the Linac tunnel length is about 1.8 km.

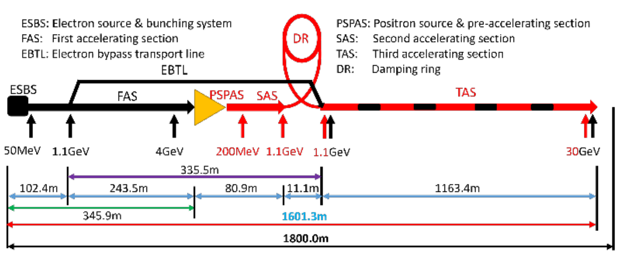

Figure 2: The layout of Linac.

Table 1: Main Parameters of Accelerating Structures

Parameter	Unit	S-band		C-band
Frequency	MHz	2860		5720
Length	m	3.1	2.0	1.8
Cavity mode		2π/3		3π/4
Aperture	mm	19~24	25	11.8~16
Gradient		22/27	22	45
Cells		85	55	89

BASIC CONSIDERATION

Wakefield

Main parameters of accelerating structures are shown in Table 1. For periodic structure, the high frequency longitudinal impedance was found by R. Gluckstern [6], with a modification by K. Yokoya and K.L.F. Bane [7], and the short-range dipole wake was given by K.L.F. Bane [8]. The Wakefields of S-band and C-band accelerating structure are shown in Fig. 3.

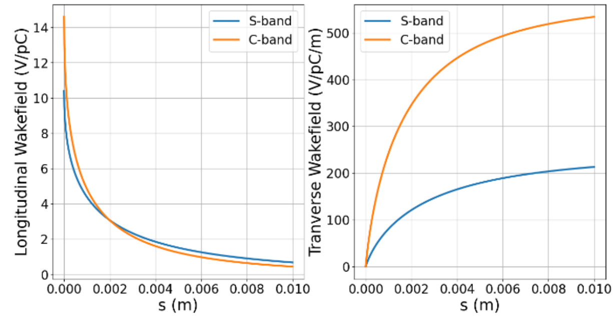

Figure 3: Wakefields of accelerating structure.

Bunch Length

We scan the bunch charge and bunch length and simulated the energy spread for the TAS, which is shown in Fig. 4. In order to meet the requirement of energy spread, we choose the bunch length as 0.4 mm. So, at the beginning of the TAS, we need a bunch compressor.

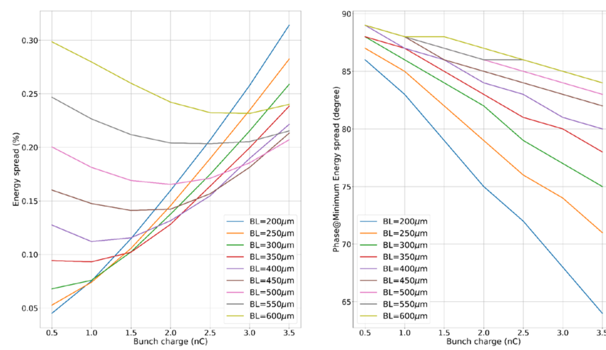

Figure 4: Energy spread with different bunch charge and bunch length.

Bunch Compressor

Generally, one bunch compressor system includes one RF cavity system providing a momentum chirp and a chicane compressing bunch length, which of the layout is shown in Fig. 5.

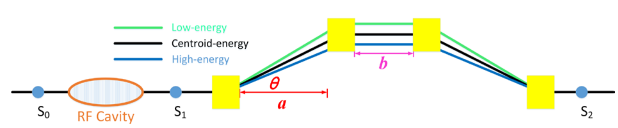

Figure 5: Layout of bunch compressor.

where *0*, *1*, *2* represent the position of the entrance of RF cavity, the entrance of and the exit of chicane, z is the longitudinal position deviation from bunch center, δ is the energy spread, E is the centroid energy, φ_0 is the synchronous phase of RF cavity. We can get the phase and voltage of RF cavity and R_{56} of chicane from the following equation:

$$F = \frac{\langle z_0^2\rangle - \langle z_2^2\rangle}{\langle z_0^2\rangle\langle z_2^2\rangle}\langle \delta_0^2\rangle \quad (1)$$

$$k = \frac{2\pi f}{c} \quad (2)$$

ISBN: 978-3-95450-236-3 ISSN: 2673-7027 doi:10.18429/JACoW-eeFACT2022-THXAT0102

$$f = \sqrt{\frac{\langle z_2^2 \rangle}{\langle z_0^2 \rangle}} \tag{3}$$

$$\varphi_0 = \arctan\left(\sqrt{\frac{k^2}{4F} - 3} - \frac{k}{2\sqrt{F}}\right) \tag{3}$$

$$V = \frac{\sqrt{F} E_0}{k \cos\varphi_0} \tag{4}$$

$$R_{56}^{ch} = \frac{(f^2-1)}{\sqrt{F}}\left(1 + \frac{\sqrt{F}\tan\varphi_0}{k}\right). \tag{5}$$

ELECTRON LINAC

The electron Linac includes ESBS, a part of FAS with energy of 1.1 GeV, EBTL and TAS. The ESBS comprise a thermal cathode electron gun, two subharmonic bunchers, a buncher, and an accelerating structure [4]. ESBS can provide electron beam with bunch charge of 10 nC. The EBTL is a local achromatic design. The electron Linac is well matched. In the last part of TAS, the period phase advance is gradually smaller to reduce the strength requirements for the quadrupole magnet. The simulation results of electron Linac are shown in Fig. 6 and Table 2, which can meet the requirements.

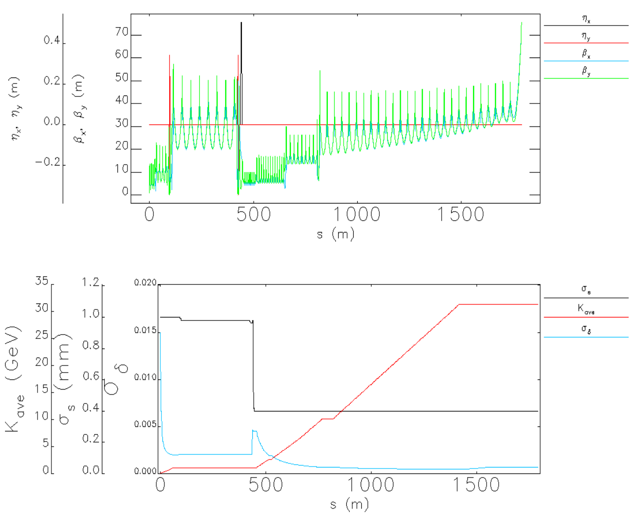

Figure 6: Dynamic results of electron Linac.

Table 2: Simulation Results of Electron Linac

Parameter	Unit	Value	Simulation Electron	
Beam energy	GeV	30	31.3	30.8
Repetition rate	Hz	100	/	
Bunch charge	nC	1.5	1.5	3.0
Energy spread		1.5×10^{-3}	0.68×10^{-3}	1.37×10^{-3}
Emittance(x/y)	nm	6.5	1.35/1.33	1.4/1.6
Bunch length	mm	/	0.4	0.4

POSITRON LINAC

The Positron Linac includes electron beam part of ESBS and FAS and positron beam part of PSPAS, SAS and TAS. S-band accelerating structures are used in FAS and the dynamic results are shown in Fig. 7. The PSPAS [9] is composed of a target, a flux concentrator which is an adiabatic matching device (AMD), 6 larger aperture S-band constant-impedance accelerating structures and a beam separation system. A schematic layout of the positron source is shown in Fig. 8. For SAS, there are 10 larger aperture accelerating structures with gradient of 22 MV/m and 8 normal S-band accelerating structures with gradient of 27 MV/m. Triplet structure is outside each accelerating structure. According to the start-to-end simulation of PAPAPAS and SAS, the positron yield is 0.45 positron particle per electron particle at energy of 1.1 GeV. Optics function of the SAS is shown in Fig. 9. After the damping ring, the positron beam is accelerated from 1.1 GeV to 30 GeV in the TAS and simulation results are shown in Fig. 10 and Table 3.

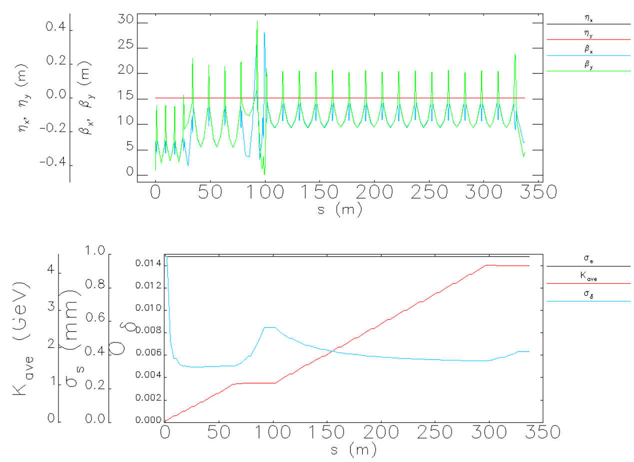

Figure 7: Dynamic results of FAS.

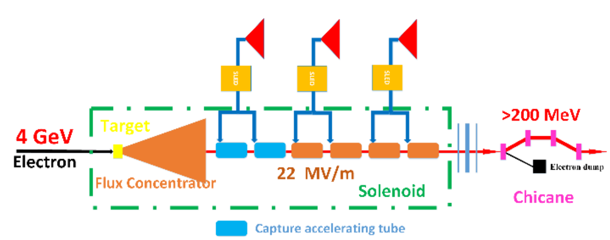

Figure 8: The layout of CEPC positron source.

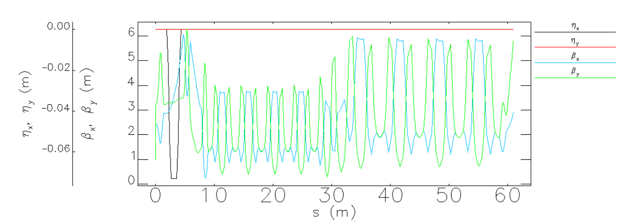

Figure 9: Optics function of SAS.

ISBN: 978-3-95450-236-3 ISSN: 2673-7027 doi:10.18429/JACoW-eeFACT2022-THXAT0102

Table 3: Simulation Results of Positron Linac

Parameter	Unit	Value	Simulation Electron	
Beam energy	GeV	30	31.3	30.8
Repetition rate	Hz	100	/	
Bunch charge	nC	1.5	1.5	3.0
Energy spread		1.5×10^{-3}	1.29×10^{-3}	2.16×10^{-3}
Emittance(x/y)	nm	6.5	3.29/1.64	3.80/1.66
Bunch length	mm	/	0.4	0.4

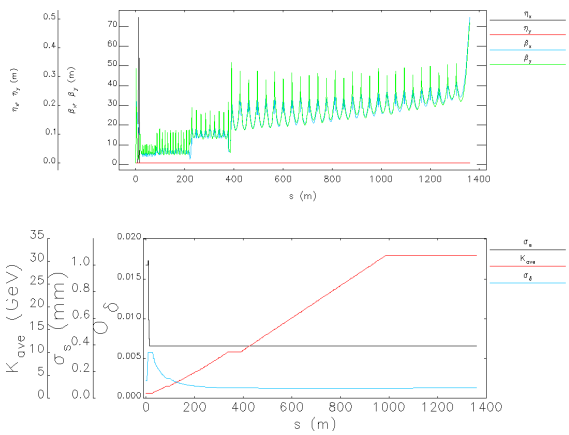

Figure 10: Dynamic results of TAS.

DOUBLE-BUNCH ACCELERATION

The repetition rate of the Linac is 100 Hz. In order to meet the injection speed requirement for Z mode, the Linac need to double the bunch repetition rate. A simpler scheme is increasing the repetition rate to 200 Hz, but it will increase the cost greatly. At last, we chose double-bunch acceleration mode. In this case, the most important issues are the frequency relationship. Considering the RF frequency of each accelerator and the time resolution ability of the detector, we give the timing related parameters and the harmonic number and beam pattern information of the collider ring, which are shown in Table 4. In order to get more flexible injection scheme and have better compatibility potential, we also consider use a RF gun. The bunch spacing in the Linac is about 70 ns, it is not too large and still can use pulse compressor even for C-band accelerating structure.

Table 4: Parameters of Timing System and Bunch Pattern Information

Parameter	Unit	High luminosity Z mode Baseline scheme	RF gun scheme
Repetition frequency	Hz	100	
Common frequency	MHz	130	
Linac common frequency	MHz	14.44	43.33
Bunch frequency	MHz	14.44	43.33
SHB1 RF frequency	MHz	158.89	/
SHB2 RF frequency	MHz	476.67	/
LINAC RF frequency	MHz	2860.00	
	MHz	5720.00	
Damping ring RF frequency	MHz	650.00	
Booster RF frequency	MHz	1300.00	
Ring RF frequency	MHz	650.00	
Bunch spacing @Collider	ns	23.08	23.08
Bunch spacing @Linac	ns	69.23	23.08
Injection scheme		bunch-by-bunch	pulse-by-pulse bunch-by-bunch
Harmonic number		45*(2k) + [10, 20, 40]	5(2k)+ [2,4]
		45*(2k+1) + [5, 25]	5(2k+1) + [1,3]
Bunch number per train		6n	2n

ISBN: 978-3-95450-236-3 ISSN: 2673-7027 doi:10.18429/JACoW-eeFACT2022-THXAT0102

CONCLUSION

The CEPC Linac is a normal conduction S-band and C-band linear accelerator with repetition rate of 100 Hz and can provide electron and positron beam with energy of 30 GeV. One conventional positron source is adopted with electron beam energy of 4 GeV. For Z mode, the Linac will run in double-bunch acceleration mode to double the injection speed. Simulation results of all the Linac was present and the design of Linac can meet the requirement.

REFERENCES

[1] ATLAS Collaboration. (G. Aad *et al.*), "Observation of a new particle in the search for the Standard Model Higgs boson with the ATLAS detector at the LHC", *Phys. Lett. B*, vol. 1, no. 716, pp. 1-29, 2012. doi:10.1016/j.physletb.2012.08.020

[2] CMS Collaboration. (S. Chatrchyan *et al.*, "Observation of a new boson at a mass of 125 GeV with the CMS experiment at the LHC", *Phys. Lett. B,* vol.1, no. 716, pp. 30-61, 2012. doi:10.1016/j.physletb.2012.08.021

[3] Y.F. Wang, "A proposal on ring-based Higgs factory in China", *2nd Symposium on Accelerator-based HEP Strategy and Development in China*, Beijing, 2012.

[4] Cai Meng *et al.*, "CEPC Linac design", *Int. J. Mod. Phys. A*, vol. 34, p. 1940005, 2019. doi:10.1142/S0217751X19400050

[5] C. Meng, J. Gao, X. P. Li, G. Pei, and J. R. Zhang, "Alternative Design of CEPC LINAC", in *Proc. IPAC'19*, Melbourne, Australia, May 2019, pp. 1005-1007. doi:10.18429/JACoW-IPAC2019-MOPTS065

[6] R. L. Gluckstern, "Longitudinal impedance of a periodic structure at high frequency", *Physical Review D,* vol. 39, p. 2780, 1989. doi:10.1103/PhysRevD.39.2780

[7] K. Yokoya and K. Bane, "The Longitudinal High-Frequency Impedance of a Periodic Accelerating Structure", in *Proc. PAC'99*, New York, 1999, p. 1725. doi:10.1109/PAC.1999.794235

[8] K. L. F. Bane, "Short range dipole wakefields in accelerating structures for the NLC", *SLAC Tech. Rep.* SLAC-PUB-9663, LCC-0116, Mar 2003.

[9] Meng, C., Li, X., Pei, G. *et al*., "CEPC positron source design", *Radiat. Detect. Technol. Methods*, vol. 3, p. 32, 2019.

ISBN: 978-3-95450-236-3 ISSN: 2673-7027 doi:10.18429/JACoW-eeFACT2022-THXAT0104

FCC-ee e^+e^- INJECTION AND BOOSTER RING

R. Ramjiawan*, M. Barnes, W. Bartmann, J. Borburgh, Y. Dutheil, M. Hofer, E. Howling
CERN, Geneva, Switzerland
A. Chance, B. Dalena, CEA, Paris, France
P. J. Hunchak, University of Saskatchewan, Saskatoon, Canada

Abstract

The Future Circular electron-positron Collider (FCC-ee) is a proposal for a 91.17 km collider, which would operate in four modes with energies ranging from 45.6 GeV (Z-pole) to 182.5 GeV ($t\bar{t}$-production). At high energies the beam lifetime could be as low as 6 minutes, requiring the beam to be continuously topped up to reach a high integrated luminosity. This top-up injection would use a separate booster ring in the same tunnel as the collider, which would accelerate the beams to the collider energy. The booster ring should achieve a lower equilibrium emittance than the collider, despite challenges such as a long damping time and no magnet-strength tapering to compensate for the impact of synchrotron radiation. For top-up injection into the collider, we consider two strategies: conventional bump injection, employing a closed orbit bump, and injection using a multipole kicker magnet. On-axis and off-axis sub-schemes will be studied for both. We compare these injection strategies on aspects including spatial constraints, machine protection, perturbation to the stored beam and hardware parameters.

INTRODUCTION

The FCC-ee

The FCC-ee [1] is a proposed, high-luminosity, circular lepton collider offering the opportunity for precision study of the Higgs and electroweak sectors. To maximise the sensitivity to new physics, it would operate in four modes, from the lowest energy Z-mode to the highest energy $t\bar{t}$-production threshold. The lowest and highest energy machine parameters are given in Table 1. The beam lifetime would be less than an hour for the highest energies because of radiative Bhabha scattering and beamstrahlung. Therefore, to achieve a high integrated luminosity there will need to be continuous full-energy, top-up injection into the collider. During injection, the disturbance to collisions and any stoppage to data-taking in the detectors should be minimised.

Top-up injection is planned via a booster ring in the same tunnel as the collider ring. The booster would be the final stage of the FCC-ee injector chain. The beam is first accelerated within a pre-injector complex, after which it will be transferred to either a pre-booster ring, such as the CERN SPS, or a 20 GeV linac. Following this, the beam will be injected into the booster ring, where the required number of bunches will be accumulated. The booster will only hold up to 10% of the charge of the collider, so that the initial filling of the collider will need 10 injections from the booster. Once the bunches are accumulated in the booster, they will be accelerated from 20 GeV to the collider energy. Operating across this energy range presents challenges for the booster, for example, achieving the necessary field quality and reproducibility between cycles at the lowest energies.

The booster ring could either be stacked vertically above the collider ring or side-by-side. Regardless of the positioning of the booster ring, injection into the collider ring must be in the horizontal plane because of the much smaller vertical emittance.

To prevent longitudinal instability of the colliding beams, the charge balance between the electron and positron beams should be kept within 3-5% of each other. This would require alternating electron and positron top-up and an injector chain which could provide bunch-to-bunch charge variations from 0-100% of the nominal value.

Table 1: FCC-ee parameters (CDR [1]) for Z- and $t\bar{t}$-operations. The beam lifetime is given as that from Bhabha scattering/beamstrahlung.

Parameter	Unit	Z	$t\bar{t}$
Beam energy	GeV	45.6	182.5
Beam lifetime	min	68/>200	39/18
Beam current	mA	1390	5.4
# bunches/beam		16 640	48
Magnetic rigidity	Tm	152.1	608.7
Emittance (x/y)	nm/pm	0.27/1.0	1.46/2.9
Energy spread	%	0.132	0.192

Injection into the Collider

The collider injection system is proposed to be located in the Long Straight Section (LSS) B. In these proceedings we consider two methods of top-up injection: conventional bump injection and multipole kicker injection (MKI), with off-axis and on-axis sub-schemes for each. A previous study of several top-up injection methods for lepton colliders established these as the most suitable [2]. Here, we present a comparison of the schemes with the goal of converging towards one.

By Liouville's theorem [3], the density of particles in phase-space stays constant while under conservative forces, meaning that you cannot inject particles into the phase-space of the stored bunches. Beams are instead injected with a separation from the stored beams and merge via synchrotron radiation damping. For *off-axis* injection, the bunches are injected with a transverse separation from the stored beam

* rebecca.louise.ramjiawan@cern.ch

ISBN: 978-3-95450-236-3 ISSN: 2673-7027 doi:10.18429/JACoW-eeFACT2022-THXAT0104

and perform betatron oscillations as they damp. With *on-axis* injection, bunches are injected with a momentum offset onto the off-momentum closed orbit and perform synchrotron oscillations. Consequently, for on-axis injection, there must be a non-zero dispersion at the septum to separate the on-momentum and off-momentum closed orbits.

For conventional bump injection (Fig. 1(a)), a dynamic orbit bump brings the stored beam close to the septum blade. The bump is collapsed within one revolution so that the injected beam is not lost on the septum. MKI (Fig. 1(b)) instead makes use of a multipole or non-linear kicker with a transverse field profile which would provide a kick to the injected bunch, off-axis, and a field-free region for the stored beam, on-axis.

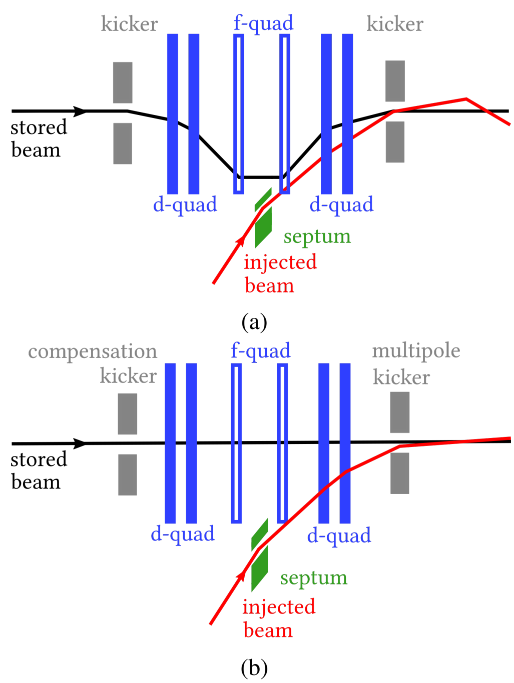

Figure 1: Schematics of the beam trajectories and beamline elements for (a) conventional bump injection and (b) multipole kicker injection [4].

In these proceedings, we consider the Z- and tt̄-operations because the Z-mode has the highest stored beam energy and tt̄-operation the highest beam rigidity. The Z-mode injection optics are presented in Fig. 2. A larger β_x-value at the septum means the septum width is smaller compared with the beam size, reducing its impact.

CONVENTIONAL BUMP INJECTION

The kickers used to create the orbit bump are separated by π-phase-advance so as to produce a closed orbit bump with only two kickers. The orbit bump must rise and fall within one revolution to avoid beam loss on the septum. Ideally, the kicker rise and fall times should fit within the abort gap of the collider ring ($\leq$ 3 µs). To reduce the beam loss at the septum, the separation between the injected and stored beams should be $> 5\sigma_i + S + 5\sigma_s$, where σ denotes the r.m.s beam size, the subscripts i and s denote the injected and stored beams, and S is the septum width. The bump amplitude must be $> 10\sigma_i + S$ to avoid losing the injected beam at the septum for subsequent revolutions.

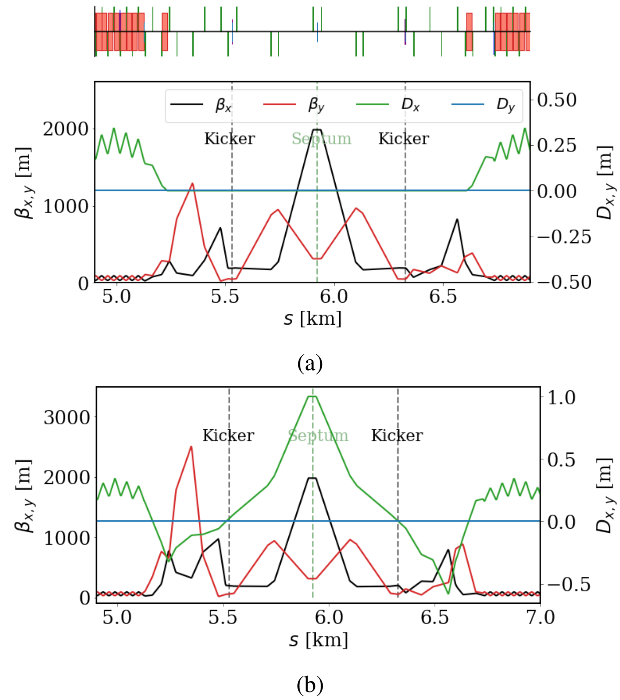

Figure 2: Injection region optics for Z-mode operation, with Twiss functions β_x (black), β_y (red) and dispersion D_x (green), D_y (blue) showing (a) off-axis injection and (b) on-axis, conventional bump injection [4]. A synoptic overview of the beamline is shown above.

Optimising the Twiss Parameters

The Twiss parameters of the injected beam at the septum should be optimised to minimise the phase space needed for the injected beam [5]. To calculate the optimum parameters, simplifying assumptions were made: $\alpha_x = 0$ and the beam angle $x' = 0$, for the stored and injected beams at the septum. For reference, the true value of α_x for the stored beam is 0.016143. The injected beam emittance was assumed to be equal to the booster ring equilibrium emittance, 0.235 nm rad for the Z-mode. Under these conditions, the optimum β for the injected beam is 550 m, corresponding to a beam size of 0.35 mm.

The beam trajectories and envelopes at injection are presented in Fig. 3. This configuration was achieved with kicker deflections of 12.5 µrad and a septum deflection of 100 µrad. If we consider 5σ envelopes for both beams this would allow for a 3 mm septum for Z-mode operation. For the other operation modes, depending on the injection-region optics and the emittances of the injected and stored beams, conventional bump injection may necessitate a very thin septum such as an electrostatic wire septum [6]. With a wire septum, we could achieve blade widths of the order of 100s of microns. Tracking studies are ongoing to estimate the

ISBN: 978-3-95450-236-3 ISSN: 2673-7027 doi:10.18429/JACoW-eeFACT2022-THXAT0104

injection efficiency in order to compare the performance with an electrostatic versus magnetic septum.

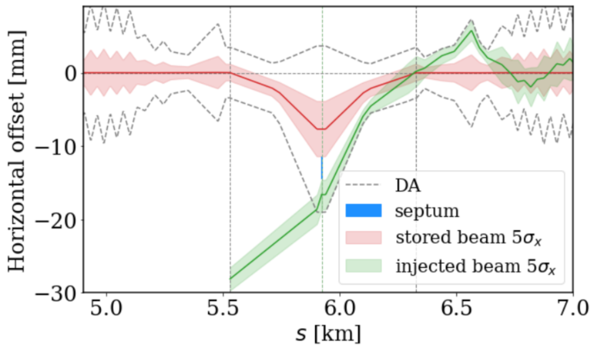

Figure 3: Injected and stored beam envelopes for off-axis conventional bump injection with optimised Twiss parameters. The 15σ dynamic aperture (DA) is indicated with a grey dashed line.

The hardware specifications at the $t\bar{t}$-threshold will be the most challenging, with a beam rigidity of 608.7 Tm. With a 182.5 GeV beam, a stripline kicker could meet the requirements for 12.5 µrad deflection, corresponding to an integrated electric field of 1.14 MV. For a 50 Ω stripline kicker, with a magnetic length of 3 m and a plate separation of 20 mm, this would require a potential difference of ±3.75 kV. If the two kickers were powered in series the ripples or jitter in the power supply would, ideally, cancel because of the π-phase-advance. However, optics errors, meaning the phase advance is not exactly π, or manufacturing and cabling differences between the two kickers would lead to leakage of the orbit bump. If this were the case, additional kickers could be needed to close the bump.

The kicker pulse length should cover the injection of the full booster ring, with a pulse flat-top >304 µs. The repetition rate for these kickers is determined by the booster cycle-time, which is 50.95 s for the Z-mode and 5.6 s for $t\bar{t}$-operation. The repetition rate for these kickers would be 0.01-0.09 Hz, taking into account the alternating electron and positron injection.

Electrostatic Wire Septa

An electrostatic wire septum comprises many contiguous wires under tension, forming a plane separating high-field and field-free regions. In reality, in the field-free regions there is still a low field, called the leakage field. In lepton machines, these septa have an increased risk sparking caused by incident synchrotron radiation (SR). Sparking risks damage to the septum and also to the machine, if not safeguarded against. To establish whether these septa would be suitable for the FCC-ee top-up injection, there will be studies into the effect of X-rays on electrostatic septa sparking rates as a function of voltage.

Here we consider a septum deflection angle of 100 µrad which could be achieved with two 3-m-long modules. We assume an effective septum width of 300 µm. At 182.5 GeV, the electric field strength would be 2.9 MV/m. The wire septum could be preceded by a thicker magnetic septum to reduce the deflection needed. The alignment of the beam with the wire septum is critical and would need a dedicated alignment system. Accident and failure scenarios must be considered and machine protection strategies developed to prevent the beam from impacting the septum.

On-axis Injection

For on-axis injection, the beam is injected with a momentum offset onto the off-momentum closed orbit; this scheme is presented in Fig. 4. The dispersion needed to separate the on- and off-momentum closed orbits leads to larger beam sizes at the septum, thus requiring a larger bump height (17.1 mm), corresponding to a kicker deflection of 27 µrad. The momentum offset for the injected bunch, $\delta = -1.9‰$, is selected such that the separation between stored and injected beams, $|D_x\delta|$, is at least $5\sigma_i + S + 5\sigma_s$.

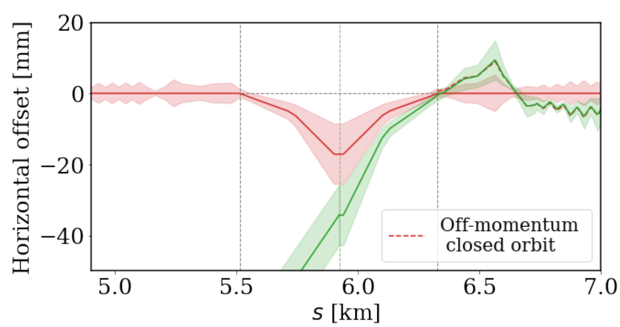

Figure 4: Beam envelopes for on-axis conventional bump injection. The beam is injected with a -1.9‰ momentum offset. The kicker and septum locations are denoted with dotted lines [4].

MULTIPOLE KICKER INJECTION

The ideal multipole kicker would have zero field for the entire stored beam and a constant field for the injected beam, i.e. a step function. The design for the MKI kicker should minimise disturbance to the trajectory and distribution of the stored beam and, consequently, may offer a less disruptive injection method with a lower impact on the luminosity. A proposal for a multipole kicker design is described in [2], based on two opposing, similarly powered, C-shaped dipoles. A 'compensation' kicker placed π-phase upstream of the MKI kicker (Fig. 1) would compensate the kicker's perturbation of the stored beam distribution and mitigate emittance blow-up. Beam distributions with and without the compensation kicker are shown in Fig. 5, highlighting its importance.

The minimum separation of the injected and stored beams at the septum ($> 5\sigma_i + S + 15\sigma_s$) is larger than for conventional bump injection. The beam is injected with a $10\sigma_x$-offset at the kicker and the septum must remain clear of the resulting betatron oscillations. A proposal for an off-axis

ISBN: 978-3-95450-236-3 ISSN: 2673-7027 doi:10.18429/JACoW-eeFACT2022-THXAT0104

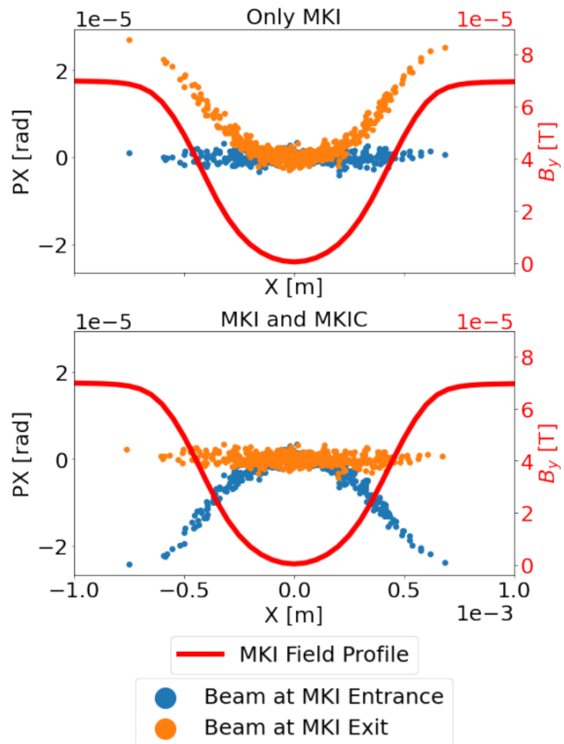

Figure 5: Tracked distributions for the stored beam at the MKI kicker entrance and exit (top) *without* a compensation kicker and (bottom) *with* a compensation kicker [7]. The MKI field profile is overlaid for comparison.

MKI injection scheme is shown in Fig. 6, with kicker deflections of 29 µrad and a septum deflection of 100 µrad . For MKI, a magnetic septum with a blade width of a few millimetres would be sufficient, here we assume 3 mm. The septum should have a deflecting-field-region gap-width of >8 mm.

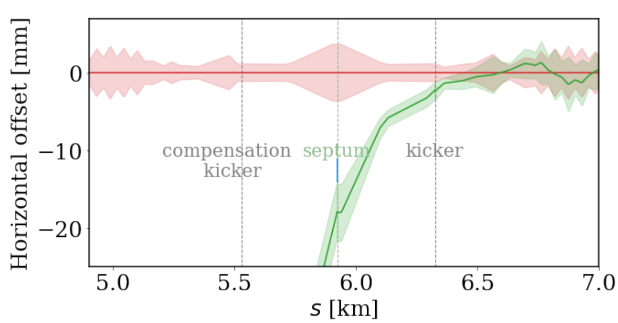

Figure 6: Beam envelopes for off-axis, multipole kicker injection [4].

Machine Protection

For all operation modes, machine protection strategies are crucial to mitigate the risk of damage to the machine. For Z-operation, there would be 20.6 MJ of stored energy per beam. The most suitable protection methods depend on the time-scales of the failure modes. The machine could be safeguarded against slower failures, e.g. changes in the septum field, with an active system, whereby the beam is dumped if the septum current varies by more than a few per mille. If there is a fault in the septum power supply, the magnetic field, B, will decay as $\Delta B/B = 1 - e^{\frac{-t}{\tau}}$, with the magnet decay constant, τ. A 0.2% change in the septum would mean a 0.3 mm offset of the injected beam at the multipole kicker and, consequently, < 1% difference in the deflection angle. If we can tolerate up to a 0.2% change in the septum, and we assume for example $\tau = 1$ s, we would need to abort the beam in less than 7 turns (2.1 ms).

Kicker failure, either failure to fire or erratic firing, would occur on a very short timescale and, therefore, would require passive protection such as an absorber. The absorber should be placed around $\frac{\pi}{2}$-phase-advance from the kicker so as to be furthest from the stored beam. An example scenario for MKI where the kicker fails to fire is shown in Fig. 7; the absorber would be placed at 6.6 km.

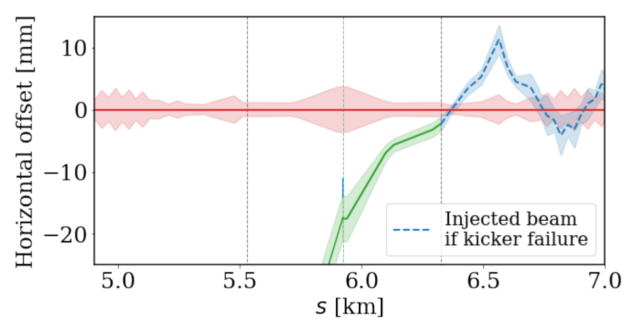

Figure 7: The injected beam trajectory if the MKI injection kicker fails to fire [4].

With conventional bump injection, the beam risks impacting the septum if the orbit bump height increases, either because of beam trajectory or kicker error, or if the beam size at the septum increases. Therefore, a mask will be needed upstream to protect the septum. Another important scenario to consider is the failure of dipoles in the transfer line from the booster to the collider. If unprotected this could lead to damage to the septum or the collider ring itself.

BOOSTER RING

The FCC-ee booster ring will accumulate beams from either a pre-booster ring or linac and accelerate them to collider energy, ready for top-up injection. The booster ring will follow the trajectory of the collider [8], except at the interaction points (IPs) where there will be a ‘bypass’ for the booster so as to minimise synchrotron radiation to the experiments and allow for the collider IP crossing angles (Fig. 8). Injection into the booster is foreseen at site PB (Fig. 9) with the RF sections at PH and PL [9]. At site PL, 11.4 m, 400 MHz cryomodules would be arranged depending on the booster extraction energy. At PH, there would be 7.5 m, 800 MHz cryomodules only for tt̄-operation. It may instead be possible to use 800 MHz RF for all operations modes [10].

ISBN: 978-3-95450-236-3 ISSN: 2673-7027 doi:10.18429/JACoW-eeFACT2022-THXAT0104

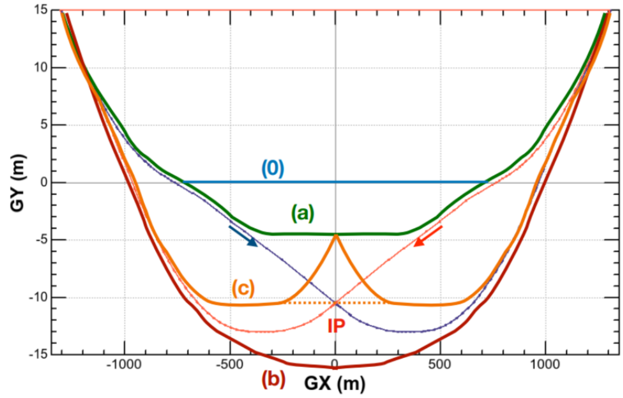

Figure 8: Options for the booster bypass regions around the collider IPs [9]. The collider-beam trajectories (thin red and blue lines) are indicated with arrows.

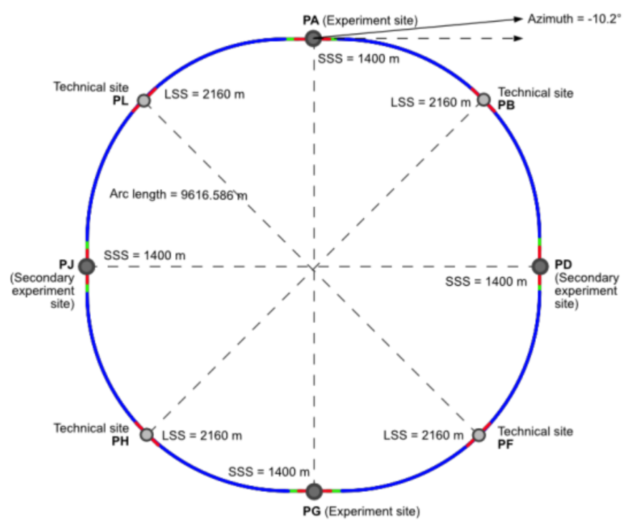

Figure 9: Booster layout indicating Long Straight Sections (LSS) and Short Straight Sections (SSS) [9].

Injection and Extraction Systems

The booster injection system could be located in the 2160 m LSS PB. If the booster is preceded by a 20 GeV linac then two-bunch pulses would be injected at 200 Hz. These would be injected into the booster between existing stored bunches and, therefore, the injection scheme must be designed so as not to disturb the stored beam. The spacing between stored bunches is insufficient to allow an injection kicker to rise and fall, eliminating the option for on-axis, single-kicker injection. In this case, off-axis conventional bump injection would be suitable [11], either in the horizontal or vertical plane. In these proceedings, we address only horizontal injection.

Proposed injection-region optics are presented in Fig. 10. These optics have an high β_x-value at the septum (302 m) to minimise the kicker deflections and to minimise the impact of the septum blade. The magnet apertures in the injection region were increased to ±40 mm to accommodate the bump injection scheme. The new optics had a maximum pole-tip field strength of 0.73 T at the highest booster energy, 182.5 GeV [11].

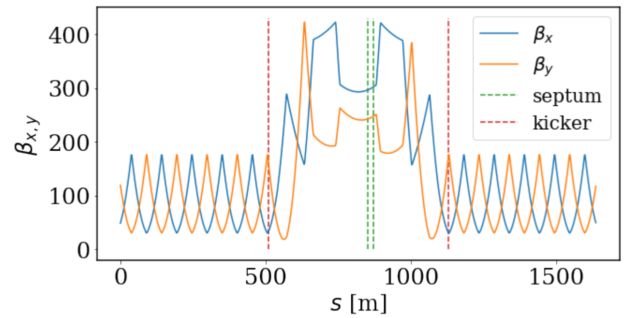

Figure 10: Booster injection-region β-functions.

This injection scheme uses two kickers, each providing deflections of 125 µrad; either magnetic or stripline kicker technology would be suitable. The trajectories and envelopes of the injected and stored beams are shown in Fig. 11(a). First, a magnetic septum, with a blade width of 10 mm, provides a deflection to the injected beam of 3 mrad (integrated B-field of 2 mT m) [11]. This is succeeded by an electrostatic septum, with a blade width of 1 mm, which then deflects the beam by 0.5 mrad (integrated E-field of 3.33 MV) [11]. Just like for the collider injection, the injected beam Twiss parameters at the septum will be optimised to improve the injection efficiency.

A preliminary proposal for the extraction system is presented in Fig. 11(b). This scheme incorporates ten kickers, each providing a deflection of 43 µrad, so that in the case one or two kickers fail the beam can still be safely extracted. A defocusing quadrupole after the kickers magnifies this deflection and, finally, two magnetic septa fully extract the beam. The septa, with blade widths of 10 mm, each provide a deflection of 4 mrad.

Equilibrium Emittance

The normalized emittance of the beam injected into the booster is expected to be 50 µm with an energy spread of 0.1%. The bunch spacing will be 15-100 ns. At the Z-pole energy for the 4IP lattice, the beam lifetime would be 1090 s so that there should be top-up injection, for each specie, every 31.61 s. This restricts the accumulation and ramp time in the booster to 24 s and 1.2 s, respectively.

Due to intra-beam scattering (IBS), the equilibrium emittance would not be reached during accumulation at 20 GeV [12]. The damping time is characterised by the second synchrotron radiation integral, I_2,

$$I_2 = \oint \frac{1}{\rho^2} ds, \quad (1)$$

with bending radius, ρ, and distance along the reference trajectory, s. The I_2 of the booster ring is too small to reach the equilibrium emittance within the 1.2 s ramp time and methods to increase it were considered.

ISBN: 978-3-95450-236-3 ISSN: 2673-7027 doi:10.18429/JACoW-eeFACT2022-THXAT0104

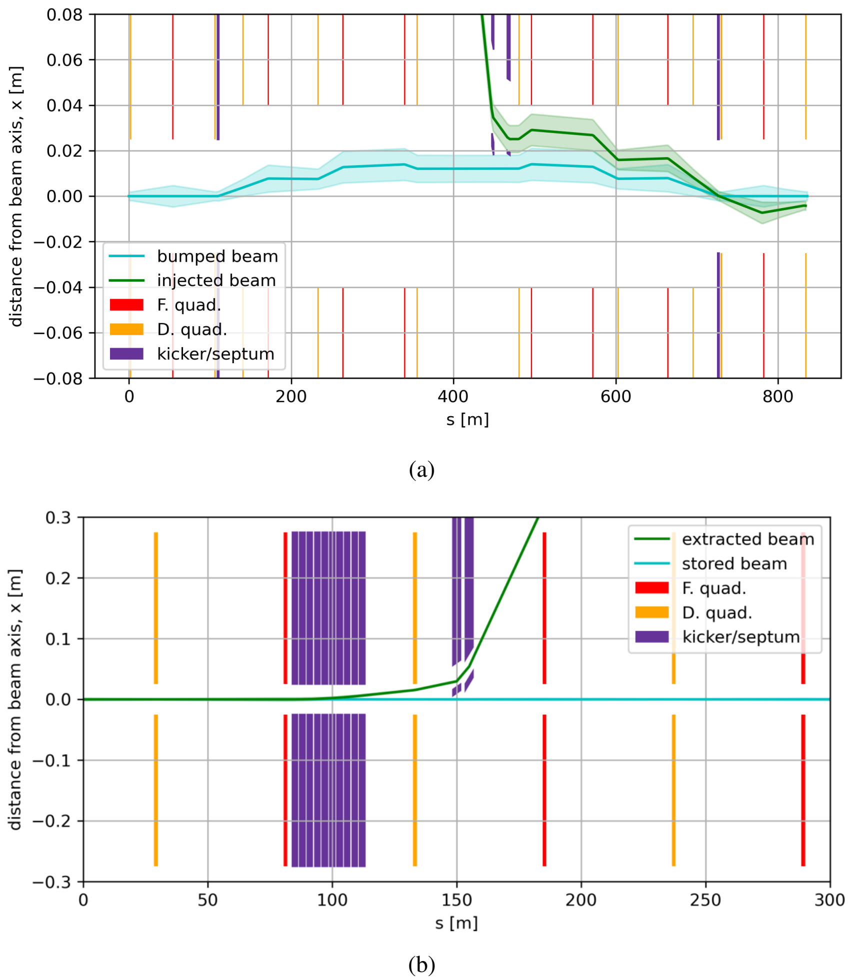

Figure 11: (a) Injected and stored beam envelopes for off-axis conventional bump injection into the booster ring. Two kickers form a closed orbit bump and two septa deflect the injected beam [11]. (b) Extracted and stored beam envelopes, with an extraction system comprising ten kickers and two magnetic septa [11]. Focusing and defocusing quadrupoles are shown in red and yellow, respectively.

ISBN: 978-3-95450-236-3 ISSN: 2673-7027 doi:10.18429/JACoW-eeFACT2022-THXAT0104

For the Z-mode, adding 2 s once at extraction energy would mean the collider emittance could be reached without needing to change the optics; this is demonstrated in Fig. 12. The drawback, however, would be an increase in the booster cycle-time. Alternatively, the addition of normal-conducting damping wigglers in the RF straight sections would reduce the damping time to order 0.1 s, although, at the expense of an increased equilibrium emittance [13]. These wigglers would be switched off during the energy ramp. Another option is to have an electron damping ring, which would help to meet vertical emittance targets [9].

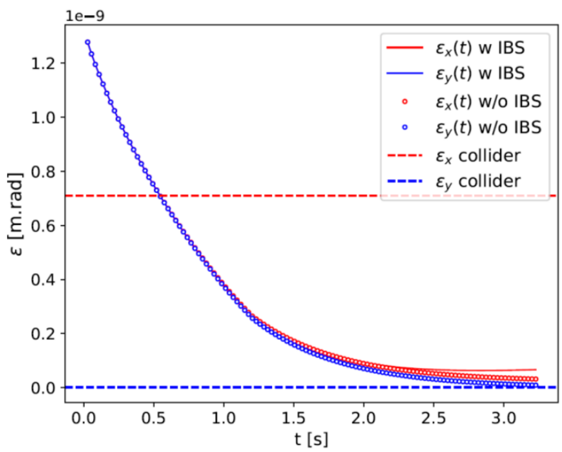

Figure 12: Emittance ($\varepsilon_{x,y}$) evolution in the booster ring during the ramp plus an additional 2 s at extraction energy [9], both with and without IBS, compared with the collider emittance.

Different booster optics were compared, including optics with phase advances $\phi_{x/y} = 90°/90°$ or $\phi_{x/y} = 60°/60°$ per FODO cell. Having the same phase advance in the horizontal and vertical planes is favourable for the chromaticity correction scheme [13]. To prevent the decrease of luminosity during top-up injection, the equilibrium emittance of the booster must be less than that of the collider ring. The equilibrium emittances for the two optics are given in Table 2, showing that only the 90°/90° lattice is suitable for H- and $t\bar{t}$-operation. To minimise IBS for the Z- and W-modes, the 60°/60° lattice is preferred.

Dynamic Aperture

For robust and efficient conventional bump injection, the dynamic aperture (DA) should be at least $15\sigma_s$. The booster DA at injection was estimated using MAD-X Thin-Lens tracking over 4500 turns. Alignment and multipole errors were included, as well as radiation damping and quantum excitation. The results for the 60°/60° optics are shown in Fig. 13. The DA for the 60°/60° optics is higher than 20σ up to a ±0.5% momentum offset, both horizontally and vertically, allowing for injection in either plane. For the 90°/90° optics, the horizontal on-momentum DA is approximately 15σ; this will be optimised to increase the beam lifetime. Although, in these proceedings we have focused on horizontal injection, for the 90°/90° optics the DA is larger in the vertical plane which could mean a better injection efficiency for vertical injection.

Table 2: Equilibrium emittances (r.m.s) for the booster and collider rings. Two different phase advances for the booster arc FODO cells are compared.

Beam Energy [GeV]	**Equilibrium Emittance** [nm rad]		
	Booster		Collider
$\phi_{x/y}$	60°/60°	90°/90°	
45.6 (Z)	0.235	0.078	0.71
80.0 (W)	0.729	0.242	2.16
120.0 (H)	4.229	0.545	0.64
175 ($t\bar{t}$)	3.540	1.172	1.49

CONCLUSION

In these proceedings we have considered two options for the top-up injection of the FCC-ee collider ring: conventional bump injection and multipole kicker injection. We study off-axis and on-axis sub-schemes for both.

We have presented a scheme for conventional bump injection, with optimised Twiss parameters to improve injection efficiency. Conventional bump injection, depending on the emittance and Twiss parameters of the injected beam, might require a thin electrostatic septum with blade width of order 100s microns. R&D would be needed to determine the expected rate of sparking of the septum due to synchrotron radiation in order to establish whether this could be a suitable means of injection for such a high-energy lepton machine. MKI injection does not require such a thin septum blade and a magnetic septum would be suitable. However, R&D and prototyping would be needed to demonstrate the field quality and alignment tolerances required for this method.

Injection-region optics will also be developed for W-, H- and $t\bar{t}$-operations and for on-axis MKI injection. These studies were for the 2IP CDR lattice [1] and will be repeated for the 4IP lattice, for which the injection insertion will need to additionally incorporate a beam crossing. Here, we have described the injection of a single beam and we will now extend this scheme to include both the electron and positron beams.

As collisions will continue during injection, the beam-beam effects during injection need careful study. The injection efficiency should be calculated and compared between the injection methods, including realistic errors and misalignments. The increased background to experiments caused by injection must also be quantified. We aim to converge to a single injection method by 2023-2024, comparing schemes based on metrics including luminosity, injection efficiency, experiment background, machine protection, feasibility, reliability and cost.

ISBN: 978-3-95450-236-3 ISSN: 2673-7027 doi:10.18429/JACoW-eeFACT2022-THXAT0104

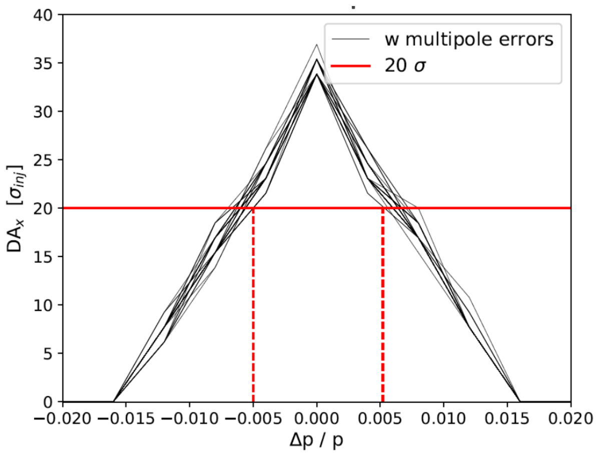

(a)

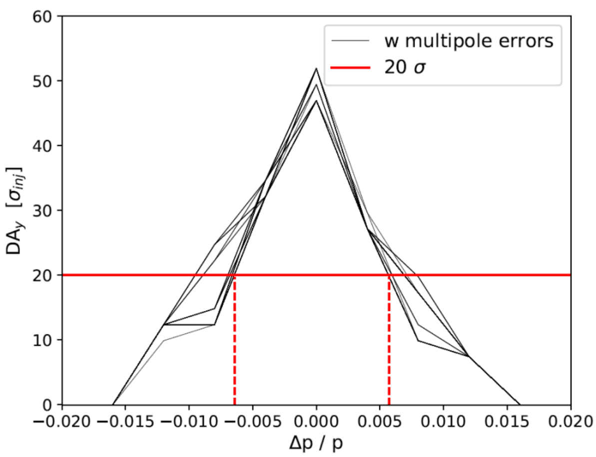

(b)

Figure 13: DA at injection for 60°/60° optics in the (a) horizontal and (b) vertical planes [9]. The grey lines show different random seeds tracked using MAD-X Thin-Lens tracking over 4500 turns.

We have given an overview of the current status of the FCC-ee booster, which will accumulate and accelerate the beams for full-energy injection into the collider. We have presented a proposal for the FCC-ee injection and extraction schemes, considering briefly the kicker and septa requirements for both. To maximise the integrated luminosity, the booster equilibrium emittance must be less than that of the collider. For the Z- and W- modes, a horizontal/vertical phase advance per FODO cell of 60°/60° was selected to reduce IBS, whereas, for the H- and $t\bar{t}$-modes, 90°/90° phase advance was chosen to minimise the equilibrium emittance. For the booster injection, we propose a conventional bump injection scheme, which would require at least a 15σ dynamic aperture. For the 60°/60° lattice, the dynamic aperture exceeded 20σ even up to a ±0.5% momentum offset. The 90°/90° lattice has sufficient DA in the vertical plane but will need optimisation to increase the horizontal DA.

ACKNOWLEDGEMENTS

We thank M. Aiba and M. Boland for helpful discussions. This project has received funding from the European Union's Horizon 2020 research and innovation programme under grant agreement No 951754.

REFERENCES

[1] FCC collaboration, "FCC-ee: The lepton collider: future circular collider conceptual design report volume 2", *Eur. Phys. J. Spec. Top.*, vol. 228, no. 2, pp. 261-623, 2019. doi:10.1140/epjst/e2019-900045-4

[2] M. Aiba, *et al.*, "Top-up injection schemes for future circular lepton collider", *Nucl. Instrum. Methods Phys. Res. Sect. A*, vol. 880, pp. 98-106, 2018. doi:10.1016/j.nima.2017.10.075

[3] R. L. Mills and A. M. Sessler, "Liouville's theorem and phase-space cooling", Lawrence Berkeley Lab., Berkeley, CA, USA, Rep. LBL-34667, 1993.

[4] R. Ramjiawan, M. Aiba, W. Bartmann, Y. Dutheil, M. Hofer, and P. J. Hunchak, "Concepts and considerations for FCC-ee top-up injection strategies", in *Proc. IPAC'22*, Bangkok, Thailand, Jun. 2022, pp. 2106–2109. doi:10.18429/JACoW-IPAC2022-WEPOTK025

[5] R. P. Filler III, "Optimal Twiss parameters for injected beam for top off injection", Brookhaven National Lab., Upton, NY, USA, Rep. Nos. NSLSII-ASD-TN-059 and BNL-211068-2019-TECH, Jul. 2018. doi:/10.2172/1504883

[6] M.J. Barnes, J. Borburgh, B. Goddard, and M. Hourican, "Injection and extraction magnets: septa", *CERN Accelerator School: Specialised Course on magnets (Report)*, CERN, Geneva, Switzerland, Rep. CERN-2010-004, pp. 167–184, 2010.

[7] P. Hunchak *et al.*, "Studies on Top-Up Injection Into the FCC-ee Collider Ring", in *Proc. IPAC'22*, Bangkok, Thailand, Jun. 2022, pp. 1699–1702. doi:10.18429/JACoW-IPAC2022-WEPOST011

[8] B. Härer, B. J. Holzer, Y. Papaphilippou, and T. Tydecks, "Status of the FCC-ee top-up booster synchrotron", in *Proc. IPAC'18*, Vancouver, BC, Canada, Apr.-May 2018, pp. 250–252. doi:10.18429/JACoW-IPAC2018-MOPMF059

[9] B. Dalena, "FCC-ee Booster Design", presented at ICHEP'22, Bologna, Italy, Jun. 2022, https://agenda.infn.it/event/28874/contributions/169171/

[10] F. Peauger, "Baseline & cavity options for FCC-ee", presented at FCC Week 2022, Sorbonne Université, Paris, France, May-Jun. 2022, https://indico.cern.ch/event/1064327/contributions/4888581/

[11] E. Howling, "Design studies towards the FCC-ee booster ring injection and extraction", CERN, Geneva, Switzerland, Rep. CERN-STUDENTS-Note-2022-146, 2022, http://cds.cern.ch/record/2826991

[12] A. Chance, "Status of the high-energy booster", presented at FCC Week 2022, Sorbonne Université, Paris, France, May-Jun. 2022, https://indico.cern.ch/event/1064327/contributions/4893280/

ISBN: 978-3-95450-236-3 ISSN: 2673-7027 doi:10.18429/JACoW-eeFACT2022-THXAT0104

[13] B. Härer and T. Tydecks, "Lattice design and dynamic aperture studies for the FCC-ee top-up booster synchrotron", *arXiv preprint arXiv:2111.14462*. doi:10.48550/arXiv.2111.14462

ISBN: 978-3-95450-236-3 ISSN: 2673-7027 doi:10.18429/JACoW-eeFACT2022-THXAS0102

STATUS AND EXPERIENCES OF THE VACUUM SYSTEM IN THE SuperKEKB MAIN RING

T. Ishibashi[1,2 †], Y. Suetsugu[1,2], K. Shibata[1,2], M. Shirai[1], S. Terui[1], K. Kanazawa[1,2], H. Hisamatsu[1], M. L. Yao[2]
[1]KEK Accelerator Laboratory, Tsukuba, Ibaraki, Japan
[2]SOKENDAI, Hayama, Kanagawa, Japan

Abstract

Since the SuperKEKB began operation in 2016, the stored beam currents in the main ring have been gradually increased. When the system was commissioned in the Spring of 2022, the maximum beam currents were ~1460 mA in the low-energy ring for positrons (LER) and ~1145 mA in the high-energy ring for electrons (HER). The beam doses are ~7312 Ah in the LER and ~6199 Ah in the HER, and vacuum scrubbing of the beam pipes is proceeding well. However, during these operations, problems such as abnormal pressure rises, vacuum leaks, and collimator damage have occurred. Here, we report on our experiences and the status of the vacuum system after its commissioning in the spring of 2019, known as Phase 3.

INTRODUCTION

The SuperKEKB accelerator is an electron–positron collider with storage rings [1]. The main ring consists of a low-energy ring (LER) for positrons (beam energy: 4 GeV; designed beam current: 3.6 A) and high-energy ring (HER) for electrons (beam energy: 7 GeV; designed beam current: 2.6 A), both with a circumference of about 3 km. Cessation of the operation of the KEKB accelerator ceased in 2010 was followed by about six years of construction of upgrades. During this period, approximately 93% of the vacuum components in the LER and approximately 20% of those in the HER were newly developed and installed [2]. Fig. 1 show the layout of the SuperKEKB main ring. Names of vertical and horizontal collimators are indicated by the letters V and H, respectively. The ring has four arc sections and four straight sections. IR: interaction region; SC: superconducting cavity region; ARES: normal-conducting RF cavity region. The ring is divided in to 12 sections, D01 to D12. Figure 2 shows a photograph of an arc-section of the ring, where: IP is ion pump; NEG is nonevaporable getter pump. Rectifiers are installed in the heater of the NEG pumps and in bending magnets in the LER, and are used to activate these while the magnets are excited

The SuperKEKB main ring began operating in 2016, and this first commissioning stage from February to June of that year was named Phase 1 [3, 4]. The second commissioning stage from March to July of 2018 was named Phase 2, and a positron-damping ring (DR) was introduced after this stage [5, 6]. In 2019, a full-scale physics experiment with the Belle II detector started; this was named Phase 3, which continues to the present.

† takuya.ishibashi@kek.jp

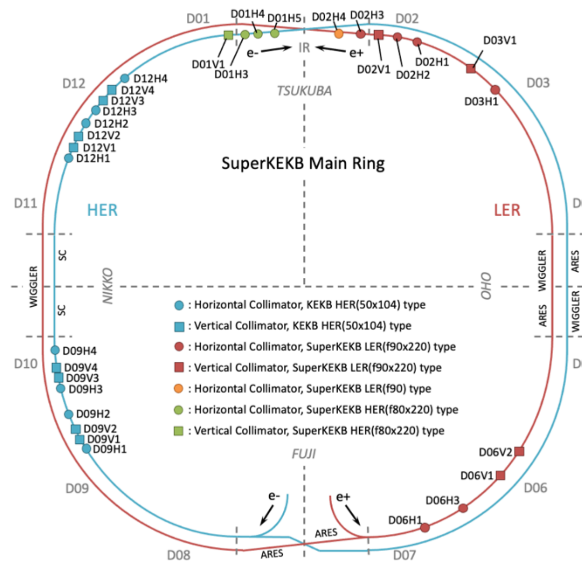

Figure 1: Layout of the SuperKEKB main ring.

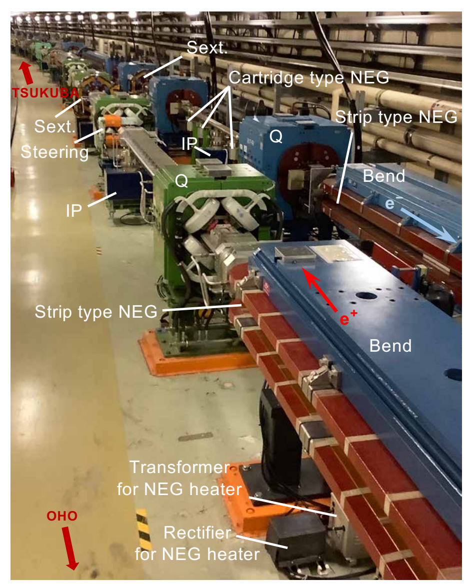

Figure 2: Photograph of an arc-section of the SuperKEKB main ring.

After breaking the world record for luminosity in 2020 [7], SuperKEKB has continued to set new records. The record peak luminosity was ~4.7 × 10^{34} cm^{-2} s^{-1} with 1.4 A in the LER and 1.1 A in the HER when the stored bunch number was 2249 during the spring run of 2022 [8].

ISBN: 978-3-95450-236-3 ISSN: 2673-7027 doi:10.18429/JACoW-eeFACT2022-THXAS0102

The highest stored beam current is ~1460 mA for the LER and ~1145 mA for the HER. The vacuum components newly developed and introduced for SuperKEKB generally operate as expected. However, troubles, such as vacuum leaks, sometimes occur, most of which are caused by the thermal load from the synchrotron radiation (SR).

The upgrading of the vacuum system and the status of the vacuum system from the start of operation in 2016 to Phase 2 operation in 2018 have been previously reported [3–6, 9, 10]. Here, we report mainly on our experiences and the current status of the SuperKEKB vacuum system since Phase 3 operation began in 2019.

OPERATION STATUS

In upgrading from KEKB to SuperKEKB, various vacuum components were newly developed and introduced. As a countermeasure to electron-cloud instability in the LER, titanium nitride (TiN)-coated beam pipes were installed almost all the way around the ring, together with beam pipes with antechambers, beam pipes with a groove structure, a clearing electrode, and permanent magnets to induce a magnetic field in the longitudinal direction [11, 12]. In addition, as a countermeasure to impedance, gate valves and bellows chambers equipped with comb-type radio-frequency (RF) shields [13], newly developed collimators [14], MO flanges with very small steps in the vacuum seal part were adopted, among other equipment [2]. These components have generally been working as expected since the start of the operation.

Figure 3 shows the operation time for each of the last six years, the percentage of time when problems were encountered, and the percentage of vacuum system that suffered problems.

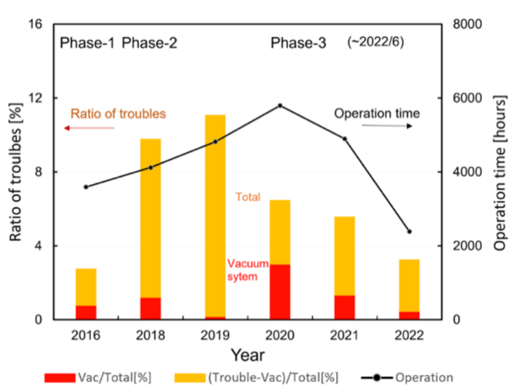

Figure 3: Operating time, ratios of total machine problems, and vacuum-system-related problems for each year since 2016.

The problems referred to here are those that stopped the beam operation. The percentage of the problems related to the vacuum systems was ~4% or less. The main vacuum-system-related problems are air leaks at flanges. In addition, collimators, especially those in the vertical direction, were frequently damaged by beam hits. In 2020 and 2021, the fact that the damaged collimator was replaced during the operating period is also a factor that increased the problem time related to the system.

Vacuum Scrubbing

The pressure increase Δp [Pa] per unit beam current ΔI [A] as a function of the beam dose in the LER and HER from the start of SuperKEKB operation to the end of the latest commissioning period on June 2022 is shown in Fig. 4. The figure also shows the photon-stimulated-desorption (PSD) coefficient η [molecules photon^{-1}] for the photon dose. The beam dose and photon dose [15] are calculated by using the following expressions:

$$(\text{beam dose}) = \int_{t_0}^{t_1} I(t)\,dt \tag{1}$$

$$(\text{photon dose}) = 8.08\times10^{11}\frac{E}{L}\int_{t_0}^{t_1} I(t)\,dt, \tag{2}$$

where I is the beam current I [A], E is the beam energy [eV], L is the photon-irradiated length [m], t_0 and t_1 are the start time of the SuperKEKB operation and the end time of the latest commissioning period. L, the total approximate length of the arc-sections in the rings, is assumed to be 2000 m.

Sets consisting of an ion pump and a cold-cathode ionization gauge (CCG) are installed around each ring at intervals of approximately 10 m. The pressure given is the average of the values indicated by the CCGs (these are conversion values in the case of nitrogen). However, the pressure at the beam channel where the beam actually passes was estimated by simulation to be approximately three times higher than that at the position where the CCGs are installed so in this paper we use a value three times the value indicated by the CCG for the pressure. The lower limit of the pressure measurement by the CCGs is 1×10^{-8} Pa. Then, in the calculations for Fig. 4, the pressure increase is divided by the beam current when the beam current is 40% or more of the maximum value at a given time.

PSD coefficient is calculated using a following formula:

$$\eta = \frac{S_{\text{eff}}}{8.08\times10^{11}kTE}\frac{\Delta p}{\Delta I}, \tag{3}$$

where S_{eff} is the effective pumping speed [m^{3}s^{-1}], k is the Boltzmann constant [J K^{-1}], and T is the temperature [K]. In calculating η, we assumed pumping speeds of 0.06 and 0.03 m^{3}s^{-1}m^{-1} in the LER and HER, respectively, and T = 300 K.

As of June 2022, the LER achieved $\Delta p/\Delta I < 1\times10^{-7}$ Pa A^{-1} for the whole ring and $\eta < 5\times10^{-7}$ molecules photon^{-1} at the arc sections with a beam dose of ~7312.1 A h. Then, the HER achieved $\Delta p/\Delta I < 1\times10^{-8}$ Pa A^{-1} for the whole ring and $\eta < 2\times10^{-8}$ molecules photon^{-1} or less at the arc sections with a beam dose of ~6199.0 A h. The value of $\Delta p/\Delta I$ in the HER is smaller than that in the LER because most of the beam pipes have been reused since the KEKB era, and their surfaces have been scrubbed for longer times than those of newly installed beam pipes.

ISBN: 978-3-95450-236-3 ISSN: 2673-7027 doi:10.18429/JACoW-eeFACT2022-THXAS0102

For LER, another beam dose of ~43400 A h is required for $\Delta p/\Delta I$ to reach $1{\times}10^{-8}$ Pa A^{-1}, which is approximately the same as the present level in the HER by extrapolation using the results of a regression analysis. The achieved beam dose in the LER during the 2022 spring run was ~440 A h month^{-1}, so it would take about 99 months operation to achieve 10^{-8} Pa A^{-1} if we assume the achieved dose rate in the latest commissioning period. In fact, the stored beam current is intended to gradually increase during future operations, so this could be achieved in a shorter operating time. Then, as the beam current increased, a pressure increase due to heating was observed especially in the LER, but note that this effect is not taken into consideration in the present discussion.

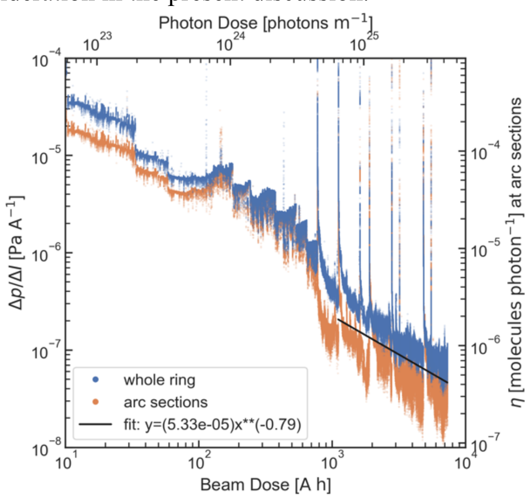

(a) LER

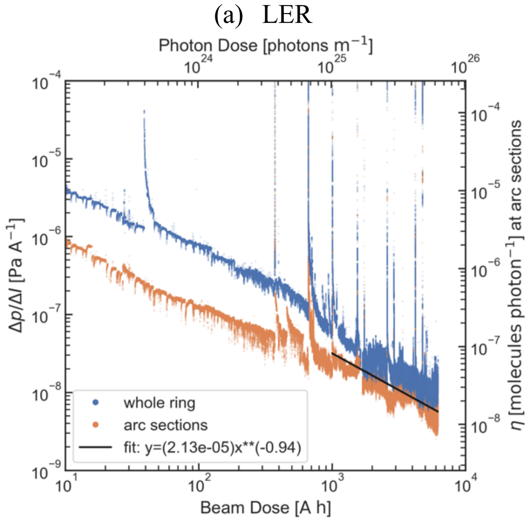

(b) HER

Figure 4: Pressure increase per unit beam current $\Delta p/\Delta I$ and PSD coefficient η at arc sections as a function of beam dose and photon dose in (a) the LER and (b) the HER from February 1st, 2016 to June 22nd, 2022. Result of regression analysis for whole rings from Phase 3 (1112.6 to 7312.1 A h in LER and 1001.9 to 6199.0 A h in HER) with $\Delta p/\Delta I = a \times (\text{beam dose})^b$, where a and b are constants, are also shown.

Residual Gas Species

Figure 5 shows the partial pressure normalized by the beam current in the LER, measured with a residual gas analyzer (RGA) during the 2019 spring run from March 11th to July 1st. It can be seen that the partial pressure of the residual gas decreased as the operating time progressed, indicating that vacuum scrubbing progressed. The RGA measuring this partial pressure is installed near an ion pump in the Tsukuba straight section of the LER, which is upstream of the interaction point.

The main gas species detected during this operation were hydrogen, carbon monoxide, water, methane, carbon dioxide, and oxygen derived from cracking of water, which are typical gas species emitted by PSD. During the shutdown period before the start of this operation, this section was once exposed to the atmosphere for vacuum works and, as a result, the partial pressure of water during this period was relatively high at the beginning of the operation.

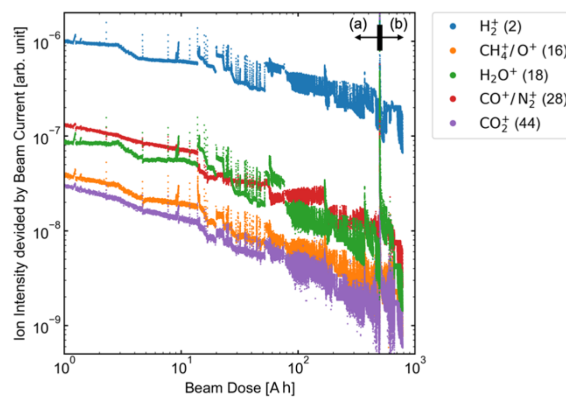

Figure 5: Ion intensity per unit beam current measured by an RGA installed in the Tsukuba straight section of the LER during (a) the spring and (b) the autumn run of 2019. The secondary-electron multiplier of the RGA was used in these measurements. Values in parentheses in the legend refer to the mass-to-charge ratio.

MAJOR PROBLEMS

In this section, we report the major problems that occurred in the SuperKEKB main ring and hindered its operation.

Cooling-Water-System Failure in the Wiggler Magnet Section

The beam in LER was aborted by the temperature interlock of the vacuum system at 17:22:54 on December 5th, 2020. Fig. 6 shows the beam current and the readings of the thermometer (a resistance temperature detector (RTD), attached to the surface of the bellows chambers in the Nikko wiggler section.

The temperatures rose rapidly, beginning at about 17:17, and the beam was then aborted, when the temperature exceeded the interlock threshold of 100 °C. The cause of this sudden rise in temperature was a failure of the water pumps and inverters in the facilities system, one of the

ISBN: 978-3-95450-236-3 ISSN: 2673-7027 doi:10.18429/JACoW-eeFACT2022-THXAS0102

infrastructures of SuperKEKB, and the water flow for the vacuum system was completely stopped in this section. A mask for SR is placed at downstream of each beam pipe, and the temperature on the SR mask rose due to a stoppage of the water flow. The temperature then rose rapidly at the flange on one side only, and we speculate that the difference in thermal expansion between the flanges caused a plastic deformation of the gaskets at that time. Later, at around 17:42, a backup pump in the cooling-water system was started, causing the temperature to drop rapidly.

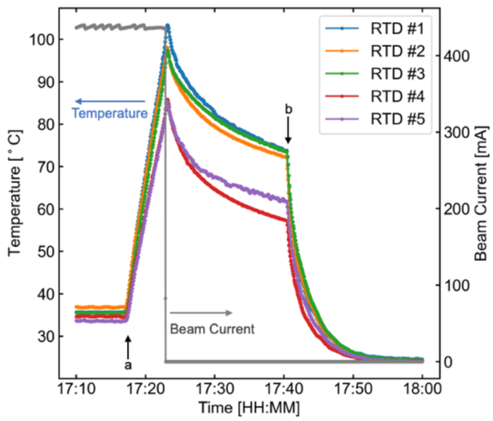

Figure 6: Temperatures of the bellows chambers in Nikko wiggler section and the beam current in the LER. The cooling water system stopped at Point a and resumed at Point b.

A behavior of the pressure after this failure is shown in Fig. 7. When the LER beam decreased or was aborted, the pressure in some CCGs in this section increased accordingly. This suggests that the beam pipes underwent thermal expansion when the beam was stored, and the gasket at the flanges was pinched. Consequently, the leak rate decreased. The beam pipes shrank when the beam was aborted, and the leak rate increased.

A leakage test was then conducted in this section, and leaks were found in a nine of the flanges. These leaks were stopped in three flanges by spraying a liquid sealant (VACSEAL, PASCAL Co. Ltd.) and by tightening the bolts at the others.

It had not been assumed that the flow of water in a section would stop completely due to a failure of the infrastructure, and no interlock system for this purpose had been constructed. Consequently, after this problem, we reconsidered the interlock system and we took appropriate countermeasures, such as issuing beam-abort requests when the water flowrate in the pumping system of the infrastructure dropped.

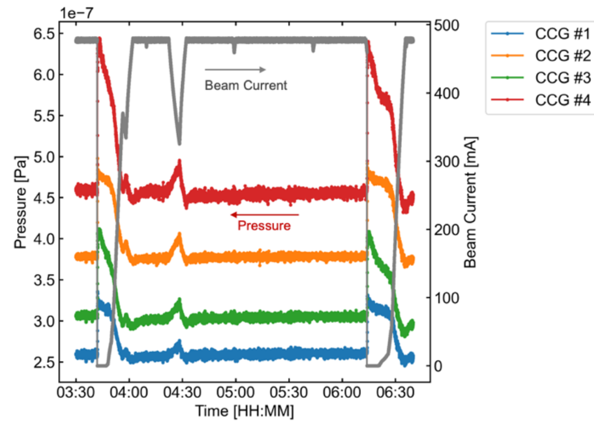

Figure 7: Pressure measured with CCG in Nikko wiggler section and beam current in LER when there are leaks.

Collimator Damage Due to Kicker Accidentally Firing

Because of the narrow physical aperture, there have been many instances in which the beam hit the jaws of the collimators, damaging them [14]. Huge beam-loss events that damage the vertical collimators are called sudden beam losses because it was observed that the beam trajectory suddenly shifted in two to three turns (20–30 μs) before being aborted [16,17]. The cause of this beam loss is still unknown.

There were also damage events for known reasons, such as damage to horizontal collimators caused by accidental firings of injection kickers in the LER. Each set of injection kickers for the main ring consists of three magnets, and two of these sets are installed with a septum magnet in between. Since a thyratron power supply drives the kicker magnet with a one-to-one correspondence, if one of the thyratrons fires and kicks the stored beam horizontally, there is nothing to kick back, so the beam hits the horizontal collimator, which has the narrow horizontal aperture downstream of the injection kickers. The beam current then had to be reduced during the operation until the frequency of accidental firings decreased.

The horizontal position of the center of gravity for each bunch, as measured with a bunch oscillation recorder [18] at the time of an accidental firing is shown in Fig. 8. The harmonic number of the main ring is 5120. Currently, the SuperKEKB main ring operates with two trains and two gaps, referred to as abort gaps, to avoid kicking the bunch on the rising of a kicker for the beam aborts. When a kicker fired accidentally, a part of the first train received a substantial kicking and was lost, as shown in Fig. 8(b). The stored beam was aborted on the next turn.

ISBN: 978-3-95450-236-3 ISSN: 2673-7027 doi:10.18429/JACoW-eeFACT2022-THXAS0102

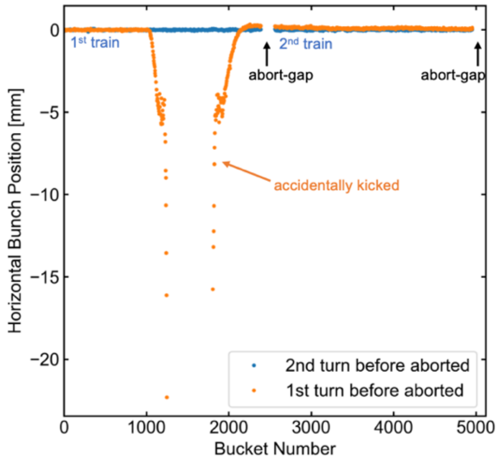

Figure 8: Horizontal position of the center of gravity for each bunch measured with a bunch oscillation recorder and the bucket number when an accidental firing of an injection kicker occurred.

At this time, a pressure burst was observed by the CCG installed near the horizontal collimator named D06H3, as shown in Fig. 9, indicating that the beam hit the jaw.

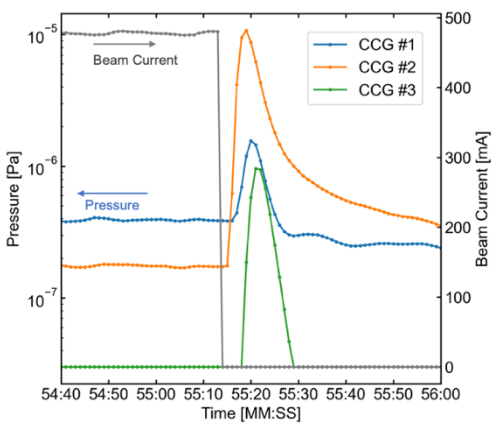

Figure 9: Pressure near D06H3 collimator and beam current in LER when an accidental-firing occurred. CCG #2 is a vacuum gauge closest to the collimator. The distance between the vacuum gauge and the tip of the jaw is approximately 1.2 m for CCG #1, 6.3 m for CCG #2, and 9.3 m for CCG #3.

Figure 10 shows the tip of a jaw located at the inner side of the ring taken from the D06H3 collimator during a shutdown period. The tip was made of tungsten, and it had a large crack and was damaged. Because the probability of a thyratron accidentally firing cannot be reduced to zero, we are developing a robust jaw made of carbon-fiber-reinforced carbon (CFC) as a countermeasure against such an event [16].

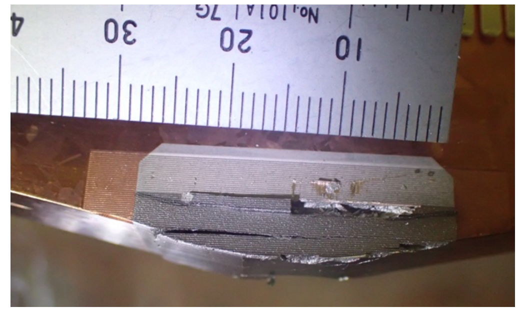

Figure 10: Photograph of a broken tungsten jaw from D06H3.

MINOR INCIDENTS

In this section, we report minor incidents that did not directly affect the operation of the accelerator.

Water Leak in a Collimator's Jaw

During the shutdown period before the start of Phase 3 in 2019, some collimators were newly installed to the main ring. After the installation of the horizontal collimator named D02H1 in the LER, when we ran the cooling water system after rough pumping with a turbomolecular pump (TMP), the high voltage of the CCGs near the collimator was turned off due to an interlock because the pressure increased to the order of 10^{-2} Pa and the number of rotations in the TMP also dropped.

The jaw of the collimator incorporates a cooling-water channel to remove the heat load caused by SR. Because the CCGs near the collimator were turned off when the water flowed, we suspected that there was a leak from the channel to the vacuum chamber. When the water in the channel was removed, the pressure decreased from 10^{-2} to 10^{-3} Pa. However, when a leak test was conducted on the cooling channel, no leak was detectable by simply spraying helium into it, and the leak was detected only after pressurizing the helium to 0.3 MPa. The leak rate was about 1×10^{-5} Pa m^3 s^{-1}.

After removing the jaw, a leak test was performed with a sniffer probe and leak-detection liquid. The leak rate in the channel, as determined by the sniffing scheme for pressurized helium, was ~5.6×10^{-4} Pa m^3 s^{-1}, and the leakage point was at a joint between copper and stainless-steel, as shown in Fig. 11.

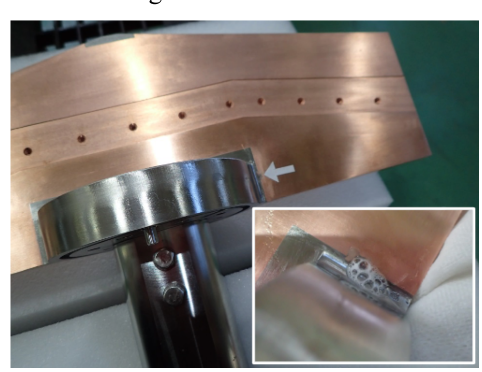

Figure 11: Leakage point of the jaw, as detected by a leak test using a foaming liquid.

ISBN: 978-3-95450-236-3 ISSN: 2673-7027 doi:10.18429/JACoW-eeFACT2022-THXAS0102

Inside this part, a stainless-steel block for the flange and a stainless-steel pipe are welded by tungsten–inert-gas (TIG) welding. In the production of the jaws, the flange and water-channel parts are sandwiched between copper blocks, and a heavy metal such as tungsten or tantalum is placed on the tip and the parts joined by hot isostatic pressing. After joining, these parts were processed into the final shape, and a part of the bead formed by the TIG welding was scraped during this processing, causing the leak.

Before the delivery of the jaws, the cooling water channel was pressurized to ~1.2 MPa with nitrogen, and a leak test was conducted by monitoring the pressure drop with a pressure gauge for at least 10 minutes; however, the item passed the test. In the jaws currently being manufactured, the structure has been improved to prevent scraping of the welding bead. In addition to a rough leak test by monitoring the pressure drop, a precise leak test of the channel with pressurized helium and a leak detector is conducted.

The remanufactured jaw was reinstalled in D02H1 for the 2019 spring operation, but it was difficult to decrease the pressure around this collimator. We consider that this is because the water that leaked at the time of the leak remained in the chamber. Therefore, the entire collimator chamber and beam pipes near it were baked in the tunnel during the 2019 summer shutdown, as shown in Fig. 12.

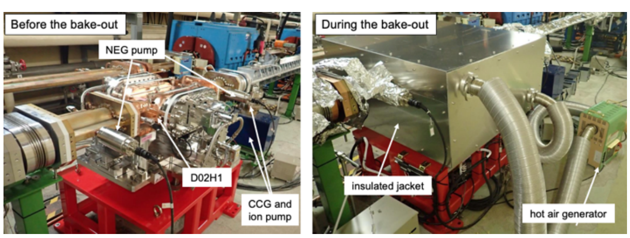

Figure 12: Photographs of the D02H1 collimator before and during baking.

Figure 13 shows the values of $\Delta p/\Delta I$ for a CCG near the D02H1 collimator during the 2019 spring and autumn runs.

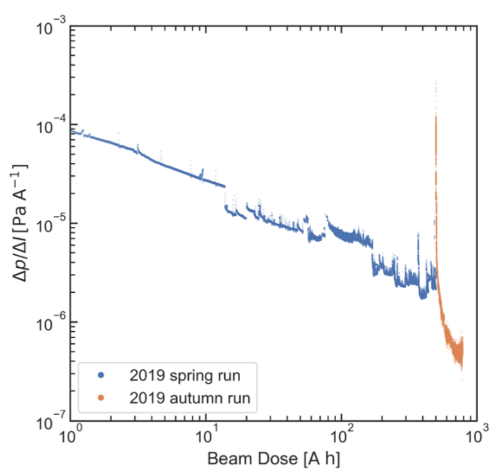

Figure 13: Pressure increase per unit beam current $\Delta p/\Delta I$ as a function of the beam dose for 2019 spring and autumn runs.

After baking, the $\Delta p/\Delta I$ value for the latter decreased rapidly by a factor of approximately six with further beam dose, indicating that baking in situ is an effective method for pumping water out of the chamber.

Abnormal Pressure Increase

Pressure increases during the beam operation have been observed in some vacuum-related components. Here, we report the case of a chamber for a luminosity monitor as an example. The luminosity monitor, named the Zero Degree Luminosity Monitor (ZDLM [19]), is installed downstream of the interaction point in the LER. As shown in Fig. 14, the beam pipe for the ZDLM has a structure in which the location where the sensor is installed protrudes toward the beam.

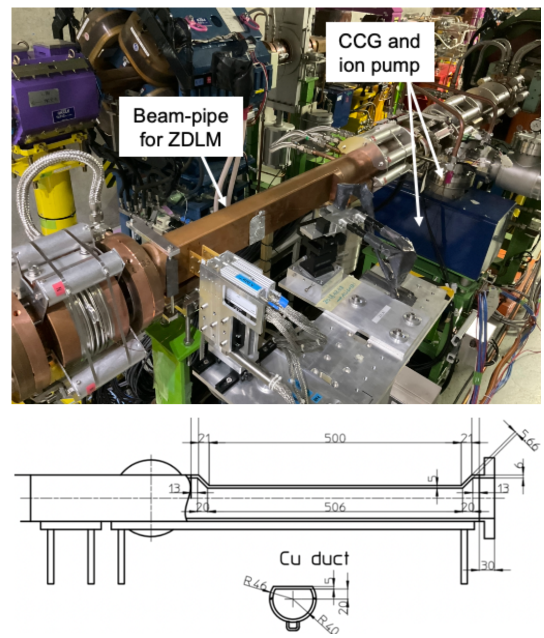

Figure 14: Photograph and drawing of the beam pipe for ZDLM.

The loss factor k_z [V C^{-1}] for a vacuum component characterizes the energy loss ΔE [J] of a bunch due to beam-impedance interaction in the longitudinal direction as the bunch passes through the component, and the energy loss can be calculated as follows:

$$\Delta E = k_z q^2, \tag{4}$$

where q is the bunch charge. The loss factor k_z in terms of the wake potential in the longitudinal direction $W_z(s)$ can then be written as:

$$k_z = \int_{-\infty}^{\infty} W_z(s)\lambda(s)\, ds \tag{5}$$

$$\lambda(s) = \frac{1}{\sqrt{2\pi}\sigma_z} \exp\left(-\frac{s^2}{2\sigma_z^2}\right), \tag{6}$$

where $\lambda(s)$ is the longitudinal charge density in the bunch. Therefore, the beam power loss due to the loss factor of a vacuum component can written as

$$P = \frac{\Delta E}{T_\mathrm{b}} = k_z I^2 T_\mathrm{b}\,, \tag{4}$$

ISBN: 978-3-95450-236-3 ISSN: 2673-7027 doi:10.18429/JACoW-eeFACT2022-THXAS0102

where P is the beam power loss [W], I is the beam current [A], T_b is the bunch [s], because $q = IT_b$. The lost beam power is finally wasted through heating of the surrounding vacuum components.

The wake potential of the beam-pipe for the ZDLM and a SuperKEKB-type horizontal collimator [14], calculated by *GdfidL* for a bunch length (σ_z) of 6 mm, is shown in Fig. 15. The horizontal collimator is one of the main sources of impedance in the ring. However, the loss factor in this beam pipe is ~0.18 V pC^{-1}, which is ~4.5 times larger than the loss factor of ~0.04 V pC^{-1} in the horizontal collimators because the wake potential in this beam-pipe is resistive, as shown in Fig. 15. The beam power loss in the beam-pipe and the collimator are then estimated to be ~1.08 kW and ~0.24 kW, respectively, for a beam current of 1.0 A and three-bunch spacing (6 ns).

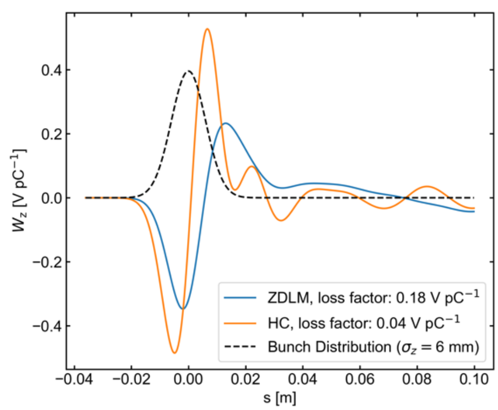

Figure 15. Longitudinal wake potential for the beam pipe for the ZDLM and the SuperKEKB-type horizontal collimator. Also plotted are the bunch distribution of σ_z = 6.0 mm. In the legend, ZDLM and HC refer to the beam-pipe for the ZDLM and the SuperKEKB-type horizontal collimator.

Pressure increases have been observed near this beam pipe, as shown in Fig. 16.

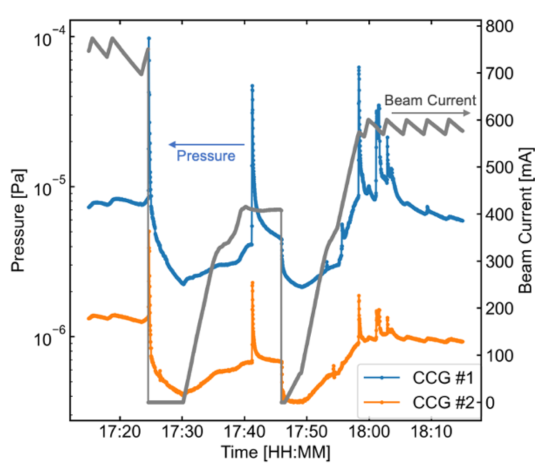

Figure 16: Pressure near the beam pipe for the ZDLM and the beam current in the LER during Phase 2 operation. The distance between the vacuum gauge and the beam pipe is approximately 1m for CCG #1 and 6 m for CCG #2.

When the LER beam current is ~800 mA, the surface temperature of this beam pipe is ~40 °C. At the same beam current, the temperature of the beam pipes in the arc sections is ~25 °C. Therefore, it is possible that the beam power loss due to the beam-impedance interaction in this beam pipe results in the pipe warming itself and nearby components, and the electromagnetic field excited in the structure might cause discharges in the slit structure of the pumping port. The observed frequency of pressure increases has been decreasing, suggesting that there is an aging effect. At present, these pressure increases do not hinder beam operations, but it may become a problem if the beam current is increased in the future.

CONCLUSION

Since the start of their operating period, newly installed components of the vacuum system of SuperKEKB have generally worked as expected. We have identified and reported some problems that occurred up to the present. Some topics that are not discussed here, such as beam-current-dependent pressure increases, beam lifetime determination by vacuum pressure, and electron-cloud instability will be addressed later [21].

ACKNOWLEDGEMENTS

We thank all the staff of the SuperKEKB accelerator and Belle II detector for their cooperation.

REFERENCES

[1] Y. Ohnishi *et al.*, "Accelerator design at SuperKEKB", *Prog. Theor. Exp. Phys.*, vol. 2013, n.3, p. 03A011, 2013. doi:10.1093/ptep/pts083

[2] Y. Suetsugu *et al.*, "Results and problems in the construction phase of SuperKEKB", *J. Vac. Sci. Technol. A*, vol. 34, p. 021605, 2016. doi:10.1116/1.4942455

[3] Y. Suetsugu *et al.*, "First Commissioning of the SuperKEKB Vacuum System", *Phys. Rev. Accel. Beams,* vol. 19, p. 121001, 2016. doi:10.1103/PhysRevAccelBeams.19.121001

[4] Y. Suetsugu *et al.*, "Achievements and problems in the first commissioning of SuperKEKB vacuum system", *J. Vac. Sci. Technol. A,* vol. 35, p. 03E103, 2017. doi:10.1116/1.4977764

[5] Y. Suetsugu *et al.*, "SuperKEKB main ring vacuum system status until the end of Phase-2 commissioning", *J. Vac. Sci. Technol. A* , vol. 37, p. 021602, 2019. doi:10.1116/1.5083928

[6] K. Shibata *et al.*, "Commissioning of vacuum system for SuperKEKB positron damping ring", *J. Vac. Sci. Technol. A*, vol. 37, p. 41601, 2019. doi:10.1116/1.5092956

[7] Y. Funakoshi et al., "The SuperKEKB has Broken the World Record of the Luminosity", *Proc. IPAC'22*, Bangkok, Thailand, Jun. 2022, pp. 1-5. doi:10.18429/JACoW-IPAC2022-MOPLXGD1

[8] "Operation status and plan on SuperKEKB", https://www-linac.kek.jp/skekb/status/web/status_plan.md.html.

ISBN: 978-3-95450-236-3 ISSN: 2673-7027 doi:10.18429/JACoW-eeFACT2022-THXAS0102

[9] K. Shibata *et al*., "Commissioning Status of SuperKEKB Vacuum System", *Proc. eeFACT2018*, Hong Kong, China, 2018, WEOAB01, pp.226–233.

[10] Y. Suetsugu *et al*., "Beam scrubbing of beam pipes during the first commissioning of SuperKEKB vacuum system", *Appl. Surf. Sci*., vol. 432, Part B, p. 347, 2018. doi:10.1016/j.apsusc.2017.06.162

[11] Y. Suetsugu *et al*., "Mitigating the electron cloud effect in the SuperKEKB positron ring", *Phys. Rev. Accel. Beams*, vol. 22, p. 023201, 2019. doi:10.1103/PhysRevAccelBeams.22.023201

[12] Y. Suetsugu *et al*., "Study to Mitigate Electron Cloud Effect in SuperKEKB", *Proc. eeFACT2018*, Hong Kong, China, 2018, TUYAA04, pp. 95–102.

[13] Y. Suetsugu *et al*., "Development of bellows and gate valves with a comb-type rf shield for high-current accelerators: Four-year beam test at KEK B-Factory", *Rev. Sci. Instrum*., vol. 78, p. 043302, 2007. doi:10.1063/1.2723747

[14] T. Ishibashi *et al*., "Movable collimator system for SuperKEKB", *Phys. Rev. Accel. Beams*, vol. 23, p. 53501, 2020. doi:10.1103/PhysRevAccelBeams.23.053501

[15] O. Gröbner *et al*., "Studies of photon induced gas desorption using synchrotron radiation", *Vacuum*, vol. 33, p. 397, 1983. doi:10.1016/0042-207X(83)90659-0

[16] S. Terui *et al*., "Development of Low-Z Collimator for SuperKEKB", *Proc. of PASJ2020*, 2020, FROT07, pp. 197–201. (in Japanese)

[17] S. Terui *et al*., "Report on Collimator Damaged Event in SuperKEKB", *Proc. IPAC'21*, Campinas, Brazil, 2021, May 2021, pp. 3541-3544. doi:10.18429/JACoW-IPAC2021-WEPAB359WEPAB359

[18] M. Tobiyama *et al*., "Development of Bunch Current and Oscillation Recorder for SuperKEKB Accelerator", *Proc. IBIC'12*, Tsukuba, Japan, 2012, MOPA36, pp. 138–142.

[19] P. Bambade *et al*., "Fast Luminosity Monitoring for the SuperKEKB Collider", *Proc. eeFACT2018*, Hong Kong, China, 2018, TUPBB06, pp. 173–178.

[20] GdfidL, http://www.gdfidl.de/

[21] Y. Suetsugu *et al*., "SuperKEKB Vacuum System in these Six Years Operation", in *Proc. IVC-22*, Sapporo, Japan, Sep. 11-16, 2022, to be published.

ISBN: 978-3-95450-236-3 ISSN: 2673-7027 doi:10.18429/JACoW-eeFACT2022-THXAS0104

VACUUM SYSTEM OF THE FCC-ee*

R. Kersevan†, CERN, Geneva, Switzerland

Abstract

The analysis and design of the vacuum system for the FCC-ee e- and e+ rings is outlined. The main vacuum-relevant parameters are recalled, with particular emphasis on the copious emission of synchrotron radiation (SR) along the rings, and its direct and indirect effects on vacuum, namely surface heating, SR-induced molecular desorption, generation of photoelectrons. A status report of the present design, analysis, and prototyping phase of several key vacuum components is also given.

VACUUM-RELEVANT MACHINE PARAMETERS

This paper refers to the version of the machine described in the Conceptual Design Report [1], i.e. the 97.756 km circumference rings. Out of the 5 beam energies foreseen for the experimental runs, see table on inset of Fig 1, we have analysed only the lowest-energy, highest beam current Z and the highest-energy, lowest beam current ttbar, as they represent all cases vacuum-wise.

All machines are bound to generate 50 MW of SR, therefore their beam currents scale as $1/E^4$, with E being the beam energy. There is therefore a large change of stored current, which makes the design challenging for vacuum, especially for the 45.6 GeV, 1390 mA, Z energy.

Synchrotron Radiation Spectra

The SR spectrum for e^-/e^+ circular accelerators is strongly dependent on beam energy. Its characteristic parameter is the critical energy ε_c of its spectrum, which varies as the third power of the beam energy E. Figure 1 shows the spectra of the five machines. The table on the figure also shows some vacuum-relevant parameter, such as the linear photon-stimulated desorption (PSD) yield, in units of mbar·l/s/m, computed assuming a molecular yield of

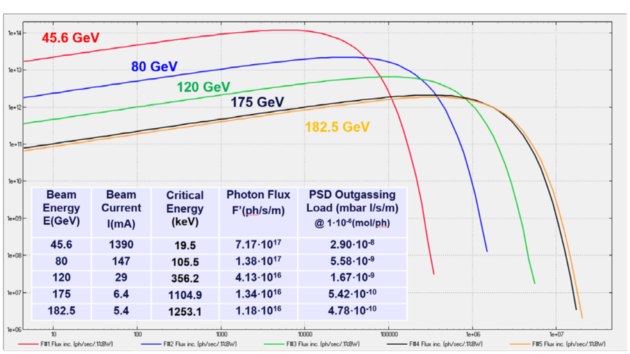

Beam Energy E(GeV)	Beam Current I(mA)	Critical Energy (keV)	Photon Flux F'(ph/s/m)	PSD Outgassing Load (mbar l/s/m) @ $1\cdot10^{-6}$(mol/ph)
45.6	1390	19.5	$7.17\cdot10^{17}$	$2.90\cdot10^{-8}$
80	147	105.5	$1.38\cdot10^{17}$	$5.58\cdot10^{-9}$
120	29	356.2	$4.13\cdot10^{16}$	$1.67\cdot10^{-9}$
175	6.4	1104.9	$1.34\cdot10^{16}$	$5.42\cdot10^{-10}$
182.5	5.4	1253.1	$1.18\cdot10^{16}$	$4.78\cdot10^{-10}$

Figure 1: SR spectra: Units: Vertical: ph/s/m/(0.1% Bandwidth); Horizontal: eV; Intervals: Vertical: [106; 2·1014]; Horizontal : [4; 5·106]; Inset table: linear photon flux, and linear PSD rate at each energy.

$1\cdot10^{-6}$ molecule/photon (mol/ph). The "per meter" unit refers to length along the arc dipole orbits, with bending radius ρ = 10.760 km.

It can be seen on Fig. 1 that the spectrum for the Z machine is almost entirely generated below the Compton threshold for aluminium or copper (~100 and 200 keV, respectively), while for all other higher energy machines there is going to be a substantial fraction of the total photon flux generated above the Compton threshold. Operation with LEP-2 at high energies has shown that this Compton-generated photons interact with the vacuum chamber material and can created a rather isotropic background of X and gamma rays, which can then re-enter the vacuum system and generate additional outgassing [2, 3]. We have therefore devised a way to contain locally this high-energy isotropic source of radiation which could otherwise activate and damage machine and tunnel components [4].

VACUUM HARDWARE

Synchrotron Radiation Absorbers

The operation timeline adopted for the FCC-ee physics program, see Fig. 3 of Ref. [1], calls for an initial 4-year time span during which the machine starts at the Z energy and then in a matter of 2 years it gets to nominal luminosity. This is a very challenging specification, as the Z machine corresponds to a very high beam current, B-factory-level, at unprecedented high energy: we need to design a very performing vacuum system, with high linear pumping speed, low dynamic desorption, and quick conditioning. To cope with this requirement and reduce the Compton-scattered background (see previous section), we have explored via numerical simulations the possibility to implement a number of short, lumped SR ures which collect and concentrate the SR that would otherwise impinge along the external wall of the vacuum chamber, like done at most modern light sources. For all machines, the linear SR power density, if the SR fan hits the external wall, is around 620 W/m (including a dipole packing factor of 0.85). Using 150 mm-long lumped absorbers we can collect the SR fan which would otherwise on average hit 5.6 m of external wall, therefore speeding up the conditioning time by a factor between 4 and 7, depending on the exponent of the power-law conditioning curve [5]. Some details and calculations are shown in Fig. 2. Correspondingly, the SR power density on the SR absorbers' surface goes up from 1.4 W/mm² to 32 W/mm² (flat wall vs inclined surface of the SR absorber) for the Z machine, and from 4 W/mm² to 115 W/mm² for the ttbar at 182.5 GeV. The material chosen for the SR absorbers is CuCrZr, and the manufacturing technology is additive manufacturing, 3D printing. The absorbers will be connected to the chamber either via brazing or using other techniques. First prototypes will be available at the beginning of 2023.

* Work supported by EU H2020 Framework Programme Grant no.951754
† roberto.kersevan@cern.ch

ISBN: 978-3-95450-236-3 ISSN: 2673-7027 doi:10.18429/JACoW-eeFACT2022-THXAS0104

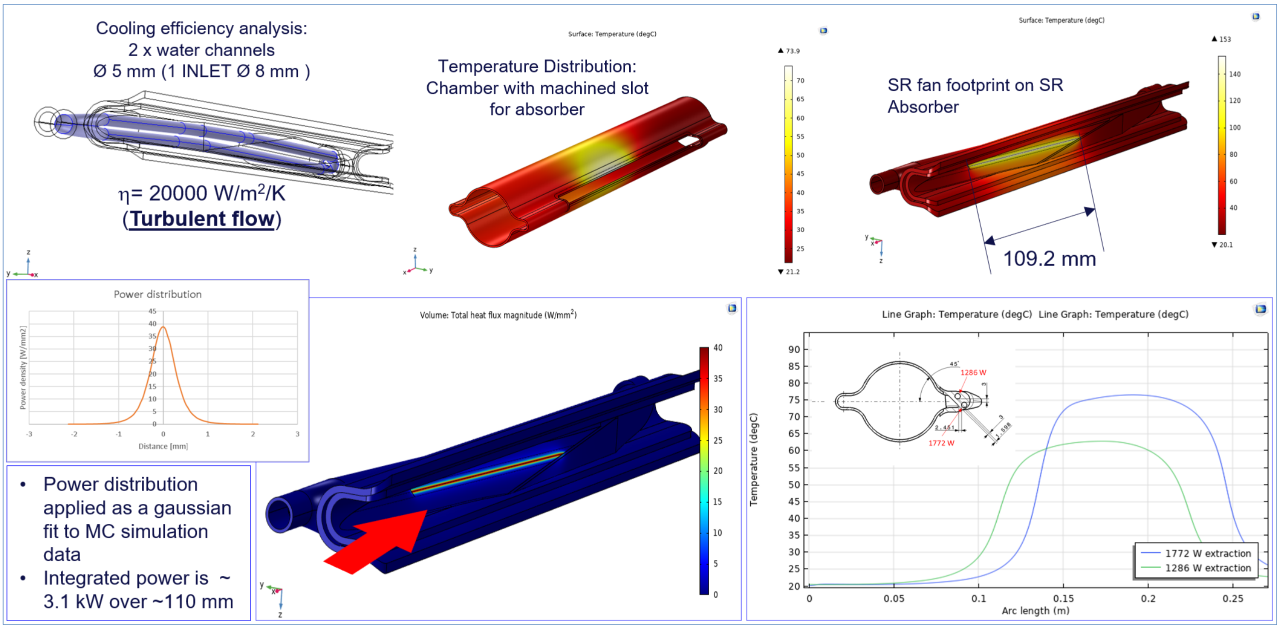

Figure 2: Composite figure showing results of calculations carried out for the SR absorbers; clockwise, from upper left: optimisation of turbulence vs pressure drop; temperature distribution near one SR absorber; temperature distribution along one absorber; wall temperature at the cooling channels vs length; SR power density along one absorber; vertical distribution of SR fan (from ray-tracing montecarlo simulation, SYNRAD+ code).

Vacuum Chamber, Surface Treatment, and Flanges

Taking advantage of the R&D program carried out for the FCC-hh study, we are adopting the shape-memory alloy (SMA) technology for sealing the flanges of the FCC-ee [6]. The maximum length of the chambers as been determined to be around 12 m, which should fit into the requirements for the fabrication of the long dipoles (up to ~ 24 m) in two segments. Based on technology developed for the HL-LHC program, we are confident that 12 m-long chambers could be NEG-coated in a horizontal position, which would greatly simplify the coating process and related costs [7]. Fig. 3 shows the tests carried out to join the oval flanges to a short vacuum chamber sample (made by wire-erosion) using the friction stir welding (FSW) technology, following the contour of the chamber placed inside a matching groove machined on the flange. The first results are very encouraging. An *ad hoc* study group has been set up to build a representative test section of the FCC-ee arcs, including short dipole, quadrupole and sextupole magnets or mock-up models of them. We are also testing additive manufacturing technology, cold plasma spray, to add thick layers of copper to the vacuum chamber extrusion and machine directly on these layers the body of the beam-position monitors (BPM). Prototyping is underway. Concerning the BPM electrodes, we are also testing the possibility to mount each of them on a small flange, again using the SMA technology to reduce the machining of holes for the screws.

NEG-coating has been proposed to keep the PSD contribution low, reduce the number of photoelectrons and their contribution to the electron-cloud effect, and provide distributed pumping to the system [8]. NEG-coating requires thermal activation to a minimum temperature of 180 °C, with the possibility to raise the temperature later should many activation cycles be needed.

We are testing a new technology based on the deposition by cold-spray of an insulating ceramic layer on top of which a thin titanium strip is also sprayed and used as ohmic heating element by running through it an appropriate current. This system is radiation resistant, an important feature for a machine like the FCC-ee which will generate copious amounts of high-energy particles and radiation. Figure 4 shows a CAD-made view of the set-up and one of the many calculations which have been carried out about this. Prototypes are already under study in our laboratories.

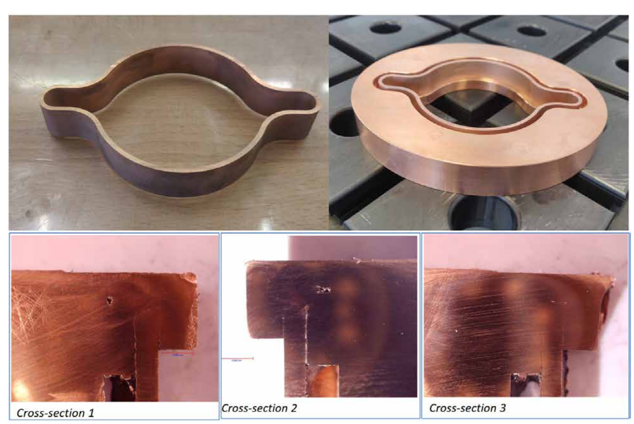

Figure 3: Short chamber extrusion, oval flange, and cross-section of the FSW tests, showing correct joining of the two parts.

ISBN: 978-3-95450-236-3 ISSN: 2673-7027 doi:10.18429/JACoW-eeFACT2022-THXAS0104

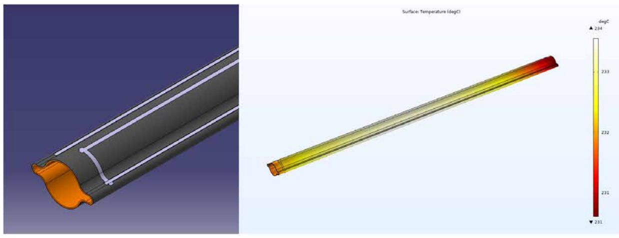

Figure 4: Left: CAD view of the chamber extrusion covered with insulating ceramic layer and sprayed Ti tracks; Right: Temperature distribution computed for a 5m-long chamber.

RF Bellows

We are designing two different bellow assembly types with RF contact fingers. One implements a modified version of the SUPERKEKB comb-type RF contacts, the second one a modified version of a contact-less type developed at CERN for the triplet area of the HL-LHC. Given the importance of minimising the impedance budget of the rings, at the same time numerical simulations of the impedance contributions of such RF contact finger geometries is underway [9].

CONCLUSIONS

The analysis and design of the vacuum system for the FCC-ee arc rings have advanced considerably. We have designed and are prepared to test soon many components of the system, utilizing novel technologies which, if validated, will allow us to simplify the design, fabrication, and installation of many components, while cutting on the cost of the vacuum system. Future refinements of the vacuum system design will include a detailed analysis of the new machine lattices, the exact position of each SR absorber, and the need to optimize the installation of the chambers on the girders, in view of quick replacement in the tunnel should it be needed in case of accidents during scheduled operation time.

ACKNOWLEDGEMENTS

The author gratefully acknowledges contributions from M. Morrone, C. Garion, S. Rorison, and F. Santangelo, CERN Vacuum Surfaces and Coatings Group.

This work was supported by EU's H2020 Framework-Programme Grant no. 951754.

REFERENCES

[1] A. Abada *et al.*, "FCC-ee: the lepton collider", *Eur. Phys. J. Spec. Top.,* vol. 228, pp. 261-262, 2019. doi:10.1140/epjst/e2019-900045-4

[2] R. Kersevan, "FCC-ee beam vacuum concept: the beam pipe of FCC-ee", in *Proc. FCC Week 2018,* Amsterdam, NL, April 9-13, 2018, https://indico.cern.ch/event/656491/contributions/2947258/

[3] M. Jimenez *et al.*, "The pressure and gas composition evolution during the operation of the LEP accelerator at 100 GeV", *Vacuum,* vol. 60, pp. 193-189, 2001. doi:10.1016/S0042-207X(00)00383-3

[4] B. Humann, "Synchrotron Radiation studies for the FCC-ee arc with FLUKA", in *Proc. FCC Week 2021,* 28 June-2 July, 2021, https://indico.cern.ch/event/995850/contributions/4405383/.

[5] O. Malyshev, "Beam Induced Desorption", in *Proc. CERN Accelerator School Vacuum For Particle Accelerators*, June 6-16, 2017, Glumslov, Sweden, https://cas.web.cern.ch/schools/glumslov-201

[6] F. Niccoli *et al.*, "NiTi shape memory alloy pipe couplers for ultrahigh vacuum systems: development and implementation", *Smart Mater. Struct.*, vol. 31, no. 6, pp. 065014, 2022. doi:10.1088/1361-665X/ac6999

[7] P. Costa Pinto, "In-situ amorphous carbon coating of the beam screen of LHC's standalone magnets", in *Proc. IPAC'20,* Caen, France, May 2020, paper THVIR02. doi:10.18429/JACoW-IPAC2020-THVIR02

[8] R. Kersevan, "FCC-ee beam vacuum challenges, concepts and future R&D plans", in *Proc. FCC Week 2019,* 24-28 June, 2019, Brussels, Belgium, https://indico.cern.ch/event/727555/contributions/3449896/.

[9] P. Krkotic, CERN, personal communication.

ISBN: 978-3-95450-236-3 ISSN: 2673-7027 doi:10.18429/JACoW-eeFACT2022-THYAT0101

POSITRON AND DAMPING RING REQUIREMENTS FOR FUTURE e^+e^- COLLIDERS*

John T. Seeman†, SLAC National Accelerator Laboratory, Menlo Park, California, USA

Abstract

Future e^+e^- colliders will need positron sources that stretch present technical capabilities. The project teams for these proposed colliders are working to extend these capabilities. A positron source encompasses many elements: an electron driver, production target, lattice optics, capture section, damping ring(s), injection/extraction short-pulse kickers, an emittance preserving complex delivery system, specific injection specifications, and (perhaps) polarization. The required technical parameters need to accommodate many beam aspects including bunch intensities, final emittances, spacings, train lengths, and desired damping times. For this note, the technical requirements for positrons related to bunch charges, number of bunches, damping ring (DR) lengths and damping times for the various positron sources for the presently proposed colliders are compared, concentrating on their DR specifications.

INTRODUCTION

An Implementation Task Force (ITF) [1] was started as a part of the Snowmass-2022 exercise that looked at the proposed future colliders. As a part of the ITF studies, positron production, accumulation, storage, and damping were briefly investigated as an important aspect of the design of the various colliders. Although positrons were not a specific part of the charge of the ITF, positron production issues entered many of the designs in a major manner. In this note some positron aspects and parameters are discussed for producing and delivering trains of positron bunches for future colliders relative to the damping rings.

ELECTRON-POSITRON COLLIDERS

The positron damping rings (DR) for fifteen e^+e^- colliders are reviewed. Four of these for past or present colliders are discussed first and, then, eleven are discussed from proposed future colliders ranging from rings to linear colliders. A brief description is given for each collider and then the technical parameters of their positron DR systems are discussed.

Over the course of the two-year Snowmass-2022 process, many of the proposed colliders changed parameters such as repetition rates, bunch charges, number of bunches, and machine lengths. The well-established proposed colliders changed only a little (e.g. ILC, FCCee, and CEPC) but some of the lesser developed changed greatly (e.g. plasma wakes, structure wakes, energy recovery proposals). Below are brief collider descriptions

The SLC [2] was a collider at SLAC operating at the Z using the SLAC copper "two mile" linac colliding single e^+ and e^- bunches.

The LEP ring collider [3] at CERN operated at the Z and higher while colliding 4 to 8 bunches.

The PEP-II ring collider [4] at SLAC operated with two rings of different energies at the Upsilon energy colliding 1732 bunches in each ring.

The present SuperKEKB collider [5] at KEK operates with two rings of different energies at the Upsilon energy colliding 2151 bunches in each ring.

The proposed FCCee ring collider [6] would use a new tunnel near CERN with two rings with energies up to ttbar colliding about 10,000 bunches in each ring.

The proposed CEPC ring collider [7] would use a new tunnel in China with two rings with energies upgradable to ttbar colliding up to 12,000 bunches in each ring.

The proposed ILC collider [8] would be a pulsed SC linac in Japan that would collide trains up to 1312 bunches per pulse initially at the Higgs energy.

The proposed CLIC collider [9] would be a pulsed, two-beam copper linac near CERN colliding trains of up to 352 bunches per pulse.

The proposed cold copper collider C3 [10] would be a pulsed cold copper linac colliding bunch trains up to 133 bunches per pulse.

The proposed circular energy recovery collider CERC [11] would use a 100 km circular tunnel to ramp up and down the two beams in energy over several turns recovering the beam energy in SC RF linacs and collision particles in damping rings with top-up injection.

The proposed energy recovery linear collider ERLC [12] would be two CW SC linacs with energy and particle recovery while operating with continuous bunches with top-up injection.

The proposed recycling linear collider ReLiC [13] would be a CW SC linac energy recovery linac operating with nearly continuous bunch trains with beam energy recovery in the linacs and particles recovery in damping rings.

The proposed plasma wake PWFA-LC [14] would be a pulsed beam-driven plasma linac, colliding single e^+ and e^- bunches up to 10,000 Hz.

The proposed laser-driven plasma wake LWFA-LC [15] would be a pulsed linac, colliding single e^+ and e^- bunches up to 50,000 Hz.

The proposed structure wake SWFA-LC [16] would be a pulsed two-beam-driven linac colliding trains of e^+ and e^- bunches.

POSITRON DAMPING RINGS

The colliders described above all need damping rings to reduce the emittances of the positron bunches either generated from scratch or being recycled after collisions and to accommodate the needed bunch spacing and trains. In Table 1 are listed the colliders, the respective DR energies, and required modes of operation. The DR energies were

* Work supported by US Department of Energy Contract DE-AC03-76SF00515.
† seeman@slac.stanford.edu

ISBN: 978-3-95450-236-3 ISSN: 2673-7027 doi:10.18429/JACoW-eeFACT2022-THYAT0101

chosen to fulfil the requirements of low beam emittances for collisions and the requisite number of bunches in each bunch train. In the ITF studies some of the above proposed pulsed colliders did not specify a DR system, neither its energy nor length. In those cases a DR energy of 3 GeV was chosen to complete our studies matching closely those of the CLIC DR parameters which was determined to technically work for them.

In Table 1 past, present, and proposed e^+e^- colliders are listed, showing the DR energy for the respective (most demanding) cases and the mode of operation [top-up (TU) or single use (SU, i.e. using the positrons once)], from low to high DR energies. From the Table is clear there is a strong trade-off between shorter damping times at higher energies but at the cost of higher equilibrium emittances.

Table 1: Past, Present, and Proposed e^+e^- Colliders

Collider	Collider Energy CM [GeV]	DR Energy [GeV]	Operation mode
SLC	98	1.21	SU
LEP	209	0.6	TU
PEP-II	3.5x9	1.21	TU
SuperKEKB	4x7	1.1	TU
Proposed:			
FCCee	91	1.54	TU
CEPC	91	1.1	TU
ILC	250	5	SU
CLIC	250	2.86	SU
C3	250	3	SU
CERC	240	8	TU
ERLC	250	5	TU
ReLiC	250	3	TU
PWFA-LC	1000	3	SU
LWFA-LC	1000	3	SU
SWFA-LC	1000	3	SU

POSITRON DAMPING RINGS

For a given collider the positron generation system must produce the needed number of positrons and bunches each second. The damping rings system must provide adequate damping to reduce the emittances. The DR length and lattice provide the needed space for the bunches and damping/storage time.

In Table 2 the designed DR bunch spacing, the damping time, and the number of damping time needed are listed for the DRs of past, present, and proposed e^+e^- Colliders.

The damping times for top-up injection colliders tend to be much longer than single use colliders as the injection rates are reduced. Furthermore, the particle recycling colliders have damping rings that need shorter storage times to allow the recycled bunches to be collided more often.

Table 2: DR properties for Past, Present, and Proposed e^+e^- Colliders

Collider Damping Ring for	DR Bunch spacing (m)	Damping time (msec)	N. damping times stored
SLC	17.6	3.1	5.5
LEP	15.7	34	330
PEP-II	17.6	3.1	5.5
SuperKEKB	28.8	10.9	3.7
Proposed:			
FCCee	15	11.6	3.8
CEPC	18.4	11.4	3.6
ILC	1.85	23.9	8.3
CLIC	0.5	2.0	10
C3	1.6	2	10
CERC	2.6	2	2
ERLC	~2	2	2
ReLiC	1.0	4	2
PWFA-LC	1.6	2	10
LWFA-LC	1.6	2	10
SWFA-LC	1.6	2	10

STORED BUNCHES AND TRAINS

Some of the future colliders need single injected positron bunches and some need trains of bunches. In Table 3 are listed DR requirements for bunch trains and number of bunches per train for the past, present and future colliders, showing the number of stored bunch trains, number of bunches per train, and the total number of bunches stored at any instant.

The requirements for the DRs are many: short damping times, number of damping times needed, number of bunch trains stored, bunches per train, and the appropriate beam energy. The cost of a DR include power components and length components. The cost components include the pulse rate, drive energy, drive beam particles, radiation losses per turn, and cooling systems. The length components include the usual elements: magnets, vacuum systems, RF cavities, tunnel, controls, and alignment. Each collider therefore has a unique set of requirements.

The plasma colliders need single bunches but many each second leading to large circumference damping rings. The pulsed SC linacs (e.g. ILC) need a few bunch trains per second but many bunches in one bunch train leading to lengthy damping rings. Top-up injection rings (e.g. FCCee and CEPC) need a steady source of positrons but at a relatively low charge per bunch so the DRs can be smaller. The particle recycling colliders (e.g. CERC, ReLiC) need a large DR circumference to store many bunches needing to be damped briefly for a few damping times before reuse.

ISBN: 978-3-95450-236-3 ISSN: 2673-7027 doi:10.18429/JACoW-eeFACT2022-THYAT0101

Table 3: DR Stored Bunch Properties for Past, Present, and Proposed e^+e^- Colliders

Collider Damping Ring for	N. stored bunch trains	N. bunches per train	Total n. stored bunches at once
SLC	2	1	2
LEP	8	1	8
PEP-II	2	1	2
SuperKEKB	2	2	4
Proposed:			
FCCee	8	2	16
CEPC	4	2	8
ILC	1	1312	1312
CLIC	1	312	312
C3	3	133	133
CERC	1	264	264
ERLC	100	1	100
ReLiC	600	20	12000
PWFA-LC	300	1	300
LWFA-LC	940	1	940
SWFA-LC	20	231	4620

DAMPING RING LENGTH

The needed minimum length L of a DR involves many technical factors and is given by:

$$L = Sb * Nsb = Sb * Nbt * Nbpt \tag{1}$$

Sb is the bunch-to-bunch separation in the DR. Nsb is the number of stored bunches. Nbt is the number of stored bunch trains. Nbpt is the number of bunches per train. The variables in play are the damping time without wigglers (e.g. SLC), wiggler based DRs (e.g. ILC, CLIC), and tunnel costs. The calculated minimum DR length does not include needed space for other functions including gaps for injection, abort kickers, ion reduction, or electron-cloud dissipation. In Table 4 are listed the positrons per bunch, needed bunch trains per second, and the derived (or actual) required DR circumference for the future colliders.

In Table 4, the positron DR of past, present, and proposed e^+e^- colliders are listed showing the number of positron per bunch, number of trains per second, and the required positron DR circumference. The resulting DRs have very difference sizes. The SLC DR is the shortest at 35 m as it stores only 2 bunches and provides a very short damping time. Long train DRs (e.g. ILC) have long lengths due to storing many bunches in a train and supporting multiple trains. Single bunch colliders with very high rates (e.g. LWFA-LC, SWFA-LC, and PWFA-LC) need large damping rings to allow many bunches to damp simultaneously.

Table 4: Number of Positron per Bunch, Number of Trains per Second, Required Positron DR Circumference

Collider DR for	DR n. positrons per bunch ($x10^{10}$)	Bunch trains per second	DR length (m)
SLC	5	120	35.3
LEP	2.5	0.09	126
PEP-II	0.9	30	35.3
SuperKEKB	4.1	50	135.5
Proposed:			
FCCee	2.2	200	242
CEPC	4.4	200	147
ILC	2	5	3200
CLIC	0.43	50	428
C3	0.63	120	650
CERC	8.1	800	1000
ERLC	0.1	5300	300
ReLiC	1.0	2200	4000
PWFA-LC	1.0	15000	500
LWFA-LC	0.12	47000	1550
SWFA-LC	0.31	5	7500

POSITRON PRODUCTION RATES

The number of positrons that need to be produced each second is a very important number since the hardware production cost is strongly correlated with this rate.

Given Tables 1 through 4, the number of positrons that need to be produced per second can be calculated. In Table 5 are listed the number of colliding bunches that need filling, the proposed injection rate, and the total number of positrons that must be produced per second.

From Table 5 several conclusions can be seen. The SLC had the highest production rate of positrons to date. Top-up injection into storage ring colliders (e.g. FCCee, CEPC, CERC, ReLiC) is the easiest from the rate perspective. The single-use high-rate colliders (e.g. ILC, CLIC, C3, LWFA-LC, PWFA-LC SWFA-LC) have production needs that are 10 to 20 times that of the SLC and are represented well by the CLIC positron system.

There are several special cases:

1) The ERLC is a CW SC collider that needs to have a cycle time of 2 seconds on and 4 seconds off for SC cavity He cooling needs. The positrons will need to be stored during the off time for the ERLC or else the positron production rate will much higher that shown in Table 5.

2) As shown in its schematic drawings, the ERLC does not have a direct DR but a single-pass-wiggler emittance-reduction system for the colliding bunches which means that the emittance disruption during collision must be quite small.

3) The CLIC based positron DR system is relatively compact compared to others and includes a pre-damping

ISBN: 978-3-95450-236-3 ISSN: 2673-7027 doi:10.18429/JACoW-eeFACT2022-THYAT0101

ring and bunch stacking. This system will likely need further investigation if it becomes the baseline for other single pass future colliders.

Table 5: Injection Requirements for Past, Present and Future Colliders.

Collider Damping Ring for	N. colliding bunches to fill	Injected bunch rate (Hz)	Total e^+ injection rate per second ($x10^{12}$)
SLC	120	120	6.0
LEP	8	100	0.12
PEP-II	1732	30	0.15
SuperKEKB	2151	100	0.2
Proposed:			
FCCee	10000	200	6.0
CEPC	12000	100	3.8
ILC	6560	6560	131
CLIC	17600	17600	100
C3	16000	16000	100
CERC	1600	160	0.16
ERLC	53000	5300	0.05
ReLiC	22000	2200	0.03
PWFA-LC	10000	10000	100
LWFA-LC	47000	47000	56
SWFA-LC	23100	23100	72

CONCLUSIONS

The various proposed future e^+e^- colliders will put additional constraints on the positron production and damping ring systems. Several of the proposed colliders require large increases in the capabilities of the positron production and damping rings compared to past systems, reaching over an order of magnitude in some cases. For those colliders, a sustained programmatic effort will be needed to reach solutions for these requirements.

ACKNOWLEDGMENTS

The author wishes to thank all the electron-positron collider proponents for sharing their technical designs, my fellow ITF members for discussions, and all the organizers and local staff of the eeFACT2022 workshop at Frascati, Italy, where these conclusions were presented.

REFERENCES

[1] T. Roser *et al*, "Report of the Snowmass 2021 Collider Implementation Task Force", arXiv:2208.06030. doi:10.48550/arXiv.2208.06030

[2] R. Erickson *et al*, "SLC Collider", SLAC-R-714, 1984.

[3] G. Arduini *et al*, "LEP Performance at 91.5 GeV", in *Proc. EPAC'98*, Stockholm, Sweden, Jun. 1998, paper WEP20H, p. 440.

[4] J. Seeman *et al,* "Achieving a Luminosity of 10^{34} cm^2/s in the PEP-II B-factory", in *Proc. EPAC'06*, Edinburgh, UK, Jun. 2006, paper MOPLS045, p. 643.

[5] Y. Funakoshi *et al*, "The SuperKEKB Has Broken the World Record of the Luminosity", in *Proc. IPAC'22*, Bangkok, Thailand, Jun. 2022, pp. 1-5. doi:10.18429/JACoW-IPAC2022-MOPLXGD1

[6] M. Benedikt *et al*, "FCC Feasibility Study overview", presented at FCC Week, 30 May - 3 June 2022, Sorbonne Université.

[7] CEPC Study Group, "Snowmass2021 White Paper AF3-CEPC", arXiv:2203.09451. doi:10.48550/arXiv.2203.09451

[8] A. Aryshev *et al*, "ILC Report to Snowmass 2021", arXiv:2203.07622. doi:10.48550/arXiv.2203.07622

[9] O. Brunner *et al*, "The CLIC project", arXiv:2203.09186. doi:10.48550/arXiv.2203.09186

[10] S. Dasu *et al*, "Strategy for Understanding the Higgs Physics: The Cool Copper Collider (C3)", arXiv:2203.07646. doi:10.48550/arXiv.2203.07646

[11] V. Litvinenko *et al*, "CERC - Circular e^+e^- Collider using Energy-Recovery Linac", arXiv:2203.07358. doi:10.48550/arXiv.2203.07358

[12] V. Telnov, "ERLC", presented at RUPAC'21, 26 Sep. - 2 Oct. 2021, Alushta, Crimea, paper TUA03.

[13] V. Litvinenko *et al*, "The ReLiC: Recycling Linear e^+e- Collider", arXiv:2203.06476. doi:10.48550/arXiv.2203.06476

[14] M. Fuchs *et al*, "PWFA-LC", arXiv:2203.08379. doi:10.48550/arXiv.2203.08379

[15] C. Benedetti *et al*, "LWFA-LC", arXiv:2203.08366. doi:10.48550/arXiv.2203.08366

[16] C. Jing *et al*, "SWFA-LC", arXiv:2203.08275. doi:10.48550/arXiv.2203.08275

ISBN: 978-3-95450-236-3 ISSN: 2673-7027 doi:10.18429/JACoW-eeFACT2022-THYAT0102

KEK e+/e- INJECTOR LINAC

T. Natsui†, M. Akemoto, D. Arakawa, H. Ego, Y. Enomoto, K. Furukawa, T. Higo, N. Iida, K. Kakihara, T. Kamitani, H. Katagiri, M. Kawamura, S. Matsumoto, T. Matsumoto, H. Matsushita, T. Miura, F. Miyahara, H. Nakajima, Y. Okayasu, I. Satake, M. Satoh, Y. Seimiya, T. Shidara, A. Shirakawa, T. Suwada, M. Tanaka, D. Wang, Y. Yano, K. Yokoyama, M. Yoshida, T. Yoshimoto, R. Zhang, X. Zhou, KEK, Ibaraki, Japan

Abstract

The KEK injector linac feeds the beams into four rings. It is called J-Linac. The SuperKEKB main rings are high-energy rings (HER) and low-energy rings (LER). The linac injects a 7 GeV electron beam to the HER and a 4 GeV positron beam to the LER. It also injects electron beams into the two light source rings. We successfully performed this simultaneous four-ring injection. We achieved this complex simultaneous injection using two electron guns, a positron source with a flux concentrator, and pulsed magnets. In SuperKEKB phase 3 operation, 2 nC electron and 3 nC positron beam injections were achieved.

INTRODUCTION

The KEK electron/positron injector linac was designed to inject different types of beams into four different rings. This injector achieved simultaneous four-ring injection at 50 pps. SuperKEKB has two rings: the HER and LER [1]. The other rings are the light source rings of the PF and PF-AR rings. An electron beam with an energy of 7 GeV and a positron beam with an energy of 4 GeV are required for the HER and LER, respectively. The energies of the PF ring and PF-AR are 2.5 GeV and 6.5 GeV, respectively.

The injector linac consists of eight sectors (sector A-C and 1-5) and a bending sector (J-arc) with a total length of 600 m. This shape resembled that of J, as shown in Fig. 1. One sector has eight klystrons, and one klystron drives four 2-m accelerating structures. The energy is adjusted from pulse to pulse by switching the accelerating or standby mode of each accelerating structure.

We used two types of electron gun: a photocathode RF gun and a thermionic cathode DC gun. An RF gun with a high-power laser was used to generate a low-emittance electron beam for the HER injection [2]. The RF gun charge and emittance design values were 5 nC and 6 mm-mrad, respectively. Positrons were generated by hitting a primary electron beam onto a tungsten target. These positrons were focused with flux concentrator (FC) [3] and accelerated with large aperture S-band (LAS) [4] accelerating structures. We obtained a 4 nC positron beam with a 10 nC primary electron beam. The generated and accelerated 1.1 GeV positron beam was injected into a damping ring to reduce the emittance. A pulse-bend magnet merged these two electron gun lines, and these beams were injected into a common acceleration beamline. A thermionic gun was used as the electron source for the light source rings.

Sector A to 2 has common optics that use DC magnets. However, sector 3 to 5 has independent optics using pulse magnets. These pulse quadrupole and steering magnet systems were developed for the SuperKEKB project and can change the optics at 50 pps.

We achieved this complex four-ring simultaneous injection using two types of electron guns: a positron source and pulsed magnet system [5].

LINAC BEAM STATUS FOR SUPERKEKB

The SuperKEKB phase 3 operation began in 2019. The linac beam quality was gradually improved. Table 1 lists the current beam status and final goal. The energy was set to the required value, and a sufficient energy margin was maintained by providing standby units. The amounts of bunch charges in operation didn't reach the target values. However, these were almost sufficient for 2022b. The emittance was improved in a step-by-step manner. Simultaneous injection to four rings and damping ring was completed.

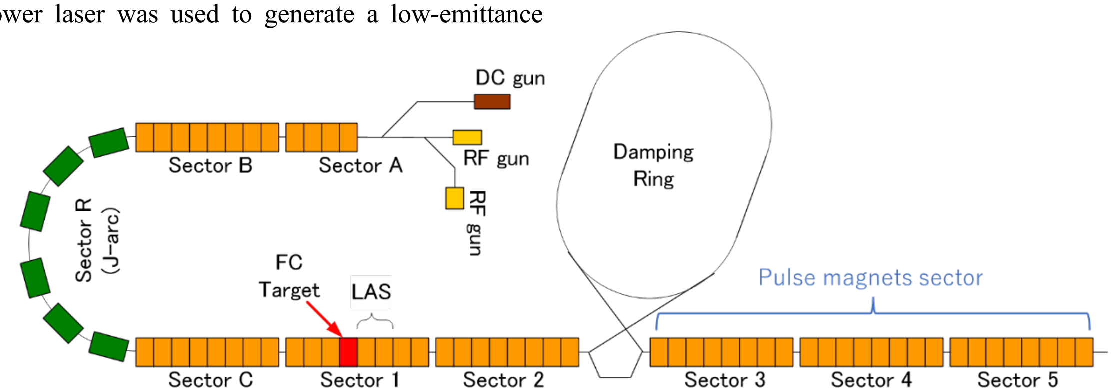

Figure 1: KEK injector linac.

† takuya.natsui@kek.jp

ISBN: 978-3-95450-236-3 ISSN: 2673-7027 doi:10.18429/JACoW-eeFACT2022-THYAT0102

Table 1: Beam Status of the Final Goal and Current Performance

	2022ab		Final goal	
Beam	e+	e-	e+	e-
Energy [GeV]	7.0	4.0	7.0	4.0
Bunch charge [nC]	(1^{st}, 2^{nd}) 3.0, 2.5	(1^{st}, 2^{nd}) 2.0, 1.5	(1^{st}, 2^{nd}) 4.0, 4.0	(1^{st}, 2^{nd}) 4.0, 4.0
Normalized emittance [mm-mrad]	(Hor., Ver.) 120, 5	(Hor., Ver.) 20-50, 20-50	(Hor., Ver.) 100, 15	(Hor., Ver.) 40, 20

Electron beam

Figure 2 shows the one-year history of the electron beam charge for the HER. 2022, stable 2 nC beam generation was achieved using a laser feedback system [6]. The amount of charge was almost sufficient in the current situation. However, the HER sometimes requires a higher bunch charge. We must increase this for the next SuperKEKB operation.

Emittance preservation is an essential issue for electron beams because a damping ring is not available for the electron beam. The emittance measured at the beamline near the RF gun is good, as shown in Fig. 3. At the linac end, the emittance is also good immediately after orbit adjustment. However, a long period with no adjustment causes gradual emittance growth; the latter part of the graph in Fig. 3 illustrates this. The cause of this emittance growth is suspected to be the long-term RF phase drift. However, the reason for this is not clearly understood, and further investigation is required.

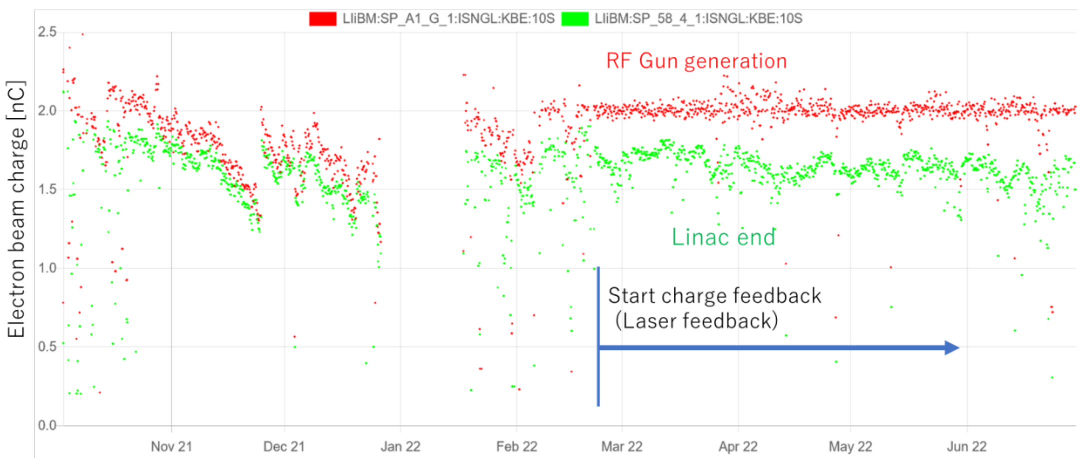

Figure 2: History of electron beam charge for the HER.

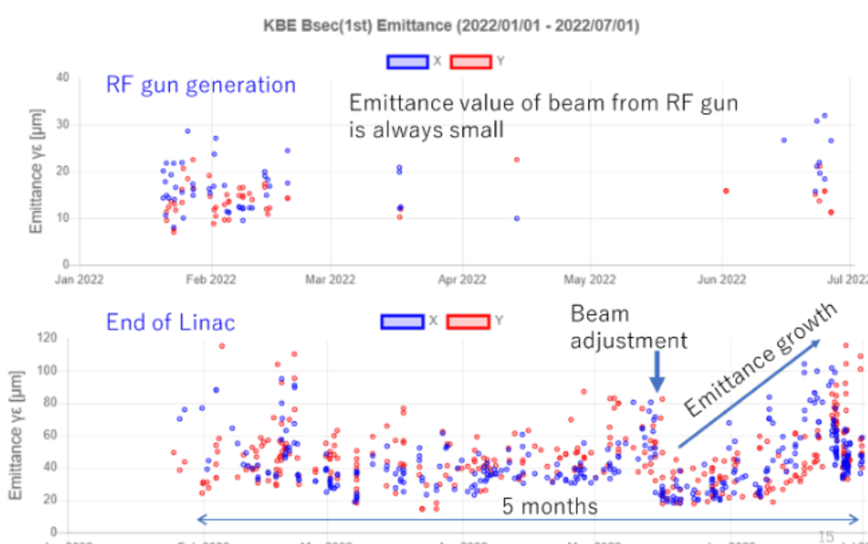

Figure 3: Long-term emittance value history of the electron beam. Emittance of RF gun beam (upper) and end of linac (lower).

ISBN: 978-3-95450-236-3 ISSN: 2673-7027 doi:10.18429/JACoW-eeFACT2022-THYAT0102

Sometimes, a two-bunch operation as shown in Fig. 4 has been attempted. However, the injection rate of the second bunch tended to be low, and we had to perform the one-bunch operation. As shown in Fig. 4, there appears to be no problem with the beam orbit. The emittance or energy spread of the second bunch would have a problem. Two-bunch operation is one of the challenges to be solved in the next operational term.

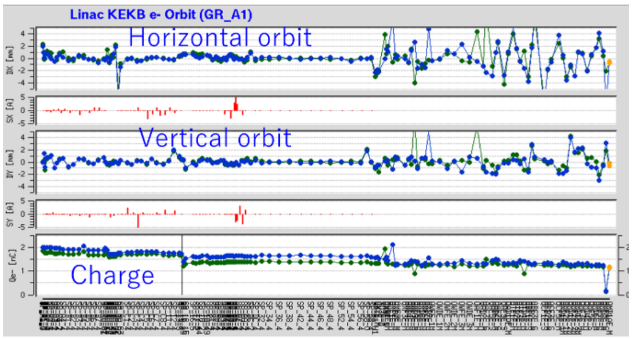

Figure 4: Two-bunch operation of the electron beam.

The stabilization of high-power laser systems also increases beam charge. We want to establish a method for emittance preservation inside the linac for high-charge operation for the next SuperKEKB operation. The issue of increased emittance in the beam transport (BT) line between the linac and ring also must be resolved. Studies on two-bunch operation and emittance preservation are essential.

Positron beam

Figure 5 shows a one-year history of the positron beam charge, including the primary electron beam charge for the LER. The beam charge was 3 nC, which is close to the final target. The thermionic gun generated a primary electron beam with a charge of 12 nC. The length of the bunch extracted from the cathode is 1 ns. We used two sub-harmonic bunchers (SHB) to compress the bunch length. The frequencies of SHB1 and SHB2 were 114 MHz and 572 MHz, respectively, and these were used to make the bunch length sufficiently shorter than the S-band RF wavelength. We used a streak camera to adjust the RF phase of the SHBs and an S-band buncher for beam bunching. In addition, we succeeded in a two-bunch operation. The second bunch charge was almost the same as the first bunch charge. We maintained a stable two-bunch injection to the LER.

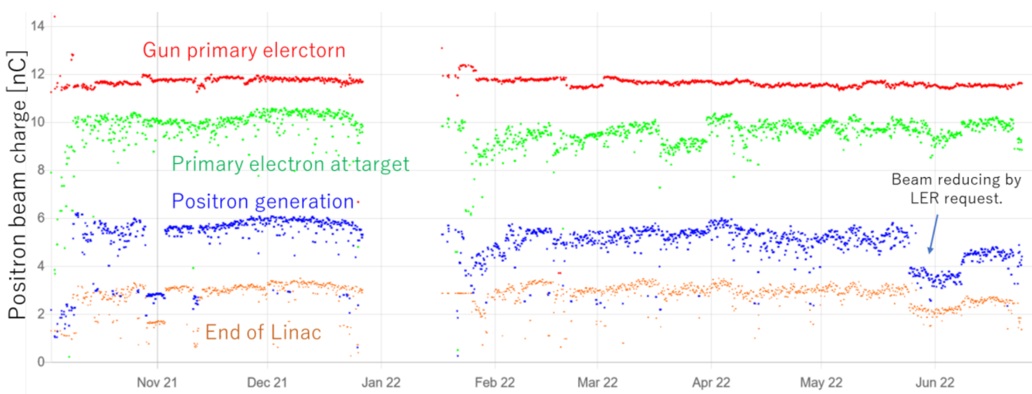

Figure 5: History of the positron beam charge for the LER.

The 2022ab SuperKEKB operation achieved a stable 3 nC two-bunch positron beam operation. Many improvements were made to achieve this stable positron beam operation. Figure 6 shows the long-term positron beam charge history. Before 2020, the beam charge was low, resulting in FC breakdown problem. This problem was solved by adopting a new robust FC and refining the applied voltage waveform [7]. Modifications were made in 2020 to increase the positron beam transportation in the LAS structure immediately after the FC. The LAS structures are in a long solenoid magnet with a transverse kick owing to their asymmetric structure. Steering magnets were added inside the solenoid magnet to compensate for the transverse kick. In 2021, positron beam transportation remarkably increased, as shown in Fig. 6. Since then, the amount of charge has been gradually increased by increasing the primary beam and improving beam transport.

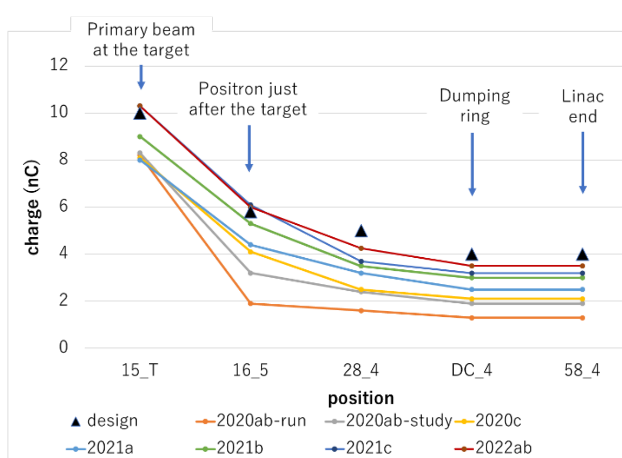

Figure 6: Long-term (a few years) charge history of the positron beam.

ISBN: 978-3-95450-236-3 ISSN: 2673-7027 doi:10.18429/JACoW-eeFACT2022-THYAT0102

LINAC UPGRADE PLAN

Currently, we are working on various linac upgrades [8]. KEK injectors have a long history, and various measures against aging and performance improvements are required.

One important issue is the replacement of accelerating structures. Old accelerating structures are operated at lower voltages owing to field emission or breakdown problems. In addition, the cooling channels are often broken. Therefore, the development of new accelerating structures is an urgent issue. We tested the newly developed structure and a new pulse compression system. Figure 7 shows the new accelerating structure, and Fig. 8 shows the spherical-cavity-type pulse compressor (SCPC) [9]. The new accelerating structure and SCPC have provided high accelerating voltages in the conditioning system, and we are testing them online. The introduction of these new structures will increase the overall injector acceleration voltage in the future.

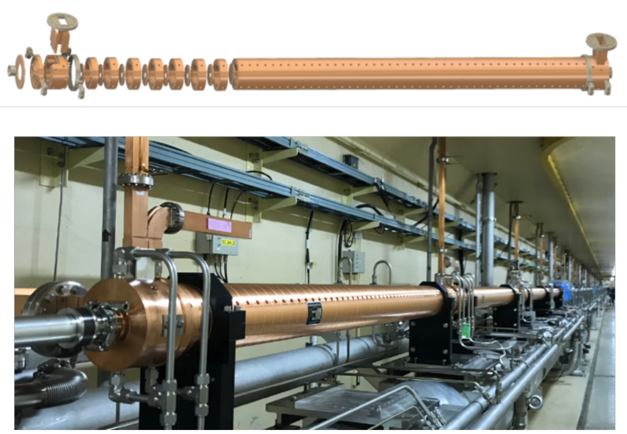

Figure 7: New accelerating structure.

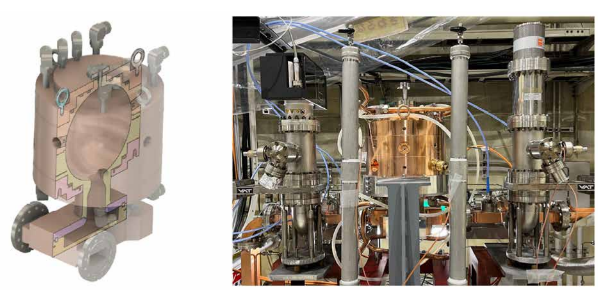

Figure 8: SCPC.

Pulse magnet upgrades are also important. Pulse magnets have already been installed in sector 3 to 5. However, DC magnets are used in sector A to 2. We must transport positron primary and electron beams in J-arc with common optics. Beam adjustment can be complicated and sometimes causes beam loss. Therefore, pulsed magnets should be installed near the J-arc. Magnets with large apertures are required in the J-arc. However, the pulse quadrupole magnets currently in use only have narrow apertures for low emittance. Developing a new magnet with a large aperture and a high-current magnet driver is necessary. The new pulse-magnet diameter was designed to be 44 mm, whereas the existing pulse-magnet aperture was 20 mm. Accordingly, the maximum current of the new pulse-magnet driver had to be increased from 300 A to 600 A. This high-power pulse-magnet driver is currently being tested.

A new device, the fast kicker, was also introduced. This kicks only on the second bunch. Sometimes, the orbit of the first and second bunches become separated owing to their energy deviation. The fast kicker was introduced to directly compensate for this orbit misalignment. The time separation between the first and second bunches was only 96 ns. The fast kicker will be tested in the next operational term.

We plan to introduce an energy compression system (ECS) in the electron beam line. Currently, the ECS is used only for the positron beam line. The 4 nC electron beam is affected significantly by its longitudinal wakefields, and it makes a large energy spread. Therefore, an electron ECS is necessary in the future.

Currently, we have to save the electric power consumed in the linac operation. In accelerators, particularly linear accelerators, the klystron efficiency dominates a large portion of the power loss. In the KEK linac, the efficiency of the conventional S-band klystrons is only 45%, which can be significantly improved. The conventional klystron output is 50 MW. We aim for an 80 MW of RF power output with the same modulator to increase the efficiency of the klystrons. We have begun designing a multibeam klystron (MBK) with an efficiency greater than 70%. In the future, installing a high-power klystron and a new accelerating structure are expected to significantly improve the performance of the KEK linac.

We will continue to make various upgrades for SuperKEKB.

SUMMARY

In the first half of 2022, the KEK injector linac provided electron/positron beams in the SuperKEKB phase 3 operation. Sufficient charge of electron/positron beams could be injected into the HER and LER while achieving simultaneous four-ring injection. During this period, various issues were identified. Emittance preservation and establishment of a two-bunch operation are required for the electron beam. The beam loss must be reduced in both the primary and positron beams. All systems of the injector are required to operate with many controlled long-term drifts. Various upgrades are planned to improve the injector performance. Replacement with new accelerating structures is gradually progressing. A pulse magnet upgrade is planned for flexible beam operation. We are currently developing high-efficiency klystrons to save power.

To further improve the performance of SuperKEKB, we will continue to perform beam studies and various upgrades in the KEK injector linac.

REFERENCES

[1] Y. Funakoshi *et al.*, "The SuperKEKB has broken the world record of the luminosity", in *Proc. IPAC'22*, Bangkok, Thailand, Jun. 2022, pp. 1-5. doi:10.18429/JACoW-IPAC2022-MOPLXGD1

[2] T. Natsui, D. Satoh, M. Yoshida, R. Zhang, and X. Zhou, "Injector linac upgrade and new RF gun development for SuperKEKB", in *Proc. eeFACT'16*, Daresbury, UK, Oct. 2016, pp. 74-78. doi:10.18429/JACoW-eeFACT2016-TUT2H2

[3] T. Kamitani *et al.*, "SuperKEKB positron source construction status", in *Proc. IPAC'14*, Dresden, Germany, Jun. 2014, pp. 579-581. doi:10.18429/JACoW-IPAC2014-MOPRI004

[4] S. Matsumoto, T. Higo, K. Kakihara, T. Kamitani, and M. Tanaka, "Large-aperture travelling-wave accelerator structure for positron capture of SuperKEKB injector linac", in *Proc. IPAC'14*, Dresden, Germany, Jun. 2014, pp. 3872-3874. doi:10.18429/JACoW-IPAC2014-THPRI047

[5] Y. Enomoto *et al.,* "Pulse-to-pulse beam modulation for 4 storage rings with 64 pulsed magnets", in *Proc. LINAC'18*, Beijing, China, Sep. 2018, pp. 609-614.

[6] R. Zhang, H. K. Kumano, N. Toyotomi, M. Yoshida, and X. Zhou, "Laser system for SuperKEKB RF gun in phase III commissioning", in *Proc. IPAC'22*, Bangkok, Thailand, Jun. 2022, pp. 2914-2916. doi:10.18429/JACoW-IPAC2022-THPOTK059

[7] Y. Enomoto, K. Abe, N. Okada, and T. Takatomi, "A new flux concentrator made of Cu alloy for the SuperKEKB positron source", in *Proc. IPAC'21*, Campinas, Brazil, May 2021, pp. 2954-2956. doi:10.18429/JACoW-IPAC2021-WEPAB144

[8] K. Furukawa *et al.*, "SuperKEKB electron positron injector linac upgrade for higher charge and lower emittance", in *Proc. IPAC'22*, Bangkok, Thailand, Jun. 2022, pp. 2461-2464. doi:10.18429/JACoW-IPAC2022-THPOST011

[9] Y. Bando *et al.*, "High power test of S-band spherical-cavity type pulse compressor", in *Proc.18th annual meeting of Particle Accelerator Society of Japan*, Japan, 2021, p. 998.

ISBN: 978-3-95450-236-3 ISSN: 2673-7027 doi:10.18429/JACoW-eeFACT2022-FRXAS0101

POWER BUDGETS AND PERFORMANCE CONSIDERATIONS FOR FUTURE HIGGS FACTORIES*

F. Zimmermann†, CERN, Geneva, Switzerland
B. List, DESY, Hamburg, Germany
S. Belomestnykh, V. Shiltsev, FNAL, Batavia, USA
J. Gao, IHEP, Beijing, China
A. Faus-Golfe, IJCLab, Orsay, France
M. Biagini, M. Boscolo, INFN-LNF, Italy
R. Rimmer, T. Satogata, JLAB, Newport News, USA
M. Koratzinos, PSI, Villigen, Switzerland
E. Nanni, P. Raimondi, T. O. Raubenheimer, J. Seeman, SLAC, Menlo Park, USA
V.N. Litvinenko, Stony Brook Univ., Stony Brook, USA
K. Oide, Univ. Geneva, Geneva, Switzerland

Abstract

A special session at eeFACT'22 reviewed the electrical power budgets and luminosity risks for eight proposed future Higgs and electroweak factories (C^3, CEPC, CERC, CLIC, FCC-ee, HELEN, ILC, and RELIC) and, in comparison, for a lepton-hadron collider (EIC) presently under construction. We report highlights of presentations and discussions.

INTRODUCTION

During the Snowmass Community Summer Study in Seattle [1], questions arose on the feasibility of power and luminosity numbers communicated for various collider proposals. The Accelerator Frontier Implementation Task Force (ITF) had received many inputs on various collider concepts and just released their evaluation report [2]. While many comparative evaluations were extremely helpful and welcome, the ITF specifically mentioned that they had not reviewed luminosity and power consumption projections (i.e., they used proponents' numbers of luminosity and power).

The following ICFA Workshop eeFACT'22, organized at Frascati in September 2022, was charged with helping the broader accelerator and HEP community by taking a look at the luminosity and power consumption projections for various e^+e^- Higgs factories and providing an "expert comparative evaluation" for them [3]. Given the strength of the cohort of anticipated participants, such "independent" evaluation was expected to be very helpful.

For this purpose, a special session was set up during eeFACT'22 [4], where representatives from all major proposals were invited to present and discuss their respective numbers and the underlying assumptions [3].

POWER CONSUMPTION

The power consumption estimates, including the underlying assumptions and level of completeness and maturity, differ significantly between proposals. The special session at eeFACT'22 [4], addressed this theme, with pertinent brief presentations from all e^+e^- Higgs and Electroweak Factory proposals. The eeFACT'22 discussions and presentations [3, 5–12], resulted in the power budgets compiled in Table 2.

For CEPC, the 260 MW power required for the Higgs factory operation is significantly lower than the value of 340 MW, which had been submitted to the ITF.

The annual power consumption in TWh numbers does not look fully consistent across various machines. As an example, for the FCC-ee, the annual power consumption is higher than the product of instantaneous power and effective physics time, since power needs during annual hardware commissioning, beam commissioning, operational downtimes, technical stops, machine development periods and shutdowns are also taken into account [13], as sketched in Table 1.

Table 1: Electrical power consumption for FCC-ee at 240 GeV c.m. energy [13] (slightly adapted), yielding a total of 1.52 TWh per year.

Mode	# days	Power [MW]
beam operation	143	301
downtime operation	42	109
h.w. & beam commissioning	30	139
machine development	20	177
technical stop	10	87
shutdown	120	61

We note that this was the first attempt to get a detailed comparative accounting of the power consumption needs, that several numbers are still missing for CERC, C^3, RELIC, etc., and that some of the numbers have not been fully critically assessed. Hence, this comparative analysis will need to be continued.

* Work supported by the European Union's H2020 Framework Programme under grant agreement no. 951754 (FCCIS), and by Fermi Research Alliance, LLC, under contract No. De-AC02-07CH11359 with the United States Department of Energy.
† frank.zimmermann@cern.ch

ISBN: 978-3-95450-236-3 ISSN: 2673-7027 doi:10.18429/JACoW-eeFACT2022-FRXAS0101

Table 2: Electrical power budgets for the proposed Higgs and Electroweak factory colliders, and, for comparison the EIC, based on invited contributions to the special session at eeFACT'22 [4]. NI: Not Included; NE: Not Estimated; –: Not Existing. ‡ILC parameters correspond to the luminosity upgrade. The total ILC power includes 4 MW margin, the one for HELEN 3.3 MW (here as part of the general services). *For HELEN, the "detector" number refers to the power required for the beam delivery system, machine detector interface, interaction region, and beam dumps, the "injector magnets" number to damping ring with wigglers. †For RELIC, the 2.5 GeV damping rings and transfer lines would use permanent magnets.

Proposal	**CEPC**		**FCC-ee**		**CERC**		**C^3**	**HELEN**	**CLIC**	**ILC‡**	**RELIC**		**EIC**
Beam energy [GeV]	120	180	120	182.5	120	182.5	125	125	190	125	120	182.5	10 or 18
Average beam current [mA]	16.7	5.5	26.7	5	2.47	0.9	0.016	0.021	0.015	0.04	38	39	0.23–2.5
Total SR power [MW]	60	100	100	100	30	30	0	3.6	2.87	7.1	0	0	9
Collider cryo [MW]	12.74	20.5	17	50	18.8	28.8	60	14.43	–	18.7	28	43	12
Collider RF [MW]	103.8	173.0	146	146	57.8	61.8	20	24.80	26.2	42.8	57.8	61.8	13
Collider magnets [MW]	52.58	119.1	39	89	13.9	32	20	10.40	19.5	9.5	2	3	25
Cooling & ventil. [MW]	39.13	60.3	36	40	NE	NE	15	10.50	18.5	15.7	NE	NE	5
General services [MW]	19.84	19.8	36	36	NE	NE	20	6.00	5.3	8.6	NE	NE	4
Injector cryo [MW]	0.64	0.6	1	1	NE	NE	6	1.96	0	2.8	NE	NE	0
Injector RF [MW]	1.44	1.4	2	2	NE	NE	5	0*	14.5	17.1	192	196	5
Injector magnets [MW]	7.45	16.8	2	4	NE	NE	4	13.07*	6.2	10.1	0†	0†	5
Pre-injector [MW]	17.685	17.7	10	10	NE	NE	–	13.37	–	–	NE	NE	10
Detector [MW]	4	4.0	8	8	NE	NE	NE	15.97*	2	5.7	NE	NE	NI
Data center [MW]	NI	NI	4	4	NE	NE	NE	NI	NI	2.7	NE	NE	NI
Total power [MW]	259.3	433.3	301	390	89	122	150	110.5	107	138	315	341	79
Lum./IP [10^{34} cm^{-2}s^{-1}]	5.0	0.8	7.7	1.3	78	28	1.3	1.35	2.3	2.7	200	200	1
Number of IPs	2	2	4 (2)	4 (2)	1	1	1	1	1	1	2	2	1 (2)
Tot. integr. lum./yr [1/fb/yr]	1300	217.1	4000 (2300)	670 (340)	10000	3600	210	390.7	276	430	79600	79000	145
Eff. physics time / yr [10^7 s]	1.3	1.3	1.24	1.24	1.3	1.3	1.6	2.89	1.2	1.6	2	2	1.45
Energy cons./yr [TWh]	0.9	1.6	1.51	1.95	0.34	0.47	0.67	0.89	0.6	0.82	2	2.2	0.32

PERFORMANCE CONSIDERATIONS

C^3 [5]

The design of and performance projections for C^3 look solid – The performance of the proposed modules, including realistic average gradient and cryogenic power required, is still to be demonstrated.

CERC [6]

CERC assumes cavity Q values of 10^{11}, which are a little higher than the present state of the art. Emittance preservation over 100s of kilometer at values smaller than for CLIC needs to be shown in simulations including alignment errors, wake fields, and optical corrections. The burnoff of particles at the high target luminosity due to radiative Bhabha scattering and beamstrahlung may be much higher than the assumed loss rate, which also means that a more powerful positron source might be required. The possible impact on overall power consumption is to be examined.

RELIC [6]

RELIC also assumes cavity Q values of 10^{11}, and a "real-estate" gradient of 12.5 MV/m in the linac sections (excluding spreaders and combiners). Such a gradient either has already been demonstrated or is close to demonstrated values. The evolution, manipulation and optimisation of the energy spread in the linac and of the bunch length in the arcs and in the interaction region probably require more studies. The electric power estimates should undergo a proper engineering evaluation.A complete accelerator and interaction-region design, validated by particle tracking, is also required to confirm the assumed particles losses. As for CERC, the luminosity related burnoff due to radiative Bhabha scattering and beamstrahlung will need to be compensated by newly injected positrons and electrons.

FCC-ee [7]

Achieved klystron efficiency is typically lower than targeted. An R&D plan has been established. A faster R&D program is executed for the twin project CEPC in China. To preserve and reuse energy, FCC is studying a waste heat management system. Two other possible energy-saving measures for FCC-ee were pointed out during the discussion [14]: (1) Energy recovery from the fast ramping booster should be considered. (2) Magnet design & magnet powering should be optimized to minimize the cable losses.

CEPC [8]

The CEPC design is similar to FCC-ee. CEPC is supported by an impressive R&D effort including massive hardware prototyping, comprising SRF cavities, cryomodules, high-efficiency klystrons, collider magnets, booster dipoles, and combinations of electrostatic separators with weak magnets for beam separation and combination, with an ambitious timeline. Earliest start of tunnel construction is in 2026.

CLIC [9]

The CLIC project aims for a 10 micron alignment over 200 m distance. The CLIC studies include using renewable energy sources, at about 10% of the project cost. CLIC operation would reduce CERN energy consumption by a factor 2 from the current level.

ISBN: 978-3-95450-236-3 ISSN: 2673-7027 doi:10.18429/JACoW-eeFACT2022-FRXAS0101

ILC [10]

The ILC has published its Technical Design Report in 2013 and is technically ready to enter an engineering design phase followed by start of construction after four years. Presently, an ILC Technology Network (ITN) is being set up to conduct further R&D on high priority items, in particular economisation of cavity and cryomodule production, positron source and the main beam dump.

Concerning the beam energy, the most important issue is achieving a sufficient average acceleration gradient with sufficient margin in beam operation. ILC design parameters have been demonstrated for industrially produced cavities [15] and cryomodules [16]. Production and operating experience from E-XFEL [17–19] and LCLS-II [20] will provide valuable input during the ITN and Engineering Design phase. Differences between the ILC and E-XFEL cryomodule designs such as a power distribution system with variable splitters will facilitate operation at maximum gradient.

Achieving the necessary accelerating gradient will be ensured by rigorous Quality Assurance during production; a 10 % overproduction of cavities is foreseen for a selection of cavities that meet the specifications. Based on the E-XFEL production experience [21] there is high confidence that projected yield and associated cost for overproduction can be achieved.

As for the luminosity performance, the critical issues concern beam intensity limitations (in particular positron source and main dumps), beam damping (damping ring design), low emittance beam transport (damping ring extraction kickers), final focussing (feedback, overall focus design) and availability. Issues connected to individual components such as kickers or the rotating positron source target will be addressed in the ITN phase by prototyping or engineering designs (main dumps).

To ensure performance of larger systems such as the damping rings or the final focus system, simulations and tests at dedicated test facilities have been conducted. These activities are planned to be continued by the ITN, e.g., at the Accelerator Test Facility [22] at KEK.

At eeFACT'22, it was suggested that the SRF target values for ILC be benchmarked against the performance of operating machines such as E-XFEL and LCLS-II, in particular the SRF gradients, static heat loads, and cryoplant efficiency. Understanding the operational performance of the E-XFEL and LCLS-II is important for a future Higgs factory, like ILC or HELEN, which will need to reach the desired energy without tripping off too often.

HELEN [11]

The HELEN approach makes use of recent advances in the SRF technology (high gradient travelling wave structures and high Q values) and looks promising. This modified design could also be an attractive option for the ILC. In the discussion, questions were raised about traveling wave phase stability.

EIC [12]

The EIC, now under construction, offers a valuable benchmark for the power consumption budgets.

STATIC HEAT LOADS

Concerning static heat loads, the best values from LCLS-II cryomodules are reported to be 5 times larger than those which had been assumed for the ILC. Based on operational experience, the 2-K static heat load per 8-cavity cryomodule is expected to be about 11 W for LCLS-II-HE [20], which is about two times higher than the value of 6 W estimated for LCLS-II in 2014 [23], and an order of magnitude higher than the static heat load per cryomodule of 1.32 W at 2 K, which had been predicted for the ILC in 2017 [24].

LCLS-II may still have some cryogenic issues to resolve. A more appropriate comparison is with the European E-XFEL. For this E-XFEL, a static heat load of 6.1 W was measured per linac cryomodule [19]. Consequently, in the latest ILC estimates, a static heat load of 6 W per cryomodule is assumed, consistent with actual E-XFEL experience [25].

CRYO EFFICIENCY

The cryoplant efficiencies at various existing facilities, like LHC, JLAB, and SLAC can be compared with the target efficiency for future projects. The LHC cryoplant efficiency at 1.9 K is 900 W/W (that is the number of Watt at room temperature required for removing one Watt at 1.9 K) [26]. For a proposed 8 GeV SC proton linac at Fermilab a cryo efficiency at 2 K of 790 W/W is considered [27]. The ILC will further improve the 2-K cryoplant efficiency to 700 W/W [28].

COLLISION SPOT SIZE

As for the final focus – the difference of the vertical spot size observed at the KEK/ATF-2 facility from the expected value, especially at nominal β_x^*, and its dependence on bunch intensity, resembles earlier findings at the SLC [29, 30] and at the FFTB [31]. The present ATF-2 optics is much relaxed compared with the design, which should greatly lower the optical aberrations. The ATF-2 would offer an opportunity to characterize the higher-order aberrations with beam and to compare them with model predictions.

POSITRON NEEDS

The Snowmass Implementation Task Force performed a review of the positron needs according to the proponents [32]. For single-pass linear colliders, like ILC and CLIC, the total rate of positrons required equals the number of particles collided per second. For circular colliders, positrons are unavoidably lost due to radiative Bhabha scattering, determined by the luminosity with little dependence on the momentum aperture, as well as due to beamstrahlung along with a limited dynamic aperture. The importance of the beamstrahlung strongly depends on the off-momentum dynamic acceptance and on several beam parameters. Also

ISBN: 978-3-95450-236-3 ISSN: 2673-7027 doi:10.18429/JACoW-eeFACT2022-FRXAS0101

for ERL-based colliders the radiative Bhabha scattering, together with beamstrahlung, determines the minimum rate of new positrons required. The differential cross section for radiative Bhabha scattering is [33]

$$\frac{d\sigma}{dk} = \frac{4r_e^2\alpha}{k}\left[\frac{4}{3} - \frac{4}{3}k + k^2\right]\left(2\ln(2\gamma) + \ln\frac{1-k}{k} - \frac{1}{2}\right) , \tag{1}$$

where r_e the classical electron radius, α the fine-structure constant, $k = E_\gamma/E_b$, $\gamma = E_b/(m_e c^2)$ and E_b the beam energy.

The total cross section for a particle loss after a single scattering is [33]

$$\sigma = \int_{k_{\min}}^{k_{\max}} \frac{d\sigma}{dk}\, dk , \tag{2}$$

with $k_{\min}$ corresponding to photon energies at the energy aperture ($\sim 2\%$) and $k_{\max} \approx 1$. In addition, Burkhardt and Kleiss [33] introduced a cut-off in the momentum transfer, on an event by event basis, at $q_{\min} = \hbar/d$ with d the average half-distance between adjacent electrons or positrons, in the rest system, namely

$$d = \sqrt{\pi}\left(\frac{\sigma_x^*\sigma_y^*\gamma\sigma_z^*}{N_b}\right)^{1/3} , \tag{3}$$

with N_b the bunch population, and the asterisk indicating rms beam size at the collision point. The applicability of this model needs to be verified; an alternative approach is described, e.g., in Ref. [34]. For FCC-ee and CEPC, we find $d \approx 2\,\mu$m, which is rather similar to the value of $d \approx 3.3\,\mu$m obtained for LEP I [33]. For all three ERL-based machines, namely RELIC, ERLC and CERC, d lies in the range 0.3–0.6 μm.

We use the program BBBREM [36] to compute the cross section $\sigma_{\mathrm{r.b.}}$, which determines the beam lifetime due to radiative Bhabha scattering, including the aforementioned cut-off based on d. The corresponding resulting minimum positron production rate required for circular colliders, or for colliders with particle recovery, is

$$\dot{N}_{e^+} = L n_{\mathrm{IP}} \sigma_{\mathrm{r.b.}} , \tag{4}$$

where L denotes the design luminosity and n_{IP} the number of interaction points with simultaneous collisions. The above is the minimum rate required, since additional particle losses occur due to beamstrahlung, which depends on horizontal beam size, bunch length, bunch charge, and (also) beam energy and momentum acceptance.

For linear colliders without particle recovery, the positron rate required at the collision point is simply

$$\dot{N}_{e^+,\mathrm{LC}} = f_{\mathrm{rep}} N_b n_b , \tag{5}$$

with f_{rep} the linac repetition rate, N_b the bunch population, and n_b the number of bunches per pulse.

Table 3 shows the computed radiative Bhabha scattering cross sections, $\sigma_{\mathrm{r.b.}}$, for different e$^+$e$^-$ circular or ERL-based Higgs factory proposals, along with the resulting minimum rates required, for all proposals, and compares the latter with the design assumptions (in the right-most column).

Table 3: Cross section for particle loss due to radiative Bhabha scattering, $\sigma_{\mathrm{r.b.}}$, as computed by BBBREM considering an energy acceptance of 2% and a cut-off based on the parameter d of Eq. (3), the resulting minimum positron production rates required for different circular and ERL based colliders ("min. requ."), compared with project assumptions compiled for Snowmass'21 [32] ("assumed"). In case of linear colliders without particle recovery, like ILC and CLIC, the required ("min. requ.") positron rate directly follows from bunch charge and bunch collision rate. Key parameters for almost all projects can be found in Table 2, those for ERLC in Ref. [35].

Proposal	**Energy** [GeV]	$\sigma_{\mathrm{r.b.}}$ [mbarn]	$\dot{N}_{e^+}$ min. requ. [10^{12} e$^+$/s]	$\dot{N}_{e^+}$ [32] assumed [10^{12} e$^+$/s]
FCC-ee	120	166	0.05	6.0
CEPC	120	166	0.03	3.8
ILC	125	—	131	131
ILC ext.	125	—	525	525
CLIC	190	—	100	100
C^3	125	—	100	100
CERC	120	154	12	0.08
ERLC	125	149	0.06	0.05
RELIC	120	147	0.6	0.02

We note that for FCC-ee and CEPC significant margins exist, of about two orders of magnitude, between the rates that can be provided from the injector complexes and the rate required to compensate the losses from radiative Bhabha scattering only. This wide a margin is due to the fact that the maximum injector production rate is specified for the more demanding running on the Z pole. We also observe that for the most easily implemented, lowest-luminosity version of the ERLC [35] considered here (namely 1.3 GHz RF cavities at 1.9 K, and pulsed operation), the production rate roughly equals the expected loss rate from radiative Bhabha scattering alone (for other versions a higher positron rate is required). By contrast, for RELIC, as presented, the loss rate due to radiative Bhabha scattering appears to be about 25 times higher than the production rate hitherto assumed, and for the CERC the loss rate is 100 times higher than the production rate. This suggests that for the latter two proposals the injector designs may need to be modified in order to provide significantly higher fluxes of fresh positrons and electrons. However, the respective cross sections still need to be validated, and possibly updated, before definite conclusions can be drawn [37].

PREDICTING PERFORMANCE

The more mature projects presented here (ILC, CLIC, FCC-ee, CEPC) have fairly established and reviewed performance figures backed by detailed simulations, although

ISBN: 978-3-95450-236-3 ISSN: 2673-7027 doi:10.18429/JACoW-eeFACT2022-FRXAS0101

of course all projects are working towards increasing performance. The newer projects (e.g., RELIC, CERC) do not yet have reviewed performance figures, neither detailed simulations demonstrating how to achieve them.

Past experience with the SLC, which after ten years of operation reached about half of its nominal luminosity [29, 38, 39], present-day struggles with obtaining the SuperKEKB design luminosity [40], and, on the other hand, actual luminosities exceeding design values at previous machines like LEP [41], PEP-II [42] and KEKB [43], highlight the importance of a fair and thorough evaluation of the luminosity risks and of the luminosity potentials. The corresponding work needs to be continued.

REFERENCES

[1] *Snowmass Community Summer Study 2021 (2022)*, http://seattlesnowmass2021.net/.

[2] T. Roser, R. Brinkmann, S. Cousineau, D. Denisov, S. Gessner, S. Gourlay, P. Lebrun, M. Narain, K. Oide, T. Raubenheimer, J. Seeman, V. Shiltsev, J. Strait, M. Turner, and L.-T. Wang, *Report of the Snowmass'21 Collider Implementation Task Force*, https://arxiv.org/abs/2208.06030.

[3] V. Shiltsev, *On Assessment of Luminosity and Power Challenges of Future Higgs/EW factories*, https://agenda.infn.it/event/21199/contributions/179782/, 2022.

[4] *eeFACT'22*, https://agenda.infn.it/event/21199/.

[5] E. Nanni, *C^3 The Cool Copper Collider — Power Discussion*, https://agenda.infn.it/event/21199/contributions/179029/, 2022.

[6] V. Litvinenko, *CERC and ReLiC: polarized e^+e^- colliders*, https://agenda.infn.it/event/21199/contributions/179027/, 2022.

[7] F. Zimmermann, *FCC-ee power & luminosity*, https://agenda.infn.it/event/21199/contributions/178817/, 2022.

[8] J. Gao, *Circular Electron Positron Collider (CEPC)*, https://agenda.infn.it/event/21199/contributions/178818/, 2022.

[9] S. Stapnes, *The Compact Linear Collider (CLIC)*, https://agenda.infn.it/event/21199/contributions/178819/, 2022.

[10] B. List, *ILC Power Consumption and Performance Risks*, https://agenda.infn.it/event/21199/contributions/178820/, 2022.

[11] S. Belomestnykh, *Higgs-Energy LEptoN (HELEN) collider*, https://agenda.infn.it/event/21199/contributions/179030/, 2022.

[12] T. Satogata, *EIC Estimated Energy Usage*, https://agenda.infn.it/event/21199/contributions/179783/, 2022.

[13] J. P. Burnet, "Update of the Power Demand for FCC-ee," *FCC Week 2022, Paris*, 2022. https://indico.cern.ch/event/1064327

[14] P. Raimondi, comments at eeFACT'22, 2022.

[15] D. Reschke *et al.*, "Performance in the vertical test of the 832 nine-cell 1.3 ghz cavities for the european x-ray free electron laser," *Phys. Rev. Accel. Beams*, vol. 20, p. 042 004, 4 2017. doi:10.1103/PhysRevAccelBeams.20.042004

[16] D. Broemmelsiek *et al.*, "Record High-Gradient SRF Beam Acceleration at Fermilab," *New J. Phys.*, vol. 20, no. 11, p. 113 018, 2018. doi:10.1088/1367-2630/aaec57

[17] D. Kostin *et al.*, "SRF Operation at XFEL: Lessons Learned After More Than One Year," in *Proc. IPAC'19*, Melbourne, pp. 12–16. doi:10.18429/JACoW-IPAC2019-MOYPLM2

[18] J. Branlard *et al.*, "Four Years of Successful Operation of the European XFEL," *JACoW*, vol. SRF2021, MOOFAV06, 2022. doi:10.18429/JACoW-SRF2021-MOOFAV06

[19] R. Ramalingam, Y. Bozhko, S. Barbanotti, and T. Schnautz, "Heat loads measurements at the xfel cold linac," *IOP Conference Series: Materials Science and Engineering*, vol. 1240, no. 1, p. 012 123, 2022. doi:10.1088/1757-899X/1240/1/012123

[20] M. Ross, "LCLS-II: Status, Issues and Plans," in *19th International Conference on RF Superconductivity (SRF 2019)*, 2019. doi:10.18429/JACoW-SRF2019-MOFAA1

[21] N. Walker, D. Reschke, J. Schaffran, L. Steder, M. Wenskat, L. Monaco, "Performance Analysis of the European XFEL SRF Cavities, From Vertical Test to Operation in Modules," in *Proc. LINAC'16*, East Lansing, MI, USA, Sep. 2016, p. 657. doi:10.18429/JACoW-LINAC2016-WE1A04

[22] A. Aryshev *et al.*, "ATF report 2020," CERN, Tech. Rep., 2020. http://cds.cern.ch/record/2742899

[23] T. Peterson et al., *LCLS-II Cryogenic Heat Load*, LCLSII-4.5-EN-0179, 2014.

[24] H. Nakai, T. Okamura, D. Delikaris, T. Peterson, and A. Yamamoto, "Cryogenic system configuration for the International Linear Collider (ILC) at mountainous site," *IOP Conf. Ser. Mater. Sci. Eng.*, vol. 171, no. 1, p. 012 036, 2017. doi:10.1088/1757-899X/171/1/012036

[25] S. Belomestnykh, private communication, 2023.

[26] L. Tavian, *Cryogenics*, CERN, 14 February 2013, https://indico.cern.ch/event/282344/.

[27] S. Belomestnykh *et al.*, "An 8 GeV Linac as the Booster Replacement in the Fermilab Power Upgrade: a Snowmass 2021 White Paper," in *2022 Snowmass Summer Study*, 2022.

[28] "The International Linear Collider Technical Design Report - Vol. 3.I: Accelerator," 2013.

[29] F. Zimmermann, *1998 SLC luminosity and pinch enhancement*, SLAC-CN-418, 1998.

[30] F. Zimmermann and P. Emma, *Chromatic and geometric spot size dilution in the present SLC final focus: Measurement and simulation*, SLAC-CN-405, 1996.

[31] D.L. Burke, for the FFTB Collaboration, "Status and Plans for the Final Focus Test Beam," in *Proceedings LC97, Zvenigorod, ed. by N. Solyak and A. Sery, available at https://www.desy.de/conferences/LC97/*.

[32] J. Seeman, "Future e+e- Collider Positron Injection Requirements," eeFACT'22, Frascati. https://agenda.infn.it/event/21199/contributions/173976/

[33] H. Burkhardt and R. Kleiss, "Beam Lifetimes in LEP," in *Proc. EPAC'94*, London, UK, Jun.-Jul. 1994, pp. 1353–1356.

ISBN: 978-3-95450-236-3 ISSN: 2673-7027 doi:10.18429/JACoW-eeFACT2022-FRXAS0101

[34] G. L. Kotkin and V. G. Serbo, "Beam-size effect at colliders and correlations of particles in a beam," *Phys. Rev. ST Accel. Beams*, vol. 7, p. 101 001, 10 2004. doi:10.1103/PhysRevSTAB.7.101001

[35] V. Telnov, "A high-luminosity superconducting twin e+e- linear collider with energy recovery," *Journal of Instrumentation*, vol. 16, no. 12, P12025, 2021. doi:10.1088/1748-0221/16/12/p12025

[36] R. Kleiss, H. Burkhardt, "BBBREM Monte Carlo simulation of radiative Bhabha scattering in the very forward direction," *Computer Physics Communications*, vol. 81, no. 3, p. 372, 1994. doi:10.1016/0010-4655(94)90085-x

[37] K. Piotrzkowski, private communication, 2023.

[38] R. Erickson et al., *SLC Design Handbook*, SLAC-R-714, 1984.

[39] R. Assmann *et al.*, "SLC: The End Game," in *7th European Particle Accelerator Conference (EPAC2000)*, 2000, p. 18.

[40] Y. Funakoshi *et al.*, "The SuperKEKB has broken the world record of the luminosity," in *Proc. IPAC'22*, Bangkok, 2022, pp. 1–5. doi:10.18429/JACoW-IPAC2022-MOPLXGD1

[41] R. Assmann, M. Lamont, S. Myers, "A brief history of the LEP collider," *Nucl. Phys. B Proc. Suppl.*, vol. 109, pp. 17–31, 2002. doi:10.1016/S0920-5632(02)90005-8

[42] J. Seeman *et al.*, "Parameters for the PEP-II B-factory at SLAC in 2008," *ICFA Beam Dyn. Newslett.*, vol. 48, pp. 72–87, 2009, available at https://icfa-usa.jlab.org/archive/newsletter/icfa_bd_nl_48.pdf.

[43] T. Abe *et al.*, "Achievements of KEKB," *PTEP*, vol. 2013, 03A001, 2013. doi:10.1093/ptep/pts102

ISBN: 978-3-95450-236-3 ISSN: 2673-7027 doi:10.18429/JACoW-eeFACT2022-FRXAS0102

CEPC ACCELERATOR TDR STATUS AND AC POWER CONSUMPTIONS*

J. Gao †, Institute of High Energy Physics, Chinese Academy of Science, Beijing, China

Abstract

The discovery of the Higgs boson at Large Hadron Collider (LHC) of CERN in July 2012 raised new opportunities for a large-scale accelerator. The Higgs boson is the heart of the Standard Model (SM) and is at the center of many mysteries of universe. In Sept. 2012, Chinese scientists proposed a 240 GeV Circular Electron Positron Collider (CEPC), having two large detectors for Higgs studies as a Higgs Factory and other topical researches. The 100 km tunnel of CEPC could also host a Super proton proton Collider (SppC) to reach energies above 100 TeV. CEPC Conceptual Design Report (CDR) has been released in Nov. 2018, and CEPC Technical Design Report (TDR) will be completed at the end of 2022. in this paper, CEPC Technical Design Report (TDR) status, upgrade possibilities and AC power consumption have been reported.

INTRODUCTION

The discovery of the Higgs boson at CERN's Large Hadron Collider (LHC) in July 2012 raised new opportunities for large-scale accelerators. The Higgs boson is the heart of the Standard Model (SM), and is at the center of our understanding the mysteries of universe. Precise measurements of the properties of the Higgs boson serve as probes of the underlying fundamental physics principles of the SM and beyond. Due to the modest Higgs boson mass of 125 GeV, it is possible to produce it in the relatively clean environment of a circular electron–positron collider with high luminosity and multi detectors. In Sept. 2012, Chinese scientists proposed a 240 GeV Circular Electron Positron Collider (CEPC), serving two large detectors for Higgs studies and other topics as shown in Fig. 1. The 100 km tunnel for such a machine could also host a Super Proton Proton Collider (SPPC) to reach energies above 100 TeV.

CEPC is a Higgs factory composed of a linac injector (10 Gev for CDR, 30 GeV for TDR), 100 km circumference full energy booster and collider ring equipped with 2 detectors. In addition to operate at center of mass energy for Higgs of 240 GeV, CEPC could operate also at different energies, such as Z-pole of 45.5 GeV, W of 80 GeV, and as last phase upgrade possibility, ttbar of 180 GeV. The Conceptual Design Report (CEPC Accelerator CDR) [1] has been released in Nov. 2018. CEPC as a Chinese proposed international large science project, it participates the international high energy strategic planning and collaborations. In May 2019, CEPC accelerator document was submitted to European High Energy Physics Strategy workshop for worldwide discussions [2]. In 2022, CEPC accelerator document was submitted to the Particle Physics Community Planning Exercise (Snowmass'21) of USA [3].

CEPC TRD PARAMETERS

According to the CEPC TDR baseline physics goals at the Higgs and Z-pole energies, the CEPC should provide e+e- collisions at the center-of-mass energy of 240 GeV and deliver a peak luminosity of $5 \times 10^{34} cm^{-2} s^{-1}$ at each interaction point. The CEPC has two IPs (two detecors) for e+e- collisions and is compatible with four energy modes (Higgs, Z-pole, W, and ttbar). At the Z-pole energy the luminosity is required to be larger than $1 \times 10^{36} cm^{-2} s^{-1}$ per IP. The experiments at ttbar energy is an energy upgrade option at the last stage of CEPC.

The CEPC TDR baseline design is a 100 km double ring scheme based on crab waist collision and 30 MW radiation power per beam at four energy modes, with the shared RF system for Higgs/ttbar energies and independent RF system for W/ Z energies. The CEPC main parameters for TDR are listed in Table 2. The luminosity at Higgs energy is $5 \times 10^{34} cm^{-2} s^{-1}$. At the Z-pole, the luminosity is $1.15 \times 10^{36} cm^{-2} s^{-1}$ for 2T detector solenoid.

The CEPC TDR power upgrade parameters of 50 MW SR power/beam at Higgs, W, Z and ttbar energy operations and the luminosities are shown in Table 3. The luminosities at Higgs and the Z-pole energies are $8.3 \times 10^{34} cm^{-2} s^{-1}$ and $1.91 \times 10^{36} cm^{-2} s^{-1}$, respectively.

CEPC TDR DESIGN STATUS

Collider Ring

For CEPC collider design, the crab-waist scheme increases the luminosity by suppressing vertical blow up, which is a must to reach high luminosity. Beamstrahlung is synchrotron radiation excited by the beam-beam force, which is a new phenomenon in a storage ring based collider especially at high energy region. It will increase the energy spread, lengthen the bunch and may reduce the beam lifetime due to the long tail of the photon spectrum. The beam-beam limit at the W/Z is mainly determined by the coherent x-z instability instead of the beamstrahlung lifetime as in the tt/Higgs mode. A smaller phase advance of the FODO cell (60/60) for the collider ring optics is chosen at the W/Z mode to suppress the beam-beam instability when we consider the beam-beam effect and longitudinal impedance consistently. The CEPC TDR design goals have been evaluated and checked from the point view of beam-beam interaction, which are feasible and achievable.

MDI

The CEPC machine detector interface (MDI) is about 14 m (±7m from the IP) in length in the Interaction Region

* On behalf of CEPC Accelerator Group. Work supported by MOST, CAS, NSFC and Scientists Studio
† email: gaoj@ihep.ac.cn

65th ICFA Adv. Beam Dyn. Workshop High Luminosity Circular e+e− Colliders eeFACT2022, Frascati, Italy JACoW Publishing
ISBN: 978-3-95450-236-3 ISSN: 2673-7027 doi:10.18429/JACoW-eeFACT2022-FRXAS0102

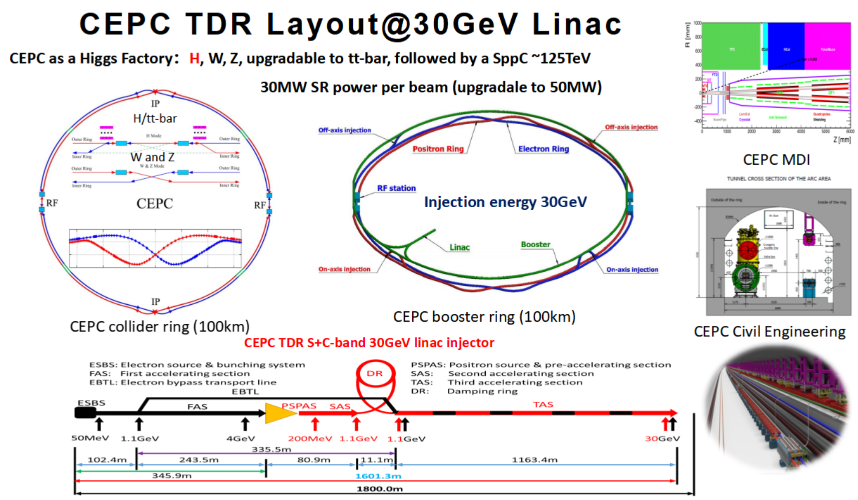

Figure 1: CEPC TDR layout.

(IR), where many elements from both detector system and accelerator components need to be installed including the detector solenoid, anti-solenoid, luminosity calorimeter (LumiCal), interaction region beam pipe, cryostat, beam position monitors (BPMs) and bellows. The cryostat includes the final doublet superconducting magnets and anti-solenoid. The CEPC detector consists of a cylindrical drift chamber surrounded by an electromagnetic calorimeter, which is immersed in a 2 to 3 T superconducting solenoid of 7.6 m in length. After optimization, the accelerator components inside the detector without shielding are within a conical space with an opening angle of 6.78 degrees. The crossing angle between electron and positron beams is 33 mrad in horizontal plane. The final focusing quadrupole is 1.9 m (L*) from the IP. A water cooling structure is required to control the heating problem of HOM in IR vacuum chamber. The diameters of beryllium pipe and the SC quadrupoles are 20 mm.

Booster

The booster provides electron and positron beams to the collider at different energies. The booster TDR design is consistent with the TDR parameters for four energy modes. The booster is in the same tunnel as the collider, placed above the collider ring except in the interaction region where there are bypasses to avoid the detectors. The injection system consists of a 30 GeV Linac, followed by a full-energy booster ring. Electron and positron beams are generated and accelerated to 30 GeV in the Linac. The beams are then accelerated to full-energy in the booster, and injected into the collider. For different beam energies of Higgs, W, Z and ttbar, experiments, there will be different particle bunch structures in the collider. The optics of booster is changed to TME structure and the emittance of booster is reduced significantly in order to match the lower emittance of collider and hence to reach higher luminosity goal in TDR. The CEPC booster TDR parameters at the injection and extraction are shown in Tables 4 and 5.

Collider and Booster SRF Systems

CEPC will use 650 MHz SCRF system for the collider and 1.3 GHz for the booster. For the first phase, CEPC will use 240 650 MHz 2-cell superconducting cavities for the collider and 96 1.3 GHz 9-cell superconducting cavities for the booster. The collider is a fully partial double-ring with common cavities for electron and positron beams in Higgs operation mode and a double ring for separate cavities for electron and positron beams in W and Z operation mode. The collider SRF system is optimized for the Higgs mode of 30 MW SR power per beam as the first priority, with enough tunnel space and operating margin to allow higher RF voltage (ttbar) and SR power (50 MW SR power per beam) by adding cavities.

RF staging and bypass scheme is proposed to unleash full potential of CEPC to reach highest luminosity at each energy and keep operational flexibility in the same time. RF staging of both the Collider and Booster is required for the CEPC power and energy upgrade. Cavity by-pass is needed to enable seamless operation mode switching, which is different from FCC-ee design.

Linac Injector

The CEPC linac injector is a normal conducting S-band and C-band linac with frequency of 2860 MHz and 5720 MHz, providing electron and positron beams at an energy of up to 30 GeV at a repetition rate of 100 Hz, as shown in Fig. 2. S-band accelerating structure is used in FAS with energy of 4 GeV and SAS with energy of 1.1 GeV and C-band accelerating structure is used in TAS form 1.1 GeV to 30 GeV. The positron source is a conventional design with a tungsten target of 15 mm in length and adiabatic matching device of 6 T in peak magnetic field. The energy of electron beam for positron production is 4 GeV and rms beam size is 0.5 mm. A positron damping ring of 1.1 GeV of circumference of 0.15 km has been design. The bunch charge is 1.5 nC and have the capability to reach 3 nC both for electron and positron beam. The linac length is 1.6 km

ISBN: 978-3-95450-236-3 ISSN: 2673-7027 doi:10.18429/JACoW-eeFACT2022-FRXAS0102

and the linac tunnel length is 1.8 km with 0.2 km as reserved space. The CEPC linac injector parameters are shown in Table 1. In the design of CEPC linac, the reliability and availability of the linac injector was emphasized because it is one of the indispensable facilities. The linac has a robust design based on well proven technologies, and about 15% backup of accelerating structures and klystrons are foreseen to reach high availability.

CEPC TDR TECHNOLOGY R&D STATUS

Intensive and full spectrum key technology R&D has been carried out during CDR and TDR periods, for example:

- CEPC 650 MHz 800 kW CW high efficiency klystrons (77 80%);
- CEPC 1.3 GHz and 650 MHz SRF accelerator systems, including SC cavities and cryomodule;
- SC quadrupole magnets including cryostate;
- High precision booster dipole magnets;
- Collider dual aperture dipole magnets, dual aperture qudrupole and sextupole magnets;
- Vacuum chamber system with NEG coating technology;
- Electrostatic-magnetic separators;
- High gradient S-band linac structures, pulse compressor, positron source, C-band linac and 80MW klystron;
- 18KW@4.5K cryoplant (Company);
- Plasma injector (alternative linac injector technology);
- SppC related high field superconducting magnets;
- Civil engineering designs in different sites; etc as shown in Fig. 2.

In synergy with other accelerator projects under construction, such as HEPS, a 6 GeV fourth generation light source by IHEP, all kinds of kickers and high precision magnets' power supplies have been developed. The CEPC TDR is scheduled to be completedat the end of 2022 and enter into Engineering Design Phase (EDR) started from 2023.

CEPC SITING STATUS

For CEPC site selection, the technical criteria are roughly quantified as follows: earthquake intensity less than seven on the Richter scale; earthquake acceleration less than 0.1 g; ground surface-vibration amplitude less than 20 nm at 1–100 Hz; granite bedrock around 50–100 m deep, and others. The site-selection process started in February 2015, preliminary studies of geological conditions for CEPC's potential site locations have been carried out in Qinhuangdao in Hebei province; Huangling county in Shanxi province; Huzhou in Zhejiang province; Changchun in Jilin province and Changsha, in Hunan province, etc. as shown in Fig. 3, and all these sites satisfies the CEPC construction requirements.

CEPC TIMELINE

CEPC has been firstly proposed by Chinese scientists in Sept. 2012 just after the Higgs Boson discovery at CERN. CEPC CDR has been completed in Nov. 2018, and accelerator TDR will be completed at the end of 2022. CEPC will enter EDR phase in 2023 and will be completed at the end of 2025. CEPC team will work closely with Chinese central government, international/industrial collaborations, and the local host government in EDR phase (2023-2025) towards the aim of putting CEPC into construction around 2027 (within the 15th five year plan of China), and into operation around 2035. At the end of CEPC operation, SppC could be put to construction, as shown in Fig. 4.

CEPC AC POWER CONSUMPTION

Corresponding to CEPC TDR parameters, the total AC powers for CEPC operation at Higgs energy with 30 MW and 50 MW SR power/beam are shown in Tables 6 and 7. The total AC power at Z-pole energy with 30 MW SR power/beam is shown in Table 8, and at ttbar energy with 50 MW SR power/beam is shown in Table 9. All these results have the rooms for further optimizations. In addition, economical using of green energies in future Higgs factories has been studied, and a 10MW solar power system has been developed at the site of the HEPS by IHEP.

CONCLUSIONS

CEPC as a Higss factory provides one of the future colliders for the high energy particle physics community and sciences in general worldwide. CEPC has developed on the timeline since it has been proposed in Sept. 2012, through pre-CDR, CDR, and TDR with international collaborations and industrial (CEPC Industrial Promotion Consortium, CIPC) participation. Continuous efforts are needed to progress forwards through CEPC EDR (2023-2025) with the aim of operating CEPC around 2035.

ACKNOWLEDGEMENTS

Thanks go to CEPC-SppC accelerator team's hardworks, international and CIPC collaboration efforts. Thanks go to the supports, encouragement, critical comments and suggestions from CEPC Institution Board (IB), Steering Committee (SC), International Advisory Committee (IAC), and International Accelerator Review Committee (IARC). Thanks go to the funds from National Natural Science Foundation of China (Grant No. 11975252), Key Research Program of Frontier Sciences, CAS(Grant No.QYZDJ-SSW-SLH004) and Scientist Studio.

REFERENCES

[1] CEPTC Study Group, "The CEPC conceptual design report, vol 1: accelerator", Rep. IHEP-CEPC-DR-2018-01. doi:10.48550/arXiv.1809.00285 Also available at: http://cepc.ihep.ac.cn/CDR_v6_201808.pdf

[2] CEPC Accelerator Study Group, "The CEPC input for the European Strategy for Particle Physics - Accelerator", preprint arXiV:1901.03169. doi:10.48550/arXiv.1901.03169

[3] CEPC Accelerator Study Group, "Snowmass2021 White Paper AF3-CEPC", preprint arXiv:2203.09451. doi:10.48550/arXiv.2203.09451

ISBN: 978-3-95450-236-3 ISSN: 2673-7027 doi:10.18429/JACoW-eeFACT2022-FRXAS0102

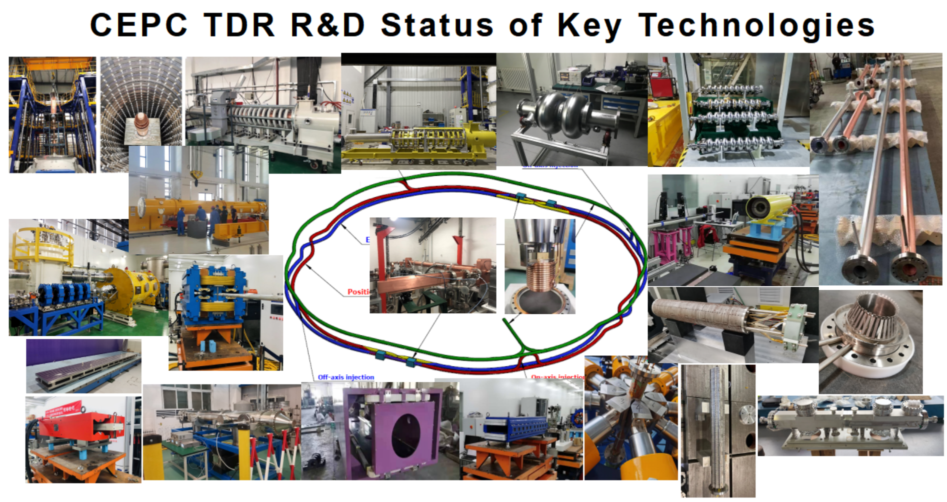

Figure 2: CEPC accelerator TDR key technology R&D status.

Figure 3: CEPC siting status.

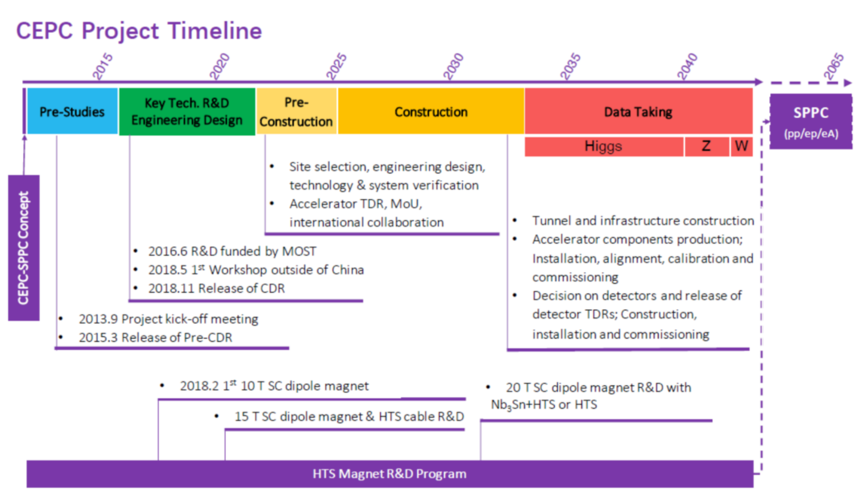

Figure 4: CEPC timeline.

ISBN: 978-3-95450-236-3 ISSN: 2673-7027 doi:10.18429/JACoW-eeFACT2022-FRXAS0102

Table 1: The CEPC TDR 30 GeV Linac Injector Parameters

Parameter	**Unit**	**Value**	**Simulated**			
			Electron		**Positron**	
Beam energy	GeV	30	31.3	30.8	31.1	30.8
Repetition rate	Hz	100	/			
Bunch charge	nC	1.5	1.5	3.0	1.5	3.0
Energy spread		1.5×10-3	1.4×10-3	1.7×10-3	1.4×10-3	1.9×10-3
Emittance	nm	6.5	1.4	1.5	3.3(H)/1.7(V)	3.5(H)/1.8(V)
Bunch length (RMS)	mm	/	0.4			

Table 2: The CEPC TDR Parameters with 30 MW SR Power/Beam

Parameter	**Higgs**	**Z**	**W**	**ttbar**
Number of IPs	2			
Circumference [km]	100.0			
SR power per beam [MW]	30			
Half crossing angle at IP [mrad]	16.5			
Bending radius [km]	10.7			
Energy [GeV]	120	45.5	80	180
Energy loss per turn [GeV]	1.8	0.037	0.357	9.1
Piwinski angle	4.88	24.68	6.08	1.21
Bunch number	268	11934	1297	35
Bunch spacing [ns]	591 (53% gap)	23 (18% gap)	257	4524 (53% gap)
Bunch population [10^{10}]	13	14	13.5	20
Beam current [mA]	16.7	803.5	84.1	3.3
Momentum compaction [10^{-5}]	0.71	1.43	1.43	0.71
Beta functions at IP (bx/by) [m/mm]	0.3/1	0.13/0.9	0.21/1	1.04/2.7
Emittance (ex/ey) [nm/pm]	0.64/1.3	0.27/1.4	0.87/1.7	1.4/4.7
Beam size at IP (sigx/sigy) [um/nm]	14/36	6/35	13/42	39/113
Bunch length (natural/total) [mm]	2.3/4.1	2.5/8.7	2.5/4.9	2.2/2.9
Energy spread (natural/total) [%]	0.10/0.17	0.04/0.13	0.07/0.14	0.15/0.20
Energy acceptance (DA/RF) [%]	1.6/2.2	1.3/1.7	1.2/2.5	2.3/2.6
Beam-beam parameters (ksix/ksiy)	0.015/0.11	0.004/0.127	0.012/0.113	0.071/0.1
RF voltage [GV]	2.2	0.12	0.7	10
RF frequency [MHz]	650	650	650	650
Longitudinal tune Qs	0.049	0.035	0.062	0.078
Beam lifetime (bhabha/beamstrahlung)[min]	39/40	80/18000	60/700	81/23
Beam lifetime [min]	20	80	55	18
Hour glass Factor	0.9	0.97	0.9	0.89
Luminosity per IP[$10^{34}/cm^2$/s]	5.0	115	16	0.5

ISBN: 978-3-95450-236-3 ISSN: 2673-7027 doi:10.18429/JACoW-eeFACT2022-FRXAS0102

Table 3: The CEPC TDR parameters with 50MW SR Power/Beam

Parameter	**Higgs**	**W**	**Z**	**ttbar**
Number of IPs	2			
Circumference [km]	100.0			
SR power per beam [MW]	50			
Half crossing angle at IP [mrad]	16.5			
Bending radius [km]	10.7			
Energy [GeV]	120	80	45.5	180
Energy loss per turn [GeV]	1.8	0.357	0.037	9.1
Piwinski angle	4.88	6.08	24.68	1.21
Bunch number	415	2162	19918	58
Bunch spacing [ns]	385	154	15(10% gap)	2640
Bunch population [10^{10}]	14	13.5	14	20
Beam current [mA]	27.8	140.2	1339.2	5.5
Momentum compaction [10^{-5}]	0.71	1.43	1.43	0.71
Phase advance of arc FODOs [degree]	90	60	60	90
Beta functions at IP (bx/by) [m/mm]	0.33/1	0.21/1	0.13/0.9	1.04/2.7
Emittance (ex/ey) [nm/pm]	0.64/1.3	0.87/1.7	0.27/1.4	1.4/4.7
Beam size at IP (sx/sy) [um/nm]	15/36	13/42	6/35	39/113
Bunch length (SR/total) [mm]	2.3/3.9	2.5/4.9	2.5/8.7	2.2/2.9
Energy spread (SR/total) [%]	0.10/0.17	0.07/0.14	0.04/0.13	0.15/0.20
Energy acceptance (DA/RF) [%]	1.7/2.2	1.2/2.5	1.3/1.7	2.3/2.6
Beam-beam parameters (xx/xy)	0.015/0.11	0.012/0.113	0.004/0.127	0.071/0.1
RF voltage [GV]	2.2 (2cell)	0.7 (2cell)	0.12 (1cell)	10 (5cell)
RF frequency [MHz]	650			
Beam lifetime [min]	20	55	80	18
Luminosity per IP[$10^{34}/cm^2$/s]	8.3	26.6	191.7	0.8

Table 4: The CEPC TDR Booster Parameters at Injection

Parameter	**Unit**	**tt**	**H**	W	**Z**	
Beam energy	GeV	30				
Bunch number		35	268	1297	3978	5967
Threshold of single bunch current	mA	8.68	6.3	5.8		
Threshold of beam current (limited by coupled bunch instability)	mA	97	106	100	93	96
Bunch charge	nC	1.1	0.78	0.81	0.87	0.9
Single bunch current	mA	3.4	2.3	2.4	2.65	2.69
Beam current	mA	0.12	0.62	3.1	10.5	16.0
Growth time (coupled bunch instability)	ms	2530	530	100	29.1	18.7
Energy spread	%	0.025				
Synchrotron radiation loss/turn	MeV	6.5				
Momentum compaction factor	10-5	1.12				
Emittance	nm	0.076				
Natural chromaticity	H/V	-372/-269				
RF voltage	MV	761.0	346.0	300.0		
Betatron tune nx/ny		321.23/117.18				
Longitudinal tune		0.14	0.0943	0.0879		
RF energy acceptance	%	5.7	3.8	3.6		
Damping time	s	3.1				
Bunch length of linac beam	mm	0.4				
Energy spread of linac beam	%	0.15				
Emittance of linac beam	nm	6.5				

ISBN: 978-3-95450-236-3 ISSN: 2673-7027 doi:10.18429/JACoW-eeFACT2022-FRXAS0102

Table 5: The CEPC TDR Booster Parameters at Extraction

Parameter	Unit	tt	H		W	Z	
		Off axis inj.	Off axis inj.	On axis inj.	Off axis inj.	Off axis inj.	
Beam energy	GeV	180	120		80	45.5	
Bunch number		35	268	261+7	1297	3978	5967
Maximum bunch charge	nC	0.99	0.7	20.3	0.73	0.8	0.81
Maximum single bunch current	mA	3.0	2.1	61.2	2.2	2.4	2.42
Threshold of single bunch current	mA	91.5	70		22.16	9.57	
Threshold of beam current (limited by RF system)	mA	0.3	1		4	16	
Beam current	mA	0.11	0.56	0.98	2.85	9.5	14.4
Growth time (coupled bunch instability)	ms	16611	2359	1215	297.8	49.5	31.6
Bunches per pulse of Linac		1	1		1	2	
Time for ramping up	s	7.1	4.3		2.4	1.0	
Injection duration for top-up (Both beams)	s	29.2	23.1	31.8	38.1	132.4	
Injection interval for top-up	s	65	38		155	153.5	
Current decay during injection interval		3%					
Energy spread	%	0.15	0.099		0.066	0.037	
Synchrotron radiation loss/turn	GeV	8.45	1.69		0.33	0.034	
Momentum compaction factor	10-5	1.12					
Emittance	nm	2.83	1.26		0.56	0.19	
Natural chromaticity	H/V	-372/-269					
Betatron tune nx/ny		321.27/117.19					
RF voltage	GV	9.7	2.17		0.87	0.46	
Longitudinal tune		0.14	0.0943		0.0879	0.0879	
RF energy acceptance	%	1.78	1.59		2.6	3.4	
Damping time	ms	14.2	47.6		160.8	879	
Natural bunch length	mm	1.8	1.85		1.3	0.75	
Full injection from empty ring	h	0.1	0.14	0.16	0.27	1.8	0.8

Table 6: The CEPC TDR AC Power Consumption (30 MW SR Power/Beam at Higgs Energy)

Parameter	Ring	Booster	LINAC	BTL	IR	Surface Building	TOTAL
RF Power Source	96.9	1.4	11.1				109.5
Cryogenic System	11.6	0.6	-		1.1		13.4
Vacuum System	1.0	3.8	1.8				6.5
Magnet Power Supplies	52.3	7.5	2.4	1.1	0.3		63.5
Instrumentation	1.3	0.7	0.2				2.2
Radiation Protection	0.3		0.1				0.4
Control System	1.0	0.6	0.2	0.0	0.0		1.8
Experimental devices					4.0		4.0
Utilities	31.8	3.5	2.0	0.6	1.2		39.1
General services	7.2		0.3	0.2	0.2	12.0	19.8
RF system			0.8				0.8
TOTAL	203.4	18.2	18.9	1.8	6.8	12.0	261.1

ISBN: 978-3-95450-236-3 ISSN: 2673-7027 doi:10.18429/JACoW-eeFACT2022-FRXAS0102

Table 7: The CEPC TDR AC Power Consumption (50 MW SR Power/Beam at Higgs Energy)

Parameter	Ring	Booster	LINAC	BTL	IR	Surface Building	TOTAL
RF Power Source	161.5	1.4	11.1				174.1
Cryogenic System	15.5	0.6	-		1.7		17.9
Vacuum System	1.0	3.8	1.8				6.5
Magnet Power Supplies	52.3	7.5	2.4	1.1	0.3		63.5
Instrumentation	1.3	0.7	0.2				2.2
Radiation Protection	0.3		0.1				0.4
Control System	1.0	0.6	0.2	0.0	0.0		1.8
Experimental devices					4.0		4.0
Utilities	42.4	3.5	2.0	0.6	1.2		49.7
General services	7.2		0.3	0.2	0.2	12.0	19.8
RF system			0.8				0.8
TOTAL	282.4	18.2	18.9	1.8	7.4	12.0	340.7

Table 8: The CEPC TDR AC Power Consumption (30 MW SR Power/Beam at Z-pole Energy)

Parameter	Ring	Booster	LINAC	BTL	IR	Surface Building	TOTAL
RF Power Source	96.9	0.1	11.1				108.1
Cryogenic System	4.1	0.6	-		1.1		5.9
Vacuum System	1.0	3.8	1.8				6.5
Magnet Power Supplies	9.6	1.4	2.4	1.1	0.3		14.7
Instrumentation	1.3	0.7	0.2				2.2
Radiation Protection	0.3		0.1				0.4
Control System	1.0	0.6	0.2	0.0	0.0		1.8
Experimental devices					4.0		4.0
Utilities	28.1	3.5	2.0	0.6	1.2		35.5
General services	7.2		0.3	0.2	0.2	12.0	19.8
RF system			0.8				0.8
TOTAL	149.4	10.8	18.9	1.8	6.8	12.0	199.7

Table 9: The CEPC TDR AC Power Consumption (50 MW SR Power/Beam at ttbar Energy)

Parameter	Ring	Booster	LINAC	BTL	IR	Surface Building	TOTAL
RF Power Source	161.5	1.4	11.1				174.1
Cryogenic System	25.2	0.6	-		1.1		26.9
Vacuum System	2.0	3.8	1.8				7.6
Magnet Power Supplies	118.8	16.8	2.4	1.1	0.3		139.3
Instrumentation	1.3	0.7	0.2				2.2
Radiation Protection	0.3		0.1				0.4
Control System	1.0	0.6	0.2	0.0	0.0		1.8
Experimental devices					4.0		4.0
Utilities	44.7	3.5	2.0	0.6	1.2		52.0
General services	7.2		0.3	0.2	0.2	12.0	19.8
RF system			0.8				0.8
TOTAL	361.9	27.5	18.9	1.8	6.8	12.0	428.9

ISBN: 978-3-95450-236-3 ISSN: 2673-7027 doi:10.18429/JACoW-eeFACT2022

ISBN: 978-3-95450-236-3 ISSN: 2673-7027 doi:10.18429/JACoW-eeFACT2022

List of Authors

Bold papercodes indicate primary authors; ~~strike through/black~~ papercodes indicate **no submission received**

ISBN: 978-3-95450-236-3 ISSN: 2673-7027 doi:10.18429/JACoW-eeFACT2022

ISBN: 978-3-95450-236-3 ISSN: 2673-7027 doi:10.18429/JACoW-eeFACT2022

ISBN: 978-3-95450-236-3 ISSN: 2673-7027 doi:10.18429/JACoW-eeFACT2022

Institutes List

ALBA-CELLS
Cerdanyola del Vallès, Spain
- Iriso, U.

APS
Silver Spring, USA
- Zimmermann, F.

BINP SB RAS
Novosibirsk, Russia
- Shatilov, D.N.

BNL
Upton, New York, USA
- Holmes, D.
- Parker, B.
- Ranjbar, V.H.
- Smith, K.S.
- Xiao, B.P.
- Xu, W.
- Zaltsman, A.

Brown University
Providence, USA
- Li, L.

CEA
Gif-sur-Yvette, France
- Chancé, A.

CEA-IRFU
Gif-sur-Yvette, France
- Antoine, C.Z.
- Dalena, B.

CERN
Meyrin, Switzerland
- Abramov, A.
- Barnes, M.J.
- Bartmann, W.
- Benedikt, M.
- Borburgh, J.C.C.M.
- Bromiley, L.
- Buffat, X.
- Calaga, R.
- Carideo, E.
- Carlier, F.S.
- Ciarma, A.
- Dutheil, Y.
- Ganis, G.
- Hofer, M.
- Iadarola, G.
- Keintzel, J.
- Kersevan, R.
- Kicsiny, P.
- Lefèvre, T.
- Mazzoni, S.
- Oide, K.
- Osborne, J.A.
- Perez, E.
- Ramjiawan, R.L.
- Schloegelhofer, A.
- Schulte, D.
- Stapnes, S.
- Tomás García, R.
- Wendt, M.
- Zimmermann, F.

DESY
Hamburg, Germany
- Chae, Y.-C.
- Li, C.
- List, B.

DPNC
Genève, Switzerland
- Oide, K.

EPFL
Lausanne, Switzerland
- Pieloni, T.
- Seidel, M.
- van Riesen-Haupt, L.
- Wu, Y.

ESRF
Grenoble, France
- Maccarrone, C.

Fermilab
Batavia, Illinois, USA
- Belomestnykh, S.A.
- Gianfelice-Wendt, E.
- Shiltsev, V.D.

HFCIM
HeFei, People's Republic of China
- Wan, Y.
- Wu, X.L.
- Zou, W.

HIT
Harbin, People's Republic of China
- Jiang, H.P.

IASF
Shenzhen, Guangdong, People's Republic of China
- Lin, C.T.

IFIC
Valencia, Spain
- Faus-Golfe, A.

IHEP
Beijing, People's Republic of China
- Bai, S.
- Chang, Y.
- Chen, F.S.
- Chen, T.
- Cui, X.
- Dai, H.L.
- Dai, J.
- Duan, Z.

ISBN: 978-3-95450-236-3 ISSN: 2673-7027 doi:10.18429/JACoW-eeFACT2022

- Gao, J.
- Guo, L.
- Huang, T.M.
- Ji, D.
- Li, D.B.
- Li, J.
- Li, M.
- Li, X.P.
- Li, Y.
- Liang, R.
- Lin, C.T.
- Lin, H.Y.
- Liu, W.B.
- Liu, Y.D.
- Luo, Y.L.
- Ma, Q.
- Ma, Y.
- Meng, C.
- Meng, F.
- Mi, Z.H.
- Na, Na,B.
- Pei, G.
- Peng, Y.M.
- Qi, H.R.
- She, X.
- Shen, C.
- Shi, H.Y.
- Tian, S.K.
- Wang, D.
- Wang, H.
- Wang, J.Q.
- Wang, N.
- Wang, Q.Y.
- Wang, Y.
- Wu, X.T.
- Wu, Y.F.
- Xia, W.H.
- Xing, J.
- Xu, G.L.
- Xu, H.S.
- Yang, M.
- Yang, X.C.
- Yu, C.H.
- Yu, L.W.
- Zhai, J.Y.
- Zhang, J.R.
- Zhang, J.
- Zhang, P.
- Zhang, X.Y.
- Zhang, Y.
- Zhang, Z.D.
- Zhang, Z.
- Zhao, F.C.
- Zheng, H.J.
- Zhu, Y.S.

INFN Genova
Genova, Italy
- Farinon, S.
- Musenich, R.

INFN-Roma
Roma, Italy
- Di Domenico, A.

INFN-Roma III
Rome, Italy
- Franceschini, R.

INFN-Roma1
Rome, Italy
- Migliorati, M.

IZTECH
Izmir, Turkey
- Yaman, F.

JLab
Newport News, Virginia, USA
- Daly, E.
- Gaskell, D.
- Guo, J.
- Henry, J.
- Matalevich, J.
- Rimmer, R.A.
- Satogata, T.
- Wang, H.
- Wang, S.

KEK
Ibaraki, Japan
- Abe, T.
- Akai, K.
- Akemoto, M.
- Aoki, K.
- Arakawa, D.A.
- Arimoto, Y.
- Ego, H.
- Enomoto, S.
- Enomoto, Y.
- Fukuma, H.
- Funakoshi, Y.
- Furukawa, K.
- Furuya, T.
- Higo, T.
- Hisamatsu, H.
- Iida, N.
- Ikeda, H.
- Ishibashi, T.
- Kabe, A.
- Kageyama, T.
- Kakihara, K.
- Kamitani, T.
- Kanazawa, K.
- Katagiri, H.
- Kawai, M.K.
- Kawamoto, T.
- Kawamura, M.
- Kobayashi, T.
- Koiso, H.
- Marutsuka, K.
- Masuzawa, M.
- Matsumoto, S.
- Matsumoto, T.
- Matsushita, H.
- Mimashi, T.
- Mitsuhashi, T.M.

ISBN: 978-3-95450-236-3 ISSN: 2673-7027 doi:10.18429/JACoW-eeFACT2022

- Mitsuka, G.
- Mitsunobu, S.
- Miura, T.
- Miyahara, F.
- Morita, A.
- Morita, Y.
- Nakajima, H.
- Nakamura, S.
- Nakanishi, K.
- Natsui, T.
- Nishiwaki, M.
- Ogasawara, S.
- Ohmi, K.
- Ohnishi, Y.
- Ohsawa, Y.
- Ohuchi, N.O.
- Oide, K.
- Okada, T.
- Okayasu, Y.
- Oki, T.
- Ono, M.
- Sakai, H.
- Sasaki, S.
- Satake, I.
- Satoh, M.
- Seimiya, Y.
- Shibata, K.
- Shidara, T.
- Shirai, M.
- Shirakawa, A.
- Suetsugu, Y.
- Sugimoto, H.
- Suwada, T.
- Takeuchi, Y.
- Tanaka, M.
- Terui, S.
- Tobiyama, M.
- Ueki, R.
- Wang, D.
- Wang, X.
- Watanabe, K.
- Yamaoka, H.
- Yano, Y.
- Yokoyama, K.
- Yoshida, M.
- Yoshida, Ma.
- Yoshimoto, S.I.
- Yoshimoto, T.
- Yoshino, K.
- Zhang, R.
- Zhou, D.
- Zhou, X.
- Zong, Z.G.

KIT
Karlsruhe, Germany
- Härer, B.
- Müller, A.-S.
- Niehues, G.
- Reißig, M.

LNF-INFN
Frascati, Italy
- Behtouei, M.
- Biagini, M.E.
- Boscolo, M.
- Spataro, B.
- Zobov, M.

ODU
Norfolk, Virginia, USA
- De Silva, S.U.
- Delayen, J.R.

PSI
Villigen PSI, Switzerland
- Auchmann, B.
- Craievich, P.
- Duda, M.
- Garcia Rodrigues, H.
- Koratzinos, M.
- Kosse, J.
- Schaer, M.
- Vallis, N.
- Zennaro, R.

Royal Holloway, University of London
Surrey, United Kingdom
- Howling, E.R.

Sapienza University of Rome
Rome, Italy
- Migliorati, M.

SLAC
Menlo Park, California, USA
- Huang, X.
- Nanni, E.A.
- Novokhatski, A.
- Raimondi, P.
- Raubenheimer, T.O.
- Seeman, J.T.
- Sullivan, M.K.

SNS
Pisa, Italy
- Lusiani, A.

Sokendai
Ibaraki, Japan
- Lee, Y.M.

Stony Brook University
Stony Brook, USA
- Litvinenko, V.

UCAS
Beijing, People's Republic of China
- Zhang, Z.D.

University of Hawaii
Honolulu,, USA
- Natochii, A.

University of Saskatchewan
Saskatoon, Canada
- Hunchak, P.J.

ISBN: 978-3-95450-236-3 ISSN: 2673-7027 doi:10.18429/JACoW-eeFACT2022

Università degli Studi di Milano
Milano, Italy
- Siano, M.

Université Paris-Saclay, CNRS/IN2P3, IJCLab
Orsay, France
- Chaikovska, I.
- Faus-Golfe, A.
- Zhang, Z.D.

USTC/NSRL
Hefei, Anhui, People's Republic of China
- Luo, Q.